

SEPTEMBER 2017

**AJNR**

VOLUME 38 • PP 1663-1848

# AJNR

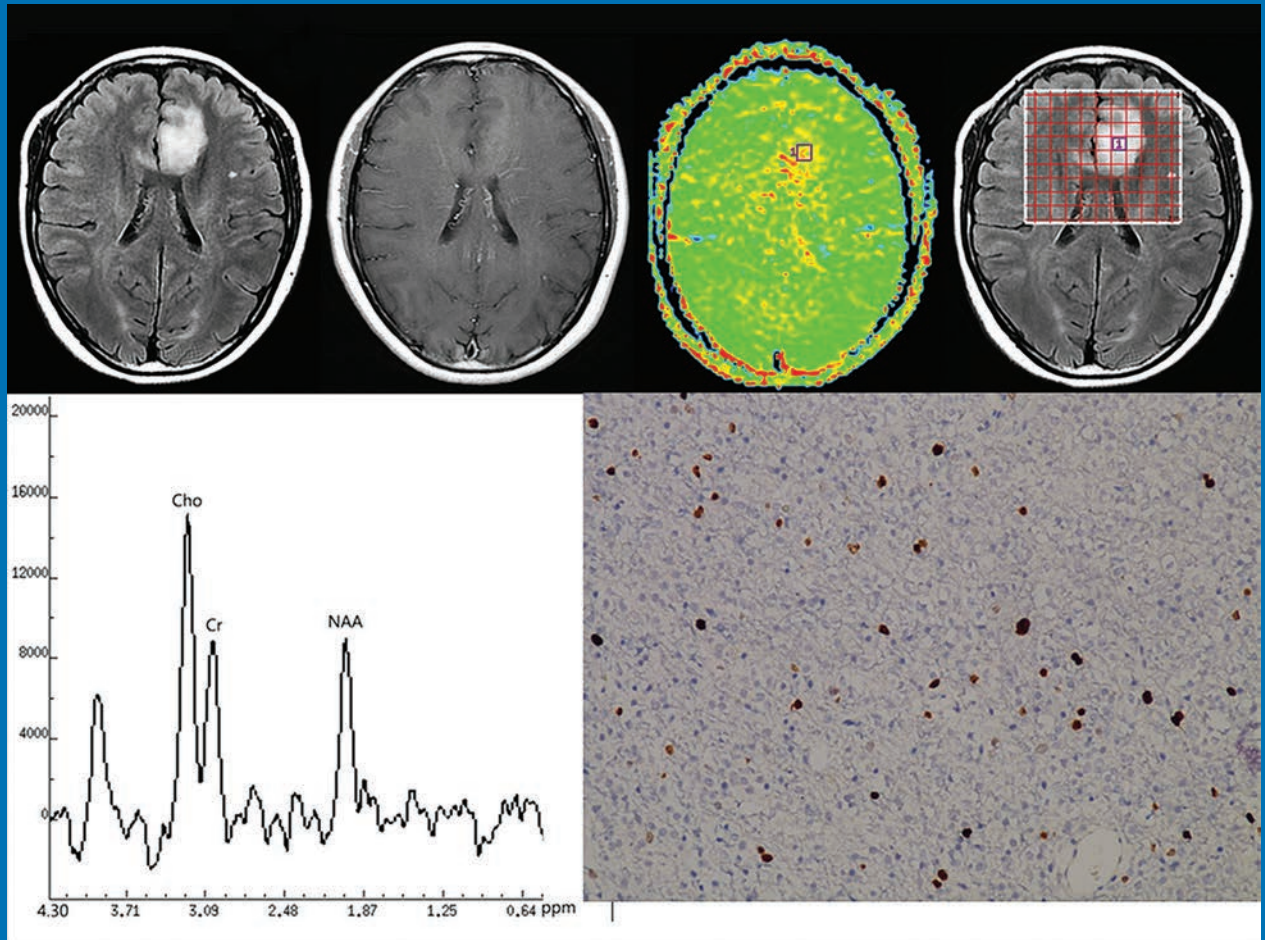
## AMERICAN JOURNAL OF NEURORADIOLOGY

SEPTEMBER 2017  
VOLUME 38  
NUMBER 9  
WWW.AJNR.ORG

THE JOURNAL OF DIAGNOSTIC AND  
INTERVENTIONAL NEURORADIOLOGY

Amide proton transfer imaging of gliomas  
3T imaging of intracranial atherosclerotic plaque components  
Pediatric brain findings after multiple exposures to  
gadobenate dimeglumine

Official Journal ASNR • ASFNR • ASHNR • ASPNR • ASSR





## Access Product Solutions



**Sofia® Plus**  
Distal Access Catheter

Soft Torqueable Catheter Optimized for Intracranial Access with Excellent Navigation and Trackability



## Neurovascular Malformation Solutions



**Scepter® XC**  
Occlusion Balloon Catheter

Clinical Applications in Four Key Areas: Balloon Remodeling, Stent Delivery, Liquid Embolic Injection, and Balloon-Test Occlusion

### INDICATIONS FOR USE:

The SOFIA® Catheter is indicated for general intravascular use, including the neuro and peripheral vasculature. The SOFIA® Catheter can be used to facilitate introduction of diagnostic or therapeutic agents. The SOFIA® Catheter is not intended for use in coronary arteries.

The Scepter C® and Scepter XC® Occlusion Balloon Catheters are intended for use in the peripheral and neuro vasculature where temporary occlusion is desired. The balloon catheters provide temporary vascular occlusion which is useful in selectively stopping or controlling blood flow. The balloon catheters also offer balloon assisted embolization of intracranial aneurysms. For use in the peripheral vasculature for the infusion of diagnostic agents, such as contrast media, and therapeutic agents such as embolization materials. For neurovascular use for the infusion of diagnostic agents such as contrast media, and therapeutic agents, such as embolization materials, that have been approved or cleared for use in the neurovasculature and are compatible with the inner diameter of the Scepter C/XC Balloon Catheter.

The LVIS® Device is intended for use with bare platinum embolic coils for the treatment of unruptured, wide neck (neck  $\geq$  4 mm or dome to neck ratio  $<$  2), intracranial, saccular aneurysms arising from a parent vessel with a diameter  $\geq$  2.5 mm and  $\leq$  4.5 mm.

The Headway® Duo Microcatheter is intended for general intravascular use, including the peripheral and coronary vasculature for the infusion of diagnostic agents, such as contrast media, and therapeutic agents, such as embolization materials. The Headway® Duo Microcatheter is intended for neurovascular use, for the infusion of diagnostic agents, such as contrast media, and therapeutic agents that have been cleared or approved for use in the neurovasculature and are compatible with the inner diameter of the Headway® Duo Microcatheter.

# A 360-Degree Approach to Neuroendovascular Therapy



## Aneurysm Therapy Solutions



**LVIS® | LVIS® Jr.**  
Intraluminal Support Device

Braided Coil Assist Stents with High Neck Coverage, Excellent Opening, and Improved Radial Force\*

\*Humanitarian Device: Authorized by Federal Law for use with bare platinum embolic coils for the treatment of unruptured, wide neck (neck  $\geq$  4 mm or dome to neck ratio  $<$  2), intracranial, saccular aneurysms arising from a parent vessel with a diameter  $\geq$  2.5 mm and  $\leq$  4.5 mm. The effectiveness of this device for this use has not been demonstrated.



## Access Product Solutions



**Headway® DUO**  
Microcatheter

Innovative Catheter Technology and Construction in a Complete Range of Sizes and Softness

For more information or a product demonstration,  
contact your local MicroVention representative:



**MicroVention, Inc.**

**Worldwide Headquarters**

PH +1.714.247.8000

35 Enterprise

Aliso Viejo, CA 92656 USA

MicroVention UK Limited

PH +44 (0) 191 258 6777

MicroVention Europe, S.A.R.L.

PH +33 (1) 39 21 77 46

MicroVention Deutschland GmbH

PH +49 211 210 798-0

**microvention.com**

## Smooth and stable.

Target Detachable Coils deliver consistently smooth deployment and exceptional microcatheter stability. Designed to work seamlessly together for framing, filling and finishing. Target Coils deliver the high performance you demand.

For more information, please visit [www.strykerneurovascular.com/Target](http://www.strykerneurovascular.com/Target) or contact your local Stryker Neurovascular sales representative.



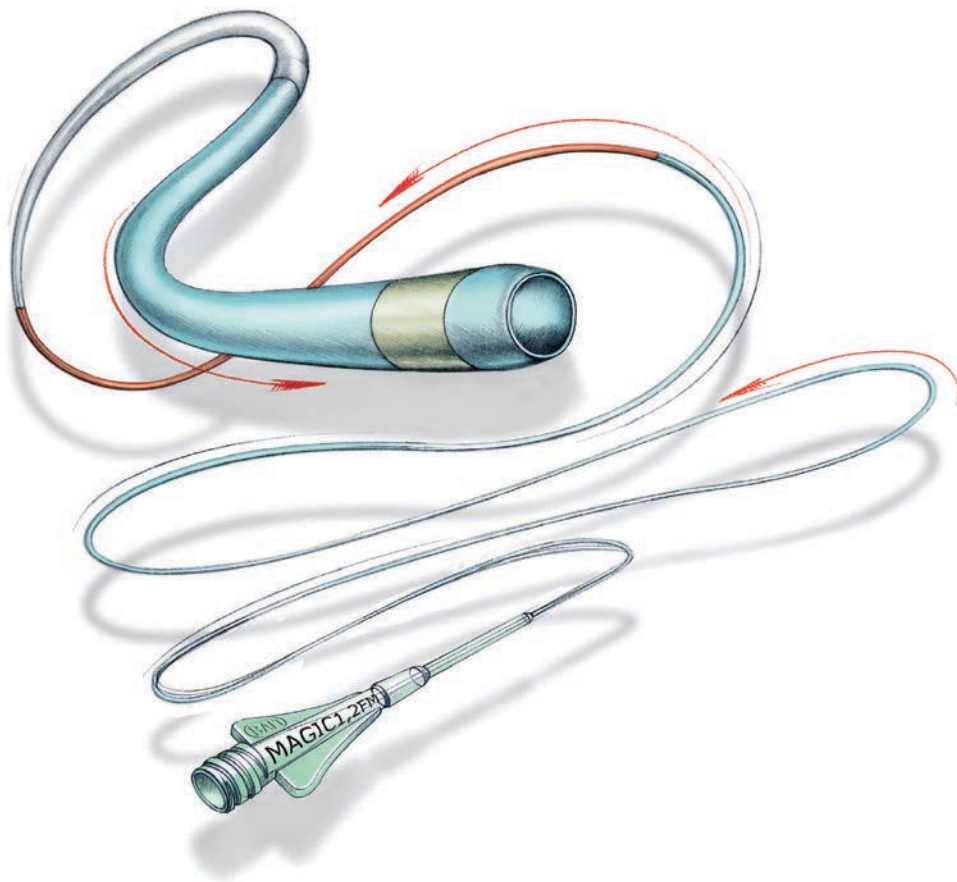
**Target**<sup>®</sup>  
DETACHABLE COILS

# Magic<sup>®</sup>



## FLOW-DEPENDENT MICROCATHETER SERIES

Now available through Balt USA



[ordermagics@balt-usa.com](mailto:ordermagics@balt-usa.com)

MAGIC catheters are designed for general intravascular use. They may be used for the controlled, selective regional infusion of therapeutic agents or embolic materials into vessels.<sup>1</sup>

Federal (USA) law restricts this device to sale, distribution by or on the order of a physician. Indications, contraindications, warnings and instructions for use can be found in the product labeling supplied with each device.

1. Magic Catheters IFU - Ind 19



BALT USA  
18 Technology Drive #169, Irvine, CA 92618  
P 949.788.1443 F 949.788.1444

© 2017 BALT USA MKTG-068 Rev. B

# Unleash Your Tiger



TIGERTRIEVER



 **RAPIDMEDICAL**  
The brain at your fingertips

[//www.rapid-medical.com](http://www.rapid-medical.com)

# ASNR 56<sup>th</sup> Annual Meeting & The Foundation of the ASNR Symposium 2018

June 2 - 7, 2018 | Vancouver, B.C., CANADA



The Vancouver Convention Centre East  
© 2013 Vancouver Convention Centre

## Welcome and Greetings

Please join us in Vancouver, CANADA for the **56th Annual Meeting of the American Society of Neuroradiology** on June 2–7, 2018 at the Vancouver Convention Centre East. Surrounded by the coastal mountains and located on the waterfront, you can enjoy these spectacular views in the heart of downtown Vancouver. With its undeniable charm and friendly atmosphere, Vancouver is known around the world as both a popular tourist attraction and one of the best places to live.

ASNR enthusiastically presents **Neuroradiology: Adding Value and Improving Healthcare** at the Symposium of the Foundation of the ASNR, as well as the common thread throughout the Annual Meeting. Implementing a value-based strategy in imaging has grasped the attention of nearly every healthcare provider; in particular with Radiologists understanding that the future will demand their imaging practices deliver better value. Value in healthcare is typically defined as those imaging strategies that yield improved outcomes, lower costs, or both. As payment transitions from a fee-for-service to a value-based system, thus creating a fundamentally different marketplace dynamic, measuring good outcomes are at the center of this changeover. At this time of uncertainty what little remains clear is that without a well-defined knowledge of their outcomes, no medical specialty will be able to succeed in the future value-based system. The Symposium will feature how Neuroradiology, in its many subspecialty areas, adds value to clinical care pathways by directing healthcare practice towards better outcomes. The annual meeting programming will continue on this theme emphasizing imaging that improves health outcomes, while considering costs, thus adding value. Our discussions will incorporate many innovative approaches to how neuroimaging currently does and will continue to improve overall healthcare performance.

As the Program Chair for ASNR 2018, it is my pleasure and honor to welcome you to Vancouver, CANADA for our annual meeting! Vancouver is known for being a very walkable city with a compact downtown core hosting many places to enjoy. So pack your comfortable walking shoes and let's tour together with our colleagues and friends!

*Pina Sanelli*

Pina C. Sanelli, MD, MPH, FACR  
ASNR 2018 Program Chair/President-Elect



ASNR 2018 ■ VANCOUVER

ASFNR ASHNR ASPNR ASSR SNIS

THE FOUNDATION OF THE ASNR



**Pina C. Sanelli, MD, MPH, FACR**

**ASNR 2018 Program Chair/President-Elect**

*Programming developed in cooperation with the...*

**American Society of Functional Neuroradiology (ASFNR)**

Max Wintermark, MD

**American Society of Head and Neck Radiology (ASHNR)**

Deborah R. Shatzkes, MD

**American Society of Pediatric Neuroradiology (ASPNR)**

Ashok Panigrahy, MD

**American Society of Spine Radiology (ASSR)**

John D. Barr, MD, FACR, FSIR, FAHA

**Society of NeuroInterventional Surgery (SNIS)**

Mahesh V. Jayaraman, MD

**ASNR Health Policy (HPC) Committee**

William D. Donovan, MD, MPH, FACR,

Gregory N. Nicola, MD, FACR

**ASNR Computer Sciences & Informatics (CSI) Committee**

John L. Go, MD, FACR

**ASNR Research Scientist Programming Committee**

Dikoma C. Shungu, PhD, Timothy P.L. Roberts, PhD

**The International Hydrocephalus Imaging Working Group (IHIWG) / CSF Flow Group**

William G. Bradley, Jr., MD, PhD, FACR, Harold L. Rekate, MD  
and Bryn A. Martin, PhD

**Abstract Deadline: Friday, December 15, 2017**

Please visit [2018.asnr.org](http://2018.asnr.org) for more information



Fairmont Waterfront  
© Copyright 2017 FRHI



Pan Pacific Vancouver  
© 2017 Pan Pacific Hotels and Resorts

**ASNR 56<sup>th</sup> Annual Meeting**

c/o American Society of Neuroradiology  
800 Enterprise Drive, Suite 205  
Oak Brook, Illinois 60523-4216  
Phone: 630-574-0220 + Fax: 630 574-0661  
[2018.asnr.org](http://2018.asnr.org)



### Official Journal:

American Society of Neuroradiology  
 American Society of Functional Neuroradiology  
 American Society of Head and Neck Radiology  
 American Society of Pediatric Neuroradiology  
 American Society of Spine Radiology

### EDITOR-IN-CHIEF

**Jeffrey S. Ross, MD**

*Professor of Radiology, Department of Radiology,  
 Mayo Clinic College of Medicine, Phoenix, AZ*

### SENIOR EDITORS

**Harry J. Cloft, MD, PhD**

*Professor of Radiology and Neurosurgery,  
 Department of Radiology, Mayo Clinic College of  
 Medicine, Rochester, MN*

**Thierry A.G.M. Huisman, MD**

*Professor of Radiology, Pediatrics, Neurology, and  
 Neurosurgery, Chairman, Department of Imaging  
 and Imaging Science, Johns Hopkins Bayview,  
 Director, Pediatric Radiology and Pediatric  
 Neuroradiology, Johns Hopkins Hospital,  
 Baltimore, MD*

**Yvonne W. Lui, MD**

*Associate Professor of Radiology,  
 Chief of Neuroradiology,  
 New York University School of Medicine,  
 New York, NY*

**C.D. Phillips, MD, FACR**

*Professor of Radiology, Weill Cornell Medical  
 College, Director of Head and Neck Imaging,  
 New York-Presbyterian Hospital, New York, NY*

**Pamela W. Schaefer, MD**

*Clinical Director of MRI and Associate Director of  
 Neuroradiology, Massachusetts General Hospital,  
 Boston, Massachusetts, Associate Professor,  
 Radiology, Harvard Medical School, Cambridge, MA*

**Charles M. Strother, MD**

*Professor of Radiology, Emeritus, University of  
 Wisconsin, Madison, WI*

### STATISTICAL SENIOR EDITOR

**Bryan A. Comstock, MS**

*Senior Biostatistician,  
 Department of Biostatistics,  
 University of Washington, Seattle, WA*

### EDITORIAL BOARD

Ashley H. Aiken, *Atlanta, GA*  
 Lea M. Alhilali, *Phoenix, AZ*  
 John D. Barr, *Dallas, TX*  
 Ari Blitz, *Baltimore, MD*  
 Barton F. Branstetter IV, *Pittsburgh, PA*  
 Jonathan L. Brisman, *Lake Success, NY*  
 Julie Bykowski, *San Diego, CA*  
 Keith Cauley, *Danville, PA*  
 Asim F. Choudhri, *Memphis, TN*  
 Alessandro Cianfoni, *Lugano, Switzerland*  
 J. Matthew Debnam, *Houston, TX*  
 Seena Dehkharghani, *New York, NY*  
 Colin Derdeyn, *Iowa City, IA*  
 Rahul S. Desikan, *San Francisco, CA*  
 Yonghong Ding, *Rochester, MN*  
 Clifford J. Eskey, *Hanover, NH*  
 Saeed Fakhraan, *Phoenix, AZ*  
 Massimo Filippi, *Milan, Italy*  
 Allan J. Fox, *Toronto, Ontario, Canada*  
 Wende N. Gibbs, *Los Angeles, CA*  
 Christine M. Glastonbury, *San Francisco, CA*  
 John L. Go, *Los Angeles, CA*  
 Allison Grayev, *Madison, WI*  
 Brent Griffith, *Detroit, MI*  
 Wan-Yuo Guo, *Taipei, Taiwan*  
 Ajay Gupta, *New York, NY*  
 Rakesh K. Gupta, *Lucknow, India*  
 Lotfi Hachein-Bey, *Sacramento, CA*  
 Christopher P. Hess, *San Francisco, CA*  
 Andrei Holodny, *New York, NY*  
 Benjamin Huang, *Chapel Hill, NC*  
 George J. Hunter, *Boston, MA*  
 Mahesh V. Jayaraman, *Providence, RI*  
 Valerie Jewells, *Chapel Hill, NC*  
 Christof Karmonik, *Houston, TX*  
 Timothy J. Kaufmann, *Rochester, MN*  
 Hillary R. Kelly, *Boston, MA*  
 Toshibumi Kinoshita, *Akita, Japan*  
 Kennith F. Layton, *Dallas, TX*  
 Michael M. Lell, *Nürnberg, Germany*  
 Michael Lev, *Boston, MA*  
 Karl-Olof Lovblad, *Geneva, Switzerland*  
 Franklin A. Marden, *Chicago, IL*  
 M. Gisele Matheus, *Charleston, SC*  
 Joseph C. McGowan, *Merion Station, PA*  
 Stephan Meckel, *Freiburg, Germany*  
 Christopher J. Moran, *St. Louis, MO*  
 Takahisa Mori, *Kamakura City, Japan*  
 Suresh Mukherji, *Ann Arbor, MI*  
 Amanda Murphy, *Toronto, Ontario, Canada*  
 Alexander J. Nemeth, *Chicago, IL*  
 Sasan Partovi, *Cleveland, OH*  
 Laurent Pierot, *Reims, France*  
 Jay J. Pillai, *Baltimore, MD*

Whitney B. Pope, *Los Angeles, CA*  
 M. Judith Donovan Post, *Miami, FL*  
 Tina Young Poussaint, *Boston, MA*  
 Joana Ramalho, *Lisbon, Portugal*  
 Otto Rapalino, *Boston, MA*  
 Álex Rovira-Cañellas, *Barcelona, Spain*  
 Paul M. Ruggieri, *Cleveland, OH*  
 Zoran Rumboldt, *Rovinj-Rovigno, Croatia*  
 Amit M. Saindane, *Atlanta, GA*  
 Erin Simon Schwartz, *Philadelphia, PA*  
 Lubdha M. Shah, *Salt Lake City, UT*  
 Aseem Sharma, *St. Louis, MO*  
 J. Keith Smith, *Chapel Hill, NC*  
 Maria Vittoria Spampinato, *Charleston, SC*  
 Gordon K. Sze, *New Haven, CT*  
 Krishnamoorthy Thamburaj, *Hershey, PA*  
 Cheng Hong Toh, *Taipei, Taiwan*  
 Thomas A. Tomsick, *Cincinnati, OH*  
 Aquilla S. Turk, *Charleston, SC*  
 Willem Jan van Rooij, *Tilburg, Netherlands*  
 Arastoo Vossough, *Philadelphia, PA*  
 Elysa Widjaja, *Toronto, Ontario, Canada*  
 Max Wintermark, *Stanford, CA*  
 Ronald L. Wolf, *Philadelphia, PA*  
 Kei Yamada, *Kyoto, Japan*  
 Carlos Zamora, *Chapel Hill, NC*

### EDITORIAL FELLOW

Vahe Zohrabian, *New Haven, CT*

### SPECIAL CONSULTANTS TO THE EDITOR

#### AJNR Blog Editor

Neil Lall, *Denver, CO*

#### Case of the Month Editor

Nicholas Stence, *Aurora, CO*

#### Case of the Week Editors

Juan Pablo Cruz, *Santiago, Chile*  
 Sapna Rawal, *Toronto, Ontario, Canada*

#### Classic Case Editor

Sandy Cheng-Yu Chen, *Taipei, Taiwan*

#### Facebook Editor

Peter Yi Shen, *Sacramento, CA*

#### Health Care and Socioeconomics Editor

Pina C. Sanelli, *New York, NY*

#### Physics Editor

Greg Zaharchuk, *Stanford, CA*

#### Podcast Editor

Wende N. Gibbs, *Los Angeles, CA*

#### Twitter Editor

Jennifer McCarty, *Atlanta, Georgia*

### YOUNG PROFESSIONALS ADVISORY COMMITTEE

Asim K. Bag, *Birmingham, AL*  
 Anna E. Nidecker, *Sacramento, CA*  
 Peter Yi Shen, *Sacramento, CA*

*Founding Editor*  
**Juan M. Taveras**

*Editors Emeriti*  
**Mauricio Castillo, Robert I. Grossman,  
 Michael S. Huckman, Robert M. Quencer**

*Managing Editor*  
**Karen Halm**

*Assistant Managing Editor*  
**Laura Wilhelm**

*Digital Publications and Social Media Coordinator*  
**Kylie Mason**

*Executive Director, ASNR*

**Mary Beth Hepp**

*Director of Communications, ASNR*

**Angelo Artemakis**

# We're Inside Every Great Neuroradiologist!

## ASNR MEMBERS RECEIVE

### *American Journal of Neuroradiology (AJNR)*

The leading neuroradiology research journal, published monthly

### *Neurographics*

Bimonthly educational journal with CME for members

### *ASNR Annual Meeting*

Discounts for members on the field's premier conference

### *eCME*

Online collection of lectures and articles with SA-CME and Category 1 credit

### *Advocacy*

Coding/reimbursement, quality standards and practice guidelines; demonstrating neuroradiology's value!

### *Networking*

Access to 5,000 peers

... And More!

Join the leaders in neuroradiology today!

Learn more at [www.asnr.org/join](http://www.asnr.org/join)

# ASNR

## American Society of Neuroradiology

800 Enterprise Dr., Suite 205, Oak Brook, IL 60523 • (630)574-0220 • [membership@asnr.org](mailto:membership@asnr.org) • [www.asnr.org](http://www.asnr.org)



© Travel Portland



© Travel Portland



© Travel Portland



© Travel Portland



© 2010 Torsten Kjellstrand

**WE'VE MOVED TO FALL 2017!**



*11<sup>th</sup> Annual Meeting of the  
American Society of*

# **FUNCTIONAL NEURORADIOLOGY**

**October 9-11, 2017 • the Nines • Portland, Oregon**

**Optional Hands-on BOLD fMRI Workshop • October 8, 2017**



**PLEASE CONTACT EDUCATIONAL SYMPOSIA AT  
813-806-1000 or [ASFNR@edusymp.com](mailto:ASFNR@edusymp.com) or visit [www.ASFNR.org](http://www.ASFNR.org) for additional information.**



## Strengthen ASNR's representation at the national level.

Your membership in the American Medical Association strengthens ASNR's representation in the AMA House of Delegates—the policymaking body of the AMA that brings forth the views and interests of all physicians to establish national policy on health, medical, professional and governance matters.

Please activate your 2017 AMA membership, visit [ama-assn.org](http://ama-assn.org) or call AMA Member Relations at (800) 262-3211. If you are currently a member, thank you.

### AMA member benefits and resources include:

- Unlimited access to **The JAMA Network**<sup>®</sup> which brings together *JAMA* and all 11 specialty journals with CME.  
[jamanetwork.com](http://jamanetwork.com)
- **STEPS Forward**<sup>™</sup>, the AMA's new practice transformation series designed to help physicians achieve the Quadruple Aim: better patient experience, better population health and lower overall costs with improved professional satisfaction.  
[stepsforward.org](http://stepsforward.org)
- Free 18-month trial of **DynaMed Plus**<sup>®</sup>, an evidence-based, clinical support tool that features thousands of images and provides immediate answers to clinical questions.  
[offers.jamanetwork.com](http://offers.jamanetwork.com)





# Simplify the MOC Process



# Manage your CME Credits Online

## CMEgateway.org

### Available to Members of Participating Societies

American Board of Radiology (ABR)  
American College of Radiology (ACR)  
American Roentgen Ray Society (ARRS)  
American Society of Neuroradiology (ASNR)  
Commission on Accreditation of Medical  
Physics Educational Programs, Inc. (CAMPEP)  
Radiological Society of North America (RSNA)  
Society of Interventional Radiology (SIR)  
SNM  
The Society for Pediatric Radiology (SPR)

### It's Easy and Free!

Log on to CME Gateway to:

- View or print reports of your CME credits from multiple societies from a single access point.
- Print an aggregated report or certificate from each participating organization.
- Link to SAMs and other tools to help with maintenance of certification.

### American Board of Radiology (ABR) participation!

By activating ABR in your organizational profile, your MOC-fulfilling CME and SAM credits can be transferred to your own personalized database on the ABR Web site.

### Sign Up Today!

go to [CMEgateway.org](http://CMEgateway.org)

## Trevo® XP ProVue Retrievers

See package insert for complete indications, complications, warnings, and instructions for use.

### INDICATIONS FOR USE

- The Trevo Retriever is indicated for use to restore blood flow in the neurovasculature by removing thrombus for the treatment of acute ischemic stroke to reduce disability in patients with a persistent, proximal anterior circulation, large vessel occlusion, and smaller core infarcts who have first received intravenous tissue plasminogen activator (IV t-PA). Endovascular therapy with the device should start within 6 hours of symptom onset.
- The Trevo Retriever is indicated to restore blood flow in the neurovasculature by removing thrombus in patients experiencing ischemic stroke within 8 hours of symptom onset. Patients who are ineligible for intravenous tissue plasminogen activator (IV t-PA) or who fail IV t-PA therapy are candidates for treatment.

### COMPLICATIONS

Procedures requiring percutaneous catheter introduction should not be attempted by physicians unfamiliar with possible complications which may occur during or after the procedure. Possible complications include, but are not limited to, the following: air embolism; hematoma or hemorrhage at puncture site; infection; distal embolization; pain/headache; vessel spasm, thrombosis, dissection, or perforation; emboli; acute occlusion; ischemia; intracranial hemorrhage; false aneurysm formation; neurological deficits including stroke; and death.

### COMPATIBILITY

3x20mm retrievers are compatible with Trevo® Pro 14 Microcatheters (REF 90231) and Trevo® Pro 18 Microcatheters (REF 90238). 4x20mm retrievers are compatible with Trevo® Pro 18 Microcatheters (REF 90238). 4x30mm retrievers are compatible with Excelsior® XT-27® Microcatheters (150cm x 6cm straight REF 275081) and Trevo® Pro 18 Microcatheters (REF 90238). 6x25mm Retrievers are compatible with Excelsior® XT-27® Microcatheters (150cm x 6cm straight REF 275081). Compatibility of the Retriever with other microcatheters has not been established. Performance of the Retriever device may be impacted if a different microcatheter is used.

Balloon Guide Catheters (such as Merci® Balloon Guide Catheter and FlowGate® Balloon Guide Catheter) are recommended for use during thrombus removal procedures.

Retrievers are compatible with the Abbott Vascular DOC® Guide Wire Extension (REF 22260).

Retrievers are compatible with Boston Scientific RHV (Ref 421242).

### SPECIFIC WARNINGS FOR INDICATION 1

- The safety and effectiveness of the Trevo Retrievers in reducing disability has not been established in patients with large core infarcts (i.e., ASPECTS  $\leq 7$ ). There may be increased risks, such as intracerebral hemorrhage, in these patients.
- The safety and effectiveness of the Trevo Retrievers in reducing disability has not been established or evaluated in patients with occlusions in the posterior circulation (e.g., basilar or vertebral arteries) or for more distal occlusions in the anterior circulation.

### WARNINGS APPLIED TO BOTH INDICATIONS

- Administration of IV t-PA should be within the FDA-approved window (within 3 hours of stroke symptom onset).
- Contents supplied STERILE, using an ethylene oxide (EO) process. Nonpyrogenic.
- To reduce risk of vessel damage, adhere to the following recommendations:
  - Take care to appropriately size Retriever to vessel diameter at intended site of deployment.
  - Do not perform more than six (6) retrieval attempts in same vessel using Retriever devices.
  - Maintain Retriever position in vessel when removing or exchanging Microcatheter.
- To reduce risk of kinking/fracture, adhere to the following recommendations:
  - Immediately after unsheathing Retriever, position Microcatheter tip marker just proximal to shaped section. Maintain Microcatheter tip marker just proximal to shaped section of Retriever during manipulation and withdrawal.
  - Do not rotate or torque Retriever.
  - Use caution when passing Retriever through stented arteries.
- Do not resterilize and reuse. Structural integrity and/or function may be impaired by reuse or cleaning.
- The Retriever is a delicate instrument and should be handled carefully. Before use and when possible during procedure, inspect device carefully for damage. Do not use a device that shows signs of damage. Damage may prevent device from functioning and may cause complications.

- Do not advance or withdraw Retriever against resistance or significant vasospasm. Moving or torquing device against resistance or significant vasospasm may result in damage to vessel or device. Assess cause of resistance using fluoroscopy and if needed resheat the device to withdraw.
- If Retriever is difficult to withdraw from the vessel, do not torque Retriever. Advance Microcatheter distally, gently pull Retriever back into Microcatheter, and remove Retriever and Microcatheter as a unit. If undue resistance is met when withdrawing the Retriever into the Microcatheter, consider extending the Retriever using the Abbott Vascular DOC guidewire extension (REF 22260) so that the Microcatheter can be exchanged for a larger diameter catheter such as a DAC® catheter. Gently withdraw the Retriever into the larger diameter catheter.
- Administer anti-coagulation and anti-platelet medications per standard institutional guidelines.

### PRECAUTIONS

- Prescription only – device restricted to use by or on order of a physician.
- Store in cool, dry, dark place.
- Do not use open or damaged packages.
- Use by “Use By” date.
- Exposure to temperatures above 54°C (130°F) may damage device and accessories. Do not autoclave.
- Do not expose Retriever to solvents.
- Use Retriever in conjunction with fluoroscopic visualization and proper anti-coagulation agents.
- To prevent thrombus formation and contrast media crystal formation, maintain a constant infusion of appropriate flush solution between guide catheter and Microcatheter and between Microcatheter and Retriever or guidewire.
- Do not attach a torque device to the shaped proximal end of DOC® Compatible Retriever. Damage may occur, preventing ability to attach DOC® Guide Wire Extension.



**Concentric Medical**  
301 East Evelyn Avenue  
Mountain View, CA 94041

**Stryker Neurovascular**  
47900 Bayside Parkway  
Fremont, CA 94538

[strykerneurovascular.com](http://strykerneurovascular.com)

Date of Release: SEP/2016

EX\_EN\_US

Copyright © 2016 Stryker  
NV00018973.AB

## Target® Detachable Coil

See package insert for complete indications, contraindications, warnings and instructions for use.

### INTENDED USE / INDICATIONS FOR USE

Target Detachable Coils are intended to endovascularly obstruct or occlude blood flow in vascular abnormalities of the neurovascular and peripheral vessels.

Target Detachable Coils are indicated for endovascular embolization of:

- Intracranial aneurysms
- Other neurovascular abnormalities such as arteriovenous malformations and arteriovenous fistulae
- Arterial and venous embolizations in the peripheral vasculature

### CONTRAINDICATIONS

None known.

### POTENTIAL ADVERSE EVENTS

Potential complications include, but are not limited to: allergic reaction, aneurysm perforation and rupture, arrhythmia, death, edema, embolus, headache, hemorrhage, infection, ischemia, neurological/intracranial sequelae, post-embolization syndrome (fever, increased white blood cell count, discomfort), TIA/stroke, vasospasm, vessel occlusion or closure, vessel perforation, dissection, trauma or damage, vessel rupture, vessel thrombosis. Other procedural complications including but not limited to: anesthetic and contrast media risks, hypotension, hypertension, access site complications.

### WARNINGS

- Contents supplied STERILE using an ethylene oxide (EO) process. Do not use if sterile barrier is damaged. If damage is found, call your Stryker Neurovascular representative.
- For single use only. Do not reuse, reprocess or resterilize. Reuse, reprocessing or resterilization may compromise the structural integrity of the device and/or lead to device failure which, in turn, may result in patient injury, illness or death. Reuse, reprocessing or resterilization may also create a risk of contamination of the device and/or cause patient infection or cross-infection, including, but not limited to, the transmission of infectious disease(s) from one patient to another. Contamination of the device may lead to injury, illness or death of the patient.

- After use, dispose of product and packaging in accordance with hospital, administrative and/or local government policy.

**This device should only be used by physicians who have received appropriate training in interventional neuroradiology or interventional radiology and preclinical training on the use of this device as established by Stryker Neurovascular.**

- Patients with hypersensitivity to 316LVM stainless steel may suffer an allergic reaction to this implant.
- MR temperature testing was not conducted in peripheral vasculature, arteriovenous malformations or fistulae models.
- The safety and performance characteristics of the Target Detachable Coil System (Target Detachable Coils, InZone Detachment Systems, delivery systems and accessories) have not been demonstrated with other manufacturer's devices (whether coils, coil delivery devices, coil detachment systems, catheters, guidewires, and/or other accessories). Due to the potential incompatibility of non Stryker Neurovascular devices with the Target Detachable Coil System, the use of other manufacturer's device(s) with the Target Detachable Coil System is not recommended.
- To reduce risk of coil migration, the diameter of the first and second coil should never be less than the width of the ostium.
- In order to achieve optimal performance of the Target Detachable Coil System and to reduce the risk of thromboembolic complications, it is critical that a continuous infusion of appropriate flush solution be maintained between a) the femoral sheath and guiding catheter, b) the 2-tip microcatheter and guiding catheters, and c) the 2-tip microcatheter and Stryker Neurovascular guidewire and delivery wire. Continuous flush also reduces the potential for thrombus formation on, and crystallization of infusate around, the detachment zone of the Target Detachable Coil.
- Do not use the product after the “Use By” date specified on the package.
- Reuse of the flush port/dispenser coil or use with any coil other than the original coil may result in contamination of, or damage to, the coil.
- Utilization of damaged coils may affect coil delivery to, and stability inside, the vessel or aneurysm, possibly resulting in coil migration and/or stretching.
- The fluoro-saver marker is designed for use with a Rotating Hemostatic Valve (RHV). If used without an RHV, the distal end of the coil may be beyond the alignment marker when the fluoro-saver marker reaches the microcatheter hub.

- If the fluoro-saver marker is not visible, do not advance the coil without fluoroscopy.
- Do not rotate delivery wire during or after delivery of the coil. Rotating the Target Detachable Coil delivery wire may result in a stretched coil or premature detachment of the coil from the delivery wire, which could result in coil migration.
- Verify there is no coil loop protrusion into the parent vessel after coil placement and prior to coil detachment. Coil loop protrusion after coil placement may result in thromboembolic events if the coil is detached.
- Verify there is no movement of the coil after coil placement and prior to coil detachment. Movement of the coil after coil placement may indicate that the coil could migrate once it is detached.
- Failure to properly close the RHV compression fitting over the delivery wire before attaching the InZone® Detachment System could result in coil movement, aneurysm rupture or vessel perforation.
- Verify repeatedly that the distal shaft of the catheter is not under stress before detaching the Target Detachable Coil. Axial compression or tension forces could be stored in the 2-tip microcatheter causing the tip to move during coil delivery. Microcatheter tip movement could cause the aneurysm or vessel to rupture.
- Advancing the delivery wire beyond the microcatheter tip once the coil has been detached involves risk of aneurysm or vessel perforation.
- The long term effect of this product on extravascular tissues has not been established so care should be taken to retain this device in the intravascular space.

Damaged delivery wires may cause detachment failures, vessel injury or unpredictable distal tip response during coil deployment. If a delivery wire is damaged at any point during the procedure, do not attempt to straighten or otherwise repair it. Do not proceed with deployment or detachment. Remove the entire coil and replace with undamaged product.

- After use, dispose of product and packaging in accordance with hospital, administrative and/or local government policy.

### CAUTIONS / PRECAUTIONS

- Federal Law (USA) restricts this device to sale by or on the order of a physician.
- Besides the number of InZone Detachment System units needed to complete the case, there must be an extra InZone Detachment System unit as back up.

- Removing the delivery wire without grasping the introducer sheath and delivery wire together may result in the detachable coil sliding out of the introducer sheath.
- Failure to remove the introducer sheath after inserting the delivery wire into the RHV of the microcatheter will interrupt normal infusion of flush solution and allow back flow of blood into the microcatheter.
- Some low level overhead light near or adjacent to the patient is required to visualize the fluoro-saver marker; monitor light alone will not allow sufficient visualization of the fluoro-saver marker.
- Advance and retract the Target Detachable Coil carefully and smoothly without excessive force. If unusual friction is noticed, slowly withdraw the Target Detachable Coil and examine for damage. If damage is present, remove and use a new Target Detachable Coil. If friction or resistance is still noted, carefully remove the Target Detachable Coil and microcatheter and examine the microcatheter for damage.
- If it is necessary to reposition the Target Detachable Coil, verify under fluoroscopy that the coil moves with a one-to-one motion. If the coil does not move with a one-to-one motion or movement is difficult, the coil may have stretched and could possibly migrate or break. Gently remove both the coil and microcatheter and replace with new devices.
- Increased detachment times may occur when:
  - Other embolic agents are present.
  - Delivery wire and microcatheter markers are not properly aligned.
  - Thrombus is present on the coil detachment zone.
- Do not use detachment systems other than the InZone Detachment System.
- Increased detachment times may occur when delivery wire and microcatheter markers are not properly aligned.
- Do not use detachment systems other than the InZone Detachment System.



**Stryker Neurovascular**  
47900 Bayside Parkway  
Fremont, CA 94538

[strykerneurovascular.com](http://strykerneurovascular.com)

Date of Release: MAR/2016

EX\_EN\_US

Copyright © 2016 Stryker  
NV00018669.AB

# AJNR

## AMERICAN JOURNAL OF NEURORADIOLOGY

SEPTEMBER 2017  
VOLUME 38  
NUMBER 9  
WWW.AJNR.ORG

Publication Preview at [www.ajnr.org](http://www.ajnr.org) features articles released in advance of print. Visit [www.ajnrblog.org](http://www.ajnrblog.org) to comment on AJNR content and chat with colleagues and AJNR's News Digest at <http://ajnrdigest.org> to read the stories behind the latest research in neuroimaging.

1663 PERSPECTIVES *S.M. Schonfeld*

### REVIEW ARTICLES

-   1664 **Current and Emerging Therapies in Multiple Sclerosis: Implications for the Radiologist, Part 1—Mechanisms, Efficacy, and Safety** *C. McNamara, et al.* **ADULT BRAIN**
-  1672 **Current and Emerging Therapies in Multiple Sclerosis: Implications for the Radiologist, Part 2—Surveillance for Treatment Complications and Disease Progression** *C. McNamara, et al.* **ADULT BRAIN**

### LEVEL 1 EBM EXPEDITED PUBLICATION

-    1681 **Comparison of Gadoterate Meglumine and Gadobutrol in the MRI Diagnosis of Primary Brain Tumors: A Double-Blind Randomized Controlled Intraindividual Crossover Study (the REMIND Study)** *K.R. Maravilla, et al.* **ADULT BRAIN**

### GENERAL CONTENTS

-   1689 **Diagnostic Performance of a 10-Minute Gadolinium-Enhanced Brain MRI Protocol Compared with the Standard Clinical Protocol for Detection of Intracranial Enhancing Lesions** *J. Fagundes, et al.* **ADULT BRAIN**
-   1695 **Relationship between Glioblastoma Heterogeneity and Survival Time: An MR Imaging Texture Analysis** *Y. Liu, et al.* **ADULT BRAIN**
-    1702 **Amide Proton Transfer Imaging Allows Detection of Glioma Grades and Tumor Proliferation: Comparison with Ki-67 Expression and Proton MR Spectroscopy Imaging** *C. Su, et al.* **ADULT BRAIN**
-   1710 **Optimization of DSC MRI Echo Times for CBV Measurements Using Error Analysis in a Pilot Study of High-Grade Gliomas** *L.C. Bell, et al.* **ADULT BRAIN**
-     1716 **Identification and Quantitative Assessment of Different Components of Intracranial Atherosclerotic Plaque by Ex Vivo 3T High-Resolution Multicontrast MRI** *Y. Jiang, et al.* **ADULT BRAIN**
-  1723 **Association between Intracranial Atherosclerotic Calcium Burden and Angiographic Luminal Stenosis Measurements** *H. Baradaran, et al.* **ADULT BRAIN**
-   1730 **Focal Low and Global High Permeability Predict the Possibility, Risk, and Location of Hemorrhagic Transformation following Intra-Arterial Thrombolysis Therapy in Acute Stroke** *Y. Li, et al.* **ADULT BRAIN INTERVENTIONAL**

AJNR (Am J Neuroradiol ISSN 0195–6108) is a journal published monthly, owned and published by the American Society of Neuroradiology (ASNR), 800 Enterprise Drive, Suite 205, Oak Brook, IL 60523. Annual dues for the ASNR include \$170.00 for journal subscription. The journal is printed by Cadmus Journal Services, 5457 Twin Knolls Road, Suite 200, Columbia, MD 21045; Periodicals postage paid at Oak Brook, IL and additional mailing offices. Printed in the U.S.A. POSTMASTER: Please send address changes to American Journal of Neuroradiology, P.O. Box 3000, Denville, NJ 07834, U.S.A. Subscription rates: nonmember \$390 (\$460 foreign) print and online, \$310 online only; institutions \$450 (\$520 foreign) print and basic online, \$895 (\$960 foreign) print and extended online, \$370 online only (basic), extended online \$805; single copies are \$35 each (\$40 foreign). Indexed by PubMed/Medline, BIOSIS Previews, Current Contents (Clinical Medicine and Life Sciences), EMBASE, Google Scholar, HighWire Press, Q-Sensei, RefSeek, Science Citation Index, and SCI Expanded. Copyright © American Society of Neuroradiology.

-   1737 **MRI of the Swallow Tail Sign: A Useful Marker in the Diagnosis of Lewy Body Dementia?** *S. Shams, et al.* **ADULT BRAIN**
-   1742 **Pericortical Enhancement on Delayed Postgadolinium Fluid-Attenuated Inversion Recovery Images in Normal Aging, Mild Cognitive Impairment, and Alzheimer Disease** *W.M. Freeze, et al.* **ADULT BRAIN**
- 1748 **How Common Is Signal-Intensity Increase in Optic Nerve Segments on 3D Double Inversion Recovery Sequences in Visually Asymptomatic Patients with Multiple Sclerosis?** *T. Sartoretti, et al.* **ADULT BRAIN**  
**HEAD & NECK**
- 1754 **Intracranial Perishunt Catheter Fluid Collections with Edema, a Sign of Shunt Malfunction: Correlation of CT/MRI and Nuclear Medicine Findings** *H.A. Kale, et al.* **ADULT BRAIN**
-   1758 **Value of Thrombus CT Characteristics in Patients with Acute Ischemic Stroke** *J. Borst, et al.* **ADULT BRAIN**
-   1765 **Risk Factor Analysis of Recanalization Timing in Coiled Aneurysms: Early versus Late Recanalization** *J.P. Jeon, et al.* **INTERVENTIONAL**
-  1771 **Influence of Carotid Siphon Anatomy on Brain Aneurysm Presentation** *E. Waihrich, et al.* **INTERVENTIONAL**
-   1776 **Carotid Plaque Morphology and Ischemic Vascular Brain Disease on MRI** *Q.J.A. van den Bouwhuisen, et al.* **EXTRACRANIAL VASCULAR**
- 1783 **Sigmoid Sinus Diverticulum, Dehiscence, and Venous Sinus Stenosis: Potential Causes of Pulsatile Tinnitus in Patients with Idiopathic Intracranial Hypertension?** *J.A. Lansley, et al.* **HEAD & NECK**
- 1789 **Increased Curvature of the Tentorium Cerebelli in Idiopathic Intracranial Hypertension** *P.P. Morris, et al.* **HEAD & NECK**
- 1794 **Ethanol Ablation of Ranulas: Short-Term Follow-Up Results and Clinoradiologic Factors for Successful Outcome** *K.H. Ryu, et al.* **HEAD & NECK**
- 1799 **T1 Signal Measurements in Pediatric Brain: Findings after Multiple Exposures to Gadobenate Dimeglumine for Imaging of Nonneurologic Disease** *G.K. Schneider, et al.* **PEDIATRICS**
- 1807 **New Ultrasound Measurements to Bridge the Gap between Prenatal and Neonatal Brain Growth Assessment** *I.V. Koning, et al.* **PEDIATRICS**
-  1814 **Analysis of 30 Spinal Angiograms Falsely Reported as Normal in 18 Patients with Subsequently Documented Spinal Vascular Malformations** *P. Barreras, et al.* **SPINE**  
**INTERVENTIONAL**
- 1820 **Diagnostic Utility of Increased STIR Signal in the Posterior Atlanto-Occipital and Atlantoaxial Membrane Complex on MRI in Acute C1–C2 Fracture** *Y.-M. Chang, et al.* **SPINE**
-  1826 **Prospective Comparison of Changes in Lumbar Spine MRI Findings over Time between Individuals with Acute Low Back Pain and Controls: An Exploratory Study** *J. Panagopoulos, et al.* **SPINE**
- 1833 **Syringohydromyelia in Patients with Chiari I Malformation: A Retrospective Analysis** *K.A. Gad, et al.* **SPINE**
-  1839 **Characteristics of CSF Velocity-Time Profile in Posttraumatic Syringomyelia** *J. Yeo, et al.* **SPINE**
-   1845 **Syringomyelia Fluid Dynamics and Cord Motion Revealed by Serendipitous Null Point Artifacts during Cine MRI** *C.M. Honey, et al.* **SPINE**
- 1848 **35 YEARS AGO IN AJNR**

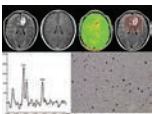
## ONLINE FEATURES

### LETTERS

- E58** **LAST<sub>2</sub> CH<sub>2</sub>ANCE: A Summary of Selection Criteria for Thrombectomy in Acute Ischemic Stroke** *P. Yang, et al.*
- E60** **Is Hippocampal Volumetry Really All That Matters?** *S. Haller*
- E62** **Reply** *T.P. Tanpitukpongse, et al.*
- E63** **FDG-PET/CT or MRI for the Diagnosis of Primary Progressive Aphasia?**  
*J.A. Matias-Guiu, et al.*
- E64** **Reply** *S.A. Sajjadi, et al.*

### BOOK REVIEWS *R.M. Quencer, Section Editor*

Please visit [www.ajnrblog.org](http://www.ajnrblog.org) to read and comment on Book Reviews.



Amide proton transfer-weighted imaging is a MR imaging technique developed to detect and quantitatively visualize endogenous proteins and peptides. APT WI is reported as asymmetry in the magnetization transfer ratio at 3.5 ppm [MTR<sub>asym</sub>(3.5ppm)]. Top row, left to right: Transverse T2-FLAIR MR image (left), C+ T1-weighted MR, APT image, location of MR spectroscopy voxel of a 45-year-old woman with grade II astrocytoma. Bottom row, left to right: MRSI indicating peaks for choline (Cho), creatine (Cr) and N-acetylaspartate (NAA); Ki-67 immunohistochemical stain. The MTR<sub>asym</sub>(3.5ppm) value was 2.83%.

 Indicates Editor's Choices selection

 Indicates Fellows' Journal Club selection

 Indicates open access to non-subscribers at [www.ajnr.org](http://www.ajnr.org)

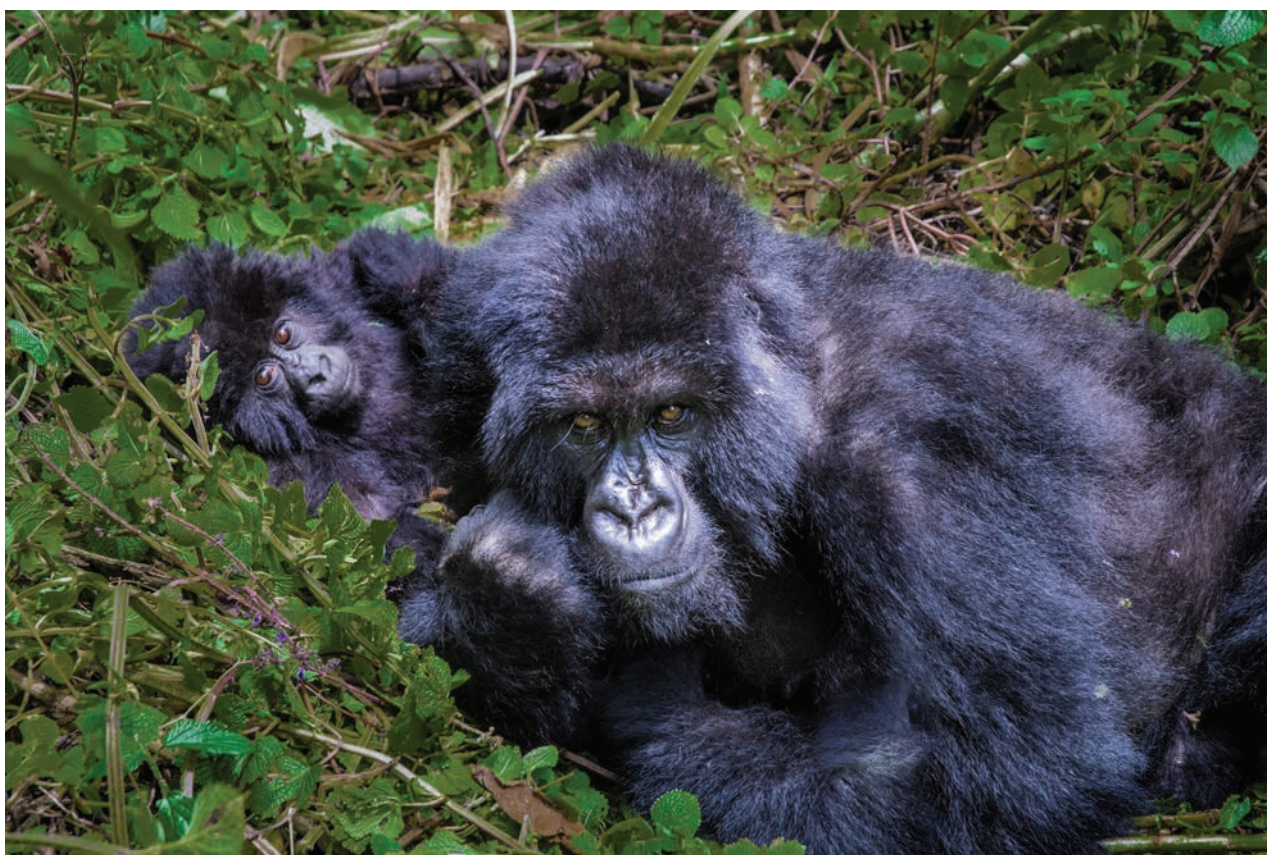
 Indicates article with supplemental on-line table

 Indicates article with supplemental on-line photo

 Indicates article with supplemental on-line video

 Evidence-Based Medicine Level 1

 Evidence-Based Medicine Level 2



Title: Mountain Gorillas, Rwanda. After 3 hours of trekking uphill in mud and jungle in the Volcanoes National Park of Rwanda, we met this mom and her baby. They are part of the Isabukuru family, one of the 10 families of Mountain Gorillas that tourists can visit. It was truly an adventure of a lifetime.

*Steven M. Schonfeld, MD, FACR, University Radiology Group, PA, East Brunswick, New Jersey*

# Current and Emerging Therapies in Multiple Sclerosis: Implications for the Radiologist, Part 1—Mechanisms, Efficacy, and Safety

 C. McNamara,  G. Sugrue,  B. Murray, and  P.J. MacMahon



## ABSTRACT

**SUMMARY:** Imaging for the diagnosis and follow-up of patients with suspected or confirmed multiple sclerosis is a common scenario for many general radiologists and subspecialty neuroradiologists. The field of MS therapeutics has rapidly evolved with multiple new agents now being used in routine clinical practice. To provide an informed opinion in discussions concerning newer MS agents, radiologists must have a working understanding of the strengths and limitations of the various novel therapies. The role of imaging in MS has advanced beyond monitoring and surveillance of disease activity to include treatment complications. An understanding of the new generation of MS drugs in conjunction with the key role that MR imaging plays in the detection of disease progression, opportunistic infections, and drug-related adverse events is of vital importance to the radiologist and clinical physician alike. Radiologists are in a unique position to detect many of the described complications well in advance of clinical symptoms. Part 1 of this review outlines recent developments in the treatment of MS and discusses the published clinical data on the efficacy and safety of the currently approved and emerging therapies in this condition as they apply to the radiologist. Part 2 will cover pharmacovigilance and the role the neuroradiologist plays in monitoring patients for signs of opportunistic infection and/or disease progression.

**ABBREVIATIONS:** IFN $\beta$  = interferon  $\beta$ ; NTZ = natalizumab; PML = progressive multifocal leukoencephalopathy; RRMS = relapsing-remitting MS

**M**ultiple sclerosis is an idiopathic chronic inflammatory demyelinating disease of the central nervous system. The median age of symptomatic onset is approximately 29 years, and the female-to-male ratio in this group approaches 3:1.<sup>1</sup> The McDonald criteria were introduced in 2001 as guidelines to facilitate a timely and accurate diagnosis of MS.<sup>2</sup> These criteria have resulted in an earlier diagnosis of this condition with a high degree of both specificity and sensitivity, allowing earlier medical intervention.<sup>3</sup> In 2010, revisions to the McDonald criteria allowed, in some instances, a more rapid diagnosis of MS, with equivalent or improved specificity and/or sensitivity compared with past criteria and allowed the clarification and simplification of the diagnostic process with fewer MR imaging examinations required.<sup>3</sup> Central to these guidelines is the use of MR imaging and the need to demonstrate the dissemination of neurologic lesions in both time and space. As a result, the radiologist plays an increasingly central

role in the multidisciplinary team care of patients diagnosed with this disease.

During the past 10 years, there has been an evolution in the treatment of relapsing-remitting MS (RRMS), with a rapid increase in the number of disease-modifying therapies available (On-line Table ). Since 2004, 7 new agents have been approved by the US Food and Drug Administration for the treatment of the relapsing form of the disease, joining what had previously been the mainstay of MS treatments: interferon  $\beta$  (IFN $\beta$ ) and glatiramer acetate.<sup>4</sup>

The radiologist has a pivotal role in the diagnosis of MS, along with monitoring and identifying complications associated with these latest treatments. Part 1 of this review details recent developments in the treatment of MS and discusses the published clinical data on the efficacy and safety of the currently approved and emerging therapies in this condition as they apply to the radiologist. Part 2 focuses on the role of the neuroradiologist in monitoring patients being treated with these medications, which includes observation for treatment complications and signs of disease progression.

## Currently Approved Agents: First-Line Therapies

**Interferon  $\beta$ .** Interferon  $\beta$  is based on a naturally occurring polypeptide predominantly produced by fibroblasts. Its anti-inflam-

From the Departments of Radiology (C.M., G.S., P.J.M.) and Neurology (B.M.), Mater Misericordiae University Hospital, Dublin, Ireland.

Please address correspondence to Peter MacMahon, FFR (RCSI), Department of Radiology, Whitty Building, North Circular Rd, Mater Misericordiae University Hospital, Dublin 7, Ireland; e-mail: pmacmahon@mater.ie; @McnamaraCillian

 Indicates open access to non-subscribers at [www.ajnr.org](http://www.ajnr.org)

 Indicates article with supplemental on-line table.

<http://dx.doi.org/10.3174/ajnr.A5147>

matory effects are largely believed to result from the inhibition of T-lymphocyte proliferation.<sup>5</sup> It is administered by intramuscular or subcutaneous injection. Phase III trials of all the IFN $\beta$  preparations have reduced the annualized relapse rate by about 30%, reduced the progression of disability in RRMS, and reduced visible MR imaging disease activity.<sup>6–8</sup> Most patients treated with IFN $\beta$  (50%–75%) experience flulike symptoms, which usually resolve within 24 hours. Liver enzymes may become elevated, and bone marrow function may be depressed, which warrants periodic surveillance of liver function and blood counts before starting therapy and every 6 months thereafter.<sup>9–11</sup> Isolated cases of severe injection-site reactions involving infection or necrosis and severe cases of acute liver failure and pancreatitis have been reported.<sup>5</sup>

**Glatiramer Acetate.** Glatiramer acetate is a pool of synthetic peptides with an amino acid composition similar to that of myelin basic protein and has widespread effects on the innate and adaptive immune systems.<sup>12</sup> It is an immunomodulatory agent that does not affect the number of circulating lymphocytes but rather switches lymphocyte polarization from a proinflammatory TH<sub>1</sub> to an anti-inflammatory TH<sub>2</sub> profile.<sup>13</sup> Glatiramer acetate is administered by subcutaneous injection. Glatiramer acetate treatment trials in RRMS have shown a significant reduction in the annualized relapse rate (29%) and a reduction in gadolinium-enhancing MR imaging activity.<sup>14,15</sup> Glatiramer acetate is usually well-tolerated, but most patients (65%) experience injection-site reactions (pain, erythema, swelling, and pruritus). About 15% report a transient self-limited systemic reaction (immediately after injection) of facial flushing and chest tightness, accompanied at times by palpitations, anxiety, and dyspnea. Other reported adverse events include lymphadenopathy and lipoatrophy.<sup>6,15,16</sup>

**Teriflunomide.** Teriflunomide (Aubagio), the active metabolite of leflunomide (an antirheumatic drug), is an oral disease-modifying therapy for RRMS, which was approved by the FDA in September 2012.<sup>17</sup> Teriflunomide reduces T- and B-cell activation, proliferation, and function in response to autoantigens by inhibiting a key mitochondrial enzyme involved in DNA replication. Teriflunomide significantly reduces relapse rates, disability progression, and MR imaging evidence of disease activity, compared with a placebo.<sup>18</sup> It showed a 31% reduction in the annualized relapse rate and a 30% reduction in disability compared with a placebo.<sup>19</sup> On MR imaging, teriflunomide was superior to a placebo in reducing the total lesion volume and the number of gadolinium-enhancing lesions.<sup>18</sup> While no radiologic-specific adverse events have been reported to date with teriflunomide, the most common clinical and biochemical adverse events include headache, diarrhea, fatigue, elevated alanine aminotransferase levels, nausea, hair thinning, influenza, and urinary tract infections.<sup>20</sup>

**Dimethyl Fumarate.** Dimethyl fumarate (Tecfidera) is an orally administered immunomodulatory agent with anti-inflammatory properties, and its mechanism of action in MS is only partially understood.<sup>5</sup> Two Phase III trials of RRMS showed that dimethyl fumarate, compared with a placebo, reduced the annualized relapse rate by 44%–53%, the rate of disability progression by 22%–

32%, and the number of gadolinium-enhancing lesions by about 75%–94%.<sup>21,22</sup> Common adverse events included flushing, nausea, diarrhea and abdominal pain, neutropenia, and elevated liver function test results.<sup>21,22</sup> Recently, a case of fatal progressive multifocal leukoencephalopathy (PML) was reported in a 54-year-old woman with MS who was treated with dimethyl fumarate.<sup>23</sup> Furthermore, 4 cases of PML have previously been described in patients with psoriasis who had received Fumaderm (related fumaric acid esters have been used in Europe since 1994 for the treatment of psoriasis).<sup>24</sup> Prolonged severe lymphopenia (<500 cells per cubic millimeter) that persists for >6 months has been suggested as a risk factor for PML in this patient cohort. Thus, Torkildsen et al<sup>5</sup> have recommended that in patients with persistent lymphopenia who are John Cunningham virus–positive, dimethyl fumarate treatment should be terminated.

### **Currently Approved Agents: Second-Line Therapies**

**Fingolimod.** Fingolimod (Gilenya), a sphingosine 1-phosphate receptor modulator, was the first oral disease-modifying therapy to be approved for the treatment of RRMS and is administered as a capsule taken once daily.<sup>25</sup> Fingolimod antagonizes the sphingosine 1-phosphate receptors on lymphocytes, inhibiting egression of lymphocytes from the lymph nodes and thereby preventing entry of lymphocytes into the blood and their subsequent infiltration into the CNS.<sup>26</sup> A 2010 study published by Cohen et al<sup>27</sup> demonstrated the superior efficacy of oral fingolimod with respect to relapse rates and MR imaging outcomes in patients with MS, compared with intramuscular IFN $\beta$ . In 2012, 2 different neurologic complications of fingolimod treatment came to light. Visser et al<sup>28</sup> reported that MS plaques paradoxically worsened after fingolimod treatment in 3 patients who started fingolimod 3–4 months after stopping another second-line therapy, natalizumab (NTZ). Furthermore, a woman who developed tumefactive MS lesions 6 months after starting fingolimod, without previously receiving NTZ, was described.<sup>28</sup>

A second complication was the development of herpes zoster encephalitis after commencement of fingolimod. Cohen et al<sup>29</sup> described 2 fatal cases of herpes encephalitis in 2 patients on fingolimod therapy. Recent studies have shown that the overall rates of varicella zoster infections in clinical trials were low with fingolimod but higher than in placebo recipients (11 versus 6 per 1000 patient-years).<sup>30</sup>

**Natalizumab.** The migration of lymphocytes across the blood-brain barrier is an important step in the creation of inflammatory lesions in MS, with the presence of leukocytes within the cerebral perivascular spaces deemed a pathologic hallmark.<sup>31</sup> Natalizumab (NTZ, Tysabri) is a monoclonal antibody administered intravenously that binds to proteins on the surface of lymphocytes and inhibits binding of the cell to the luminal surface of blood vessel walls.<sup>32</sup> On MR imaging, NTZ has demonstrated a reduction in the development of new gadolinium-enhancing lesions,<sup>33</sup> and a significant reduction in the conversion of gadolinium-enhancing lesions to T1-hypointense lesions.<sup>34,35</sup> This reduction in lesion formation was greater than the previous reduction of 50%–80% and 30% reported with IFN $\beta$  and glati-

ramer acetate, respectively.<sup>14,36</sup> Even within 2 months of treatment, NTZ has been associated with a >90% reduction in new MR imaging gadolinium-enhancing lesions compared with a placebo.<sup>32</sup> Clinically, patients treated with NTZ have significantly fewer clinical relapses, and it is currently the only disease-modifying therapy to actually improve the Expanded Disability Status Scale in select patients.<sup>37</sup>

In 2005, NTZ was withdrawn from the market as a result of the potentially lethal adverse effect of PML occurring in 3 separately reported patients.<sup>38–40</sup> PML results from an opportunistic infection of the oligodendrocytes caused by the reactivation and replication of the John Cunningham polyomavirus.<sup>41</sup> As of March 4, 2016, 635 cases of PML in patients treated with NTZ have been reported.<sup>42</sup> Despite a widespread understanding of the major risk factors for PML, the overall rate of NTZ-associated PML has nearly doubled between 2012 and 2015.<sup>43</sup> The imaging features of PML are discussed in the Part 2 of this review.

**Alemtuzumab.** Alemtuzumab (Lemtrada) is a monoclonal antibody that effects circulating T- and B-lymphocytes, leading to alterations in the number and functions of lymphocyte subsets.<sup>44</sup> Alemtuzumab received FDA approval in the treatment of RRMS in November 2014. It is administered intravenously during 2 treatment courses for a total of 8 days and is associated with infusion reactions in essentially all treated patients. In its Phase III trials, alemtuzumab, compared with IFN $\beta$  given subcutaneously, reduced the annualized relapse rate by 49%–55%, the rate of disability progression by 30%–42%, and the number of gadolinium-enhancing lesions by 61%–63%.<sup>44,45</sup> Tuohy et al<sup>46</sup> reported secondary autoimmunity as the most frequently reported adverse event posttreatment. Such conditions included thyroid disorders (41% of 86 patients treated) most commonly, followed by immune thrombocytopenic purpura (3.5%) and, rarely, nephropathies, namely Goodpasture syndrome (<1%).<sup>46</sup> Thyroid disorders included hyperthyroidism, hypothyroidism, thyroiditis, and rarely goiter formation. Most cases occurred within 2 years of the last infusion.<sup>45</sup> On the basis of the risk of autoimmune-mediated conditions, monthly blood and urine analyses are recommended for 4 years after the last dose of alemtuzumab.<sup>5</sup>

**Mitoxantrone.** Mitoxantrone is an anthracenedione chemotherapeutic agent that inhibits T-cell activation and reduces proliferation of B- and T-cells.<sup>19</sup> Limited efficacy data are available, but controlled studies of patients with highly active RRMS have shown significant efficacy of the treatment, as shown by a 60%–70% reduction in the relapse rate (compared with placebo or IV steroids) and reduced disability progression and MR imaging evidence of disease activity.<sup>5,47,48</sup> Mitoxantrone is currently the only agent approved to treat secondary-progressive multiple sclerosis.<sup>49</sup> Adverse events such as transient nausea, fatigue, mild hair loss (for days to a week), and menstrual disturbances are frequent (60%–70%).<sup>49</sup> Additional adverse events are urinary tract infection (about 30%) and elevated liver enzymes and leukopenia (about 15%–20%). Although not in the Phase III trial, lethal congestive heart failure and therapy-related leukemia have been reported in treated patients, even years after treatment ends.<sup>50,51</sup> Due to this potential cardiotoxicity, echocardiograms should be performed before, during, and after treatment. Mitoxantrone is

teratogenic and is absolutely contraindicated in pregnancy. The use of mitoxantrone has rapidly decreased due to the risk of severe complications and the increasing number of alternative highly effective and less toxic treatment options.<sup>5</sup>

### **Future Therapeutic Directions**

**Monoclonal Antibodies.** Several other monoclonal antibodies against various lymphocyte surface markers are currently being investigated in the treatment of MS.<sup>4</sup> Daclizumab, an antibody against CD25<sup>+</sup> T-cells, is presently in late-stage clinical trials.<sup>52</sup> Ocrelizumab<sup>53</sup> and ofatumumab,<sup>54</sup> monoclonal antibodies directed against the CD20 surface marker on B-cells, have been designed to minimize infusion-related reactions and are currently under investigation for various forms of MS. Rituximab, a human-mouse chimeric monoclonal antibody against CD20, has also been used off-label for a small group of patients who did not respond to the approved second-line treatments.<sup>55</sup>

**Autologous Hematopoietic Stem Cell Transplantation.** There are published reports of >600 bone marrow–based transplants performed primarily for the treatment of MS.<sup>56</sup> Hematopoietic stem cell transplantation appears to be most beneficial for patients with highly active MS who are progressing and who are refractory to conventional MS therapies.<sup>56,57</sup> It is too early, however, to recommend a more widespread use of hematopoietic stem cell transplantation until more data from randomized controlled trials are available. Currently, there is at least 1 Phase III trial addressing this issue.<sup>57</sup>

### **Role of the Radiologist in MS Surveillance and Pharmacovigilance**

**Standardized Imaging.** MR imaging is the most sensitive tool currently available for monitoring inflammatory disease activity in MS. Clinical assessments far underestimate disease activity and burden compared with MR imaging.<sup>58</sup> The challenge with using MR imaging as a surrogate for clinical outcomes is the lack of standardization and the variability in the interpretation of findings.<sup>58</sup>

The use of MR imaging in the routine follow-up of patients with MS is less straightforward than its use in the diagnostic process, owing largely to the experimental nature of many of the techniques that have been used to measure disease progression.<sup>59</sup> Although follow-up MR imaging studies should be as consistent as possible with baseline or reference scans, fewer sequences are necessary than have been recommended for the initial diagnosis of MS and can be completed in 20–25 minutes.<sup>59,60</sup> Often follow-up imaging can be tailored on the basis of the specific indication. For example, to assess treatment efficacy, FLAIR and T2-weighted spin-echo sequences should be used, whereas DWI, and SWI if available, should also be included for patients at risk of PML.<sup>58,59,61,62</sup>

Gadolinium has routinely been administered in many centers as part of their MS follow-up imaging protocol. Gadolinium-enhancing lesions are considered a marker of blood-brain barrier disruption, which has been associated with acute inflammation in patients with MS.<sup>58,63</sup> Contrast-enhancing lesions are also typically easier to identify than new and/or enlarged T2 hyperintense

### Summary of imaging parameters

Segment	Sequences	Plane	FOV (mm)	Matrix	Thickness (mm)	TR (ms)	TE (ms)	TI (ms)	No. of Signals Acquired
Brain	T2	Axial	220	512 × 384	4	6000.0	100.0	–	1
Brain	FLAIR	Axial	220	320 × 224	4	7500.0	81.0	2500 ms	1
Brain	FLAIR	Sagittal	220	320 × 224	4	7500.0	81.0	2500 ms	1
Brain	T1	Sagittal	230	224 × 224	0.9	2300.0	2.3	–	1
Cervical	T2	Axial	180	256 × 218	3	555.0	17.0	–	2
Cervical	T2	Sagittal	240	384 × 269	3	3000.0	102.0	–	1
Cervical	T1	Sagittal	240	384 × 269	3	600.0	9.5	–	2

lesions, and the process is also less dependent on technical factors such as scan repositioning. Furthermore, some new T2 hyperintense lesions are only detected after being identified as new enhancing lesions, owing to their small size or location in areas with confluent lesions.<sup>64</sup> Interobserver accuracy is also significantly better when looking for gadolinium-enhancing lesions rather than new T2-lesions. A 2013 study by Erbayat Altay et al<sup>65</sup> found that concordance correlation was high (0.8–0.96) for gadolinium-positive lesions, intermediate (0.6–0.8) for new T2 lesions, and very poor (0.0–0.14) for T2 enlarging lesions.

On the other hand, recognition of disease activity cannot rely exclusively on enhancing lesions. New inflammatory lesions take up gadolinium for approximately 3–4 weeks after their development, and the recommended interval between baseline and follow-up scans is typically 6 months.<sup>66</sup> Therefore, although enhancing lesions are useful, they are not sufficiently sensitive to act as sole measures of disease activity.<sup>59</sup> Recent studies have suggested that gadolinium-based contrast agents can accumulate in the brains of patients who have undergone multiple contrast-enhanced MR imaging studies.<sup>67</sup> The most recent guidelines recommend that clinicians carefully evaluate the necessity of gadolinium use and limit it only to those cases in which the additional information provided is clinically significant.<sup>68,69</sup> In light of these studies and the transient nature of enhancing lesions, contrast administration for patients undergoing surveillance MR imaging is not routinely performed at our institution unless there is an unexpected change of clinical status or a high clinical suspicion for relapse of disease.

Standardized patient head positioning and image acquisition, ideally with the same field strength, and access to prior MR imaging are critical for the accurate assessment of changes in lesion size and number with time.<sup>62</sup> All scans should be obtained at field strengths of at least 1.5T. Higher field strengths, for example 3T, have the advantage of detecting a higher lesion load compared with 1.5T imaging.<sup>70</sup> Imaging findings should not be taken out of clinical context. A study performed by Neema et al<sup>71</sup> demonstrated that in healthy subjects, the total number and volume of discrete FLAIR hyperintense foci of age-related and incidental hyperintensities were nearly double on 3T versus 1.5T. In our practice, when comparing 3T imaging with prior 1.5T imaging, we are careful to only declare lesions as new if they are of a size and signal intensity that would have been visible if present on prior 1.5T imaging.

In our institution, MR imaging in suspected or known MS is performed using a 3T MR imaging system (Magnetom Skyra; Siemens, Erlangen, Germany) with acquisition parameters outlined in the Table. We use a guideline-based<sup>58,60,62,72</sup> standardized diagnostic MS brain MR imaging protocol. For brain imaging, we

always include axial 2D T2 TSE, 2D axial and sagittal FLAIR, and 3D pre- and post-contrast-enhanced T1 sequences. Additional sequences may include axial diffusion-weighted imaging and SWI, depending on clinical circumstances. For brain MR imaging surveillance, we do not routinely acquire contrast-enhanced T1 imaging. Our standardized diagnostic and surveillance cervical spinal cord MR imaging protocol always includes sagittal T2 TSE and axial T2 gradient-echo sequences. Optional sequences in the cervical spine include an additional T2-weighted sagittal sequence (eg, STIR and pre- and postcontrast T1 imaging in the sagittal and axial planes). Gadolinium is administered (single dose, 0.1 mmol/kg body weight) with a minimum 5-minute delay before postgadolinium T1 sequence acquisition.<sup>73</sup> A further dose of gadolinium is not administered for MR imaging of the cervical spine, provided it immediately follows the contrast-enhanced brain MR imaging study.

While MR imaging is a powerful noninvasive tool routinely used in the diagnosis and monitoring of MS, certain limitations of conventional MR images exist. FLAIR is one of the most sensitive techniques for visualization of supratentorial white matter lesions<sup>74,75</sup>; however, it is less sensitive than 2D T2 TSE in detecting posterior fossa lesions.<sup>75,76</sup> This difference can be compensated for by using FLAIR at a higher strength magnetic field (3T) and/or with a 3D T2 FLAIR sequence, but T2 TSE remains slightly more sensitive in the detection of infratentorial lesions.<sup>77–79</sup> MS protocols should thus include a T2 TSE sequence, which should be specifically examined when assessing the infratentorial brain.

A second pitfall of routine brain MR imaging sequences is the difficulty in detection of gray matter MS lesions.<sup>80</sup> White matter lesions are readily detected on standard MR imaging protocols; however, most cortical gray matter plaques are not. Cortical gray matter lesions are common in MS<sup>81</sup> and are associated with physical disability and cognitive impairment.<sup>82,83</sup> The difficulty in the detection of cortical gray matter lesions is mainly due to their small size<sup>84</sup> but also due to the lower degree of inflammation associated with cortical lesions, the lower amount of myelin in the cortex compared with white matter, and partial volume artifacts from the adjacent CSF and white matter.<sup>85</sup> Although not routinely available, ultra-high-field MR imaging (for example, 7T) has significantly improved the detection of gray matter cortical lesions.<sup>86</sup> Furthermore, advances in pulse sequences, including double inversion recovery<sup>87,88</sup> or phase-sensitive inversion recovery,<sup>89</sup> are recently developed techniques to overcome this obstacle, which may become more widespread in time.

Third, MR spinal cord imaging is more challenging than brain MR imaging<sup>90</sup> because the spinal cord is long, thin, and mobile. Imaging is made more difficult by ghosting (from

breathing and pulsation of CSF and blood) and truncation artifacts.<sup>91</sup> Poor histopathologic correlation between T2 imaging and MS-associated pathologic spinal cord change is well-described.<sup>92,93</sup> Some authors recommend 2 sets of sagittal images to improve confidence in lesion detection.<sup>90,94</sup> Sagittal sequences could include T2, proton density, STIR, or T1-weighted inversion recovery with phase-sensitive inversion recovery. In our experience, axial imaging is a much more reliable and sensitive technique in the detection of small plaques that often have a more lateral location in the cord (where volume-averaging artifacts are more common on sagittal sequences). We routinely acquire axial imaging through the entire cervical cord (rather than acquire a second sagittal sequence) and more targeted axial imaging in the thoracic cord and conus if potential lesions are seen on sagittal imaging.

### **Imaging the Brain versus the Spinal Cord**

Focal abnormalities in the spinal cord are present in most patients with MS, affecting the cervical region more frequently than the thoracic and lumbar regions.<sup>95</sup> MR imaging of the spinal cord is more challenging than brain MR imaging for reasons outlined above. These inherent features make it difficult to image subtle pathologic changes and to ensure comparability in follow-up examinations. Sagittal T2-weighted MR imaging can demonstrate larger lesions and should always be examined, but axial T2-weighted imaging is the most accurate and useful in detecting the commonly small peripheral lesions.<sup>96</sup>

Although newer imaging modalities have improved the detection of spinal cord lesions in MS,<sup>95</sup> conventional MR imaging still lacks the necessary histopathologic specificity.<sup>97</sup> Recent research has been focused on quantitative techniques such as the measurement of spinal cord atrophy. Spinal cord atrophy correlates with clinical disability,<sup>98-100</sup> and its association with disability is stronger than with focal lesion load.<sup>101</sup> Quantification of spinal cord volume or cross-sectional area with MR imaging may be a potential marker for monitoring the disease course or treatment effectiveness in the future.

Brain imaging is still considered a more sensitive surveillance tool than spinal cord imaging for longitudinal monitoring of patients with MS.<sup>59</sup> Brain imaging is more likely to identify subclinical inflammation, whereas inflammation affecting the spinal cord is more likely to be symptomatic.<sup>102</sup> Several studies have shown that MR imaging of the spinal cord is less sensitive than brain MR imaging for detecting disease activity, particularly with regard to contrast-enhancing lesions, relating mostly to image artifacts associated with vascular and CSF pulsation. Routine spinal imaging is therefore not currently recommended as part of MR imaging surveillance schedules.<sup>103,104</sup> MR imaging of the spinal cord may be indicated when there is significant clinical worsening with few changes on brain MR imaging or to rule out an alternative cause of progressive myelopathy, such as cervical spondylosis or a tumor. Routine follow-up with spinal cord imaging may be useful in patients with known spinal cord disease, in rare cases of recurrent transverse myelitis to assess response to therapy, or in new disease activity.<sup>58</sup>

### **Pharmacovigilance on Disease-Modifying Therapy and Frequency of Surveillance**

Several guidelines have attempted to define the indications for and frequency of serial MR imaging in patients with an established diagnosis of MS.<sup>62,105,106</sup>

Follow-up MR imaging should be performed on at least an annual basis in patients with MS, especially for the first 2 or 3 years after starting therapy. However, certain patients at risk of serious treatment-related adverse events may need to be monitored more frequently, for example, every 3–4 months.<sup>59</sup> A 2015 publication by the Magnetic Resonance Imaging in MS Consortium recommends that patients be evaluated with MR imaging after each unexpected clinical presentation whether typical or atypical of MS.<sup>59</sup>

Since the approval of the most recent generation of MS therapeutics, the importance of the role of MR imaging in MS drug surveillance is increasing. The aims of MR imaging drug surveillance include detection of unexpected MS disease activity, paradoxical reactions (eg, tumefactive demyelinating lesions), comorbidities (eg, vascular, neoplastic), and adverse effects such as PML and other opportunistic infections.<sup>107,108</sup> The importance of strict pharmacovigilance has been recognized for many years, but it has gained additional clinical relevance with the potential for a broader spectrum of adverse findings than with earlier therapies.<sup>109</sup>

Part 2 of this review will discuss the recommended frequency of MR imaging for patients, depending on their treatment regimen and their unique risk profile. Further, it will focus on the imaging features that are important for neuroradiologists to be aware of when interpreting images in patients being treated with the most recent MS medications. The second part of this review will also examine the various methods for assessing the radiologic response to MS therapies. Finally, it covers future areas and technologies that may make the accomplishment of the above tasks more reliable and efficient.

### **REFERENCES**

1. Orton SM, Herrera BM, Yee IM, et al; Canadian Collaborative Study Group. **Sex ratio of multiple sclerosis in Canada: a longitudinal study.** *Lancet Neurol* 2006;5:932–36 CrossRef Medline
2. McDonald WI, Compston A, Edan G, et al. **Recommended diagnostic criteria for multiple sclerosis: guidelines from the International Panel on the Diagnosis of Multiple Sclerosis.** *Ann Neurol* 2001;50:121–27 CrossRef Medline
3. Polman CH, Reingold SC, Banwell B, et al. **Diagnostic criteria for multiple sclerosis: 2010 revisions to the McDonald criteria.** *Ann Neurol* 2011;69:292–302 CrossRef Medline
4. Straus Farber R, Harel A, Lublin F. **Novel agents for relapsing forms of multiple sclerosis.** *Annu Rev Med.* 2016;67:309–21 CrossRef Medline
5. Torkildsen Ø, Myhr KM, Bø L. **Disease-modifying treatments for multiple sclerosis: a review of approved medications.** *Eur J Neurol* 2016;23(suppl 1):18–27 CrossRef Medline
6. IFNB Multiple Sclerosis Study Group. **Interferon beta-1b is effective in relapsing-remitting multiple sclerosis, I: clinical results of a multicenter, randomized, double-blind, placebo-controlled trial.** *Neurology* 1993;43:655–61 CrossRef Medline
7. Jacobs LD, Cookfair DL, Rudick RA, et al. **Intramuscular interferon beta-1a for disease progression in relapsing multiple sclerosis: the Multiple Sclerosis Collaborative Research Group (MSCRG).** *Ann Neurol* 1996;39:285–94 CrossRef Medline
8. Ebers GC; PRISMS (Prevention of Relapses and Disability by Inter-

- feron  $\beta$ -1a Subcutaneously in Multiple Sclerosis) Study Group. **Randomised double-blind placebo-controlled study of interferon beta-1a in relapsing/remitting multiple sclerosis.** *Lancet* 1998;352:1498–504 CrossRef Medline
9. Kappos L, Polman CH, Freedman MS, et al. **Treatment with interferon beta-1b delays conversion to clinically definite and McDonald MS in patients with clinically isolated syndromes.** *Neurology* 2006;67:1242–49 CrossRef Medline
  10. Jacobs LD, Beck RW, Simon JH, et al. **Intramuscular interferon beta-1a therapy initiated during a first demyelinating event in multiple sclerosis: CHAMPS Study Group.** *N Engl J Med* 2000;343:898–904 CrossRef Medline
  11. Comi G, Filippi M, Barkhof F, et al; Early Treatment of Multiple Sclerosis Study Group. **Effect of early interferon treatment on conversion to definite multiple sclerosis: a randomised study.** *Lancet* 2001;357:1576–82 CrossRef Medline
  12. Weinstock-Guttman B. **An update on new and emerging therapies for relapsing-remitting multiple sclerosis.** *Am J Manag Care* 2013;19(17 suppl):s343–54 Medline
  13. Michel L, Laroche C, Prat A. **Update on treatments in multiple sclerosis.** *Presse Med* 2015;44(4 pt 2):e137–51 CrossRef Medline
  14. Comi G, Filippi M, Wolinsky JS. **European/Canadian multicenter, double-blind, randomized, placebo-controlled study of the effects of glatiramer acetate on magnetic resonance imaging-measured disease activity and burden in patients with relapsing multiple sclerosis: European/Canadian Glatiramer Acetate Study Group.** *Ann Neurol* 2001;49:290–97 Medline
  15. Johnson KP, Brooks BR, Cohen JAM, et al; Copolymer 1 Multiple Sclerosis Study Group. **Copolymer 1 reduces relapse rate and improves disability in relapsing-remitting multiple sclerosis: results of a phase III multicenter, double-blind, placebo-controlled trial.** *Neurology* 1995;45:1268–76 CrossRef Medline
  16. Wingerchuk DM, Carter JL. **Multiple sclerosis: current and emerging disease-modifying therapies and treatment strategies.** *Mayo Clin Proc* 2014;89:225–40 CrossRef Medline
  17. English C, Aloji JJ. **New FDA-approved disease-modifying therapies for multiple sclerosis.** *Clin Ther* 2015;37:691–715 CrossRef Medline
  18. O'Connor P, Wolinsky JS, Confavreux C, et al; TEMSO Trial Group. **Randomized trial of oral teriflunomide for relapsing multiple sclerosis.** *N Engl J Med* 2011;365:1293–303 CrossRef Medline
  19. Cross AH, Naismith RT. **Established and novel disease-modifying treatments in multiple sclerosis.** *J Intern Med* 2014;275:350–63 CrossRef Medline
  20. He D, Xu Z, Dong S, et al. **Teriflunomide for multiple sclerosis.** *Cochrane Database Syst Rev* 2012;12:CD009882 CrossRef Medline
  21. Gold R, Kappos L, Arnold DL, et al; DEFINE Study Investigators. **Placebo-controlled phase 3 study of oral BG-12 for relapsing multiple sclerosis.** *N Engl J Med* 2012;367:1098–107 CrossRef Medline
  22. Fox RJ, Miller DH, Phillips JT, et al; CONFIRM Study Investigators. **Placebo-controlled phase 3 study of oral BG-12 or glatiramer in multiple sclerosis.** *N Engl J Med* 2012;367:1087–97 CrossRef Medline
  23. Rosenkranz T, Novas M, Terborg C. **PML in a patient with lymphocytopenia treated with dimethyl fumarate.** *N Engl J Med* 2015;372:1476–78 CrossRef Medline
  24. Sweetser MT, Dawson KT, Bozic C. **Manufacturer's response to case reports of PML.** *N Engl J Med* 2013;368:1659–61 CrossRef Medline
  25. Izquierdo G, O'Connor P, Montalban X, et al. **Five-year results from a phase 2 study of oral fingolimod in relapsing multiple sclerosis.** *Mult Scler J* 2014;20:877–81 CrossRef Medline
  26. Bourdette D, Gilden D. **Fingolimod and multiple sclerosis: four cautionary tales.** *Neurology* 2012;79:1942–43 CrossRef Medline
  27. Cohen JA, Barkhof F, Comi G, et al; TRANSFORMS Study Group. **Oral fingolimod or intramuscular interferon for relapsing multiple sclerosis.** *N Engl J Med* 2010;362:402–15 CrossRef Medline
  28. Visser F, Wattjes MP, Pouwels PJ, et al. **Tumefactive multiple sclerosis lesions under fingolimod treatment.** *Neurology* 2012;79:2000–03 CrossRef Medline
  29. Cohen JA, Chun J. **Mechanisms of fingolimod's efficacy and adverse effects in multiple sclerosis.** *Ann Neurol* 2011;69:759–77 CrossRef Medline
  30. Arvin AM, Wolinsky JS, Kappos L, et al. **Varicella-zoster virus infections in patients treated with fingolimod: risk assessment and consensus recommendations for management.** *JAMA Neurol* 2015;72:31–39 CrossRef Medline
  31. Lucchinetti C, Brück W, Parisi J, et al. **Heterogeneity of multiple sclerosis lesions: implications for the pathogenesis of demyelination.** *Ann Neurol* 2000;47:707–17 Medline
  32. Polman CH, O'Connor PW, Havrdova E, et al; AFFIRM Investigators. **A randomized, placebo-controlled trial of natalizumab for relapsing multiple sclerosis.** *N Engl J Med* 2006;354:899–910 CrossRef Medline
  33. Miller DH, Khan OA, Sheremata WA, et al; International Natalizumab Multiple Sclerosis Trial Group. **A controlled trial of natalizumab for relapsing multiple sclerosis.** *N Engl J Med* 2003;348:15–23 CrossRef Medline
  34. Rudick R, Polman C, Clifford D, et al. **Natalizumab: bench to bedside and beyond.** *JAMA Neurol* 2013;70:172–82 CrossRef Medline
  35. Dalton CM, Miszkiel KA, Barker GJ, et al. **Effect of natalizumab on conversion of gadolinium enhancing lesions to T1 hypointense lesions in relapsing multiple sclerosis.** *J Neurol* 2004;251:407–13 CrossRef Medline
  36. Li DKB, Paty DW. **Magnetic resonance imaging results of the PRISMS trial: a randomized, double-blind, placebo-controlled study of interferon- $\beta$ 1a in relapsing-remitting multiple sclerosis: prevention of relapses and disability by interferon-beta 1a subcutaneously in multiple sclerosis.** *Ann Neurol* 1999;46:197–206 Medline
  37. Belachew S, Phan-Ba R, Bartholomé E, et al. **Natalizumab induces a rapid improvement of disability status and ambulation after failure of previous therapy in relapsing-remitting multiple sclerosis.** *Eur J Neurol* 2011;18:240–45 CrossRef Medline
  38. Kleinschmidt-DeMasters BK, Tyler KL. **Progressive multifocal leukoencephalopathy complicating treatment with natalizumab and interferon beta-1a for multiple sclerosis.** *N Engl J Med* 2005;353:369–74 CrossRef Medline
  39. Langer-Gould A, Atlas SW, Green AJ, et al. **Progressive multifocal leukoencephalopathy in a patient treated with natalizumab.** *N Engl J Med* 2005;353:375–81 CrossRef Medline
  40. Van Assche G, Van Ranst M, Sciot R, et al. **Progressive multifocal leukoencephalopathy after natalizumab therapy for Crohn's disease.** *N Engl J Med* 2005;353:362–68 CrossRef Medline
  41. Clifford DB, De Luca A, DeLuca A, et al. **Natalizumab-associated progressive multifocal leukoencephalopathy in patients with multiple sclerosis: lessons from 28 cases.** *Lancet Neurol* 2010;9:438–46 CrossRef Medline
  42. Biogen Idec MedInfo. <https://medinfo.biogenidec.com/>. Accessed June 15, 2016
  43. Berger JR, Fox RJ. **Reassessing the risk of natalizumab-associated PML.** *J Neurovirol* 2016;22:533–35 CrossRef Medline
  44. Cohen JA, Coles AJ, Arnold DL, et al; CARE-MS I investigators. **Alemtuzumab versus interferon beta 1a as first-line treatment for patients with relapsing-remitting multiple sclerosis: a randomised controlled phase 3 trial.** *Lancet* 2012;380:1819–28 CrossRef Medline
  45. Coles AJ, Twyman CL, Arnold DL, et al; CARE-MS II investigators. **Alemtuzumab for patients with relapsing multiple sclerosis after disease-modifying therapy: a randomised controlled phase 3 trial.** *Lancet* 2012;380:1829–39 CrossRef Medline
  46. Tuohy O, Costelloe L, Hill-Cawthorne G, et al. **Alemtuzumab treatment of multiple sclerosis: long-term safety and efficacy.** *J Neurol Neurosurg Psychiatry* 2015;86:208–15 CrossRef Medline
  47. Millefiorini E, Gasperini C, Pozzilli C, et al. **Randomized placebo-controlled trial of mitoxantrone in relapsing-remitting multiple**

- sclerosis: 24-month clinical and MRI outcome. *J Neurol* 1997;244: 153–59 CrossRef Medline
48. Martinelli V, Radaelli M, Straffi L, et al; Mitoxantrone in Multiple Sclerosis Study Group (MIMS). **Mitoxantrone: benefits and risks in multiple sclerosis patients.** *Neurol Sci* 2009;30(suppl 2):S167–70 CrossRef Medline
  49. Hartung H-P, Gonsette R, König N, et al. **Mitoxantrone in progressive multiple sclerosis: a placebo-controlled, double-blind, randomised, multicentre trial.** *Lancet* 2002;360:2018–25 CrossRef Medline
  50. Martinelli V, Cocco E, Capra R, et al; Italian Mitoxantrone Group. **Acute myeloid leukemia in Italian patients with multiple sclerosis treated with mitoxantrone.** *Neurology* 2011;77: 1887–95 CrossRef Medline
  51. Ellis R, Brown S, Boggild M. **Therapy-related acute leukaemia with mitoxantrone: four years on, what is the risk and can it be limited?** *Mult Scler* 2015;21:642–45 CrossRef Medline
  52. Wynn D, Kaufman M, Montalban X, et al; CHOICE investigators. **Daclizumab in active relapsing multiple sclerosis (CHOICE study): a phase 2, randomised, double-blind, placebo-controlled, add-on trial with interferon beta.** *Lancet Neurol* 2010;9:381–90 CrossRef Medline
  53. Kappos L, Li D, Calabresi PA, et al. **Ocrelizumab in relapsing-remitting multiple sclerosis: a phase 2, randomised, placebo-controlled, multicentre trial.** *Lancet* 2011;378:1779–87 CrossRef Medline
  54. Sorensen PS, Lisby S, Grove R, et al. **Safety and efficacy of ofatumumab in relapsing-remitting multiple sclerosis: a phase 2 study.** *Neurology* 2014;82:573–81 CrossRef Medline
  55. Hauser SL, Waubant E, Arnold DL, et al; HERMES Trial Group. **B-cell depletion with rituximab in relapsing-remitting multiple sclerosis.** *N Engl J Med* 2005;358:676–88 Medline
  56. Atkins HL, Freedman MS. **Hematopoietic stem cell therapy for multiple sclerosis: top 10 lessons learned.** *Neurotherapeutics*. 2013; 10:68–76 CrossRef Medline
  57. Burman J, Iacobaeus E, Svenningsson A, et al. **Autologous haematopoietic stem cell transplantation for aggressive multiple sclerosis: the Swedish experience.** *J Neurol Neurosurg Psychiatry* 2014;85:1116–21 CrossRef Medline
  58. Traboulsee A, Simon JH, Stone L, et al. **Revised recommendations of the Consortium of MS Centers Task Force for a standardized MRI protocol and clinical guidelines for the diagnosis and follow-up of multiple sclerosis.** *AJNR Am J Neuroradiol* 2016; 37:394–401 CrossRef Medline
  59. Wattjes MP, Rovira À, Miller D, et al; MAGNIMS study group. **Evidence-based guidelines: MAGNIMS consensus guidelines on the use of MRI in multiple sclerosis—establishing disease prognosis and monitoring patients.** *Nat Rev Neurol* 2015;11:597–606 CrossRef Medline
  60. Rovira À, Wattjes MP, Tintoré M, et al; MAGNIMS study group. **Evidence-based guidelines: MAGNIMS consensus guidelines on the use of MRI in multiple sclerosis—clinical implementation in the diagnostic process.** *Nat Rev Neurol* 2015;11:471–82 CrossRef Medline
  61. Hodel J, Outteryck O, Dubron C, et al. **Asymptomatic progressive multifocal leukoencephalopathy associated with natalizumab: diagnostic precision with MR imaging.** *Radiology* 2016;278:863–72 CrossRef Medline
  62. Simon JH, Li D, Traboulsee A, et al. **Standardized MR imaging protocol for multiple sclerosis: Consortium of MS Centers consensus guidelines.** *AJNR Am J Neuroradiol* 2006;27:455–61 Medline
  63. Rovira À, Auger C, Alonso J. **Magnetic resonance monitoring of lesion evolution in multiple sclerosis.** *Ther Adv Neurol Disord* 2013; 6:298–310 CrossRef Medline
  64. Miller DH, Barkhof F, Nauta JP. **Gadolinium enhancement increases the sensitivity of MRI in detecting disease activity in multiple sclerosis.** *Brain* 1993;116:1077–94 CrossRef Medline
  65. Erbayat Altay EE, Fisher E, Jones SE, et al. **Reliability of classifying multiple sclerosis disease activity using magnetic resonance imaging in a multiple sclerosis clinic.** *JAMA Neurol* 2013;70:338–44 CrossRef Medline
  66. Cotton F, Weiner HL, Jolesz FA, et al. **MRI contrast uptake in new lesions in relapsing-remitting MS followed at weekly intervals.** *Neurology* 2003;60:640–46 CrossRef Medline
  67. Kanda T, Fukusato T, Matsuda M, et al. **Gadolinium-based contrast agent accumulates in the brain even in subjects without severe renal dysfunction: evaluation of autopsy brain specimens with inductively coupled plasma mass spectroscopy.** *Radiology* 2015;276:228–32 CrossRef Medline
  68. Stojanov D, Aracki-Trenkic A, Benedeto-Stojanov D. **Gadolinium deposition within the dentate nucleus and globus pallidus after repeated administrations of gadolinium-based contrast agents: current status.** *Neuroradiology* 2016;58:433–41 CrossRef Medline
  69. Gadolinium-based contrast agents for magnetic resonance imaging (MRI): drug safety communication – FDA evaluating the risk of brain deposits with repeated use. July 27, 2015. <https://www.fda.gov/Safety/MedWatch/SafetyInformation/SafetyAlertsforHumanMedicalProducts/ucm456012.htm>. Accessed May 9, 2016
  70. Stankiewicz JM, Glanz BI, Healy BC, et al. **Brain MRI lesion load at 1.5T and 3T versus clinical status in multiple sclerosis.** *J Neuroimaging* 2011;21:e50–e6 CrossRef Medline
  71. Neema M, Guss ZD, Stankiewicz JM, et al. **Normal findings on brain fluid-attenuated inversion recovery MRI scans at 3T.** *AJNR Am J Neuroradiol* 2009;30:911–16 CrossRef Medline
  72. Lövsblad KO, Anzalone N, Dörfler A, et al. **MR imaging in multiple sclerosis: review and recommendations for current practice.** *AJNR Am J Neuroradiol* 2010;31:983–89 CrossRef Medline
  73. Uysal E, Erturk SM, Yildirim H, et al. **Sensitivity of immediate and delayed gadolinium-enhanced MRI after injection of 0.5 M and 1.0 M gadolinium chelates for detecting multiple sclerosis lesions.** *AJR Am J Roentgenol* 2007;188:697–702 CrossRef Medline
  74. Bakshi R, Ariyaratana S, Benedict RH, et al. **Fluid-attenuated inversion recovery magnetic resonance imaging detects cortical and juxtacortical multiple sclerosis lesions.** *Arch Neurol* 2001;58: 742–78 CrossRef Medline
  75. Gawne-Cain ML, O’Riordan JI, Thompson AJ, et al. **Multiple sclerosis lesion detection in the brain: a comparison of fast fluid-attenuated inversion recovery and conventional T2-weighted dual spin echo.** *Neurology* 1997;49:364–70 CrossRef Medline
  76. Youstry TA, Filippi M, Becker C, et al. **Comparison of MR pulse sequences in the detection of multiple sclerosis lesions.** *AJNR Am J Neuroradiol* 1997;18:959–63 Medline
  77. Wattjes MP, Lutterbey GG, Harzheim M, et al. **Imaging of inflammatory lesions at 3.0 Tesla in patients with clinically isolated syndromes suggestive of multiple sclerosis: a comparison of fluid-attenuated inversion recovery with T2 turbo spin-echo.** *Eur Radiol* 2006;16:1494–500 CrossRef Medline
  78. Mills RJ, Young CA, Smith ETS. **3D MRI in multiple sclerosis: a study of three sequences at 3 T.** *Br J Radiol* 2007;80:307–20 CrossRef Medline
  79. Moraal B, Roosendaal SD, Pouwels PJ, et al. **Multi-contrast, isotropic, single-slab 3D MR imaging in multiple sclerosis.** *Eur Radiol* 2008;18:2311–20 CrossRef Medline
  80. Daams M, Geurts JJ, Barkhof F. **Cortical imaging in multiple sclerosis: recent findings and ‘grand challenges.’** *Curr Opin Neurol* 2013;26:345–52 CrossRef Medline
  81. Kutzelnigg A, Lucchinetti CF, Stadelmann C, et al. **Cortical demyelination and diffuse white matter injury in multiple sclerosis.** *Brain* 2005;128(pt 11):2705–12 CrossRef Medline
  82. Fisniku LK, Chard DT, Jackson JS, et al. **Gray matter atrophy is related to long-term disability in multiple sclerosis.** *Ann Neurol* 2008;64:247–54 CrossRef Medline
  83. Morgen K, Sammer G, Courtney SM, et al. **Evidence for a direct association between cortical atrophy and cognitive impairment in relapsing-remitting MS.** *Neuroimage* 2006;30:891–98 CrossRef Medline

84. Seewann AM, Kooi EJ, Roosendaal SD, et al. **Postmortem verification of MS cortical lesion detection with 3D DIR.** *Neurology* 2012; 78:302–08 CrossRef Medline
85. Peterson JW, Bö L, Mörk S, et al. **Transected neurites, apoptotic neurons, and reduced inflammation in cortical multiple sclerosis lesions.** *Ann Neurol* 2001;50:389–400 CrossRef Medline
86. Kilsdonk ID, Jonkman LE, Klaver R, et al. **Increased cortical grey matter lesion detection in multiple sclerosis with 7 T MRI: a post-mortem verification study.** *Brain* 2016;139(pt 5):1472–81 CrossRef Medline
87. Nelson F, Poonawalla AH, Hou P, et al. **Improved identification of intracortical lesions in multiple sclerosis with phase-sensitive inversion recovery in combination with fast double inversion recovery MR imaging.** *AJNR Am J Neuroradiol* 2007;28:1645–49 CrossRef Medline
88. Wattjes MP, Lutterbey GG, Gieseke J, et al. **Double inversion recovery brain imaging at 3T: diagnostic value in the detection of multiple sclerosis lesions.** *AJNR Am J Neuroradiol* 2007;28:54–59 Medline
89. Sethi V, Yousry TA, Muhlert N, et al. **Improved detection of cortical MS lesions with phase-sensitive inversion recovery MRI.** *J Neurol Neurosurg Psychiatry* 2012;83:877–82 CrossRef Medline
90. Lycklama G, Thompson A, Filippi M, et al. **Spinal-cord MRI in multiple sclerosis.** *Lancet Neurol* 2003;2:555–62 CrossRef Medline
91. Curtin AJ, Chakeres DW, Bulas R, et al. **MR imaging artifacts of the axial internal anatomy of the cervical spinal cord.** *AJR Am J Roentgenol* 1989;152:835–42 CrossRef Medline
92. Bergers E, Bot JC, van der Valk VP, et al. **Diffuse signal abnormalities in the spinal cord in multiple sclerosis: direct postmortem in situ magnetic resonance imaging correlated with in vitro high-resolution magnetic resonance imaging and histopathology.** *Ann Neurol* 2002;51:652–56 CrossRef Medline
93. Bergers E, Bot JC, De Groot CJ, et al. **Axonal damage in the spinal cord of MS patients occurs largely independent of T2 MRI lesions.** *Neurology* 2002;59:1766–71 CrossRef Medline
94. Stankiewicz JM, Neema M, Alsop DC, et al. **Spinal cord lesions and clinical status in multiple sclerosis: a 1.5 T and 3 T MRI study.** *J Neurol Sci* 2009;279:99–105 CrossRef Medline
95. Lukas C, Sombekke MH, Bellenberg B, et al. **Relevance of spinal cord abnormalities to clinical disability in multiple sclerosis: MR imaging findings in a large cohort of patients.** *Radiology* 2013;269: 542–52 CrossRef Medline
96. Lycklama à Nijeholt GJ, Barkhof F, Castelijns JA, et al. **Comparison of two MR sequences for the detection of multiple sclerosis lesions in the spinal cord.** *AJNR Am J Neuroradiol* 1996;17:1533–38 Medline
97. Kidd D, Thorpe JW, Thompson AJ, et al. **Spinal cord MRI using multi-array coils and fast spin echo, II: findings in multiple sclerosis.** *Neurology* 1993;43:2632–37 CrossRef Medline
98. Liu C, Edwards S, Gong Q, et al. **Three dimensional MRI estimates of brain and spinal cord atrophy in multiple sclerosis.** *J Neurol Neurosurg Psychiatry* 1999;66:323–30 CrossRef Medline
99. Bakshi R, Dandamudi VS, Neema M, et al. **Measurement of brain and spinal cord atrophy by magnetic resonance imaging as a tool to monitor multiple sclerosis.** *J Neuroimaging* 2005;15(4 suppl): 30S–45S CrossRef Medline
100. Rashid W, Davies GR, Chard DT, et al. **Increasing cord atrophy in early relapsing-remitting multiple sclerosis: a 3-year study.** *J Neurol Neurosurg Psychiatry* 2006;77:51–55 CrossRef Medline
101. Furby J, Hayton T, Anderson V, et al. **Magnetic resonance imaging measures of brain and spinal cord atrophy correlate with clinical impairment in secondary progressive multiple sclerosis.** *Mult Scler* 2008;14:1068–75 CrossRef Medline
102. Klawiter EC. **Current and new directions in MRI in multiple sclerosis.** *Continuum (Minneapolis Minn)* 2013;19(4 Multiple Sclerosis): 1058–73 CrossRef Medline
103. Silver NC, Good CD, Sormani MP, et al. **A modified protocol to improve the detection of enhancing brain and spinal cord lesions in multiple sclerosis.** *J Neurol* 2001;248:215–24 CrossRef Medline
104. Thorpe JW, Kidd DM, Moseley IF, et al. **Serial gadolinium-enhanced MRI of the brain and spinal cord in early relapsing-remitting multiple sclerosis.** *Neurology* 1996;46:373–78 CrossRef Medline
105. Cook SD, Dhib-Jalbut S, Dowling P, et al. **Use of magnetic resonance imaging as well as clinical disease activity in the clinical classification of multiple sclerosis and assessment of its course: a report from an international CMSC Consensus Conference, March 5–7, 2010.** *Int J MS Care* 2012;14:105–14 CrossRef Medline
106. Verhey LH, Narayanan S, Banwell B. **Standardized magnetic resonance imaging acquisition and reporting in pediatric multiple sclerosis.** *Neuroimaging Clin N Am* 2013;23:217–26.e7 CrossRef Medline
107. Rommer PS, Zettl UK, Kieser B, et al. **Requirement for safety monitoring for approved multiple sclerosis therapies: an overview.** *Clin Exp Immunol* 2014;175:397–407 CrossRef Medline
108. Weber MS, Menge T, Lehmann-Horn K, et al. **Current treatment strategies for multiple sclerosis: efficacy versus neurological adverse effects.** *Curr Pharm Des* 2012;18:209–19 CrossRef Medline
109. Wattjes MP, Steenwijk MD, Stangel M. **MRI in the diagnosis and monitoring of multiple sclerosis: an update.** *Clin Neuroradiol* 2015; 25(suppl 2):157–65 CrossRef Medline

# Current and Emerging Therapies in Multiple Sclerosis: Implications for the Radiologist, Part 2—Surveillance for Treatment Complications and Disease Progression

C. McNamara, G. Sugrue, B. Murray, and P.J. MacMahon



## ABSTRACT

**SUMMARY:** An understanding of the new generation of MS drugs in conjunction with the key role MR imaging plays in the detection of disease progression, opportunistic infections, and drug-related adverse effects is of vital importance to the neuroradiologist. Part 1 of this review outlined the current treatment options available for MS and examined the mechanisms of action of the various medications. It also covered specific complications associated with each form of therapy. Part 2, in turn deals with the subject of pharmacovigilance and the optimal frequency of MRI monitoring for each individual patient, depending on his or her unique risk profile. Special attention is given to the diagnosing of progressive multifocal leukoencephalopathy in patients treated with natalizumab as this is a key area in which neuroradiologists can contribute to improved patient outcomes. This article also outlines the aims of treatment and reviews the possibility of “no evidence of disease activity” becoming a treatment goal with the availability of more effective therapies. Potential future areas and technologies including image subtraction, brain volume measurement and advanced imaging techniques such as double inversion recovery are also reviewed. It is anticipated that such advancements in this rapidly developing field will improve the accuracy of monitoring an individual patient’s response to treatment.

**ABBREVIATIONS:** BV = brain volume; DIR = double inversion recovery; DMT = disease-modifying therapy; IRIS = immune reconstitution inflammatory syndrome; JC virus = John Cunningham virus; MTR = magnetization transfer ratio; NEDA = no evidence of disease activity; NTZ = natalizumab; NTZ PML = natalizumab-associated PML; PML = progressive multifocal leukoencephalopathy; PML IRIS = PML-associated IRIS; PSIR = phase-sensitive inversion recovery

Part 1 of this review covered recent developments in the treatment of MS and discussed the published clinical data on the efficacy and safety of the currently approved and emerging therapies in this condition as they apply to the radiologist. Part 2 will focus on the role of the radiologist in monitoring patients being treated with these medications and will focus on pharmacovigilance, which includes observation for treatment complications and signs of disease progression.

### Frequency of MR Imaging for Drug Monitoring

MR imaging is recommended before the initiation or modification of disease-modifying therapy (DMT) and approximately 6 months after a treatment switch to allow sufficient time for the new therapy to reach its therapeutic potential.<sup>1</sup> Therefore, some authors suggest that the reference scan should be obtained no earlier than 3 months after treatment initiation/change to over-

come the uncertainty about new lesions occurring before the treatment becomes effective.<sup>2</sup> Continued or worsening disease activity on MR imaging while a patient is on a DMT may prompt a change in therapy. There is evolving evidence that ongoing MR imaging activity can be indicative of a suboptimal therapeutic response<sup>3</sup>; however, due to variable pharmacodynamics, the time until MR imaging activity is suppressed differs among the immunomodulatory agents.<sup>4</sup>

Several studies have attempted to define criteria and strategies for the early identification of suboptimal response in individual patients via a combination of clinical and MR imaging measures during the first 6–12 months after treatment initiation.<sup>5–7</sup> These criteria are partially or completely based on the detection of disease activity on follow-up brain MR imaging studies, defined as new gadolinium-enhancing lesions or new and/or enlarging T2 hyperintense lesions.<sup>8</sup>

More frequent surveillance may be indicated in clinically aggressive cases or unusual patterns (eg, tumefactive MS) (Table 1). Clinical judgment and experience are critical in such cases. While guidelines on a tolerable threshold for new lesion activity that warrants a change in therapy have been proposed, individual factors will impact the clinician’s decision as to the exact frequency of MR imaging monitoring and time to switch ther-

From the Departments of Radiology (C.M., G.S., P.J.M.) and Neurology (B.M.), Mater Misericordiae University Hospital, Dublin, Ireland.

Please address correspondence to Peter MacMahon, MD, Department of Radiology, Whitty Bldg, North Circular Rd, Mater Misericordiae University Hospital, Dublin 7, Ireland; e-mail: pmacmahon@mater.ie; @McnamaraCillian

Indicates open access to non-subscribers at www.ajnr.org

<http://dx.doi.org/10.3174/ajnr.A5148>

**Table 1: Frequency of MRI surveillance**

Clinical Indication	Frequency of Imaging	Imaging Protocol
RRMS, routine surveillance	Annually for at least the first 2 or 3 years after starting therapy or switching DMT	T2-weighted and contrast-enhanced T1-weighted
Higher risk patients (positive for JC virus serum antibodies) with >24 mo of NTZ exposure	Every 3–6 months	T2WI, T2 FLAIR, DWI, SWI (if indicated)
Low risk of PML (negative for JC virus serum antibodies)	Annually	T2WI, T2 FLAIR, DWI, SWI (if indicated)
Patients at high risk of developing opportunistic infections who are switching DMT	MRI when the current treatment is discontinued and 3–6 months after the new treatment is started	T2WI, T2 FLAIR, DWI, SWI (if indicated)
Patients who switch from NTZ to other therapeutics (including fingolimod, alemtuzumab, and dimethyl fumarate)	Enhanced pharmacovigilance, including brain MRI every 3–4 mo for up to 12 mo	T2WI, T2 FLAIR, DWI, SWI (if indicated)
Patients who require enhanced pharmacovigilance for other reasons	Every 3–6 mo	As indicated

**Note:**—RRMS indicates relapsing-remitting MS.

**Table 2: Risk stratification of natalizumab-associated PML**

Risk Factors for PML Development in Patients Treated with NTZ	Duration of Therapy $\geq$ 24 Months
Risk stratification of patients	
High risk	Prior immunosuppressive therapy Evidence of JCV antibody seropositivity Presence of anti-JCV antibodies Increased treatment duration, especially beyond 2 yr Immunosuppressant use prior to receiving NTZ High JCV titers
Low risk	Patients negative for anti-JCV antibody (risk is <0.09/1000)
Methods of reducing risk	All patients receiving NTZ should be screened for previous JCV infection Serologic testing for patients negative for JCV every 6 mo Patients positive for JCV who have been treated with NTZ for >2 yr should be switched to another second-line therapy Increased frequency of imaging surveillance for high-risk patients (eg, every 3–4 mo) Comparison of surveillance images with previous MR imaging

**Note:**—JCV indicates John Cunningham virus.

apy.<sup>1,7,9</sup> Isolated worsening on the neurologic examination or brain MR imaging should lead to closer monitoring rather than an immediate switch of therapy; with silent brain MR imaging activity, reassessing the MR imaging in several months is recommended.<sup>10</sup>

### Imaging Surveillance for Opportunistic Infections

Particularly high-risk patients (natalizumab [NTZ] treatment longer than 24 months, serology positive for John Cunningham [JC] virus serology, prior immunosuppression) should be screened every 3–6 months with at least a curtailed MR imaging protocol to include FLAIR, T2-weighted, DWI, and SWI sequences if available.<sup>8</sup> Low-risk patients (JC virus seronegative) can be imaged on an annual basis (Table 2).<sup>8,11</sup> MR imaging-based monitoring of patients for early progressive multifocal leukoencephalopathy (PML) detection is not recommended for those patients treated with NTZ exclusively, but also for patients being treated with other DMTs, including alemtuzumab, fingolimod, and dimethyl fumarate.<sup>12,13</sup> In addition, PML is not the only opportunistic infection that can be observed during MS treatment. MS treatment-related infections include a wide-ranging

spectrum of pathogens such as varicella zoster virus, as has been described in patients treated with fingolimod.<sup>14</sup>

There is now growing evidence that drug-related adverse effects can occur when MS medication is discontinued or even several months after a new treatment is started (so-called “carry over opportunistic infections”). Therefore, strict pharmacovigilance, including frequent MR imaging, should be performed in patients who switch therapies, to detect resurgent MS disease activity and adverse effects such as opportunistic infections.<sup>15–17</sup> In patients at high risk of developing opportunistic infections (eg, immunocompromised patients, those recently treated with a course of immunosuppressants) who are switching DMTs, brain MR imaging is recommended when the current treatment is

discontinued and after the new treatment is started. Thus, heightened pharmacovigilance, including brain MR imaging every 3–4 months for up to 12 months, is required in patients who switch from NTZ to other medications (such as fingolimod, alemtuzumab, and dimethyl fumarate).<sup>8</sup> To date, among patients switching to fingolimod treatment after previous natalizumab therapy, there have been 17 suspected cases of PML.<sup>18</sup>

### Diagnosing PML

Although differentiating between a new MS lesion and an evolving PML lesion can be challenging, radiologists must be familiar with the key imaging features associated with PML because a timely and accurate diagnosis at the asymptomatic stage is associated with improved survival and functional outcome compared with patients identified at the symptomatic stage.<sup>19</sup> MR imaging has been shown to be sensitive in the detection of PML lesions and can identify such lesions several months before the onset of clinical symptoms.<sup>20</sup>

The current diagnostic criteria for PML as established by the American Academy of Neurology include the presence of 3 components: a clinical picture suggestive of PML (eg, behavioral and

**Table 3: MRI Features of PML**

Features	
Location	Subcortical white matter U-fibers Predilection for frontal lobe > occipital lobe > parietal lobe
Size	Small, <3 cm when asymptomatic In symptomatic patients, lesions are often large (>3 cm)
Morphology	Punctate lesions often identified in asymptomatic PML Symptomatic PML typically demonstrates more confluent and diffuse lesions Microcysts No associated edema or mass effect
T1WI and T2WI	FLAIR hyperintensity with corresponding T1 hypointense lesions T1 hypointensity is less pronounced in asymptomatic PML
DWI	Hyperintensity on DWI
T1 postcontrast	30% will demonstrate linear or punctate enhancing lesions; if nodular or rim enhancement is present, active MS plaque or IRIS should be considered
SWI	Low signal intensity in U-fibers
Differential diagnosis	MS plaque Acute disseminated encephalomyelitis Tumefactive lesion Ischemic changes Posterior reversible encephalopathy syndrome

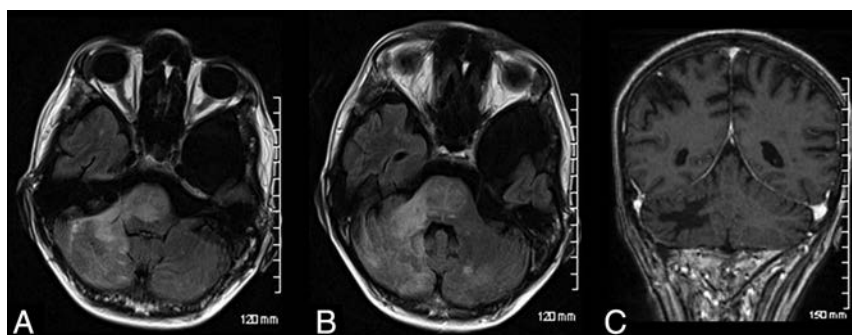


**FIG 1.** Infratentorial natalizumab-associated PML. Axial FLAIR (A and B) images of a patient demonstrating extensive hyperintense signal involving the cerebellum, middle cerebellar peduncle, and pons. This had progressed from prior imaging. Note minimal mass effect. Postadministration of gadolinium, there is no enhancement demonstrated (C).

cognitive abnormalities, progressive weakness, gait abnormalities, visual field deficits, speech and language disturbances, and/or incoordination), biochemical and/or histologic evidence of the JC virus, and MR imaging findings.<sup>21</sup> Compared with symptomatic PML, in which the lesion dissemination typically involves multiple lobes affecting both hemispheres, patients with asymptomatic PML present more frequently with a localized disease in a unilobar and focal distribution.<sup>19,20</sup> Most interesting, compared with other PML cohorts, contrast enhancement can be observed quite frequently in natalizumab-associated PML (NTZ PML), occurring in approximately 30% of all patients at diagnosis, and can be the leading radiologic sign in asymptomatic patients.<sup>22-24</sup>

Substantial evidence indicates that FLAIR is the most sensitive sequence for detecting PML.<sup>22</sup> DWI is known to be highly sensitive for depicting acute demyelination but can also aid in the differentiation of acute PML lesions from chronic and subacute demyelinating MS lesions.<sup>22</sup> In patients with MR imaging lesions suggestive of PML, the MR imaging protocol should be extended to include pre- and postcontrast T1-weighted imaging to detect inflammatory features and the possible coincidence of PML and

PML-immune reconstitution inflammatory syndrome, particularly during MS follow-up imaging.<sup>25,26</sup>

The most common area to be affected by NTZ PML is the frontal lobe, followed in frequency by the occipital lobe and then the parietal lobe (Table 3).<sup>27,28</sup> Like other aggressive infiltrating lesions, PML can also infiltrate the corpus callosum, though isolated corpus callosal involvement is rare.<sup>29</sup> PML lesions occur in the posterior fossa in early PML in approximately 10% of cases at initial presentation (Fig 1).<sup>28</sup> These most commonly involve the cerebellum and middle cerebellar peduncles, though the brain stem can be affected.<sup>27,30</sup> Crescent-shaped lesions involving the middle cerebellar peduncles and adjacent cerebellar and/or pontine white matter may be specific to PML, rather than MS, because they have, so far, only been reported in patients with PML.<sup>30-32</sup> Deep gray matter (including the thalamus and dentate nuclei) PML lesions are unusual (5%) in NTZ PML, particularly in the early disease course.<sup>22</sup>

A 2016 study published in *Radiology* by Hodel et al<sup>27</sup> investigated the radiologic findings of NTZ PML at the asymptomatic stage. They concluded that hyperintensity on DWI and involvement of U-fibers were the most predictive MR imaging features for the diagnosis of asymptomatic NTZ PML. Their results also suggested that punctate lesions may be a highly specific finding

for NTZ PML, being exclusively observed in patients with NTZ PML. Most of the lesions observed in their study involved the frontal lobe as has been previously reported in other studies.<sup>28</sup> They also found that comparison of the patient's current MR images with those from previous MR imaging examinations significantly improved the specificity for the detection of NTZ PML lesions and for the diagnosis of PML (from 88% without to 100% with previous MR imaging;  $P = .05$ ). Recent evidence also suggests that SWI may be of value in the early diagnosis of PML (Fig 2). In particular, low signal intensity observed in U-fibers identified with SWI has been reported as a unique finding in early PML.<sup>33,34</sup> Most interesting, the rate of PML in patients treated for <1 year remains virtually zero. Thus, the patient's length of treatment with natalizumab should be provided to the radiologist when interpreting MR imaging findings.

#### **PML-Immune Reconstitution Inflammatory Syndrome**

In a bid to halt the progression of PML, plasma exchange or immunoadsorption can be used to remove NTZ from the circulation, which allows lymphocytes to cross the BBB once again.<sup>35</sup>

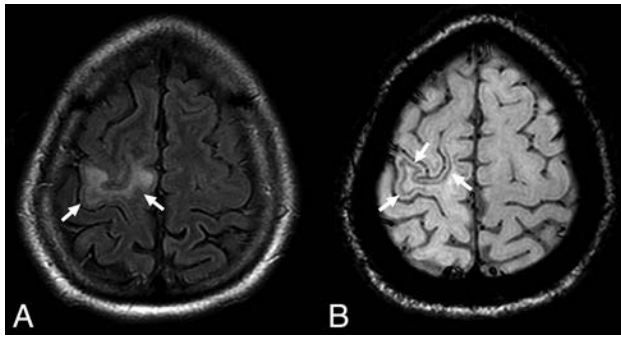


**FIG 2.** A typical example of natalizumab-associated PML. There is a FLAIR hyperintense lesion involving the right precentral gyrus (A, arrows) abutting the cortex. The susceptibility-weighted sequence reveals a hypointense rim involving the subcortical U-fibers adjacent to the PML lesion (B, arrows). Reprinted from Hodel et al.<sup>34</sup>

This sudden restoration of cellular immunity can paradoxically result in the worsening of the patient's neurologic status with the development of immune reconstitution inflammatory syndrome (IRIS).<sup>36</sup> The development of IRIS occurs days to weeks following treatment with plasma exchange or immunoadsorption.<sup>35,36</sup> PML-associated IRIS (PML IRIS) can, however, also occur following the cessation of NTZ alone without plasma exchange.<sup>26</sup> In such cases, immunologic rebound with IRIS takes approximately 3 months postcessation, in keeping with the long half-life of the drug.<sup>37</sup> This represents a challenge for the radiologist because neurologic dysfunction and white matter lesions occurring after NTZ interruption may also be caused by MS exacerbations.<sup>38</sup> The literature suggests that PML IRIS tends to occur first in such cases followed by recurrences of MS activity at later follow-up imaging, suggesting that timing is key to reaching a diagnosis.<sup>17,25,28</sup>

Imaging findings that can assist in the diagnosis of PML IRIS include contrast enhancement and rapid progression of existing PML lesions, which begin to exert mass effect through swelling and edema.<sup>37,39,40</sup> Current data, though limited, suggest that contrast enhancement with either a patchy or punctate pattern in the border of the PML lesion is the most frequent imaging sign in early PML IRIS (Fig 3).<sup>39</sup> Gheuens et al<sup>41</sup> have developed a diagnostic model using proton MR spectroscopy to help differentiate PML IRIS lesions from lesions without IRIS on the basis of their metabolic profile and the presence contrast enhancement.

### Assessing Radiologic Response to Therapy

Several studies have demonstrated that the occurrence of new T2 lesions or gadolinium-enhancing lesions during the first year of a treatment (most studies have investigated treatment with interferon  $\beta$ ) correlates with progression of disability.<sup>42,43</sup> These 2 measures have relevant differences. While contrast-enhancing lesions are considered a marker of acute inflammation in patients with MS, new T2 hyperintense lesions reflect the permanent footprint from a previous focal inflammatory lesion that developed in the interval between 2 scans.<sup>44</sup>

Determining ongoing radiologic stability is based on the presence or absence of new lesions (whether T2-weighted or contrast-enhancing lesions).<sup>5,42,43,45,46</sup> In a large retrospective study of patients with MS on therapy, the presence of  $>2$  contrast-enhancing lesions at 1 year was predictive of poor clinical outcome at 5

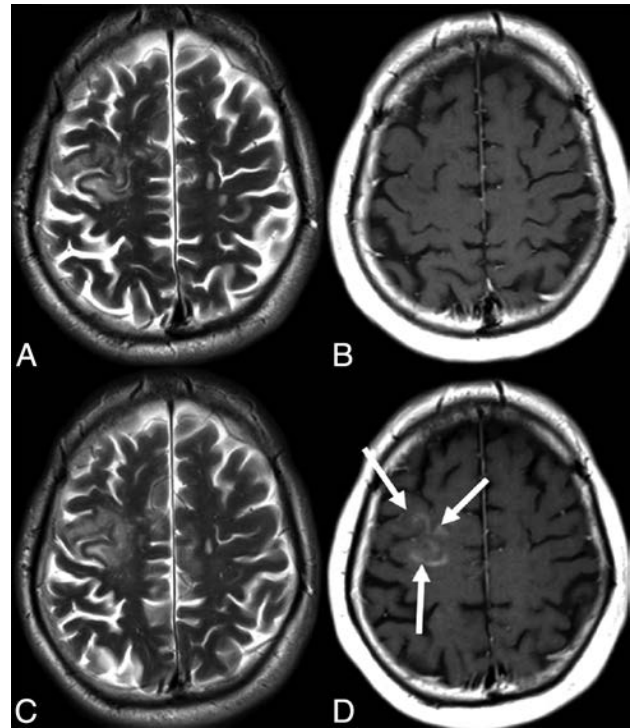


**FIG 3.** Axial T2-weighted and contrast-enhanced T1-weighted images showing imaging signs suggestive of natalizumab-associated PML (A and B) with follow-up imaging post-withdrawal of medication suggestive of PML-immune reconstitution inflammatory syndrome. This patient demonstrates the most frequent pattern of PML IRIS, with patchy contrast enhancement in the border of the lesion (arrows). Reproduced from Wattjes et al<sup>39</sup> with permission from BMJ Publishing Group Ltd.

years.<sup>47</sup> The Barcelona and Cleveland Clinic groups have both shown that the accumulation of a certain number of new T2 lesions, with or without clinical relapse, has a predictive value for disability progression during the next few years.<sup>3,43,48</sup> For example, Rio et al<sup>49</sup> showed that  $\pm 3$  lesions after 1 year of treatment predicted increased disability after 2 years (OR = 8.3, 71% sensitivity, 71% specificity).

A scoring system proposed by Rio et al<sup>50</sup> combines commonly used, short-term (ie, 1-year) treatment measures of disease activity, such as clinical relapses, Expanded Disability Status Scale progression, and active MR imaging lesions, to identify patients at risk of developing new clinical activity (ie, relapses) during the ensuing years. The other novelty provided by this proposed score is the use of the number of new T2 hyperintense MR imaging lesions instead of gadolinium-enhancing lesions. Previous approaches have used gadolinium-enhancing lesions to assess MR imaging activity because they are easier to detect as already mentioned.<sup>42,43,51</sup> The Rio Criteria or the Modified Rio Criteria are guides to prognosis; but unfortunately, their sensitivity and specificity are not considered accurate enough for routine clinical practice.<sup>5,6</sup>

Critics have dismissed T2 lesions as a predictive biomarker because of the moderate-to-poor short-term correlation between the accumulation of lesions and outcome. However, long-term studies are much more informative. For example, in the Queen Square 21-year clinically isolated syndromes follow-up study, T2 lesion load was highly predictive of a poor clinical outcome.<sup>52</sup> In a

meta-analysis from 23 randomized placebo-controlled clinical trials involving 6591 patients, regression models demonstrated that the treatment effect on T2 hyperintense lesions correlated with the effect on relapses.<sup>46</sup> Most interesting, the development of new T2 lesions in patients with MS on DMT is much more predictive of long-term outcome compared with the development of new T2 lesions in patients on no treatment or a placebo.<sup>53-55</sup> Such data make a compelling case for suppressing the development of T2 lesions as a treatment target, with the aim of delaying or preventing the onset of secondary-progressive MS. One drawback of such an approach is that the detection of new T2 hyperintense lesions can be challenging, especially if there is a preexisting high load of lesions, and one has to factor in variable positioning on serial scans and 1.5T-versus-3T lesion detection.<sup>56</sup>

Whereas the classification of new T2 lesions can be more difficult and is more time-consuming, T2 signal alterations are a durable “footprint” of plaque formation and thus a relatively reliable means of ascertaining lesion accumulation.<sup>5</sup> Some of the limitations of T2 lesion counting could be overcome by technological innovations, for example emerging registration and subtraction techniques.<sup>57</sup>

### **Defining “Nonresponders”**

Effective DMT treatment has been shown to be especially beneficial early in the course of MS. Thus, rapid identification of nonresponders is crucial to determine the need for a therapeutic switch.<sup>58</sup> Patients with MS who continue to experience clinical and/or radiologic disease activity despite treatment with DMT are categorized as “nonresponders.”<sup>43,48,50</sup> The response of patients with MS to DMT is very heterogeneous; thus, it is especially difficult to determine whether a particular treatment of choice is producing the desired effect.<sup>48</sup> Proposed scoring methods to identify patients with a suboptimal treatment response on the basis of combined clinical and radiologic measures at follow-up have shown considerable variation.<sup>8</sup> Moreover, such criteria have been developed almost exclusively in patients receiving different formulations of interferon  $\beta$ . Few data are available from patients undergoing treatment with the newer DMTs in clinical practice.<sup>8</sup>

### **Advancing toward “No Evidence of Disease Activity”**

With the introduction of new, more effective therapies, there has been a shift in treatment expectations from partial response to potential remission, with no evidence of disease activity (NEDA) being the new treatment target. NEDA is defined as the following: 1) absence of relapses, 2) absence of sustained disability worsening, and 3) absence of radiologic activity, seen as gadolinium-enhancing lesions or new/enlarged T2-hyperintense lesions (NEDA-3).<sup>59</sup> More recently, this composite outcome has been implemented by also considering the absence of brain volume loss (NEDA-4).<sup>60</sup> The clinical significance of NEDA in the long-term, however, is still lacking, and the concept is still evolving because there is debate over additional measures that could or should be included, such as loss of brain volume as a marker.<sup>61,62</sup> Realistically because DMT is only partially effective, some lesion accumulation is an expected outcome for patients treated with these therapies and neurologists do not routinely switch DMTs with minor asymptomatic relapses.<sup>61</sup> While new T2 lesions during treatment

are undesirable, studies are heterogeneous in relation to the number of new lesions considered significant disease activity. In a recent systematic review investigating the role of MR imaging in the assessment of treatment response to interferon  $\beta$ , pooled data of new T2 lesions did not show statistical significance for those patients with only 1 new T2 lesion per year.<sup>63</sup> A 2016 study published by Prosperini et al<sup>64</sup> showed that 34% of patients treated with natalizumab achieved NEDA-3 at 7-year follow-up.

From the clinician’s point of view, there are multiple justifications for switching therapies. First, MS involves diverse pathologic mechanisms that no single DMT addresses. Second, MS is heterogeneous, and one might expect a given agent to work better in one patient than another. Third and perhaps most important, no DMT actually cures MS. Approximately 30% of patients show a suboptimal therapeutic response during the early treatment years.<sup>65,66</sup> Therefore, NEDA may be an unrealistic long-term expectation, especially when economic factors and adverse effects are taken into account. There are no uniform criteria for choosing the initial DMT to be trialed in an individual patient. This decision is guided by drug, disease, and patient considerations; personal preferences and experiences; and economic and availability factors. Most initial treatment choices would involve a first-line agent before consideration is given to a second-line agent such as NTZ.

### **Future Areas**

**Brain Atrophy as a Marker.** Numerous studies have used MR imaging–derived methods to assess brain volume (BV) changes in MS, revealing that atrophy can be present even in the early stages of the condition and that it progresses during the disease course.<sup>67,68</sup> Several MR imaging studies consistently reported associations between whole-brain gray matter loss and increases of lesion load.<sup>69,70</sup> The clinical relevance of brain atrophy is well-known: Compared with measures of lesion load, brain atrophy shows better correlations with progression of disability and cognitive impairment, with gray matter atrophy being more closely associated with clinical dysfunction than white matter atrophy.<sup>71</sup> The overall effect of treatment on brain atrophy can be reflective of the effect of the therapy on disability.<sup>55</sup> The more recent DMTs have been shown to decrease rates of brain atrophy when compared with a placebo.<sup>72</sup> Thus, recent clinical trials have incorporated BV outcomes as a measure of treatment effect.<sup>73</sup> Current methods for measuring BV in radiology are usually automated software that either uses a segmentation-based approach (such as statistical parametric mapping) for cross-sectional data or a registration-based approach (such as structural image evaluation with normalization of atrophy) for longitudinal analysis.<sup>72</sup> Unfortunately, the clinical interpretation of BV loss in patients with MS can often be difficult with other confounding factors such as hydration status and ongoing inflammation at the time of treatment onset.<sup>74</sup> Moreover, differences in the quality and capabilities of MR imaging hardware and in the software packages used for analysis or processing can generate notable variability in brain atrophy assessment.<sup>71,75</sup>

In many trials, DMTs have produced only moderate evidence of a reduction in BV loss. This is because anti-inflammatory agents have been shown to increase the rate of BV reduction

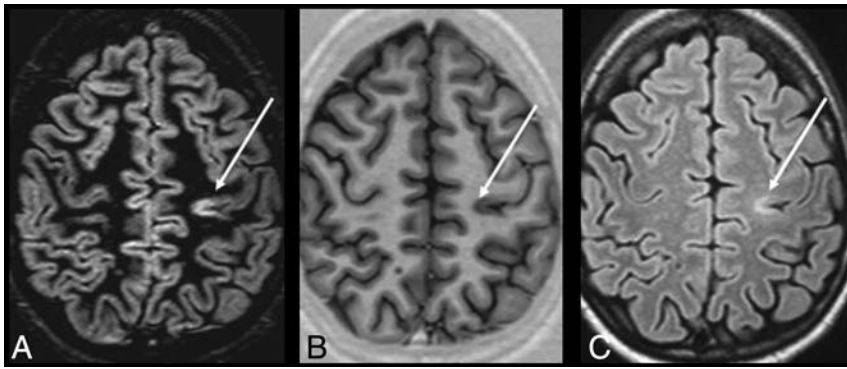


**FIG 4.** DIR (A), PSIR (B), and FLAIR (C) images from a single patient with MS at the same section location. An intracortical lesion is evident in the left parietal area. Also, note the excellent overall delineation of the gray-white matter border on PSIR. Reprinted from Nelson et al.<sup>100</sup>

within the first 6 months to 1 year of treatment, followed by stabilization during the second year of treatment.<sup>76</sup> Resolution of this inflammation will lead to an initial accelerated BV loss that has been described as a “pseudoatrophy” effect.<sup>73</sup> Therefore, the most clinically efficacious drugs (with a high impact on inflammation), such as natalizumab,<sup>77–79</sup> fingolimod<sup>80</sup> or high-dose interferon  $\beta$ ,<sup>81</sup> will tend to produce larger-than-placebo BV decreases during the first months of therapy, which, at least in part, may not be related to true tissue damage. The difficulties in clinical interpretation of BV loss outlined above such as the pseudoatrophy effect explain why this novel technique is not currently employed in routine clinical use.

**Image Subtraction to Detect New Lesions.** A second area of growing interest is the accurate detection of active lesions and its achievement. Both new and enlarging lesions, imaged with standard serial nonregistered 2D images, are complicated by repositioning errors and a background of unaltered nonactive lesions.<sup>82</sup> Subtraction images, after image registration, provide an alternative strategy in which the effect of repositioning errors is reduced, cancelling out radiologically stable disease. In both single-center and multicenter settings, 2D subtraction images depicted higher numbers of active lesions with greater interobserver agreement compared with nonregistered 2D T2-weighted spin-echo images.<sup>83,84</sup> Image subtraction can overcome issues associated with differentiating old T2 lesions from new T2 lesions, thus providing good visualization and quantification of active and resolving lesions.<sup>85</sup> Recent data have shown that automated identification of new or enlarging T2 lesions is robust, accurate, and sensitive, thus supporting its use for evaluating treatment efficacy in clinical trials.<sup>86</sup> Long-interval T2-weighted sequences can be processed with automated subtraction, which has been used in a multicenter trial to provide greater power for assessing treatment efficacy than is possible with monthly contrast-enhanced T1-weighted imaging.<sup>85,87</sup> However, subtraction requires time-consuming postprocessing steps, and the process can be susceptible to imaging artifacts.

**Advanced Imaging Techniques.** A broadening spectrum of emerging MR imaging techniques allows a more specific evaluation of MS pathology. Included in these new methods are the following: magnetization transfer ratio (MTR), diffusion tensor

imaging, restricted proton fraction, and positron-emission tomography techniques.<sup>4</sup> Furthermore, additional pulse sequences such as double inversion recovery (DIR) and phase-sensitive inversion recovery (PSIR) have improved the detection rate of cortical lesions.<sup>88,89</sup>

Although conventional MR imaging is very sensitive to macroscopic lesions, it lacks sensitivity to the microscopic pathology. Diffusion MR imaging techniques, including DTI and diffusional kurtosis imaging, are sensitive to diffuse microscopic injury in the normal-appearing white matter and gray matter of patients with MS.<sup>90</sup> These techniques provide quantitative parameters such as

fractional anisotropy and mean diffusivity, which correlate well with tissue damage that is not visible on T2 and FLAIR imaging.<sup>91</sup> DTI may also assist in evaluating the structural integrity of white matter and can be used for probabilistic or deterministic tractography.<sup>92</sup> In one in vivo study of MS, radial diffusivity appeared to provide the closest correlation with tissue integrity.<sup>93</sup> A multicenter validation study indicated that fractional anisotropy was the most comparable DTI measure across centers and endorsed its use in multicenter clinical trials.<sup>94</sup> Werring et al<sup>95</sup> demonstrated that a steady and moderate increase of the apparent diffusion coefficient can precede the development of new plaques by 6–8 months, and they indicated that structural changes in prelesion normal-appearing white matter occur before inflammation and BBB leakage.

MTR is a technique based on the transfer of magnetization between semisolid and water protons in different structural environments.<sup>92</sup> Longitudinal studies demonstrate decreases in MTR preceding contrast enhancement. The magnitude of the MTR decline during gadolinium enhancement predicts whether a lesion will evolve into a T1 hypointense one.<sup>96</sup> Thus, MTR alteration has been proposed as a marker of overall lesion severity. Partial or complete resolution of the MTR may occur as inflammation is reduced and remyelination ensues.<sup>97</sup> Due to these features, this technique provides a promising primary outcome measure to evaluate remyelinating therapies in clinical trials. Several metrics that have been proposed for further study include intralésional MTR and whole-brain MTR.<sup>98</sup>

DIR sequences simultaneously suppress CSF and white matter signals, thereby increasing the detectability of gray and white matter lesions in MS significantly.<sup>99</sup> Several reports have shown the utility of DIR and PSIR images for detecting MS plaques, especially in intracortical or mixed white matter–gray matter areas compared with FLAIR and T2-weighted images (Fig 4).<sup>88,100,101</sup> Hagiwara et al<sup>102</sup> recently showed that such sequences could be recreated by using synthetic MR imaging techniques, which lead to greater diagnostic accuracy than conventional MR images in comparable acquisition times.

Last, there have been studies that have combined the above imaging advances with promising results. Calabrese et al<sup>103</sup> showed that the combination of DIR and DTI constitutes a substantial step forward in the analysis of cortical disease in MS. They

combined these techniques to analyze the cortex of patients with relapsing-remitting MS and found that fractional anisotropy was significantly increased in cortical lesions compared with normal-appearing gray matter. Their study concluded that there is a high correlation between the fractional anisotropy of normal-appearing gray matter and the progression of physical disability during a 3-year follow-up. Another example is the combined use of DIR and PSIR, which allows more reliable detection of cortical lesions in MS than DIR techniques alone. The addition of PSIR also provides better delineation of lesion boundaries, which results in a more confident classification of lesions as purely intracortical, mixed, or juxtacortical.<sup>100</sup>

Although the use of quantitative MR imaging measures for disease monitoring shows much promise, their use in routine clinical practice is, in part, hindered by the longer acquisition and postprocessing times and a current lack of standardization.

## CONCLUSIONS

The field of MS therapeutics is a rapidly evolving one. For radiologists to provide an informed opinion in discussions of newer MS agents, they must have a working understanding of the strengths and limitations of various novel therapies. The role of imaging in MS has advanced beyond confirmation of disease presence to include the monitoring and surveillance of disease activity and treatment complications. An understanding of the new generation of MS drugs in conjunction with the key role MR imaging plays in the detection of disease progression, opportunistic infections, and drug-related adverse effects is of vital importance to the radiologist and physician alike. Radiologists are in a unique position to detect many of the described complications well in advance of clinical symptoms. This rapidly expanding area will see much change in the years to come, and it is more important than ever for the neurologist and radiologist to work together in the pursuit of improved outcomes for the patient with MS.

## ACKNOWLEDGMENTS

The authors thank Drs Seamus Looby and Ronan P. Killeen for providing images for the article.

## REFERENCES

- Traboulsee A, Simon JH, Stone L, et al. **Revised Recommendations of the Consortium of MS Centers Task Force for a Standardized MRI Protocol and Clinical Guidelines for the Diagnosis and Follow-Up of Multiple Sclerosis.** *AJNR Am J Neuroradiol* 2016;37:394–401 CrossRef Medline
- Stangel M, Penner IK, Kallmann BA, et al. **Towards the implementation of ‘no evidence of disease activity’ in multiple sclerosis treatment: the multiple sclerosis decision model.** *Ther Adv Neurol Disord* 2015;8:3–13 CrossRef Medline
- Rudick RA, Lee JC, Simon J, et al. **Significance of T2 lesions in multiple sclerosis: a 13-year longitudinal study.** *Ann Neurol* 2006; 60:236–42 CrossRef Medline
- Wattjes MP, Steenwijk MD, Stangel M. **MRI in the diagnosis and monitoring of multiple sclerosis: an update.** *Clin Neuroradiol* 2015; 25(suppl 2):157–65 CrossRef Medline
- Sormani M, Rio J, Tintorè M, et al. **Scoring treatment response in patients with relapsing multiple sclerosis.** *Mult Scler* 2013;19: 605–12 CrossRef Medline
- Sormani MP, Signori A, Stromillo ML, et al. **Refining response to treatment as defined by the Modified Rio Score.** *Mult Scler* 2013; 19:1246–47 CrossRef Medline
- Freedman MS, Selchen D, Arnold DL, et al. **Treatment optimization in MS: Canadian MS Working Group updated recommendations.** *Can J Neurol Sci* 2013;40:307–23 CrossRef Medline
- Wattjes MP, Rovira À, Miller D, et al; MAGNIMS study group. **Evidence-based guidelines: MAGNIMS consensus guidelines on the use of MRI in multiple sclerosis—establishing disease prognosis and monitoring patients.** *Nat Rev Neurol* 2015;11:597–606 CrossRef Medline
- Wiendl H, Toyka KV, Rieckmann P, et al; Multiple Sclerosis Therapy Consensus Group (MSTCG). **Basic and escalating immunomodulatory treatments in multiple sclerosis: current therapeutic recommendations.** *J Neurol* 2008;255:1449–63 CrossRef Medline
- Coyle PK. **Switching therapies in multiple sclerosis.** *CNS Drugs* 2013;27:239–47 CrossRef Medline
- Wattjes MP, Barkhof F. **Diagnosis of natalizumab-associated progressive multifocal leukoencephalopathy using MRI.** *Cur Opin Neurol* 2014;27:260–70 CrossRef Medline
- Rommer PS, Zettl UK, Kieseier B, et al. **Requirement for safety monitoring for approved multiple sclerosis therapies: an overview.** *Clin Exp Immunol* 2014;175:397–407 CrossRef Medline
- van Oosten BW, Killestein J, Barkhof F, et al. **PML in a patient treated with dimethyl fumarate from a compounding pharmacy.** *N Engl J Med* 2013;368:1658–59 CrossRef Medline
- Arvin AM, Wolinsky JS, Kappos L, et al. **Varicella-zoster virus infections in patients treated with fingolimod: risk assessment and consensus recommendations for management.** *JAMA Neurol* 2015;72:31–39 CrossRef Medline
- Fine AJ, Sorbello A, Kortepeter C, et al. **Progressive multifocal leukoencephalopathy after natalizumab discontinuation.** *Ann Neurol* 2014;75:108–15 CrossRef Medline
- Wattjes MP, Killestein J. **Progressive multifocal leukoencephalopathy after natalizumab discontinuation: few and true?** *Ann Neurol* 2014;75:462 CrossRef Medline
- Killestein J, Vennegoor A, van Golde AE, et al. **PML-IRIS during fingolimod diagnosed after natalizumab discontinuation.** *Case Rep Neurol Med* 2014;2014:307872 CrossRef Medline
- Dubey D, Cano CA, Stüve O. **Update on monitoring and adverse effects of approved second-generation disease-modifying therapies in relapsing forms of multiple sclerosis.** *Curr Opin Neurol* 2016;29:278–85 CrossRef Medline
- Dong-Si T, Richman S, Wattjes MP, et al. **Outcome and survival of asymptomatic PML in natalizumab-treated MS patients.** *Ann Clin Transl Neurol* 2014;1:755–64 CrossRef Medline
- Wattjes MP, Vennegoor A, Steenwijk MD, et al. **MRI pattern in asymptomatic natalizumab-associated PML.** *J Neurol Neurosurg Psychiatry* 2015;86:793–98 CrossRef Medline
- Wattjes MP, Vennegoor A, Mostert J, et al. **Diagnosis of asymptomatic natalizumab-associated PML: are we between a rock and a hard place?** *J Neurol* 2014;261:1139–43 CrossRef Medline
- Richert N, Bloomgren G, Cadavid D, et al. **Imaging findings for PML in natalizumab-treated MS patients.** *Mult Scler* 2012;18(suppl 4):27. Oral 99 CrossRef
- Phan-Ba R, Lommers E, Tshibanda L, et al. **MRI preclinical detection and asymptomatic course of a progressive multifocal leukoencephalopathy (PML) under natalizumab therapy.** *J Neurol Neurosurg Psychiatry* 2012;83:224–26 CrossRef Medline
- Wattjes MP, Verhoeff L, Zentjens W, et al. **Punctate lesion pattern suggestive of perivascular inflammation in acute natalizumab-associated progressive multifocal leukoencephalopathy: productive JC virus infection or preclinical PML-IRIS manifestation?** *J Neurol Neurosurg Psychiatry* 2013;84:1176–77 CrossRef Medline
- Yousry TA, Pelletier D, Cadavid D, et al. **Magnetic resonance imaging pattern in natalizumab-associated progressive multifocal leukoencephalopathy.** *Ann Neurol* 2012;72:779–87 CrossRef Medline
- Gheuens S, Smith DR, Wang X, et al. **Simultaneous PML-IRIS after**

- discontinuation of natalizumab in a patient with MS. *Neurology* 2012;78:1390–93 CrossRef Medline
27. Hodel J, Outteryck O, Dubron C, et al. **Asymptomatic progressive multifocal leukoencephalopathy associated with natalizumab: diagnostic precision with MR imaging.** *Radiology* 2016;278:863–72 CrossRef Medline
  28. Wattjes MP, Richert ND, Killestein J, et al. **The chameleon of neuroinflammation: magnetic resonance imaging characteristics of natalizumab-associated progressive multifocal leukoencephalopathy.** *Mult Scler* 2013;19:1826–40 CrossRef Medline
  29. Honce JM, Nagae L, Nyberg E. **Neuroimaging of natalizumab complications in multiple sclerosis: PML and other associated entities.** *Mult Scler Int* 2015;2015:809252 CrossRef Medline
  30. Kastrop O, Maschke M, Diener H, et al. **Progressive multifocal leukoencephalopathy limited to the brain stem.** *Neuroradiology* 2002;44:227–29 CrossRef Medline
  31. Mathew RM, Murnane M. **MRI in PML: bilateral medullary lesions.** *Neurology* 2004;63:2380 CrossRef Medline
  32. Svensson PA, Larsson EM. **Infratentorial progressive multifocal leukoencephalopathy (PML) in a patient with SLE (2008: 4b).** *Eur Radiol* 2008;18:1526–28 CrossRef Medline
  33. Miyagawa M, Maeda M, Umino M, et al. **Low signal intensity in U-fiber identified by susceptibility-weighted imaging in two cases of progressive multifocal leukoencephalopathy.** *J Neurol Sci* 2014;344:198–202 CrossRef Medline
  34. Hodel J, Outteryck O, Vercluyte S, et al. **Brain magnetic susceptibility changes in patients with natalizumab-associated progressive multifocal leukoencephalopathy.** *AJNR Am J Neuroradiol* 2015;36:2296–302 CrossRef Medline
  35. Clifford DB, De Luca A, DeLuca A, et al. **Natalizumab-associated progressive multifocal leukoencephalopathy in patients with multiple sclerosis: lessons from 28 cases.** *Lancet Neurol* 2010;9:438–46 CrossRef Medline
  36. Tan IL, McArthur JC, Clifford DB, et al. **Immune reconstitution inflammatory syndrome in natalizumab-associated PML.** *Neurology* 2011;77:1061–67 CrossRef Medline
  37. Kleinschmidt-DeMasters BK, Miravalle A, Schowinsky J, et al. **Update on PML and PML-IRIS occurring in multiple sclerosis patients treated with natalizumab.** *J Neuropathol Exp Neurol* 2012;71:604–17 CrossRef Medline
  38. Miravalle A, Jensen R, Kinkel RP. **Immune reconstitution inflammatory syndrome in patients with multiple sclerosis following cessation of natalizumab therapy.** *Arch Neurol* 2011;68:186–91 CrossRef Medline
  39. Wattjes MP, Wijburg MT, Vennegoor A, et al; Dutch-Belgian Natalizumab-associated PML study group. **MRI characteristics of early PML-IRIS after natalizumab treatment in patients with MS.** *J Neurol Neurosurg Psychiatry* 2016;87:879–84 CrossRef Medline
  40. Wenning W, Haghikia A, Laubenberger J, et al. **Treatment of progressive multifocal leukoencephalopathy associated with natalizumab.** *N Engl J Med* 2009;361:1075–80 CrossRef Medline
  41. Gheuens S, Ngo L, Wang X, et al. **Metabolic profile of PML lesions in patients with and without IRIS: an observational study.** *Neurology* 2012;79:1041–48 CrossRef Medline
  42. Prosperini L, Gallo V, Petsas N, et al. **One-year MRI scan predicts clinical response to interferon beta in multiple sclerosis.** *Eur J Neurol* 2009;16:1202–09 CrossRef Medline
  43. Río J, Castelló J, Rovira A, et al. **Measures in the first year of therapy predict the response to interferon beta in MS.** *Mult Scler* 2009;15:848–53 CrossRef Medline
  44. Rovira A, Auger C, Alonso J. **Magnetic resonance monitoring of lesion evolution in multiple sclerosis.** *Ther Adv Neurol Disord* 2013;6:298–310 CrossRef Medline
  45. Simon JH, Bermel RA, Rudick RA. **Simple MRI metrics contribute to optimal care of the patient with multiple sclerosis.** *AJNR Am J Neuroradiol* 2014;35:831–32 CrossRef Medline
  46. Sormani MP, Bonzano L, Roccatagliata L, et al. **Magnetic resonance imaging as a potential surrogate for relapses in multiple sclerosis: a meta-analytic approach.** *Ann Neurol* 2009;65:268–75 CrossRef Medline
  47. Romeo M, Martinelli V, Perego M, et al. **Brain MRI activity after disease-modifying treatment may predict disability progression after 5 years in relapsing remitting multiple sclerosis patients.** In: *Proceedings of the 5th Joint Triennial Congress of the European and Americas Committees for Treatment and Research in Multiple Sclerosis*, Amsterdam, the Netherlands. October 19–22, 2011; abstract 29
  48. Río J, Nos C, Tintoré M, et al. **Defining the response to interferon-beta in relapsing-remitting multiple sclerosis patients.** *Ann Neurol* 2006;59:344–52 CrossRef Medline
  49. Río J, Rovira A, Tintoré M, et al. **Relationship between MRI lesion activity and response to IFN-beta in relapsing-remitting multiple sclerosis patients.** *Mult Scler* 2008;14:479–84 CrossRef Medline
  50. Río J, Comabella M, Montalban X. **Predicting responders to therapies for multiple sclerosis.** *Nat Rev Neurol* 2009;5:553–60 CrossRef Medline
  51. Tomassini V, Paolillo A, Russo P, et al. **Predictors of long-term clinical response to interferon beta therapy in relapsing multiple sclerosis.** *J Neurol* 2006;253:287–93 CrossRef Medline
  52. Fisniku LK, Brex PA, Altmann DR, et al. **Disability and T2 MRI lesions: a 20-year follow-up of patients with relapse onset of multiple sclerosis.** *Brain* 2008;131:808–17 CrossRef Medline
  53. Goodin DS, Traboulsee A, Knappertz V, et al; 16-Year Long Term Follow-up Study Investigators. **Relationship between early clinical characteristics and long term disability outcomes: 16-year cohort study (follow-up) of the pivotal interferon  $\beta$ -1b trial in multiple sclerosis.** *J Neurol Neurosurg Psychiatry* 2012;83:282–87 CrossRef Medline
  54. Bermel RA, You X, Foulds P, et al. **Predictors of long-term outcome in multiple sclerosis patients treated with interferon  $\beta$ .** *Ann Neurol* 2013;73:95–103 CrossRef Medline
  55. Sormani MP, Arnold DL, De Stefano N. **Treatment effect on brain atrophy correlates with treatment effect on disability in multiple sclerosis.** *Ann Neurol* 2014;75:43–49 CrossRef Medline
  56. Erbayat Altay E, Fisher E, Jones SE, et al. **Reliability of classifying multiple sclerosis disease activity using magnetic resonance imaging in a multiple sclerosis clinic.** *JAMA Neurol* 2013;70:338–44 CrossRef Medline
  57. Vrenken H, Jenkinson M, Horsfield MA, et al; MAGNIMS Study Group. **Recommendations to improve imaging and analysis of brain lesion load and atrophy in longitudinal studies of multiple sclerosis.** *J Neurol* 2013;260:2458–71 CrossRef Medline
  58. Michel L, Laroche C, Prat A. **Update on treatments in multiple sclerosis.** *Presse Med* 2015;44(4 pt 2):e137–51 CrossRef Medline
  59. Havrdova E. **Freedom from disease activity in multiple sclerosis.** *Neurology* 2010;74(suppl 3):S3–7 CrossRef Medline
  60. Giovannoni G, Turner B, Gnanapavan S, et al. **Is it time to target no evident disease activity (NEDA) in multiple sclerosis?** *Mult Scler Rel Disord* 2015;4:329–33 CrossRef Medline
  61. Río J. **Any evident MRI T2 lesion activity should guide change of therapy in multiple sclerosis: no.** *Mult Scler* 2015;21:132–33 CrossRef Medline
  62. Ziemssen T, Derfuss T, de Stefano N, et al. **Optimizing treatment success in multiple sclerosis.** *J Neurol* 2016;263:1053–65 CrossRef Medline
  63. Dobson R, Rudick RA, Turner B, et al. **Assessing treatment response to interferon- $\beta$ : is there a role for MRI?** *Neurology* 2014;82:248–54 CrossRef Medline
  64. Prosperini L, Fanelli F, Pozzilli C. **Long-term assessment of No Evidence of Disease Activity with natalizumab in relapsing multiple sclerosis.** *J Neurol Sci* 2016;364:145–47 CrossRef Medline
  65. Coyle PK. **Switching algorithms: from one immunomodulatory agent to another.** *J Neurol* 2008;255:44–50 CrossRef Medline
  66. Río J, Tintoré M, Sastre-Garriga J, et al. **Change in the clinical activity of multiple sclerosis after treatment switch for suboptimal response.** *Eur J Neurol* 2012;19:899–904 CrossRef Medline
  67. De Stefano N. **Assessing brain atrophy rates in a large population**

- of untreated multiple sclerosis subtypes. *Neurology* 2010;74:1868–76 CrossRef Medline
68. Fisher E, Lee JC, Nakamura K, et al. **Gray matter atrophy in multiple sclerosis: a longitudinal study.** *Ann Neurol* 2008;64:255–65 CrossRef Medline
  69. Steenwijk MD, Daams M, Pouwels PJ, et al. **What explains gray matter atrophy in long-standing multiple sclerosis?** *Radiology* 2014;272:832–42 CrossRef Medline
  70. Bergsland N, Laganà MM, Tavazzi E, et al. **Corticospinal tract integrity is related to primary motor cortex thinning in relapsing-remitting multiple sclerosis.** *Mult Scler* 2015;21:1771–80 CrossRef Medline
  71. De Stefano N, Airas L, Grigoriadis N, et al. **Clinical relevance of brain volume measures in multiple sclerosis.** *CNS Drugs* 2014;28:147–56 CrossRef Medline
  72. Vidal-Jordana A, Sastre-Garriga J, Rovira A, et al. **Treating relapsing-remitting multiple sclerosis: therapy effects on brain atrophy.** *J Neurol* 2015;262:2617–26 CrossRef Medline
  73. Zivadinov R. **Mechanisms of action of disease-modifying agents and brain volume changes in multiple sclerosis.** *Neurology* 2008;71:136–44 CrossRef Medline
  74. Enzinger C, Fazekas F, Matthews PM, et al. **Risk factors for progression of brain atrophy in aging: six-year follow-up of normal subjects.** *Neurology* 2005;64:1704–11 CrossRef Medline
  75. Huppertz HJ, Kröll-Seger J, Klöppel S, et al. **Intra- and interscanner variability of automated voxel-based volumetry based on a 3D probabilistic atlas of human cerebral structures.** *Neuroimage* 2010;49:2216–24 CrossRef Medline
  76. Jacobsen C, Hagemeyer J, Myhr KM, et al. **Brain atrophy and disability progression in multiple sclerosis patients: a 10-year follow-up study.** *J Neurol Neurosurg Psychiatry* 2014;85:1109–15 CrossRef Medline
  77. Miller DH, Soon D, Fernando KT, et al; AFFIRM Investigators. **MRI outcomes in a placebo-controlled trial of natalizumab in relapsing MS.** *Neurology* 2007;68:1390–401 CrossRef Medline
  78. Radue EW, Stuart WH, Calabresi PA, et al; SENTINEL Investigators. **Natalizumab plus interferon beta-1a reduces lesion formation in relapsing multiple sclerosis.** *J Neurol Sci* 2010;292:28–35 CrossRef Medline
  79. Magraner M, Coret F, Casanova B. **The relationship between inflammatory activity and brain atrophy in natalizumab treated patients.** *Eur J Neurol* 2012;81:3485–90 CrossRef
  80. Radue EW, O'Connor P, Polman CH, et al; FTY720 Research Evaluating Effects of Daily Oral Therapy in Multiple Sclerosis (FREEDOMS) Study Group. **Impact of fingolimod therapy on magnetic resonance imaging outcomes in patients with multiple sclerosis.** *Arch Neurol* 2012;69:1259–69 CrossRef Medline
  81. Kappos L, Traboulsee A, Constantinescu C, et al. **Long-term subcutaneous interferon beta-1a therapy in patients with relapsing-remitting MS.** *Neurology* 2006;67:944–53 CrossRef Medline
  82. Goodkin DE, Vanderburg-Medendorp S, Ross JT. **The effect of repositioning error on serial magnetic resonance imaging scans.** *Arch Neurol* 1993;50:569–70 Medline
  83. Tan IL, van Schijndel RA, Fazekas F, et al. **Image registration and subtraction to detect active T (2) lesions in MS: an interobserver study.** *J Neurol* 2002;249:767–73 CrossRef Medline
  84. Moraal B, Meier DS, Poppe PA, et al. **Subtraction MR images in a multiple sclerosis multicenter clinical trial setting.** *Radiology* 2009;250:506–14 CrossRef Medline
  85. Moraal B, Wattjes MP, Geurts JJ, et al. **Improved detection of active multiple sclerosis lesions: 3D subtraction imaging.** *Radiology* 2010;255:154–63 CrossRef Medline
  86. Battaglini M, Rossi F, Grove RA, et al. **Automated identification of brain new lesions in multiple sclerosis using subtraction images.** *J Magn Reson Imaging* 2014;39:1543–49 CrossRef Medline
  87. Moraal B, van den Elskamp IJ, Knol DL, et al. **Long-interval T2-weighted subtraction magnetic resonance imaging: a powerful new outcome measure in multiple sclerosis trials.** *Ann Neurol* 2010;67:667–75 CrossRef Medline
  88. Wattjes MP, Lutterbey GG, Gieseke J, et al. **Double inversion recovery brain imaging at 3T: diagnostic value in the detection of multiple sclerosis lesions.** *AJNR Am J Neuroradiol* 2007;28:54–59 Medline
  89. Sethi V, Yousry TA, Muhlert N, et al. **Improved detection of cortical MS lesions with phase-sensitive inversion recovery MRI.** *J Neurol Neurosurg Psychiatry* 2012;83:877–82 CrossRef Medline
  90. de Kouchkovsky I, Fieremans E, Fleysher L, et al. **Quantification of normal-appearing white matter tract integrity in multiple sclerosis: a diffusion kurtosis imaging study.** *J Neurol* 2016;263:1146–55 CrossRef Medline
  91. Testaverde L, Caporali L, Venditti E, et al. **Diffusion tensor imaging applications in multiple sclerosis patients using 3T magnetic resonance: a preliminary study.** *Eur Radiol* 2012;22:990–97 CrossRef Medline
  92. Klawiter EC. **Current and new directions in MRI in multiple sclerosis.** *Continuum (Minneapolis)* 2013;19(4 multiple sclerosis):1058–73 CrossRef Medline
  93. Naismith RT. **Increased diffusivity in acute multiple sclerosis lesions predicts risk of black hole.** *Neurology* 2010;74:1694–701 CrossRef Medline
  94. Fox RJ, Sakaie K, Lee JC, et al. **A validation study of multicenter diffusion tensor imaging: reliability of fractional anisotropy and diffusivity values.** *AJNR Am J Neuroradiol* 2012;33:695–700 CrossRef Medline
  95. Werring DJ, Brassat D, Droogan AG, et al. **The pathogenesis of lesions and normal-appearing white matter changes in multiple sclerosis: a serial diffusion MRI study.** *Brain* 2000;123(pt 8):1667–76 CrossRef Medline
  96. Rovira A, León A. **MR in the diagnosis and monitoring of multiple sclerosis: an overview.** *Eur J Radiol* 2008;67:409–14 CrossRef Medline
  97. Chen JT, Collins DL, Atkins HL, et al; Canadian MS/BMT Study Group. **Magnetization transfer ratio evolution with demyelination and remyelination in multiple sclerosis lesions.** *Ann Neurol* 2008;63:254–62 CrossRef Medline
  98. van den Elskamp IJ, Knol DL, Vrenken H, et al. **Lesional magnetization transfer ratio: a feasible outcome for remyelinating treatment trials in multiple sclerosis.** *Mult Scler* 2010;16:660–69 CrossRef Medline
  99. Simon B, Schmidt S, Lukas C, et al. **Improved in vivo detection of cortical lesions in multiple sclerosis using double inversion recovery MR imaging at 3 Tesla.** *Eur Radiol* 2010;20:1675–83 CrossRef Medline
  100. Nelson F, Poonawalla AH, Hou P, et al. **Improved identification of intracortical lesions in multiple sclerosis with phase-sensitive inversion recovery in combination with fast double inversion recovery MR imaging.** *AJNR Am J Neuroradiol* 2007;28:1645–49 CrossRef Medline
  101. Geurts JJ, Pouwels PJ, Uitdehaag BM, et al. **Intracortical lesions in multiple sclerosis: improved detection with 3D double inversion-recovery MR imaging.** *Radiology* 2005;236:254–60 CrossRef Medline
  102. Hagiwara A, Hori M, Yokoyama K, et al. **Synthetic MRI in the detection of multiple sclerosis plaques.** *AJNR Am J Neuroradiol* 2016 Dec 8. [Epub ahead of print] CrossRef Medline
  103. Calabrese M, Rinaldi F, Seppi D, et al. **Cortical diffusion-tensor imaging abnormalities in multiple sclerosis: a 3-year longitudinal study.** *Radiology* 2011;261:891–98 CrossRef Medline

# Comparison of Gadoterate Meglumine and Gadobutrol in the MRI Diagnosis of Primary Brain Tumors: A Double-Blind Randomized Controlled Intraindividual Crossover Study (the REMIND Study)

K.R. Maravilla, D. San-Juan, S.J. Kim, G. Elizondo-Riojas, J.R. Fink, W. Escobar, A. Bag, D.R. Roberts, J. Hao, C. Pitrou, A.J. Tsiouris, E. Herskovits, and J.B. Fiebach



## ABSTRACT

**BACKGROUND AND PURPOSE:** Effective management of patients with brain tumors depends on accurate detection and characterization of lesions. This study aimed to demonstrate the noninferiority of gadoterate meglumine versus gadobutrol for overall visualization and characterization of primary brain tumors.

**MATERIALS AND METHODS:** This multicenter, double-blind, randomized, controlled intraindividual, crossover, noninferiority study included 279 patients. Both contrast agents (dose = 0.1 mmol/kg of body weight) were assessed with 2 identical MRIs at a time interval of 2–14 days. The primary end point was overall lesion visualization and characterization, scored independently by 3 off-site readers on a 4-point scale, ranging from “poor” to “excellent.” Secondary end points were qualitative assessments (lesion border delineation, internal morphology, degree of contrast enhancement, diagnostic confidence), quantitative measurements (signal intensity), and safety (adverse events). All qualitative assessments were also performed on-site.

**RESULTS:** For all 3 readers, images of most patients (>90%) were scored good or excellent for overall lesion visualization and characterization with either contrast agent; and the noninferiority of gadoterate meglumine versus gadobutrol was statistically demonstrated. No significant differences were observed between the 2 contrast agents regarding qualitative end points despite quantitative mean lesion percentage enhancement being higher with gadobutrol ( $P < .001$ ). Diagnostic confidence was high/excellent for all readers in >81% of the patients with both contrast agents. Similar percentages of patients with adverse events related to the contrast agents were observed with gadoterate meglumine (7.8%) and gadobutrol (7.3%), mainly injection site pain.

**CONCLUSIONS:** The noninferiority of gadoterate meglumine versus gadobutrol for overall visualization and characterization of primary brain tumors was demonstrated.

**ABBREVIATIONS:** AE = adverse event; CNR = contrast-to-noise ratio; GBCA = gadolinium-based contrast agent; LS = least-squares;  $r_1$  = relaxivity

Gadolinium-based contrast agents (GBCAs) have led to improvement in the diagnostic accuracy and sensitivity of MR imaging. GBCAs can be classified into linear or macrocyclic agents according to their chemical structure, with macrocyclic GBCAs showing a higher kinetic stability.

Gadoterate meglumine is an ionic macrocyclic GBCA with a

measured T1 relaxivity ( $r_1$ ) range in plasma at 37°C of 3.4–3.8  $L \times mmol^{-1} \times s^{-1}$  at 1.5T and 3.3–3.7  $L \times mmol^{-1} \times s^{-1}$  at 3T.<sup>1</sup> Gadobutrol is a nonionic macrocyclic GBCA with a higher  $r_1$  range of 4.9–5.5  $L \times mmol^{-1} \times s^{-1}$  at 1.5T and 4.7–5.3  $L \times mmol^{-1} \times s^{-1}$  at 3T in plasma at 37°C.<sup>1</sup>

Gadobutrol is the only GBCA formulated at a concentration of 1 mmol/mL, while gadoterate meglumine is formulated at 0.5 mmol/mL, as are all other commercially available GBCAs approved for CNS imaging. Both are administered intravenously at a dose of 0.1 mmol/kg of body weight; thus, gadobutrol is administered at half the volume of gadoterate meglumine. However,

Received May 3, 2017; accepted after revision June 6.

From the Department of Radiology (K.R.M., J.R.F.), University of Washington Medical Center, Seattle, Washington; Clinical Research Department (D.S.-J.), National Institute of Neurology and Neurosurgery, Mexico City, Mexico; Department of Radiology (S.J.K.), Asan Medical Center, University of Ulsan College of Medicine, Seoul, Korea; Universidad Autonoma de Nuevo Leon (G.E.-R.), Hospital Universitario Dr. Jose Eleuterio Gonzalez, Monterrey, Mexico; Centro Medico Imbanaco (W.E.), Cali, Colombia; Department of Radiology (A.B.), University of Alabama, Birmingham, Alabama; Medical University of South Carolina (D.R.R.), Charleston, South Carolina; Guerbet (J.H., C.P.), Roissy–Charles de Gaulle, France; Department of Radiology (A.J.T.), Weill Cornell Medical College, New York, New York; Department of Radiology (E.H.), University of Maryland, Baltimore, Maryland; and Center for Stroke Research Berlin (J.B.F.), Charité–Universitätsmedizin, Berlin, Germany.

This study was supported by Guerbet.

Please address correspondence to Kenneth R. Maravilla, MD, Department of Radiology, University of Washington, 1959 NE Pacific, Box 357115, Seattle, WA 98195; e-mail: kmarav@uw.edu

Indicates open access to non-subscribers at www.ajnr.org

Indicates article with supplemental on-line tables.

Evidence-Based Medicine Level 1.

<http://dx.doi.org/10.3174/ajnr.A5316>

despite the small differences in relaxivity and in formulated drug concentration, several neuroimaging studies have failed to conclusively demonstrate a clinical advantage for gadobutrol compared with other GBCAs.<sup>2-4</sup>

The primary objective of this study was to determine whether gadoterate meglumine is noninferior to gadobutrol for overall visualization and characterization of primary brain tumors, using an intraindividual crossover comparison design.

## MATERIALS AND METHODS

### Study Design

This study was a multicenter, double-blind, randomized, controlled intraindividual, 2-sequence, 2-period, crossover noninferiority study. Patients underwent 2 identical MR imaging examinations, 1 with each contrast agent, gadoterate meglumine and gadobutrol. The sequence of contrast agent administration (gadoterate meglumine followed by gadobutrol or vice versa) was randomly assigned to each patient with a 1:1 allocation ratio. This study was conducted according to the principles in the Declaration of Helsinki and the Good Clinical Practices guidelines of the International Conference on Harmonization. In the United States, the protocol was compliant with the Health Insurance Portability and Accountability Act. The study was approved by the local ethics committee or institutional review board for human subject research of each institution in which the study was performed. Written informed consent was obtained from all participating patients. The study was registered on <https://clinicaltrials.gov> with identifier NCT02034708.

### Patients

A total of 279 adult patients were enrolled in the study at 27 centers worldwide (Mexico, United States, South Korea, and Colombia) between June 2014 and September 2015. Patients with known or highly suspected primary brain (intracranial) tumors detected by previous CT or MR imaging examination and who were scheduled for contrast-enhanced MR imaging were included. Patients were not included if they had a rapidly evolving brain tumor that could change in appearance between the 2 MR imaging examinations or if they were receiving treatment that could result in a change of lesion appearance between the 2 MR imaging examinations (eg, radiation therapy, an operation, or chemotherapy). Additional noninclusion criteria were the following: patients who were pregnant or breastfeeding, had a contraindication to MR imaging, had known severely impaired renal function (estimated glomerular filtration rate of  $<30$  mL/min/1.73 m<sup>2</sup>), had known class III/IV congestive heart failure (New York Heart Association Classification), had a known severe adverse drug reaction or contraindication to GBCA, had received any contrast agent within 48 hours before first study contrast agent injection or were expected to receive any other contrast agent within 24 hours following the last study contrast agent injection, or were included in another clinical trial involving an investigational drug within 30 days before the first contrast agent injection.

### Contrast Agent Administration

Gadoterate meglumine (Dotarem; Guerbet, Aulnay-sous-Bois, France) and gadobutrol (Gadovist, Bayer Schering Pharma, Ber-

lin, Germany; or Gadavist, Bayer HealthCare Pharmaceuticals, Wayne, New Jersey) were each administered at a single dose of 0.1 mmol/kg of body weight (0.2 mL/kg for gadoterate meglumine, 0.1 mL/kg for gadobutrol) by intravenous bolus injection at a rate of 2 mL/s with an automatic injector. Contrast agent injection was immediately followed by a saline flush of 20–30 mL at the same injection rate. To ensure that on-site evaluation of the contrast agent was performed under blinded conditions, a third party performed the injection. The patient was not aware of the identity of the injected contrast agent. The 2 MR imaging examinations were performed with a minimum time interval of 48 hours to allow contrast washout and prevent any effect of contrast agent carry-over, and a maximum time interval of 14 days to minimize any potential for lesion change and thus ensure comparability of the 2 examinations.

### MR Imaging

MR imaging was performed on 1.5T systems in 15 centers and on 3T systems in 12 centers. Each MR imaging scanner was previously evaluated for qualification for the study by BioClinica (Princeton, New Jersey). It was mandatory that the same MR imaging scanner and same parameters be used for both examinations in each patient. Imaging protocol included 3 unenhanced sequences: axial T1-weighted (2D spin-echo or gradient recalled-echo, or TSE with an echo-train length of  $\leq 3$ ), axial T2-weighted (2D TSE), and axial T2-weighted FLAIR (2D or 3D FLAIR); and 1 axial T1-weighted sequence post contrast-agent injection acquired with imaging parameters identical to those of the precontrast axial T1 sequence (On-line Table 1). The postcontrast T1-weighted imaging was initiated  $5 \pm 1$  minutes after the end of the contrast agent injection.

### Image Evaluation

All images were evaluated by 3 independent blinded off-site readers. All were experienced (at least 12 years of experience with an everyday practice in neuroradiology) and analyzed the images for the following qualitative criteria: overall lesion visualization and characterization (as the primary end point), lesion border delineation, visualization of lesion internal morphology, degree of contrast enhancement, and level of diagnostic confidence.

Overall visualization and characterization of the lesion (or most representative lesion, ie, enhancing and/or largest if there was  $>1$  lesion present) were assessed on a 4-point scale (0 = poor, inadequate; 1 = fair, partial; 2 = good, adequate; and 3 = excellent).

The level of diagnostic confidence was evaluated on a 5-point scale according to the percentage of confidence (1 = nil, 0%–4%; 2 = poor, 5%–35%; 3 = moderate, 36%–65%; 4 = high, 66%–95%; and 5 = excellent, 96%–100%) for each patient based on the most representative lesion. All available sequences (FLAIR, T2, and T1 with and without contrast administration) were available for readers to review and evaluate.

Border delineation and internal morphology were scored on a 3-point scale (0 = unevaluable; 1 = seen, but imperfectly; and 2 = seen completely/perfectly), as was the degree of contrast enhancement (0 = nil; 1 = mild enhancement; and 2 = strong enhancement). These 3 criteria were assessed on up to 3 of the most

representative lesions. For each of these 3 criteria, a sum of scores was calculated at the patient level as follows:  $\text{score}_{\text{lesion } 1} (+ \text{score}_{\text{lesion } 2} + \text{score}_{\text{lesion } 3}, \text{ if applicable})$  and was recorded as a continuous variable. Sums of scores were therefore related to the number of detected lesions. According to the results for sums of scores, images were classified as “gadoterate meglumine preferred” when the sum of scores of the patient was superior with gadoterate meglumine; as “no preference” when the sums of scores were equal with both contrast agents; and as “gadobutrol preferred” when the sum of scores was superior with gadobutrol.

Off-site readers also performed quantitative measures of signal intensity on up to 3 of the most representative lesions using ROI markers to determine SNR, contrast-to-noise ratio (CNR), and lesion percentage enhancement. ROIs were placed on unenhanced and enhanced T1 sequences.

The 3 off-site readers were blinded to all patient data and to the time point of the MR imaging examination (first or second), diagnostic results of the imaging procedures, findings of any other readers (ie, investigators, on-site readers, other off-site readers), and the contrast agent administered. Readers were trained on an independent dataset of 15 MR imaging examinations to ensure a harmonized understanding of the reading criteria and were qualified after evaluation of inter- and intrareader variability on 15 new MR imaging examinations.

Study examinations were read in batches of approximately 30 examinations randomly distributed to each reader. Each reader was permitted to analyze a maximum of 1 batch during any given 24-hour period. A “washout” period of at least 2 weeks between examinations from the same patient was applied, and images were distributed in random order between the 2 time points to minimize recall bias.

In conditions more closely simulating the usual practice, an on-site radiologist, blinded to the identity of the contrast agent, also evaluated all images of patients included in his or her site with the same qualitative criteria as described for the blinded readers. These readings were used for patient management.

### **Safety**

All adverse events (AEs) were recorded from the time of patient enrollment in the study until 30 minutes after the last contrast agent injection. The intensity of each adverse event was graded as mild, moderate, or severe, and the causal relationship to the contrast agent was assessed by the investigator as being not related, doubtfully related, or possibly related. All AEs were classified according to the *Medical Dictionary for Regulatory Activities*, Version 18.1 (<https://www.meddra.org/>) index terms.

### **Statistical Methods**

Statistical analyses were performed by using SAS software (SAS Institute, Cary, North Carolina), Version 9.2.

Primary and secondary criteria were presented on the per-protocol set, including all randomized patients who had a valid off-site assessment of the primary criterion without major protocol deviation. The primary criterion, the noninferiority of gadoterate meglumine-enhanced MR imaging compared with gadobutrol-enhanced MR imaging for overall lesion visualization and characterization (dichotomized as good/excellent versus

poor/fair), was assessed with a noninferiority margin set at  $-10\%$ , which was considered clinically acceptable. If one assumed that approximately 85% of patients would have good or excellent lesion visualization and characterization (minimum score of 2) for each contrast agent and each independent reader, approximately 235 patients undergoing the 2 MR imaging examinations were needed to ensure that the difference between the 2 examinations did not exceed the noninferiority margin. Assuming that 15% of patients would withdraw from the study, 270 patients were planned for randomization to achieve the study objective.

The noninferiority of gadoterate meglumine to gadobutrol was declared if the lower limit of the 95% CI of the difference in overall lesion visualization and characterization was above the noninferiority margin for at least 2 of 3 off-site readers, using a normal test of equality of paired proportions with a 1-sided 2.5% significance level. To test the difference between the 2 contrast agents, we performed a multiple logistic regression model for correlated data. Secondary criteria were considered exploratory. Comparison between the 2 contrast agents for continuous variables was performed with the differences of least-squares (LS) mean from a mixed model for correlated data. The frequency of the 3 classifications of sums of scores was compared using the Wilcoxon signed rank test. The intra- and interreader agreement for the evaluation of the overall lesion visualization and characterization was assessed for each contrast agent and presented as agreement proportion. Intrareader agreement was analyzed by rereading 10% of all MR images, randomly determined. The 3 off-site readers reread the images without knowledge that it was a second reading.

## **RESULTS**

### **Patient Characteristics**

A total of 279 patients were enrolled in the study. Five were not randomized due to deviation from the plan specified in the protocol (3 patients) or because they withdrew consent (2 patients). A total of 274 patients were randomized to either the gadoterate meglumine/gadobutrol arm (140 patients) or the gadobutrol/gadoterate meglumine arm (134 patients) to undergo 2 identical MR imaging examinations. Six patients did not receive the first contrast agent, leading to a total of 268 patients receiving at least 1 injection of contrast agent (safety set). Of these, 249 patients underwent a second MR imaging with contrast agent injection and completed the study with both contrast-enhanced MR imaging examinations performed. Patient disposition is summarized in Fig 1.

Among the 249 randomized patients who underwent both MR imaging examinations, 15 were excluded from the per protocol set because they presented with at least 1 major protocol deviation: differences of MR imaging DICOM parameters at T1 sequences between the 2 MR imaging examinations that could adversely affect the comparability of lesion visualization and characterization ( $n = 3$ ), technical injection failure in 1 of the MRIs ( $n = 3$ ), a difference in injection rate of  $\geq 1.5$  mL/s between the 2 contrast agent administrations ( $n = 3$ ), a difference of  $\geq 10\%$  between the 2 actual doses administered to a single patient ( $n = 2$ ), patients without detected tumoral lesions according to at least 2 off-site readers at both examinations ( $n = 3$ ), and loss of the second MR

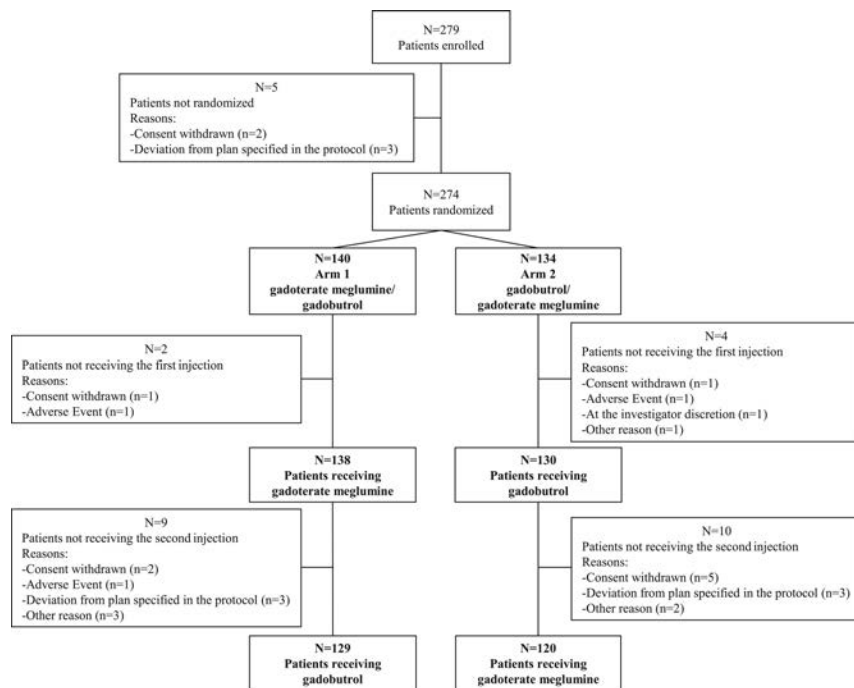


**FIG 1.** Patient disposition with numbers of patients enrolled ( $n = 279$ ) and randomized ( $n = 274$ ) to undergo 2 identical MR imaging examinations with gadoterate meglumine followed by gadobutrol (arm 1) or with gadobutrol followed by gadoterate meglumine (arm 2). A total of 268 patients received the first contrast agent injection, and 249 patients completed the study with the 2 examinations performed.

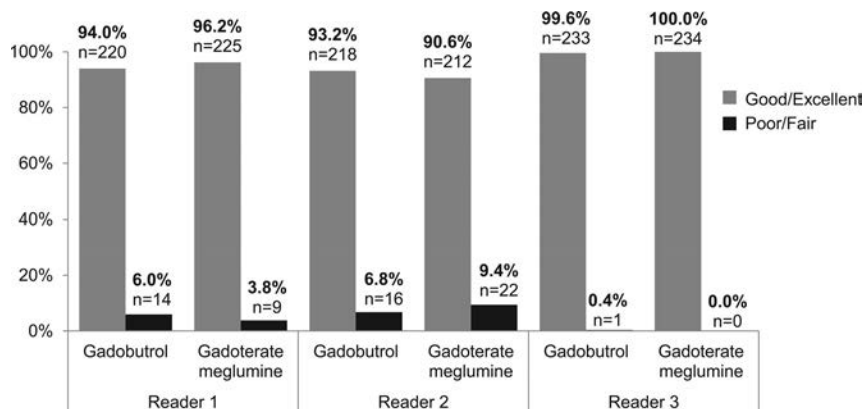


**FIG 2.** Rate of patients with overall lesion visualization and characterization scored good/excellent or poor/fair. The bar graph shows the rate of patients with overall lesion visualization and characterization scored good/excellent or poor/fair according to each contrast agent and each off-site reader ( $n = 234$  patients for all readers).

imaging data ( $n = 1$ ). Therefore, the per-protocol set used for analysis of evaluation criteria included 234 patients, 120 in the gadoterate meglumine/gadobutrol arm and 114 in the gadobutrol/gadoterate meglumine arm.

The 2 arms showed comparable demographic characteristics (On-line Table 2). Patients ranged in age from 18 to 98 years, with a mean of  $53.6 \pm 15.1$  years. There were more female than male patients (64.2% versus 35.8%). Body mass index ranged from 17.4 to 51.2 kg/m<sup>2</sup>, with a mean of  $27.7 \pm 5.3$  kg/m<sup>2</sup>. At the time of the last brain imaging evaluation, the patients' diagnoses were tumor of the meninges (49.3%), glioma (14.9%), tumor not otherwise specified (13.1%), pituitary adenoma (11.9%), nerve sheath tumor (9.0%), tumor metastases (1.5%), and other (0.4%). Among

the 268 patients, 170 (63.4%) had a previous examination with GBCA administration and only 1 of these patients (0.4%) experienced a nonsevere adverse reaction to the GBCA administered.

### Primary Criterion: Overall Lesion Visualization and Characterization

Figure 2 shows the results of the 3 blinded off-site readers for overall lesion visualization and characterization. For all readers, the overwhelming majority of patients (>90%) presented with good or excellent overall lesion visualization and characterization with either of the 2 contrast agents. Reader 3 scored overall lesion visualization and characterization as good or excellent for all patients with gadoterate meglumine and for all patients except 1 with gadobutrol. Therefore, a difference between these GBCAs was not statistically evaluable for this reader.

For the 2 other off-site readers, the estimated difference and 95% CI between gadoterate meglumine and gadobutrol (as reference) was 2.3% (95% CI,  $-1.3$  to  $5.9$ ) for reader 1 and  $-2.5\%$  (95% CI,  $-6.5$  to  $1.4$ ) for reader 2 with lower limits of 95% CI above the noninferiority limit set at  $-10\%$ . The noninferiority of gadoterate meglumine compared with gadobutrol was therefore demonstrated.

Figures 3 and 4 illustrate 2 case examples that demonstrate the identical appearance in lesion visualization and characterization observed for the 2 contrast agents.

Inter- and intrareader agreement for the assessment of overall lesion visualization and characterization was high on the basis of agreement proportion, with interreader agreement ranging from 91% to 96% and intrareader agreement, from 96% to 100%.

The noninferiority of gadoterate meglumine compared with gadobutrol was also demonstrated by on-site readers, with >96% of patients presenting good or excellent overall lesion visualization and characterization with both contrast agents and an estimated difference between them of 0.6% (95% CI,  $-1.8$  to  $3.1$ ).

### Qualitative Secondary Criteria

The 3 off-site readers scored border delineation, internal morphology, and degree of contrast enhancement on up to 3 of the most representative lesions; a sum of scores was calculated per patient for each of these criteria (On-line Table 3). More than 87% of patients had only 1 lesion, 5%–10% had 2 lesions, and

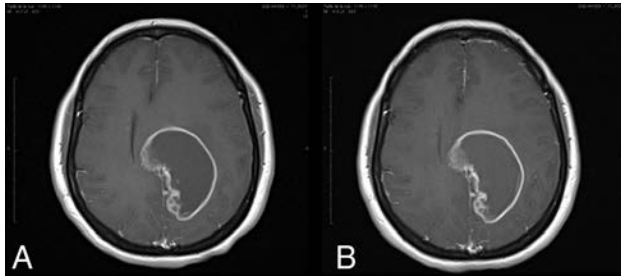


**FIG 3.** A 46-year-old woman with glioblastoma. T1 spin-echo images (1.5T) after administration of 0.1 mmol/kg of gadoterate meglumine (A) and gadobutrol (B) show an approximate 65-mm lesion. The time between the 2 MR imaging examinations was 7 days. Lesion visualization and characterization were scored as excellent by all 3 blinded readers. The enhancing rim of the lesion is clearly seen on both examinations.

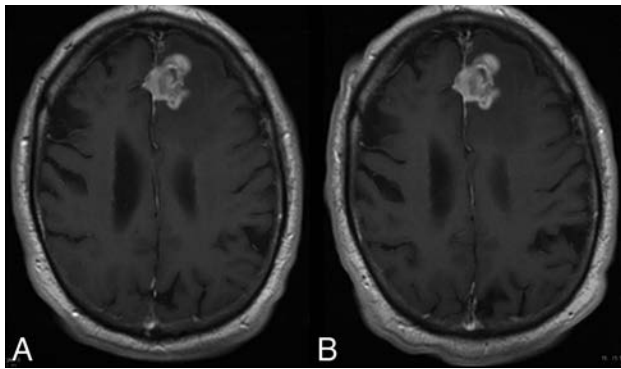


**FIG 4.** A 74-year-old man with a high-grade glioma. T1 spin-echo images (1.5T) after administration of 0.1 mmol/kg of gadoterate meglumine (A) and gadobutrol (B) show an approximate 30-mm mass. The time between the 2 MR imaging examinations was 8 days. Lesion visualization and characterization were scored as excellent by all 3 blinded readers. The mass is clearly seen on both examinations and shows no difference in contrast enhancement.

<4% had  $\geq 3$  lesions. Lesion border delineation showed no significant differences between contrast agents for readers 1 and 2; however, a minimal statistically significant difference ( $P = .049$ ) was observed in favor of gadobutrol for reader 3. No statistically significant differences between contrast agents were shown for any of the 3 readers for visualization of lesion internal morphology or for qualitative assessment of the degree of lesion contrast enhancement.

The analysis by calculated preference of border delineation, internal morphology, and degree of contrast enhancement between the 2 contrast agents showed no preference of the off-site readers for most patients (68%–89%) (Fig 5). For the other patients ( $\leq 33\%$  of patients), a slight calculated preference for gadobutrol was observed for readers 2 and 3, while a slight calculated preference for gadoterate meglumine was seen for reader 1. These differences were not statistically significant.

The mean level of diagnostic confidence was high or excellent with both GBCAs in  $>81\%$  of patients, according to all off-site readers. No significant difference in diagnostic confidence was observed between the 2 contrast agents.

Similar results were observed between on-site and off-site readers regarding all the qualitative secondary criteria.

### Quantitative Secondary Criteria: Signal-Intensity Measurements

Results of signal-intensity measurements are presented in the Table. LS mean SNR and CNR were higher with gadobutrol than with gadoterate meglumine for all off-site readers, with an LS mean difference ranging from  $-10.3$  to  $-14.6$  for SNR and from  $-7.4$  to  $-23.6$  for CNR. Statistically significant LS mean differences were observed for SNR for reader 1 ( $P < .001$ ) and for CNR for readers 1 and 3 ( $P < .001$  and  $P = .008$ ). Significantly ( $P < .001$ ) higher values of lesion percentage enhancement were reported with gadobutrol compared with gadoterate meglumine, according to all readers, with LS mean differences ranging from  $-13.2$  to  $-15.7$ .

### Adverse Events

A similar percentage of patients with postinjection AEs related to contrast agent was observed with gadoterate meglumine (7.8%,  $n = 20$  patients) and gadobutrol (7.3%,  $n = 19$  patients). The most frequent AEs related to gadoterate meglumine were injection site pain ( $n = 11$ ) and paraesthesia at the injection site ( $n = 2$ ) and at other sites ( $n = 2$ ), while the most frequent AEs related to gadobutrol were injection site pain ( $n = 13$ ), dizziness ( $n = 2$ ), and nausea ( $n = 2$ ). All these postinjection AEs related to the contrast agents were mild or moderate in intensity and resolved. Two patients had serious AEs during the study (1 before and the other 8 days after contrast agent administration). For both patients, the serious AEs were considered related to their primary brain tumor and not related to the contrast agent.

### DISCUSSION

The results from this study support the noninferiority of gadoterate meglumine compared with gadobutrol, 2 macrocyclic GBCAs, for the diagnosis and evaluation of primary brain (intracranial) tumors. Most patients ( $>90\%$ ) presented with lesions that were scored good/excellent for overall lesion visualization and characterization by the readers with each contrast agent. No statistically significant differences were observed between the 2 GBCAs regarding the assessment of lesion border delineation (except for 1 reader), lesion internal morphology, degree of contrast enhancement, or level of diagnostic confidence. The results for blinded calculated reader preference based on the sum of scores at the patient level for 3 of the secondary end points showed no preference for either contrast agent in most cases (68%–89%). When a preference was expressed for one or the other contrast agent, the statistical analysis including the no preference subgroup failed to show any statistically significant difference. Despite an LS mean difference in CNR, SNR, and lesion percentage enhancement in favor of gadobutrol, which is considered clinically minimal when relating it to the LS mean value of either of the 2 contrast agents, no discernible clinical effect was observed on lesion visualization and characterization score. This suggests that the level of contrast enhancement obtained with gadoterate meglumine provides comparable contrast visualization for evaluation of primary brain tumors.

Several previous studies compared the efficacy of gadoterate meglumine with that of other GBCAs with slightly different relax-

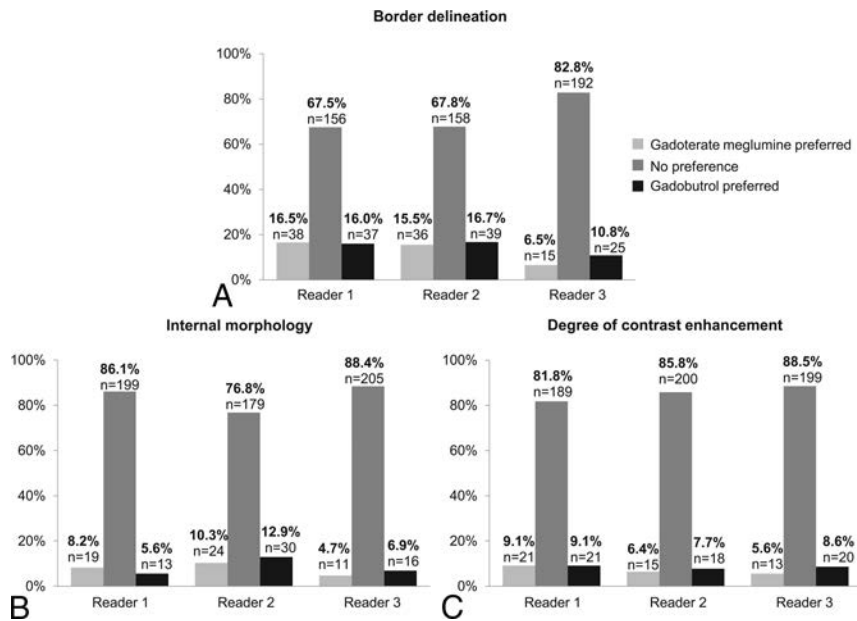


**FIG 5.** Classification in preference subgroups for lesion border delineation (A), lesion internal morphology (B), and degree of contrast enhancement (C). The bar graphs show the rate of patients classified in preference subgroups for lesion border delineation (A), lesion internal morphology (B), and degree of contrast enhancement (C), according to each off-site reader ( $n = 234$  patients for all readers;  $n = 231$  patients for reader 1;  $n = 233$  patients for reader 2;  $n = 232$  patients for reader 3), with  $P > .1$  for the 3 end points for all readers (Wilcoxon signed rank test).

#### Signal-intensity measurements

	LS Mean <sup>a</sup> (SE)		LS Mean <sup>a</sup> Difference (95% CI)	P Value
	Gadoterate Meglumine	Gadobutrol		
<b>SNR</b>				
Reader 1	266.79 (5.00)	281.41 (5.02)	-14.61 (-22.77 to -6.46)	<.001
Reader 2	157.21 (4.75)	167.46 (4.75)	-10.26 (-21.58 to 1.07)	.076
Reader 3	192.94 (4.98)	203.35 (4.97)	-10.41 (-22.75 to 1.93)	.098
<b>CNR</b>				
Reader 1	117.22 (7.83)	140.84 (7.84)	-23.62 (-33.25 to -13.99)	<.001
Reader 2	64.59 (4.19)	72.02 (4.19)	-7.42 (-14.87 to 0.03)	.051
Reader 3	82.96 (5.16)	96.44 (5.15)	-13.48 (-23.43 to -3.54)	.008
<b>Percentage enhancement</b>				
Reader 1	107.61 (3.93)	121.72 (3.93)	-14.12 (-18.38 to -9.85)	<.001
Reader 2	93.90 (3.63)	107.12 (3.63)	-13.22 (-17.28 to -9.16)	<.001
Reader 3	98.82 (3.77)	114.47 (3.76)	-15.66 (-20.52 to -10.79)	<.001

**Note:**—SE indicates standard error.

<sup>a</sup> LS means are the means controlled for covariates of the model.

ivity values. Oudkerk et al<sup>5</sup> compared gadoterate meglumine with gadopentetate dimeglumine, a linear ionic GBCA, in 1038 patients with CNS pathologies and showed comparable image quality with both contrast agents. However, one of the limitations of the study is the lack of a crossover design. More recently, Anzalone et al<sup>2</sup> performed a single-blind, crossover comparison study of gadobutrol versus gadoterate meglumine in 136 patients with known brain lesions who underwent 2 identical MR imaging examinations, one with each contrast agent. MR images were read by 3 independent blinded readers in a matched-pairs comparison in which both MR imaging series were displayed simultaneously. Readers scored an overall preference for one or the other MR imaging examination or “no preference” by using a 3-point scale: 1 = gadobutrol better than gadoterate meglumine, 0 = no pref-

erence, and -1 = gadobutrol worse than gadoterate meglumine. Secondary end point evaluations included a preference regarding the intensity of lesion enhancement, lesion delineation, and internal lesion structure. A statistically significant overall preference for gadobutrol was noted by 2 of 3 readers. However, no preference was expressed by the off-site readers in the largest proportion of cases (47% of patients). For secondary assessment, a statistically significant preference in favor of gadobutrol was noted by the 3 readers for the level of enhancement but by only 1 reader for internal lesion structure and by none of the readers for lesion delineation. A major bias of the statistical analysis of this study was that it excluded the “no preference” assessment group, which was the largest group.<sup>6</sup> Quantitative assessment of the lesion-to-brain ratio and lesion percentage enhancement showed a statistically significant difference in favor of gadobutrol, which probably reflects the small difference in r1 between the 2 contrast agents. Most important, no clinical advantage for either treatment group was demonstrated in this study, and no differences were reported in the number of lesions detected with either contrast agent.

Gadobutrol was also compared with other GBCAs in several studies. A comparison of the diagnostic performance of gadobutrol and gadoteridol, another macrocyclic agent with r1 relaxivity comparable with that of gadoterate meglumine, was conducted by Katakami et al<sup>4</sup> in 175 patients with known or suspected brain metastases. In this single-blind, randomized, controlled intraindividual crossover study, a single dose

and a double dose of gadobutrol, 1.0 mol/L (0.1 and 0.2 mmol/kg of body weight, respectively), were demonstrated to be noninferior to a double dose of gadoteridol, 0.5 mol/L (0.2 mmol/kg of body weight), at detecting brain metastases, with a comparable mean number of lesions detected. A major limitation of this study is that MR imaging examinations with gadoteridol were performed only after the double dose; this feature did not allow a head-to-head comparison of single doses of both contrast agents.

Maravilla et al<sup>3</sup> reported a randomized double-blind crossover study also comparing gadobutrol with gadoteridol, both at the single dose of 0.1 mmol/kg. This study, including 229 patients, showed the noninferiority of gadoteridol compared with gadobutrol for overall diagnostic lesion preference using a matched-pairs comparison study design, as well as for secondary end points

of lesion border delineation, internal morphology, lesion extent, and lesion contrast enhancement. In addition, a blinded reader assessment of the diagnostic characterization of lesions as benign or malignant showed no statistically significant difference between the 2 contrast agents for 2 of 3 readers.

Another limitation of the study is that nearly 60% of patients presented with extra-axial tumors, meningiomas, or nerve sheath tumors, which should readily enhance regardless of agent and magnetic field strength.

Therefore, the results of the present study are consistent with previous reports showing no difference in clinical benefit between the 2 contrast agents, with slightly different relaxivity values. In our study, a rigorous, double-blind, controlled intraindividual, 2-sequence, 2-period crossover design was chosen to compare gadoterate meglumine with gadobutrol. The study design differs slightly from some other crossover comparison studies because blinded readers used a 4-point scale graded from poor to excellent to rank the primary end point of overall lesion visualization and characterization for each individual MR imaging examination independently and in a randomized order. The present methodology aimed to simulate the clinical daily practice in which contrast-enhanced MR imaging must allow good visualization and characterization of lesions, which ensures appropriate medical care of patients. The very high interreader agreement proportion, ranging from 91% to 96% for the assessment of overall lesion visualization and characterization, and the consistency observed between off-site and on-site readers demonstrate the robustness of our results.

Unlike in Maravilla et al,<sup>3</sup> the accuracy for lesion characterization with histopathologic confirmation was not appraised in our study. The level of diagnostic confidence and radiologic diagnosis was assessed, but histopathologic confirmation ensuring the validity of the diagnosis was lacking. Another limitation of this study was that we did not evaluate the impact of contrast-enhanced MR imaging on patient medical management. A follow-up study evaluating patient management after contrast-enhanced MR imaging with gadoterate meglumine or gadobutrol would be needed to confirm the clinical significance of these results.

The use of any contrast agent must be based on clinical need and diagnostic indications. Once the diagnostic indications are met, the choice of which contrast agent to use is based on balancing the benefit to be gained (eg, adequate visualization) versus the risk of use. Gadoterate meglumine has been used for >28 years as a safe and efficient MR imaging GBCA. There have been >60 million doses administered worldwide, with an excellent safety profile for immediate adverse drug reactions and a low incidence of serious AEs, comparable with other extracellular GBCAs.<sup>7</sup> This study confirms the low incidence of immediate AEs reported with gadoterate meglumine and with gadobutrol as demonstrated in multiple previous studies.<sup>7,8</sup> All AEs were mild or moderate in degree and resolved; no serious AEs related to either contrast agent were reported during the study.

Thus, the present results also support the comparable safety profile of gadoterate meglumine versus gadobutrol.

The discovery of the association of GBCAs with nephrogenic systemic fibrosis in patients with severe renal failure<sup>9,10</sup> and, more recently, with brain gadolinium deposition<sup>11-13</sup> in patients with

normal renal function raises important safety concerns in the field of contrast-enhanced MR imaging, which influence radiologic practice. Most important, no or very few cases of nephrogenic systemic fibrosis have been reported after highly stable macrocyclic GBCA administration (no cases of nephrogenic systemic fibrosis associated with unconfounded single-agent administration of gadoterate meglumine), and brain T1 hyperintensities have not been observed after administration of any of the macrocyclic GBCAs.<sup>12-16</sup> The emergence of these safety issues related to the use of GBCAs should encourage the choice of the most stable macrocyclic contrast agents in clinical practice.

## CONCLUSIONS

This multicenter, randomized, double-blind, controlled intraindividual crossover study demonstrates the noninferiority of gadoterate meglumine versus gadobutrol for overall visualization and characterization of primary brain tumors in 234 patients, supported by no preference of the readers for either contrast agent, in most cases, regarding border delineation, internal morphology, and the qualitative degree of contrast enhancement. Despite the difference in relaxivity between these 2 GBCAs, no measurable difference in clinical benefit was observed in our study. A similar safety profile was also demonstrated for both contrast agents.

## ACKNOWLEDGMENTS

The authors thank all participating investigators, Pr K.J. Ahn, Dr A. Arbelaez, Dr E. Caro Osorio, Dr R. Carmody, Dr S.H. Cha, Dr J.W. Choi, Dr G.H. Chung, Dr A.H. Gil Valadez, Dr J.L. Jasso Rico, Dr J.F. Moreno, Dr F. Moser, Dr J. Nickerson, Dr J.A. Romero Figueroa, Dr H. Schwartz, Dr S. Seidman, Dr G. Shah, Dr P. Shah, Dr A.J. Schlesinger, Dr H.R. Vazquez Sanchez, Dr P. Woodward; all study site coordinators; as well as S. Rollin and L. Maho for operational aspects. They also thank B. Piednoir for his statistical input and A.-C. Laurent for her support in editorial assistance.

Disclosures: Kenneth R. Maravilla—*RELATED: Grant: Guerbet, Comments: grant for clinical trial study site\*; Consulting Fee or Honorarium: Guerbet, Comments: consultant for study design and blinded image reviewer design; Support for Travel to Meetings for the Study or Other Purposes: Guerbet, Comments: travel support for consultant meetings; UNRELATED: Consultancy: Bracco, Guerbet. Daniel San-Juan—RELATED: Provision of Writing Assistance, Medicines, Equipment, or Administrative Support: Clinical Research Institute, Comments: I received the contrast agents to test in my center.\* Sang Joon Kim—RELATED: Grant: Guerbet, Comments: sponsor-initiated trial. James R. Fink—RELATED: Grant: Guerbet, Comments: research salary support (approximately 1% full time equivalent)\*; UNRELATED: Grants/Grants Pending: Guerbet, Comments: research salary support (approximately 1% full time equivalent)\*. William Escobar—RELATED: Consulting Fee or Honorarium: Centro Medico Imbanaco\*; UNRELATED: Payment for Lectures Including Service on Speakers Bureaus: Centro Medico Imbanaco.\* Asim Bag—RELATED: Grant: Guerbet, Comments: University of Alabama at Birmingham was one of the many sites where the clinical trial was conducted. Guerbet supported all the trial-related expenditures.\* Donna R. Roberts—RELATED: Grant: Quintiles/Guerbet, Comments: My university received funding to conduct the clinical trial. I served as site principal investigator\*; Support for Travel to Meetings for the Study or Other Purposes: Guerbet, Comments: I received travel support from Guerbet to present the findings of this study at the American Society of Neuroradiology Annual Meeting; UNRELATED: Board Membership: Guerbet, Comments: I serve as a consultant and advisory board member for Guerbet; Consultancy: Guerbet, Comments: I serve as a consultant and advisory board member for Guerbet; Grants/Grants Pending: Guerbet, Comments: grant support for an investigator-initiated study; Payment for Lectures Including Service on Speakers Bureaus: Guerbet, Comments: I have given presentations at scientific meetings. Jing Hao—UNRELATED: Employment: Guerbet, Comments: I am an employee of Guerbet. Camille Pitrou—RELATED: Other: Guerbet, Comments: Guerbet employee; UNRELATED: Employment: Guerbet. Apostolos J. Tsiouris—RELATED:*

Other: BioClinica, *Comments*: reimbursed for reviewing MRI scans for this study through BioClinica as a blinded independent observer. Edward Herskovits—*RELATED: Consulting Fee or Honorarium*: BioClinica, *Comments*: consulting fee for reviewing brain MR imaging examinations; *UNRELATED: Board Membership*: Galileo CDS, *Comments*: stock grant for board membership, consulting, software development; *Consultancy*: Galileo CDS, RadOptimal, *Comments*: software development, scientific advisor; *Expert Testimony*: medicolegal consulting; *Patents (Planned, Pending or Issued)*: Galileo CDS, patent pending; *Stock/Stock Options*: Galileo CDS, RadOptimal, Jochen B. Fiebach—*RELATED: Consulting Fee or Honorarium*: Guerbet, *Comments*: honorarium for blinded reading of study MRI examinations; *UNRELATED: Board Membership*: European Union Seventh Framework Program (FP7/2007–2013), *Comments*: grant agreement No. 278276 (WAKE-Up study)\*; *Consultancy*: BioClinica, Cerevast, Artemida, Brainomix, Lundbeck, *Comments*: consulting and blinded reading of study CT/PET/MRI examinations; *Grants/Grants Pending*: German Federal Ministry of Education and Research, *Comments*: Principal Investigator in 01EO0801 and 01EI01301. \*Money paid to the institution.

## REFERENCES

- Rohrer M, Bauer H, Mintorovitch J, et al. **Comparison of magnetic properties of MRI contrast media solutions at different magnetic field strengths.** *Invest Radiol* 2005;40:715–24 CrossRef Medline
- Anzalone N, Scarabino T, Venturi C, et al. **Cerebral neoplastic enhancing lesions: multicenter, randomized, crossover intraindividual comparison between gadobutrol (1.0M) and gadoterate meglumine (0.5M) at 0.1 mmol Gd/kg body weight in a clinical setting.** *Eur J Radiol* 2013;82:139–45 CrossRef Medline
- Maravilla KR, Smith MP, Vymazal J, et al. **Are there differences between macrocyclic gadolinium contrast agents for brain tumor imaging? Results of a multicenter intraindividual crossover comparison of gadobutrol with gadoteridol (the TRUTH study).** *AJNR Am J Neuroradiol* 2015;36:14–23 CrossRef Medline
- Katakami N, Inaba Y, Sugata S, et al. **Magnetic resonance evaluation of brain metastases from systemic malignancies with two doses of gadobutrol 1.0 m compared with gadoteridol: a multicenter, phase ii/iii study in patients with known or suspected brain metastases.** *Invest Radiol* 2011;46:411–18 CrossRef Medline
- Oudkerk M, Sijens PE, Van Beek EJ, et al. **Safety and efficacy of Dotarem (Gd-DOTA) versus Magnevist (Gd-DTPA) in magnetic resonance imaging of the central nervous system.** *Invest Radiol* 1995;30:75–78 CrossRef Medline
- Desché P. **Re: cerebral neoplastic enhancing lesions—multicenter, randomized, crossover intraindividual comparison between gadobutrol (1.0M) and gadoterate meglumine (0.5M) at 0.1 mmol Gd/kg body weight in a clinical setting.** *Eur J Radiol* 2012;81:e967; author reply 2925–26 CrossRef Medline
- de Kerviler E, Maravilla K, Meder JF, et al. **Adverse reactions to gadoterate meglumine: review of over 25 years of clinical use and more than 50 million doses.** *Invest Radiol* 2016;51:544–51 CrossRef Medline
- Endrikat J, Vogtlaender K, Dohanish S, et al. **Safety of gadobutrol: results from 42 clinical phase II to IV studies and postmarketing surveillance after 29 million applications.** *Invest Radiol* 2016;51:537–43 CrossRef Medline
- Grobner T. **Gadolinium—a specific trigger for the development of nephrogenic fibrosing dermopathy and nephrogenic systemic fibrosis? Nephrol Dial Transplant** 2006;21:1104–08 Medline
- Marckmann P, Skov L, Rossen K, et al. **Nephrogenic systemic fibrosis: suspected causative role of gadodiamide used for contrast-enhanced magnetic resonance imaging.** *J Am Soc Nephrol* 2006;17:2359–62 CrossRef Medline
- Kanda T, Ishii K, Kawaguchi H, et al. **High signal intensity in the dentate nucleus and globus pallidus on unenhanced T1-weighted MR images: relationship with increasing cumulative dose of a gadolinium-based contrast material.** *Radiology* 2014;270:834–41 CrossRef Medline
- Kanda T, Fukusato T, Matsuda M, et al. **Gadolinium-based contrast agent accumulates in the brain even in subjects without severe renal dysfunction: evaluation of autopsy brain specimens with inductively coupled plasma mass spectroscopy.** *Radiology* 2015;276:228–32 CrossRef Medline
- McDonald RJ, McDonald JS, Kallmes DF, et al. **Intracranial gadolinium deposition after contrast-enhanced MR imaging.** *Radiology* 2015;275:772–82 CrossRef Medline
- Radbruch A, Weberling LD, Kieslich PJ, et al. **Gadolinium retention in the dentate nucleus and globus pallidus is dependent on the class of contrast agent.** *Radiology* 2015;275:783–91 CrossRef Medline
- Radbruch A, Haase R, Kieslich PJ, et al. **No signal intensity increase in the dentate nucleus on unenhanced T1-weighted MR images after more than 20 serial injections of macrocyclic gadolinium-based contrast agents.** *Radiology* 2017;282:699–707 CrossRef Medline
- Cao Y, Huang DQ, Shih G, et al. **Signal change in the dentate nucleus on T1-weighted MR images after multiple administrations of gadopentetate dimeglumine versus gadobutrol.** *AJR Am J Roentgenol* 2016;206:414–19 CrossRef Medline

# Diagnostic Performance of a 10-Minute Gadolinium-Enhanced Brain MRI Protocol Compared with the Standard Clinical Protocol for Detection of Intracranial Enhancing Lesions

J. Fagundes, M.G. Longo, S.Y. Huang, B.R. Rosen, T. Witzel, K. Heberlein, R.G. Gonzalez, P. Schaefer, and O. Ropalino



## ABSTRACT

**BACKGROUND AND PURPOSE:** The development of new MR imaging scanners with stronger gradients and improvement in coil technology, allied with emerging fast imaging techniques, has allowed a substantial reduction in MR imaging scan times. Our goal was to develop a 10-minute gadolinium-enhanced brain MR imaging protocol with accelerated sequences and to evaluate its diagnostic performance compared with the standard clinical protocol.

**MATERIALS AND METHODS:** Fifty-three patients referred for brain MR imaging with contrast were scanned with a 3T scanner. Each MR image consisted of 5 basic fast precontrast sequences plus standard and accelerated versions of the same postcontrast T1WI sequences. Two neuroradiologists assessed the image quality and the final diagnosis for each set of postcontrast sequences and compared their performances.

**RESULTS:** The acquisition time of the combined accelerated pre- and postcontrast sequences was 10 minutes and 15 seconds; and of the fast postcontrast sequences, 3 minutes and 36 seconds, 46% of the standard sequences. The 10-minute postcontrast axial T1WI had fewer image artifacts ( $P < .001$ ) and better overall diagnostic quality ( $P < .001$ ). Although the 10-minute MPRAGE sequence showed a tendency to have more artifacts than the standard sequence ( $P = .08$ ), the overall diagnostic quality was similar ( $P = .66$ ). Moreover, there was no statistically significant difference in the diagnostic performance between the protocols. The sensitivity, specificity, and accuracy values for the 10-minute protocol were 100.0%, 88.9%, and 98.1%.

**CONCLUSIONS:** The 10-minute brain MR imaging protocol with contrast is comparable in diagnostic performance with the standard protocol in an inpatient motion-prone population, with the additional benefits of reducing acquisition times and image artifacts.

**ABBREVIATIONS:** GRAPPA = generalized autocalibrating partially parallel acquisition; GRE = gradient-echo; SE = spin-echo

The prolonged acquisition time of MR imaging is uncomfortable for patients, introduces the potential for motion-related artifacts (especially in critically ill patients), limits clinical availability, and increases cost. Consequently, in the past decade, there has been a concerted effort to develop fast and ultrafast MR imaging protocols.<sup>1-7</sup>

For many years, continual development of new scanners with

stronger gradients and the improvement of coil technology,<sup>8-10</sup> allied with a number of emerging fast imaging techniques, has allowed substantial reduction in MR imaging scan times.<sup>1,11-13</sup> More recently, the development of parallel imaging, a robust method for accelerating MR imaging data acquisitions based on obtaining simultaneous information from arrays of coils, allowing decreased filling of  $k$ -space lines, has been the preferred method for decreasing acquisition times.<sup>14-16</sup>

This study is in accord with recent effort within the neuroradiology research community to accelerate the clinical MR imaging studies and expands on a 5-minute noncontrast brain MR

Received March 6, 2017; accepted after revision May 12.

From the Clínica de Diagnóstico por Imagem (J.F.), Rio de Janeiro, Brazil; Department of Radiology (M.G.L., S.Y.H., R.G.G., P.S., O.R.), Massachusetts General Hospital, Boston, Massachusetts; Athinoula A. Martinos Center for Biomedical Imaging (B.R.R., T.W.), Charlestown, Massachusetts; and Siemens Medical Solutions (K.H.), Malvern, Pennsylvania.

J. Fagundes, M.G. Longo, and K. Heberlein received financial support from Siemens Medical Solutions.

This work was conducted with support from Harvard Catalyst and The Harvard Clinical and Translational Science Center (National Center for Research Resources and the National Center for Advancing Translational Sciences, National Institutes of Health Award ULI TR001102) and financial contributions from Harvard University and its affiliated academic health care centers.

The content is solely the responsibility of the authors and does not necessarily represent the official views of Harvard Catalyst, Harvard University and its affiliated academic health care centers, or the National Institutes of Health.

Please address correspondence to Otto Ropalino, MD, Department of Radiology, Massachusetts General Hospital, 55 Fruit St, Boston, MA 02114-2622; e-mail: oropalino@mgh.harvard.edu.

Indicates article with supplemental on-line table.

<http://dx.doi.org/10.3174/ajnr.A5293>

**Table 1: Clinical characteristics of patients**

Characteristic	No. of Cases (%)
Male	25 (47%)
Age (mean) (yr)	53.4 ± 16.1
Clinical indication for MRI	
New focal neurologic deficit	3 (5.7%)
Altered mental status	4 (7.6%)
Seizures	2 (3.8%)
Brain tumor	26 (49.1%)
Postoperative evaluation	8 (15.1%)
Others	10 (18.9%)

imaging protocol previously validated by our group.<sup>11</sup> We previously demonstrated similar image quality and diagnostic accuracy of a 5-minute brain MR imaging protocol compared with the conventional protocol in a motion-prone clinical population. The aim of this study was to develop a 10-minute gadolinium-enhanced brain MR imaging protocol with accelerated sequences and to evaluate its diagnostic performance compared with a standard clinical protocol in a similar clinical population.

## MATERIALS AND METHODS

### Study Design

A prospective comparative study was performed in 69 consecutive neurologic/neurosurgical patients in the intensive care unit who underwent brain MR imaging with contrast, from February through June 2016. None of the patients were sedated. Sixteen patients were excluded because of incomplete datasets due to technical or compliance issues. The remaining 53 patients (25 men; mean age, 53.4 ± 16.1 years) were included. Demographic information, including age, sex, and clinical indication for undergoing MR imaging, is described in Table 1. This study was Health Insurance Portability and Accountability Act–compliant and was approved by the Massachusetts General Hospital institutional review board. Because all brain MR imaging studies included were acquired for clinical purposes and no significant time was added to the study, informed consent was waived by the institutional review board.

### MR Imaging Protocol

All studies included 5 basic fast sequences that have been previously validated (5-minute brain)<sup>11</sup> and standard and fast versions of 2 common clinically used postcontrast sequences: axial 5-mm T1-weighted and 3D MPRAGE. Because the acquisition time of the precontrast sequences in addition to the fast postcontrast sequences was close to 10 minutes, we decided to call this novel protocol the “10-minute brain MR imaging protocol.” All MR imaging studies were performed with a clinical 3T MR imaging scanner (Magnetom Skyra; Siemens, Erlangen, Germany) with maximum gradient strength of 45 mT/m, a slew rate of 200 T/m/s, and a 32-channel multiarray receiver head coil. All scans began with 4 sequences from the 5-minute brain protocol (fast sagittal T1-weighted, axial FLAIR, axial T2\*-weighted, and axial diffusion-weighted images),<sup>11</sup> followed by a fast gradient-echo (GRE) T1-weighted sequence. Following the intravenous injection of gadolinium, an axial T2-weighted sequence, also developed for the 5-minute protocol, was performed to allow a minimum time required for the contrast to properly enhance brain lesions.<sup>17</sup> The

standard axial TSE T1-weighted, 10-minute protocol fast axial GRE T1-weighted, and standard and accelerated MPRAGE sequences were then acquired in a randomized order. The fast axial GRE T1 and fast MPRAGE sequences were shortened with generalized autocalibrating partially parallel acquisition (GRAPPA).<sup>18</sup> In addition, manual intersequence adjustments were eliminated with the automatic section positioning technique. This technique was developed by van der Kouwe et al,<sup>19</sup> with a probabilistic method to align a 3D localizer to a statistical atlas, which contains the probability of a given tissue type occurring at a given location based on the MR imaging intensity values.

A detailed summary of sequence parameters is found in the On-line Table. The elapsed times before the beginning of each sequence were measured and compared between both protocols (standard and 10-minute). Elapsed time was defined as a time from the start of the MR imaging study (localizer scan) to the start of each sequence in each protocol.<sup>11</sup>

### Qualitative Image Evaluation

The DICOM datasets were transferred to a predetermined workstation and anonymized before randomization. Blinded to patient information and protocol type, 2 neuroradiologists (O.R., S.Y.H.) with 16 and 6 years of experience independently reviewed all DICOM datasets with a DICOM viewer (OsiriX Imaging Software; <http://www.osirix-viewer.com>). To obtain optimal visualization, we allowed adjustments of window widths and levels. A research team member not involved in the data assessment was responsible for maintaining anonymization and randomization keys.

### Individual Analysis

Regarding the individual analysis, each patient had 2 DICOM datasets: 1 containing the 10-minute postcontrast protocol and 1 containing the standard protocol images (both shared the same 5 basic sequences from the 5-minute brain protocol already mentioned and a standard precontrast 5-mm axial T1-weighted sequence). Both datasets were distributed in a randomized fashion throughout the reading sessions so that no patient had his or her standard and 10-minute protocols read at the same session.

Individual datasets for each protocol were assessed for diagnostic performance, and accuracy was calculated with the standard protocol as the criterion standard. The readers were asked to determine the number of lesions, the degree of enhancement, and the presumed diagnosis (without knowledge of clinical information) after they analyzed the entire protocol. Only pathological enhancing lesions were included. The degree of enhancement was determined on the basis of a predefined 4-point scale: 0 (none), not visualized on 1 (or both) of the postcontrast sequences; 1 (subtle), faintly visualized on 3D sequences but better visualized on axial images (or vice versa); 2 (adequate), moderate degree of enhancement, equally seen in both 3D and axial sequences; and 3 (excellent), strong and sharply demarcated enhancement on both sequences.<sup>20</sup> Disagreements between readers were resolved by consensus review for presumed diagnoses and adjudicated by a third reader (P.S.) with 20 years of experience for the remaining variables.

**Table 2: Presumed diagnosis based on imaging findings without clinical information**

Diagnosis	Standard Protocol		10-Minute Protocol		P <sup>a</sup>
	No. Cases (%)	Mean No. of Lesions (95% CI)	No. Cases (%)	Mean No. of Lesions (95% CI)	
Normal findings	8 <sup>b</sup> (15.1%)	0	9 <sup>b</sup> (17.0%)	0	1.00
Neoplastic disease	21 (39.6%)	4.8 (1.8–7.7)	21 (39.6%)	4.8 (1.8–7.7)	
Inflammatory disease	2 (3.8%)	2.5 (–16.5–1.6)	2 (3.8%)	2.5 (–16.5–21.6)	
CNS infection	0 (0%)	0	0 (0%)	0	
Vascular pathologies	5 <sup>b</sup> (9.4%)	2 (0.8–3.2)	4 <sup>b</sup> (7.6%)	1.5 (–0.1–3.1)	
Posttreatment and/or postsurgical changes	15 (28.3%)	2.9 (2.2–3.7)	15 (28.3%)	2.9 (2.2–3.7)	
Undetermined	2 (3.8%)	1	2 (3.8%)	1	

<sup>a</sup> McNemar test between standard and 10-minute protocols.

<sup>b</sup> A case was diagnosed as a vascular lesion in the standard protocol sequences, but it was considered normal enhancement in the 10-minute protocol. Retrospectively, this lesion was present in the 10-minute protocol sequences and compatible with a small capillary telangiectasia.

### Head-to-Head Analysis

A separate review session was performed to compare the presence of image artifacts, visualization of normal anatomic structures, and overall diagnostic quality. Each case had side-by-side comparison of the standard and 10-minute versions of the T1-weighted axial postcontrast sequences and side-by-side comparison of the standard and 10-minute versions of the MPRAGE postcontrast sequences. Both datasets (10-minute and standard) were presented simultaneously in a random left-right order and in a blinded fashion to the observers. The observers documented which sequence was superior (left or right) or whether they were equivalent. A different member of the research team, who was not blinded to the assignments, used these scores and rearranged them following a previously described scoring method.<sup>21</sup> A third reader (P.S.) resolved any disagreements. Image quality was defined as image degradation by artifacts and was assessed by using a 5-point scale: –2, artifacts are seen only on the left sequence; –1, artifacts are worse on the left sequence; 0, comparable artifacts are seen in both protocols; +1, artifacts are worse on the right sequence; +2, artifacts are seen only on the right sequence. The overall diagnostic quality was defined as the ability to identify findings despite the presence of artifacts and was assessed by a similar comparative 5-point scale: –2, left sequences are nondiagnostic; –1, right sequences are superior to the left sequences, but both are diagnostic; 0, both protocols are diagnostic and equal in terms of overall quality; +1, left sequences are superior to the 10-minute sequences, but both are diagnostic; +2, right sequences are nondiagnostic.<sup>21</sup>

### Statistical Analysis

The descriptive data were presented by means and SDs or medians and ranges for parametric and nonparametric variables, respectively. Fisher exact and Wilcoxon signed rank tests were used to analyze the results of elapsed time, head-to-head, and individual analyses, considering categorical and continuous variables, respectively, on the basis of the data from the described scores after the adjudication. The comparison of individual analyses regarding the diagnostic performance was evaluated with the McNemar test.

Proportions of agreement between readers regarding the individual analysis were reported with the Cohen  $\kappa$  coefficient. This coefficient was interpreted as follows: 0.00–0.20, slight agreement; 0.21–0.40, fair agreement; 0.41–0.60, moderate agreement; 0.61–0.80, substantial agreement; and >0.80, almost perfect agreement.<sup>22</sup>

*P* values < .05 were considered statistically significant. All statistical calculations were performed with STATA, Version 14.0 (StataCorp, College Station, Texas).

## RESULTS

### Elapsed-Time Comparison

There was no statistically significant difference between the elapsed time of the standard and 10-minute sequences (*P* > .05). These results reinforce the order of the scanning being truly randomized, and they did not influence image quality.

### Individual Analysis

The observers decided by consensus a presumed diagnosis based on the MR imaging features (Table 2). These diagnoses were concordant between the 10-minute and standard protocol groups in 52 cases (98.1%). The only case in which they disagreed was diagnosed as a vascular pathology in the standard protocol sequences, but it was considered normal vascular enhancement in the 10-minute protocol. Retrospectively, this lesion was present in the 10-minute protocol sequences and was compatible with a small capillary telangiectasia. The sensitivity, specificity, and accuracy of the 10-minute protocol were 100.0% (95% CI, 92%–100%), 88.9% (95% CI, 51.8%–99.7%), and 98.1% (95% CI, 89.9%–99.9%), respectively.

Regarding the enhancing lesions, the median number and statistical distribution of the lesions for each group were similar. The observers identified the same number of lesions in both protocols (162 lesions in 45 patients). From these 45 patients in whom the presence of at least 1 enhancing lesion was described, 18 (40%) underwent the standard protocol first, and 27 (60%), the 10-minute protocol first. Just 1 lesion was more conspicuous in the standard protocol but was also identified on the 10-minute protocol sequences. In this particular case, the standard postcontrast sequences were acquired after the 10-minute postcontrast sequences, and the increased leakage of gadolinium within the lesion may explain this difference. The  $\kappa$  for the interobserver agreement was 0.96 for the standard sequences and 1.0 for the 10-minute sequences. The observers classified slightly more lesions with a higher degree of enhancement in the 10-minute sequences; 97 lesions were classified as degree 3 in the standard protocol, while 111 lesions were classified as degree 3 in the 10-minute protocol (*P* < .001). The  $\kappa$  for the interobserver agreement for this variable was 0.71 for the standard sequences and 0.70 for the 10-minute sequences.

### Head-to-Head Analysis

The 10-minute axial GRE T1-weighted postcontrast sequence was considered superior (in terms of the presence of artifacts and overall diagnostic quality) compared with the standard postcontrast spin-echo (SE) T1-weighted sequence. For most cases (51/53) (96.2%),

**Table 3: Head-to-head evaluation**

Sequence	Favor 10-Minute	Equal	Favor Standard	P <sup>a</sup>
Image artifacts (No.) (%)				
Axial T1 (SE or GRE)	51 (96.22%)	1 (1.88%)	1 (1.88%)	<.001
MPRAGE	11 (20.75%)	21 (39.62%)	21 (39.62%)	.08
Overall diagnostic quality (No.) (%)				
Axial T1 (SE or GRE)	40 (75.47%)	12 (22.64%)	1 (1.88%)	<.001
MPRAGE	2 (3.77%)	48 (90.57%)	3 (5.66%)	.66

<sup>a</sup>Wilcoxon signed rank test.

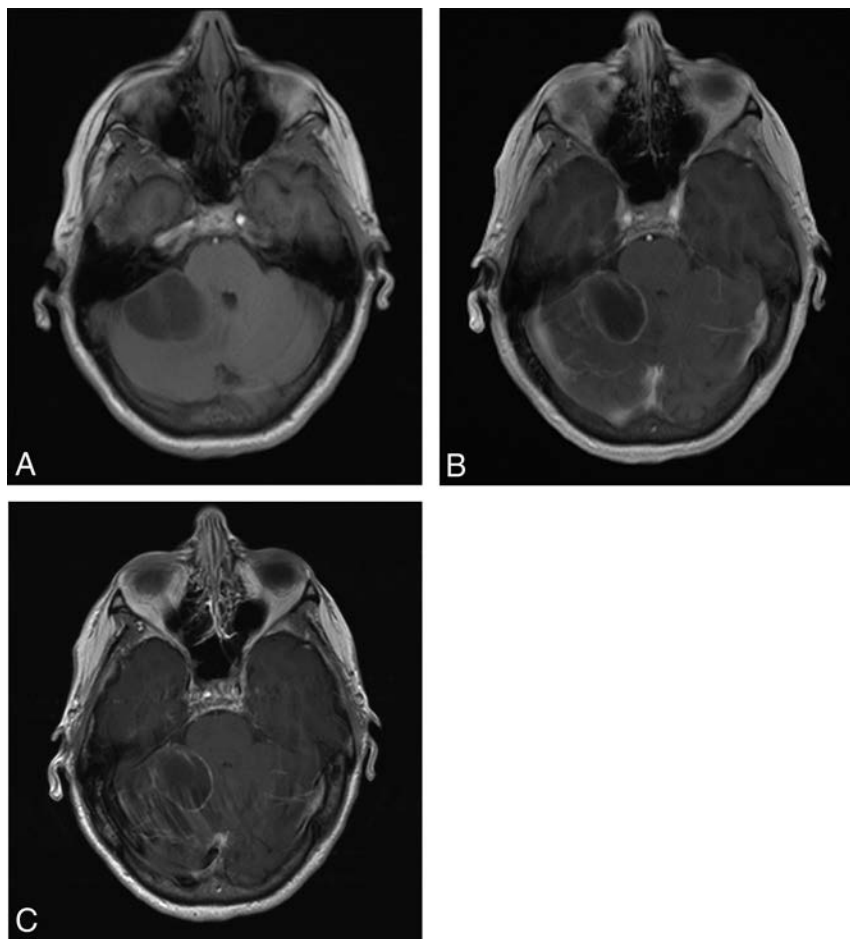


**FIG 1.** Postcontrast T1-weighted axial images obtained from a 66-year-old woman with a history of non-small cell lung cancer showing a metastatic cystic lesion with peripheral enhancement in the right cerebellar hemisphere. Precontrast axial GRE T1-weighted (A), postcontrast axial GRE T1-weighted (B), and postcontrast axial SE T1-weighted (C) images. The 10-minute axial GRE T1WI shows fewer artifacts compared with the standard axial T1WI. The conspicuity of the lesion is comparable on both postcontrast sequences.

the 10-minute GRE T1-weighted sequence had fewer artifacts compared with the standard SE T1-weighted sequence ( $P < .001$ ) (Table 3 and Fig 1).

Most of the MPRAGE postcontrast evaluations reported that the sequences were equivalent. However, there was a trend among the observers to find more artifacts on the 10-minute sequence, though the difference was not statistically significant ( $P = .08$ ). The presence of these artifacts did not influence the overall diagnostic quality ( $P = .66$ ) (Fig 2).

## DISCUSSION

Our results suggest that the proposed 10-minute contrast-enhanced protocol may improve imaging of motion-prone patients

in an inpatient setting. We demonstrated that an optimized 10-minute protocol with contrast (sagittal T1-weighted, axial T2-weighted, axial FLAIR, axial T2\*WI, axial DWI, axial T1-weighted pre- and postcontrast, and 3D-MPRAGE postcontrast) has similar diagnostic accuracy and diagnostic image quality compared with a conventional postcontrast MR imaging protocol.

In fact, the 10-minute GRE T1-weighted axial postcontrast sequence performed better in terms of artifacts and diagnostic image quality compared with the standard SE T1-weighted postcontrast sequence. One reason for this difference in performance could be due to intrinsic differences in these pulse sequences, resulting in faster acquisition times and less motion artifacts with GRE sequences. However, even the initial studies >2 decades ago reported that SE sequences showed more contrast compared with GRE.<sup>23</sup> The improvements in scanner hardware and the higher field strengths of the 3T scanners might have helped to reduce this difference in contrast. Another contribution of our findings is that the TE of the GRE sequence is almost 3 times shorter than the TE of the SE sequence, which could also reduce pulsation artifacts.<sup>24</sup>

The 10-minute-protocol MPRAGE sequence had similar diagnostic performance compared with the standard sequence, though it had a non-statistically significant trend to present more artifacts. The likely cause is the reduction in the signal-to-noise ratio, typical of parallel imaging, which is more evident in 3D sequences.<sup>25,26</sup> Nevertheless, having no influence on the diagnostic performance and the decrease in the acquisition time may justify the use of this sequence.

The shortened acquisition time is one of the most significant benefits of the 10-minute protocol, especially in a group of unstable and motion-prone patients as seen in our cohort. The scan time of our 10-minute protocol was 10 minutes and 15 seconds compared with at least 19 minutes and 3 seconds for a typical conventional protocol (without using acceleration techniques, even for the precontrast sequences), which represents an acquisition time reduction of almost 50%. The acquisition time of the combined postcontrast sequences (GRE T1-weighted axial and 3D MPRAGE) in the 10-minute protocol was 3 minutes and 36 seconds compared with 7 minutes and 49 seconds for the standard postcontrast sequences. This reduction was possible without compromising diagnostic performance and maintaining an accuracy of almost 100%.

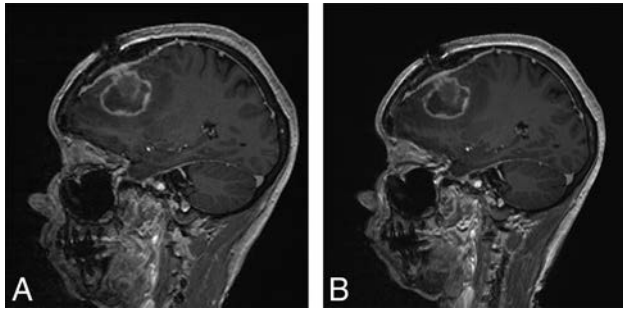


**FIG 2.** Sagittal postcontrast MPRAGE images from a 53-year-old woman with history of breast cancer showing postoperative findings after resection of a brain metastasis. Ten-minute sagittal 3D MPRAGE (A) and standard sagittal 3D MPRAGE (B) images both show comparable diagnostic quality.

We decided to maintain both sequences, 2D T1-weighted axial and 3D MPRAGE, to increase our sensitivity for the detection of enhancing lesions and to be in agreement with the standard protocol in our department, which includes 2 different T1-weighted sequences after contrast administration. Considering the clinical importance of the postcontrast sequences in this population, we believe that maintaining both sequences is useful in case of patient movement during the MR imaging acquisition. While the 3D MPRAGE is known to have higher spatial resolution compared with 2D sequences, it may have decreased the conspicuity of enhancement for small lesions in some cases, supporting the complementary use of both sequences.<sup>27,28</sup>

Parallel imaging relies on a more efficient scan technique, which uses a higher percentage of the scan time for data acquisition (instead of image reconstruction). More specifically, multiple independent receiver coils are used, and the spatial information provided by these independent coils is exploited to encode multiple MR imaging echoes simultaneously.<sup>15,18</sup> Although parallel imaging has many advantages, it has an SNR penalty. Our protocol is optimized for 3T MR imaging with a 32-channel head coil to compensate and mitigate these constraints<sup>16</sup> and should be adapted if 1.5T scanners or head coils with fewer channels are used.

In accordance with our results, previous studies demonstrated the benefits of using parallel imaging sequences in ischemic stroke and pediatric central nervous system disorders,<sup>3,29,30</sup> with consistently reduced acquisition times and comparable image quality. In the study of Nael et al,<sup>29</sup> postcontrast sequences, MR angiography and dynamic susceptibility contrast perfusion, were tested in an acute stroke setting. This study used echo-planar imaging as an acceleration factor for most sequences and yet reached a similar accuracy between the fast and conventional protocols. Our previous study demonstrated the feasibility of fast sequences without contrast in an inpatient setting, with comparable diagnostic accuracy with standard sequences for multiple CNS pathologies in an adult population.<sup>11</sup> Our current results with postcontrast sequences reinforced and expanded on those findings.

Our study has several limitations. First, it included a relatively small sample size. Although we enrolled only 53 patients, we were able to compare the enhancement pattern of >160 lesions. Second, we decided to use our standard protocol as the criterion standard, which may overestimate the accuracy of the protocols.

Third, the time lag between the reading sections was imprecise, increasing the risk of reader-order bias. To address this issue, we performed assessments separated by at least 1 week from each other in a random order.<sup>31</sup> Fourth, our analysis was predominantly qualitative and subjective rather than with quantitative and automated measures. Nevertheless, our  $\kappa$  coefficients for interobserver agreement for enhancement characteristics and the number of lesions were in the range of substantial-to-near-complete agreement, and the diagnostic concordance rate between the standard and 10-minute protocols was very high (98.1%).

## CONCLUSIONS

The 10-minute brain MR imaging protocol with contrast is at least comparable with the standard protocol in an inpatient motion-prone clinical setting, with the substantial benefit of reducing the acquisition time (by nearly 50%). Further use of this protocol in larger and different patient populations is warranted to determine the extent of its clinical utility.

Disclosures: Joana Fagundes—RELATED: Consulting Fee or Honorarium: Siemens Medical Solutions USA, Comments: scholarship to conduct the research. Maria Gabriela Longo—RELATED: Consulting Fee or Honorarium: Siemens Medical Solution USA, Comments: scholarship to conduct the research. Keith Heberlein—UNRELATED: Employment: Siemens Medical Solution USA, Comments: I am a full-time employee. Ramon G. Gonzalez—UNRELATED: Expert Testimony: For the US Attorney in Florida.

## REFERENCES

1. Tsao J. **Ultrafast imaging: principles, pitfalls, solutions, and applications.** *J Magn Reson Imaging* 2010;32:252–66 CrossRef Medline
2. Heidemann RM, Ozsarlak O, Parizel PM, et al. **A brief review of parallel magnetic resonance imaging.** *Eur Radiol* 2003;13:2323–37 CrossRef Medline
3. Woodfield J, Kealey S. **Magnetic resonance imaging acquisition techniques intended to decrease movement artefact in paediatric brain imaging: a systematic review.** *Pediatr Radiol* 2015;45:1271–81 CrossRef Medline
4. Bilgic B, Gagoski BA, Cauley SF, et al. **Wave-CAIPI for highly accelerated 3D imaging.** *Magn Reson Med* 2015;73:2152–62 CrossRef Medline
5. Jacobs J, Stich J, Zahneisen B, et al. **Fast fMRI provides high statistical power in the analysis of epileptic networks.** *Neuroimage* 2014;88:282–94 CrossRef Medline
6. Geethanath S, Reddy R, Konar AS, et al. **Compressed sensing MRI: a review.** *Crit Rev Biomed Eng* 2013;41:183–204 CrossRef Medline
7. Ma D, Gulani V, Seiberlich N, et al. **Magnetic resonance fingerprinting.** *Nature* 2013;495:187–92 CrossRef Medline
8. Wiggins GC, Polimeni JR, Potthast A, et al. **96-channel receive-only head coil for 3 Tesla: design optimization and evaluation.** *Magn Reson Med* 2009;62:754–62 CrossRef Medline
9. Wiggins GC, Triantafyllou C, Potthast A, et al. **32-channel 3 Tesla receive-only phased-array head coil with soccer-ball element geometry.** *Magn Reson Med* 2006;56:216–23 CrossRef Medline
10. Keil B, Blau JN, Biber S, et al. **A 64-channel 3T array coil for accelerated brain MRI.** *Magn Reson Med* 2013;70:248–58 CrossRef Medline
11. Prakkamakul S, Witzel T, Huang S, et al. **Ultrafast brain MRI: clinical deployment and comparison to conventional brain MRI at 3T.** *J Neuroimaging* 2016;26:503–10 CrossRef Medline
12. Feinberg DA, Moeller S, Smith SM, et al. **Multiplexed echo planar imaging for sub-second whole brain fMRI and fast diffusion imaging.** *PLoS One* 2010;5:e15710 CrossRef Medline
13. Feinberg DA, Setsompop K. **Ultra-fast MRI of the human brain with simultaneous multi-slice imaging.** *J Magn Reson* 2013;229:90–100 CrossRef Medline
14. Deshmane A, Gulani V, Griswold MA, et al. **Parallel MR imaging.** *J Magn Reson Imaging* 2012;36:55–72 CrossRef Medline

15. Yanasak NE, Kelly MJ. **MR imaging artifacts and parallel imaging techniques with calibration scanning: a new twist on old problems.** *Radiographics* 2014;34:532–48 CrossRef Medline
16. Zhu Y, Hardy CJ, Sodickson DK, et al. **Highly parallel volumetric imaging with a 32-element RF coil array.** *Magn Reson Med* 2004;52: 869–77 CrossRef Medline
17. Akeson P, Nordström C, Holtås S. **Time-dependency in brain lesion enhancement with gadodiamide injection.** *Acta Radiol* 1997;38: 19–24 Medline
18. Griswold MA, Jakob PM, Heidemann RM, et al. **Generalized auto-calibrating partially parallel acquisitions (GRAPPA).** *Magn Reson Med* 2002;47:1202–10 CrossRef Medline
19. van der Kouwe AJ, Benner T, Fischl B, et al. **On-line automatic slice positioning for brain MR imaging.** *Neuroimage* 2005;27:222–30 CrossRef Medline
20. Gutierrez JE, Rosenberg M, Seemann J, et al. **Safety and efficacy of gadobutrol for contrast-enhanced magnetic resonance imaging of the central nervous system: results from a multicenter, double-blind, randomized, comparator study.** *Magn Reson Insights* 2015;8: 1–10 CrossRef Medline
21. Soman S, Holdsworth SJ, Barnes PD, et al. **Improved T2\* imaging without increase in scan time: SWI processing of 2D gradient echo.** *AJNR Am J Neuroradiol* 2013;34:2092–97 CrossRef Medline
22. Viera AJ, Garrett JM. **Understanding interobserver agreement: the kappa statistic.** *Fam Med* 2005;37:360–63 Medline
23. Chappell PM, Pelc NJ, Foo TK, et al. **Comparison of lesion enhancement on spin-echo and gradient-echo images.** *AJNR Am J Neuroradiol* 1994;15:37–44 Medline
24. Crombé A, Saranathan M, Ruet A, et al. **MS lesions are better detected with 3D T1 gradient-echo than with 2D T1 spin-echo gadolinium-enhanced imaging at 3T.** *AJNR Am J Neuroradiol* 2015;36: 501–07 CrossRef Medline
25. Li T, Mirowitz SA. **Comparative study of fast MR imaging: quantitative analysis on image quality and efficiency among various time frames and contrast behaviors.** *Magn Reson Imaging* 2002;20:471–78 CrossRef Medline
26. Li T, Mirowitz SA. **Fast T2-weighted MR imaging: impact of variation in pulse sequence parameters on image quality and artifacts.** *Magn Reson Imaging* 2003;21:745–53 CrossRef Medline
27. Rand S, Maravilla KR, Schmiedl U. **Lesion enhancement in radio-frequency spoiled gradient-echo imaging: theory, experimental evaluation, and clinical implications.** *AJNR Am J Neuroradiol* 1994; 15:27–35 Medline
28. Mugler JP 3rd, Brookeman JR. **Theoretical analysis of gadopentetate dimeglumine enhancement in T1-weighted imaging of the brain: comparison of two-dimensional spin-echo and three-dimensional gradient-echo sequences.** *J Magn Reson Imaging* 1993;3:761–69 CrossRef Medline
29. Nael K, Khan R, Choudhary G, et al. **Six-minute magnetic resonance imaging protocol for evaluation of acute ischemic stroke: pushing the boundaries.** *Stroke* 2014;45:1985–91 CrossRef Medline
30. Meshksar A, Villablanca JP, Khan R, et al. **Role of EPI-FLAIR in patients with acute stroke: a comparative analysis with FLAIR.** *AJNR Am J Neuroradiol* 2014;39:878–83 CrossRef Medline
31. Sica GT. **Bias in research studies.** *Radiology* 2006;238:780–89 CrossRef Medline

# Relationship between Glioblastoma Heterogeneity and Survival Time: An MR Imaging Texture Analysis

Y. Liu, X. Xu, L. Yin, X. Zhang, L. Li, and H. Lu



## ABSTRACT

**BACKGROUND AND PURPOSE:** The heterogeneity of glioblastoma contributes to the poor and variant prognosis. The aim of this retrospective study was to assess the glioblastoma heterogeneity with MR imaging textures and to evaluate its impact on survival time.

**MATERIALS AND METHODS:** A total of 133 patients with primary glioblastoma who underwent postcontrast T1-weighted imaging (acquired before treatment) and whose data were filed with the survival times were selected from the Cancer Genome Atlas. On the basis of overall survival, the patients were divided into 2 groups: long-term ( $\geq 12$  months,  $n = 67$ ) and short-term ( $< 12$  months,  $n = 66$ ) survival. To measure heterogeneity, we extracted 3 types of textures, co-occurrence matrix, run-length matrix, and histogram, reflecting local, regional, and global spatial variations, respectively. Then the support vector machine classification was used to determine how different texture types perform in differentiating the 2 groups, both alone and in combination. Finally, a recursive feature-elimination method was used to find an optimal feature subset with the best differentiation performance.

**RESULTS:** When used alone, the co-occurrence matrix performed best, while all the features combined obtained the best survival stratification. According to feature selection and ranking, 43 top-ranked features were selected as the optimal subset. Among them, the top 10 features included 7 run-length matrix and 3 co-occurrence matrix features, in which all 6 regional run-length matrix features emphasizing high gray-levels ranked in the top 7.

**CONCLUSIONS:** The results suggest that local and regional heterogeneity may play an important role in the survival stratification of patients with glioblastoma.

**ABBREVIATIONS:** CM = co-occurrence matrix; GBM = glioblastoma; RFE-SVM = recursive feature-elimination-based support vector machine classifier; RLM = run-length matrix; ROC = receiver operating characteristic; SVM = support vector machine; TCGA = the Cancer Genome Atlas

Glioblastoma (GBM) is the most common malignant brain tumor.<sup>1</sup> Despite maximal safe surgery plus radiation therapy and chemotherapy, the prognosis of patients with GBM remains poor. The median survival of patients with GBM is only 10~14 months,<sup>2</sup> though some patients can survive longer than 36

months.<sup>3</sup> Because the heterogeneity of GBM contributes to its poor and variant prognosis,<sup>4</sup> it is very important to evaluate the heterogeneity and analyze the relationship between GBM heterogeneity and survival time.

As a common method to explore intratumoral characterization in the clinic, percutaneous biopsy can only provide limited information about a tumor at the biopsy site and does not represent the heterogeneity of the entire tumor.<sup>5</sup> With the development of medical imaging, an image-based approach may avoid the risks of biopsy and assess heterogeneity more comprehensively.<sup>6,7</sup> Tumor heterogeneity occurs at the molecular level, but heterogeneity can be macroscopically reflected by the texture patterns observed in medical imaging. Texture analysis refers to the various mathematic methods that allow pattern evaluation of gray-level intensities and pixel positions on medical images, which have been proved an effective way to measure tumor heterogeneity, as shown in studies related to breast cancer,<sup>8</sup> lung cancer,<sup>9</sup> colorectal cancer,<sup>10</sup> and so forth. These

Received January 26, 2017; accepted after revision April 25.

From the School of Biomedical Engineering (Y.L., X.P.X., L.L.Y., X.Z., H.B.L.), Fourth Military Medical University, Xi'an, Shaanxi, China; and Department of Engineering Science and Physics (L.H.L.), City University of New York at College of Staten Island, Staten Island, New York.

Yang Liu and Xiaopan Xu contributed equally to this work.

This work was supported by the National Natural Science Foundation of China (grant Nos. 81230035 and 81402049) and the Military Science Foundation of China (grant No. BW514J038).

Please address correspondence to Hongbing Lu, PhD, School of Biomedical Engineering, Fourth Military Medical University, Xi'an 710032, Shaanxi, China; e-mail: luhb@fmmu.edu.cn

Indicates open access to non-subscribers at [www.ajnr.org](http://www.ajnr.org)

<http://dx.doi.org/10.3174/ajnr.A5279>

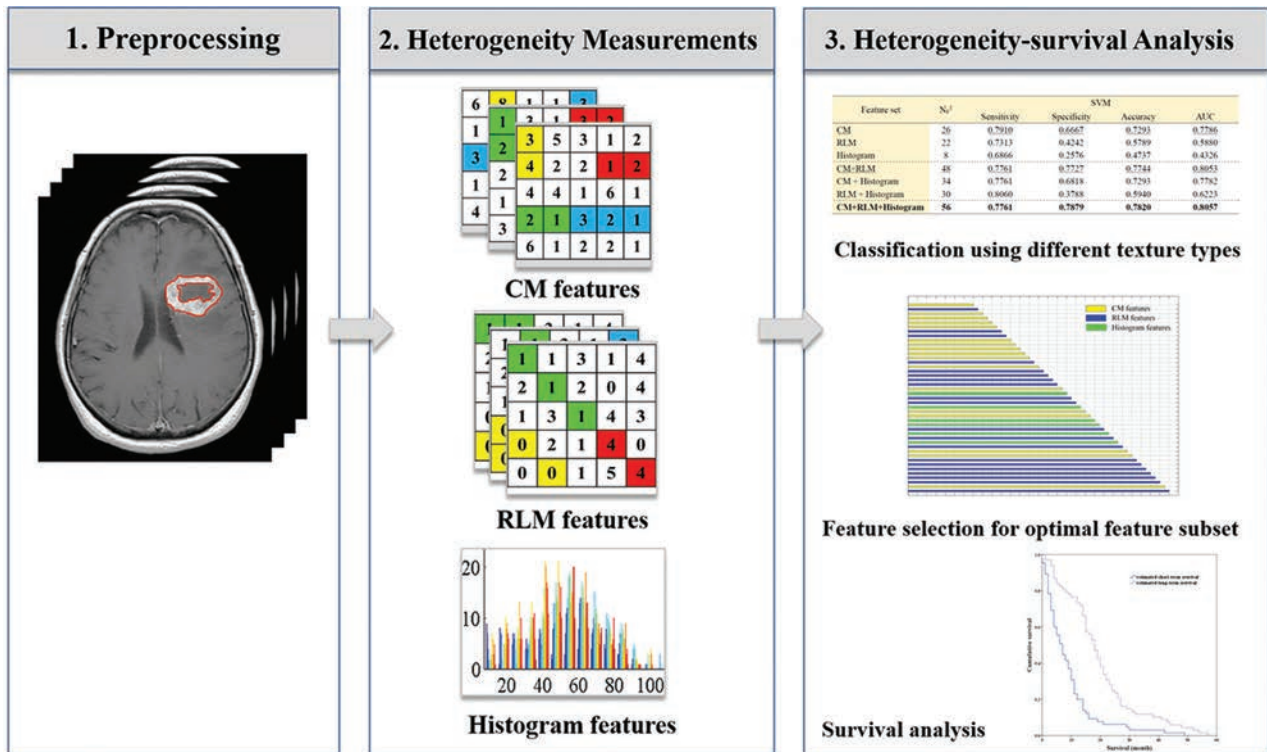


**FIG 1.** The schematic diagram for data processing and analysis.

studies suggest that texture analysis would be effective in evaluating GBM heterogeneity and its correlation with survival time.

As a type of heterogeneous tumor,<sup>4,11</sup> GBM varies across geographic regions. Thus, some researchers segmented the heterogeneous GBM into multiple regions, including active tumor, necrosis, and edema and used the texture features of these regions to predict prognosis.<sup>12,13</sup> Considering that the region of active tumor better reflects the molecular activities in GBM, Itakura et al<sup>14</sup> further used the enhanced region of postcontrast T1-weighted MR imaging to identify different phenotypic subtypes of GBM. On the basis of the relationship between the GBM heterogeneity and the enhanced region of postcontrast T1WI, recently Molina et al<sup>15</sup> used the Cox proportional hazards analysis to correlate the texture features of the enhanced region with GBM heterogeneity. Although they verified that the texture analysis could assess the heterogeneity of GBM and predict prognosis,<sup>15</sup> the types of texture features that could better characterize the heterogeneity and which heterogeneous characterizations play a key role in prognosis prediction are still unknown.

## MATERIALS AND METHODS

### Study Design

In this study, we aimed to investigate the relationship between GBM heterogeneity characterized by MR imaging texture analysis and survival time. The data processing mainly included 3 parts: 1) Preprocessing, based on the contrast-enhanced regions of post-contrast T1WI (the tumor regions were manually contoured); 2) Heterogeneity Measurements, the co-occurrence matrix (CM), run-length matrix (RLM), and histogram-based features, reflecting the local, regional, and global spatial variations of tumor, respectively, extracted to measure the heterogeneity on

**Table 1: Summary of patient characteristics of long- and short-term groups**

Group	Sex (Male/Female)	Age (Median, Range) (yr)	Overall Survival (Median, Range) (days)
Long-term group	40:27	59, 14~81	600, 370~1731
Short-term group	43:23	64, 17~85	145, 16~357

different scales; and 3) Heterogeneity-Survival Analysis, the support vector machine (SVM) classification used to determine how the 3 texture types perform in differentiating the 2 groups, both alone and in combination. After that, the recursive feature-elimination-based SVM classifier (RFE-SVM) was used to obtain an optimal feature subset with the best differentiation performance.<sup>16</sup> On the basis of the optimal feature subset, the model for survival stratification of the patients with GBM can be built. With the model, the stratification of all patients with GBM was estimated, and Kaplan-Meier plots were used to assess the model. The schematic diagram for the data processing is shown in Fig 1.

### Dataset

A dataset of 133 patients with primary GBM was collected from the Cancer Genome Atlas (TCGA, <https://wiki.cancerimagingarchive.net/display/Public/TCGA-GBM>). Although the dataset contains >200 GBM cases, only the cases scanned with postcontrast T1WI and filed with a clinical survival time were included. On the basis of the overall survival, the patients were divided into 2 groups: long-term survival (overall survival,  $\geq 12$  months,  $n = 67$ ) and short-term survival (overall survival, <12 months,  $n = 66$ ). A summary of patient characteristics of long-

term and short-term groups is shown in Table 1. All MR images were acquired before treatment, and the patients were subsequently diagnosed as having GBM on the basis of histologic examination. Because all the patient data in TCGA were de-identified, an institutional review board approval was waived.

### Image Preprocessing

All MR images in this study were acquired in axial sections. The postcontrast T1WI was acquired with a spin- or gradient-echo sequence with the following range of parameters: TE/TR = 2.48~20/7.62~880 ms, section thickness = 1~6 mm, spacing between sections = 0.8~7.8 mm, and matrix size = 256 × 256 or 512 × 512.

In light of the different imaging parameters, we preprocessed the MR images to standardize the data analysis across patients. On the basis of the contrast-enhanced regions of the postcontrast T1WI, ROIs were manually contoured by 2 neuroradiologists with a custom-developed package in Matlab R2012b (Math-Works, Natick, Massachusetts). The 2 neuroradiologists had 23 and 8 years of MR imaging interpretation experience. During the delineation, they were blinded to all the clinical information and delineated the contours of the tumors from each patient slice by slice, independently. Then, they worked together on the outlined contours of each patient via a consensus reading. Finally, matrices above 256 × 256 were resampled to this resolution, to avoid the effect of resolution on the textural analysis.<sup>17</sup>

### Heterogeneity Measurements

To alleviate the effect of variations in the section thickness and spacing on the feature analysis, we extracted 2D texture features from each tumor ROI. In this study, the image section for the 2D analysis was judged by the maximum tumor area. Then, the 2D texture features were computed to measure the heterogeneity of the tumors.<sup>18</sup> According to the different scales, we used the CM, RLM, and histogram-based features to quantify the local,<sup>15</sup> regional,<sup>17,19</sup> and global heterogeneity in the ROIs of the tumor.<sup>20</sup>

The CM features proposed by Haralick et al<sup>21</sup> describe the arrangements of pixel pairs within 2D images.<sup>22</sup> They are defined to measure the relations between 2 neighboring pixels and reflect the local heterogeneity of the tumor region.<sup>15</sup> In this study, for each 2D tumor region, 4 CMs were constructed along 4 directions (0°, 45°, 90°, and 135°). For each CM, Haralick et al proposed 13 features, named “Haralick features.” Thus, the 13 Haralick features were successively extracted from 4 directions. The mean and range (the difference between the maximum and minimum values) of the 13 features were calculated to keep the features rotationally invariant.

The RLM features essentially describe the distribution of the gray-level runs, in which the run length is defined to measure the contiguous gray-levels along a specific orientation.<sup>19,23</sup> Thus, the RLM features can characterize groups of pixels within the tumor to represent the regional heterogeneity information.<sup>17,19</sup> In the tumor region, fine textures tend to have a short run length, while coarser textures would result in a longer run length. In this study, we calculated the mean and range of the 11 RLM features over 4 directions (0°, 45°, 90°, and 135°), to constitute the final RLM features.

**Table 2: Texture features extracted from ROIs of GBM images**

Feature Group/ Feature ID	Description
CM features	
CM <sub>1</sub>	Energy
CM <sub>2</sub>	Contrast
CM <sub>3</sub>	Correlation
CM <sub>4</sub>	Variance
CM <sub>5</sub>	Inverse difference moment
CM <sub>6</sub>	Sum average
CM <sub>7</sub>	Sum variance
CM <sub>8</sub>	Sum entropy
CM <sub>9</sub>	Entropy
CM <sub>10</sub>	Difference variance
CM <sub>11</sub>	Difference entropy
CM <sub>12</sub>	Information measures I of correlation
CM <sub>13</sub>	Information measures II of correlation
RCM <sub>1</sub> –RCM <sub>13</sub>	Range of corresponding features listed above
RLM features	
RLM <sub>1</sub>	Short-run emphasis
RLM <sub>2</sub>	Long-run emphasis
RLM <sub>3</sub>	Gray-level nonuniformity
RLM <sub>4</sub>	Run-length nonuniformity
RLM <sub>5</sub>	Run percentage
RLM <sub>6</sub>	Low gray-level run emphasis
RLM <sub>7</sub>	High gray-level run emphasis
RLM <sub>8</sub>	Short-run low gray-level emphasis
RLM <sub>9</sub>	Short-run high gray-level emphasis
RLM <sub>10</sub>	Long-run low gray-level emphasis
RLM <sub>11</sub>	Long-run high gray-level emphasis
RRLM <sub>1</sub> –RRLM <sub>11</sub>	Range of corresponding features listed above
Histogram-based features	
H <sub>1</sub>	Mean
H <sub>2</sub>	Entropy
H <sub>3</sub>	Uniformity
H <sub>4</sub>	SD
H <sub>5</sub>	Smoothness
H <sub>6</sub>	Skewness
H <sub>7</sub>	Third-order moment
H <sub>8</sub>	Kurtosis

**Note:**—ID indicates identification; RCM, range of co-occurrence matrix; RRLM, range of run-length matrix; H, histogram.

The histogram shows the number of pixels in the whole image having the same intensity. The common histogram-based features include the mean, entropy, uniformity, SD, smoothness, skewness, third-order moment, kurtosis, and so forth.<sup>24</sup> These features represent the statistical properties of an image and further describe the heterogeneity of the entire tumor.<sup>20,25</sup>

We used 26 CM features, 22 RLM features, and 8 commonly used histogram-based features, taken together, to measure GBM heterogeneity on different scales (Table 2). In this study, all the features were extracted with a custom-developed package in Matlab R2012b.

### Classification Performance with Different Texture Types

To evaluate the performance of different texture types in the differentiation task, we performed an SVM classifier with a radial basis function kernel implemented by the LIBSVM package (<https://www.csie.ntu.edu.tw/~cjlin/libsvm/>).<sup>26</sup> After all the features were normalized to [−1, 1], the grid search method was used to search for the optimal parameter combination of an SVM clas-

**Table 3: The performance of feature combinations with the SVM classifier in differentiating long- and short-term survival time**

Feature Set	N <sub>F</sub> <sup>a</sup>	SVM			
		Sensitivity	Specificity	Accuracy	AUC
CM <sup>b</sup>	26	0.7910	0.6667	0.7293	0.7786
RLM	22	0.7313	0.4242	0.5789	0.5880
Histogram	8	0.6866	0.2576	0.4737	0.4326
CM + RLM <sup>b</sup>	48	0.7761	0.7727	0.7744	0.8053
CM + histogram	34	0.7761	0.6818	0.7293	0.7782
RLM + histogram	30	0.8060	0.3788	0.5940	0.6223
CM + RLM + histogram <sup>c</sup>	56	0.7761	0.7879	0.7820	0.8057

**Note:**—AUC indicates area under the curve.

<sup>a</sup> The number of features in each subset.

<sup>b</sup> The best classification when the feature type is used alone or pair-combined.

<sup>c</sup> The best classification result when all features are used.

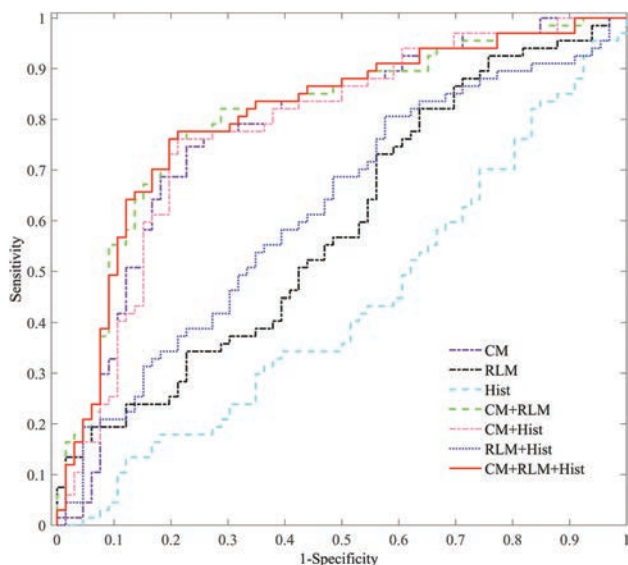


**FIG 2.** ROC curves of the different feature combinations with the SVM classifier (CM, RLM, and Hist stand for the co-occurrence matrix, run-length matrix, and histogram-based texture types, respectively).

sifier.<sup>27,28</sup> Then, a 10-fold cross-validation was implemented to extensively evaluate the performance of different feature combinations.<sup>29</sup>

After classification, the results, namely the sensitivity, specificity, accuracy, and area under the curve of the receiver operating characteristic (ROC), were calculated to evaluate the classification performance.

### Feature Selection for the Optimal Feature Subset

Considering that the correlation and redundancy among the features would inevitably affect the classification performance,<sup>30-32</sup> the RFE-SVM method was used to first find the optimal feature subset and then verify its overall performance in the prediction. According to feature selection and ranking, the optimal feature subset, containing the first *N* features with the highest mean accuracy, was finally determined with the SVM and a 10-fold cross-validation. On the basis of the optimal feature subset, we can build a model to predict the survival stratifications of patients with GBM.

### Survival Analysis

On the basis of the model built in the above section, the survival stratifications of all 133 patients with GBM were estimated. Then, a

Kaplan-Meier plot and a log-rank analysis were used to assess the model, performed by SPSS software, Version 22.0.00 (IBM, Armonk, New York).

## RESULTS

### Classification Performance with the Different Texture Types

The performances of the different combinations of the 3 texture types (CM, RLM, and histogram) in the differentiation of patients with GBM with long- and short-term survival times were compared (Table 3). When used alone,

the CM was the best texture type for classification performance. When combined in pairs, the combination of CM and RLM obtained the best classification performance. When all the features were used, the specificity, accuracy, and area under the curve reached the highest value.

The ROC curves of the feature combinations with the SVM classifier were plotted, as shown in Fig 2. Consistent with results shown in Table 3, any combination including CM or CM alone demonstrated a better classification performance. Furthermore, the combination of the 3 texture types showed the best performance.

### Optimal Feature Subset Selection with RFE-SVM

Applying the RFE-SVM method on all 56 features, the selection process for the optimal feature subset and the corresponding ROC curve are shown in Fig 3. Finally, the feature subset consisting of 43 top-ranked features was selected as the optimal subset, which obtained the optimal classification performance (sensitivity = 0.7910, specificity = 0.7727, accuracy = 0.7820, area under the curve = 0.8104). The relative ranking orders of all features in the optimal subset are shown in Fig 4. The length of each bar represents the iteration number at which the feature was rejected by RFE. The longer the bar is, the higher the feature ranks. Furthermore, the top 3 features, short-run high gray-level emphasis (RLM<sub>9</sub>), variance (CM<sub>4</sub>), and long-run high gray-level emphasis (RLM<sub>11</sub>), can obtain a relatively stable accuracy (0.7519).

### Survival Analysis

On the basis of the model built by the optimal feature subset, the survival stratifications (long- and short-term survival groups) of 133 patients with GBM were estimated. The Kaplan-Meier plot of the 2 groups indicated that their survival difference was significant (log-rank test, *P* < .001), as shown in Fig 5.

## DISCUSSION

Tumor heterogeneity is one of the major causes of treatment resistance in GBM,<sup>33</sup> directly affecting the prognosis.<sup>8,34</sup> On the basis of the MR imaging data from the TCGA, the heterogeneity was first characterized by texture features on different scales. On this basis, the present study investigated the impact of heterogeneity on survival time and obtained an optimal feature combination for survival stratification. The results indicate that CM and

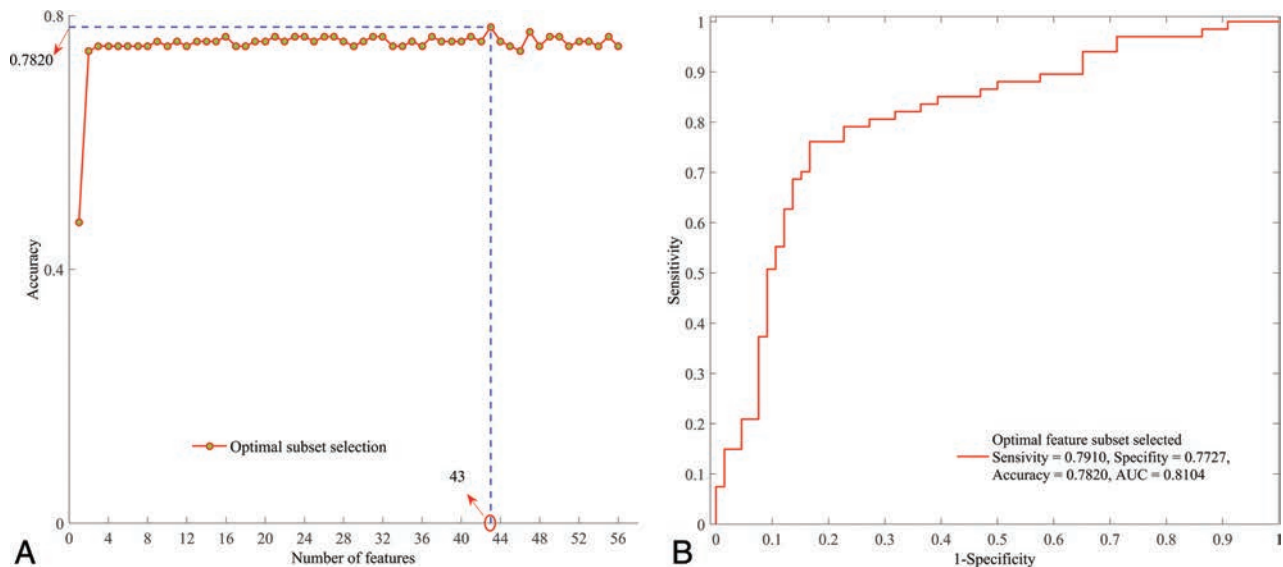


**FIG 3.** Optimal feature subset selection. A, Selection process of the optimal feature subset with RFE-SVM. B, ROC curve of the optimal feature subset selected.

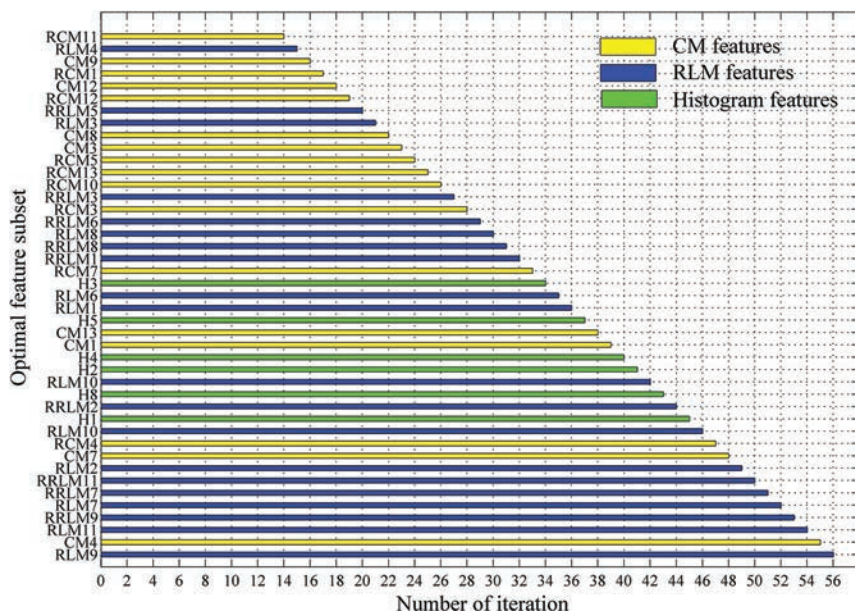


**FIG 4.** Ranking orders of all features in the optimal subset. The length of each bar represents the iteration number at which the feature was rejected by the RFE.

RLM type features, which reflect the local and regional heterogeneity, play an important role in survival stratification. Furthermore, regional features that emphasize high gray-level distribution ranked higher in the optimal feature subset and contributed more to prognosis.

As a powerful description of the spatial distribution of the pixel intensity within images, the texture features are sensitive to the reflection of tissue types and pathologic properties.<sup>35,36</sup> Among the texture features, the first-order features were derived from the gray-level histogram. They mainly take into account the frequency of the appearance of each gray-level within the tumor, rather than the relative spatial position of pixels (eg, histogram-based features used in this study). Second-order texture features describe the gray-level relationship

of the nearby pixel pairs, thereby reflecting the spatial distribution of pixels in a local way. The CM used in this study is a typical second-order texture description method. The high-order features measure the regional distributions (ie, groups of pixels with the same gray-level values). The RLM is a high-order texture method designed to characterize the regions with the same gray-level in the tumor. Therefore, the CM, RLM, and histogram features used in this study can characterize the local,<sup>15</sup> regional,<sup>17,19</sup> and global heterogeneity<sup>20,25</sup> of GBM on different scales. Only the features reflecting GBM heterogeneity were included in the present study because the present study aimed to investigate the impact of the different heterogeneous characterizations on the prognosis, though it may result in a lower accuracy in differentiating the long- and short-term groups.

Although texture features are capable of characterizing the gray-level heterogeneity of GBM, different types of textures may make different contributions to the survival stratification. The results (as shown in Table 3 and Fig 2) indicated that local heterogeneity, identified by the CM features, played a key role in the survival stratification, while global heterogeneity (histogram features) had little effect. Although the classification performance using the RLM alone was not good, its performance improved greatly when it was combined with the CM features. Taken together, the local and regional heterogeneity may have more impact on the prognosis. Meanwhile, the combination of multiple types of features might complement each other, thus improving the classification performance.

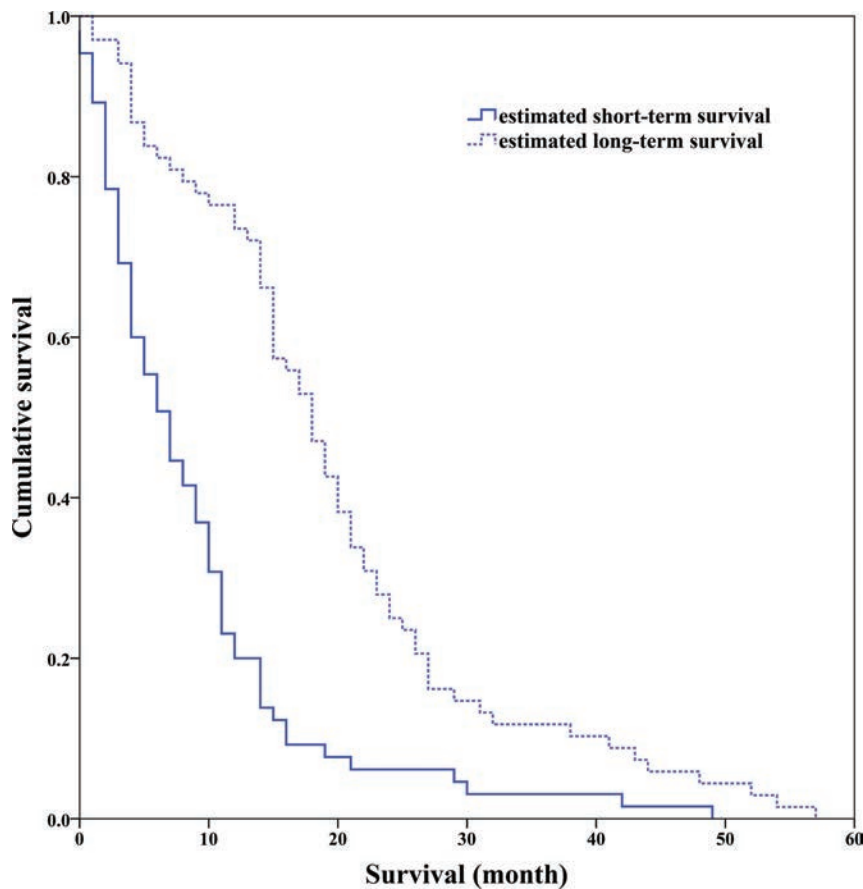


**FIG 5.** Kaplan-Meier survival curves determined by the log-rank test ( $P < .001$ ).

Except for the evaluation of the different texture types on the prognosis, the ranking orders and optimal subset of all features were calculated on the basis of the maximum accuracy from the SVM. The top 10 features include 7 RLM features and 3 CM features, supporting the conclusion of the texture type analysis in the last paragraph. Although the CM features demonstrate a high performance compared with other texture types, the RLM features performed better in the optimal subset. This is probably derived from the RLM properties, which reflect relatively moderate (regional) heterogeneity information. In particular, all 6 RLM features emphasized high gray-levels (RLM<sub>7</sub>, RLM<sub>9</sub>, RLM<sub>11</sub>, and their ranges) ranked in the top 7 of the optimal subset, indicating that the tumor regions with high gray-levels or intensity in postcontrast T1WI might contribute more to the prognosis of patients with GBM. This may also indicate that the further segmentation of the active tumor into multiple subregions spatially and the prognosis prediction within these subregions may improve the predictive performance.

Some limitations still need further investigation. First, as a retrospective study, the MR imaging data were acquired on a variety of imaging platforms with different protocols, imaging parameters, and gadolinium-based contrast agents. Second, we divided all the patients into short- and long-term survival with the criterion of 12 months. If more patients with GBM are recruited, a more detailed classification (eg, 6-, 12-, and 24 months) would be further performed. Third, the demographic and treatment in-

formation of the patients with GBM might also influence the survival. The adjustment for the demographic and treatment factors should be considered in future studies. Fourth, considering the large section thickness and spacing in most data, we used the 2D texture analysis instead of the 3D analysis, which may result in certain information missing. Finally, only a portion of the subjects in TCGA had multimodality data. Because it was a primary study, our aim was to examine the relationship between GBM heterogeneity characterized by texture features in postcontrast T1WI and survival time. Further study may benefit from the combined use of more anatomic and functional images.

## CONCLUSIONS

We used the postcontrast T1WI of patients with GBM from the TCGA to investigate the impact of different heterogeneous characterizations on survival stratification, characterized by texture features on different scales. The results of our study indicated that local and regional heterogeneity may play an important role in the survival stratification.

Disclosures: Yang Liu—RELATED: Grant: Military Science Foundation of China, Comments: grant No. BWS14J038.\* Xiaopan Xu—RELATED: Grant: National Natural Science Foundation of China, Comments: grant No. 81230035.\* Lulu Yin—RELATED: Grant: National Natural Science Foundation of China, Comments: grant No. 81402049.\* Xi Zhang—RELATED: Grant: National Natural Science Foundation of China, Comments: grant No. 81230035.\* Hongbing Lu—RELATED: Grant: National Natural Science Foundation of China, Comments: grant No. 81230035.\* \*Money paid to the institution.

## REFERENCES

- Ostrom QT, Gittleman H, Stetson L, et al. **Epidemiology of gliomas.** *Cancer Treat Res* 2015;163:1–14 CrossRef Medline
- Van Meir EG, Hadjipanayis CG, Norden AD, et al. **Exciting new advances in neuro-oncology: the avenue to a cure for malignant glioma.** *CA Cancer J Clin* 2010;60:166–93 CrossRef Medline
- Smoll NR, Schaller K, Gautschi OP. **Long-term survival of patients with glioblastoma multiforme (GBM).** *J Clin Neurosci* 2013;20:670–75 CrossRef Medline
- Sottoriva A, Spiteri I, Piccirillo SG, et al. **Intratumor heterogeneity in human glioblastoma reflects cancer evolutionary dynamics.** *Proc Natl Acad Sci U S A* 2013;110:4009–14 CrossRef Medline
- Bedard PL, Hansen AR, Ratain MJ, et al. **Tumour heterogeneity in the clinic.** *Nature* 2013;501:355–64 CrossRef Medline
- Kumar V, Gu Y, Basu S, et al. **Radiomics: the process and the challenges.** *Magn Reson Imaging* 2012;30:1234–48 CrossRef Medline
- Gillies RJ, Kinahan PE, Hricak H. **Radiomics: images are more than pictures, they are data.** *Radiology* 2016;278:563–77 CrossRef Medline
- Kim JH, Ko ES, Lim Y, et al. **Breast cancer heterogeneity: MR imaging texture analysis and survival outcomes.** *Radiology* 2017;282:665–75 CrossRef Medline
- Yoon SH, Park CM, Park SJ, et al. **Tumor heterogeneity in lung**

- cancer: assessment with dynamic contrast-enhanced MR imaging.** *Radiology* 2016;280:940–48 CrossRef Medline
10. Ng F, Kozarski R, Ganeshan B, et al. **Assessment of tumor heterogeneity by CT texture analysis: can the largest cross-sectional area be used as an alternative to whole tumor analysis?** *Eur J Radiol* 2013;82:342–48 CrossRef Medline
  11. Verhaak RG, Hoadley KA, Purdom E, et al; Cancer Genome Atlas Research Network. **Integrated genomic analysis identifies clinically relevant subtypes of glioblastoma characterized by abnormalities in PDGFRA, IDH1, EGFR, and NF1.** *Cancer Cell* 2010;17:98–110 CrossRef Medline
  12. Chaddad A, Tanougast C. **Extracted magnetic resonance texture features discriminate between phenotypes and are associated with overall survival in glioblastoma multiforme patients.** *Med Biol Eng Comput* 2016;54:1707–18 CrossRef Medline
  13. Cui Y, Tha KK, Terasaka S, et al. **Prognostic imaging biomarkers in glioblastoma: development and independent validation on the basis of multiregion and quantitative analysis of MR images.** *Radiology* 2016;278:546–53 CrossRef Medline
  14. Itakura H, Achrol AS, Mitchell LA, et al. **Magnetic resonance image features identify glioblastoma phenotypic subtypes with distinct molecular pathway activities.** *Sci Transl Med* 2015;7:303ra138 CrossRef Medline
  15. Molina D, Perez-Beteta J, Luque B, et al. **Tumour heterogeneity in glioblastoma assessed by MRI texture analysis: a potential marker of survival.** *Br J Radiol* 2016 Jul 4. [Epub ahead of print] Medline
  16. Simões R, van Cappellen van Walsum AM, Slump CH. **Classification and localization of early-stage Alzheimer's disease in magnetic resonance images using a patch-based classifier ensemble.** *Neuroradiology* 2014;56:709–21 CrossRef Medline
  17. Molina D, Pérez-Beteta J, Martínez-González A, et al. **Influence of gray level and space discretization on brain tumor heterogeneity measures obtained from magnetic resonance images.** *Comput Biol Med* 2016;78:49–57 CrossRef Medline
  18. Tixier F, Hatt M, Le Rest CC, et al. **Reproducibility of tumor uptake heterogeneity characterization through textural feature analysis in 18F-FDG PET.** *J Nucl Med* 2012;53:693–700 CrossRef Medline
  19. Tang X. **Texture information in run-length matrices.** *IEEE Trans Image Process* 1998;7:1602–09 CrossRef Medline
  20. Just N. **Improving tumour heterogeneity MRI assessment with histograms.** *Br J Cancer* 2014;111:2205–13 CrossRef Medline
  21. Haralick RM, Shanmugam K, Dinstein IH. **Texture features for image classification.** *IEEE Trans Syst Man Cybern Syst* 1973;smc-3:610–21 CrossRef
  22. Castellano G, Bonilha L, Li LM, et al. **Texture analysis of medical images.** *Clin Radiol* 2004;59:1061–69 CrossRef Medline
  23. Galloway MM. **Texture analysis using gray level run lengths.** *Computer Graphics and Image Processing* 1975;4:172–79 CrossRef
  24. Xu X, Liu Y, Zhang X, et al. **Preoperative prediction of muscular invasiveness of bladder cancer with radiomic features on conventional MRI and its high-order derivative maps.** *Abdom Radiol (NY)* 2017 Feb 20. [Epub ahead of print] CrossRef Medline
  25. Kang Y, Choi SH, Kim YJ, et al. **Gliomas: histogram analysis of apparent diffusion coefficient maps with standard- or high-b-value diffusion-weighted MR imaging: correlation with tumor grade.** *Radiology* 2011;261:882–90 CrossRef Medline
  26. Chang CC, Lin CJ. **LIBSVM: a library for support vector machines.** *ACM Trans Intell Syst Technol* 2011;2:1–27 CrossRef
  27. Han F, Wang H, Zhang G, et al. **Texture feature analysis for computer-aided diagnosis on pulmonary nodules.** *J Digit Imaging* 2015;28:99–115 CrossRef Medline
  28. Song B, Zhang G, Lu H, et al. **Volumetric texture features from higher-order images for diagnosis of colon lesions via CT colonography.** *Int J Comput Assist Radiol Surg* 2014;9:1021–31 CrossRef Medline
  29. Rakotomamonjy A. **Variable selection using SVM-based criteria.** *J Mach Learn Res* 2003;3:1357–70
  30. Zacharaki EI, Wang S, Chawla S, et al. **Classification of brain tumor type and grade using MRI texture and shape in a machine learning scheme.** *Magn Reson Med* 2009;62:1609–18 CrossRef Medline
  31. Zou J, Ji Q, Nagy G. **A comparative study of local matching approach for face recognition.** *IEEE Trans Image Process* 2007;16:2617–28 CrossRef Medline
  32. Xu X, Zhang X, Tian Q, et al. **Three-dimensional texture features from intensity and high-order derivative maps for the discrimination between bladder tumors and wall tissues via MRI.** *Int J Comput Assist Radiol Surg* 2017;12:645–56 CrossRef Medline
  33. Inda MM, Bonavia R, Seoane J. **Glioblastoma multiforme: a look inside its heterogeneous nature.** *Cancers (Basel)* 2014;6:226–39 CrossRef Medline
  34. Yang Z, Tang LH, Klimstra DS. **Effect of tumor heterogeneity on the assessment of Ki67 labeling index in well-differentiated neuroendocrine tumors metastatic to the liver: implications for prognostic stratification.** *Am J Surg Pathol* 2011;35:853–60 CrossRef Medline
  35. Lerski RA, Straughan K, Schad LR, et al. **MR image texture analysis: an approach to tissue characterization.** *Magn Reson Imaging* 1993;11:873–87 CrossRef Medline
  36. Fetit AE, Novak J, Peet AC, et al. **Three-dimensional textural features of conventional MRI improve diagnostic classification of childhood brain tumours.** *NMR Biomed* 2015;28:1174–84 CrossRef Medline

# Amide Proton Transfer Imaging Allows Detection of Glioma Grades and Tumor Proliferation: Comparison with Ki-67 Expression and Proton MR Spectroscopy Imaging

C. Su, C. Liu, L. Zhao, J. Jiang, J. Zhang, S. Li, W. Zhu, and J. Wang



## ABSTRACT

**BACKGROUND AND PURPOSE:** Prognosis in glioma depends strongly on tumor grade and proliferation. In this prospective study of patients with untreated primary cerebral gliomas, we investigated whether amide proton transfer–weighted imaging could reveal tumor proliferation and reliably distinguish low-grade from high-grade gliomas compared with Ki-67 expression and proton MR spectroscopy imaging.

**MATERIALS AND METHODS:** This study included 42 patients with low-grade ( $n = 28$ ) or high-grade ( $n = 14$ ) glioma, all of whom underwent conventional MR imaging, proton MR spectroscopy imaging, and amide proton transfer–weighted imaging on the same 3T scanner within 2 weeks before surgery. We assessed metabolites of choline and *N*-acetylaspartate from proton MR spectroscopy imaging and the asymmetric magnetization transfer ratio at 3.5 ppm from amide proton transfer–weighted imaging and compared them with histopathologic grade and immunohistochemical expression of the proliferation marker Ki-67 in the resected specimens.

**RESULTS:** The asymmetric magnetization transfer ratio at 3.5 ppm values measured by different readers showed good concordance and were significantly higher in high-grade gliomas than in low-grade gliomas ( $3.61\% \pm 0.155$  versus  $2.64\% \pm 0.185$ ,  $P = .0016$ ), with sensitivity and specificity values of 92.9% and 71.4%, respectively, at a cutoff value of 2.93%. The asymmetric magnetization transfer ratio at 3.5 ppm values correlated with tumor grade ( $r = 0.506$ ,  $P = .0006$ ) and Ki-67 labeling index ( $r = 0.502$ ,  $P = .002$ ). For all patients, the asymmetric magnetization transfer ratio at 3.5 ppm correlated positively with choline ( $r = 0.43$ ,  $P = .009$ ) and choline/*N*-acetylaspartate ratio ( $r = 0.42$ ,  $P = .01$ ) and negatively with *N*-acetylaspartate ( $r = -0.455$ ,  $P = .005$ ). These correlations held for patients with low-grade gliomas versus those with high-grade gliomas, but the correlation coefficients were higher in high-grade gliomas (choline:  $r = 0.547$ ,  $P = .053$ ; *N*-acetylaspartate:  $r = -0.644$ ,  $P = .017$ ; choline/*N*-acetylaspartate:  $r = 0.583$ ,  $P = .036$ ).

**CONCLUSIONS:** The asymmetric magnetization transfer ratio at 3.5 ppm may serve as a potential biomarker not only for assessing proliferation, but also for predicting histopathologic grades in gliomas.

**ABBREVIATIONS:** APT = amide proton transfer; APTWI = amide proton transfer–weighted imaging; MRSI =  $^1\text{H}$  proton MR spectroscopy imaging; MTRasym(3.5ppm) = asymmetric magnetization transfer ratio at 3.5ppm; NAA = *N*-acetylaspartate; WHO = World Health Organization

Gliomas are the most common primary cerebral tumors and are classified into 4 grades based on histology and biologic behavior.<sup>1</sup> The median survival time depends greatly on tumor grade, being longer for patients with lower-grade tumors.<sup>2–4</sup> Another important marker of prognosis in glioma is Ki-67, a protein

reflecting cellular proliferation and malignancy; higher Ki-67 values correspond to greater malignancy. Indeed, some investigators have proposed that the Ki-67 labeling index could be superior to histologic grading as an indicator of prognosis.<sup>5,6</sup> A noninvasive imaging method that could reveal proliferative features at the molecular level and enable accurate tumor grading before surgery would be of great importance for the clinical management of gliomas.

MR imaging is widely used in the clinical management of gliomas. However, conventional MR imaging is not sufficient for accurate assessments of tumor grade and proliferation.  $^1\text{H}$  proton MR spectroscopy imaging (MRSI) allows noninvasive measure-

Received December 17, 2016; accepted after revision May 7, 2017.

From the Department of Radiology (C.S., C.L., L.Z., J.J., J.Z., S.L., W.Z.), Tongji Hospital of Tongji Medical College, Huazhong University of Science and Technology, Hankou, Wuhan, People's Republic of China; and Department of Radiation Physics (J.W.), The University of Texas MD Anderson Cancer Center, Houston, Texas.

This work was supported by grants from the National Program of the Ministry of Science and Technology of China during the "12th Five-Year Plan" (ID: 2011BAI08B10) and the National Natural Science Foundation of China (No. 81171308 and No. 81570462).

Please address correspondence to Wenzhen Zhu, MD, Department of Radiology, Tongji Hospital of Tongji Medical College, Huazhong University of Science and Technology, No. 1095 Jiefang Ave, Hankou, Wuhan, 430030 PR China; e-mail: zhuwenzhen8612@163.com

Indicates open access to non-subscribers at [www.ajnr.org](http://www.ajnr.org)

Indicates article with supplemental on-line photos.

<http://dx.doi.org/10.3174/ajnr.A5301>

**Table 1: Patient characteristics in the 2 correlational analyses**

Characteristics	Value or No. of Patients (%)					
	MTRasym(3.5ppm) vs Ki-67			MTRasym(3.5ppm) vs MR Spectroscopy		
	Low-Grade Glioma (n = 28)	High-Grade Glioma (n = 14)	P Value	Low-Grade Glioma (n = 23)	High-Grade Glioma (n = 13)	P Value
Age, y <sup>a</sup>	44.00 ± 2.81	44.64 ± 3.70	.89	42.96 ± 3.04	43.31 ± 3.73	.94
Sex, no. (%)			.82			.97
Male	19 (68)	9 (64)		14 (61)	8 (57)	
Female	9 (32)	5 (36)		9 (39)	5 (43)	
Tumor grade, no. (%) <sup>b</sup>						
II	28 (100)	0		23 (100)	0	
III	0	6 (43)		0	6 (46)	
IV	0	8 (57)		0	7 (54)	

<sup>a</sup> Mean ± standard deviation.

<sup>b</sup> Confirmed on histopathologic examination.

ment of metabolites in tissues, among the most common of which are choline and *N*-acetylaspartate (NAA). Choline is a metabolic marker of cell membrane density and integrity, reflecting cellular proliferation and tumor progression.<sup>7,8</sup> NAA is a marker of neuronal health, viability, and number<sup>9</sup>; NAA levels are inversely associated with glioma grade and are considered a useful indicator of secondary neuronal damage caused by tumor growth.<sup>10</sup> MRSI can detect regions within gliomas that contain aggressive growth or upgrading because of strong correlations between choline and NAA levels and the Ki-67 histopathologic proliferation index.<sup>11</sup> Therefore, MRSI can provide important supplementary information for the management of gliomas.

Amide proton transfer–weighted imaging (APTWI) is a novel molecular MR imaging technique developed to detect and quantitatively visualize endogenous proteins and peptides.<sup>12</sup> APTWI is usually reported in terms of asymmetry in the magnetization transfer ratio at 3.5 ppm [MTRasym(3.5ppm)] and is measured as a reduction in bulk water intensity caused by chemical exchange with magnetically labeled backbone amide protons (at ~3.5 ppm downfield of the water resonance) of endogenous mobile proteins and peptides. Previous studies have demonstrated that APTWI can detect response to therapy in glioma<sup>13-15</sup> and correlates with grade in adult diffuse gliomas.<sup>16</sup> However, a further consideration sustained by multiple methods with bigger samples is required to investigate whether APTWI accurately reflects cellular proliferation in patients with glioma.

We previously observed that choline and NAA levels measured by MRSI correlated with MTRasym(3.5ppm) in a patient with anaplastic astrocytoma. Because APTWI and MRSI can produce similar information regarding tumor proliferation, we hypothesized that MTRasym(3.5ppm) could correlate with the metabolic profiles from MRSI. The purpose of this study was to prospectively explore the utility of the amide proton transfer (APT)–derived measurement MTRasym(3.5ppm) as a noninvasive biomarker of glioma proliferation and histopathologic grade by comparing APTWI with Ki-67 expression and with MRSI by using voxel-to-voxel analysis.

## MATERIALS AND METHODS

### Patients

This prospective study was initiated after approval by the institutional ethics committee of Tongji Hospital, and all activities abided by the statement of ethical standards. From June 23, 2015

to January 24, 2016, we identified 66 consecutive patients suspected of having a primary cerebral tumor; none had had chemotherapy or radiation treatment within 6 months before surgery, and all provided informed consent before MR imaging scanning. Inclusion criteria were as follows: 1) undergoing routine MR imaging, APTWI, and MRSI in the same scanner and 2) histopathologic confirmation of glioma. Exclusion criteria were 1) not having surgery or having surgery more than 2 weeks after the MR imaging; 2) having nonglioma tumors; 3) having motion artifacts on imaging; and 4) having missing or unstable baseline MRSI data. Of the 66 patients originally identified, 24 were excluded (6 for not having tumor resection, 14 for having lesions other than glioma, 2 for head motion, 1 for massive intratumoral hemorrhage, and 1 for having a pilocytic astrocytoma with a large cyst and minimal solid tumor). The remaining 42 patients, all of whom underwent tumor resection, were the subjects of this analysis. According to the World Health Organization (WHO) criteria, lesions in 28 patients were low-grade glioma (19 astrocytoma [1 grade I, 18 grade II], 7 oligodendroglioma, and 2 oligoastrocytoma) and lesions in 14 patients were high-grade glioma (1 anaplastic oligodendroglioma, 5 anaplastic astrocytoma [grade III], and 8 glioblastoma [grade IV]). Of these 42 patients, 6 were excluded from the voxel-to-voxel analysis (described under “Data Processing and Analysis”) because of poor-quality MRSI. Patient and treatment characteristics are shown in Table 1.

### Data Acquisition

All patients underwent MR imaging before surgery, with images obtained with a Discovery MR750 3T scanner (GE Healthcare, Milwaukee, Wisconsin). Routine and gadolinium contrast-enhanced MR imaging were included in the basic scanning protocol, which consisted of transverse T1 fluid-attenuated inversion recovery, transverse T2 fast spin-echo, and transverse T2 fluid-attenuated inversion recovery. All routine sequences had the same section thickness, spacing, and FOV (5 mm/1.5 mm, 20 sections, and 240 × 240 mm<sup>2</sup>, respectively). All sequences had the same scan coverage, and the range covered the entire brain. Routine and contrast-enhanced images were used as anatomic references for functional imaging scan localization.

APT data were collected during the routine MR imaging scanning session before the intravenous bolus injection of chelated gadolinium. Any other unrelated contrast-enhancement scan-

**Table 2: Independent t test and receiver operating characteristic curve analysis of low-/high-grade glioma**

MTRAsym(3.5ppm)	Low-Grade Gliomas (n = 28)	High-Grade Gliomas (n = 14)	P Value	Area Under the Curve <sup>a</sup>	Optimal Threshold (%)	Sensitivity (%)	Specificity (%)
Reader 1	2.65% ± 0.20	3.74% ± 0.17	.001	.813 (.675, .95)	3.11	92.9	71.4
Reader 2	2.63% ± 0.18	3.47% ± 0.16	.004	.770 (.623, .918)	2.85	92.9	71.4
Mean MTRAsym(3.5ppm)	2.64% ± 0.18	3.61% ± 0.155	.002	.791 (.650, .931)	2.93	92.9	71.4
Mean Ki-67 labeling index	4.98% ± 1.02 (n = 24)	24.15% ± 5.04 (n = 13)	.003	.867 (.702, 1.00)	6.5	84.6	83.3

<sup>a</sup>Data in parentheses are 95% CIs.

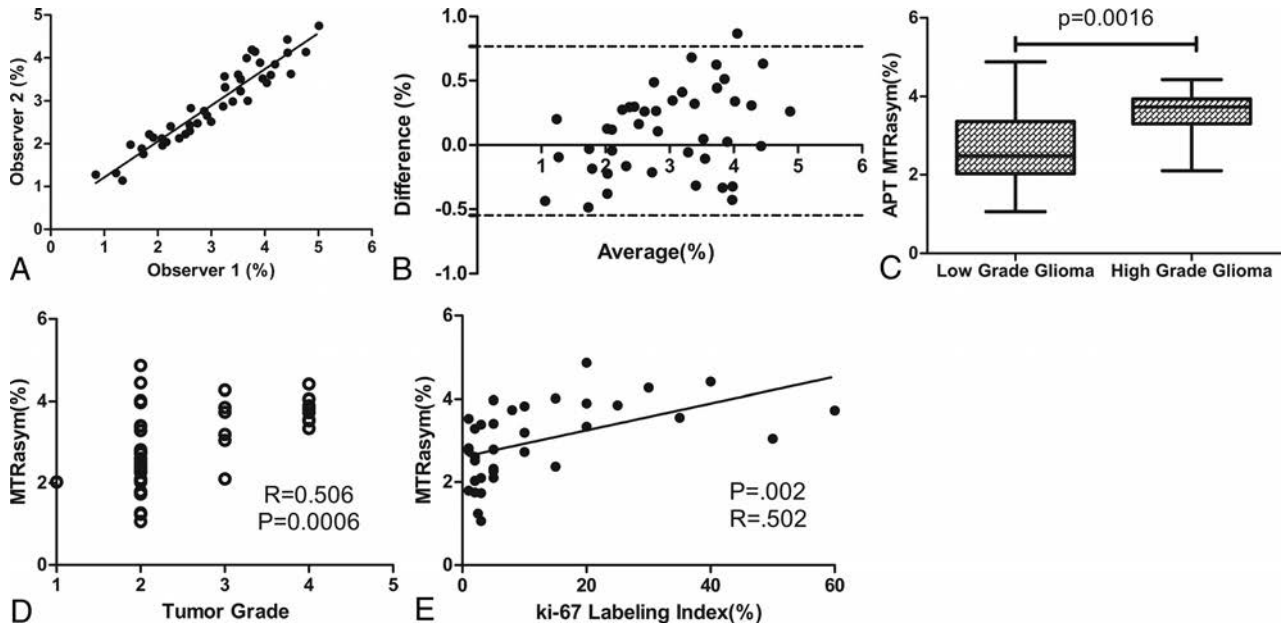


**FIG 1.** A, Intraclass agreement for the 2 readers who evaluated the MTRAsym(3.5ppm) of the solid parts of tumors in 42 patients was excellent, with an intraclass correlation coefficient of 0.94 (95% CI, 0.89–0.96). B, Bland-Altman analysis of the difference in MTRAsym(3.5ppm) by the 2 readers also showed excellent concordance. C, MTRAsym(3.5ppm) values were higher for high-grade gliomas than for low-grade gliomas ( $P = .0016$ , Student  $t$  test). D, The correlation between MTRAsym(3.5ppm) and tumor grade was moderate (Pearson  $r = 0.506$ ;  $P = .0006$ ). E, The correlation between the Ki-67 staining index and the APT MTRAsym(3.5ppm) was also moderate (Pearson  $r = 0.502$ ;  $P = .002$ ).

ning was to be done at least 24 hours before or after amide proton scanning to avoid interference with the APT signal.<sup>17</sup> Single-section transverse imaging was used at the center of the tumor for the APT data, with TR/TE, 3000/22.6 ms; matrix size, 128 × 128; FOV, 240 × 240 mm<sup>2</sup>; and section thickness, 5 mm. The power of the radiofrequency saturation pulse for the APT sequence was 2.0 μT and the length was 400 ms. Data were acquired with 2 NEX in a saturation frequency list of 15.6, ±6, ±5, ±4.5, ±4, ±3.75, ±3.5, ±3.25, ±3, ±2.5, ±2, ±1.5, ±1, ±0.75, ±0.5, ±0.25, and 0 ppm and 1 no-saturation map, resulting in 66 images being acquired in 3 minutes 18 seconds. The MTRAsym(3.5ppm) was calculated at 3.5 ppm, and B0 correction was performed by shifting the minimum signal of the z spectrum to 0 Hz.

For MRSI, we used 2D multivoxel <sup>1</sup>H imaging based on the point-resolved spectroscopy pulse sequence (PRESS). VOIs were centered on the same section as the position for APTWI based on anatomic reference images, with the following parameters: TR, 1000 ms; TE, 144 ms; FOV, 240 mm<sup>2</sup>; section thickness, 14 mm; NEX, 0.8; and pixel dimension, 7.5 mm × 7.5 mm × 14 mm with a total scanning time of 4 minutes 20 seconds. The VOIs were chosen carefully to avoid areas of hemorrhage, calcification, cystic components, large vessels, and strong interference from subcutaneous fat and lipid of the skull; saturation slabs were applied in 6 directions to further reduce potential artifacts.

### Data Processing and Analysis

All raw data were transferred to an AW4.6 workstation (GE Healthcare). To study the ability of MTRAsym(3.5ppm) to reflect tumor proliferation, we compared APT MTRAsym(3.5ppm) with MRSI and Ki-67, and the ROIs were drawn on the APT images in 2 ways. First, for the voxel-to-voxel correlation of MTRAsym(3.5ppm) with MRSI, spectral analyses were done. The following steps were included: 1) filtering of the signal to reduce noise, 2) zero-filling of the signal, 3) the suppression of water molecules signal, 4) translating of the signal from the time domain to the frequency domain with fast Fourier transformation, 5) baseline correction and phase correction. The calculation of quantitative parameters was based on curve fitting, and information on the location of each VOI was collected on the anatomic images. Then, a parametric MTRAsym(3.5ppm) map was created and automatically matched with the anatomic images. The grids that come with the postprocessing FuncTool software (GE Healthcare) were used to segment the APT maps based on anatomic images, and the size of each grid was adjusted in the same way as for the MR spectroscopy (On-line Fig 1). The grid with the largest mean APT asymmetry value was selected as the target to analyze. In the second approach, to evaluate potential correlations between Ki-67 expression and APTWI, 2 readers who were blinded to the histopathologic diagnosis indepen-

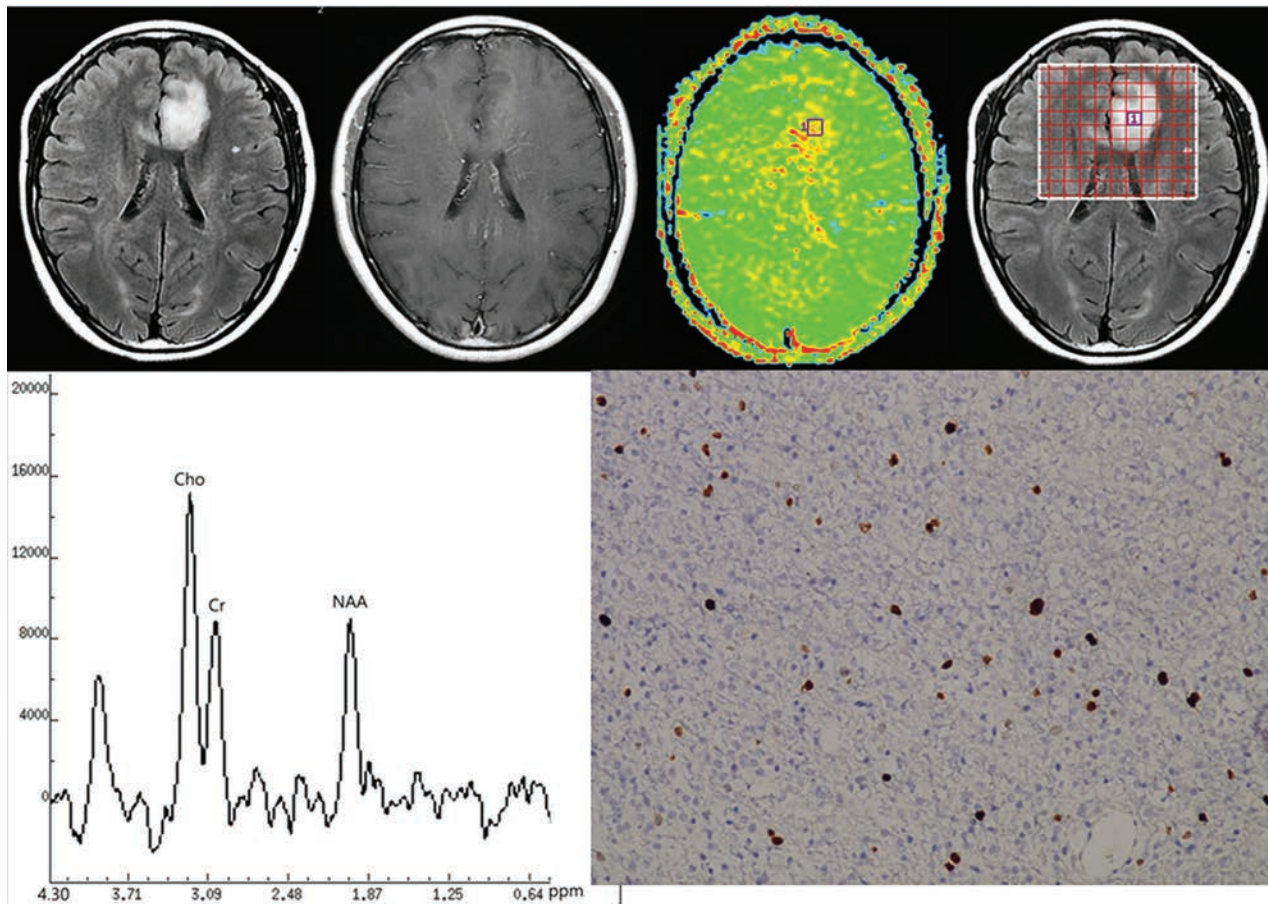


**FIG 2.** Top row, left to right: Transverse T2-FLAIR MR image (left), postgadolinium T1-weighted MR image, APT image, and the location of MR spectroscopy voxel of a 45-year-old woman with diffuse astrocytoma (grade II). Bottom row, left to right: MRSI indicating peaks for choline (Cho), creatine (Cr) and *N*-acetylaspartate (NAA); Ki-67 immunohistochemical stain for the same patient. The MTRasym(3.5ppm) value for this patient was 2.83%; the choline peak was slightly increased and the NAA peak slightly decreased; and the Ki-67 labeling index was 5%.

dently drew 4 circular ROIs on the APT images, taking care to place them so as to include solid tumor in the area with the highest MTRasym(3.5ppm) but to avoid cystic, large necrotic, or hemorrhagic components of the tumor with reference to conventional MR imaging. The measured MTRasym(3.5ppm) in the 4 ROIs were averaged to represent the tumor, as shown in On-line Fig 2.

### **Surgery and Pathologic Evaluation**

Tumor grade was assigned based on the pathologic diagnosis of the surgical specimens according to the 2007 WHO classification; the Ki-67 labeling index was also measured by using standard immunohistochemical staining procedures in samples from 37 patients (2 samples from the other 5 patients were too small). Tumor sections were reviewed and Ki-67 quantified based on the percentage of positive cells in the highest density of the stained areas; all cells with nuclear staining of any intensity were considered positive, and the Ki-67 labeling index was defined as the percentage of positive cells among the total number of counted cells.

### **Statistical Analysis**

All values are expressed as means  $\pm$  standard deviations. Interobserver agreement on tumor MTRasym(3.5ppm) values made by

the 2 readers was analyzed by calculating the intraclass correlation coefficient with MedCalc (MedCalc Software, Ostend, Belgium). Intraclass correlation coefficients  $>0.74$  indicate excellent correlation. Overall correlations between the MTRasym(3.5ppm) values and the MRSI features as well as subgroup correlations were analyzed with the Pearson correlation coefficient. The correlation between Ki-67 expression and MTRasym(3.5ppm) was also assessed with the Pearson correlation analysis. Independent sample *t* tests were used to compare differences in MTRasym(3.5ppm) and Ki-67 between the high- and low-grade gliomas. Receiver operating characteristic curve analysis was used to evaluate the accuracy of MTRasym(3.5ppm) for determining glioma grade and to establish optimal cutoff values. A default  $\alpha$  level of .05 was used for all tests, and all tests were 2-tailed. Statistical analyses were done with SPSS (IBM, Armonk, New York), IBM 19 (IBM), or Prism 5.0 GraphPad software (GraphPad Software, San Diego, California).

## **RESULTS**

### **MTRasym(3.5ppm) and Glioma Grade**

Both readers found that the APT MTRasym(3.5ppm) values were lower in low-grade gliomas than in high-grade gliomas (reader 1,  $2.65\% \pm 0.20$  versus  $3.74\% \pm 0.17$ ,  $P = .001$  by Student *t* test;

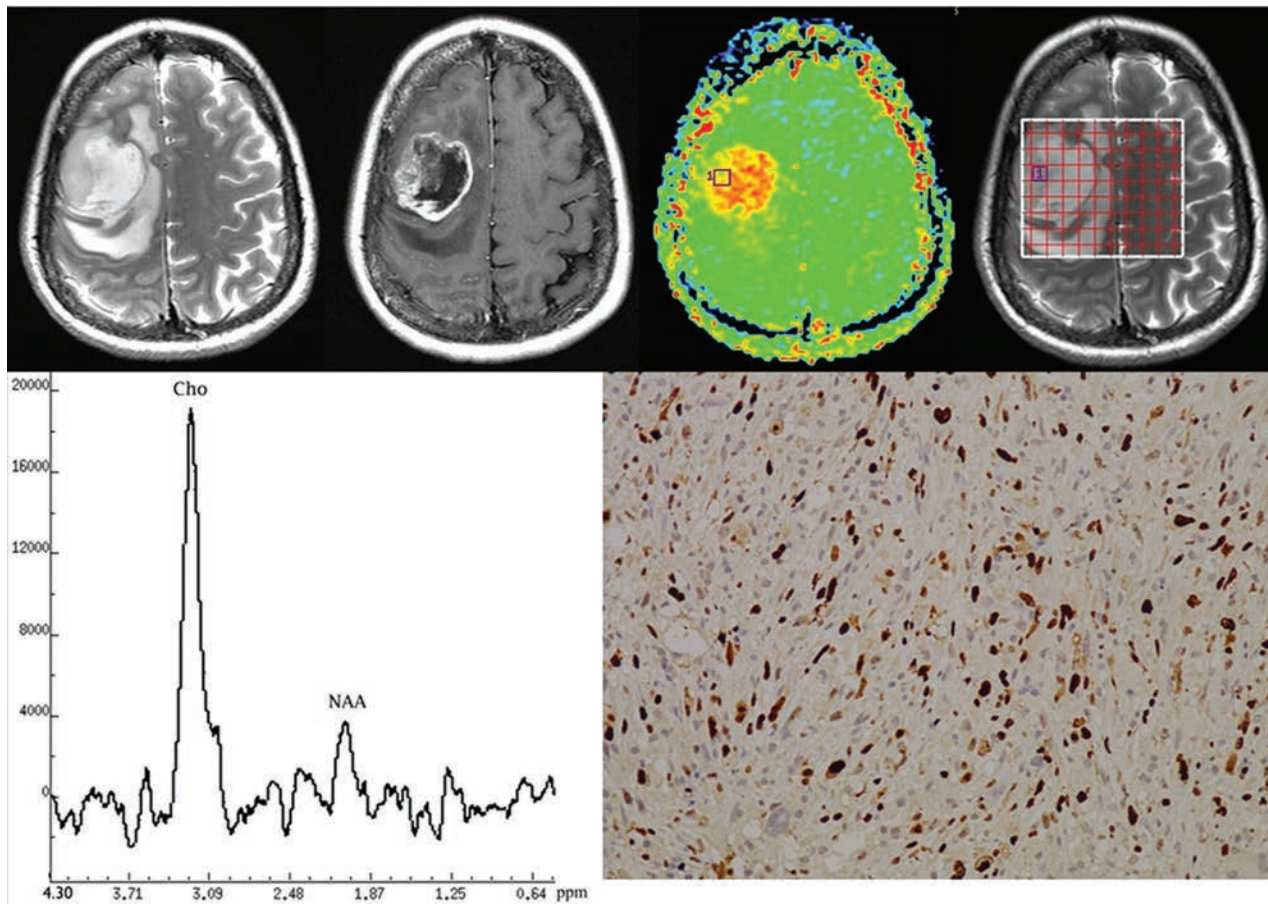


**FIG 3.** Top row, left to right: T2 FSE MR image, postgadolinium T1-weighted MR image, APT image, and the location of MR spectroscopy voxel of a 46-year-old woman with anaplastic oligodendroma (grade III). Bottom row, left to right: MRSI indicating peaks for choline (Cho) and *N*-acetylaspartate (NAA), and Ki-67 immunohistochemical staining for the same patient. The MTRAsym(3.5ppm) value for this patient was 4.39%; the choline peak was obviously increased and the NAA peak obviously decreased; and the Ki-67 labeling index was 30%.

reader 2,  $2.63\% \pm 0.18$  versus  $3.47\% \pm 0.16$ ,  $P = .004$  by Student *t* test) (Table 2). The sensitivity and specificity values for discriminating low-grade from high-grade gliomas were 92.9% and 71.4%, respectively, when cutoff values for MTRAsym(3.5ppm) were 3.11% for reader 1 and 2.85% for reader 2. Areas under the curve of MTRAsym(3.5ppm) were 0.813 (95% CI, 0.675–0.95) for reader 1 and 0.770 (95% CI, 0.623–0.918) for reader 2 (Table 2). Interobserver agreement between the 2 readers was excellent, with an intraclass correlation coefficient of 0.94 (95% CI, 0.89–0.96) and a regression equation of  $y = 0.8928x + 0.3550$  ( $P < .0001$ ) (Fig 1A). The Bland-Altman analysis of the difference in MTRAsym(3.5ppm) assessed by the 2 readers also showed excellent concordance, with only 1 value beyond the 95% limits of agreement (Fig 1B). The mean MTRAsym(3.5ppm) values of both readers' measurements were significantly lower for low-grade gliomas than for high-grade gliomas ( $2.64\% \pm 0.185$  versus  $3.61\% \pm 0.155$ ,  $P = .0016$  by Student *t* test) (Fig 1C, Table 2). Correlation analysis further demonstrated that MTRAsym(3.5ppm) values correlated with tumor grade ( $r = 0.506$ ,  $P = .0006$ ) (Fig 1D).

#### **MTRAsym(3.5ppm) and Ki-67 Expression**

The mean Ki-67 labeling index was significantly lower in low-grade gliomas than in high-grade gliomas ( $4.98\% \pm 1.02$  versus

$24.15\% \pm 5.04$ ,  $P = .003$ ) (Table 2). Correlation analysis revealed that the MTRAsym(3.5ppm) values were moderately positively correlated with Ki-67 expression levels ( $r = 0.502$ ,  $P = .002$ ) (Fig 1E), with a higher MTRAsym(3.5ppm) indicating greater proliferative activity and greater malignancy. Findings from APTWI, Ki-67 staining, and MRSI from 2 representative patients, one with low-grade glioma and the other with high-grade glioma, are shown separately in Figs 2 and 3.

#### **Correlation of MTRAsym(3.5ppm) with Metabolite Measurements on MRSI**

Overall Pearson correlation analysis showed that the MTRAsym(3.5ppm) values were moderately positively correlated with choline ( $r = 0.429$ ,  $P = .009$ ) and the choline/NAA ratio ( $r = 0.423$ ,  $P = .01$ ) and were moderately negatively correlated with NAA ( $r = -0.455$ ,  $P = .005$ ) (Fig 4A). This correlation pattern was similar in the subgroup analysis of low- and high-grade gliomas. In low-grade gliomas, MTRAsym(3.5ppm) showed moderate correlation with metabolite measurements (choline,  $r = 0.442$ ,  $P = .031$ ; NAA,  $r = -0.474$ ,  $P = .019$ ; choline/NAA ratio,  $r = 0.448$ ,  $P = .028$ ) (Fig 4B). The correlation was similar in high-grade gliomas, but the absolute correlation coefficients were greater (choline,  $r = 0.547$ ,  $P = .053$ ; NAA,  $r = -0.644$ ,  $P = .017$ ; choline/NAA ratio,  $r = 0.583$ ,  $P = .036$ ) (Fig 4C).

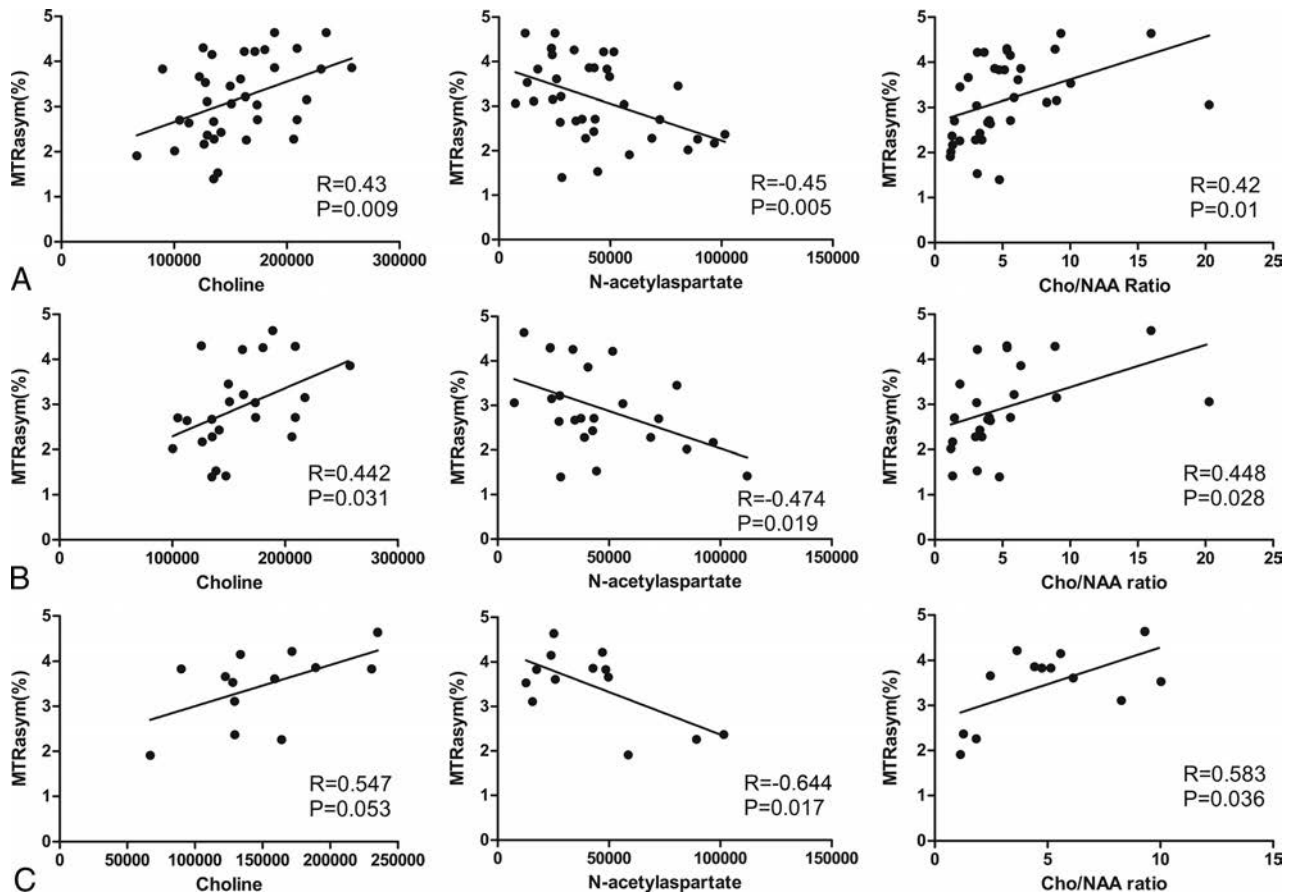


**FIG 4.** The voxel-to-voxel correlational analyses of MTRAsym(3.5ppm) with choline (Cho), N-acetylaspartate (NAA), and Cho/NAA ratio in patients with glioma. *A*, For all patients (regardless of glioma grade), MTRAsym(3.5ppm) showed mildly positive correlations with Cho ( $r = 0.43$ ,  $P = .009$ ) and the Cho/NAA ratio ( $r = 0.42$ ,  $P = .01$ ) and a slightly stronger negative correlation with NAA ( $r = -0.45$ ,  $P = .005$ ). *B*, Subgroup analyses of low-grade gliomas revealed that MTRAsym(3.5ppm) correlated with Cho ( $r = 0.442$ ,  $P = .031$ ), NAA ( $r = -0.474$ ,  $P = .019$ ), and the Cho/NAA ratio ( $r = 0.448$ ,  $P = .028$ ). *C*, Subgroup analyses of high-grade gliomas revealed a similar pattern of correlation, though the absolute values of the correlation coefficients were higher for the high-grade tumors (Cho:  $r = 0.547$ ,  $P = .053$ ; NAA:  $r = -0.644$ ,  $P = .017$ ; Cho/NAA:  $r = 0.583$ ,  $P = .036$ ).

## DISCUSSION

Our key findings were as follows. First, the MTRAsym(3.5ppm) values correlated with glioma grades, and MTRAsym(3.5ppm) could reliably distinguish low-grade from high-grade gliomas. Moreover, these MTRAsym(3.5ppm) values also correlated with choline and NAA levels on MRSI in both low- and high-grade gliomas, with stronger correlation in high-grade gliomas. Finally, the MTRAsym(3.5ppm) values correlated moderately with the Ki-67 labeling index. Collectively, these findings suggest that MTRAsym(3.5ppm) may be useful as a noninvasive biomarker of glioma proliferation and grade.

We further found that high-grade gliomas showed significantly higher MTRAsym(3.5ppm) values than low-grade gliomas and that the increase of MTRAsym(3.5ppm) correlated positively with the cellular proliferation marker Ki-67 and glioma grade. Our findings were partly consistent with those results of another group,<sup>16</sup> who reported that the amide protons of endogenous mobile proteins and peptides in the cytoplasm are the main source of the APT signal. To further clarify the value of MTRAsym(3.5ppm) with regard to tumor proliferation, we compared MTRAsym(3.5ppm) with MRSI variables and observed modest correlations between the 2 types of measurements. High-

grade gliomas are characterized by particularly rapid proliferation and atypical cytoarchitecture, as well as the presence of necrotic areas, vascular thrombosis, and microvascular proliferation. Because higher-grade gliomas have more actively proliferating tumor cells, and because the concentrations of mobile macromolecules (such as proteins and peptides) increase with the tumor cell density and glioma grades,<sup>18</sup> one could expect that the MTRAsym(3.5ppm) values would be different in high-grade versus low-grade gliomas. Factors other than intracellular components can also affect APT MTRAsym(3.5ppm); for example, tumors with necrosis showed higher MTRAsym(3.5ppm) values than tumors without necrosis.<sup>16</sup> Highly concentrated mobile proteins and peptides in the extracellular space, such as microscopic necrosis or fluid collection in the microcystic space, may also increase MTRAsym(3.5ppm) in tumors. In addition, the amide proton exchange rate is base-catalyzed in the physiologic pH range. Tissue pH in gliomas has been shown to be higher than that in normal tissue (up to 0.2 pH units)<sup>19,20</sup>; a higher pH increases the proton exchange rate, which in turn increases MTRAsym(3.5ppm). These findings, in combination with our own discovery that MTRAsym(3.5ppm) correlates positively with the Ki-67 labeling index and glioma grade, provide further support for the

concept that APT MTRAsym(3.5ppm) may be valuable as a non-invasive biomarker of tumor proliferation.

In our study, MTRAsym(3.5ppm) values correlated positively with choline level and choline/NAA ratio and negatively with NAA level, which suggests that the MTRAsym(3.5ppm) of the solid parts of gliomas may reflect both the proliferative activity of the tumor and the extent of neuron damage caused by tumor growth. As an important imaging method based on the metabolic characteristics of tissues,<sup>21,22</sup> MRSI has been used to map changes in phospholipid metabolism in brain tumors. Increases in total choline have been linked with increases in membrane turnover and cellular density<sup>7,8</sup> and with the extent of fiber destruction caused by gliomas.<sup>23</sup> Conversely, NAA levels reflect neuronal activity and, thus, decrease in parallel with the growth of brain tumors such as gliomas.<sup>21</sup> Our findings on the correlations between MTRAsym (3.5ppm) and choline/NAA ratios were consistent in part with those reported by Park et al,<sup>15</sup> who used single-voxel MR spectroscopy, and their VOIs were somewhat larger than our multi-voxel MRSI findings. Because gliomas are often heterogeneous, using smaller VOIs carries a lower risk of accidentally including cystic and necrotic areas and allows more precise measurement of the tumor areas of interest, which could provide an important part of a comprehensive comparison between MR spectroscopy and APT imaging. Our voxel-to-voxel correlation results, combined with the findings reported by Park et al,<sup>15</sup> indicate that MTRAsym(3.5ppm) could be a noninvasive means of assessing not only tumor proliferation, but also the extent of secondary neuronal injury in vivo, which would be very important for targeted biopsy and local therapy.

Our findings also demonstrated that APT MTRAsym(3.5ppm) provided better sensitivity (93%) and specificity (71.4%) with a cutoff value of 2.93% in distinguishing low- from high-grade gliomas, and the MTRAsym(3.5ppm) values correlated with metabolite levels from MRSI. Previous studies<sup>10,24</sup> have shown that MRSI is useful for distinguishing among types and grades of brain tumors. However, the reported accuracy in identifying glioma grades by choline levels was not sufficient, having high sensitivity but low specificity. Further, MRSI is limited by heterogeneities in the tumor.<sup>11</sup> With the exception of a uniform magnetic field, accurate and reliable measurements also require not only excellent scanning done by a skilled MR imaging technologist, but also careful placement of ROIs to avoid areas of calcification, cysts, hemorrhage, and adjacent bone structures. As for APTWI scanning, these disadvantages are not a major problem. Moreover, in addition to the ability to distinguish malignant brain tumors from peritumoral edema and to distinguish low-grade from high-grade tumors,<sup>12,25,26</sup> MTRAsym(3.5ppm) can also be used to depict tumor core areas based on its ability to visualize amide proton contrast. Our results also showed that MTRAsym(3.5ppm) values correlated positively with glioma grade, with higher MTRAsym (3.5ppm) associated with greater malignancy. Sakata et al<sup>27</sup> reported that APTWI analysis of a single representative image section could distinguish low-grade from high-grade gliomas as accurately as could APTWI of the entire tumor, and single sections can be acquired within a reasonably short scan time. Collectively, these findings imply that APT can be an efficient tool for assessing glioma malignancy in a clinical setting.

This study had 2 major limitations. First, although the ROIs for the APT measurements were roughly in the same areas as those used to assess Ki-67, a point-to-point match was not done. Resected specimens for Ki-67 examination possess little locational information, and without intraoperative MR imaging, the accuracy of a direct match between MR imaging and samples for immunohistochemical staining would be a challenge, especially when a single-axis section is used for imaging. Second, relatively few patients in this study had high-grade gliomas, though the correlations were statistically significant.

## CONCLUSIONS

Comparing APTWI with immunohistochemical staining of Ki-67 and MRSI by using voxel-to-voxel analysis in patients with glioma, we found that MTRAsym(3.5ppm) correlated with Ki-67 labeling index, with histopathologic grade, and with key metabolites from MR spectroscopy. We concluded that MTRAsym(3.5ppm) may be a useful biomarker not only for assessing tumor proliferation, but also for predicting histopathologic grade, which could have an important impact on the clinical therapy strategy for patients with glioma.

## REFERENCES

1. Louis DN, Ohgaki H, Wiestler OD, et al. **The 2007 WHO classification of tumours of the central nervous system.** *Acta Neuropathol* 2007;114:97–109 CrossRef Medline
2. Wen PY, Kesari S. **Malignant gliomas in adults.** *N Engl J Med* 2008; 359:492–507 CrossRef Medline
3. Stupp R, Mason WP, van den Bent MJ, et al. **Radiotherapy plus concomitant and adjuvant temozolomide for glioblastoma.** *N Engl J Med* 2005;352:987–96 CrossRef Medline
4. Cancer Genome Atlas Research Network, Brat DJ, Verhaak RG, et al. **Comprehensive, integrative genomic analysis of diffuse lower-grade gliomas.** *N Engl J Med* 2015;372:2481–98 CrossRef Medline
5. Hoshino T, Ahn D, Prados MD, et al. **Prognostic significance of the proliferative potential of intracranial gliomas measured by bromodeoxyuridine labeling.** *Int J Cancer* 1993;53:550–55 CrossRef Medline
6. Sallinen PK, Haapasalo HK, Visakorpi T, et al. **Prognostication of astrocytoma patient survival by Ki-67 (MIB-1), PCNA, and S-phase fraction using archival paraffin-embedded samples.** *J Pathol* 1994; 174:275–82 CrossRef Medline
7. Tamiya T, Kinoshita K, Ono Y, et al. **Proton magnetic resonance spectroscopy reflects cellular proliferative activity in astrocytomas.** *Neuroradiology* 2000;42:333–38 CrossRef Medline
8. Tedeschi G, Lundbom N, Raman R, et al. **Increased choline signal coinciding with malignant degeneration of cerebral gliomas: a serial proton magnetic resonance spectroscopy imaging study.** *J Neurosurg* 1997;87:516–24 CrossRef Medline
9. Moffett JR, Ross B, Arun P, et al. **N-Acetylaspartate in the CNS: from neurodiagnostics to neurobiology.** *Prog Neurobiol* 2007;81:89–131 CrossRef Medline
10. Stadlbauer A, Gruber S, Nimsky C, et al. **Preoperative grading of gliomas by using metabolite quantification with high-spatial-resolution proton MR spectroscopic imaging.** *Radiology* 2006;238: 958–69 CrossRef Medline
11. Bulik M, Jancalek R, Vanicek J, et al. **Potential of MR spectroscopy for assessment of glioma grading.** *Clin Neurol Neurosurg* 2013;115: 146–53 CrossRef Medline
12. Zhou J, Lal B, Wilson DA, et al. **Amide proton transfer (APT) contrast for imaging of brain tumors.** *Magn Reson Med* 2003;50: 1120–26 CrossRef Medline
13. Sagiya K, Mashimo T, Togao O, et al. **In vivo chemical exchange saturation transfer imaging allows early detection of a therapeutic**

- response in glioblastoma. *Proc Natl Acad Sci U S A* 2014;111:4542–47 CrossRef Medline
14. Zhou J, Tryggstad E, Wen Z, et al. **Differentiation between glioma and radiation necrosis using molecular magnetic resonance imaging of endogenous proteins and peptides.** *Nat Med* 2011;17:130–34 CrossRef Medline
  15. Park JE, Kim HS, Park KJ, et al. **Pre- and posttreatment glioma: comparison of amide proton transfer imaging with MR spectroscopy for biomarkers of tumor proliferation.** *Radiology* 2016;278:514–23 CrossRef Medline
  16. Togao O, Yoshiura T, Keupp J, et al. **Amide proton transfer imaging of adult diffuse gliomas: correlation with histopathological grades.** *Neuro Oncol* 2014;16:441–48 CrossRef Medline
  17. Tee YK, Donahue MJ, Harston GW, et al. **Quantification of amide proton transfer effect pre- and post-gadolinium contrast agent administration.** *J Magn Reson Imaging* 2014;40:832–38 CrossRef Medline
  18. Howe FA, Barton SJ, Cudlip SA, et al. **Metabolic profiles of human brain tumors using quantitative in vivo 1H magnetic resonance spectroscopy.** *Magn Reson Med* 2003;49:223–32 CrossRef Medline
  19. Maintz D, Heindel W, Kugel H, et al. **Phosphorus-31 MR spectroscopy of normal adult human brain and brain tumours.** *NMR Biomed* 2002;15:18–27 CrossRef Medline
  20. Ha DH, Choi S, Oh JY, et al. **Application of 31P MR spectroscopy to the brain tumors.** *Korean J Radiol* 2013;14:477–86 CrossRef Medline
  21. Howe FA, Opstad KS. **1H MR spectroscopy of brain tumours and masses.** *NMR Biomed* 2003;16:123–31 CrossRef Medline
  22. Nelson SJ. **Multivoxel magnetic resonance spectroscopy of brain tumors.** *Mol Cancer Ther* 2003;2:497–507 Medline
  23. Stadlbauer A, Hammen T, Buchfelder M, et al. **Differences in metabolism of fiber tract alterations in gliomas: a combined fiber density mapping and magnetic resonance spectroscopic imaging study.** *Neurosurgery* 2012;71:454–63 CrossRef Medline
  24. Zeng QS, Li CF, Liu H, et al. **Distinction between recurrent glioma and radiation injury using magnetic resonance spectroscopy in combination with diffusion-weighted imaging.** *Int J Radiat Oncol Biol Phys* 2007;68:151–58 CrossRef Medline
  25. Zhou J, Blakeley JO, Hua J, et al. **Practical data acquisition method for human brain tumor amide proton transfer (APT) imaging.** *Magn Reson Med* 2008;60:842–49 CrossRef Medline
  26. Zhou J, Zhu H, Lim M, et al. **Three-dimensional amide proton transfer MR imaging of gliomas: initial experience and comparison with gadolinium enhancement.** *J Magn Reson Imaging* 2013;38:1119–28 CrossRef Medline
  27. Sakata A, Okada T, Yamamoto A, et al. **Grading glial tumors with amide proton transfer MR imaging: different analytical approaches.** *J Neurooncol* 2015;122:339–48 CrossRef Medline

# Optimization of DSC MRI Echo Times for CBV Measurements Using Error Analysis in a Pilot Study of High-Grade Gliomas

 L.C. Bell,  M.D. Does,  A.M. Stokes,  L.C. Baxter,  K.M. Schmainda,  A.C. Dueck, and  C.C. Quarles



## ABSTRACT

**BACKGROUND AND PURPOSE:** The optimal TE must be calculated to minimize the variance in CBV measurements made with DSC MR imaging. Simulations can be used to determine the influence of the TE on CBV, but they may not adequately recapitulate the in vivo heterogeneity of precontrast T2\*, contrast agent kinetics, and the biophysical basis of contrast agent–induced T2\* changes. The purpose of this study was to combine quantitative multiecho DSC MRI T2\* time curves with error analysis in order to compute the optimal TE for a traditional single-echo acquisition.

**MATERIALS AND METHODS:** Eleven subjects with high-grade gliomas were scanned at 3T with a dual-echo DSC MR imaging sequence to quantify contrast agent–induced T2\* changes in this retrospective study. Optimized TEs were calculated with propagation of error analysis for high-grade glial tumors, normal-appearing white matter, and arterial input function estimation.

**RESULTS:** The optimal TE is a weighted average of the T2\* values that occur as a contrast agent bolus transverses a voxel. The mean optimal TEs were 30.0 ± 7.4 ms for high-grade glial tumors, 36.3 ± 4.6 ms for normal-appearing white matter, and 11.8 ± 1.4 ms for arterial input function estimation (repeated-measures ANOVA,  $P < .001$ ).

**CONCLUSIONS:** Greater heterogeneity was observed in the optimal TE values for high-grade gliomas, and mean values of all 3 ROIs were statistically significant. The optimal TE for the arterial input function estimation is much shorter; this finding implies that quantitative DSC MR imaging acquisitions would benefit from multiecho acquisitions. In the case of a single-echo acquisition, the optimal TE prescribed should be 30–35 ms (without a preload) and 20–30 ms (with a standard full-dose preload).

**ABBREVIATIONS:** AIF = arterial input function; CA = contrast agent; NAWM = normal-appearing white matter

Dynamic susceptibility contrast MR imaging is increasingly used to map cerebral blood volume in patients with brain tumor, owing to its potential to predict treatment response, improve image-guided biopsies, and differentiate posttreatment radiation effects and glioma progression.<sup>1–9</sup>

CBV is typically acquired by using a dynamic susceptibility contrast MR imaging and tracking the gadolinium-based contrast

agent (CA)–induced T2\* changes with time. To optimally capture the MR signal changes due to the T2\* changes, one must prescribe an optimal TE during the acquisition. Previous studies have used simulations to determine optimal TEs for spin-echo-based DSC MR imaging<sup>10</sup>; however, to the best of our knowledge, an optimal TE has not been determined for gradient-echo-based DSC MR imaging. Recently, the American Society of Functional Neuro-radiology recommended gradient-echo-based DSC MR imaging for brain tumor imaging because of the higher signal to noise, better sensitivity, and more uniform vessel-size sensitivity compared with spin-echo imaging.<sup>11</sup> Accordingly, it is important to determine an optimal TE for gradient-echo-based DSC MR imaging.

Optimal TEs have been previously suggested in the literature. It has been suggested that the optimal TE should be on the order of the expected T2\* values before CA administration.<sup>12,13</sup> In contrast, Boxerman et al<sup>10</sup> demonstrated, with propagation of error analysis, that the optimal TE should be a weighted average of the precontrast and postcontrast T2\* values, though they did not rec-

Received December 2, 2016; accepted after revision May 7, 2017.

From the Division of Imaging Research (L.C. Bell, A.M.S., L.C. Baxter, C.C.Q.), Barrow Neurological Institute, Phoenix, Arizona; Department of Biomedical Engineering (M.D.D.), Vanderbilt University Institute of Imaging Science, Nashville, Tennessee; Departments of Biophysics and Radiology (K.M.S.), Medical College of Wisconsin, Milwaukee, Wisconsin; and Division of Health Sciences Research (A.C.D.), Section of Biostatistics, Mayo Clinic, Scottsdale, Arizona.

This work was supported by the National Institutes of Health/National Cancer Institute R01 CA158079.

Please address correspondence to C. Chad Quarles, PhD, Barrow Neurological Institute, 350 W Thomas Rd, Phoenix, Arizona 85018; e-mail: chad.quarles@barrowneuro.org

 Indicates open access to non-subscribers at [www.ajnr.org](http://www.ajnr.org)

 Indicates article with supplemental on-line photo.

<http://dx.doi.org/10.3174/ajnr.A5295>

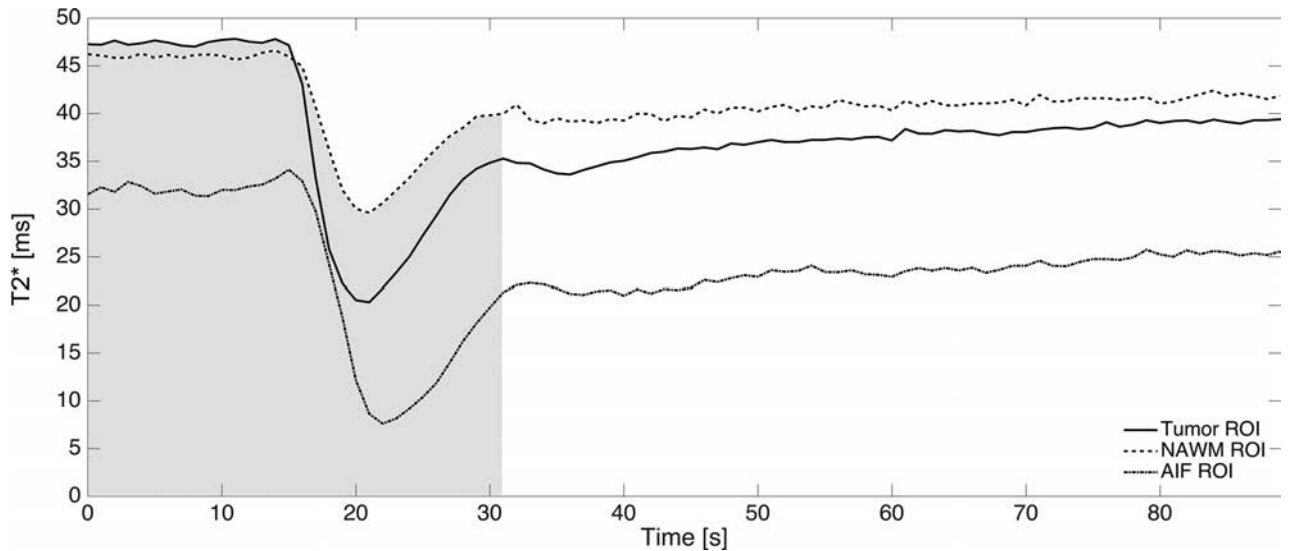


**FIG 1.** An example from 1 patient of the absolute T2\* time curves for tumor (solid), NAWM (dash dash), and the AIF (dash dot) ROIs. As described in Equation 6, the optimal TE is proportional to the weighted average of absolute T2\* values during the first pass (as indicated by the shaded gray area) of the contrast agent.

commend a specific TE. The optimal TE in a DSC experiment is most likely different for voxels used to identify the arterial input function (AIF) and normal-appearing white matter (NAWM) due to the higher contrast agent concentration encountered within arteries and the associated potential signal saturation.<sup>14</sup>

While simulations and error analysis can be used to systematically investigate the influence of TE on CBV accuracy, they cannot recapitulate in vivo heterogeneity of precontrast T2\*, CA kinetics, and the biophysical basis of CA-induced T2\* changes. With multiecho-based DSC MR imaging acquisitions, voxelwise T2\* values before and after CA administration can be quantified across tissue types by assuming a monoexponential decay. The goal of this study was to combine quantitative multiecho DSC MR imaging T2\* time curves with propagation of error analysis to compute the optimal gradient-echo TEs for high-grade glial tumors, NAWM, and AIF estimation.

## MATERIALS AND METHODS

### Theory

During the contrast agent bolus passage in a DSC MR image, the T2\* of the perfused voxel changes with time. From the literature, it is assumed that this change in the transverse relaxation rate,  $\Delta R_2^*(t) = 1/\Delta T_2^*(t)$ , is linear with CA concentration, and therefore the relative CBV (rCBV) can be approximated by

$$1) \quad rCBV = \int_0^T \Delta R_2^*(t) dt,$$

assuming a single-echo acquisition,  $\Delta R_2^*(t)$  is

$$2) \quad \Delta R_2^*(t) = R_2^*(t) - R_{20}^* = -\frac{1}{TE} \ln\left(\frac{S(t)}{S_{pre}}\right).$$

Here  $R_{20}^*$  is the baseline apparent transverse relaxation rate before contrast arrival. The generalized signal equation, after contrast agent injection, for a spoiled gradient-echo acquisition is

$$3) \quad S(t) = S_0 \sin \alpha \exp[-TE \times R_2^*(t)] \frac{1 - \exp[-TR \times R_1(t)]}{1 - \cos \alpha \exp[-TR \times R_1(t)]} = \eta \exp[-TE \times R_2^*(t)].$$

For simplification, the constant  $\eta$  includes all the terms that are independent of the TE.

If we assume that the baseline (precontrast) signal points are acquired with a sufficient signal-to-noise ratio, we note that the variance in the apparent transverse relaxation is mainly due to the variance in the signal with time. If one applies propagation of error to Equation 2, the variance in  $R_2^*(t)$  is

$$4) \quad \sigma_R^2 = \frac{k\sigma_S^2 \exp[2TE \times R_2^*(t)]}{TE^2},$$

where  $k$  is a proportionality constant. Similar to the approach taken by Boxerman et al,<sup>10</sup> the variance in a CBV measurement can then be determined by

$$5) \quad \sigma_{CBV}^2 = \Delta t \sum_{i=1}^N \sigma_R^2(t_i) = \frac{k\sigma_S^2 \Delta t}{TE^2} \sum_{i=1}^N \exp[2TE \times R_2^*(t_i)].$$

Last, the derivative of Equation 5 is taken with respect to TE and solved when equal to zero to determine the optimal TE that minimizes the variance in CBV measurements:

$$6) \quad TE_{opt} = \frac{\sum_{i=1}^N \exp[2TE_{opt} \times R_2^*(t_i)]}{\sum_{i=1}^N R_2^*(t_i) \exp[2TE_{opt} \times R_2^*(t_i)]}.$$

The optimal TE can now be solved numerically from Equation 6. Note that the optimal TE is, essentially, the weighted average of T2\* values during the contrast agent passage (illustrated by Fig 1).

## MR Imaging Protocol

This article is a retrospective analysis from 2 separate subject cohorts approved by the Barrow Neurological Institute's (1st subject cohort) and Vanderbilt University's (2nd subject cohort) institutional review boards. Both cohorts of patients had World Health Organization grade III and IV primary high-grade gliomas undergoing preoperative imaging for surgical resection. All patients had contrast-enhancing lesions.

We analyzed 2 separate subject cohorts to evaluate optimal TE values in scans acquired with and without a contrast agent preload. In the clinic, a preload ranging from 0.025 to 0.1 mmol/kg is typically administered 6 minutes before the DSC imaging to reduce CA-induced T1 leakage effects. The first cohort of subjects was used for calculation of optimal TE (described in detail below) without a preload. The second cohort of subjects was scanned with multiecho DSC MR imaging for 7.5 minutes, making it an ideal dataset to quantify T2\* changes 6 minutes after contrast agent injection, mimicking a preload situation in the clinic. These results allowed us to understand how a preload would affect the calculated optimal TE.

The first subject cohort consisted of 11 datasets randomly selected from an ongoing study (mean age,  $49.9 \pm 12.9$  years; 7 men, 4 women). Each subject was scanned on a single 3T MR imaging system (Signa HDx; GE Healthcare, Milwaukee, Wisconsin) with a dedicated 8-channel phased array brain coil. A 2D single-shot dual-echo spiral DSC sequence was used with the following parameters: TR/TE1/TE2 = 1000/5.6/28 ms, flip angle =  $60^\circ$ , FOV =  $22 \times 22$  cm, section thickness = 5 mm, section spacing = 0 mm, number of sections = 16, and acquired matrix = 128 (frequency)  $\times$  128 (phase). Gadobenate dimeglumine (MultiHance; Bracco Diagnostics, Princeton, New Jersey) was administered at 0.1 mmol/kg (a standard dose) by using a power injector for each perfusion scan at a rate of 5 mL/s. The injection occurred 20 seconds after the start of the DSC scan, and the total length of the scan was 3 minutes. Last, T1-weighted spoiled gradient-echo images were acquired (TR/TE = 6.7/2.8 ms, flip angle =  $13^\circ$ , FOV =  $32 \times 24$  cm<sup>2</sup>, section thickness = 2 mm, acquired resolution =  $0.51 \times 0.51 \times 2$  mm<sup>3</sup>) after the perfusion scan to delineate enhancing tumor and NAWM ROIs.

The second subject cohort consisted of 5 datasets (mean age,  $47.0 \pm 7.2$  years; 4 men, 1 woman) acquired by using a combined spin- and gradient-echo DSC sequence. Each subject was scanned on a single 3T MR imaging system (Achieva; Philips Healthcare, Best, the Netherlands) with a 32-channel head coil. A 2D single-shot spin- and gradient-echo DSC sequence was used with the following parameters: 2 gradient-echoes, 2 asymmetric spin-echoes, and 1 true spin-echo, TR = 1800 ms, TE1–TE5 = 8.8/26/55/72/90 ms, flip angle =  $90^\circ$ , FOV =  $24 \times 24$  cm<sup>2</sup>, section thickness = 5 mm, section spacing = 0 mm, number of sections = 15, and acquired matrix = 76 (frequency)  $\times$  76 (phase). Partial Fourier encoding and sensitivity encoding (acceleration factors 0.73 and 2.0, respectively) were used to obtain acceptable TEs. Gadopentetate dimeglumine (Magnevist; Bayer HealthCare Pharmaceuticals, Wayne, New Jersey) was administered at 0.1 mmol/kg (a standard dose), with a power injector at a rate of 4 mL/s. The injection occurred 60 seconds after the start of the DSC scan, and the total length of the scan was 7.5 minutes. Last, 3D T1-weighted spoiled

gradient-echo images were acquired (TR/TE = 8.9/4.6 ms, flip angle =  $9^\circ$ , FOV =  $25.6 \times 25.6 \times 17.0$  cm<sup>3</sup>, acquired resolution =  $1 \times 1 \times 1$  mm<sup>3</sup>) after the perfusion scan to delineate enhancing tumor and NAWM ROIs.

## Postprocessing for Optimal TE Calculation

The T1-weighted, anatomic data were coregistered to the DSC perfusion data by using rigid registration with the FMRIB Software Library (FSL; <http://www.fmrib.ox.ac.uk/fsl>).<sup>15</sup> The DSC perfusion data were analyzed with Matlab (MathWorks, Natick, Massachusetts).

From both the dual-echo spiral and spin- and gradient-echo DSC sequences,  $R_2^*(t)$  was calculated voxel by voxel by assuming a monoexponential decay in T2\*<sup>16</sup>:

$$7) \quad R_2^*(t) = \frac{1}{TE2 - TE1} \ln \left[ \frac{S_{TE1}(t)}{S_{TE2}(t)} \right].$$

With this information, the optimal TE was calculated by numerically solving Equation 6 over the first pass of CA. To determine the temporal duration of the first pass, we first calculated the mean whole brain (WB)  $\Delta R_2^*(t)$  to determine the mean peak time point. The slope of the whole brain WB  $\Delta R_2^*(t)$  was then calculated. A positive slope indicated wash-in of CA, whereas a negative slope indicated washout, and a slope of zero, no change in CA. Starting at the peak time point, the time point in which the slope equaled zero was identified and set as the end of the first passage. The first passage of CA was approximately 22.5 seconds from the time of injection across all subjects (see Fig 1 for an illustrative example of the first-pass integration limits).

Three ROIs were used for analysis: tumor, NAWM, and voxels selected for AIF estimation. The tumor and NAWM ROIs were selected by using K-means clustering, with data partitioned into 4 clusters with the T1-weighted anatomic data (On-line Figure). The largest centroid value (brightest signal intensity) consisted of the enhancing tumor along with other unwanted regions such as fat around the skull and eyes. The enhancing tumor was manually selected section by section to separate it from the unwanted regions. The NAWM mask was determined by the second largest centroid value. Finally, voxels with the selected ROIs exhibiting a signal drop of at least 5 SDs from the baseline precontrast signal were used for analysis to ensure sufficient contrast-to-noise for the time curves. The AIF was identified on the DSC perfusion dataset with previously established automated algorithms.<sup>17,18</sup> This automatic AIF algorithm typically selects AIF pixels in the internal carotid, vertebral, and middle cerebral arteries. All ROI selections were approved by an investigator with >15 years of experience in brain tumor imaging (C.C.Q.).

In addition to the above measurements and calculations, we calculated T2\* 6 minutes after the CA injection from the second cohort of subjects. The percentage difference in T2\* ( $1/R_2^*$ ) between precontrast T2\* ( $t = 0$ ) and postcontrast ( $t = 6$  minutes) was calculated to determine the potential effect of a standard dose (0.1 mmol/kg) preload on the measured baseline T2\* values in a DSC scan. The estimated optimal TE with a preload was then calculated by scaling the calculated optimal TE without a preload by the percentage difference in T2\*.

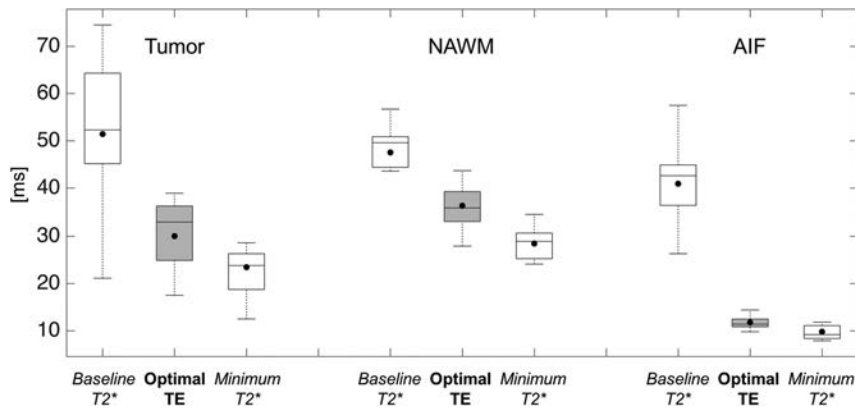


**FIG 2.** Boxplot representation of baseline and minimum T2\* values (white boxplots) along with their respective calculated optimal TE (gray boxplots) in the brain tumor, NAWM, and AIF. Baseline T2\* is defined as the T2\* of the ROI before contrast arrival, and the minimum T2\* is defined as the T2\* value at the peak signal drop. Solid lines represent median values, whereas solid dots represent means across subjects in these boxplots.

### Statistical Analysis

Mean optimal TE values were compared across tumor, NAWM, and AIF ROIs using a multivariate approach with a repeated-measures analysis of variance with post hoc pair-wise comparisons using paired *t* tests. With 11 subjects, this study had an 80% power to detect a 0.94 SD difference between a pair of ROIs with a 2-sided  $\alpha = .05$  paired *t* test. To test for mean differences in the minimum T2\* of the 2 cohorts of subjects imaged, we performed a Student unpaired *t* test. Statistical significance was detected for a *P* value < .05.

### RESULTS

Figure 1 illustrates a typical T2\* time curve for a single patient in the tumor, NAWM, and AIF. Figure 2 summarizes the baseline and minimum T2\* along with the corresponding optimal TE across all 11 subjects from the first cohort. Mean optimal TE values (mean  $\pm$  1 SD) were  $30.0 \pm 7.4$  ms for tumor,  $36.3 \pm 4.6$  ms for NAWM, and  $11.8 \pm 1.4$  ms for AIF (repeated-measures ANOVA, *P* < .001; post hoc paired *t* tests: tumor versus NAWM, *P* = .005; tumor versus AIF, *P* < .001; NAWM versus AIF, *P* < .001). Tumor ROIs exhibited a wide range of optimal TE values compared with healthy tissue. In all ROIs, mean optimal TE values were closer to the minimum T2\* than the baseline values.

Results from the second cohort of subjects indicated that the mean tumor T2\* was 35% lower than baseline 6 minutes after the CA injection. Additionally, the mean NAWM and AIF T2\* were 15% and 10%, respectively, lower than baseline. If one assumed a respective percentage decrease of each region in T2\* 6 minutes after CA injection and the optimal TE results from the first cohort of subjects presented above, the estimated mean optimal TE values with a standard preload dose were  $19.5 \pm 4.8$  ms for tumor,  $30.8 \pm 3.9$  ms for NAWM, and  $10.6 \pm 1.3$  ms for AIF.

The concentration of gadolinium between the populations must be similar to apply the results of the second to the first cohort of subjects. Because the concentration of gadolinium is proportional to  $\Delta R_2^*$ , we estimated the similarity between cohorts by comparing the peak  $\Delta R_2^*$  change. The mean peak  $\Delta R_2^*$  for the first-versus-second cohort of subjects was  $22.9 \pm 12.9$  versus  $23.7 \pm 10.8$  ms for tumor (*P* = .90),  $14.3 \pm 4.2$  versus  $12.9 \pm 5.8$

ms for the NAWM (*P* = .65), and  $94.5 \pm 18.3$  versus  $103.2 \pm 30.6$  ms for the AIF (*P* = .40).

### DISCUSSION

This study determined the optimal TE for a typical single-echo DSC MR imaging acquisition by minimizing the variance in CBV. Using error analysis, we determined that the optimal TE is a weighted average of T2\* values that occur before and after the CA passage and is dependent on the ROI type.

For an imaging protocol using no preload dose and a standard injection dose at 3T, the optimal TE in brain tumor is  $30.0 \pm 7.4$  ms. The larger range of optimal TEs in the tumor regions is expected, given the greater variability of

blood volume values and CA-induced T2\* leakage effects both within and across subjects.<sup>19</sup> The optimal TE for NAWM is roughly 20% longer (optimal TE =  $36.3 \pm 4.6$  ms) than that found in tumor. The optimal TE for the AIF is roughly 300% shorter (optimal TE =  $11.8 \pm 1.4$  ms) than that found in tumor. For an imaging protocol using both a standard preload and injection dose at 3T, we estimated the optimal TE in brain tumor to be  $19.5 \pm 4.8$  ms. The estimated optimal TE for NAWM is roughly 65% longer (optimal TE =  $30.8 \pm 3.9$  ms) than that found in tumor. The optimal TE for the AIF is roughly 200% shorter (optimal TE =  $10.6 \pm 1.3$  ms) than that found in tumor. Because a statistically significant difference was detected among the optimal TEs for each of the 3 regions for both imaging options (no preload and preload), multiecho acquisitions are warranted for quantitative DSC MR imaging studies requiring the use of the AIF, supporting previous hypotheses in the literature.<sup>20</sup>

To quantify T2\* values throughout the passage of CA in the selected ROIs, we analyzed data from dual-echo spiral acquisitions. The dual-echo data are advantageous because the influence of CA-induced T1 changes that may be present in blood or in situations in which the blood-brain barrier has been compromised has been removed.<sup>16</sup> Additionally, the calculation of T2\* based on dual-echo data is computationally simple. While more TEs could potentially improve the T2\* quantification, Stokes and Quarles<sup>21</sup> have shown that T2\* measurements derived from 2 echoes are consistent with those derived from a 5-echo acquisition. Our reported quantitative T2\* values for NAWM ( $47.5 \pm 6.8$  ms) are within the ranges previously reported in the literature:  $48.4$  ms,<sup>21</sup>  $49$  ms,<sup>22</sup>  $50 \pm 8$  ms,<sup>23</sup> and  $67.6 \pm 11.0$  ms.<sup>20</sup> However, comparison of the quantitative T2\* values for the AIF in this study with those in literature (eg, bulk arterial blood T2\*) is difficult because the voxels used to estimate the AIF likely contain brain tissue and arteries due to partial volume effects. Nevertheless, our results indicate that a much shorter optimal TE is needed for AIF estimation, which is consistent with previously published observations.<sup>20</sup>

The optimal TEs reported in this study are specific to a field strength of 3T and the CA dose protocol (no preload and 1 stan-

dard dose of CA). At a different field strength, such as 1.5T, the optimal TE would be expected to lengthen. A preload of CA is typically administered before the DSC MR imaging to decrease the CA-induced T1 leakage effects. Such preloads could potentially decrease baseline T2\* values due to residual CA in the blood and tumor tissue, thereby shortening the optimal TE. To estimate the impact of a standard full dose of preload, we retrospectively analyzed, in a separate cohort of 5 patients with gliomas, multi-echo DSC MR imaging data that were acquired for a total of 7.5 minutes. We found that tumor T2\* was 35% lower than baseline 6 minutes after the CA injection (additionally, NAWM was 15% and AIF was 10% lower than baseline). If we assume a 35% decrease in T2\* with a preload, the optimal TE will be 35% shorter than a no-preload-dose scheme or an estimated  $19.5 \pm 4.8$  ms for tumor.

There were several limitations to this study. First, our results are specific to 3T and to both a standard preload and injection dose. Although T2\* is expected to be longer at 1.5T than at 3T, implying that the optimal TE would also increase, we are not able to demonstrate this expectation experimentally. For clinical sites with less than a standard dose for either the preload or injection dose, our results do not apply. However, our derivations and methodology for optimal TE can be easily applied to data acquired at any field strength or dosing scheme of interest. Second, as noted, a statistically significant difference was found among the optimal TEs among tumor, NAWM, and AIF. The extent of using a nonoptimal TE on CBV is unknown. The influence of TE on the accuracy of CBV can be explored both experimentally and through simulations and is currently saved for future work. Third, we have calculated the optimal TE in a small cohort of patients. However, power statistics did demonstrate that our sample size had an 80% power to detect a 0.94 SD in our measurements. It is unlikely that additional patients would substantially (or practically) shift the calculated optimal TE values. Last, the estimation of the optimal TE from 2 separate cohorts to understand the effect of a preload on the optimal TE is not ideal. Calculation of the optimal TE from multiecho DSC data acquired with a preload would have been ideal. However, clinically, single-echo DSC MR imaging is acquired with a preload, and changes in absolute T2\* cannot be obtained from single-echo data for optimal TE calculation. When a multiecho DSC acquisition is acquired in the clinic, a preload is typically not administered because the T1 leakage effects are eliminated. Additionally, our 2 separate cohorts used a standard dose injection of 2 different contrast agents. However, the calculated optimal TE values should not change appreciably because the expected change in T2\* due to its relaxation rate is similar<sup>22,23</sup> across both contrast agents and we found no significant statistical differences in the average gadolinium concentration between the 2 cohorts.

## CONCLUSIONS

The results of this study demonstrate that for conventional single-echo-, gradient-echo-based DSC MR imaging, the optimal TE for CBV mapping in brain tumors and NAWM is 30–36 ms at 3T if no preload has been administered. The accuracy of the AIF will be diminished, to an unknown degree, due to the longer-than-optimal TE. In this situation, CBV should only be calculated in the

tumor and the NAWM. If multiple TEs can be prescribed, then a shorter TE of 10 ms should be prescribed for the AIF and a longer TE of 30–36 ms should be prescribed for the brain tissue and tumor. Given the recommendation of the American Society of Functional Neuroradiology that a preload should be used for DSC MR imaging studies in patients with glioma, the error analysis and patient data described in this study provide experimental evidence that CBV estimates may benefit from lower TEs (~20 ms) than the recommended value of 30 ms.

## ACKNOWLEDGMENTS

We acknowledge Kelly Gardener and Samuel McGee for their valuable help.

Disclosures: Laura C. Bell—RELATED: Grant: National Institutes of Health/National Cancer Institute R01 CA158079\*. Ashley M. Stokes—RELATED: Grant: National Institute of Health/National Cancer Institute, Comments: R01 CA158079.\* Leslie C. Baxter—RELATED: Grant: National Cancer Institute\*. Kathleen M. Schmainda—RELATED: Grant: National Institutes of Health, Comments: R01 CA082500, U01 CA176110\*. UNRELATED: Other: Imaging Biometrics, Comments: ownership interest. C. Chad Quarles—RELATED: Grant: National Institutes of Health.\* Amylou C. Dueck—RELATED: Grant: National Institutes of Health/National Cancer Institute, Comments: CA158079\*. \*Money paid to the institution.

## REFERENCES

1. Fink JR, Muzi M, Peck M, et al. **Multimodality brain tumor imaging: MR imaging, PET, and PET/MR imaging.** *J Nucl Med* 2015;56:1554–61 CrossRef Medline
2. Boxerman JL, Ellingson BM, Jeyapalan S, et al. **Longitudinal DSC-MRI for distinguishing tumor recurrence from pseudoprogression in patients with a high-grade glioma.** *Am J Clin Oncol* 2017;40:228–34 CrossRef Medline
3. Ellingson BM, Zaw T, Cloughesy TF, et al. **Comparison between intensity normalization techniques for dynamic susceptibility contrast (DSC)-MRI estimates of cerebral blood volume (CBV) in human gliomas.** *J Magn Reson Imaging* 2012;35:1472–77 CrossRef Medline
4. Chaskis C, Stadnik T, Michotte A, et al. **Prognostic value of perfusion-weighted imaging in brain glioma: a prospective study.** *Acta Neurochir (Wien)* 2006;148:277–85; discussion 285 CrossRef Medline
5. Maia AC Jr, Malheiros SM, da Rocha AJ, et al. **Stereotactic biopsy guidance in adults with supratentorial nonenhancing gliomas: role of perfusion-weighted magnetic resonance imaging.** *J Neurosurg* 2004;101:970–76 CrossRef Medline
6. Barajas RF Jr, Chang JS, Segal MR, et al. **Differentiation of recurrent glioblastoma multiforme from radiation necrosis after external beam radiation therapy with dynamic susceptibility-weighted contrast-enhanced perfusion MR imaging.** *Radiology* 2009;253:486–96 CrossRef Medline
7. Hu LS, Baxter LC, Smith KA, et al. **Relative cerebral blood volume values to differentiate high-grade glioma recurrence from posttreatment radiation effect: direct correlation between image-guided tissue histopathology and localized dynamic susceptibility-weighted contrast-enhanced perfusion MR imaging measurements.** *AJNR Am J Neuroradiol* 2009;30:552–58 CrossRef Medline
8. Danchavijitr N, Waldman AD, Tozer DJ, et al. **Low-grade gliomas: do changes in rCBV measurements at longitudinal perfusion-weighted MR imaging predict malignant transformation?** *Radiology* 2008;247:170–78 CrossRef Medline
9. Rossi Espagnet MC, Romano A, Mancuso V, et al. **Multiparametric evaluation of low grade gliomas at follow-up: comparison between diffusion and perfusion MR with <sup>18</sup>F-FDOPA PET.** *Br J Radiol* 2016;89:20160476 CrossRef Medline
10. Boxerman JL, Rosen BR, Weisskoff RM. **Signal-to-noise analysis of cerebral blood volume maps from dynamic NMR imaging studies.** *J Magn Reson Imaging* 1997;7:528–37 CrossRef Medline

11. Welker K, Boxerman J, Kalnin A, et al; American Society of Functional Neuroradiology MR Perfusion Standards and Practice Subcommittee of the ASFNR Clinical Practice Committee. **ASFNR recommendations for clinical performance of MR dynamic susceptibility contrast perfusion imaging of the brain.** *AJNR Am J Neuroradiol* 2015;36:E41–51 [CrossRef Medline](#)
12. Willats L, Calamante F. **The 39 steps: evading error and deciphering the secrets for accurate dynamic susceptibility contrast MRI.** *NMR Biomed* 2013;26:913–31 [CrossRef Medline](#)
13. Thilmann O, Larsson EM, Björkman-Burtscher I, et al. **Effects of echo time variation on perfusion assessment using dynamic susceptibility contrast MR imaging at 3 Tesla.** *Magn Reson Imaging* 2004;22:929–35 [CrossRef Medline](#)
14. Jochimsen TH, Newbould RD, Skare ST, et al. **Identifying systematic errors in quantitative dynamic-susceptibility contrast perfusion imaging by high-resolution multi-echo parallel EPI.** *NMR Biomed* 2007;20:429–38 [CrossRef Medline](#)
15. Woolrich MW, Jbabdi S, Patenaude B, et al. **Bayesian analysis of neuroimaging data in FSL.** *Neuroimage* 2009;45:S173–86 [CrossRef Medline](#)
16. Schmainda KM, Paulson ES, Prah DE, inventors; Imaging Biometrics Llc, assignee. Multiparameter perfusion imaging with leakage correction. US patent 8670602. May 22, 2007
17. Newton AT, Skinner JT, Quarles CC. **Automatic AIF estimation in multi-echo DSC-MRI of pediatric patients: avoiding the noise floor.** In: *Proceedings of the International Society for Magnetic Resonance in Medicine*, Salt Lake City, Utah. April 20–26, 2013;21
18. Mouridsen K, Christensen S, Gyldensted L, et al. **Automatic selection of arterial input function using cluster analysis.** *Magn Reson Med* 2006;55:524–31 [CrossRef Medline](#)
19. Semmineh NB, Xu J, Skinner JT, et al. **Assessing tumor cytoarchitecture using multiecho DSC-MRI derived measures of the transverse relaxivity at tracer equilibrium (TRATE).** *Magn Reson Med* 2015;74:772–84 [CrossRef Medline](#)
20. Newbould RD, Skare ST, Jochimsen TH, et al. **Perfusion mapping with multiecho multishot parallel imaging EPI.** *Magn Reson Med* 2007;58:70–81 [CrossRef Medline](#)
21. Stokes AM, Quarles CC. **A simplified spin and gradient echo approach for brain tumor perfusion imaging.** *Magn Reson Med*. 2016; 75:356–62 [CrossRef Medline](#)
22. Weinmann HJ, Bauer H, Ebert W, et al. **Comparative studies on the efficacy of MRI contrast agents in MRA.** *Acad Radiol* 2002;9:S135–36 [CrossRef Medline](#)
23. Pintaske J, Martirosian P, Graf H, et al. **Relaxivity of gadopentetate dimeglumine (Magnevist), gadobutrol (Gadovist), and gadobenate dimeglumine (MultiHance) in human blood plasma at 0.2, 1.5, and 3 Tesla.** *Invest Radiol* 2006;41:213–21 [CrossRef Medline](#)

# Identification and Quantitative Assessment of Different Components of Intracranial Atherosclerotic Plaque by Ex Vivo 3T High-Resolution Multicontrast MRI

Y. Jiang, W. Peng, B. Tian, C. Zhu, L. Chen, X. Wang, Q. Liu, Y. Wang, Z. Xiang, A.J. Degnan, Z. Teng, D. Saloner, and J. Lu



## ABSTRACT

**BACKGROUND AND PURPOSE:** High-resolution 3T MR imaging can visualize intracranial atherosclerotic plaque. However, histologic validation is still lacking. This study aimed to evaluate the ability of 3T MR imaging to identify and quantitatively assess intracranial atherosclerotic plaque components ex vivo with histologic validation.

**MATERIALS AND METHODS:** Fifty-three intracranial arterial specimens with atherosclerotic plaques from 20 cadavers were imaged by 3T MR imaging with T1, T2, and proton-density-weighted FSE and STIR sequences. The signal characteristics and areas of fibrous cap, lipid core, calcification, fibrous tissue, and healthy vessel wall were recorded on MR images and compared with histology. Fibrous cap thickness and maximum wall thickness were also quantified. The percentage of areas of the main plaque components, the ratio of fibrous cap thickness to maximum wall thickness, and plaque burden were calculated and compared.

**RESULTS:** The signal intensity of the lipid core was significantly lower than that of the fibrous cap on T2-weighted, proton-density, and STIR sequences ( $P < .01$ ) and was comparable on T1-weighted sequences ( $P = 1.00$ ). Optimal contrast between the lipid core and fibrous cap was found on T2-weighted images. Plaque component mean percentages were comparable between MR imaging and histology: fibrous component ( $81.86\% \pm 10.59\%$  versus  $81.87\% \pm 11.59\%$ ,  $P = .999$ ), lipid core ( $19.51\% \pm 10.76\%$  versus  $19.86\% \pm 11.56\%$ ,  $P = .863$ ), and fibrous cap ( $31.10\% \pm 11.28\%$  versus  $30.83\% \pm 8.51\%$ ,  $P = .463$ ). However, MR imaging overestimated mean calcification ( $9.68\% \pm 5.21\%$  versus  $8.83\% \pm 5.67\%$ ,  $P = .030$ ) and plaque burden ( $65.18\% \pm 9.01\%$  versus  $52.71\% \pm 14.58\%$ ,  $P < .001$ ).

**CONCLUSIONS:** Ex vivo 3T MR imaging can accurately identify and quantitatively assess intracranial atherosclerotic plaque components, providing a direct reference for in vivo intracranial plaque imaging.

**ABBREVIATIONS:** ICC = intraclass correlation coefficient; PD = proton-density

Intracranial atherosclerotic disease is one of the most common causes of stroke.<sup>1</sup> It has a high prevalence in the Asian popula-

tion<sup>2</sup> with a high recurrence rate.<sup>3</sup> Due to its high morbidity and mortality, early diagnosis and prognostic evaluation are particularly important. High-resolution vessel wall MR imaging is a promising noninvasive method to evaluate intracranial plaque in vivo, with excellent soft-tissue contrast.<sup>4</sup> In recent years, a few studies have attempted to characterize intracranial atherosclerotic plaque composition by in vivo MR imaging.<sup>5-9</sup> Intracranial plaque imaging with MR imaging has identified high-risk plaque correlated with infarct territory and plaque associated with stroke recurrence.<sup>10-13</sup> However, these studies have mostly focused on plaque enhancement to ascertain plaque risk. Moreover, the determination of plaque composition in other studies has been based on the MR imaging characteristics of extracranial carotid plaque, while direct histologic validation of in vivo MR imaging of

Received March 10, 2016; accepted after revision April 23, 2017.

From the Department of Radiology (Y.J.), Wuhan General Hospital of the People's Liberation Army, Wuhan, China; Departments of Radiology (Y.J., W.P., B.T., L.C., X.W., Q.L., J.L.) and Pathology (Y.W., Z.X.), Changhai Hospital, Shanghai, China; Department of Radiology and Biomedical Imaging (C.Z., D.S.), University of California, San Francisco, San Francisco, California; Department of Radiology (A.J.D.), University of Pittsburgh Medical Center, Pittsburgh, Pennsylvania; and Department of Radiology (Z.T.), University of Cambridge, Cambridge, UK.

Y. Jiang, W. Peng, and B. Tian contributed equally to this work.

This work was supported by the Twelfth Five-Year Plan Medical Key Project of the People's Liberation Army, China (BWS12J026); Shanghai Hospital Development Center grant (SHDC12013110); the National Nature Science Foundation of China (NSFC31470910, NSFC81270413); and the National Institutes of Health grants R01HL114118 and R01NS059944.

Please address correspondence to Jianping Lu, MD, Department of Radiology, Changhai Hospital of Shanghai, 168 Changhai Rd, Shanghai, China, 20043; e-mail: cjr.lujianping@vip.163.com; and Chengcheng Zhu, PhD, Department of Radiology and Biomedical Imaging, University of California, San Francisco, Room BA34, VA Medical Center, 4150 Clement St, San Francisco, CA 94121; e-mail: Chengcheng.Zhu@ucsf.edu

Indicates open access to non-subscribers at [www.ajnr.org](http://www.ajnr.org)

Indicates article with supplemental on-line tables.

Indicates article with supplemental on-line photos.

<http://dx.doi.org/10.3174/ajnr.A5266>

intracranial plaque is still lacking, except for 1 individual case study.<sup>14</sup>

Ex vivo MR imaging of intracranial atherosclerotic plaque specimens provides a way to understand intracranial plaque. A few studies have reported ex vivo MR imaging characteristics of intracranial plaque with 7T research scanners.<sup>15-17</sup> However, these results cannot be transferred to 3T for the clinical evaluation of intracranial arterial disease because the MR relaxometry is different at 3T and 7T. Very few studies have reported intracranial plaque characteristics at 3T, the highest field strength that is clinically relevant.<sup>14,18</sup> Thus, there is an urgent need to investigate whether clinical 3T scanners provide sufficient contrast for the evaluation of intracranial plaque composition. In addition, most of these 7T studies focused on the qualitative classification of plaque components and lacked quantitative assessment of high-risk plaque features, including the lipid core area, fibrous cap thickness, and plaque burden, all of which play an important role in atherosclerotic plaque progression and rupture.<sup>19,20</sup>

The purpose of this study was to report the signal characteristics of plaque components on multicontrast MR imaging at 3T and evaluate the ability of MR imaging to quantify plaque components with histologic validation.

## **MATERIALS AND METHODS**

### **Study Population**

The study was approved by our hospital ethics committee, and informed consent was obtained from the patients' relatives. Patients 45 years of age or older who underwent a postmortem examination in our hospital (Changhai Hospital) from January 2013 to June 2015 were recruited for the study. Among 120 cadavers, 20 with possible atherosclerotic specimens of the circle of Willis were selected on the basis of macroscopic examination by a pathologist during the postmortem examination. The time between death and the postmortem examination was <1 month; however, the exact time window was unknown due to the limitations of our local ethics committee. The same specimens were evaluated in a previous study<sup>18</sup>; however, the current study addresses distinctly different research questions, specifically performing a quantitative analysis of the identification of plaque components on multicontrast imaging. The demographics of the cadavers were reported in the previous publication.<sup>18</sup> All specimens were rinsed carefully with saline to remove blood clots. The same pathologist excised possible atherosclerotic arteries according to gross morphologic changes. All excised arteries were then stored at 4°C. The time between the postmortem examination and imaging was <24 hours. Photographs of gross specimens of the circle of Willis are shown in On-line Fig 1.

### **MR Imaging Protocol**

MR imaging was undertaken in a 3T whole-body system (Magnetom Skyra; Siemens, Erlangen, Germany) with a loop coil (4 cm in diameter). Before imaging, arteries were embedded in Fomblin (Solvey Solexis, Milan, Italy), which is a fluorinated fluid with no MR signal. Careful flushing of the lumen and outer surfaces of specimens was performed to ensure that gas bubbles were removed. The experimental setup is shown in On-line Fig 2. Multiple imaging sequences, including T1, T2, and proton-density

(PD) weighted FSE and STIR were acquired perpendicular to the longitudinal axis of the arterial segments. The scanning parameters were identical to those in a previous study.<sup>18</sup>

### **Histology**

The specimens were fixed for 24 hours in formal saline (10% formalin in 0.9% sodium chloride) following imaging. After decalcification, samples were cut into sections between 4 and 5 mm in length and numbered to assist the coregistration. Each section was then sliced at a 5- $\mu$ m thickness with an interval of 0.5 mm. Specimens were stained with hematoxylin-eosin and Masson trichrome to visualize arterial architecture, including atherosclerotic components. The histology sections were digitized with a digital microscope at 20 $\times$  magnification (BX53 microscope; Olympus, Tokyo, Japan).

Five experienced radiologists were involved in the image analysis: coregistration of MR imaging and histology (Y.J.), measurement of signal intensities (B.T.), classification of plaque components (W.P.), and measurement and quantification of plaque component area/thickness (Q.L. and X.W.).

### **Image Coregistration**

An experienced radiologist (Y.J.) matched the MR imaging sections and histologic sections carefully according to location. The gross morphologic features, such as vessel size and shape, plaque configuration, and specific plaque components (eg, calcification), were considered during the coregistration.

### **Image Analysis**

Image analysis was performed in 2 steps. First, the signal intensity of plaque components on MR images was quantified with histology as a reference for plaque component categorization. Second, images containing advanced lesion types were selected for plaque component area quantification.

### **Analysis of Signal Intensities of Plaque Components**

One experienced pathologist identified and segmented the main components of the plaque in every matched histologic section, including intraplaque hemorrhage, fibrous cap, lipid core, calcification, fibrous tissue (ie, smooth-muscle cell and dense collagen not including fibrous cap or healthy vessel wall), and healthy vessel wall according to the American Heart Association classification,<sup>21</sup> as well as judging the lesion types—types I–II: initial lesion with foam cells or fatty streaks with multiple foam cell layers; type III: atheroma with extracellular lipid pools; types IV–V: plaque with a fibrous cap and lipid core; type VI: complex plaque with a surface defect, hemorrhage, or thrombus; type VII: calcified plaque; and type VIII: fibrotic plaque without a lipid core.<sup>22</sup> According to the histologic results, a radiologist (B.T.) segmented plaque components on corresponding T2-weighted images with CMRtools (Cardiovascular Imaging Solutions, London, UK), and the contours on T2-weighted images were copied to the same anatomic sections of other MR images. This process allowed quantification of the signal intensity of plaque components. Because only a single segment of the vessel was imaged in our study, the signal of the healthy vessel wall that did not include any atheroma (mostly media) was used as a reference. A second radiolo-

**Table 1: The criteria for plaque component identification by multicontrast MRI**

	Lipid Core	Fibrous Cap	Calcification
T1	Isointense/hyperintense	Isointense	Hypointense
T2	Isointense/hypointense	Isointense/hyperintense	Hypointense
PD	Isointense/hypointense	Isointense/hyperintense	Hypointense
STIR	Hypointense	Hyperintense	Hypointense

gist (W.P.), blinded to histology results, identified the main plaque components on the basis of a criterion developed in prior histology–MR imaging comparative analysis (Table 1).

### Quantification of Plaque Component Area

Sections containing advanced lesion types (types IV–VII) were included in the area analysis. Histologic sections were segmented and measured with ImageJ software (Version 1.47; National Institutes of Health, Bethesda, Maryland) by a pathologist blinded to MR imaging results. The lumen, vessel wall, and each plaque component were contoured, and the areas were recorded. We calculated the following metrics: vessel wall area (Vessel Wall Area = Total Vessel Area – Lumen Area); fibrous component area (ie, smooth-muscle cells and dense collagen including the fibrous cap and healthy wall) (Fibrous Component Area = Vessel Wall Area – Other Component Area); the percentage of the area of each major plaque component (% Plaque Component = Specific Component Area / Vessel Wall Area × 100%); and plaque burden (Plaque Burden = Vessel Wall Area / Total Vessel Area × 100%).<sup>23</sup> Both the fibrous cap thickness and the maximum wall thickness were also measured on sections containing a lipid core. Because of shrinkage during histologic processing,<sup>24</sup> the percentage of the plaque component area/thickness in addition to absolute area/thickness was used for histology-imaging comparison. Two radiologists (Q.L. and X.W.) segmented the components on MR imaging and measured the area/thickness blinded to histology results. One of the radiologists (X.W.) repeated the measurements 1 month later.

### Statistics

Statistical analysis was performed in SPSS (Version 21.0; IBM, Armonk, New York). Normality assumptions were assessed by using a Shapiro-Wilk test. Categorical data were presented as counts, and continuous variables were presented as mean ± SD or median (interquartile range). Considering that multiple measurements were obtained from each subject, a linear mixed-effects model was used to assess the differences among the signal intensities of different components and the differences between histology measurements and MR imaging measurements. The Cohen  $\kappa$  with 95% CIs was used to estimate the agreement of plaque component identification on MR imaging compared with histology. To evaluate the agreement of measurements between MR imaging and histology and intraobserver/interobserver reproducibility of MR imaging measurements, we calculated the intraclass correlation coefficient (ICC) with 95% CIs. A  $P$  value < .05 was considered significant. All  $P$  values were 2-sided.

## RESULTS

Fifty-three intracranial arterial sections (1–7 arterial sections from each specimen) from 20 subjects with atherosclerotic plaques were excised; 207 sections with matched MR imaging and

histology were included in the analysis. The details of specimens and plaque types were reported in the previous publication.<sup>18</sup>

### Signal Intensity Characteristics

Representative multicontrast MR images of the specimens and their corresponding histologic sections are shown in Figs 1 and 2. MR imaging characteristics of the main plaque components are shown in Table 1. Signal intensities of plaque components on multiple MR images are summarized in On-line Table 1. Overall, there were significant differences among signal intensities of different plaque components on multiple sequences ( $P < .05$ ). The best contrast between lipid core and fibrous cap assessment was achieved with T2-weighted images. Post hoc pair-wise tests showed that the signal intensity of the lipid core was significantly lower than that of the fibrous cap on T2-weighted, PD, and STIR sequences ( $P < .01$ ) and was not significantly different on T1-weighted imaging ( $P = 1.00$ ). The signal intensities of the fibrous cap, fibrous tissue, and healthy wall were similar on all sequences ( $P > .05$ ). Lipid core and healthy wall had similar signal intensities on all sequences. Calcification showed the lowest signal intensity on T2-weighted, PD, and T1-weighted sequences ( $P < .001$ ). Pair-wise test results of the signal intensity of each 2 components are provided in On-line Table 2.

### Utility of MR Imaging for Plaque Component Characterization

The sensitivity and specificity were 90.53% and 69.64% for identifying fibrous cap and lipid core and 83.33% and 100% for calcification on a combination of weightings. Cohen  $\kappa$  values were 0.59 for the fibrous cap and lipid core and 0.90 for calcification.

### Quantitative Analysis

Only sections containing  $\geq 2$  components (types IV–V or VII) were selected for quantitative analysis. Fifty-seven sections were used for further analysis (Figs 1 and 2). The agreement between manual measurements performed on MR images and histology sections is shown in On-line Table 3. The absolute values were larger on MR imaging compared with histology, likely due to the shrinkage of the specimen during the histologic processing. Good-to-excellent correlation was observed ( $r = 0.72$ – $0.93$ , ICC = 0.69–0.85), but fibrous cap thickness measurements had only a moderate correlation ( $r = 0.50$ , ICC = 0.46). Table 2 shows the comparison between MR imaging and histology for the percentages of areas and thicknesses. Generally, there was good-to-excellent agreement ( $r = 0.86$ – $0.93$ , ICC = 0.77–0.93), except that the agreement of the percentage of the fibrous cap was moderate ( $r = 0.44$ , ICC = 0.42). The percentages of plaque component areas and thicknesses were comparable between MR imaging and histology, but MR imaging significantly overestimated calcification ( $9.68\% \pm 5.21\%$  versus  $8.83\% \pm 5.67\%$ ,  $P = .030$ ) and plaque burden ( $65.18\% \pm 9.01\%$  versus  $52.71\% \pm 14.58\%$ ,  $P < .001$ ).

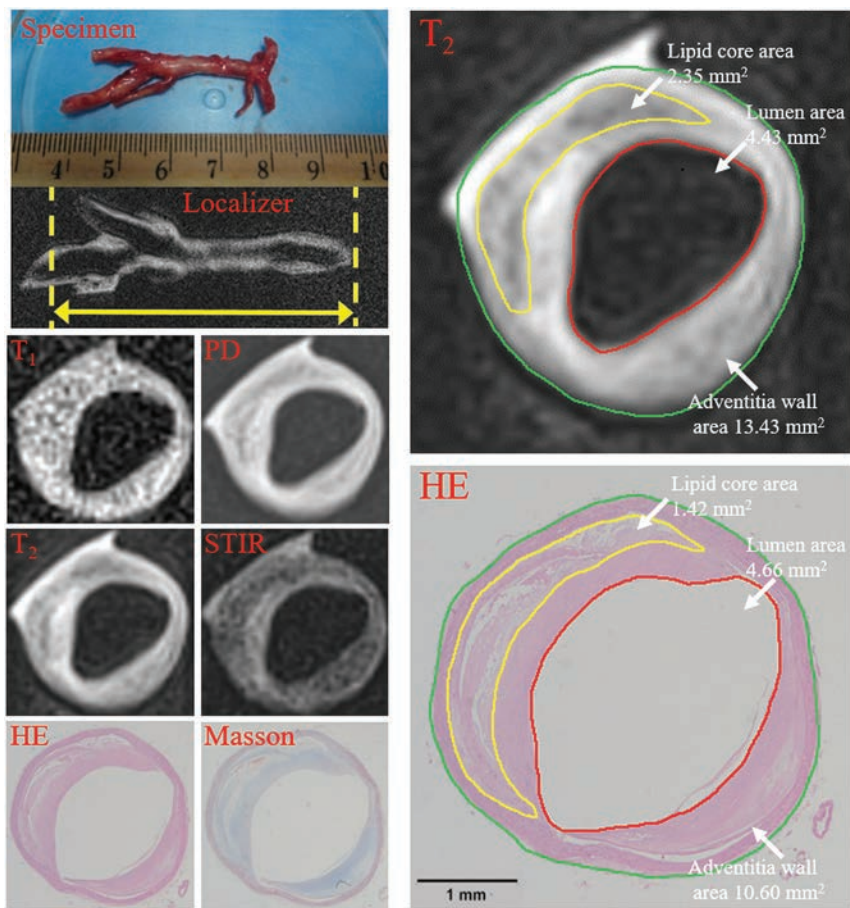


**FIG 1.** A basilar artery plaque with a thick fibrous cap and a large lipid core (type IV–V) was identified on multicontrast MR imaging and matched histology (20 $\times$  magnification). Contours have been drawn for the lumen (red), vessel wall (green), and lipid core (yellow) on a T<sub>2</sub>-weighted image and hematoxylin-eosin-stained section. The lumen, total vessel, and lipid core areas were 4.34, 13.43, and 2.35 mm<sup>2</sup> and 4.66, 10.60, and 1.42 mm<sup>2</sup> for MR imaging and histology. The vessel wall areas calculated by total vessel area minus lumen area were 9.09 and 6.00 mm<sup>2</sup>. The fibrous component areas calculated by vessel wall area minus lipid core area were 6.70 and 4.56 mm<sup>2</sup>. The percentages of plaque components (Specific Component Area / Vessel Wall Area  $\times$  100%) were 25.85% versus 23.63% for the lipid core and 74.15% versus 76.37% for fibrous tissue. Plaque burden (Vessel Wall Area / Total Vessel Area  $\times$  100%) was 67.68% versus 56.24%.

### Reproducibility of Quantitative MR Imaging Measurements

Both intraobserver and interobserver reproducibility were good to excellent for the percentage of plaque component areas and thicknesses as well as plaque burden (ICC = 0.779–0.985). Detailed measurements and analysis are shown in On-line Tables 4 and 5.

### DISCUSSION

To our knowledge, this is the first study to assess intracranial atherosclerotic plaque characteristics quantitatively with 3T MR imaging with histologic validation. Our results confirm that 3T high-resolution multicontrast MR imaging can provide sufficient contrast to discriminate and quantitatively assess intracranial atherosclerotic plaque components ex vivo; this discrimination provides a reference for in vivo intracranial plaque imaging.

The ability of multicontrast MR imaging to ascertain the composition of extracranial carotid plaque has been extensively studied and validated against histology, with several of these plaque features correlated to increased risk of stroke.<sup>25</sup> Histologic valida-

tion of intracranial plaque imaging, however, is still very limited, mostly due to the challenge of collecting postmortem specimens. Only a few histology validation studies have been undertaken at 7T.<sup>15–17</sup> The scan parameters of multicontrast MR imaging in this study were close to those in standard protocols used in clinical in vivo studies at 3T, except that this study used higher resolution settings.<sup>9,26</sup> Therefore, the criteria established in this study (Table 1) could be used when assessing images obtained in vivo.

Prior studies have demonstrated that intracranial plaque burden, lipid core area, and fibrous cap thickness are closely related to plaque vulnerability.<sup>9,20,27</sup> Teng et al<sup>9</sup> found that culprit lesions (ie, lesions in patients with clinical symptoms arising on the side referable to the location of an ischemic stroke on neuroimaging) had greater plaque burden compared with nonculprit lesions in the MCA. In a postmortem study of MCA atherosclerosis, plaques containing >40% lipid area were more often associated with cerebral infarct.<sup>27</sup> We found that our ex vivo high-resolution protocol can reliably quantify lipid core area but overestimated overall plaque burden. This finding may be attributed to tissue shrinkage and distortion during histologic processing, which are difficult to account for in our analysis.<sup>24</sup> Moreover, the accuracy in characterizing fibrous cap thickness was marginal. This finding may be attributed to

the thin fibrous cap seen in most intracranial atherosclerotic plaques, which differs from that in carotid atherosclerotic disease. Therefore, it would be more challenging for in vivo imaging protocols (typically with a resolution of 0.4  $\times$  0.4  $\times$  2 mm<sup>3</sup> for 2D imaging)<sup>28</sup> to visualize a thin fibrous cap.

Calcification area was slightly overestimated by MR imaging; this overestimation was similar to previous findings from an in vivo MR imaging study of carotid plaque.<sup>23</sup> This is because due to partial volume averaging, voxels that only partially contain calcification can appear hypointense on MR imaging. In general, due to the short T<sub>2</sub> and T<sub>2</sub>\* of calcium, it is challenging for MR imaging to depict calcifications. Also, histology could possibly underestimate the amount of calcification because specimen processing included decalcification before tissue sectioning.

It has been shown that intraplaque hemorrhage is a high-risk feature in the carotid plaque.<sup>29</sup> However, intraplaque hemorrhage was not present in any of the lesions in this study. The reason could be that plaques obtained in this study were mostly asymptomatic and stable. However, it is also possible that the

mechanism of stroke caused by intracranial arterial plaque is different from that in carotid plaques because it has been reported that there is a lower incidence of intraplaque hemorrhage in intracranial plaques.<sup>8</sup>

Multicontrast MR imaging has been used for plaque composition characterization due to the limitation of 1 single sequence to distinguish all plaque components.<sup>30-33</sup> Our results showed that the fibrous cap yielded higher signal intensities than the lipid core on T2-weighted, PD, and STIR sequences, and calcification showed the lowest signal intensity on T2-weighted, PD, and T1-weighted sequences; these findings are similar to previous

observations in carotid imaging.<sup>30,31</sup> The best contrast and image quality were observed on T2-weighted imaging; thus, the segmentation of the fibrous cap and lipid core was performed on T2-weighted images. Lipid core and fibrous cap were difficult to distinguish on T1-weighted images; this finding agrees with those in previous carotid studies.<sup>31,33</sup> Although the T1 values of the lipid core and fibrous cap might be different,<sup>17</sup> the clinical T1-weighted FSE sequence is known to have reduced T1 contrast because of the long echo train.

Intracranial atherosclerosis is increasingly recognized as an important cause of stroke worldwide. As with carotid atherosclerosis, there is increasing recognition that aggressive (dual) antiplatelet therapy may be warranted and may mitigate the risk of major events such as stroke.

However, aggressive medical management is not without risk; therefore, aggressive medical management for intracranial atherosclerosis should be targeted to the patient population in whom the benefit exceeds the risks (eg, bleeding) associated with antiplatelet therapy. Imaging of intracranial atherosclerosis may serve a role in stratifying patients into groups with differing levels of risk based on the nature and extent of atherosclerotic plaque.<sup>34</sup>

There are some limitations to this study. First, the properties of postmortem intracranial arteries might be different from those in arteries in vivo because of changes in the chemical nature and structure of the arterial wall and plaque components related to processing such as dehydration and protein degradation, which could potentially affect the accuracy of results.<sup>24</sup> Second, the sample size was small ( $n = 20$ ). Specifically, only 57 sections could be used for quantitative assessment, and only 10 sections contained calcification, which may bias the results. Third, MR image thickness (1 mm) and histologic section thickness (5  $\mu\text{m}$ ) did not match, especially for complex plaques in which plaque components may vary over a short distance. Fourth, the various inflammatory components of intracranial atherosclerotic

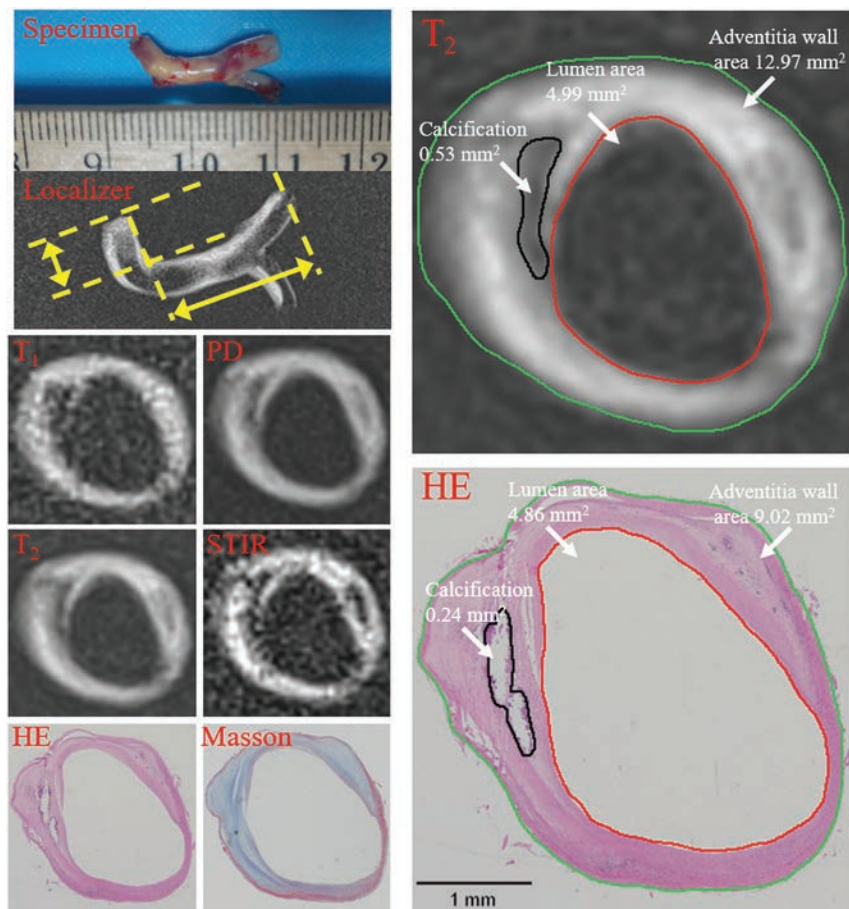


**FIG 2.** Vertebral artery plaque with fibrous tissue and calcification was identified on multicontrast MR imaging and matched histology (20 $\times$  magnification). Contours have been drawn for lumen (red), outer vessel wall (green), and calcification (black) on T2-weighted imaging and a hematoxylin-eosin-stained section. The lumen, total vessel, and calcification areas were 4.99, 12.97, and 0.53 mm<sup>2</sup> on MR imaging and 4.86, 9.02, and 0.24 mm<sup>2</sup> on histology. The vessel wall areas calculated by total vessel area minus lumen area were 7.98 and 4.16 mm<sup>2</sup>. The fibrous component area calculated by vessel wall area minus the calcification area was 7.45 and 3.93 mm<sup>2</sup>. The percentages of components (Specific Component Area / Vessel Wall Area  $\times$  100%) were 6.64% versus 5.73% for calcification and 93.36% versus 94.27% for fibrous tissue. Plaque burden (Vessel Wall Area / Total Vessel Area  $\times$  100%) was 61.52% versus 46.09%.

**Table 2: Comparison of the percentages of areas and thicknesses and overall plaque burden between MRI and histology<sup>a</sup>**

	MRI	Histology	P	r	ICC (95% CI)
Fibrous component area (%)	81.86 $\pm$ 10.59	81.87 $\pm$ 11.59	.997	0.901	0.898 (0.832–0.938)
Lipid core area (%)	19.51 $\pm$ 10.76	19.86 $\pm$ 11.56	.660	0.888	0.885 (0.804–0.934)
Calcification area (%)	9.68 $\pm$ 5.21	8.83 $\pm$ 5.67	.030	0.933	0.930 (0.745–0.982)
Fibrous cap thickness (%)	31.10 $\pm$ 11.28	30.83 $\pm$ 8.51	.890	0.438	0.421 (0.155–0.630)
Plaque burden area (%)	65.18 $\pm$ 9.01	52.71 $\pm$ 14.58	<.001	0.862	0.771 (0.640–0.858)

**Note:**—r indicates the Pearson correlation coefficient.

<sup>a</sup>Results are expressed as mean  $\pm$  SD with P values derived from a linear mixed-effects model.

plaque were not included in the analysis. Future in vivo studies could evaluate the inflammatory components by including contrast-enhanced 3D T1 black-blood imaging.<sup>35</sup> Fifth, sequences with lower resolution as typically used in clinical MR imaging were not evaluated in this study, and future investigation is needed. Also, in this study, no intraplaque hemorrhage was found as previously discussed. Another limitation related to the ex vivo nature of this study is the effect of specimen processing and temperature on plaque size and signal properties. Prior work with carotid atherosclerotic plaque observed small but significant increases in plaque size (4%–7%) and T2 (8 ms) in imaging samples at room temperature compared with body temperature.<sup>24</sup> While many recent ex vivo imaging studies were performed at room temperature,<sup>15–17,36</sup> scanning specimens at room temperature may result in small increases in plaque volume and can nominally prolong the T2 of plaque tissue. These potential small errors in measurement would be expected to occur equally across specimens.

## CONCLUSIONS

In the evaluation of intracranial atherosclerosis on ex vivo specimens, 3T high-resolution multicontrast MR imaging can accurately identify different plaque components and quantitatively measure the relative volumes of those components, providing a direct reference for in vivo intracranial plaque imaging.

Disclosures: Yuanliang Jiang—RELATED: Grant: Twelfth Five-Year Plan Medical Key Project of the People's Liberation Army, China (BWS12J026); Shanghai Hospital Development Center grant (SHDC12013110); the National Nature Science Foundation of China (31470910). \* Wenjia Peng—RELATED: Grant: Twelfth Five-Year Plan Medical Key Project of the People's Liberation Army, China (BWS12J026); Shanghai Hospital Development Center grant (SHDC12013110); the National Nature Science Foundation of China (31470910). \* Chengcheng Zhu—RELATED: Grant: National Institutes of Health grants R01NS059944 and R01HL114118. Qi Liu—RELATED: Grant: Twelfth Five-Year Plan Medical Key Project of the People's Liberation Army, China (BWS12J026), the Emerging Frontier Technology Joint Research Program of Shanghai Municipal Hospital (research grant from Shanghai Hospital Development Center), China (SHDC12013110); and the National Nature Science Foundation of China (31470910). \* Jianping Lu—RELATED: Grant: Twelfth Five-Year Plan Medical Key Project of the People's Liberation Army, China (BWS12J026); Shanghai Hospital Development Center grant (SHDC12013110); the National Nature Science Foundation of China (31470910). \* Money paid to the institution.

## REFERENCES

- Holmstedt CA, Turan TN, Chimowitz MI. **Atherosclerotic intracranial arterial stenosis: risk factors, diagnosis, and treatment.** *Lancet Neurol* 2013;12:1106–14 CrossRef Medline
- Wong KS, Huang YN, Gao S, et al. **Intracranial stenosis in Chinese patients with acute stroke.** *Neurology* 1998;50:812–13 CrossRef Medline
- Kern R, Steinke W, Daffertshofer M, et al. **Stroke recurrences in patients with symptomatic vs asymptomatic middle cerebral artery disease.** *Neurology* 2005;65:859–64 CrossRef Medline
- Bodley JD, Feldmann E, Swartz RH, et al. **High-resolution magnetic resonance imaging: an emerging tool for evaluating intracranial arterial disease.** *Stroke* 2013;44:287–92 CrossRef Medline
- Klein IF, Lavallée PC, Touboul PJ, et al. **In vivo middle cerebral artery plaque imaging by high-resolution MRI.** *Neurology* 2006;67:327–29 CrossRef Medline
- Swartz RH, Bhuta SS, Farb RI, et al. **Intracranial arterial wall imaging using high-resolution 3-Tesla contrast-enhanced MRI.** *Neurology* 2009;72:627–34 CrossRef Medline
- van der Kolk AG, Zwanenburg JJ, Brundel M, et al. **Intracranial vessel wall imaging at 7.0-T MRI.** *Stroke* 2011;42:2478–84 CrossRef Medline
- Xu WH, Li ML, Gao S, et al. **Middle cerebral artery intraplaque hemorrhage: prevalence and clinical relevance.** *Ann Neurol* 2012;71:195–98 CrossRef Medline
- Teng Z, Peng W, Zhan Q, et al. **An assessment on the incremental value of high-resolution magnetic resonance imaging to identify culprit plaques in atherosclerotic disease of the middle cerebral artery.** *Eur Radiol* 2016;26:2206–14 CrossRef Medline
- Skarpathiotakis M, Mandell DM, Swartz RH, et al. **Intracranial atherosclerotic plaque enhancement in patients with ischemic stroke.** *AJNR Am J Neuroradiol* 2013;34:299–304 CrossRef Medline
- Vakil P, Vranic J, Hurley MC, et al. **T1 gadolinium enhancement of intracranial atherosclerotic plaques associated with symptomatic ischemic presentations.** *AJNR Am J Neuroradiol* 2013;34:2252–58 CrossRef Medline
- Qiao Y, Zeiler SR, Mirbagheri S, et al. **Intracranial plaque enhancement in patients with cerebrovascular events on high-spatial-resolution MR images.** *Radiology* 2014;271:534–42 CrossRef Medline
- Kim JM, Jung KH, Sohn CH, et al. **Intracranial plaque enhancement from high resolution vessel wall magnetic resonance imaging predicts stroke recurrence.** *Int J Stroke* 2016;11:171–79 CrossRef Medline
- Turan TN, Rumboldt Z, Granholm AC, et al. **Intracranial atherosclerosis: correlation between in-vivo 3T high resolution MRI and pathology.** *Atherosclerosis* 2014;237:460–63 CrossRef Medline
- Majidi S, Sein J, Watanabe M, et al. **Intracranial-derived atherosclerosis assessment: an in vitro comparison between virtual histology by intravascular ultrasonography, 7T MRI, and histopathologic findings.** *AJNR Am J Neuroradiol* 2013;34:2259–64 CrossRef Medline
- van der Kolk AG, Zwanenburg JJ, Denswil NP, et al. **Imaging the intracranial atherosclerotic vessel wall using 7T MRI: initial comparison with histopathology.** *AJNR Am J Neuroradiol* 2015;36:694–701 CrossRef Medline
- Harteveld AA, Denswil NP, Siero JC, et al. **Quantitative intracranial atherosclerotic plaque characterization at 7T MRI: an ex vivo study with histologic validation.** *AJNR Am J Neuroradiol* 2016;37:802–10 CrossRef Medline
- Jiang Y, Zhu C, Peng W, et al. **Ex-vivo imaging and plaque type classification of intracranial atherosclerotic plaque using high resolution MRI.** *Atherosclerosis* 2016;249:10–16 CrossRef Medline
- Naghavi M, Libby P, Falk E, et al. **From vulnerable plaque to vulnerable patient: a call for new definitions and risk assessment strategies—Part 1.** *Circulation* 2003;108:1664–72 CrossRef Medline
- Ravn HB, Falk E. **Histopathology of plaque rupture.** *Cardiol Clin* 1999;17:263–70, vii Medline
- Stary HC, Chandler AB, Dinsmore RE, et al. **A definition of advanced types of atherosclerotic lesions and a histological classification of atherosclerosis: a report from the Committee on Vascular Lesions of the Council on Arteriosclerosis, American Heart Association.** *Arterioscler Thromb Vasc Biol* 1995;15:1512–31 CrossRef Medline
- Cai JM, Hatsukami TS, Ferguson MS, et al. **Classification of human carotid atherosclerotic lesions with in vivo multicontrast magnetic resonance imaging.** *Circulation* 2002;106:1368–73 CrossRef Medline
- Saam T, Ferguson MS, Yarnykh VL, et al. **Quantitative evaluation of carotid plaque composition by in vivo MRI.** *Arterioscler Thromb Vasc Biol* 2005;25:234–39 Medline
- Dalager-Pedersen S, Falk E, Ringgaard S, et al. **Effects of temperature and histopathologic preparation on the size and morphology of atherosclerotic carotid arteries as imaged by MRI.** *J Magn Reson Imaging* 1999;10:876–85 CrossRef Medline
- Gupta A, Baradaran H, Schweitzer AD, et al. **Carotid plaque MRI and stroke risk: a systematic review and meta-analysis.** *Stroke* 2013;44:3071–77 CrossRef Medline
- Zhang X, Zhu C, Peng W, et al. **Scan-rescan reproducibility of high resolution magnetic resonance imaging of atherosclerotic plaque in the middle cerebral artery.** *PLoS One* 2015;10:e0134913 CrossRef Medline

27. Chen XY, Wong KS, Lam WW, et al. **Middle cerebral artery atherosclerosis: histological comparison between plaques associated with and not associated with infarct in a postmortem study.** *Cerebrovasc Dis* 2008;25:74–80 Medline
28. Dieleman N, van der Kolk AG, Zwanenburg JJ, et al. **Imaging intracranial vessel wall pathology with magnetic resonance imaging: current prospects and future directions.** *Circulation* 2014;130:192–201 CrossRef Medline
29. Saam T, Hetterich H, Hoffmann V, et al. **Meta-analysis and systematic review of the predictive value of carotid plaque hemorrhage on cerebrovascular events by magnetic resonance imaging.** *J Am Coll Cardiol* 2013;62:1081–91 CrossRef Medline
30. Clarke SE, Hammond RR, Mitchell JR, et al. **Quantitative assessment of carotid plaque composition using multicontrast MRI and registered histology.** *Magn Reson Med* 2003;50:1199–208 CrossRef Medline
31. Fabiano S, Mancino S, Stefanini M, et al. **High-resolution multicontrast weighted MR imaging from human carotid endarterectomy specimens to assess carotid plaque components.** *Eur Radiol* 2008;18:2912–21 CrossRef Medline
32. Shinnar M, Fallon JT, Wehrli S, et al. **The diagnostic accuracy of ex vivo MRI for human atherosclerotic plaque characterization.** *Arterioscler Thromb Vasc Biol* 1999;19:2756–61 CrossRef Medline
33. Yuan C, Mitsumori LM, Ferguson MS, et al. **In vivo accuracy of multispectral magnetic resonance imaging for identifying lipid-rich necrotic cores and intraplaque hemorrhage in advanced human carotid plaques.** *Circulation* 2001;104:2051–56 CrossRef Medline
34. van den Wijngaard IR, Holswilder G, van Walderveen MA, et al. **Treatment and imaging of intracranial atherosclerotic stenosis: current perspectives and future directions.** *Brain Behav* 2016;6:e00536 CrossRef Medline
35. Zhu C, Haraldsson H, Tian B, et al. **High resolution imaging of the intracranial vessel wall at 3 and 7 T using 3D fast spin echo MRI.** *MAGMA* 2016;29:559–70 CrossRef Medline
36. Degnan AJ, Young VE, Tang TY, et al. **Ex vivo study of carotid endarterectomy specimens: quantitative relaxation times within atherosclerotic plaque tissues.** *Magn Reson Imaging* 2012;30:1017–21 CrossRef Medline

# Association between Intracranial Atherosclerotic Calcium Burden and Angiographic Luminal Stenosis Measurements

H. Baradaran, P. Patel, G. Gialdini, A. Giambone, M.P. Lerario, B.B. Navi, J.K. Min, C. Iadecola, H. Kamel, and A. Gupta



## ABSTRACT

**BACKGROUND AND PURPOSE:** Calcification of the intracranial vasculature is an independent risk factor for stroke. The relationship between luminal stenosis and calcium burden in the intracranial circulation is incompletely understood. We evaluated the relationship between atherosclerotic calcification and luminal stenosis in the intracranial ICAs.

**MATERIALS AND METHODS:** Using a prospective stroke registry, we identified patients who had both NCCT and CTA or MRA examinations as part of a diagnostic evaluation for ischemic stroke. We used NCCTs to qualitatively (modified Woodcock Visual Score) and quantitatively (Agatston-Janowitz Calcium Score) measure ICA calcium burden and used angiography to measure arterial stenosis. We calculated correlation coefficients between the degree of narrowing and calcium burden measures.

**RESULTS:** In 470 unique carotid arteries (235 patients), 372 (79.1%) had atherosclerotic calcification detectable on CT compared with 160 (34%) with measurable arterial stenosis on CTA or MRA ( $P < .001$ ). We found a weak linear correlation between qualitative ( $R = 0.48$ ) and quantitative ( $R = 0.42$ ) measures of calcium burden and the degree of luminal stenosis ( $P < .001$  for both). Of 310 ICAs with 0% luminal stenosis, 216 (69.7%) had measurable calcium scores.

**CONCLUSIONS:** There is a weak correlation between intracranial atherosclerotic calcium scores and luminal narrowing, which may be explained by the greater sensitivity of CT than angiography in detecting the presence of measurable atherosclerotic disease. Future studies are warranted to evaluate the relationship between stenosis and calcium burden in predicting stroke risk.

**ABBREVIATIONS:** WASID = warfarin-aspirin symptomatic intracranial disease; MWVS = Modified Woodcock Visual Score; AJ-130 = Agatston-Janowitz 130

Intracranial atherosclerotic disease is one of the most common causes of stroke worldwide.<sup>1</sup> Although commonly seen in Asian and African populations, intracranial atherosclerotic disease is also highly prevalent and occurs in over 80% of older, white populations as well.<sup>2</sup> The most well-recognized biomarker to assess for future ischemic stroke risk attributable to intracranial atherosclerosis is the degree of luminal stenosis as measured on angiography.<sup>3,4</sup> Although the composition of intracranial atherosclerotic plaque has largely

been ignored in favor of luminal stenosis measurements,<sup>5</sup> the Rotterdam Study, a large prospective population-based cohort, demonstrated that intracranial carotid artery wall calcification as detected on NCCT is an independent risk factor for incident stroke.<sup>6</sup> Such data are consistent with the large body of literature showing that coronary calcium scores are a marker for the severity of coronary artery disease and a predictor of future myocardial infarction.<sup>7,8</sup>

Although both intracranial arterial stenosis and calcification are signs of atherosclerosis, the relationship between calcium burden and stenosis is incompletely understood.<sup>9</sup> For CT calcium scoring of the intracranial ICA to be a more useful tool in stroke risk prediction, it is necessary to improve our understanding of the relationship between atherosclerotic calcification and the degree of arterial narrowing. Therefore, the purpose of this study was to evaluate the relationship between calcium burden and luminal stenosis in the intracranial ICA in patients presenting with ischemic stroke.

## MATERIALS AND METHODS

### Patient Selection

Patients with acute ischemic stroke admitted to New York Presbyterian Hospital/Weill Cornell Medical College in 2013 were

Received January 11, 2017; accepted after revision April 13.

From the Departments of Radiology (H.B., P.P., A. Gupta), Healthcare Policy and Research (A. Giambone), and Neurology (M.P.L., B.B.N., C.I., H.K.), Clinical and Translational Neuroscience Unit, Feil Family Brain and Mind Research Institute (H.B., G.G., M.P.L., B.B.N., C.I., H.K., A. Gupta), and Dalio Institute of Cardiovascular Imaging (J.K.M.), Weill Cornell Medical College, New York, New York.

This work was supported by National Institutes of Health/National Center for Advancing Translational Sciences Grant #KL2TR000458 to Ajay Gupta and National Institutes of Health/National Institute of Neurological Disorders and Stroke Grant # K23NS082367 to Hooman Kamel.

Please address correspondence to Ajay Gupta, MD, 525 East 68th St, Box 141, Starr 8A, New York, NY 10065; e-mail: ajg9004@med.cornell.edu

Indicates open access to non-subscribers at www.ajnr.org

<http://dx.doi.org/10.3174/ajnr.A5310>

prospectively included in the Cornell Acute Stroke Academic Registry (CAESAR). Patients were registered after an attending vascular neurologist confirmed the diagnosis of ischemic stroke. Because we were interested in comparing the degree of intracranial arterial narrowing with arterial calcification, we only included patients who had CTA or MRA examinations and NCCT with 2.5-mm section thickness examinations within 30 days of their admission for stroke. We excluded any patients with complete occlusion of their intracranial ICA and any patients in whom motion degradation precluded interpretation of their images. The institutional review board at Weill Cornell Medical College approved the collection of these data and additionally waived the need for informed consent because all medical information was already obtained for standard clinical purposes.

Trained hospital personnel collected data regarding patient demographics, the NIHSS score on admission, and vascular risk factors including tobacco use, diabetes, hypertension, dyslipidemia, atrial fibrillation, congestive heart failure, coronary heart disease, peripheral vascular disease, and cardiac valvular disease. Using the TOAST classification scheme,<sup>10</sup> 2 neurologists used all available medical records to independently assign a stroke etiology with a third neurologist independently resolving any disagreements.

### **Imaging Technique**

We performed all head CT and CTA studies on one of the CT scanners at our institution: the Optima 660, LightSpeed Xtra, Discovery HD 750, or the LightSpeed Pro (GE Healthcare, Milwaukee, Wisconsin). We performed the CT examinations according to standard protocol for patients with suspected or known acute stroke. Head CT coverage extended from the foramen magnum to the skull vertex, with 22-cm display FOV, by using 120 kVp and with mA of 250–300, and with all images being reconstructed at 2.5-mm axial sections. In patients who had multiple CT studies during their admission, we used the CT performed closest to the time of admission for stroke. We acquired CTA studies in helical scanning mode with coverage extending from the aortic arch to the C1 ring. Studies were collimated at 0.625 mm, with a kVp of 120 and auto-mA with a rotation time of 0.5 seconds. Approximately 90 mL of nonionic iodinated contrast (iohexol; Omnipaque, GE Healthcare) was administered via an 18-gauge peripheral intravenous catheter at 4–5 mL/s by using a power injector and a SmartPrep (GE Healthcare) ROI on the aortic arch.

MRA examinations were performed on either 1.5T or 3T Signa (GE Healthcare) scanners. We performed 3D-TOF acquisitions with an FOV of 20 cm, 1.4-mm section thickness, and a matrix of 320 × 192 and 320 × 224 on 1.5T and 3T, respectively.

### **Degree of Stenosis Measurements**

The degree of intracranial ICA stenosis was measured by using the warfarin-aspirin symptomatic intracranial disease (WASID) method<sup>11</sup> with the following equation:

$$\text{percent stenosis} = [1 - (D_{\text{stenosis}}/D_{\text{normal}})] \times 100$$

where  $D_{\text{stenosis}}$  is the diameter of the artery at the site of the most severe degree of stenosis and  $D_{\text{normal}}$  is the diameter of the prox-

imal normal artery at its widest, nontortuous, normal segment. To maximize the accuracy of stenosis measurements, we used a combination of MIP and axial MRA source images and multiplanar reformations and axial 0.625-mm sections on CTA. The degree of stenosis was calculated for each ICA and categorized as 0% reflecting no detectable stenosis, >0%–29%, 30%–49%, 50%–69%, and 70%–99%. ICAs that were completely occluded were excluded from analysis. For intracranial ICAs without qualitative evidence of any degree of stenosis, we did not perform formal WASID measurements and considered the ICA to have 0% stenosis. To evaluate for the reproducibility of our measurements, a second radiologist independently reassessed WASID stenosis measurements on a subset of 50 intracranial ICAs.

### **Calcium Scoring**

We measured both qualitative and semiautomated quantitative calcium scoring of each ICA separately, beginning just above its exit from the petrous temporal bone up to the level of the terminal ICA bifurcation. We excluded the petrous segment of each ICA because separating arterial wall calcification from the adjacent temporal bone was difficult. Each research imaging study was interpreted by a single radiologist who was blinded to clinical and other imaging data.

### **Qualitative Visual Calcium Scoring**

For qualitative calcium scoring, we used the Modified Woodcock Visual Score (MWVS) scale,<sup>12,13</sup> which uses a 0–3 scoring scale to reflect the severity of calcification on each section of an NCCT. The scoring begins just distal to the petrous temporal bone and ends at the terminal ICA bifurcation. The scoring scale is as follows: 0 indicates no calcification; 1 reflects thin, discontinuous calcification; 2 indicates thin and continuous or thick and discontinuous calcification; and 3 reflects thick, continuous calcification. Separate scores for each right and left ICA were created by summing each axial section. For a reproducibility assessment, another radiologist independently reevaluated a subset of 50 MWVS scores.

### **Semiautomated Quantitative Calcium Scoring**

For quantitative calcium scoring, we used a commercially available program, Smartscore 4.0 software (GE Healthcare), to calculate Agatston-Janowitz 130 (AJ-130) Calcium Scores for each ICA.<sup>14</sup> In the Smartscore 4.0 software, a radiologist used the manual drawing tool to circle the region containing visible calcifications within the ICA on each axial NCCT section. The software identifies calcifications with an HU value >130 and then multiplies the area by an attenuation factor (130–199 HU:1; 200–299 HU:2; 300–399 HU:3; 400+ HU:4) to calculate a calcium score for each section. A second radiologist independently drew ROIs to reassess reproducibility in a subset of 50 AJ-130 measurements.

### **Statistical Analysis**

For comparing the proportions of patients with detectable WASID stenosis with arteries with detectable calcification, we used a McNemar test for correlated proportions. ANOVA was used to assess differences in MWVS and AJ-130 among the degree

**Table 1: Patient demographics**

Characteristic	Overall (%) (N = 235)	Detectable	No Detectable	P Value	Detectable (>0%)	No Detectable (0%)	P Value
		Calcification in Either ICA (%) (n = 200)	Calcification in Either ICA (%) (n = 35)		Stenosis in Either ICA (%) (n = 91)	Stenosis in Either ICA (%) (n = 144)	
Age	71.7 ± 14.5	74.9 ± 12.1	53.2 ± 13.3	<.0001	76.9 ± 10.6	68.4 ± 15.7	<.0001
Female	118 (50.2)	100 (50.0)	18 (51.4)	.88	45 (49.5)	73 (50.7)	.85
Race				.91			.35
White	210 (89.4)	179 (89.5)	31 (88.6)		78 (85.7)	132 (91.7)	
Black	13 (5.5)	11 (5.5)	2 (5.7)		7 (7.7)	6 (4.2)	
Other	12 (5.1)	10 (5.0)	2 (5.7)		6 (6.6)	6 (4.2)	
Atrial fibrillation	46 (19.6)	44 (22.0)	2 (5.7)	.02	20 (22.0)	26 (18.1)	.46
Coronary artery disease	50 (21.3)	47 (23.5)	3 (8.6)	.05	26 (28.6)	24 (16.7)	.03
Carotid artery stenosis	8 (3.4)	8 (4.0)	0 (0)	.61	4 (4.4)	4 (2.8)	.71
Diabetes mellitus	69 (29.4)	64 (32.0)	5 (14.3)	.03	38 (41.8)	31 (21.5)	.001
Hypertension	163 (69.4)	149 (74.5)	14 (40.0)	<.0001	77 (84.6)	86 (59.7)	<.0001
Dyslipidemia	120 (51.1)	113 (56.5)	7 (20.0)	<.0001	57 (62.6)	63 (43.8)	.01
NIHSS score				.16			.39
1	49 (20.9)	37 (18.5)	12 (34.3)		14 (15.4)	35 (24.3)	
2	57 (24.3)	51 (25.5)	6 (17.1)		22 (24.2)	35 (24.3)	
3	36 (15.3)	30 (15.0)	6 (17.1)		15 (16.5)	21 (14.6)	
4	93 (39.6)	82 (41.0)	11 (31.4)		40 (44.0)	53 (36.8)	
Prior stroke	71 (30.2)	66 (33.0)	5 (14.3)	.03	30 (33.0)	41 (28.5)	.46
Peripheral vascular disease	17 (7.2)	15 (7.5)	2 (5.7)	1.00	8 (8.8)	9 (6.3)	.46
Active tobacco use	20 (8.5)	16 (8.0)	4 (11.4)	.51	8 (8.8)	12 (8.3)	.90
IV tPA administered	33 (14.0)	23 (11.5)	10 (28.6)	.01	8 (8.8)	25 (17.4)	.07
Valvular disease	6 (2.6)	6 (3.0)	0 (0)	.60	2 (2.2)	4 (2.8)	1.00

of WASID stenosis. Pearson correlation coefficients were used to determine the linear relationship between AJ-130 and WASID stenosis, between MWVS and WASID stenosis, and between right and left arteries for MWVS, AJ-130, and WASID stenosis. Histograms were used to plot the distribution of AJ-130, MWVS, and WASID stenosis across all arteries. Interobserver agreement was assessed with a  $\kappa$  coefficient and 95% CI for MWVS and WASID stenosis and an intraclass correlation coefficient and 95% CI for AJ-130. All *P* values were 2-sided and evaluated at the .05  $\alpha$  level. All analyses were performed in SAS v9.3 (SAS Institute, Cary, North Carolina).

## RESULTS

### Patient Characteristics

Of the 335 patients from CAESAR in 2013, we excluded 56 patients because they did not have either an MRA or CTA examination, 34 patients because they did not have a 2.5-mm NCCT of the head, 7 patients because their intracranial ICAs were completely occluded, and 3 patients because motion degradation rendered their CT or MRA/CTA uninterpretable. Of the 235 patients included in our study, the mean age was 71.7 years (Table 1). We made WASID stenosis measurements on CTA for 84 patients and on MRA for 151 patients. Compared with patients without calcification in their intracranial ICA, patients who had detectable ICA calcification were significantly older and had a significantly higher prevalence of diabetes mellitus, hypertension, dyslipidemia, atrial fibrillation, and history of prior stroke. Patients with detectable (nonzero) stenosis of either intracranial ICA were more likely to be older and have hypertension, dyslipidemia, and coronary artery disease. Among 470 ICAs studied, 372 (79.1%) arteries demonstrated atherosclerotic calcification detectable on NCCT, whereas 160 (34%) arteries demonstrated stenosis detectable on CTA or MRA (*P* < .0001).

There was a wide range of calcium scores and degree of WASID stenosis in our cohort, with most plaques causing <50% luminal stenosis (Fig 1, Table 2). There were 310 intracranial ICAs with no detectable WASID stenosis (0% stenosis). Of these 310 ICAs without detectable intracranial stenosis, 216 (69.7%) arteries had measurable calcium scores, which varied widely in magnitude (Fig 2). Conversely, only 4% of patients with no detectable calcium had measurable WASID stenosis (Fig 3). A total of 156/470 arteries (33.2%) had neither detectable ICA stenosis nor detectable ICA calcification.

Measures of reproducibility demonstrated a  $\kappa$  coefficient of 0.89 (95% CI, 0.78–0.99) for the MWVS and 0.85 (95% CI, 0.72–0.98) for WASID stenosis measurements. The intraclass correlation coefficient was 0.998 for the AJ-130 score (95% CI, 0.996–0.999), indicating outstanding interobserver reproducibility.

### Correlation Analyses

There was a wide range of calcium scores in the intracranial ICAs, with a weak linear positive correlation between both quantitative and qualitative calcium scores and intracranial stenosis (*R* = 0.48 and *R* = 0.42, respectively; *P* < .0001) (Fig 4). We found no statistical difference in correlations of quantitative and qualitative calcium scores and intracranial stenosis when WASID stenosis was measured on CTA alone or MRA alone (*P* = .54 and *P* = .39, respectively). There was a strong correlation between the quantitative and qualitative calcium scoring systems (*R* = 0.85, *P* < .0001). There was also a strong correlation between right and left intracranial ICAs for each patient's MWVSs and AJ-130 calcium scores (*R* = 0.91, *P* < .0001 and *R* = 0.90, *P* < .0001, respectively) and moderate correlation between ICAs in each patient in WASID stenosis scores (*R* = 0.66, *P* < .0001).

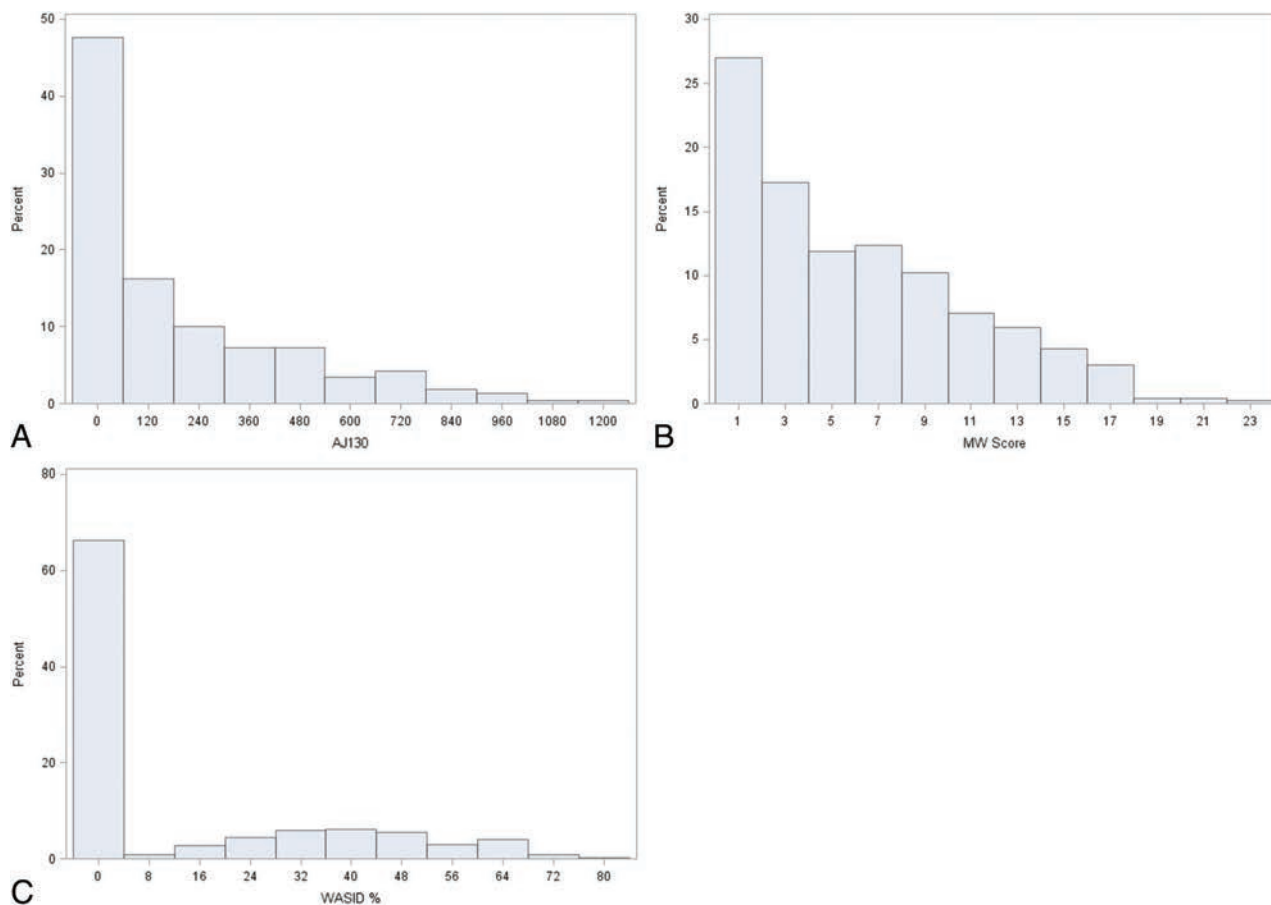


**FIG 1.** A, Distribution of all 470 arteries by quantitative calcium score. B, Distribution of all 470 arteries by qualitative calcium score. C, Distribution of all 470 subjects by WASID stenosis.

**Table 2: Degree of intracranial WASID stenosis compared with quantitative and qualitative measures of calcium**

Degree of WASID Stenosis	Number of Arteries	MWVS Mean $\pm$ SD, Median (Q1, Q3)	AJ-130 Mean $\pm$ SD, Median (Q1, Q3)
0%	310	4 $\pm$ 4.4, 2.5 (0, 7)	114.8 $\pm$ 194.6, 23 (0, 144)
>0%–29%	42	7.8 $\pm$ 4, 7 (5, 11)	278.8 $\pm$ 219.1, 261.5 (106, 411)
30%–49%	73	8.3 $\pm$ 4.5, 8 (5, 12)	339.5 $\pm$ 271.9, 331 (97, 557)
50%–69%	41	9.1 $\pm$ 5.2, 8 (5, 15)	438.7 $\pm$ 324.6, 427 (155, 698)
70%–99%	4	11.3 $\pm$ 4.5, 12.5 (8, 14.5)	593.8 $\pm$ 391.9, 682 (330.5, 857)
P value		<.0001	<.0001

**Note:**—Q indicates quartile.

## DISCUSSION

In an analysis of 470 intracranial ICAs from a prospective stroke registry, we found only a weak correlation between measures of intracranial atherosclerotic calcium burden and the degree of stenosis. In addition, we found that substantially more patients had atherosclerotic calcium detected on CT compared with intracranial stenosis detected on angiography, suggesting that a routine NCCT is more sensitive in detecting the presence of any intracranial atherosclerosis than isolated CTA or MRA studies. For instance, among 310 ICAs with 0% stenosis by WASID criteria, nearly 70% had measurable atherosclerotic calcification on CT. We also found that there were strong correlations between calcium scores in right and left intracranial ICAs within each patient, but only moderate correlation in the degree of WASID stenosis between sides. Our findings of a weak correlation between

the degree of intracranial stenosis and the intracranial atherosclerotic calcium burden<sup>15</sup> and a strong correlation between qualitative and quantitative measures of intracranial atherosclerotic calcium burden are similar to the existing literature.<sup>16</sup> Our work uniquely builds upon this knowledge by using NCCT to measure calcium burden and adapting a commonly used method for coronary calcium scoring (Agatston Score) to the intracranial ICA.

Our findings suggest that arterial calcium and degree of stenosis may provide complementary rather than overlapping data regarding atherosclerotic pathobiology and stroke risk. Histopathologic studies of the coronary arteries have shown that plaque calcification can predict overall atherosclerotic plaque burden better than the degree of arterial narrowing.<sup>17</sup> Although NCCT is capable of detecting vessel wall calcification with high sensitivity, angiographic techniques provide detailed information about luminal caliber. The relationship between ICA calcification and stroke risk is likely multifactorial. The presence of calcified intracranial atherosclerotic disease may indicate a general state of elevated cardiovascular risk, or the calcified plaque itself may cause either flow-limiting stenosis or distal thromboembolism.<sup>18–21</sup> The relationship between cal-

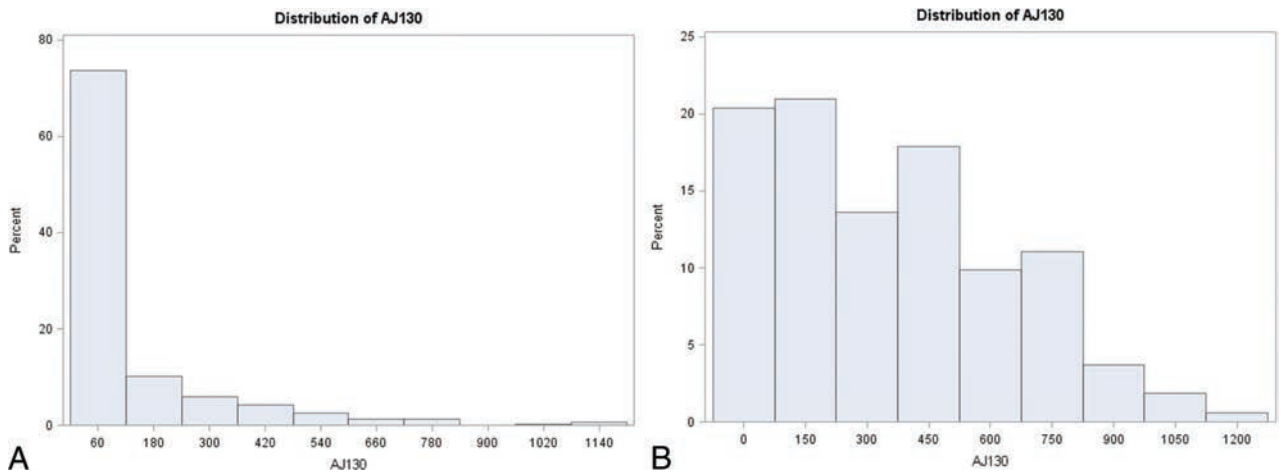


**FIG 2.** A, Distribution of AJ-130 scores in patients with no detectable (0%) WASID stenosis. B, Distribution of AJ-130 scores in patients with detectable WASID stenosis (>0%).

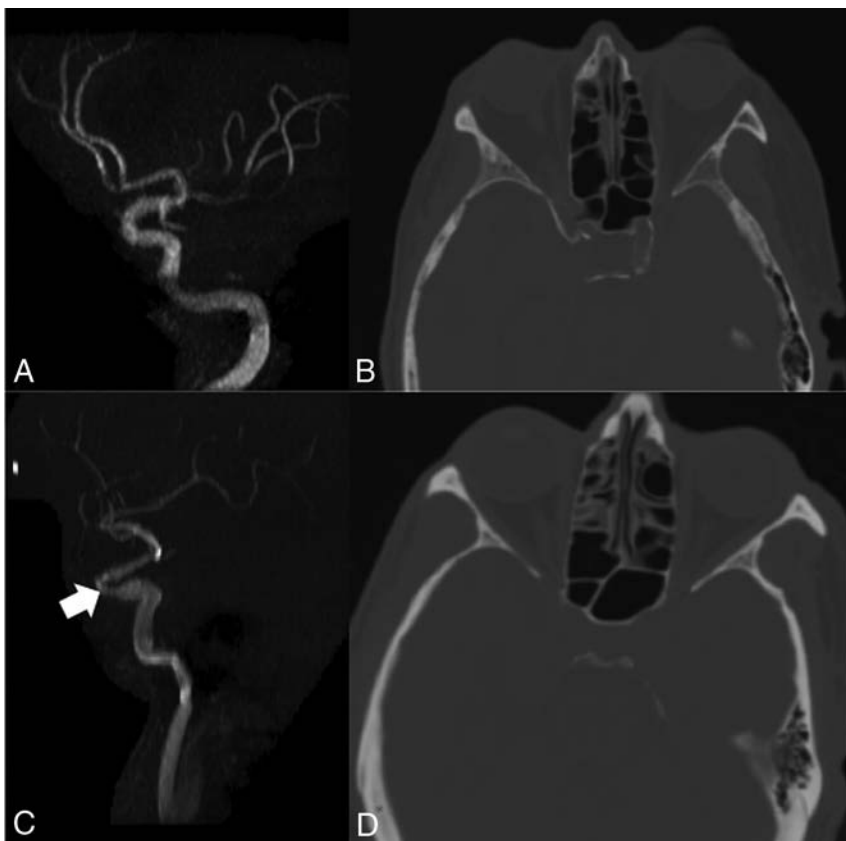


**FIG 3.** Imaging examples. A patient with no detectable stenosis (A) of the left intracranial ICA also has NCCT showing significant calcification of the visualized intracranial left ICA (B). This patient had an AJ-130 score of 604 and an MWVS of 9. Conversely, another patient had approximately 40% stenosis of the left intracranial ICA (C, arrow) but an NCCT (D) demonstrated no calcification in the left intracranial ICA, with an AJ-130 score of 0 and an MWVS of 0.

cified intracranial vasculature and flow-limiting stenosis may also be complicated by arterial remodeling<sup>22,23</sup> such that even with an extensive plaque burden, a vessel may not be significantly narrowed because of compensatory arterial expansion.<sup>24</sup> Additional studies evaluating the association between nonstenosing arterial calcification and vulnerable plaque elements, such as high-resolution vessel wall MR imaging,<sup>25</sup> may

be helpful in clarifying the pathobiology of intracranial atherosclerosis.

Historically, evaluation of luminal stenosis has been the main strategy to characterize intracranial atherosclerosis for both diagnostic and treatment purposes. For example, in most stroke classification schemes, a plaque must cause  $\geq 50\%$  stenosis for a stroke to be recognized as having an atherosclerotic etiology.<sup>10,26</sup> In addition, stroke treatment guidelines from the American Heart Association currently dictate that only patients with  $\geq 50\%$  stenosis be treated with intensive lipid-modification therapy.<sup>27</sup> Similarly, intracranial luminal stenosis measures have been used as the imaging biomarker for patient selection into endovascular or medical treatment trials.<sup>5</sup> Because our findings suggest that  $\sim 70\%$  of ICAs with calcification have no detectable narrowing on cross-sectional angiographic studies, many patients are likely harboring easily detectable atherosclerosis that may be ignored and, therefore, potentially undertreated. Because NCCT is nearly universally performed for patients with acute ischemic strokes, ICA calcium scoring represents a potentially useful imaging biomarker that could provide a more detailed evaluation of atherosclerotic disease burden.

Our study has several limitations. First, our study had a low proportion of patients with high-grade intracranial stenosis, likely resulting from our predominantly white population. Future studies in patient populations with a higher prevalence of intracranial stenosis, such as is found in Asian populations, may be helpful to further elucidate the relationship between severely stenotic ICAs and calcium burden. Second, whereas

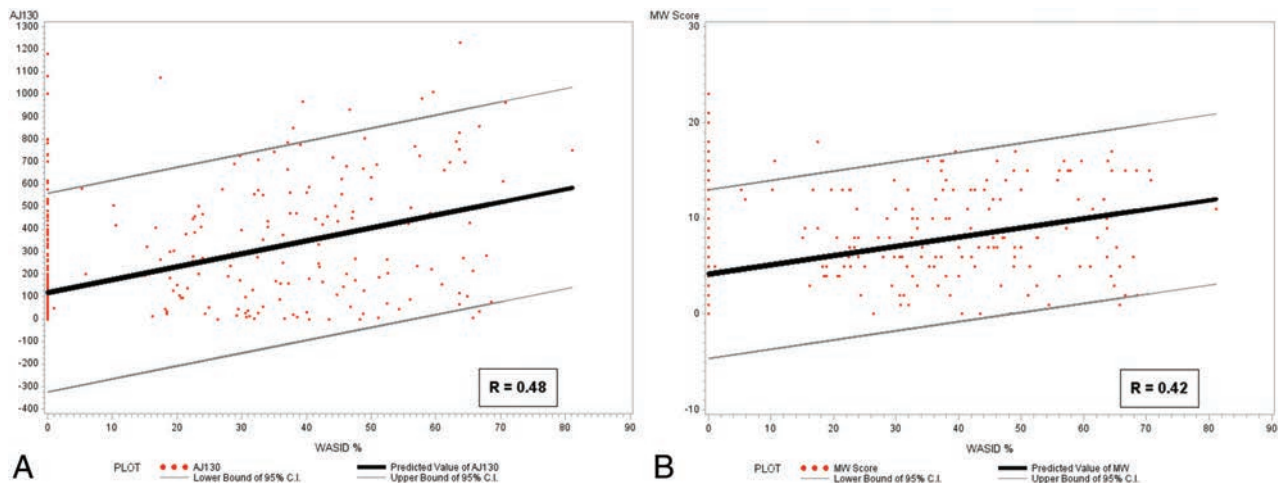


**FIG 4.** A, Correlation between quantitative (AJ-130) calcium score and WASID stenosis. B, Correlation between qualitative calcium score and WASID stenosis.

obtaining NCCT is relatively inexpensive and widely available, the manual postprocessing involved in calculating quantitative calcium scores can be modestly time-consuming, potentially adding up to 5 minutes per scan because, unlike the coronary arteries, no automated calcium scoring software currently exists for the intracranial circulation. Because our results show that the qualitative and quantitative calcium scores were similar in assessing intracranial atherosclerosis, using qualitative MWVS (requiring approximately 1 minute per case) could provide an alternative to manual quantitative calcium scoring until automated methods become more widely available. Third, our study was cross-sectional in nature, and although it provided important information regarding the relationship between intracranial stenosis and calcification, future large prospective studies are needed to evaluate the incremental utility of atherosclerotic calcium burden to predict stroke. In addition, our methods did not take into account calcification in the petrous segment of the ICA because the MWVS definition does not include the petrous segment of the ICA. The petrous segment was also excluded from analysis because evaluation of calcium burden in this segment is challenging and requires meticulous delineation of lumen from adjacent bone, a process that increases overall interpretation time and reduces the clinical utility of the technique. Last, measurements of WASID stenosis were performed on either CTA or MRA examinations, which have different sensitivities for detecting intracranial stenosis. Despite the differences in technique, we found no statistical difference in the correlation between WASID stenosis and calcium score when using CTA compared with MRA.

## CONCLUSIONS

In summary, we found a relatively weak association between intracranial atherosclerotic calcification and the degree of luminal stenosis. This finding suggests that CT may be more sensitive than angiographic studies in detecting the presence of measurable atherosclerotic disease. Given that stenosis and calcium burden may be 2 largely independent features of atherosclerotic plaque, future studies are warranted to evaluate

the relationship between stenosis and calcium burden in predicting stroke risk.

Disclosures: Babak Navi—RELATED: Grant: National Institutes of Health grant K23NS091395\*. James K. Min—UNRELATED: Board Membership: Arineta; Grants/Grants Pending: National Institutes of Health, GE Healthcare, Comments: Dr. Min is program director/principal or co-investigator on 5 National Institutes of Health grants and a sponsored research agreement related to cardiovascular research that is unrelated and has not funded the research discussed in this paper\*; Stock/Stock Options: Heartflow, Inc., Comments: equity/ownership stock options; Other: MDDX, Comments: medical advisor and 43% ownership. Ajay Gupta—RELATED: Grant: National Institutes of Health\*. \*Money paid to the institution.

## REFERENCES

- Holmstedt CA, Turan TN, Chimowitz MI. Atherosclerotic intracranial arterial stenosis: risk factors, diagnosis, and treatment. *Lancet Neurol* 2013;12:1106–14 CrossRef Medline
- Bos D, van der Rijk MJ, Geeraedts TE, et al. Intracranial carotid artery atherosclerosis: prevalence and risk factors in the general population. *Stroke* 2012;43:1878–84 Medline
- Gorelick PB, Wong KS, Bae HJ, et al. Large artery intracranial occlusive disease: a large worldwide burden but a relatively neglected frontier. *Stroke* 2008;39:2396–99 CrossRef Medline
- Kasner SE, Chimowitz MI, Lynn MJ, et al. Predictors of ischemic stroke in the territory of a symptomatic intracranial arterial stenosis. *Circulation* 2006;113:555–63 CrossRef Medline
- Derdeyn CP, Chimowitz MI, Lynn MJ, et al. Aggressive medical treatment with or without stenting in high-risk patients with intracranial artery stenosis (SAMMPRIS): the final results of a randomized trial. *Lancet* 2014;383:333–41 CrossRef Medline
- Bos D, Portegies ML, van der Lugt A, et al. Intracranial carotid artery atherosclerosis and the risk of stroke in whites: the Rotterdam Study. *JAMA Neurol* 2014;71:405–11 CrossRef Medline
- Shaw LJ, Giambone AE, Blaha MJ, et al. Long-term prognosis after coronary artery calcification testing in asymptomatic patients: a cohort study. *Ann Intern Med* 2015;163:14–21 CrossRef Medline
- Detrano R, Guerci AD, Carr JJ, et al. Coronary calcium as a predictor of coronary events in four racial or ethnic groups. *N Engl J Med* 2008;358:1336–45 CrossRef Medline
- Chimowitz MI, Caplan LR. Is calcification of intracranial arteries important and how? *JAMA Neurol* 2014;71:401–02 CrossRef Medline
- Adams HP, Bendixen BH, Kappelle LJ, et al. Classification of subtype of acute ischemic stroke. Definitions for use in a multicenter clinical

- cal trial. **Toast. Trial of org 10172 in acute stroke treatment.** *Stroke* 1993;24:35–41 CrossRef Medline
11. Samuels OB, Joseph GJ, Lynn MJ, et al. **A standardized method for measuring intracranial arterial stenosis.** *AJNR Am J Neuroradiol* 2000;21:643–46 Medline
  12. Woodcock RJ Jr, Goldstein JH, Kallmes DF, et al. **Angiographic correlation of CT calcification in the carotid siphon.** *AJNR Am J Neuroradiol* 1999;20:495–99 Medline
  13. Subedi D, Zishan US, Chappell F, et al. **Intracranial carotid calcification on cranial computed tomography visual scoring methods, semiautomated scores, and volume measurements in patients with stroke.** *Stroke* 2015;46:2504–09 CrossRef Medline
  14. Agatston AS, Janowitz WR, Hildner FJ, et al. **Quantification of coronary artery calcium using ultrafast computed tomography.** *J Am Coll Cardiol* 1990;15:827–32 CrossRef Medline
  15. Marquering HA, Nederkoorn PJ, Bleeker L, et al. **Intracranial carotid artery disease in patients with recent neurological symptoms: high prevalence on CTA.** *Neuroradiology* 2013;55:179–85 CrossRef Medline
  16. Bleeker L, Marquering HA, van den Berg R, et al. **Semi-automatic quantitative measurements of intracranial internal carotid artery stenosis and calcification using CT angiography.** *Neuroradiology* 2012;54:919–27 CrossRef Medline
  17. Sangiorgi G, Rumberger JA, Severson A, et al. **Arterial calcification and not lumen stenosis is highly correlated with atherosclerotic plaque burden in humans: a histologic study of 723 coronary artery segments using nondecalcifying methodology.** *J Am Coll Cardiol* 1998;31:126–33 CrossRef Medline
  18. Cheung HM, Moody AR, Singh N, et al. **Late stage complicated atheroma in low-grade stenotic carotid disease: MR imaging depiction—prevalence and risk factors.** *Radiology* 2011;260:841–47 CrossRef Medline
  19. Freilinger TM, Schindler A, Schmidt C, et al. **Prevalence of nonstenosing, complicated atherosclerotic plaques in cryptogenic stroke.** *JACC Cardiovasc Imaging* 2012;5:397–405 CrossRef Medline
  20. Gupta A, Gialdini G, Giambone AE, et al. **Association between nonstenosing carotid artery plaque on MR angiography and acute ischemic stroke.** *JACC Cardiovasc Imaging* 2016;9:1228–29 CrossRef Medline
  21. Gupta A, Gialdini G, Lerario MP, et al. **Magnetic resonance angiography detection of abnormal carotid artery plaque in patients with cryptogenic stroke.** *J Am Heart Assoc* 2015;4:e002012 CrossRef Medline
  22. Clarkson TB, Prichard RW, Morgan TM, et al. **Remodeling of coronary arteries in human and nonhuman primates.** *JAMA* 1994;271:289–94 CrossRef Medline
  23. Qiao Y, Anwar Z, Intrapirromkul J, et al. **Patterns and implications of intracranial arterial remodeling in stroke patients.** *Stroke* 2016;47:434–40 CrossRef Medline
  24. Astor BC, Sharrett AR, Coresh J, et al. **Remodeling of carotid arteries detected with MR imaging: atherosclerosis risk in communities carotid MRI study.** *Radiology* 2010;256:879–86 CrossRef Medline
  25. Mossa-Basha M, Hwang WD, De Havenon A, et al. **Multicontrast high-resolution vessel wall magnetic resonance imaging and its value in differentiating intracranial vasculopathic processes.** *Stroke* 2015;46:1567–73 CrossRef Medline
  26. Amarenco P, Bogousslavsky J, Caplan L, et al. **The ASCOD phenotyping of ischemic stroke (updated ASCO phenotyping).** *Cerebrovasc Dis* 2013;36:1–5 CrossRef Medline
  27. Kernan WN, Ovbiagele B, Black HR, et al. **Guidelines for the prevention of stroke in patients with stroke and transient ischemic attack: a guideline for healthcare professionals from the American Heart Association/American Stroke Association.** *Stroke* 2014;45:2160–236 CrossRef Medline

# Focal Low and Global High Permeability Predict the Possibility, Risk, and Location of Hemorrhagic Transformation following Intra-Arterial Thrombolysis Therapy in Acute Stroke

Y. Li, Y. Xia, H. Chen, N. Liu, A. Jackson, M. Wintermark, Y. Zhang, J. Hu, B. Wu, W. Zhang, J. Tu, Z. Su, and G. Zhu



## ABSTRACT

**BACKGROUND AND PURPOSE:** The contrast volume transfer coefficient ( $K^{trans}$ ), which reflects blood-brain barrier permeability, is influenced by circulation and measurement conditions. We hypothesized that focal low BBB permeability values can predict the spatial distribution of hemorrhagic transformation and global high BBB permeability values can predict the likelihood of hemorrhagic transformation.

**MATERIALS AND METHODS:** We retrospectively enrolled 106 patients with hemispheric stroke who received intra-arterial thrombolytic treatment.  $K^{trans}$  maps were obtained with first-pass perfusion CT data. The  $K^{trans}$  values at the region level, obtained with the Alberta Stroke Program Early CT Score system, were compared to determine the differences between the hemorrhagic transformation and nonhemorrhagic transformation regions. The  $K^{trans}$  values of the whole ischemic region based on baseline perfusion CT were obtained as a variable to hemorrhagic transformation possibility at the global level.

**RESULTS:** Forty-eight (45.3%) patients had hemorrhagic transformation, and 21 (19.8%) had symptomatic intracranial hemorrhage. At the region level, there were 82 ROIs with hemorrhagic transformation and parenchymal hemorrhage with a mean  $K^{trans}$ ,  $0.5 \pm 0.5$ /min, which was significantly lower than that in the nonhemorrhagic transformation regions ( $P < .01$ ). The mean  $K^{trans}$  value of 615 nonhemorrhagic transformation ROIs was  $0.7 \pm 0.6$ /min. At the global level, there was a significant difference ( $P = .01$ ) between the mean  $K^{trans}$  values of patients with symptomatic intracranial hemorrhage ( $1.3 \pm 0.9$ ) and those without symptomatic intracranial hemorrhage ( $0.8 \pm 0.4$ ). Only a high  $K^{trans}$  value at the global level could predict the occurrence of symptomatic intracranial hemorrhage ( $P < .01$ ; OR = 5.04; 95% CI, 2.01–12.65).

**CONCLUSIONS:** Global high  $K^{trans}$  values can predict the likelihood of hemorrhagic transformation or symptomatic intracranial hemorrhage at the patient level, whereas focal low  $K^{trans}$  values can predict the spatial distributions of hemorrhagic transformation at the region level.

**ABBREVIATIONS:** AIS = acute ischemic stroke; HI = hemorrhagic infarction; HT = hemorrhagic transformation; IAT = intra-arterial thrombolysis;  $K^{trans}$  = contrast volume transfer coefficient; PCT = perfusion CT; PH = parenchymal hemorrhage; sICH = symptomatic intracranial hemorrhage

Hemorrhagic transformation (HT) is a dreaded complication of reperfusion therapy after acute ischemic stroke (AIS). HT is nearly 5 times more likely following intravenous thrombolysis

compared with controls<sup>1</sup> and even more common following intra-arterial thrombolysis (IAT).<sup>2</sup> Symptomatic intracranial hemorrhage (sICH), the most serious complication after reperfusion therapy, is associated with an independent increase in mortality at 3 months after acute ischemia stroke.<sup>3</sup> It is therefore crucial to be able to predict the risks of HT and sICH before making a decision to use reperfusion therapy, especially intra-arterial procedures.

Received September 7, 2016; accepted after revision May 6, 2017.

From the Department of Neurology (Y.L., H.C., N.L., W.Z.), PLA Army General Hospital, Beijing, China; Department of Critical Care Medicine (Y.X.), Yantai Yuhuangding Hospital, Shandong, China; Wolfson Molecular Imaging Centre (A.J.), University of Manchester, Manchester, UK; Department of Radiology (Y.L., M.W.), Neuroradiology Section, Stanford University, Stanford, California; Department of Neurology (Y.Z.), Changhai Hospital, Second Military Medical University, Shanghai, China; Department of Neurology (J.H., G.Z.), Southwest Hospital, Third Military Medical University, Chongqing, China; Department of Radiology (B.W.), PLA Army General Hospital, Beijing, China; Outpatient Department (J.T.), PLA 61889 Army, Beijing, China; and GE Healthcare (Z.S.), Beijing, China.

Ying Li and Yonghong Xia contributed equally to this study.

This work was supported by the National Natural Science Foundation of China (grant Nos. 81371286 and 81501024) and the Clinical Innovation Foundation of Southwest Hospital (grant No. SWH2013LC20).

Please address correspondence to Guangming Zhu, MD, PhD, Department of Neurology, Southwest Hospital, Third Military Medical University, Chongqing, 400038, China; e-mail: zhugmdc@aliyun.com; Zihua Su, PhD, Advanced Application Department, Life Science, GE Healthcare, Beijing 100176, China; e-mail: zihua.su@qq.com

Indicates open access to non-subscribers at www.ajnr.org

Indicates article with supplemental on-line tables.

<http://dx.doi.org/10.3174/ajnr.A5287>

A number of clinical risk factors, including age, diabetes mellitus, infarction volume, and anticoagulant or antiplatelet therapy, are associated with increased risk of HT.<sup>3,4</sup> In addition, focal ischemia and reperfusion injury may lead to blood-brain barrier disruption, which is seen as early as 6 hours after infarction and increases with time,<sup>5</sup> and HT often appears in these areas. Clinical features alone provide poor predictive power for the risk of HT, and recent studies have assessed biomarkers of perfusion and endothelial permeability derived from dynamic contrast-enhanced imaging, specifically the contrast volume transfer coefficient ( $K^{trans}$ ).<sup>6,7</sup>  $K^{trans}$  represents the product of endothelial permeability and endothelial surface and governs the leakage of contrast from the vascular to the extravascular compartment. Several of these studies have suggested that increased blood-brain barrier permeability of an ischemic area predisposes to HT after reperfusion therapy.<sup>8-11</sup>

In our previous study, we proposed that  $K^{trans}$ , based on the model of Patlak and Blasberg,<sup>12</sup> derived from standard first-pass perfusion CT (PCT), can predict the relative risk of HT following intra-arterial reperfusion. However, in contrast to other studies, we found that HT was most likely to develop in the areas within the infarct that had lower permeability values.<sup>13</sup> We hypothesized that this apparent discrepancy arose from previous studies focusing on the mean values of  $K^{trans}$  derived from within the entire infarct volume as a predictive feature for HT, whereas in our previous study, we studied  $K^{trans}$  values measured specifically in areas of the brain that subsequently develop HT. Taken in combination, the studies suggest that HT is more common in infarcts characterized by high mean  $K^{trans}$  but is most likely to occur within the infarcted area in those who develop hemorrhage after IAT therapy, characterized by low values of  $K^{trans}$ .

In this study, we tested the hypotheses that in patients with AIS treated with IAT with tPA, high average values of  $K^{trans}$  within the infarct predict the risk of HT or sICH after reperfusion, and focal areas with low  $K^{trans}$  predict the geographic location of HT.

## MATERIALS AND METHODS

### Patients

The clinical and imaging data presented in this study were extracted from a repository created from data collected as part of standard clinical stroke care at 3 participating institutions: the PLA Army General Hospital, Beijing; Southwest Hospital, Chongqing; and Changhai Hospital, Shanghai, China. The respective institutional review boards approved collection and analysis of data from the repository.

We retrospectively enrolled consecutive patients who were admitted to these institutions with signs and symptoms suggesting hemispheric stroke, from January 2011 to January 2014, who met the following inclusion criteria: National Institutes of Health Stroke Scale scores on admission of 4–22; completion of a stroke CT imaging work-up including noncontrast CT, CT angiography, and PCT on admission; no high density that suggested intracranial hemorrhage on baseline noncontrast CT; treatment with IAT, with <12 hours from symptom onset to IAT completion; coagulation function normal before IAT; no anticoagulation or antiplatelet agent given within 24 hours after IAT; and MR imaging

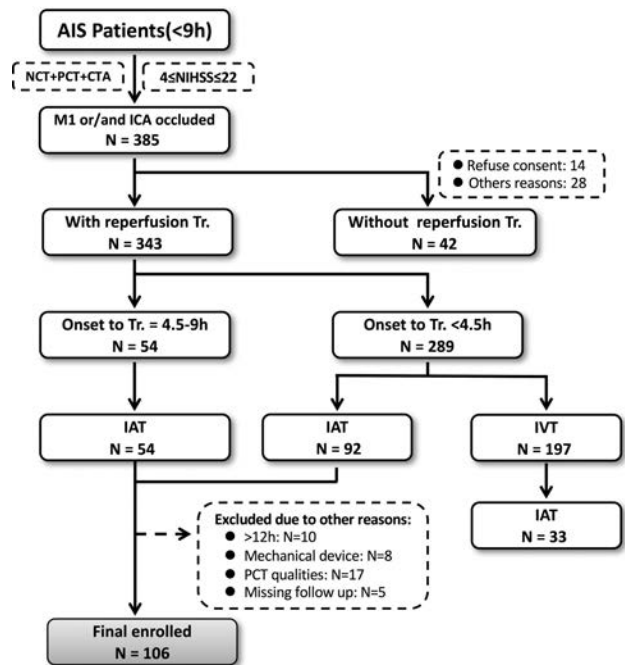


**FIG 1.** Flow chart outlining patient selection. Tr. indicates treatment; IVT, intravenous thrombolysis; NCT, noncontrast CT.

performed on the third day after therapy. A flow chart outlining the rules for patient selection is shown in Fig 1.

We recorded the following demographic and clinical variables: age, sex, medical history, vascular risk factors, time from symptom onset to treatment, the National Institutes of Health Stroke Scale score on admission, and the modified Rankin Scale score at 90 days. The 90-day outcomes were assessed in an outpatient clinic or over the telephone. An mRS of  $\leq 2$  was considered a good clinical outcome. Death was coded as mRS = 6.

Stroke mechanisms were subtyped by using the Trial of Org 10172 in Acute Stroke Treatment classification<sup>14</sup> and were diagnosed by the consensus of 2 stroke neurologists (J.H. and Y.Z.). The sICH was recorded as clinical neurologic worsening or death after therapy caused by parenchymal hemorrhage (PH) or hemorrhagic infarction (HI).<sup>15</sup>

### Imaging Protocol

**PCT Image Acquisition.** PCT studies were performed on similarly specified 64-section CT scanners (Discovery CT750 HD; GE Healthcare, Milwaukee, Wisconsin). Each PCT study involved successive gantry rotations performed in cine mode during intravenous administration of 2 boluses of 40 mL of iohexol (Omnipaque 350; GE Healthcare, Piscataway, New Jersey) at an injection rate of 4 mL/s. First-pass PCT acquisitions ranged from 50 to 70 seconds, with a sampling interval of either 1 or 2 seconds. Total PCT coverage was 40 mm. Acquisition parameters were 80 kVp and 100 mAs.

**CTA Imaging Protocol.** CTA studies of the cervical and intracranial arteries were performed at 120 kVp/200–300 mAs with the following acquisition parameters: helical mode; 0.5- to 0.8-second gantry rotation; pitch, 1-.375:1; section thickness, 0.625–1.25 mm; and reconstruction interval, 0.5–1 mm. A caudocranial

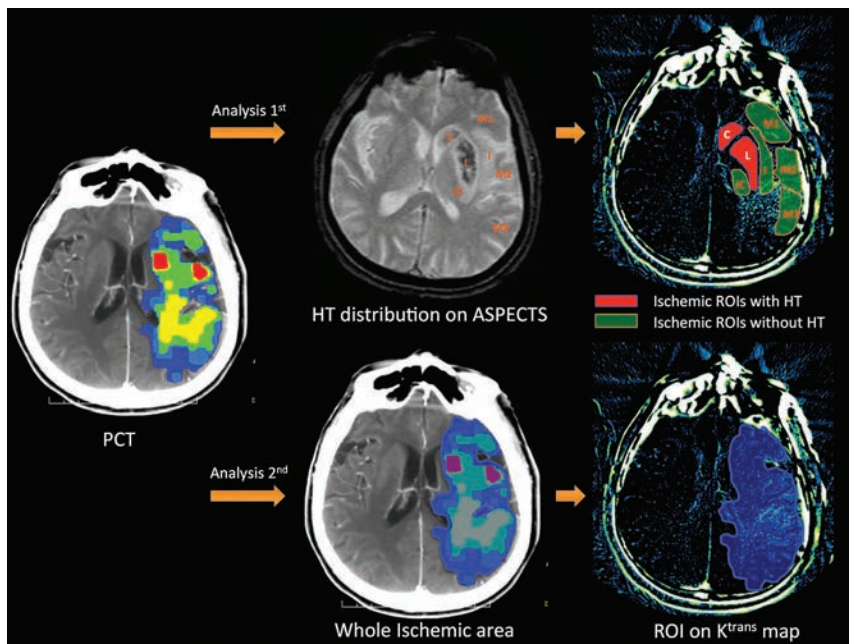


**FIG 2.** Protocol used to define ROIs (HT area and non-HT area) on  $K^{\text{trans}}$  maps. First analysis: the ASPECTS system was used to manually draw the distribution of the ischemic area on  $K^{\text{trans}}$  maps and determine the permeability values of each ROI. Second analysis: the entire ischemic area from PCT imaging is overlapped on the  $K^{\text{trans}}$  maps to determine the ROI, and the permeability value is restricted to this area.

scanning direction was selected covering the midchest to the vertex of the skull. CTA scans were obtained with 50 mL of iohexol (Omnipaque 350) administered via power injector at 5 mL/s.

**DSA Imaging Protocol.** DSA was performed with a dedicated biplane cerebral angiographic system (Axiom Artis dBA Twin; Siemens, Erlangen, Germany). Images during injection of each internal and external carotid artery and at least 1 vertebral artery were acquired and stored. All patients underwent IAT. Reperfusion status was assessed on DSA after IAT, and successful recanalization was defined as TIC1 2b and 3.

**MR Imaging Protocol.** MR imaging was performed on 1.5T MR imaging scanners (Signa; GE Healthcare). Gradient recalled-echo sequence parameters were as follows: TR, 600 ms; TE, 20 ms; flip angle, 20°; matrix size, 256 × 160; section thickness, 6 mm; intersection gap, 1 mm; 20 axial sections; and FOV, 250 × 180 mm.

### Image Processing

A neurologist (H.C.) with 13 years of experience reviewed all non-contrast CT, PCT, and CTA data. She measured the Alberta Stroke Program Early CT Score<sup>16</sup> and the hyperdense middle cerebral artery sign<sup>17</sup> on noncontrast CT and the infarct core and penumbra volumes on PCT. A neurologist (N.L.) with 14 years of experience reviewed the follow-up MR images to measure the final infarct volumes. Both reviewers were blinded to the initial clinical interpretation of these studies and were provided with only the side of the signs and symptoms.

Conventional perfusion parameters were calculated from PCT data with the commercially available software MISTar (Apollo Medical Imaging Technology, Melbourne, Australia).

The software applies singular value decomposition with delay- and dispersion-correction to calculate parametric perfusion maps and to automatically measure the volumes of infarct and penumbra.<sup>18</sup> Cerebral tissue with delay time >3 seconds, which includes penumbra and infarct core, was integrated as ischemic.<sup>19</sup> Parametric maps of  $K^{\text{trans}}$  were calculated from PCT data with prototype software (Omni-Kinetics; GE Healthcare, Beijing, China),<sup>20</sup> which is based on the model of Patlak et al.<sup>21</sup>  $K^{\text{trans}}$  maps were loaded into ImageJ 1.47 for Mac OS (National Institutes of Health, Bethesda, Maryland). A neurologist (Y.L.) defined ROIs with a manual drawing based on PCT, deriving mean  $K^{\text{trans}}$  values for each ROI.

HT was defined on the basis of the gradient-echo T2\*-weighted<sup>22</sup> images obtained on day 3, using the European Cooperative Acute Stroke Study<sup>23</sup> classification of hemorrhagic infarct: 1) no HT; 2) HI; and 3) PH.

Here we built 2 levels of permeability values: a region level and global level. In the region level,  $K^{\text{trans}}$  values of all patients were assessed according to the ASPECTS system. The 10 ASPECTS regions included the following: caudate, lenticula, internal capsule, insular ribbon, and M1–M6. On the basis of the PCT data at admission and the follow-up gradient-echo T2\*-weighted images, the ASPECTS regions in each patient were divided into 4 categories: 1) ischemic tissue without HT (simplified as non-HT); 2) ischemic tissue with HI (simplified as HI); 3) ischemic tissue with PH (simplified as PH); and 4) normal tissue without ischemia (simplified as normal). The  $K^{\text{trans}}$  values in the 3 categories, including the ischemic areas with non-HT, HI, or PH, were measured. Of note, here we did not include the normal tissue without ischemia. The  $K^{\text{trans}}$  values within non-HT areas were calculated as controls. The protocol used to define the ROIs on the basis of the ASPECTS system is illustrated in Fig 2.

In the global level, the ROIs were drawn on the basis of the whole ischemic regions observed on the output imaging of PCT, as described above; these ROIs were then imported into the  $K^{\text{trans}}$  maps to measure the permeability values of the entire ischemic region. The protocol used to define the ROIs for the entire ischemic region is illustrated in Fig 2. The mean permeability values in ischemic tissue for each patient were calculated and recorded because there were multiple sections on PCT imaging.

### Outcome Measurements

There were 3 outcomes in this study: 1) the presence or absence of HT based on follow-up imaging data, 2) the occurrence (or absence) of sICH, and 3) favorable (mRS > 2) versus unfavorable (mRS ≤ 2) clinical outcome.

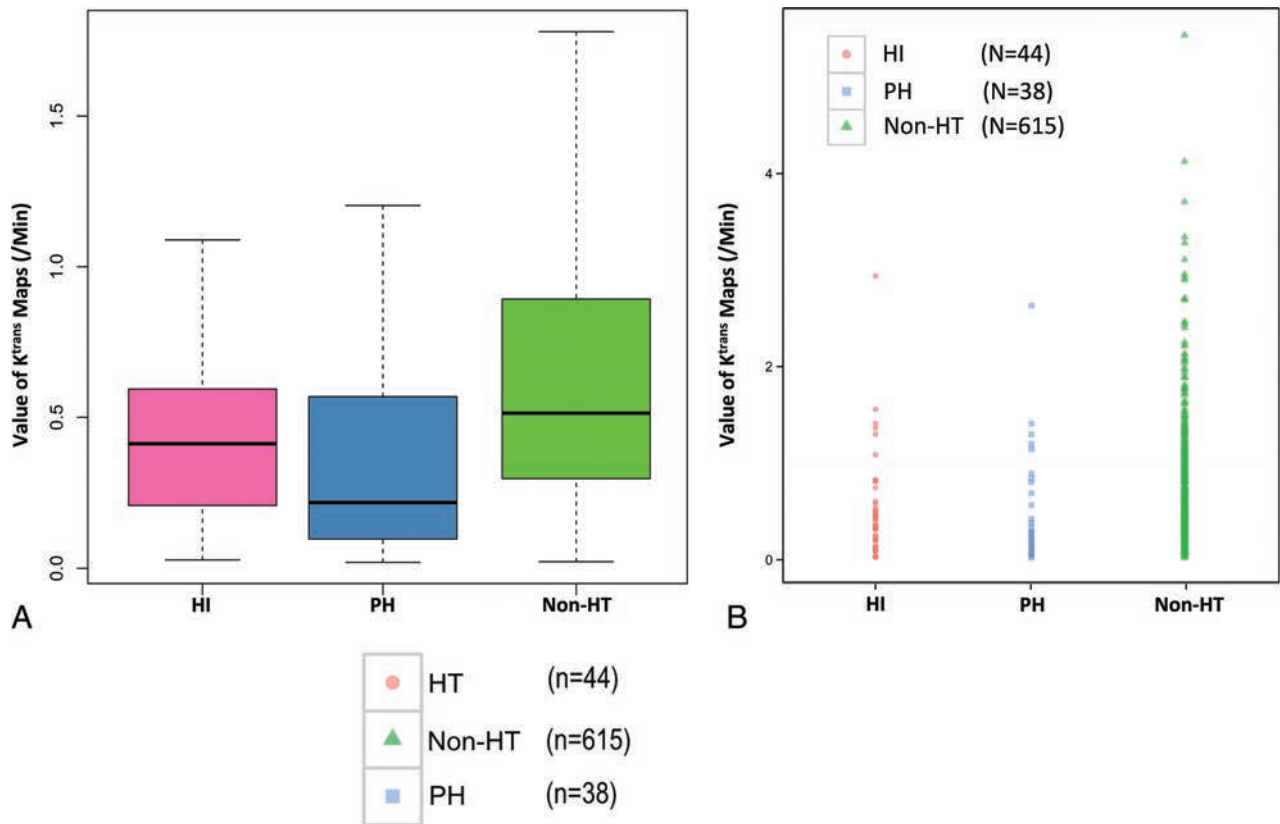


**FIG 3.** Boxplots and value distribution of  $K^{trans}$  values in the ASPECTS regions. A, Boxplots of  $K^{trans}$  values in the HI, PH, and non-HT ASPECTS regions. In each box, the median, 95% CI, and first and third quartile values are illustrated. B, The graph illustrates the distribution of the  $K^{trans}$  values, grouped into the HI, PH, and non-HT regions.

### Statistical Analyses

All data were presented as mean, median with interquartile range, or number with percentages. The baseline characteristics were compared on the basis of different outcomes such as HT, sICH, and good clinical outcome. Age and systolic and diastolic blood pressure on admission were analyzed with Student *t* tests. The time from symptom onset to CT, NIHSS score on admission, ASPECTS, collateral flow score, percentage of carotid artery stenosis, PCT infarct core, PCT ischemic penumbra, permeability value of the HT regions, permeability value of the non-HT regions, and mRS at 90 days ( $\leq 2$ ) were analyzed with Wilcoxon rank sum tests. The Pearson  $\chi^2$  test was used to analyze the relationship between stroke subtypes and the sites of occlusion. The effect of sex, hypertension, diabetes, hyperlipidemia, atrial fibrillation, current smoking, and the use of statins on admission was compared using the Pearson  $\chi^2$  test with a Yates continuity correction. Coronary heart disease and recanalization were analyzed with the Fisher exact test.

At the region level, mean  $K^{trans}$  values of ROIs with HI, PH, and non-HT based on the ASPECTS system were compared using the Kruskal-Wallis rank sum test. Mean  $K^{trans}$  values of the HT (HI plus PH) and non-HT ischemic regions were compared using the Wilcoxon rank sum test and a receiver operating characteristic curve.

At the global level, mean  $K^{trans}$  values of whole ischemic regions were entered into 3 multiple logistic regression analyses to determine whether they were independent predictors of HT,

sICH, and good clinical outcome. We entered the baseline predictors into multivariate models in cases with  $P < .05$  in the univariate analysis. The results were reported as odds ratios with 95% confidence intervals. All statistical analyses were performed with SAS, Version 9.3 (SAS Institute, Cary, North Carolina). A  $P$  value  $< .05$  was considered statistically significant.

### RESULTS

Our study population consisted of 106 patients, including 47 (44.3%) women; the mean age was  $65.3 \pm 13.9$  years. Eighty-six (81.1%) patients had successful recanalization. Of the 48 (45.3%) patients with HT, 21 (19.8%) had sICH. Moreover, 54 (50.9%) patients had a good clinical outcome (mRS  $< 2$ ). The details of clinical and imaging characteristics and outcome are described in On-line Tables 1 and 2.

The first analysis considered a total of 697 ischemic ROIs determined on the basis of the ASPECTS system. Of these ROIs, 44 had HI on follow-up and a mean  $K^{trans}$  value of  $0.5 \pm 0.5$ /min, whereas 38 showed PH on follow-up and a mean  $K^{trans}$  value of  $0.4 \pm 0.5$ /min. The mean  $K^{trans}$  value of 615 non-HT ROIs was  $0.7 \pm 0.6$ /min (Fig 3). The mean  $K^{trans}$  value of the ROIs in the patients with HT and PH ( $0.5 \pm 0.5$ /min) was significantly lower than that in the non-HT regions ( $0.7 \pm 0.6$ /min,  $P < .01$ , Fig 4A). The mean  $K^{trans}$  value of the normal tissue ROIs was  $0.2 \pm 0.2$ /min. These HT distributions were most commonly located in the lenticular nucleus (25/82) based on the ASPECTS system, with a mean  $K^{trans}$  value of  $0.2 \pm 0.2$ . Other locations included the insu-

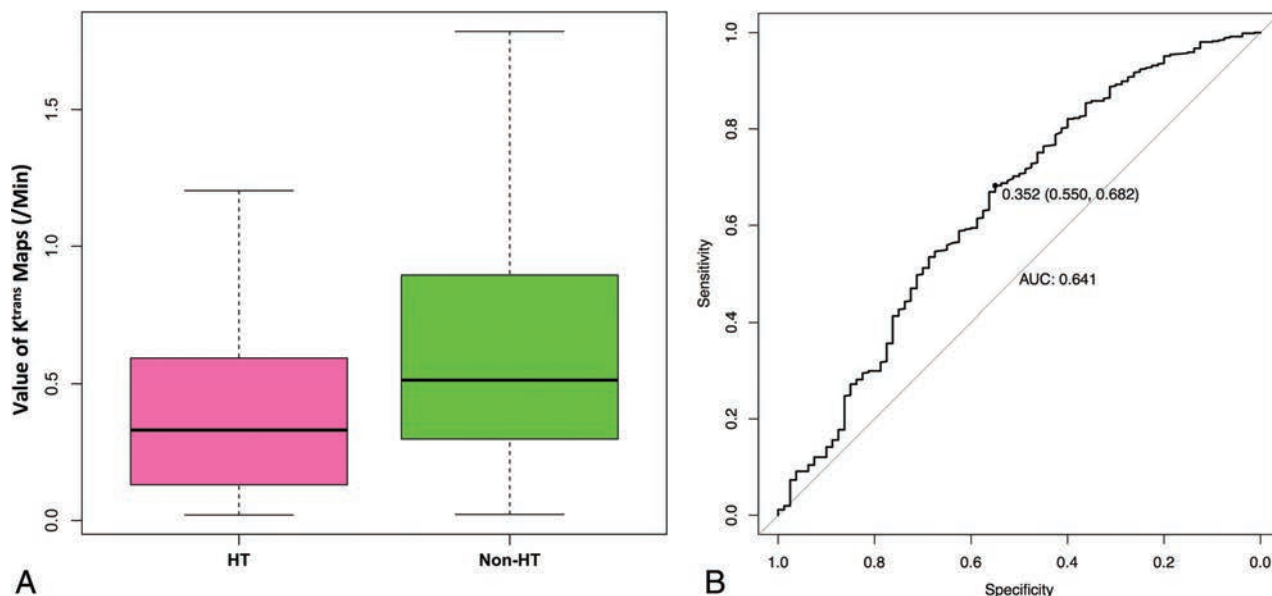


**FIG 4.** Boxplots of  $K^{\text{trans}}$  values of HT and non-HT regions and the receiver operating characteristic curve. **A**, Boxplots of  $K^{\text{trans}}$  values in HT and non-HT regions. In each box, the median, 95% CI, and first and third quartile values are illustrated. **B**, The optimal cutoff value of the  $K^{\text{trans}}$  value for the prediction of HT is identified with receiver operating characteristic curve analysis.

**Predictor variables determined to be uniquely associated with different outcomes**

Outcomes	Variable	Factors	Standard Error	Wald $\chi^2$	P Value	OR	OR 95%CI
HT vs non-HT	Intercept	2.8	1.2	5.9	.02		
	ASPECTS	-0.5	0.1	11.2	.00	0.6	0.5–0.8
	$K^{\text{trans}}$ value at patient level	1.0	0.4	5.4	.02	2.7	1.2–6.5
sICH vs non-sICH	Intercept	-3.0	0.6	28.8	.00		
	$K^{\text{trans}}$ value at patient level	1.6	0.5	11.9	.00	5.0	2.0–12.7
mRS $\leq 2$ vs mRS $> 2$	Intercept	-4.6	1.6	8.9	.00		
	Age	0.1	0.0	13.5	.00	1.1	1.0–1.1
	NIHSS score on admission	0.1	0.1	6.2	.01	1.1	1.0–1.3
	Recanalization	-2.6	0.8	11.2	.00	0.1	0.0–0.3

lar lobe (16/82) with a mean  $K^{\text{trans}}$  value of  $0.6 \pm 0.5$  and the caudate nuclei (15/82) with a mean  $K^{\text{trans}}$  value of  $0.2 \pm 0.1$ , but there were very few in the capsula interna (2/82) with a mean  $K^{\text{trans}}$  value of  $0.3 \pm 0.2$ . Receiver operating characteristic curve analysis indicated an optimal cutoff value for  $K^{\text{trans}}$  of 0.35/min, which produced a mean area under the curve of  $0.64 \pm 0.06$ . The sensitivity and specificity at this threshold were 55.0% and 68.2%, respectively (Fig 4B).

The first logistic regression model for the prediction of HT indicated that the ASPECTS was the most powerful independent significant predictor ( $P < .01$ , OR = 0.61; 95% CI, 0.46–0.82). The  $K^{\text{trans}}$  value was also a significant independent predictive factor ( $P = .02$ , OR = 2.75; 95% CI, 1.17–6.46).

The second logistic regression model for the prediction of sICH showed that only the  $K^{\text{trans}}$  value was a significant independent predictive factor ( $P < .01$ , OR = 5.04; 95% CI, 2.01–12.65). Both models suggested that an overall increase in the  $K^{\text{trans}}$  values in the ischemic regions predicted a higher probability of HT or sICH.

The third logistic regression model for the prediction of clinical outcome did not show that the  $K^{\text{trans}}$  value was an independent predictor. Instead, age was the most significant predictive factor ( $P < .01$ , OR = 1.08; 95% CI, 1.03–1.12) for clinical outcome. The NIHSS scores on admission and recanalization were

also found to be predictive factors ( $P = .01$ , OR = 1.14; 95% CI, 1.03–1.26; and  $P < .01$ , OR = 0.08; 95% CI, 0.03–0.34, respectively). The details are shown in the Table.

**DISCUSSION**

AIS is the leading cause of mortality in China and is the second most common cause of mortality worldwide.<sup>24,25</sup> Recent studies suggest that endovascular reperfusion therapy during the 6-hour time window,<sup>26,27</sup> or even during the 12-hour time window, can be effective for patients with proximal intracranial artery occlusion. However, HT remains a dangerous complication after reperfusion therapy. Furthermore, sICH—one of the most serious types of HT after AIS—increases the risk of stroke morbidity and mortality.<sup>28</sup> The prediction of HT or sICH before making a decision about reperfusion therapy could have important implications.

In the present study, 106 patients with AIS received IAT therapy. Moreover, 48 patients developed HT and 21 patients developed sICH. The  $K^{\text{trans}}$  values in the entire ischemic region were higher in patients with HT or sICH on follow-up compared with those without HT/sICH, which is consistent with previous studies.<sup>10</sup>

Many factors are associated with HT after AIS, including age, pretreatment NIHSS, ASPECTS, sex, blood pressure, and diabetes

mellitus. Recent studies focused on multimodal imaging, including perfusion and permeability imaging, to predict HT.<sup>6,7</sup> In fact, ischemia and reperfusion injury may lead to BBB disruption, and HT often develops in the area with BBB disruption. BBB disruption can develop as early as 6 hours after cerebral infarction, and the severity increases with time.<sup>5</sup> Moreover, first-pass dynamic PCT can be used to assess BBB permeability.<sup>10</sup> Another study using PCT imaging indicated that pretreatment BBB permeability measurement had a sensitivity of 100% and specificity of 79% in the prediction of sICH and malignant edema.<sup>11</sup> In fact, abnormal pretreatment permeability may be associated with an increased risk of PH following recanalization therapy, not only in patients with acute anterior circulation ischemic stroke but also in patients with acute posterior circulation ischemic stroke.<sup>29</sup>

However, our previous study, which included 41 patients with AIS with HT, showed that a low  $K^{\text{trans}}$  value predicted the site where HT would occur with perfect sensitivity and specificity.<sup>13</sup> Our interpretation of this result is that HT is more likely to develop in areas with the most severe hypoperfusion and ischemic injury, and that the  $K^{\text{trans}}$  values are low despite a significant elevation of BBB permeability. The main reason of the mismatch between the  $K^{\text{trans}}$  value and BBB permeability is that the blood flow and delivery of contrast agent are severely limited in the infarct core; therefore, the permeability of these areas could not be estimated correctly from a  $K^{\text{trans}}$  map. This finding is consistent with that of studies that suggest that very low cerebral blood volume,<sup>30</sup> admission PCT-based hypoperfused tissue volume,<sup>31</sup> time-to-maximum of >8 seconds, and lesion volumes are all independent predictors of PH in patients with acute stroke.<sup>32</sup> All these studies suggest that the low perfusion areas or severely infarcted tissue is more likely to develop HT after reperfusion therapy. In the current study, we compared the difference in the  $K^{\text{trans}}$  values between non-HT and HT areas on the basis of the 10 regions derived from the ASPECTS system. In the present study as well, the regions with low  $K^{\text{trans}}$  values indicated the location of HT, though the sensitivity and specificity (55.0% and 68.2%) were not as suitable as in our previous study. Nevertheless, the threshold of  $K^{\text{trans}}$  for predicting HT in the present study (0.35/min) was similar to that in the previous study (0.33/min).

When assessing the overall BBB permeability values, including those of the entire ischemic area (rather than specific regions where HT developed), the patients with HT had significantly higher mean  $K^{\text{trans}}$  values compared with those without HT. The difference was even more significant when comparing patients with sICH with those without sICH. Although the  $K^{\text{trans}}$  value did not predict the clinical outcome, it was still a significant predictor for HT or sICH. Our interpretation of this finding is that the severity of BBB disruption reflects the severity of ischemia and thus predicts the likelihood of HT. Age, NIHSS score on admission, and recanalization are significant predictors of 90-day mRS values; this finding is consistent with those in previous studies. In the present study, we have also observed that the ASPECTS is a predictor of HT. This finding is consistent with that in another study that demonstrated that a decreased ASPECTS/diffusion-weighted imaging score increased the likelihood of HT after thrombolysis.<sup>3</sup>

The present study has several limitations. First, this is a retrospective analysis with a study population of only 106 cases. Sec-

ond, we used only 1 permeability parameter,  $K^{\text{trans}}$ , to characterize the BBB permeability. Other permeability parameters, such as permeability surface-area product and vascular permeability, could also have been assessed. We used first-pass data from PCT, which is not the standard method for the assessment of BBB permeability. These data are more sensitive to noise and more easily overestimated because of the delayed flow in ischemic regions.<sup>31</sup> All the above could be reasons that the receiver operating characteristic curve in this study is not great at differentiating HT from non-HT. Further study may need more carefully selected candidates with other more meticulous methods, such as delayed-acquisition perfusion CT or dynamic contrast-enhanced MR imaging. Last, the results from the data base with intra-arterial thrombolysis cannot be generalized to other reperfusion therapies such as IV thrombolysis and mechanical recanalization. However, IAT is still an effective method in the clinical setting to assess patients in the hyperacute phase of AIS within limited reperfusion time windows.

## CONCLUSIONS

This study demonstrates that global high  $K^{\text{trans}}$  values may be one of the predictors of the likelihood of HT or sICH and that focal low  $K^{\text{trans}}$  values predict the spatial distribution of HT after intra-arterial reperfusion treatment. Further studies are needed to examine the role of permeability imaging in the decision-making process in patients with AIS.

## ACKNOWLEDGMENTS

We thank Statistical Elite (<http://www.tjstat.com/>) for statistical analysis and Editage (<https://www.editage.cn/>) for language editing.

Disclosures: Max Wintermark—UNRELATED: board membership: GE NFL Advisory Board.

## REFERENCES

1. Hacke W, Donnan G, Fieschi C, et al; ATLANTIS Trials Investigators, ECASS Trials Investigators, NINDS rt-PA Study Group Investigators. **Association of outcome with early stroke treatment: pooled analysis of ATLANTIS, ECASS, and NINDS rt-PA stroke trials.** *Lancet* 2004;363:768–74 CrossRef Medline
2. O'Rourke K, Berge E, Walsh CD, et al. **Percutaneous vascular interventions for acute ischaemic stroke.** *Cochrane Database Syst Rev* 2010:CD007574 CrossRef Medline
3. Hong KS, Kang DW, Koo JS, et al. **Impact of neurological and medical complications on 3-month outcomes in acute ischaemic stroke.** *Eur J Neurol* 2008;15:1324–31 CrossRef Medline
4. Zhang PL, Wang YX, Chen Y, et al. **Analysis on the correlation factors for hemorrhagic transformation after intravenous thrombolytic therapy.** *Eur Rev Med Pharmacol Sci* 2015;19:1001–08 Medline
5. Moriya Y, Takahashi W, Kijima C, et al. **Predictors for hemorrhagic transformation with intravenous tissue plasminogen activator in acute ischemic stroke.** *Tokai J Exp Clin Med* 2013;38:24–27 Medline
6. Jiang Q, Ewing JR, Chopp M. **MRI of blood-brain barrier permeability in cerebral ischemia.** *Transl Stroke Res* 2012;3:56–64 CrossRef Medline
7. Jain AR, Jain M, Kanthala AR, et al. **Association of CT perfusion parameters with hemorrhagic transformation in acute ischemic stroke.** *AJNR Am J Neuroradiol* 2013;34:1895–900 CrossRef Medline
8. Ozkul-Wermester O, Guegan-Massardier E, Triquenot A, et al. **Increased blood-brain barrier permeability on perfusion computed**

- tomography predicts hemorrhagic transformation in acute ischemic stroke. *Eur Neurol* 2014;72:45–53 CrossRef Medline
9. Campbell BC, Christensen S, Parsons MW, et al; EPITHET and DEFUSE Investigators. **Advanced imaging improves prediction of hemorrhage after stroke thrombolysis.** *Ann Neurol* 2013;73:510–19 CrossRef Medline
  10. Lin K, Kazmi KS, Law M, et al. **Measuring elevated microvascular permeability and predicting hemorrhagic transformation in acute ischemic stroke using first-pass dynamic perfusion CT imaging.** *AJNR Am J Neuroradiol* 2007;28:1292–98 CrossRef Medline
  11. Hom J, Dankbaar JW, Soares BP, et al. **Blood-brain barrier permeability assessed by perfusion CT predicts symptomatic hemorrhagic transformation and malignant edema in acute ischemic stroke.** *AJNR Am J Neuroradiol* 2011;32:41–48 CrossRef Medline
  12. Patlak CS, Blasberg RG. **Graphical evaluation of blood-to-brain transfer constants from multiple-time uptake data: generalizations.** *J Cereb Blood Flow Metab* 1985;5:584–90 CrossRef Medline
  13. Chen H, Liu N, Li Y, et al. **Mismatch of low perfusion and high permeability predicts hemorrhagic transformation region in acute ischemic stroke patients treated with intra-arterial thrombolysis.** *Sci Rep* 2016;6:27950 CrossRef Medline
  14. Adams HP Jr, Bendixen BH, Kappelle LJ, et al; TOAST Investigators. **Classification of subtype of acute ischemic stroke: definitions for use in a multicenter clinical trial.** *Stroke* 1993;24:35–41 Medline
  15. Berger C, Fiorelli M, Steiner T, et al. **Hemorrhagic transformation of ischemic brain tissue: asymptomatic or symptomatic?** *Stroke* 2001;32:1330–35 CrossRef Medline
  16. Barber PA, Demchuk AM, Zhang J, et al. **Validity and reliability of a quantitative computed tomography score in predicting outcome of hyperacute stroke before thrombolytic therapy: ASPECTS Study Group—Alberta Stroke Programme Early CT Score.** *Lancet* 2000;355:1670–74 CrossRef Medline
  17. Man S, Hussain MS, Wisco D, et al. **The location of pretreatment hyperdense middle cerebral artery sign predicts the outcome of intraarterial thrombectomy for acute stroke.** *J Neuroimaging* 2015;25:263–68 CrossRef Medline
  18. Yang Q, inventor; Apollo Medical Imaging Technology Pty Ltd, assignee. **Method and system for mapping tissue status of acute stroke.** US patent 8942451. January 27, 2015
  19. Bivard A, Levi C, Krishnamurthy V, et al. **Perfusion computed tomography to assist decision making for stroke thrombolysis.** *Brain* 2015;138(pt 7):1919–31 CrossRef Medline
  20. Sourbron SP, Buckley DL. **Classic models for dynamic contrast-enhanced MRI.** *NMR Biomed* 2013;26:1004–27 CrossRef Medline
  21. Patlak CS, Blasberg RG, Fenstermacher JD. **Graphical evaluation of blood-to-brain transfer constants from multiple-time uptake data.** *J Cereb Blood Flow Metab* 1983;3:1–7 CrossRef Medline
  22. Arnould MC, Grandin CB, Peeters A, et al. **Comparison of CT and three MR sequences for detecting and categorizing early (48 hours) hemorrhagic transformation in hyperacute ischemic stroke.** *AJNR Am J Neuroradiol* 2004;25:939–44 Medline
  23. Hacke W, Kaste M, Fieschi C, et al. **Randomised double-blind placebo-controlled trial of thrombolytic therapy with intravenous alteplase in acute ischaemic stroke (ECASS II): Second European-Australasian Acute Stroke Study Investigators.** *Lancet* 1998;352:1245–51 CrossRef Medline
  24. Goldstein LB, Bushnell CD, Adams RJ, et al; American Heart Association Stroke Council, Council on Cardiovascular Nursing, Council on Epidemiology and Prevention, Council for High Blood Pressure Research, Council on Peripheral Vascular Disease, and Interdisciplinary Council on Quality of Care and Outcomes Research. **Guidelines for the primary prevention of stroke: a guideline for healthcare professionals from the American Heart Association/American Stroke Association.** *Stroke* 2011;42:517–84 CrossRef Medline
  25. Wang YJ, Zhang SM, Zhang L, et al. **Chinese guidelines for the secondary prevention of ischemic stroke and transient ischemic attack 2010.** *CNS Neurosci Ther* 2012;18:93–101 CrossRef Medline
  26. Gobert F, Cho TH, Desilles JP, et al. **Magnetic resonance imaging-based intravenous thrombolysis 6 hours after onset of minor cerebellar stroke.** *Arch Neurol* 2011;68:678 CrossRef Medline
  27. Newman DH, Shreves AE. **Thrombolysis in acute ischaemic stroke.** *Lancet* 2012;380:1053–54; author reply 1054–55 CrossRef Medline
  28. Whiteley WN, Thompson D, Murray G, et al; IST-3 Collaborative Group. **Targeting recombinant tissue-type plasminogen activator in acute ischemic stroke based on risk of intracranial hemorrhage or poor functional outcome: an analysis of the third international stroke trial.** *Stroke* 2014;45:1000–06 CrossRef Medline
  29. Lee M, Saver JL, Alger JR, et al. **Blood-brain barrier permeability derangements in posterior circulation ischemic stroke: frequency and relation to hemorrhagic transformation.** *J Neurol Sci* 2012;313:142–46 CrossRef Medline
  30. Hermitte L, Cho TH, Ozanne B, et al. **Very low cerebral blood volume predicts parenchymal hematoma in acute ischemic stroke.** *Stroke* 2013;44:2318–20 CrossRef Medline
  31. Schneider T, Hom J, Bredno J, et al. **Delay correction for the assessment of blood-brain barrier permeability using first-pass dynamic perfusion CT.** *AJNR Am J Neuroradiol* 2011;32:E134–38 CrossRef Medline
  32. Yassi N, Parsons MW, Christensen S, et al. **Prediction of poststroke hemorrhagic transformation using computed tomography perfusion.** *Stroke* 2013;44:3039–43 CrossRef Medline

# MRI of the Swallow Tail Sign: A Useful Marker in the Diagnosis of Lewy Body Dementia?

 S. Shams,  D. Fällmar,  S. Schwarz,  L.-O. Wahlund,  D. van Westen,  O. Hansson,  E.-M. Larsson, and  S. Haller



## ABSTRACT

**BACKGROUND AND PURPOSE:** There are, to date, no MR imaging diagnostic markers for Lewy body dementia. Nigrosome 1, containing dopaminergic cells, in the substantia nigra pars compacta is hyperintense on SWI and has been called the swallow tail sign, disappearing with Parkinson disease. We aimed to study the swallow tail sign and its clinical applicability in Lewy body dementia and hypothesized that the sign would be likewise applicable in Lewy body dementia.

**MATERIALS AND METHODS:** This was a retrospective cross-sectional multicenter study including 97 patients (mean age, 65 ± 10 years; 46% women), consisting of the following: controls ( $n = 21$ ) and those with Lewy body dementia ( $n = 19$ ), Alzheimer disease ( $n = 20$ ), frontotemporal lobe dementia ( $n = 20$ ), and mild cognitive impairment ( $n = 17$ ). All patients underwent brain MR imaging, with susceptibility-weighted imaging at 1.5T ( $n = 46$ ) and 3T ( $n = 51$ ). The swallow tail sign was assessed independently by 2 neuroradiologists.

**RESULTS:** Interrater agreement was moderate ( $\kappa = 0.4$ ) between raters. An abnormal swallow tail sign was most common in Lewy body dementia (63%; 95% CI, 41%–85%;  $P < .001$ ) and had a predictive value only in Lewy body dementia with an odds ratio of 9 (95% CI, 3–28;  $P < .001$ ). The consensus rating for Lewy body dementia showed a sensitivity of 63%, a specificity of 79%, a negative predictive value of 89%, and an accuracy of 76%; values were higher on 3T compared with 1.5T. The usefulness of the swallow tail sign was rater-dependent with the highest sensitivity equating 100%.

**CONCLUSIONS:** The swallow tail sign has diagnostic potential in Lewy body dementia and may be a complement in the diagnostic work-up of this condition.

**ABBREVIATIONS:** AD = Alzheimer disease; FTD = frontotemporal lobe dementia; LBD = Lewy body dementia; MCI = mild cognitive impairment; PD = Parkinson disease

Lewy body dementia (LBD) is often regarded as the second most common dementia in older individuals after Alzheimer disease,<sup>1,2</sup> possibly sharing the second place with vascular dementia.<sup>3</sup> Clinical symptoms of LBD are similar to those of Parkinson

disease (PD) dementia and include fluctuating cognitive decline, recurrent visual hallucinations, and parkinsonism.<sup>2,4</sup> LBD and PD dementia are separated by the arbitrary 1-year rule: If dementia exists within 12 months of parkinsonism, the patient is classified as having LBD.<sup>2,4</sup> More than 12 months of parkinsonism before the onset of dementia is termed “PD dementia.”<sup>2,4</sup>

Differential diagnostics between LBD and Alzheimer disease (AD) can be difficult, with both clinical and pathologic overlap.<sup>2,5,6</sup> LBD distinguishes itself from AD on MR imaging by having a lesser degree of generalized atrophy and commonly sparing or having less severe atrophy of the medial temporal lobes.<sup>6</sup> Besides the loss of atrophy, which in itself is nonspecific, no accurate MR imaging signs for the distinction of LBD and other neurodegenerative diagnoses exist. Functional imaging is useful in diagnostic differentiation and typically shows reduced perfusion and

Received December 8, 2016; accepted after revision April 17, 2017.

From the Department of Clinical Science, Intervention, and Technology (S. Shams), Division of Medical Imaging and Technology, and Department of Neurobiology, Care Sciences, and Society (L.-O.W.), Karolinska Institutet, Stockholm, Sweden; Department of Radiology (S. Shams) and Division of Clinical Geriatrics (L.-O.W.), Karolinska University Hospital, Stockholm, Sweden; Department of Surgical Sciences (D.F., E.-M.L.), Department of Radiology, Uppsala University, Uppsala, Sweden; Radiological Sciences (S. Schwarz), Division of Clinical Neurosciences, School of Medicine, University of Nottingham, Nottingham, UK; Department of Radiology (E.-M.L., D.v.W.) and Memory Clinic (O.H.), Skåne University Hospital and Clinical Memory Research Unit, Department of Clinical Sciences, Malmö, Lund University, Lund, Sweden; and Affidea CDRC Centre de Diagnostic Radiologique de Carouge SA (S.H.), Carouge GE, Geneva, Switzerland.

This work was supported by the Stockholm County Council, the Karolinska Institutet, and the Swedish Dementia Association.

Please address correspondence to Sara Shams, MD, PhD, Department of Radiology, Karolinska University Hospital, SE-14186 Stockholm, Sweden; e-mail: sara.shams@ki.se

 Indicates open access to non-subscribers at [www.ajnr.org](http://www.ajnr.org)

 Indicates article with supplemental on-line table.

<http://dx.doi.org/10.3174/ajnr.A5274>

**Table 1: Mean age and sex distribution across diagnoses<sup>a</sup>**

	Whole Cohort (n = 97)	Controls (n = 21)	LBD (n = 19)	FTD (n = 20)	AD (n = 20)	MCI (n = 17)
Mean age (yr)	65 ± 10	60 ± 6	72 ± 6	64 ± 11	72 ± 6	62 ± 12
Female (No.) (mean age) (yr)	45, 46%; 64 ± 11	10, 48%; 58 ± 5	5, 26%; 74 ± 65	10, 50%; 63 ± 13	12, 60%; 68 ± 8	8, 47%; 60 ± 12
Male (No.) (mean age) (yr)	52, 54%; 67 ± 10	11, 52%; 62 ± 6	14, 74%; 72 ± 6	10, 50%; 66 ± 9	8, 40%; 70 ± 13	9, 53%; 64 ± 11
MMSE (mean)	26 ± 4	30 ± 0	22 ± 3	27 ± 2	23 ± 4	28 ± 2
Hypertension (No.) (%)	8 (9)	3 (14)	0	1 (5)	2 (10)	2 (12)
Diabetes (No.) (%)	2 (2)	1 (5)	0	0	1 (5)	0
Hyperlipidemia (No.) (%)	6 (7)	2 (10)	0	1 (5)	2 (10)	1 (6)
CSF amyloid (median) (IQR) (ng/L)	575 (403–1250)	1160 (697–1370)	–	565 (528–565)	391 (342–524)	737 (448–1138)
CSF T- $\tau$ (median) (IQR) (ng/L)	52 (36–73)	274 (211–364)	–	214 (129–214)	502 (398–873)	198 (129–417)
CSF P- $\tau$ (median) (IQR) (ng/L)	307 (192–458)	55 (36–75)	–	36 (22–36)	84 (61–115)	37 (28–67)
CSF/serum albumin ratio (median) (IQR)	249 (153–322)	230 (166–345)	–	322 (153–322)	307 (206–730)	155 (106–376)

**Note:**—P- $\tau$  indicates phosphorylated  $\tau$ ; T- $\tau$ , total  $\tau$ ; MMSE, Mini-Mental State Examination.

<sup>a</sup> All patients, except 8 with LBD, had data on hypertension, hyperlipidemia, and diabetes. CSF data were available for a subgroup of 56 patients (controls = 18; LBD = 0; FTD = 8; AD = 16; MCI = 14).

glucose metabolism in an AD-like pattern, sparing the medial temporal lobes, with additional involvement of the occipital regions.<sup>6–9</sup> Dopaminergic transporter imaging with SPECT is another reliable method of differentiation, with less binding in the striatum suggesting LBD.<sup>6</sup>

In recent years, MR imaging of the substantia nigra has shown great promise as a diagnostic tool in Parkinson disease.<sup>10–14</sup> Pathophysiologically, PD is characterized by loss of pigmented dopaminergic neurons of the substantia nigra pars compacta; 60%–80% of neurons are lost even before manifestation of motor symptoms.<sup>15</sup> Clusters of dopamine-containing neurons in calbindin-poor zones in the substantia nigra are termed nigrosomes.<sup>16</sup> Nigrosome 1, located in the caudal and posterolateral part of the substantia nigra pars compacta, is the largest dopamine-containing cluster and is mostly affected by PD.<sup>17</sup> Recently, nigrosome 1 has been described as hyperintense on iron-sensitive SWI sequences,<sup>14</sup> resembling a swallow tail.<sup>11</sup> The presence of a swallow tail sign has been shown to be sensitive and specific and has a high negative predictive value in PD on 3T MR imaging,<sup>11</sup> but its clinical applicability in LBD warrants further investigation.

Due to the similarity in pathophysiology of PD and LBD, the swallow tail sign should be of diagnostic value even in LBD.<sup>18</sup> We aimed to determine the clinical applicability of the swallow tail sign in a memory clinic population with a focus on LBD.

## MATERIALS AND METHODS

### Patients

This study received institutional review board approval. Informed consent was obtained from each patient or a legal guardian in case of severe dementia, according to the Declaration of Helsinki. This was a retrospective multicenter cross-sectional study with patient recruitment from memory clinics at the Karolinska, Uppsala, and Lund University Hospitals. All patients were recruited at initial work-up of their disease, and the MR imaging brain scan was obtained concomitantly as part of the memory investigation. Inclusion criteria were the presence of SWI sequences, a diagnosis of subjective cognitive impairment (used as controls), LBD, frontotemporal lobe dementia (FTD), AD, or mild cognitive impairment (MCI). The exclusion criterion was insufficient scan quality. We aimed to have around 20 patients per diagnostic group and recruited the total amount of consecutive patients with SWI from each center ( $n = 100$ ). Three patients were excluded because of insufficient scan quality due to motion artifacts. In total, we included 97 patients: subjective cognitive impairment (controls)

**Table 2: Overview of MRI scanners, SWI sequence parameters, and diagnostic distribution**

	Karolinska University Hospital		Lund University Hospital	
	Avanto <sup>a</sup>	Tim Trio <sup>a</sup>	Achieva <sup>b</sup>	Skyra <sup>a</sup>
Field strength	1.5T	3T	3T	3T
TE (ms)	40	20	25	20
TR (ms)	49	28	17	27
Flip angle	15°	15°	15°	15°
Section thickness (mm)	2.0	1.6	2	1.5
Patients (No.) (%)	43 (43)	37 (40)	9 (9)	8 (8)
Controls ( $n = 21$ ) (No.) (%)	12 (57)	9 (43)	–	–
LBD ( $n = 19$ ) (No.) (%)	4 (21)	5 (26)	2 (11)	8 (42)
FTD ( $n = 20$ ) (No.) (%)	7 (35)	6 (30)	7 (35)	–
AD ( $n = 20$ ) (No.) (%)	13 (65)	7 (35)	–	–
MCI ( $n = 17$ ) (No.) (%)	7 (41)	10 (59)	–	–

<sup>a</sup> Siemens, Erlangen, Germany.

<sup>b</sup> Philips Healthcare, Best, the Netherlands.

( $n = 21$ ), LBD ( $n = 19$ ), FTD ( $n = 20$ ), AD ( $n = 20$ ), and MCI ( $n = 17$ ).

Patient demographics are detailed in Table 1. Patients with LBD were recruited from all 3 sites; those with FTD, from Uppsala University Hospital; and the remaining patients, from the Karolinska University Hospital.<sup>19</sup> All patients had their diagnosis set according to the International Classification of Diseases-10, the clinically used classification criteria in our country. Diagnosis was determined in multidisciplinary rounds, with consideration of all data (clinical, lab, imaging, and neuropsychological) after a thorough memory clinic investigation. CSF analysis was performed as previously described<sup>20</sup> on a subgroup of 56 patients and is seen in Table 1.

### MR Imaging and Image Assessment

All patients were scanned with full MR imaging protocols, including an SWI sequence (VenBOLD; Philips Healthcare, Best, the Netherlands) on 1.5 and 3T scanners; parameters and distribution across scanners are included in Table 2. Patients were assigned to the different scanners on the basis of clinical availability; the proportions of patients scanned at 3T were the following: LBD,  $n = 15$ , 74%; AD,  $n = 7$ , 35%; MCI,  $n = 10$ , 59%; FTD,  $n = 13$ , 65%; and controls,  $n = 9$ , 43%.

Images were assessed by 2 neuroradiologists (S.H. with 16 years of experience, and S. Schwarz with 9 years of experience). Ratings were performed independently and blinded to diagnosis and the other raters' assessments. One month after independent ratings, a consensus rating, blinded to diagnosis, was performed

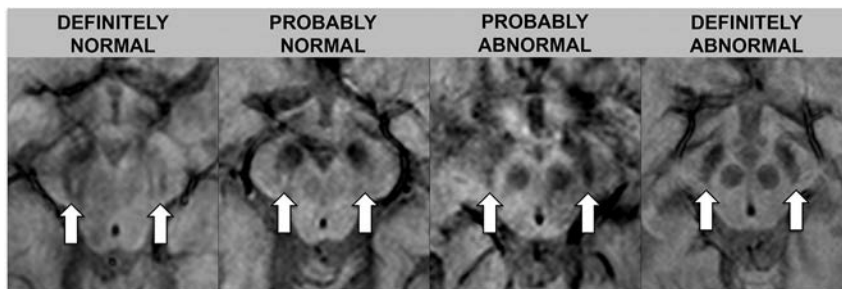


**FIG 1.** Rating scale for the swallow tail sign. The rating scale for the swallow tail sign is detailed in this figure; arrows indicate the normal/abnormal swallow tail signs on SWI sequences.

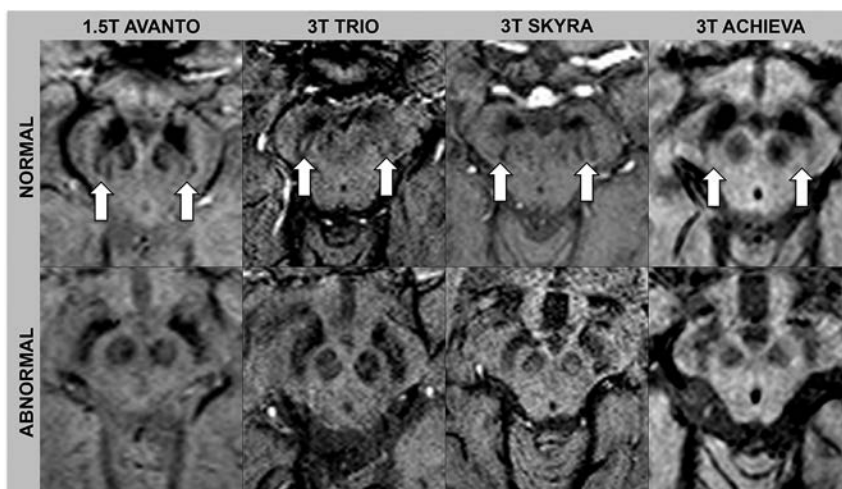


**FIG 2.** Normal and abnormal swallow tail signs across scanners. Arrows indicate the normal swallow tail signs on SWI sequences.

between the 2 initial raters in conjunction with a third neuro-radiologist (E.-M.L with 30 years of experience). The swallow tail sign was rated on an ordinal scale with 5 increments: 0 = unsure, 1 = definitely normal, 2 = probably normal, 3 = probably abnormal, 4 = definitely abnormal. For statistical analysis, the results were dichotomized into normal (ratings 1 and 2) and abnormal (ratings 3 and 4). Raters looked at the nigrosome 1 appearance, located in the posterior third part of the substantia nigra, resembling a swallow tail (Figs 1 and 2).<sup>11</sup> Cases with unilateral abnormal findings were considered abnormal. Figures 1 and 2 depict the swallow tail sign.

### Statistical Analysis

Descriptive data are presented as numbers and percentages. Rating increments for the swallow tail sign were dichotomized into normal (ratings 1 and 2) and abnormal (ratings 3 and 4). Sensitivity, specificity, negative and positive predictive values, and accuracy were calculated.  $\chi^2$  and Fischer exact tests were used for categoric data. Binary logistic regression analysis was used to see whether ratings could predict diagnosis. Diagnosis was set as the dependent variable with the controls as a reference. Rating was dichotomized into normal and abnormal and used as an independent variable. The regression model was controlled for field strength and section thickness (by adding them as covariates in our model). SPSS, Version 22.0 (IBM, Armonk, New York) was used for statistical analysis, and  $P < .05$  was set as the threshold of

significance, equaling a corrected level of 0.033 after adjustment for the false discovery rate according to the Benjamini-Hochberg procedure.<sup>21</sup>

### RESULTS

The  $\kappa$  between raters was 0.4, equaling a moderate agreement, on all scans, as well as on only 1.5T and 3T scans. Table 3 shows the distribution of ratings across raters and diagnoses. The distribution of normal and abnormal swallow tail signs varied significantly across diagnoses ( $P < .001$ ) (Table 3), and nonsignificantly across different MR imaging scanners ( $P = .138$ ) for both raters. An abnormal swallow tail sign was significantly more common in LBD than in all other diagnoses ( $P < .001$ ). The swallow tail sign was abnormal on 1.5 and 3T on consensus rating in the following: controls, 10% (95% CI 0%–23%); LBD, 63% (95% CI, 41%–85%); FTD, 35% (95% CI, 14%–56%); AD, 25% (95% CI, 6%–44%); and MCI, 6% (95% CI, 0%–12%) (Table 3). For rater 1, two patients (2%) had only one of their nigrosomes rated as abnormal, resulting in an abnormal case; the rest of the nigrosomes were bilaterally the same. For rater 2, the corresponding number was 3 (3%) patients. The cases mentioned were not the

same for the raters.

Table 4 shows sensitivity, specificity, positive predictive value, negative predictive value, and accuracies across raters and field strengths for LBD. The highest sensitivity and negative predictive value were descriptively obtained by rater 2 on 3T (Table 4). Similar values for AD, MCI, and FTD are seen in the On-line Table, showing that the swallow tail sign is only applicable in LBD. In binary logistic regression analysis, controlled for field strength and section thickness, the odds of having LBD with an abnormal swallow tail sign were significant; the swallow tail sign had no predictive value (ie, it was insignificant, in the other diagnoses; Table 5).

When comparing the number of abnormal swallow tail signs on 1.5- and 1.6-mm section thicknesses versus 2.0-mm, abnormal swallow tail signs were more frequently seen on 1.5- and 1.6-mm section thicknesses ( $P = .03$ ). Similarly, descriptively, sensitivity, specificity, positive predictive values, and accuracy were higher with 1.5- and 1.6-mm section thicknesses (Table 4).

### DISCUSSION

Considering that no other MR imaging markers for LBD exist, the swallow tail sign may be a useful complement in the diagnosis of LBD. A normal swallow tail sign has a high negative predictive value for exclusion of an LBD diagnosis. However, because 37% of patients with LBD had a normal swallow tail sign, the sign does

**Table 3: Distribution of the abnormal swallow tail sign across diagnoses<sup>a</sup>**

	Controls (n = 21)	LBD (n = 19)	FTD (n = 20)	AD (n = 20)	MCI (n = 17)
Abnormal, 1.5T and 3T (No.) (%)					
Rater 1	2 (10)	9 (47)	7 (35)	5 (25)	2 (12)
Rater 2	5 (24)	18 (95)	8 (40)	9 (45)	4 (24)
Consensus	2 (10)	12 (63)	7 (35)	5 (25)	1 (6)
1.5T	n = 12	n = 4	n = 7	n = 13	n = 7
Abnormal, 1.5T (No.) (%)					
Rater 1	2 (17)	1 (25)	3 (43)	3 (23)	2 (29)
Rater 2	4 (33)	4 (100)	1 (14)	6 (46)	1 (14)
Consensus	2 (17)	3 (75)	4 (57)	3 (23)	1 (14)
3T	n = 9	n = 15	n = 13	n = 7	n = 10
Rater 1	0 (0)	8 (53)	4 (31)	2 (29)	0 (0)
Rater 2	1 (11)	14 (93)	7 (54)	3 (43)	3 (30)
Consensus	0 (0)	9 (60)	3 (23)	2 (29)	0 (0)

<sup>a</sup>Rater 1, S.H.; rater 2, S.S. Missing cases represent unsure raters due to low-quality images.

**Table 4: Sensitivity, specificity, positive predictive value, negative predictive value, and accuracy for Lewy body dementia with the abnormal swallow tail sign**

	Sensitivity (%)	Specificity (%)	PPV (%)	NPV (%)	Accuracy (%)
1.5 and 3T					
Rater 1	50	79	36	87	74
Rater 2	95	66	41	98	72
Consensus	63	79	44	89	76
Consensus, 1.5- and 1.6-mm ST	69	91	75	88	84
Consensus, 2-mm ST	50	69	20	90	67
1.5T					
Rater 1, 1.5T	25	75	9	91	70
Rater 2, 1.5T	80	70	25	97	71
Consensus, 1.5T	60	72	23	93	71
3T					
Rater 1, 3T	57	84	57	84	76
Rater 2, 3T	100	61	50	100	72
Consensus, 3T	64	86	64	86	80

**Note:**—PPV indicates positive predictive value; NPV, negative predictive value; ST, section thickness.

**Table 5: Predictive role of an abnormal swallow tail sign in cognitive impairment<sup>a</sup>**

	LBD, OR (95% CI)	FTD, OR (95% CI)	AD, OR (95% CI)	MCI, OR (95% CI)
Rater 1	4 (1–14), <i>P</i> = .010	6 (1–39), <i>P</i> = .060	3 (1–17), <i>P</i> = .248	2 (0–14), <i>P</i> = .668
Rater 2	31 (4–244), <i>P</i> = .001	11 (0–276), <i>P</i> = .236	4 (1–20), <i>P</i> = .070	1 (0–4), <i>P</i> = .831
Consensus	9 (3–28), <i>P</i> < .001	7 (1–50), <i>P</i> = .060	3 (1–19), <i>P</i> = .229	1 (0–10), <i>P</i> = .746

**Note:**—OR indicates odds ratio.

<sup>a</sup>The regression model is controlled for field strength and section thickness.

not qualify as the sole diagnostic test. Accuracy and sensitivity increase with optimized imaging techniques.

To date, the swallow tail sign has mainly been studied in PD. An abnormal swallow tail sign has been shown to be a useful marker in PD with a 100% sensitivity and negative predictive value, 95% specificity, and 69% positive predictive value.<sup>11</sup> The swallow tail sign has not been shown to discriminate typical and atypical PD.<sup>22</sup> In LBD, the sensitivity and negative predictive value on 3T SWI has been shown to be 93%, with a 87% specificity and positive predictive value.<sup>23</sup> No studies exist examining the swallow tail sign in PD dementia. The lower positive predictive value and specificity, as reflected in our study, shows that the swallow tail sign may be abnormal even in other diseases and healthy individuals. However, values may be improved with optimized imaging sequences and techniques.

All our patients were included and had an MR imaging brain scan during their diagnostic work-up. The patients with LBD could thus be considered in their early stages of disease. Thus, this

may explain the number of patients rated with a normal swallow tail sign. A similar study with patients in later stages of disease would have been of interest, to see whether results differ. Furthermore, abnormal swallow tail signs were seen in a range of diagnoses, such as in AD and FTD. No study has assessed the distribution and associations of an abnormal swallow tail sign in a large-scale or prospectively acquired memory clinic cohort, to our knowledge. The reason for an abnormal swallow tail sign is not fully known and may be multifactorial. It may represent dopaminergic neuronal loss, neuromelanin loss, or a change in iron storage and oxidation.<sup>11,14,24</sup> As the hyperintense feature of the nigrosome 1 decreases, the surrounding hypointensity may increase; this change reduces the demarcation of the nigrosome 1. It would be interesting to see whether dementia-related gait changes, especially because they are more common in dementia than healthy aging,<sup>25</sup> are associated with an abnormal swallow tail sign. An abnormal swallow tail sign across dementia diagnoses may also suggest a large overlap in the pathophysiology of cognitive impairment.

Our results demonstrate interindividual variation in the assessment of the swallow tail sign. Despite the use of experienced neuroradiologists, our interrater agreement was moderate, and our interrater variability equals that of another study of swallow tail assessment in PD.<sup>22</sup> Consensus ratings resulted in values between both initial ratings. Rater 2 more readily called the swallow tail sign

abnormal and, consequently, had a higher sensitivity, at the price of a lower specificity, for LBD. Meanwhile consensus ratings were closer to those of rater 1, showing that rating of the swallow tail sign in a clinical setting is difficult. While the rating was clear and distinct between normal and abnormal in most cases, a substantial portion of patients had less clear findings. This outcome allows individual interpretation of when to call the swallow tail sign abnormal and reflects the challenge of assessing the swallow tail sign and using it as a diagnostic test. Adding to the difficulty of rating and probably lowering our agreement is the inclusion of different MR imaging scanners, field strengths, and section thicknesses in our study. However, this also contributes to our study being more clinically generalizable. Rating of the swallow tail sign, the only MR imaging marker with potential diagnostic value in LBD, should therefore be improved, to increase clinical utility and reliability. We suggest optimizing MR imaging parameters of SWI, including high spatial resolution and high contrast, which should be

standardized across MR imaging scanners. Interrater agreement and rating reliability may further be increased with established rating scales,<sup>11</sup> such as the one in Fig 1.

Field strength is of importance for the clinical applicability of the swallow tail sign. Accuracy has been shown to be higher at 7T, decreasing with 3T.<sup>26</sup> In our cohort, we included both 1.5 and 3T scans, and sensitivity, specificity, positive predictive value, and accuracy for LBD were higher on 3T. Nevertheless, even at 1.5T, the assessment of the swallow tail provided significant information for the diagnosis of LBD. In the absence of other established imaging findings, we argue that though ideally performed at 3T, assessment of the swallow tail sign at 1.5T may still provide added clinical value. Similarly, a thinner section thickness resulted in higher sensitivity for LBD and should be implemented for clinical imaging.

Limitations in our study include the use of multiple scanners and 1.5 and 3T field strengths. However, we performed our statistical analysis subdivided for the different field strengths, and the use of multiple scanners may better reflect the clinical reality. Besides, section thickness and field strength were both corrected for in our regression model. Including the pretest probability of the diagnoses included in our study would have added further insight into the diagnostic use of the swallow tail sign. It would also have increased the external validity of our study, because positive and negative predictive values are influenced by the prevalence of diseases in the population. Subjective cognitive impairment was used as a control group, and to date, clinical methods of detecting whether these individuals may have prodromal disease are scarce. "Subjective cognitive impairment" means patients with no observable clinical or pathologic findings, but with subjective feelings of cognitive decline. Thus, no disease was detected, but using healthy elderly as controls would have provided a cleaner control group. Strengths include a large and well-classified cohort and the use of experienced raters.

## CONCLUSIONS

The swallow tail sign may be a complement in the diagnosis of LBD but does not qualify as a sole diagnostic marker.

## REFERENCES

- Haller S, Garibotto V, Kövari E, et al. **Neuroimaging of dementia in 2013: what radiologists need to know.** *Eur Radiol* 2013;23:3393–404 CrossRef Medline
- McKeith I. **Dementia with Lewy bodies.** *Dialogues Clin Neurosci* 2004;6:333–41 Medline
- McVeigh C, Passmore P. **Vascular dementia: prevention and treatment.** *Clin Interv Aging* 2006;1:229–35 CrossRef Medline
- McKeith IG, Dickson DW, Lowe J, et al; Consortium on DLB. **Diagnosis and management of dementia with Lewy bodies: third report of the DLB Consortium.** *Neurology* 2005;65:1863–72 CrossRef Medline
- Mrak RE, Griffin WS. **Dementia with Lewy bodies: definition, diagnosis, and pathogenic relationship to Alzheimer's disease.** *Neuropsychiatr Dis Treat* 2007;3:619–25 Medline
- Mak E, Su L, Williams GB, et al. **Neuroimaging characteristics of dementia with Lewy bodies.** *Alzheimers Res Ther* 2014;6:18 CrossRef Medline
- Brown RK, Bohnen NI, Wong KK, et al. **Brain PET in suspected dementia: patterns of altered FDG metabolism.** *Radiographics* 2014;34:684–701 CrossRef Medline
- Binnewijzend MA, Kuijjer JP, Benedictus MR, et al. **Cerebral blood flow measured with 3D pseudocontinuous arterial spin-labeling MR imaging in Alzheimer disease and mild cognitive impairment: a marker for disease severity.** *Radiology* 2013;267:221–30 CrossRef Medline
- O'Brien JT, Firbank MJ, Davison C, et al. **18F-FDG PET and perfusion SPECT in the diagnosis of Alzheimer and Lewy body dementias.** *J Nucl Med* 2014;55:1959–65 CrossRef Medline
- Kwon DH, Kim JM, Oh SH, et al. **Seven-Tesla magnetic resonance images of the substantia nigra in Parkinson disease.** *Ann Neurol* 2012;71:267–77 CrossRef Medline
- Schwarz ST, Afzal M, Morgan PS, et al. **The "swallow tail" appearance of the healthy nigrosome: a new accurate test of Parkinson's disease—a case-control and retrospective cross-sectional MRI study at 3T.** *PLoS One* 2014;9:e93814 CrossRef Medline
- Bae YJ, Kim JM, Kim E, et al. **Loss of nigral hyperintensity on 3 Tesla MRI of parkinsonism: comparison with (123) I-FP-CIT SPECT.** *Mov Disord* 2016;31:684–92 CrossRef Medline
- Kim JM, Jeong HJ, Bae YJ, et al. **Loss of substantia nigra hyperintensity on 7 Tesla MRI of Parkinson's disease, multiple system atrophy, and progressive supranuclear palsy.** *Parkinsonism Relat Disord* 2016;26:47–54 CrossRef Medline
- Blazejewska AI, Schwarz ST, Pitiot A, et al. **Visualization of nigrosome 1 and its loss in PD: pathoanatomical correlation and in vivo 7 T MRI.** *Neurology* 2013;81:534–40 CrossRef Medline
- Fearnley JM, Lees AJ. **Ageing and Parkinson's disease: substantia nigra regional selectivity.** *Brain* 1991;114(pt 5):2283–301 CrossRef Medline
- Damier P, Hirsch EC, Agid Y, et al. **The substantia nigra of the human brain, I: nigrosomes and the nigral matrix, a compartmental organization based on calbindin D(28K) immunohistochemistry.** *Brain* 1999;122(pt 8):1421–36 CrossRef Medline
- Damier P, Hirsch EC, Agid Y, et al. **The substantia nigra of the human brain, II: patterns of loss of dopamine-containing neurons in Parkinson's disease.** *Brain* 1999;122(pt 8):1437–48 CrossRef Medline
- Haller S, Fällmar D, Larsson EM. **Susceptibility weighted imaging in dementia with Lewy bodies: will it resolve the blind spot of MRI?** *Neuroradiology* 2016;58:217–18 CrossRef Medline
- Shams S, Martola J, Granberg T, et al. **Cerebral microbleeds: different prevalence, topography, and risk factors depending on dementia diagnosis—the Karolinska Imaging Dementia Study.** *AJNR Am J Neuroradiol* 2015;36:661–66 CrossRef Medline
- Shams S, Granberg T, Martola J, et al. **Cerebrospinal fluid profiles with increasing number of cerebral microbleeds in a continuum of cognitive impairment.** *J Cereb Blood Flow Metab* 2016;36:621–28 CrossRef Medline
- Benjamini Y, Hochberg Y. **Controlling the false discovery rate: a practical and powerful approach to multiple testing.** *J R Stat Soc Series B Stat Methodol* 1995;57:289–300
- Meijer FJ, Steens SC, van Rumund A, et al. **Nigrosome-1 on susceptibility weighted imaging to differentiate Parkinson's disease from atypical parkinsonism: an in vivo and ex vivo pilot study.** *Pol J Radiol* 2016;81:363–69 CrossRef Medline
- Kamagata K, Nakatsuka T, Sakakibara R, et al. **Diagnostic imaging of dementia with Lewy bodies by susceptibility-weighted imaging of nigrosomes versus striatal dopamine transporter single-photon emission computed tomography: a retrospective observational study.** *Neuroradiology* 2017;59:89–98 CrossRef Medline
- Zecca L, Casella L, Albertini A, et al. **Neuromelanin can protect against iron-mediated oxidative damage in system modeling iron overload of brain aging and Parkinson's disease.** *J Neurochem* 2008;106:1866–75 Medline
- Beauchet O, Allali G, Berrut G, et al. **Gait analysis in demented subjects: interests and perspectives.** *Neuropsychiatr Dis Treat* 2008;4:155–60 Medline
- Cosottini M, Frosini D, Pesaresi I, et al. **Comparison of 3T and 7T susceptibility-weighted angiography of the substantia nigra in diagnosing Parkinson disease.** *AJNR Am J Neuroradiol* 2015;36:461–66 CrossRef Medline

# Pericortical Enhancement on Delayed Postgadolinium Fluid-Attenuated Inversion Recovery Images in Normal Aging, Mild Cognitive Impairment, and Alzheimer Disease

W.M. Freeze, R.S. Schnerr, W.M. Palm, J.F. Jansen, H.I. Jacobs, E.I. Hoff, F.R. Verhey, and W.H. Backes



## ABSTRACT

**BACKGROUND AND PURPOSE:** Breakdown of BBB integrity occurs in dementia and may lead to neurodegeneration and cognitive decline. We assessed whether extravasation of gadolinium chelate could be visualized on delayed postcontrast FLAIR images in older individuals with and without cognitive impairment.

**MATERIALS AND METHODS:** Seventy-four individuals participated in this study (15 with Alzheimer disease, 33 with mild cognitive impairment, and 26 with normal cognition). We assessed the appearance of pericortical enhancement after contrast administration, MR imaging markers of cerebrovascular damage, and medial temporal lobe atrophy. Three participants who were positive for pericortical enhancement (1 with normal cognition and 2 with mild cognitive impairment) were followed up for approximately 2 years. In vitro experiments with a range of gadolinium concentrations served to elucidate the mechanisms underlying the postcontrast FLAIR signals.

**RESULTS:** Postcontrast pericortical enhancement was observed in 21 participants (28%), including 6 individuals with Alzheimer disease (40%), 10 with mild cognitive impairment (30%), and 5 with normal cognition (19%). Pericortical enhancement was positively associated with age ( $P < .02$ ) and ischemic stroke ( $P < .05$ ), but not with cognitive status ( $P = .3$ ). Foci with enhanced signal remained stable across time in all follow-up cases. The in vitro measurements confirmed that FLAIR imaging is highly sensitive for the detection of low gadolinium concentrations in CSF, but not in cerebral tissue.

**CONCLUSIONS:** Postcontrast pericortical enhancement on FLAIR images occurs in older individuals with normal cognition, mild cognitive impairment, and dementia. It may represent chronic focal superficial BBB leakage. Future longitudinal studies are needed to determine its clinical significance.

**ABBREVIATIONS:** AD = Alzheimer disease; ApoE = apolipoprotein E; MCI = mild cognitive impairment; MMSE = Mini-Mental State Examination; MTA = medial temporal lobe atrophy

Alzheimer disease (AD) is the most common form of dementia, and is clinically characterized by progressive cognitive decline and associated functional impairment in daily living. Accumulating evidence suggests that microvascular dysregulation and BBB disruption are early events in the multifactorial disease cascade that leads to continuous neuronal loss.<sup>1,2</sup> During the past decades, the development of gadolinium-based contrast agents

has enabled detailed in vivo examination of BBB leakage by detection of extravasated gadolinium with postcontrast T1WI. Thus, previous studies reported subtle changes in vascular permeability in the cortex, white matter, and hippocampus in early-stage AD.<sup>3,4</sup> Small changes in the dynamics of contrast agent leakage in ventricular CSF have also been reported in AD.<sup>5</sup> It is likely that vascular permeability changes also occur in vessels adjacent to the CSF along the cortical surface or leptomeninges. However, T1-weighted BBB permeability imaging around the cortex in disease conditions with subtle changes to BBB integrity is probably difficult because the leptomeninges are highly vascularized and

Received December 12, 2016; accepted after revision April 19, 2017.

From the Department of Psychiatry and Neuropsychology (W.M.F., H.I.J., F.R.V.), Maastricht University, School for Mental Health and Neuroscience, Alzheimer Center Limburg, Maastricht, the Netherlands; Department of Radiology and Nuclear Medicine (W.M.F., R.S.S., J.F.J., W.M.P., W.H.B.), Maastricht University Medical Center, School for Mental Health and Neuroscience, Maastricht, the Netherlands; and Department of Neurology (E.I.H.), Zuyderland Medical Center Heerlen, Heerlen, the Netherlands.

This research was supported by Alzheimer Nederland (research grant WE-03-2012-40).

Paper previously presented in part at: International Congress on Vascular Dementia, October 16–18, 2015; Ljubljana, Slovenia; and Alzheimer's Association International Conference, July 22–28, 2016; Toronto, Ontario, Canada.

Please address correspondence to Whitney M. Freeze, MSc, Department of Psychiatry and Neuropsychology, School for Mental Health and Neuroscience, Maastricht University, PO Box 616, 6200MD, Maastricht, the Netherlands; e-mail: w.freeze@maastrichtuniversity.nl

 Indicates article with supplemental on-line table.

 Indicates article with supplemental on-line photos.

<http://dx.doi.org/10.3174/ajnr.A5273>

become relatively strongly enhanced due to high gadolinium concentrations within the blood vessels. Furthermore, when gadolinium chelate leaks into the CSF, convection and diffusion may dilute the contrast agent at concentrations that become too low to detect.

Delayed postcontrast FLAIR imaging yields up to 10-fold higher sensitivity compared with postcontrast T1WI for the detection of low amounts of gadolinium chelate in the CSF.<sup>6,7</sup> Previous studies that used postcontrast FLAIR imaging reported pericortical gadolinium leakage that appears as signal enhancement in the CSF in various clinical disease conditions with BBB leakage, including acute ischemic stroke and MS.<sup>8,9</sup> The application of the postcontrast FLAIR technique has not yet been evaluated in patients in memory clinics and in normal aging, to our knowledge.

The primary objective of this study was to explore the utility of postcontrast FLAIR imaging in identifying pericortical enhancement in AD, mild cognitive impairment (MCI), and age-matched cognitively healthy individuals. We hypothesized that pericortical BBB leakage is more common in patients with AD and MCI compared with cognitively healthy individuals and that it is associated with MR imaging markers of cerebrovascular damage. Finally, to investigate whether signal alterations could result from leakage of contrast medium into cortical tissue or into the CSF, we performed *in vitro* experiments to mimic the FLAIR signal effects of different concentrations of gadolinium in CSF and cerebral tissue.

## MATERIALS AND METHODS

### Participants

Patients were prospectively recruited at 2 memory clinics (Maastricht University Medical Center and Zuyderland Medical Center Heerlen) between November 2014 and December 2016, and healthy controls were enrolled via a local newspaper advertisement in the same period. Detailed neuropsychological assessment, medical history, and educational level<sup>10</sup> were recorded for all participants. Inclusion criteria for patients were a clinical diagnosis of subjective cognitive decline,<sup>11</sup> MCI<sup>12</sup> or AD,<sup>13</sup> and a Mini-Mental State Examination (MMSE)<sup>14</sup> score of  $\geq 20$ . Control participants reported no subjective cognitive impairment and were screened to ensure cognitive health (MMSE score,  $\geq 27$ ). Inclusion criteria for all participants were 55 years of age or older and eligibility for undergoing MR imaging and gadolinium contrast administration. Exclusion criteria for all participants included impaired renal function (estimated glomerular filtration rate of  $< 30$  mL/min) and the presence of psychiatric or neurologic disorders that might have caused the cognitive impairment, other than AD, cerebral small-vessel disease, or noninvalidating stroke. Participants with recent (eg,  $< 3$  months before inclusion) ischemic or hemorrhagic stroke were excluded. Informed consent was obtained from all participants before participation. This study was performed in accordance with the rules and regulations of the local institutional review boards and approved by the medical ethics committee in Maastricht.

### MR Imaging Protocol

MR images were acquired on a 3T MR imaging system with a 32-channel head coil (Achieva TX; Philips Healthcare, Best, the

Netherlands). The imaging protocol was relatively long because other sequences that are not relevant to this article were included, and it was split into 2 separate sessions for the participants' comfort. During the first session without contrast administration, 3D T1-weighted gradient-echo (TR/TE, 8/4 ms; acquisition matrix,  $256 \times 256$ ; 160 sections; 1-mm section thickness) and 3D T2-FLAIR (TR/TE/TI, 4800/290/1650 ms; acquisition matrix,  $256 \times 256$ ; 200 sections; 1-mm section thickness) images were acquired, as well as multisection T2-weighted TSE and T2-weighted fast-field echo images with a section thickness of 5 mm in the transverse plane. During a second session (median time between scans 2 days; interquartile range, 0–5.5 days), the same FLAIR sequence was acquired 16 minutes after intravenous administration of 0.1 mmol/kg of gadobutrol in the antecubital vein (injection rate, 3 mL/s; 20-mL saline flush).

### Image Analysis

Pericortical enhancement was defined as hyperintense signal substantially brighter than the proximal parenchymal signal intensity, occurring in the subarachnoid space on postcontrast FLAIR images, but not on precontrast images. Two raters blinded to clinical data (W.M.F., W.M.P.) independently evaluated the scans for the presence of pericortical enhancement. Discrepancies and cases of uncertainty (Cohen  $\kappa = 0.50$ ) were evaluated during consensus meetings, after which both raters agreed on all cases. When present, pericortical enhancement was classified according to vascular territory (anterior, middle, or posterior cerebral artery), hemisphere (left/right), location (within a sulcus, along the cortical convexity, or within the longitudinal fissure), and number of foci.

White matter hyperintensities were scored on precontrast FLAIR images according to the Fazekas scale.<sup>15</sup> Old lacunar infarcts were scored as subcortical round or ovoid structures of 3–15 mm in diameter with low signal intensity on FLAIR images and CSF-like signal intensity on T2WI.<sup>16</sup> Cerebral microbleeds were scored as round or ovoid areas of signal void with associated blooming on T2-weighted fast-field echo images in cortical or subcortical regions, excluding potential mimics such as bilateral iron/calcium deposits in the basal ganglia, bone, or vessel flow voids.<sup>17</sup> Old ischemic stroke of  $> 15$  mm was scored on T2-weighted TSE and FLAIR images, and old cerebral hemorrhage was scored on T2-weighted fast-field echo images. Medial temporal lobe atrophy (MTA) was rated bilaterally on coronal T1WI with a previously described visual rating scale.<sup>18</sup> The average score of the left and right sides was taken as the final MTA score. Vascular markers and MTA were scored by an experienced neuroradiologist (W.M.P.), who was blinded to clinical data.

### Genetic Risk Factor Assessment

Blood samples were collected and *apolipoprotein E* (*ApoE*) genotyping was performed with polymerase chain reaction. Individuals with at least 1  $\epsilon 4$  allele were classified as *ApoE4*-positive.

### Follow-Up

One cognitively healthy participant and 2 patients with MCI who were positive for pericortical enhancement were followed up after

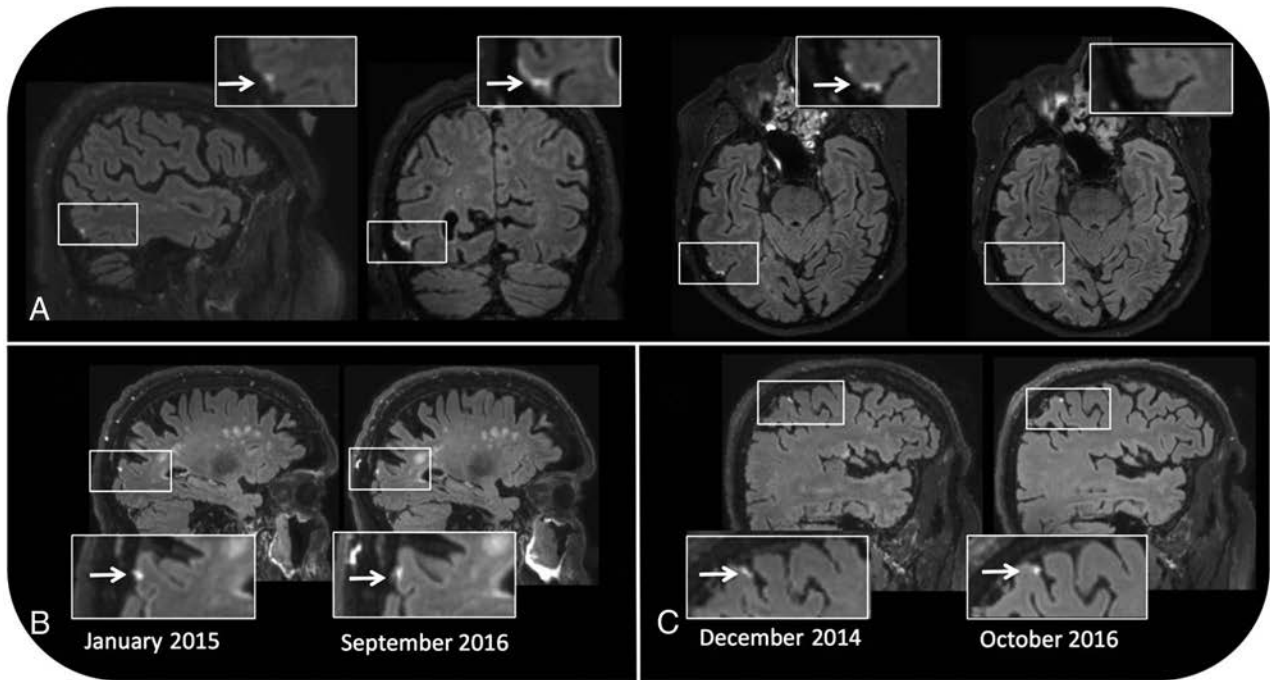


**FIG 1.** Pericortical enhancement is evident on sagittal, coronal, and transverse postcontrast FLAIR images of a 76-year-old male patient with MCI. No signal enhancement is apparent on the precontrast FLAIR image (*upper right*) (A). Pericortical enhancement remains stable across time in a male healthy control participant 87 years of age at baseline (B) and in a male MCI participant 71 years of age at baseline (C).

21–22 months. The same scan protocol was applied as described earlier, but all scans were acquired in 1 single session.

### Statistical Analyses

Differences between individuals with and without pericortical enhancement were assessed with the  $\chi^2$  or Fisher exact test (when applicable) for categorical variables. For continuous variables with a normal data distribution, independent 2-sample *t* tests were performed to compare the means of the 2 groups. Mann-Whitney *U* tests were performed in case of non-normal data distribution.

To assess differences between the diagnostic groups (cognitively normal, MCI, and AD), we performed ANOVA for continuous variables with normal data distribution and Kruskal-Wallis tests for continuous variables with non-normal data distribution. The  $\chi^2$  or Fisher exact test was used for categorical variables. A threshold of  $\alpha < .05$  was used to determine statistical significance, all *P* values were 2-tailed, and analyses were conducted with SPSS statistical software (Version 24.0; IBM, Armonk, New York).

### In Vitro Experiment

Gadobutrol was dissolved in demineralized water in plastic Falcon tubes (50 mL; Corning, Corning, New York) in different concentrations (0.004, 0.008, 0.016, 0.031, 0.063, 0.125, 0.250, 0.500, and 1.0 mmol/L), mimicking in vivo gadolinium concentrations with a range of leakage severity in the CSF. The same gadolinium concentrations were adopted for a solution mimicking cerebral tissue, which was prepared by dissolving 0.08-mmol/L  $MnCl_2$  in demineralized water. The T1 and T2 relaxation times of this  $MnCl_2$  solution were determined by using signal intensities from inversion recovery TSE images with TR = 3000 ms and varying TIs (50, 100, 200, 400, 600, 800, 1000, and 1500 ms) and T2-

weighted images with a fixed TR = 453 ms and varying TEs (20, 40, 60, 80, 100, 120, 140, 160, 180, and 200 ms). The T1 and T2 relaxation times (On-line Fig 1) of the tissue phantom approximated previously reported values of the cerebral cortex at 3T with 1170 and 122 ms, respectively.<sup>19</sup>

The samples mimicking CSF and tissue with different concentrations of gadolinium were scanned with the T1 and FLAIR sequences described above.

## RESULTS

### Neuroradiologic Imaging

Seventy-four participants with a mean age of  $71.2 \pm 6.2$  years were enrolled in this study, including 26 cognitively healthy participants (13 healthy controls and 13 with subjective cognitive decline), 33 with MCI, and 15 with AD. Participants' characteristics according to cognitive status (normal cognition, MCI, or AD) are provided in the On-line Table.

Twenty-one individuals showed evidence of abnormal pericortical enhancement on postcontrast FLAIR images (Fig 1). Overall, there were 32 foci, among which 10 (31%) were located within the posterior, 9 (28%) within the middle, and 13 (41%) within the anterior cerebral artery territory. Fifteen foci (47%) were located in the left and 17 (53%), in the right hemisphere. Most foci were located on the cortical convexity (12/32, 38%) or within a sulcus (12/32, 38%), but 1 (3%) traversed several sulci and 7 (22%) were located within the longitudinal fissure. Pericortical enhancement was observed as a single focus in most cases (13/21, 62%). Three subjects with MCI and 2 subjects with dementia showed 2 foci, and 1 subject with MCI and 2 subjects with AD showed 3 foci (Fig 2).

In the 3 subjects positive for enhancement with a follow-up

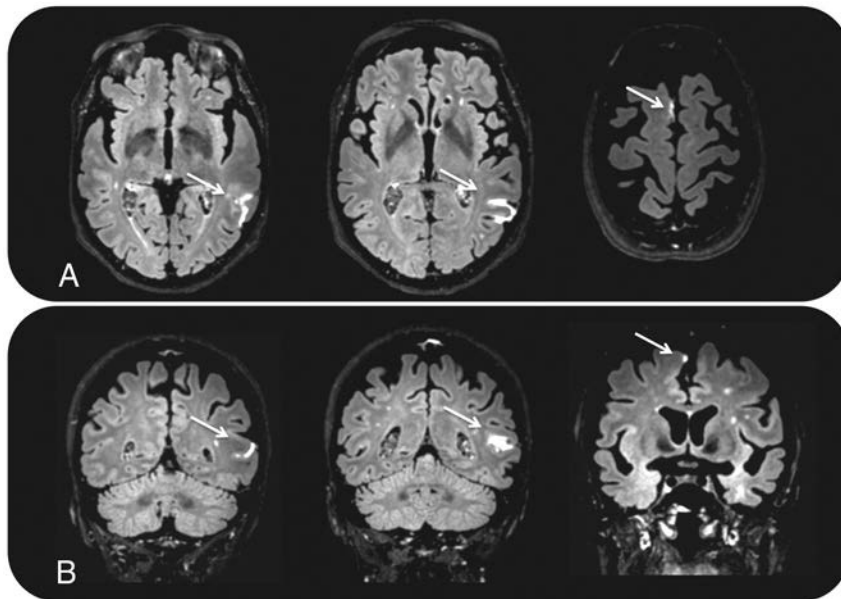


**FIG 2.** Two foci of pericortical enhancement on transverse (A) and coronal (B) postcontrast FLAIR images in a 73-year-old female participant with AD.

#### Characteristics of pericortical enhancement

	Pericortical Enhancement		P Value
	Yes (n = 21)	No (n = 53)	
<b>Demographics</b>			
Age (mean) (SD) (yr)	73.5 (4.8)	70.2 (6.4)	.02 <sup>a</sup>
Female sex (No) (%)	10 (48)	22 (42)	.8
<b>Clinical subtype (No) (%)</b>			
Normal cognition	5 (19)	21 (81)	.3
MCI	10 (30)	23 (70)	
AD	6 (40)	9 (60)	
<b>MRI characteristics</b>			
Fazekas scale score (median) (IQR)	1.0 (1.0–3.0)	1.0 (1.0–2.0)	.4
Lacunar infarct present (No) (%)	7 (33)	8 (15)	.11
Ischemic stroke present (No) (%)	4 (19)	3 (6)	.18
Lacunar and/or ischemic stroke present (No) (%)	9 (43)	10 (19)	.04 <sup>a</sup>
Microbleed present (No) (%)	2 (10)	7 (13)	1.0
Hemorrhagic stroke present (No) (%)	1 (5)	1 (2)	1.0
MTA score (median) (IQR)	1.0 (0.5–2.25)	0.5 (0–1.5)	.08
Gadobutrol dosage (mean) (SD) (mL)	7.3 (1.2)	7.3 (1.1)	.98
<b>Cognitive performance</b>			
MMSE (median) (IQR) <sup>b</sup>	28 (25–28)	28 (26–29)	.97
<b>Genotype</b>			
ApoE4-positive (No) (%) <sup>c</sup>	6 (30)	25 (47)	.3

**Note:**—IQR indicates interquartile range.

<sup>a</sup> Significant.

<sup>b</sup> Data were missing for 2 cases.

<sup>c</sup> Data were missing for 1 case.

time between 21 and 22 months, the foci remained stable across time regarding location, size, and shape (Fig 1).

In addition to the pericortical foci, 1 focus of signal enhancement was found in what appeared to be a perivascular space on the post-contrast but not on the precontrast FLAIR images (On-line Fig 2). No signal attenuation was observed in other fluid-containing structures, including lacunar infarcts, the ventricular system, or the eyes.

The group characteristics of individuals with pericortical enhancement are summarized in the Table. The prevalence per diagnostic group was 5/26 (19%) in cognitively healthy individuals, 10/33 (30%) in individuals with MCI, and 6/15 (40%) in individ-

uals with AD. Although the prevalence of pericortical enhancement was higher in the AD and MCI groups compared with the cognitively healthy individuals, there were no statistically significant group differences (Fisher exact test,  $P = .3$ ). Individuals with pericortical enhancement were significantly older ( $t[50] = 2.4$ ,  $P < .02$ ) and more often had ischemic stroke ( $\chi^2 = 4.5$ ,  $df = 2$ ,  $P = .04$ ) when lacunar infarct and ischemic stroke data were pooled. No associations were apparent among pericortical enhancement and sex, amount of contrast agent administered, MMSE score, ApoE genotype, and other MR imaging markers of cerebrovascular damage (Table). The location of pericortical enhancement did not correspond to the location of other MR imaging markers of cerebrovascular damage.

#### In Vitro Measurements

The phantom imaging experiment shows that relatively low concentrations of gadolinium in the CSF appear bright on FLAIR images, while at higher concentrations, the signal declines. On T1WI, low concentrations of gadolinium in the CSF appear dark, while at higher concentrations, the signal increases. In contrast, the FLAIR images of tissue phantoms with low gadolinium concentrations show only very little signal enhancement, while the signal decreases at higher concentrations. On T1WI, a gradual signal increase can be observed with increasing gadolinium concentrations (On-line Figs 3 and 4).

#### DISCUSSION

Delayed postcontrast FLAIR imaging revealed pericortical signal enhancement in 28% of all participants who underwent MR imaging. This signal enhancement likely results from leakage of gadolinium chelate through

cortical or leptomeningeal vessels and, as such, represents a marker for focal loss of BBB integrity. Although pericortical enhancement occurred more often in MCI or AD compared with cognitively healthy individuals, there were no statistical group differences. Pericortical enhancement was associated with increasing age and ischemic stroke. Most interesting, in the 3 subjects who were followed up, the pericortical enhancement remained stable for 21–22 months. A possible explanation for this imaging phenomenon is chronic inflammation with BBB disruption in the leptomeninges or superficial cortical vessels.

The potential of postcontrast FLAIR imaging for the detection of contrast agent leakage through the BBB was already described by Mathews et al in 1999.<sup>20</sup> Since then, several studies on the application of this technique have been published. Many of these describe postischemic diffuse enhancement in the CSF in 1 or both hemispheres, a phenomenon called “hyperintense acute reperfusion marker.”<sup>7,9,21,22</sup> Similar to its acute presentation after ischemic stroke or transient ischemic attack, the appearance of the hyperintense acute reperfusion marker has also been described after hemorrhagic stroke, cardiac surgery, and carotid revascularization.<sup>23-25</sup> These findings suggest a common process of rapid pericortical BBB leakage following cerebral ischemia or hypoxia. In addition to its relationship with ischemia, pericortical BBB leakage on postcontrast FLAIR images has been described in infectious diseases of the CNS, including meningitis and MS.<sup>8,26</sup> Together, these studies suggest that (chronic) hypoxic and/or inflammatory processes in the cortex and leptomeninges may underlie this neuroimaging phenomenon. Pericortical enhancement is likely not specific for a particular disease and also occurs in the context of normal aging.<sup>27,28</sup>

We found no association between pericortical enhancement and diagnostic group, *ApoE* genotype, MTA score, or global cognition. Hence, the clinical relevance of pericortical enhancement in our study population remains unclear. Although delayed postcontrast FLAIR imaging is not routinely used in clinical examinations, the CSF signal change should not be confused with other causes of signal increase in the subarachnoid space on FLAIR images such as subarachnoid hemorrhage or meningeal metastasis.<sup>29</sup>

Because the signal enhancement on postcontrast FLAIR images appears very close to the cortical surface, we aimed to assess whether the focal enhancement occurs in the CSF or cortical tissue. Our phantom study showed that FLAIR imaging is relatively insensitive for the detection of gadolinium in brain tissue, while strong signal enhancement is observed in CSF, mimicking phantom solutions at low gadolinium concentrations (ie, 10–500  $\mu\text{mol/L}$ ). We therefore interpret the pericortical enhancement as leakage and accumulation of low gadolinium concentrations in the pericortical CSF.

Previous studies have shown 2 advantages of postcontrast FLAIR imaging over T1WI in detecting pericortical BBB leakage. First, postcontrast FLAIR imaging is superior to postcontrast T1WI in detecting low gadolinium concentrations (ie, 10–500  $\mu\text{mol/L}$ ) in the CSF.<sup>7,20</sup> Because of the long T1 relaxation time of CSF, FLAIR is relatively sensitive to subtle shortening of the T1 relaxation time caused by low concentrations of gadolinium. Second, previous work has shown that unlike T1WI, FLAIR is rather insensitive to the effects of contrast medium within blood vessels because the shortening of the T2 relaxation time at higher gadolinium concentrations and the effects of blood flow both result in a strong signal decay.<sup>26</sup>

The strengths of this study include the availability of both pre- and postcontrast FLAIR images obtained in individuals with a wide range of cognitive performance. The availability of other MR imaging sequences allowed us to look for associations between postcontrast FLAIR enhancement and various markers of cerebrovascular damage. The timeframe of 16 minutes between contrast injection and FLAIR imaging proved suitable for detecting

pericortical enhancement in a relatively high number (ie, 28%) of participants in our study.

Limitations of this study include the relatively small sample size, which limits our ability to draw conclusions about the presence or absence of associations between BBB leakage and variables of interest. Because we did not include markers more specific for neurodegeneration than MTA and AD, the biomarkers amyloid  $\beta$  and  $\tau$  were not measured, and their association with pericortical enhancement remains unknown. Although the sensitivity of postcontrast FLAIR imaging compared with T1WI was assessed in our phantom study, we did not set out to make this comparison in vivo. We expect that the enhancement of the leptomeningeal vessels due to intravascular gadolinium complicates the detection of focal pericortical enhancement on postcontrast T1-weighted images.

Future studies are needed to elucidate the pathophysiology and clinical relevance of pericortical BBB leakage in relation to neurodegeneration. The potential of pericortical enhancement as a biomarker for cognitive decline and dementia could be explored by future studies that compare the cognitive profile of individuals with and without pericortical enhancement within the same diagnostic group (ie, normal cognition, MCI, dementia) and by following individuals across time to assess conversion rates to MCI or dementia. The optimal timeframe between contrast injection and scan acquisition remains to be explored, as well as whether this phenomenon also occurs in younger individuals. In the future, larger study samples and longitudinal studies may shed light on the clinical consequences following signs of pericortical BBB disruption in aging, dementia, and other disorders of the CNS.

## CONCLUSIONS

This study identified focal pericortical BBB leakage on delayed postcontrast FLAIR images in a substantial proportion of patients with AD and MCI as well as cognitively healthy participants. Pericortical signal enhancement was associated with increasing age and previous ischemic stroke. In all 3 follow-up cases, the focal BBB leakage persisted and remained stable across time. The results of our study demonstrate the suitability of postcontrast FLAIR imaging as a tool for detecting possible chronic pericortical vascular leaks in a memory clinic setting and in cognitively healthy older individuals.

## ACKNOWLEDGMENTS

We thank Danique Hellebrekers and Tiny Simons for their assistance with participant inclusion; Jos Slenter, Ivo Pooters, and Joost Löring for their contribution to the phantom study; and Paul Hofman for his advice on image interpretation.

Disclosures: Whitney M. Freeze—RELATED: Grant: Alzheimer Nederland, Comments: This grant supports study costs including MRI scanning, analysis of blood samples, and my salary as a PhD student in the Netherlands\*; Support for Travel to Meetings for the Study or Other Purposes: Alzheimer Nederland, Comments: I received €500 to support my attendance to present part of this work at the Alzheimer’s Association International Conference that took place in Toronto, Ontario, Canada in July 2016. Heidi I. Jacobs—RELATED: Grant: Alzheimer Nederland; Comments: money for MRI scans; UNRELATED: Employment: Netherlands Organisation for Scientific Research, Comments: grant for salary of Dr Heidi Jacobs\*; Grants/Grants Pending: Memorabel ZonMw, Comments: grant submitted on December 8\*; Travel/Accommodations/Meeting Expenses Unrelated to Activities Listed: Alzheimer’s Association, Human Amyloid Imaging, Alzheimer Nederland, Comments: travel fellowship for conference.\* Frans R. Verhey—UNRELATED: Grant: ZonMw National

## REFERENCES

1. Zlokovic BV. **Neurovascular pathways to neurodegeneration in Alzheimer's disease and other disorders.** *Nat Rev Neurosci* 2011;12:723–38 CrossRef Medline
2. Iturria-Medina Y, Sotero RC, Toussaint PJ, et al; Alzheimer's Disease Neuroimaging Initiative. **Early role of vascular dysregulation on late-onset Alzheimer's disease based on multifactorial data-driven analysis.** *Nat Commun* 2016;7:11934 CrossRef Medline
3. Montagne A, Barnes SR, Sweeney MD, et al. **Blood-brain barrier breakdown in the aging human hippocampus.** *Neuron* 2015;85:296–302 CrossRef Medline
4. van de Haar HJ, Burgmans S, Jansen JF, et al. **Blood-brain barrier leakage in patients with early Alzheimer disease.** *Radiology* 2016;281:527–35 CrossRef Medline
5. Starr JM, Farrall AJ, Armitage P, et al. **Blood-brain barrier permeability in Alzheimer's disease: a case-control MRI study.** *Psychiatry Res* 2009;171:232–41 CrossRef Medline
6. Mamourian AC, Hoopes PJ, Lewis LD. **Visualization of intravenously administered contrast material in the CSF on fluid-attenuated inversion-recovery MR images: an in vitro and animal-model investigation.** *AJNR Am J Neuroradiol* 2000;21:105–11 Medline
7. Köhrmann M, Struffert T, Frenzel T, et al. **The hyperintense acute reperfusion marker on fluid-attenuated inversion recovery magnetic resonance imaging is caused by gadolinium in the cerebrospinal fluid.** *Stroke* 2012;43:259–61 CrossRef Medline
8. Absinta M, Vuolo L, Rao A, et al. **Gadolinium-based MRI characterization of leptomeningeal inflammation in multiple sclerosis.** *Neurology* 2015;85:18–28 CrossRef Medline
9. Latour LL, Kang DW, Ezzeddine MA, et al. **Early blood-brain barrier disruption in human focal brain ischemia.** *Ann Neurol* 2004;56:468–77 CrossRef Medline
10. Verhage F. **Intelligence and age in a Dutch sample.** *Human Development* 1965;8:238–45 CrossRef
11. Jessen F, Amariglio RE, van Boxtel M, et al; Subjective Cognitive Decline Initiative (SCD-I) Working Group. **A conceptual framework for research on subjective cognitive decline in preclinical Alzheimer's disease.** *Alzheimers Dement* 2014;10:844–52 CrossRef Medline
12. Petersen RC. **Mild cognitive impairment as a diagnostic entity.** *J Intern Med* 2004;256:183–94 CrossRef Medline
13. McKhann G, Drachman D, Folstein M, et al. **Clinical diagnosis of Alzheimer's disease: report of the NINCDS-ADRDA Work Group under the auspices of Department of Health and Human Services Task Force on Alzheimer's Disease.** *Neurology* 1984;34:939–44 CrossRef Medline
14. Folstein MF, Folstein SE, McHugh PR. **"Mini-Mental State": a practical method for grading the cognitive state of patients for the clinician.** *J Psychiatr Res* 1975;12:189–98 CrossRef Medline
15. Fazekas F, Chawluk JB, Alavi A, et al. **MR signal abnormalities at 1.5 T in Alzheimer's dementia and normal aging.** *AJR Am J Roentgenol* 1987;149:351–56 CrossRef Medline
16. Wardlaw JM, Smith EE, Biessels GJ, et al; STandards for Reporting Vascular changes on nEuroimaging (STRIVE v1). **Neuroimaging standards for research into small vessel disease and its contribution to ageing and neurodegeneration.** *Lancet Neurol* 2013;12:822–38 CrossRef Medline
17. Greenberg SM, Vernooij MW, Cordonnier C, et al; Microbleed Study Group. **Cerebral microbleeds: a guide to detection and interpretation.** *Lancet Neurol* 2009;8:165–74 CrossRef Medline
18. Scheltens P, Leys D, Barkhof F, et al. **Atrophy of medial temporal lobes on MRI in "probable" Alzheimer's disease and normal ageing: diagnostic value and neuropsychological correlates.** *J Neurol Neurosurg Psychiatry* 1992;55:967–72 CrossRef Medline
19. Wansapura JP, Holland SK, Dunn RS, et al. **NMR relaxation times in the human brain at 3.0 Tesla.** *J Magn Reson Imaging* 1999;9:531–38 CrossRef Medline
20. Mathews VP, Caldemeyer KS, Lowe MJ, et al. **Brain: gadolinium-enhanced fast fluid-attenuated inversion-recovery MR imaging.** *Radiology* 1999;211:257–63 CrossRef Medline
21. Warach S, Latour LL. **Evidence of reperfusion injury, exacerbated by thrombolytic therapy, in human focal brain ischemia using a novel imaging marker of early blood-brain barrier disruption.** *Stroke* 2004;35:2659–61 CrossRef Medline
22. Förster A, Wenz H, Groden C. **Hyperintense acute reperfusion marker on FLAIR in a patient with transient ischemic attack.** *Case Rep Radiol* 2016;2016:9829823 CrossRef Medline
23. Kidwell CS, Burgess R, Menon R, et al. **Hyperacute injury marker (HARM) in primary hemorrhage: a distinct form of CNS barrier disruption.** *Neurology* 2011;77:1725–28 CrossRef Medline
24. Merino JG, Latour LL, Tso A, et al. **Blood-brain barrier disruption after cardiac surgery.** *AJNR Am J Neuroradiol* 2013;34:518–23 CrossRef Medline
25. Cho AH, Suh DC, Kim GE, et al. **MRI evidence of reperfusion injury associated with neurological deficits after carotid revascularization procedures.** *Eur J Neurol* 2009;16:1066–69 CrossRef Medline
26. Fukuoka H, Hirai T, Okuda T, et al. **Comparison of the added value of contrast-enhanced 3D fluid-attenuated inversion recovery and magnetization-prepared rapid acquisition of gradient echo sequences in relation to conventional postcontrast T1-weighted images for the evaluation of leptomeningeal diseases at 3T.** *AJNR Am J Neuroradiol* 2010;31:868–73 CrossRef Medline
27. Erdő F, Denes L, de Lange E. **Age-associated physiological and pathological changes at the blood-brain barrier: a review.** *J Cereb Blood Flow Metab* 2017;37:4–24 CrossRef Medline
28. Farrall AJ, Wardlaw JM. **Blood-brain barrier: ageing and microvascular disease—systematic review and meta-analysis.** *Neurobiol Aging* 2009;30:337–52 CrossRef Medline
29. Stuckey SL, Goh TD, Heffernan T, et al. **Hyperintensity in the subarachnoid space on FLAIR MRI.** *AJR Am J Roentgenol* 2007;189:913–21 CrossRef Medline

# How Common Is Signal-Intensity Increase in Optic Nerve Segments on 3D Double Inversion Recovery Sequences in Visually Asymptomatic Patients with Multiple Sclerosis?

T. Sartoretti, E. Sartoretti, S. Rauch, C. Binkert, M. Wyss, D. Czell, and S. Sartoretti-Schefer

## ABSTRACT

**BACKGROUND AND PURPOSE:** In postmortem studies, subclinical optic nerve demyelination is very common in patients with MS but radiologic demonstration is difficult and mainly based on STIR T2WI. Our aim was to evaluate 3D double inversion recovery MR imaging for the detection of subclinical demyelinating lesions within optic nerve segments.

**MATERIALS AND METHODS:** The signal intensities in 4 different optic nerve segments (ie, retrobulbar, canalicular, prechiasmatic, and chiasm) were evaluated on 3D double inversion recovery MR imaging in 95 patients with MS without visual symptoms within the past 3 years and in 50 patients without optic nerve pathology. We compared the signal intensities with those of the adjacent lateral rectus muscle. The evaluation was performed by a student group and an expert neuroradiologist. Statistical evaluation (the Cohen  $\kappa$  test) was performed.

**RESULTS:** On the 3D double inversion recovery sequence, optic nerve segments in the comparison group were all hypointense, and an isointense nerve sheath surrounded the retrobulbar nerve segment. At least 1 optic nerve segment was isointense or hyperintense in 68 patients (72%) in the group with MS on the basis of the results of the expert neuroradiologist. Student raters were able to correctly identify optic nerve hypersignal in 97%.

**CONCLUSIONS:** A hypersignal in at least 1 optic nerve segment on the 3D double inversion recovery sequence compared with hyposignal in optic nerve segments in the comparison group was very common in visually asymptomatic patients with MS. The signal-intensity rating of optic nerve segments could also be performed by inexperienced student readers.

**ABBREVIATION:** DIR = double inversion recovery

MR imaging contributes to not only the diagnosis and differential diagnosis of MS but also the monitoring and follow-up of patients.<sup>1</sup> T1-weighted postcontrast, T2-weighted, proton-density, FLAIR, and double inversion recovery (DIR) images are recommended to detect acute and chronic demyelinating lesions in typical locations.<sup>1-9</sup>

Acute optic neuritis is an inflammatory demyelination of the optic nerve causing acute visual loss.<sup>10-13</sup> After recovery, patients are often visually asymptomatic, but careful visual testing by vi-

sually evoked potentials, optical coherence tomography, and visual disability evaluation may reveal persistent slight visual deficits.<sup>14-17</sup> These deficits are also observed in patients without any history of previous acute optic neuritis due to a suspected subclinical disease known as subclinical optic nerve demyelination.<sup>14-17</sup>

Acute optic neuritis is easily diagnosed on MR imaging by focal nerve swelling and segmental T2-weighted hyperintensity, especially on STIR images or on fat-suppressed T2-weighted images and by segmental gadolinium enhancement on T1-weighted fat-suppressed images.<sup>10,18-22</sup> The enhancement is present for a mean of 30 days after the onset of visual symptoms.<sup>21,23-31</sup>

Subclinical optic nerve demyelination, however, is not easily visible on MR imaging. Routine T2-weighted images without fat suppression and contrast-enhanced T1-weighted FSE images do not show any signal abnormality in the affected optic nerve. Fat-suppressed T2-weighted FSE images, especially STIR T2-weighted images, may detect a signal-intensity abnormality in subclinical optic nerve demyelination.<sup>23,32,33</sup> The highly diagnostic value of fat-suppressed FLAIR images and fat-suppressed 3D

Received February 16, 2017; accepted after revision April 12.

From the Institut für Radiologie (T.S., E.S., S.R., C.B., M.W., S.S.-S.) and Klinik für Innere Medizin (D.C.), Abteilung für Neurologie, Kantonsspital Winterthur, Winterthur, Switzerland.

Thomas Sartoretti and Elisabeth Sartoretti contributed equally to this article. Institutional review board approval was obtained by the ethics commission of Kanton Zürich on September 26, 2016; Basec No. 2016-01396.

Please address correspondence to Sabine Sartoretti-Schefer, MD, Institute of Radiology, Kantonsspital Winterthur, Brauerstr 15, 8401 Winterthur, Switzerland; e-mail: sabine.sartoretti@ksw.ch

<http://dx.doi.org/10.3174/ajnr.A5262>

DIR images in the detection of any pathologic signal intensity in the optic nerve has been evaluated in acute optic nerve demyelination.<sup>10,34,35</sup> In a few patients with subclinical optic nerve demyelination, signal-intensity abnormalities have been reported on 3D FLAIR.<sup>34</sup> However, there are few data about the use of the 3D DIR sequence in the evaluation of subclinical optic nerve demyelination.<sup>36</sup>

In our department, patients with MS are routinely and regularly monitored for disease progression by a standard protocol with 3D FLAIR, 3D DIR, T2-weighted FSE, and 3D T1-weighted postcontrast images. 3D DIR is added to our standard protocol for improved detection of juxtacortical, cortical, and infratentorial demyelinating lesions.<sup>1-9</sup> On the basis of postmortem and clinical studies having already shown a high percentage of subclinical optic nerve demyelination with ongoing axonal loss in patients with MS,<sup>37-41</sup> we wanted to test 2 hypotheses: first, that it is possible to detect signal-intensity changes in optic nerve segments on the 3D DIR sequence without the additional application of a STIR T2-weighted sequence over the orbits in patients with MS without a history of clinically obvious visual loss and without a history of acute optic neuritis during the previous 3 years; and second, that the signal-intensity changes on 3D DIR are so obvious that even inexperienced readers can detect them. This second hypothesis is important because in our department, MR imaging examinations of patients with MS are evaluated not only by trained neuroradiologists but also general radiologists. Therefore, it is desirable that the lack of neuroradiologic experience be compensated by the application of an easily readable MR image, and the 3D DIR sequence is routinely acquired in our department for the follow-up of patients with MS.

For comparison, the signal intensities of normal healthy optic nerve segments in patients evaluated by the identical 3D DIR sequence for different diseases (ie, epileptic seizures and posttraumatic sequelae) were analyzed as well.

## MATERIALS AND METHODS

From November 2012 to September 2016, cerebral 3D DIR images were obtained on a 3T MR imaging unit, Achieva (Philips Healthcare, Best, the Netherlands), in both a comparison group and the group of patients with MS.

The comparison group consisted of 50 patients (30 females, 20 males; mean age, 42.5 years; range, 13–78 years) evaluated for epileptic seizures or posttraumatic sequelae after head trauma without any known optic nerve pathology.

The group of patients with MS comprised 95 patients (68 females and 27 males; mean age, 44.5 years; range, 16–77 years) without clinically obvious visual loss and without any history of previous optic neuritis during the past 3 years. The diagnosis of MS had been present in these patients for a mean of 8.9 years (range, 4.2–26.7 years). Clinical data were obtained with our hospital information system.

In all patients, the 3D DIR sequence was acquired in the sagittal plane. The parameters of this sequence are presented in Table 1. Coronal reconstructions with 2-mm section thickness and 2-mm increments were performed parallel to the long axis of the brain stem covering the orbits and the whole brain.

The optic nerve is divided into 4 segments (ie, the retrobulbar

**Table 1: Imaging parameters of the 3D DIR sequence**

	Double Inversion Recovery
Acquisition mode	3D TSE
Acquisition plane	Sagittal
Coverage	Whole head
Reconstructions, section thickness (mm)	Coronal, 2
TR/TE (ms)	5500/246
T1 (ms)	2550/450
FOV (mm)	250 × 250 × 195
Matrix	240 × 240 × 310
Acquired voxel size (mm)	1.2 × 1.2 × 0.65
No. of sections	300
Fat suppression	SPIR
NEX	2
Acquisition time	6 min 19 sec

**Note:**—SPIR indicates spectral presaturation with inversion recovery.

segment within the orbit, the canalicular segment as the nerve passes through the bony optic canal, the prechiasmatic segment within the suprasellar cistern, and the chiasm). Both prechiasmatic segments join at the optic chiasm.<sup>23,42</sup> The term optic system comprises all optic nerve segments.

The evaluation of the signal intensity of the optic nerve segments in both the comparison group and the group of patients with MS was by visual inspection. First, a bilateral analysis of the signal intensity of the 4 optic nerve segments on 3D DIR was performed in the asymptomatic comparison group. Second, the signal intensity of the 4 optic nerve segments on 3D DIR in the group of patients with MS was evaluated.

The signal intensity was separately evaluated for the left and the right optic nerves and for the optic nerve sheath. In the comparison group, 100 retrobulbar, 100 canalicular, and 100 prechiasmatic nerve segments and 50 chiasms were evaluated. In the group of patients with MS, 190 retrobulbar, 190 intracanalicular, and 190 prechiasmatic nerve segments and 95 chiasms were analyzed. The signal intensity of the optic nerve segments and of the optic nerve sheath was rated as hypointense, isointense, or hyperintense compared with the signal intensity of the directly adjacent lateral rectus muscle, thus allowing an easy comparison.

The signal intensity was jointly evaluated by a group of 2 students (T.S. and E.S.) inexperienced in the evaluation of MR images and by an expert neuroradiologist with 23 years of experience (S.S.-S.). The 2 students had been previously instructed and trained by the expert neuroradiologist by jointly performing correct signal-intensity ratings in 15 randomly chosen MR imaging examinations not included in this study.

The level of the interobserver agreement for the detection of signal abnormalities, considering the different nerve segments, was determined on the basis of the Cohen  $\kappa$  test, and the results are shown in Tables 2 and 3. The  $\kappa$  values were interpreted as follows<sup>10</sup>: A  $\kappa$  value of zero indicated poor agreement; a  $\kappa$  value of 0.01–0.20, minor agreement; a  $\kappa$  value of 0.21–0.40, fair agreement; a  $\kappa$  value of 0.41–0.60, moderate agreement; a  $\kappa$  value of 0.61–0.80, good agreement; and a  $\kappa$  value of 0.81–1, excellent agreement. Comparisons of  $\kappa$  values were performed to determine whether the agreements were different for the evaluation of optic nerve signal abnormality.

This retrospective study with the number Basec 2016–01396 was approved by the institutional review board Kantonale Ethik-

**Table 2:  $\kappa$  values and their confidence intervals for 3D DIR, based on nerve segments in the group of patients with MS**

3D DIR (No. of Valid Cases)	Symmetric Measures					
	Value MoA ( $\kappa$ )	Asymp. SE <sup>a</sup>	Approx. T <sup>b</sup>	Approx. Sig.	Exact Sig.	95% CI
Retrolubar (190)	.942	.023	15.091	.000	.000	0.896–0.987
Canalicular (190)	1.000	.000	15.891	.000	.000	1.000–1.000
Prechiasmatic (190)	.704	.065	13.886	.000	.000	0.576–0.832
Chiasm (95)	.918	.081	10.084	.000	.000	0.759–1.077

**Note:**—MoA indicates measure of agreement; asymp. SE, asymptomatic standard error; approx., approximative; sig., significance.

<sup>a</sup> Not assuming the null hypothesis.

<sup>b</sup> Using the asymptomatic SE assuming the null hypothesis.

**Table 3:  $\kappa$  values and their confidence intervals for 3D DIR, in the group of patients with MS in all 665 nerve segments combined**

3D DIR	Symmetric Measures					
	Value MoA ( $\kappa$ )	Asymp. SE <sup>a</sup>	Approx. T <sup>b</sup>	Approx. Sig.	Exact Sig.	95% CI
665 Valid cases (all nerve segments)	.931	.015	29.761	.000	.000	0.901–0.961

**Note:**—MoA indicates measure of agreement; asymp. SE, asymptomatic standard error; approx., approximative; sig., significance.

<sup>a</sup> Not assuming the null hypothesis.

<sup>b</sup> Using the asymptotic SE assuming the null hypothesis.

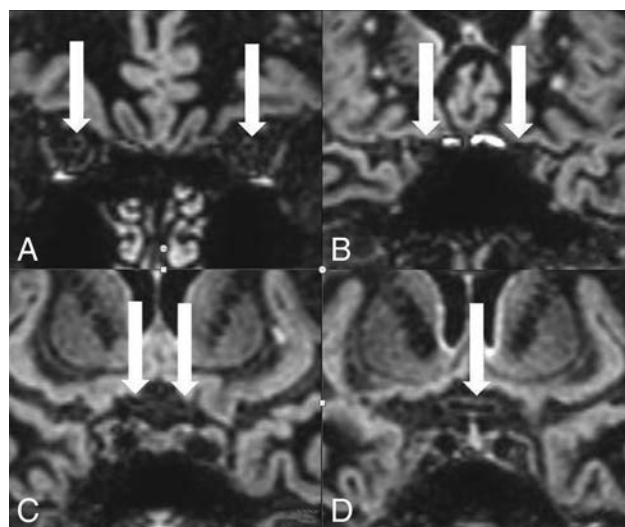


**FIG 1.** On 3D DIR, bilaterally normal hypointense retrobulbar (A), canalicular (B), and prechiasmatic (C) optic nerve segments and a normal hypointense chiasm (D). The normal nerve segments are marked with white arrows. The normal hypointense retrobulbar optic nerve is surrounded by an isointense nerve sheath on 3D DIR (A).

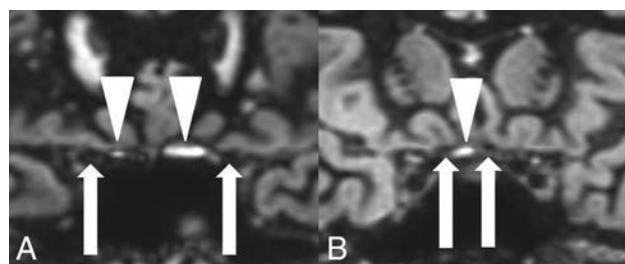


**FIG 2.** Hyperintense susceptibility artifacts (white arrowheads) at the air-bone interface next to the canalicular nerve segments (A) and next to the prechiasmatic nerve segments (B). Optic nerve segments are marked with white arrows.

kommision Zürich on September 26, 2016, without additional informed consent. This article did not receive any grant support and has not been presented at any meetings.

## RESULTS

### Interobserver Agreement

The agreement was excellent in the assessment of the signal intensity of the optic nerve segments on 3D DIR for the comparison group. No interobserver difference was seen. All nerve segments in the comparison group were deemed hypointense for all subjects by the expert reader and the student group.

In the patients with MS group, on 3D DIR, the signal intensity in 6 retrobulbar (3%) and 12 prechiasmatic segments (6%) and 1 chiasm (0.5%) was rated differently by the student group and the expert reader. The final rating of the signal intensity on 3D DIR was defined according to the rating of the expert neuroradiologist. A correct rating of the signal intensity of the different nerve segments on 3D DIR was performed in 97% of all 665 nerve segments by the student reader group.

The level of the interobserver agreement for the detection of signal abnormalities considering the different nerve segments was determined on the basis of the Cohen  $\kappa$  test (Tables 2 and 3).

Statistical evaluation yielded an excellent interobserver agreement in the comparison group and in the group of patients with MS, for all  $\kappa$  values were  $>0.8$  (Tables 2 and 3). The 95% confidence interval with a value of 0.901–0.961 for all nerve segments together proved the very good interobserver agreement.

The level of the interobserver agreement for the detection of signal abnormalities considering the different nerve segments was determined on the basis of the Cohen  $\kappa$  test (Tables 2 and 3). Statistical evaluation yielded an excellent interobserver agreement in the comparison group and in the group of patients with MS, for all  $\kappa$  values were  $>0.8$  (Tables 2 and 3). The 95% confidence interval with a value of 0.901–0.961 for all nerve segments together proved the very good interobserver agreement.

### Signal Intensity in Different Optic Nerve Segments in the Comparison Group

In the comparison group, 100 retrobulbar, 100 canalicular, 100 prechiasmatic, and 50 chiasmatic nerve segments were hypointense on 3D DIR (Fig 1). No isointense or hyperintense nerve signal was observed. The optic nerve sheath was seen as an isointense rim surrounding the hypointense retrobulbar optic nerve (Fig 1A). Small hyperintense artifacts were present at the air-bone interface in 57% of the examinations, both in the comparison group (Fig 2) and in the patients with MS group.

### Signal Intensity in Different Optic Nerve Segments in the Patients with MS Group

The results of the signal-intensity rating of the different nerve segments are depicted in Table 4.

On 3D DIR, 27 (28%) of the patients with MS presented with a hypointense optic system without any pathologic signal-intensity increase. However, 68 (72%) of the patients with MS presented with an isointense or hyperintense optic nerve signal in at least 1 optic nerve segment on 3D DIR (Fig 3).

**Table 4: Signal intensity of optic nerve segments evaluated on 3D DIR in patients with MS**

Optic Nerve Segment (No. of Nerves Evaluated)	Signal Intensity on 3D DIR Compared with Signal Intensity of the Lateral Rectus Muscle (%)			
	Hypointense	Isointense	Hyperintense	Isointense or Hyperintense
Retrobulbar (190)	108 (57%)	8	74	82 (43%)
Canalicular (190)	129 (68%)	9	52	61 (32%)
Prechiasmatic (190)	178 (93.5%)	9	4	13 (6.5%)
Chiasm (95)	89 (93.5%)	5	1	6 (6.5%)

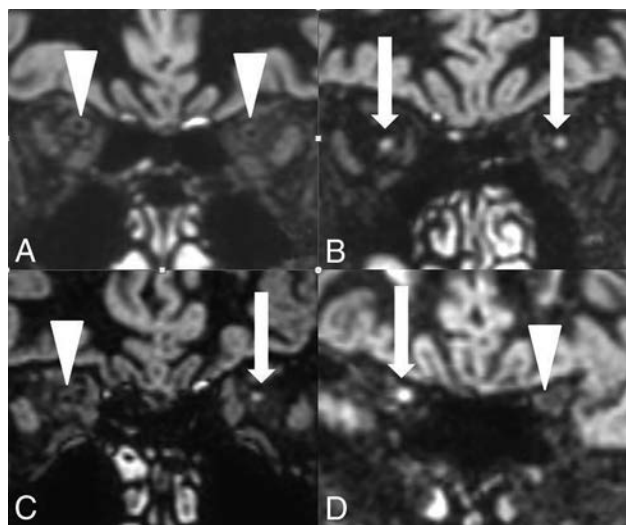


**FIG 3.** On 3D DIR, bilateral normal hypointense retrobulbar nerve segments (A) are compared with bilateral pathologic hyperintense retrobulbar nerve segments (B), with a unilateral pathologic hyperintense retrobulbar nerve segment on the left side (C) and a unilateral pathologic hyperintense canalicular nerve segment on the right side (D) in 3 different asymptomatic patients with MS. The hyperintense optic nerve segments are marked with white arrows. The normal hypointense optic nerve segments are marked with white arrowheads.

## DISCUSSION

The optic system comprises 4 different optic nerve segments, namely the retrobulbar, canalicular, and prechiasmatic segments and the chiasm.<sup>23,42</sup> An analysis of the signal intensity of the different optic nerve segments in a comparison group without any known optic nerve pathology showed that these 4 optic nerve segments presented with hypointensity on 3D DIR compared with the signal intensity of the directly adjacent lateral rectus muscle. This finding allowed us to define optic nerve segments in patients in the comparison group as hypointense on 3D DIR. A meningeal sheath that presented as an isointense circular rim around the hypointense optic nerve on 3D DIR surrounded the retrobulbar optic nerve segment.<sup>42</sup>

The signal-intensity rating of the different optic nerve segments could be easily performed by visual inspection by both inexperienced readers and expert readers, leading to very good interobserver reliability in our study. The inexperienced student readers were able to perform a correct rating of the signal intensity of the different nerve segments on 3D DIR in 97% of all nerve segments based on a  $\kappa$  value of  $>0.8$  in the Cohen  $\kappa$  interobserver agreement test. Therefore, the 3D DIR sequence allows recognizing signal intensity changes in optic nerve segments even if the reader is not an experienced neuroradiologist. Differences in

the signal-intensity rating between the student group and the expert reader could be explained by 2 possibilities: First, hyperintense susceptibility artifacts at the skull base common on 3D DIR were present in 57% of all examinations (in both the comparison group and the group of patients with MS) in various intensities and obscured the correct identification of 12 prechiasmatic

nerve segments and 1 chiasm for the student readers and prevented accurate signal-intensity analysis of these nerve segments on 3D DIR for the unexperienced readers.<sup>10</sup> No artifacts were observed along the retrobulbar and the canalicular nerve segments on 3D DIR.

Second, a prominent isointense optic nerve sheath masked the central hypointense optic nerve segment on 3D DIR and was therefore confused with increased signal intensity of the retrobulbar optic nerve itself in 6 retrobulbar nerve segments, leading to an incorrect pathologic signal-intensity rating in the student reader group.

Acute optic neuritis is easily diagnosed by contrast enhancement on T1-weighted fat-suppressed images and T2-weighted hyperintensity on fat-suppressed T2-weighted FSE images and FLAIR images<sup>10,24-26,30-31,34,35</sup> or by hypersignal on 3D DIR,<sup>10</sup> for the 3D DIR sequence suppresses fat, white matter, and fluid and gives optimal contrast between a pathologic hyperintense lesion and the surrounding suppressed background.<sup>10</sup>

The diagnosis of subclinical optic nerve demyelination, however, is challenging on MR imaging. Contrast enhancement of the optic nerve segments on T1-weighted MR images is absent. Slight optic nerve atrophy is possible.<sup>37</sup> It has been reported that a signal intensity increase of optic nerve segments in subclinical demyelination can be demonstrated on T2-weighted FSE sequences with fat suppression and on STIR T2-weighted images, and there are also rare reports of optic nerve hypersignal on FLAIR sequences.<sup>23,32,34</sup>

In a very recent study of 25 patients with MS, an optic nerve hypersignal was found on 3D DIR in 38.5% of optic nerves without a history of previous optic neuritis.<sup>36</sup> Our systematic investigation of the reliability of the 3D DIR sequence in the detection of subclinical optic nerve demyelination in a large group of patients with MS without clinically obvious visual symptoms and without any previous history of optic nerve neuritis within the last 3 years showed an even higher percentage of pathologic hypersignal in optic nerves in 78% of patients. Only 28% of all patients in the MS group did not present with an increased signal intensity in the optic system on 3D DIR. Therefore, a high value of the 3D DIR sequence in the diagnosis of subclinical optic nerve demyelination can be suspected according to the results of our study. Moreover, the 3D DIR sequence has the great advantage of being easily read even by inexperienced readers who are not routinely assessing neuroradiologic examinations. Thus, in patients with MS, a hypersignal in an optic nerve segment on 3D DIR that is different from a hypointense optic nerve signal in the comparison group should be considered pathologic.

The presence of a 3D DIR hypersignal in 78% of visually

asymptomatic patients with MS in our study also correlates very well with the results of postmortem and clinical studies that have already shown the high percentage of subclinical optic nerve demyelination with ongoing axonal loss in patients with MS.<sup>25,36,38-41</sup> The high percentage of optic nerve hypersignal on DIR in the retrobulbar nerve segments in 43% and in the canaliculular nerve segments in 32% of the patients with MS but with only rare hypersignal in the prechiasmatic segment and the chiasm in 6.5% of patients with MS correlates with the distribution of acute demyelinating lesions in optic nerves.<sup>26,30</sup> In postmortem studies, however, chronic demyelinating lesions are very common, not only in retrobulbar and canaliculular but also in intracranial nerve segments.<sup>30,38,39</sup> Evidently, the evaluation of demyelination in intracranial nerve segments on MR imaging seems to be difficult with the MR images currently available. This subclinical optic nerve demyelination occurs with or without previous clinical episodes of acute optic neuritis.<sup>36,38-41,43-45</sup> The ongoing axonal loss correlates with functional disability and quality of life in these patients.<sup>14-17,36,46-48</sup>

However, we cannot be sure whether our patients with MS who were visually asymptomatic had subtle visual deficits that would have been obvious only by special visual testing (visual-evoked potentials, optical coherence tomography, visual disability evaluation<sup>36</sup>), for our patients had not been specifically examined before the MR imaging examination. Additionally, a possible episode of acute optic neuritis in the years before the 3 years included in our study design could have been possible. Thus, subtle visual deficits may have gone undetected in our study, and further studies combining radiologic findings of DIR hypersignal within optic nerve segments and clinical correlation based on specific visual testing with visual evoked potentials and optical coherence tomography and visual disability testing<sup>36</sup> are mandatory.

There are several limitations to this study. First, the main one is that optic nerve signal intensity was not assessed with a standard sequence, specifically the STIR T2WI sequence of the orbits. As a result, the sensitivity and specificity of the 3D DIR sequence could not be evaluated.

Second, we have assumed that a signal-intensity increase in different optic nerve segments, based on hypersignal of optic nerve segments on 3D DIR compared with the signal intensity of the lateral rectus muscle, was always pathologic because of the hyposignal of optic nerve segments in 50 patients in the comparison group. This assumption may be wrong.

Third, the hypersignal of different optic nerve segments on 3D DIR in patients with MS was always related to possible subclinical optic nerve demyelination, even though it also could have been caused by other concomitant disease processes such as, for example, ischemic optic neuropathy.

Fourth, it has been assumed that subclinical optic nerve demyelination always leads to hypersignal of optic nerve segments on 3D DIR. However, we did not know whether subclinical nerve demyelination could also go undetected on 3D DIR.

Fifth, a correlation between hypersignal of optic nerve segments on 3D DIR and histologic findings and specific visual testing as mentioned above had not been performed.

Sixth, the patients in the comparison group evaluated for epileptic seizures or posttraumatic sequelae might also have had

subclinical optic nerve damage and thus did not really represent a reliable control group.

## CONCLUSIONS

Compared with hypointense optic nerve segments in patients without MS, in 72% of clinically asymptomatic patients with MS, 3D DIR showed hypersignal in at least 1 optic nerve segment. We have speculated about whether the hypersignal of the different optic nerve segments on 3D DIR in the group of patients with MS was related to subclinical optic nerve demyelination. The signal intensity of the different optic nerve segments could easily and reliably be determined on 3D DIR by both inexperienced and expert readers; therefore, evaluation of subclinical optic nerve pathology in patients with MS can also be performed without an experienced neuroradiologist.

## ACKNOWLEDGMENTS

Statistical tests were performed by Nicole Tracy Graf, Graf Biostatistics, Winterthur, Switzerland.

Disclosures: Simon Rauch—UNRELATED: Employment: Kantonsspital Winterthur Hospital.

## REFERENCES

1. Wattjes MP, Rovira À, Miller D, et al; MAGNIMS study group. **Evidence-based guidelines: MAGNIMS consensus guidelines on the use of MRI in multiple sclerosis—establishing disease prognosis and monitoring patients.** *Nat Rev Neurol* 2015;11:597–606 CrossRef Medline
2. Polman CH, Reingold SC, Edan G, et al. **Diagnostic criteria for multiple sclerosis: 2005 revisions to the “McDonald Criteria.”** *Ann Neurol* 2005;58:840–46 CrossRef Medline
3. Polman CH, Reingold SC, Banwell B, et al. **Diagnostic criteria for multiple sclerosis: 2010 revisions to the McDonald criteria.** *Ann Neurol* 2011;69:292–302 CrossRef Medline
4. Swanton JK, Rovira A, Tintore M, et al. **MRI criteria for multiple sclerosis in patients presenting with clinically isolated syndromes: a multicentre retrospective study.** *Lancet Neurol* 2007;6:677–86 CrossRef Medline
5. McDonald WI, Compston A, Edan G, et al. **Recommended diagnostic criteria for multiple sclerosis: guidelines from the International Panel on the diagnosis of multiple sclerosis.** *Ann Neurol* 2001;50:121–27 CrossRef Medline
6. Geurts JJ, Pouwels PJ, Uitdehaag BM, et al. **Intracortical lesions in multiple sclerosis: improved detection with 3D double inversion-recovery MR imaging.** *Radiology* 2005;236:254–60 CrossRef Medline
7. Simon B, Schmidt S, Lukas C, et al. **Improved in vivo detection of cortical lesions in multiple sclerosis using double inversion recovery MR imaging at 3 Tesla.** *Eur Radiol* 2010;20:1675–83 CrossRef Medline
8. Coebergh JA, Roosendaal SD, Polman CH, et al. **Acute severe memory impairment as a presenting symptom of multiple sclerosis: a clinical case study with 3D double inversion recovery MR imaging.** *Mult Scler* 2010;16:1521–24 CrossRef Medline
9. Wattjes MP, Lutterbey GG, Gieseke J, et al. **Double inversion recovery brain imaging at 3T: diagnostic value in the detection of multiple sclerosis lesions.** *AJNR Am J Neuroradiol* 2007;28:54–49 Medline
10. Hodel J, Outteryck O, Bocher AL, et al. **Comparison of 3D double inversion recovery and 2D STIR FLAIR MR sequences for the imaging of optic neuritis: pilot study.** *Eur Radiol* 2014;24:3069–75 CrossRef Medline
11. Balcer LJ. **Clinical practice: optic neuritis.** *N Engl J Med* 2006;354:1273–80 CrossRef Medline

12. Foroozan R, Buono LM, Savino PJ, et al. **Acute demyelinating optic neuritis.** *Curr Opin Ophthalmol* 2002;13:375–80 CrossRef Medline
13. Frohman EM, Frohman TC, Zee DS, et al. **The neuro-ophthalmology of multiple sclerosis.** *Lancet Neurol* 2005;4:111–21 CrossRef Medline
14. Hickman SJ, Toosy AT, Miszkiel KA, et al. **Visual recovery following acute optic neuritis: a clinical, electrophysiological and magnetic resonance imaging study.** *J Neurol* 2004;251:996–1005 Medline
15. Beck RW, Gal RL, Bhatti MT, et al; Optic Neuritis Study Group. **Visual function more than 10 years after optic neuritis: experience of the optic neuritis treatment trial.** *Am J Ophthalmol* 2004;137:77–83 CrossRef Medline
16. Brusa A, Jones SJ, Plant GT. **Long-term remyelination after optic neuritis: a 2-year visual evoked potential and psychophysical serial study.** *Brain* 2001;124:468–79 CrossRef Medline
17. Cleary PA, Beck RW, Bourque LB, et al. **Visual symptoms after optic neuritis: results from the Optic Neuritis Treatment Trial.** *J Neuroophthalmol* 1997;17:18–23; quiz 24–28 Medline
18. Guy J, Mao J, Bidgood WD Jr, et al. **Enhancement and demyelination of the intraorbital optic nerve: fat suppression magnetic resonance imaging.** *Ophthalmology* 1992;99:713–19 CrossRef Medline
19. Guy J, Fitzsimmons J, Ellis EA, et al. **Intraorbital optic nerve and experimental optic neuritis: correlation of fat suppression magnetic resonance imaging and electron microscopy.** *Ophthalmology* 1992;99:720–25 CrossRef Medline
20. Hendrix L, Kneeland JB, Haughton VM, et al. **MR imaging of optic nerve lesions: value of gadopentetate dimeglumine and fat-suppression technique.** *AJR Am J Roentgenol* 1990;155:849–54 CrossRef Medline
21. Johnson G, Miller DH, MacManus D, et al. **STIR sequences in NMR imaging of the optic nerve.** *Neuroradiology* 1987;29:238–45 CrossRef Medline
22. Sartoretti-Schefer S, Wichmann W, Valavanis A. **Optic neuritis: characteristic magnetic resonance features and differential diagnosis.** *Int J Neuroradiol* 1997;3:417–27
23. Gala F. **Magnetic resonance imaging of optic nerve.** *Indian J Radiol Imaging* 2015;25:421–38 CrossRef Medline
24. Rizzo JF 3rd, Andreoli CM, Rabinov JD. **Use of magnetic resonance imaging to differentiate optic neuritis and nonarteritic anterior ischemic optic neuropathy.** *Ophthalmology* 2002;109:1679–84 CrossRef Medline
25. Rocca MA, Hickman SJ, Bö L, et al. **Imaging the optic nerve in multiple sclerosis.** *Mult Scler* 2005;11:537–41 CrossRef Medline
26. Kupersmith MJ, Alban T, Zeiffer B, et al. **Contrast-enhanced MRI in acute optic neuritis: relationship to visual performance.** *Brain* 2002;125:812–22 CrossRef Medline
27. Hickman SJ, Miszkiel KA, Plant GT, et al. **The optic nerve sheath on MRI in acute optic neuritis.** *Neuroradiology* 2005;47:51–55 CrossRef Medline
28. Youl BD, Turano G, Towell AD, et al. **Optic neuritis: swelling and atrophy.** *Electroencephalogr Clin Neurophysiol Suppl* 1996;46:173–79 Medline
29. Youl BD, Turano G, Miller DH, et al. **The pathophysiology of acute optic neuritis: an association of gadolinium leakage with clinical and electrophysiological deficits.** *Brain* 1991;114:2437–50 CrossRef Medline
30. Miller DH, Newton MR, van der Poel JC, et al. **Magnetic resonance imaging of the optic nerve in optic neuritis.** *Neurology* 1988;38:175–79 CrossRef Medline
31. Jackson A, Sheppard S, Laitt RD, et al. **Optic neuritis: MR imaging with combined fat- and water-suppression techniques.** *Radiology* 1998;206:57–63 CrossRef Medline
32. Davies MB, Williams R, Haq N, et al. **MRI of optic nerve and postchiasmatic visual pathways and visual evoked potentials in secondary progressive multiple sclerosis.** *Neuroradiology* 1998;40:765–70 CrossRef Medline
33. Kadtare A, Ursekar M. **Systematic imaging review: multiple sclerosis.** *Ann Indian Acad Neurol* 2015;18(suppl 1):S24–29 CrossRef Medline
34. Aiken AH, Mukherjee P, Green AJ, et al. **MR imaging of optic neuropathy with extended echo-train acquisition fluid-attenuated inversion recovery.** *AJNR Am J Neuroradiol* 2011;32:301–05 CrossRef Medline
35. McKinney AM, Lohman BD, Sarikaya B, et al. **Accuracy of routine fat-suppressed FLAIR and diffusion-weighted images in detecting clinically evident acute optic neuritis.** *Acta Radiol* 2013;54:455–61 CrossRef Medline
36. Hadjhoum N, Hodel J, Defoort-Dhellemmes S, et al. **Length of optic nerve double inversion recovery hypersignal is associated with retinal axonal loss.** *Mult Scler J* 2016;22:649–58 CrossRef Medline
37. Tur C, Goodkin O, Altmann DR, et al. **Longitudinal evidence for anterograde trans-synaptic degeneration after optic neuritis.** *Brain* 2016;139:816–28 CrossRef Medline
38. Ikuta F, Zimmerman HM. **Distribution of plaques in seventy autopsy cases of multiple sclerosis in the United States.** *Neurology* 1976;26:26–28 CrossRef Medline
39. Toussaint D, Périer O, Verstaepen A, et al. **Clinicopathological study of the visual pathways, eyes, and cerebral hemispheres in 32 cases of disseminated sclerosis.** *J Clin Neuroophthalmol* 1983;3:211–20 CrossRef Medline
40. Frohman EM, Costello F, Stüve O, et al. **Modeling axonal degeneration within the anterior visual system: implications for demonstrating neuroprotection in multiple sclerosis.** *Arch Neurol* 2008;65:26–35 Medline
41. Frohman EM, Fujimoto JG, Frohman TC, et al. **Optical coherence tomography: a window into the mechanisms of multiple sclerosis.** *Nat Clin Pract Neurol* 2008;4:664–75 Medline
42. Hayreh SS. **Structure of the optic nerve.** In: Hayreh SS, ed. *Ischemic Optic Neuropathies.* Heidelberg: Springer; 2011:7–34
43. Lamirel C, Newman NJ, Bioussé V. **Optical coherence tomography (OCT) in optic neuritis and multiple sclerosis.** *Rev Neurol (Paris)* 2010;166:978–86 CrossRef Medline
44. Thrower BW. **Clinically isolated syndromes: predicting and delaying multiple sclerosis.** *Neurology* 2007;68:S12–25 CrossRef Medline
45. Frisén L, Hoyt WF. **Insidious atrophy of retinal nerve fibers in multiple sclerosis: funduscopic identification in patients with and without visual complaints.** *Arch Ophthalmol* 1974;92:91–97 CrossRef Medline
46. Bambo MP, Garcia-Martin E, Perez-Olivan S, et al. **Detecting optic atrophy in multiple sclerosis patients using new colorimetric analysis software: from idea to application.** *Semin Ophthalmol* 2016;31:459–62 CrossRef Medline
47. Garcia-Martin E, Rodriguez-Mena D, Herrero R, et al. **Neuro-ophthalmologic evaluation, quality of life and functional disability in patients with MS.** *Neurology* 2013;81:76–83 CrossRef Medline
48. Garcia-Martin E, Pueyo V, Ara JR, et al. **Effect of optic neuritis on progressive axonal damage in multiple sclerosis patients.** *Mult Scler* 2011;17:830–37 CrossRef Medline

# Intracranial Perishunt Catheter Fluid Collections with Edema, a Sign of Shunt Malfunction: Correlation of CT/MRI and Nuclear Medicine Findings

H.A. Kale, A. Muthukrishnan, S.V. Hegde, and V. Agarwal

## ABSTRACT

**SUMMARY:** Fluid collections with edema along the intracranial tract of ventriculoperitoneal shunt catheters in adults are rare and are more frequently seen in children. The imaging appearance of these fluid collections is frequently confusing and presents a diagnostic dilemma. We present 6 cases of adult patients noted to have collections with edema along the tract of ventriculoperitoneal shunt catheters. To our knowledge, there are no previous studies correlating the CT/MR imaging findings with nuclear medicine scans in this entity. We hypothesized that when seen in adults, the imaging findings of a CSF-like fluid collection around the intracranial ventriculoperitoneal shunt catheter on CT/MR imaging may suggest areas of CSF accumulation with interstitial edema. It is important to recognize this rare ventriculoperitoneal shunt complication in adults to prevent misdiagnosis of an abscess or cystic tumor.

**ABBREVIATIONS:** NM = nuclear medicine; VP = ventriculoperitoneal

Ventriculoperitoneal (VP) shunt catheters are placed for drainage of CSF for a wide variety of etiologies, such as hydrocephalus and idiopathic intracranial hypertension (pseudotumor cerebri). Fluid collections along the tract of an intracranial VP shunt catheter with edema are rarely seen in adults<sup>1-5</sup> and more frequently seen in children.<sup>6-10</sup> VP shunt catheters may be complicated by blockage, kinking, or fracture of the catheter; overdrainage; infection; and malposition. Some of these complications can be treated by merely changing the shunt settings. In other situations, the catheters may have to be removed and replaced either along the same tract or at a new site.<sup>11,12</sup> Shunt malfunction is a serious complication, and the most frequent reason for shunt revision. The rate of shunt failure after 1 year has been reported to be up to 30%, with 50% of shunts requiring some form of revision within 6 years of placement.<sup>13,14</sup> The basic components of a CSF shunt include a proximal catheter, reservoir, valve, and distal catheter.<sup>1,11</sup> In adults, distal catheter obstruction is more common. In children, proximal cath-

eter obstruction is more frequent and commonly occurs early after an operation.

Initial evaluation of shunt malfunction is with a shunt series and CT or MR imaging of the head and, if necessary, the abdomen/pelvis. Typically, VP shunt catheter malfunction results in inadequate drainage of CSF and is seen on imaging as an increase in ventricular size. VP shunt nuclear scintigraphy is usually performed to evaluate the patency and function of a VP shunt system. The patient is typically placed in a supine position, and the patient's scalp overlying the shunt reservoir/valve is prepared with iodine and draped. The neurosurgeon then injects a small volume, about 0.5 mL, of the radiotracer into the shunt reservoir/valve while manually applying pressure to the valve on the overlying skin to demonstrate reflux of tracer activity into the ventricles. Indium-111 disodium pentetate (<sup>111</sup>In] DTPA) is the preferred radioactive tracer of choice, though technetium Tc99m DTPA has also been used in some institutions. Sequential spot planar imaging of the head, neck, chest, and abdomen is acquired in multiple projections with a gamma camera. The radiotracer flow through the proximal and distal portion of the catheter tubing is imaged immediately after injection and at 15-minute intervals.

When there is absent or substantially delayed tracer migration from the ventricular system into the abdomen, a diagnosis of shunt malfunction should be inferred. Pericatheter cyst with edema around VP shunt catheters are rare in adults. In our review of the literature, there were only 5 case reports in adults with pericatheter cyst and edema associated with VP shunt catheters. The purpose of our study was to illustrate the benefit of combin-

Received February 2, 2017; accepted after revision April 8.

From the Department of Radiology, University of Pittsburgh Medical Center, Pittsburgh, Pennsylvania.

Paper previously presented, in part, as an oral presentation, at: Annual Meeting of the American Society of Neuroradiology and the Foundation of the ASNR Symposium, May 21-26, 2016; Washington, DC.

Please address correspondence to Hrishikesh Kale, MBBS, University of Pittsburgh Medical Center, 200 Lothrop St, Presby South Tower, 3rd Floor, Suite 3950, Pittsburgh, PA 15213; e-mail: kaleh@upmc.edu

<http://dx.doi.org/10.3174/ajnr.A5291>

ing the utility of anatomic CT/MR imaging with functional nuclear medicine (NM) information in arriving at a correct diagnosis of shunt malfunction.

### Case Series

The institutional Radiology Information System and PACS were used to retrospectively identify patients who presented with perishunt catheter collections on either CT or MR imaging who subsequently underwent evaluation with [<sup>111</sup>In] DTPA examinations. Patients who had pericatheter hemor-

rhage on immediate postoperative examinations were excluded. Likewise, patients who did not have NM examinations were also excluded. The study was fully Health Insurance Portability and Accountability Act–compliant and was approved by the local institutional review board. We retrospectively evaluated the CT/MR imaging and [<sup>111</sup>In] DTPA NM findings in 6 patients with peri-VP shunt catheter collections who presented to our institution through a search of our Radiology Information System and PACS.

In our group of patients, all 6 had an abnormal NM findings with delayed or absent detection of tracer in the proximal or proximal and distal limbs of the VP shunt catheter. Of these patients, 5 were treated surgically with shunt removal and replacement. The sixth patient was initially clinically stable and subsequently lost to follow-up. There was a near-complete resolution of the cyst after shunt replacement in all operated patients (Table).

#### Patient demographics

Total No. of patients	6
Age range (yr); sex (M:F)	24–46; 4:2
Indication for shunt placement (No.)	
Pseudotumor cerebri	4
Chiari I malformation	1
Postoperative pseudomeningocele	1
Presenting symptoms prior to shunt replacement (No.)	
Headache	5
Abdominal pain	1
Time to development of cyst after surgery	16 days to 5 years
Site of shunt catheter obstruction (No.)	
Proximal	3
Proximal and distal	3

**Case 1.** A 38-year-old woman with pseudotumor cerebri presented with new onset of headaches after placement of a VP shunt catheter. The duration between her initial catheter placement and clinical presentation was 12 months. CT performed at presentation showed edema and a fluid collection along the tract of the right-frontal-approach catheter (Fig 1A). An NM study showed no evidence of distal VP shunt obstruction with free tracer transit

into the peritoneal cavity (Fig 1B, -C).

However, there was focal accumulation of tracer activity on both early and delayed images in the right frontal fluid collection seen on the most recent head CT, suggesting an area of CSF accumulation. The patient was clinically stable with some improvement in symptoms. No shunt revision was performed. The patient was subsequently lost to follow-up.

**Case 2.** A 43-year-old man status post subependymoma resection with a postoperative pseudomeningocele treated with VP shunt placement presented with posterior headaches. The duration between catheter placement and presentation was 45 months. CT and MR imaging showed a right frontal fluid collection along the shunt catheter tract (Fig 2A). An NM study showed no evidence of radiotracer transit through the shunt tubing into the peritoneal cavity, suggesting a distal obstruction (Fig 2B). Also, focal tracer intracranial activity was noted corresponding to the area of the right frontal hypoattenuation seen on the head CT, suggesting a proximal obstruction. The patient subsequently underwent shunt revision. Immediate follow-up CT showed a decreased size of the collection and resolution of the cyst at 1 year.

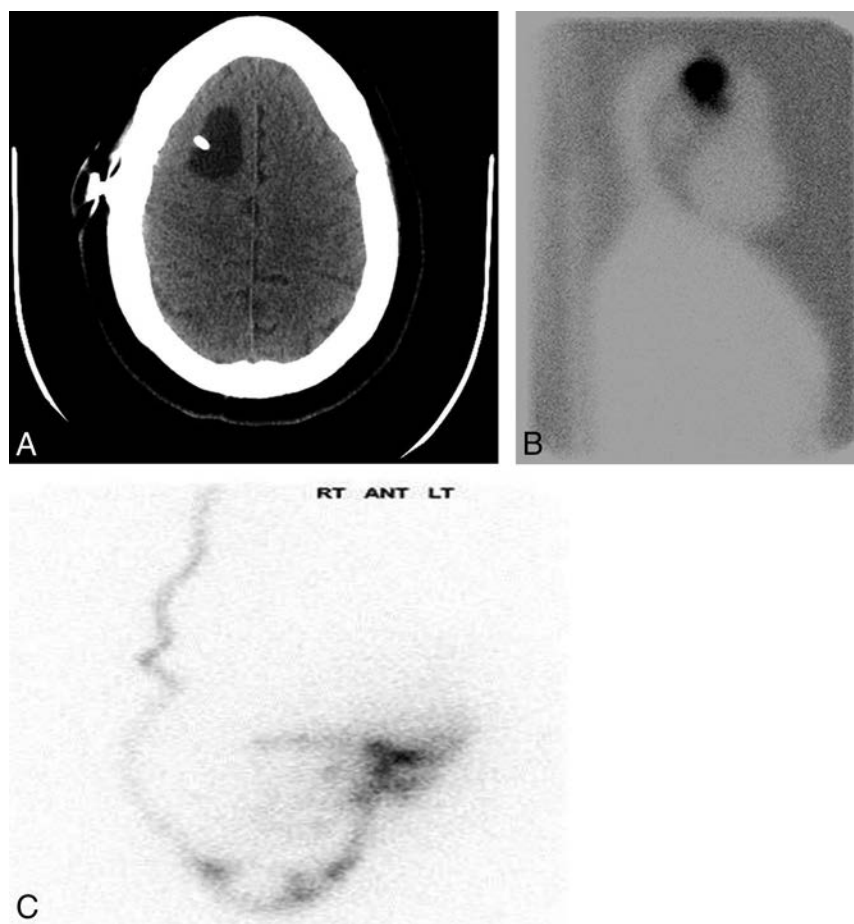


**FIG 1.** A, CT shows a fluid collection in the right frontal lobe along the tract of a VP shunt with surrounding edema. B, NM scan shows a focal accumulation of tracer in a right frontal cyst. C, NM scan shows normal transit of the radiotracer to the peritoneum.

**Case 3.** A 24-year-old woman with a history of pseudotumor cerebri was treated with VP shunt placement. She initially presented with abdominal pain and increased abdominal fluid. The interval between catheter placement and presentation was 60 months. CT of the head showed a fluid collection and edema along the right frontal shunt tract (Fig 3A). An NM study showed delayed passage of tracer distally into the peritoneum (Fig 3B). There was focal tracer accumulation within the right frontal region (Fig 3C), corresponding to the focal fluid collection on CT, suggesting an area of CSF accumulation. After initial conservative management, the shunt was ultimately revised.

**Case 4.** A 43-year-old woman with a history of Chari I malformation with hydrocephalus treated with VP shunt placement presented with headaches. The duration between shunt placement and presentation was 3 months. CT and MR imaging showed fluid collection/edema along the left frontal shunt tract. An NM study showed free spillage of tracer into the peritoneal cavity; however, there was focal tracer retention within the left frontal region corresponding to the fluid collection on the CT of the head. The VP shunt catheter was subsequently revised.

**Case 5.** A 46-year-old woman with a history of pseudotumor cerebri had a shunt placed. Sixteen days after shunt placement, she presented with headaches. CT and MR imaging showed fluid collection/edema along the shunt tract. An NM study showed distal obstruction of the shunt with no evidence of tracer transit into the distal portions of the VP shunt tubing or peritoneum. In addition, there was focal intracranial accumulation of the tracer, with the right frontal region corresponding to the right frontal

fluid collection seen on the head CT, suggesting proximal obstruction. The VP shunt catheter was subsequently revised.

**Case 6.** A 36-year-old man with a history of pseudotumor cerebri had a shunt placed. Fifteen months after shunt placement, he presented with headaches, tinnitus, and blurred vision. CT and MR imaging showed fluid collection/edema along the shunt tract. An NM study showed no evidence of intracranial tracer movement through the distal portions of the shunt tubing into the peritoneum, consistent with a distal obstruction. Substantial tracer collection at the shunt reservoir, the site of the tracer administration, was also noted. On more delayed images, a small area of intracranial focal activity corresponded to the right frontal fluid collection seen on the head CT, suggesting additional proximal obstruction. The VP shunt catheter was subsequently revised.

## DISCUSSION

Our study of peri-VP shunt catheter fluid collections showed a CSF-like attenuation/signal within the collections with extensive surrounding edema on both CT and MR imaging without substantial ventricular dilation. On subsequent nuclear medicine studies, there was shunt obstruction noted in all the VP shunt catheters. These findings are important because the presence of a cystic mass with surrounding edema may lead to an incorrect suspicion of an abscess or cystic tumor.

Bianchi et al<sup>1</sup> reported a case of pericatheter cyst mimicking a cystic tumor. In their report, the patient had a VP shunt catheter placed for hydrocephalus associated with a myelomeningocele. The patient presented with a motor deficit. At the operation, discontinuity of the intraventricular portion of the catheter to the rest of the shunt was found. Amans and Dillon<sup>2</sup> reported a pericatheter cyst around a VP shunt catheter placed for communicating hydrocephalus. In the case reported by Vajramani and Fugleholm,<sup>3</sup> the VP shunt catheter was placed for recurrent meningioma with symptomatic hydrocephalus.

Bianchi et al<sup>1</sup> and Amans and Dillon<sup>2</sup> demonstrated a proximally obstructed malfunctioning VP shunt catheter. Vajramani and Fugleholm<sup>3</sup> hypothesized radiation-induced changes responsible for the cyst development rather than shunt malfunction.

In our series, the age range was 24–46 years. The collections were seen at an interval of 16 days to 60 months from the time of VP shunt catheter placement. All patients had postoperative CT or MR imaging, which did not reveal a collection. The patients

included 4 men and 2 women. All patients in our series demonstrated a fluid collection along the tract of the VP shunt catheter with surrounding edema on CT. There was proximal shunt obstruction in 4 patients and proximal and distal obstruction in 2 patients. The indication for shunt placement was a pseudotumor in 4 patients and Chiari malformation and postoperative pseudomeningocele in 1 each. The indication for repeat imaging was headache in 5 patients and abdominal pain in 1 patient. The shunt was replaced in 5 patients, and 1 patient was followed conserva-

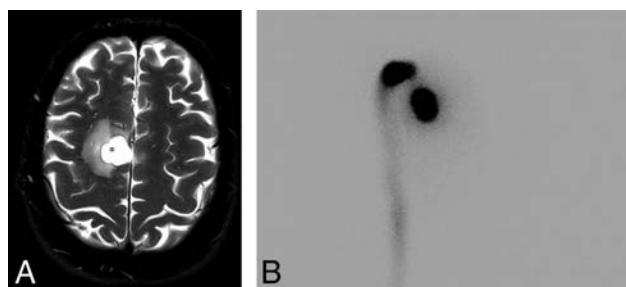


**FIG 2.** A, MR imaging shows a cyst in the right frontal region. B, NM scan shows focal accumulation of the tracer in a right frontal cyst.

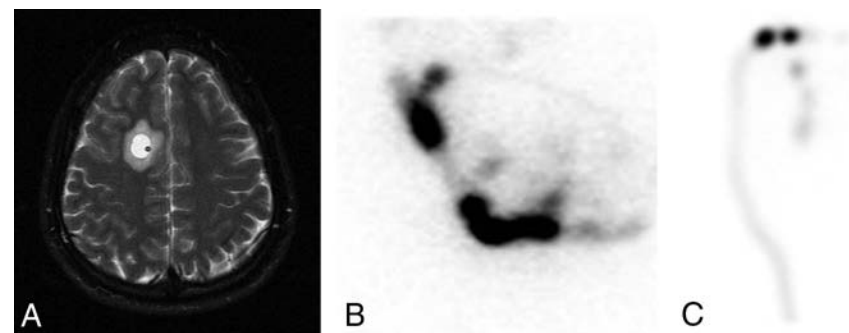


**FIG 3.** A, MR imaging shows a cyst in the right frontal region with surrounding edema. B, NM scan shows delayed passage of radiotracer to the peritoneum. C, NM scan shows focal accumulation of the tracer in a right frontal cyst.

tively because this patient was subsequently asymptomatic. The time between the cyst being reported and shunt revision was <1 month in 3 patients and >1 year in 2 patients. The ventricular size was nondilated in 5 patients and mildly dilated in 1 patient. In our series, one of the patients is asymptomatic and continues to show persistence of the collection and surrounding edema on a follow-up examination. We believe this finding may represent early partial or complete obstruction of the catheter, which, if followed, will ultimately result in shunt failure.

Four of the 6 patients had VP shunt catheters placed for refractory increased intracranial pressure (pseudotumor). VP shunt catheter placement is an established surgical treatment for refractory increased intracranial pressure.<sup>15,16</sup> Previously, its use was thought to be increasing.<sup>17</sup>

VP shunt catheters are the main treatment option available for hydrocephalus due to various causes. Shunt malfunction is a serious problem. The initial diagnostic evaluation for VP shunt malfunction is CT or MR imaging and a plain film evaluation for shunt integrity. The typical CT/MR imaging findings in shunt malfunction include hydrocephalus, fracture, migration, and overdrainage with slit-like ventricles and extra-axial fluid collections. Pericatheter cyst and edema around VP shunt catheters are rare, with a few case reports mostly described in children.

Most of the patent well-functioning VP shunt systems demonstrate good ventricular reflux of the tracer activity. Also, the entire portion of the shunt system will be visualized with uninterrupted passage of the tracer into the distal portions of the shunt tubing, with free spilling of the tracer into the peritoneal cavity (the pleural cavity in case of a ventriculopleural shunt) within the first 15 minutes of the injection of the radiotracer. Delayed or no clearance of the radioactivity through the distal portions of the shunt tubing, in general, is useful in confirming and localizing distal obstruction. However, in case of proximal obstruction of the ventricular portion of the tubing, the absence of ventricular reflux is considered a more reliable imaging finding.

Collections with edema around VP shunt catheters are uncommon in adults. Although these findings may be confused with infection or tumor, shunt malfunction should be considered. The exact etiology of pericatheter collections is unclear. Findings may represent accumulation of CSF in the brain parenchyma as a result of differential pressure between the intraventricular CSF and brain parenchyma. This finding would explain the higher incidence in children, with the softer more pliable pediatric brains being more amenable to yielding to pressure. This would also explain the relatively younger adult patients in our series (24–46 years). Edema around the VP shunt tract is probably a precursor or an associated finding. Other proposed mechanisms have been CSF leak into the pericatheter space/fibrous tunnel, slit ventricle syndrome, and subependymal dislocation of holes of the catheter.<sup>1</sup>

In the series of cases presented here, all patients demonstrated absence of radiotracer reflux into the ventricles. Also, there was focal accumulation of radiotracer corresponding to the loculated fluid collection as seen on head CT or MR images. Some patients also had good passage of the radiotracer through the distal portions of the tubing, which should not be mistaken for a well-functioning shunt system, especially in the absence of ventricular reflux and the presence of an intracranial loculated collection of radiotracer activity.

Combining the benefits of the anatomic imaging (CT/MR imaging) and functional information (NM study) can help make the diagnosis of shunt malfunction, especially related to proximal obstruction; however, management remains controversial.

A limitation of this case series is the low number of cases; however, given the relative frequency with which VP shunt catheters are placed, though rare, this entity is probably underdiagnosed.

## CONCLUSIONS

Pericatheter fluid collection with edema along the tract of the VP shunt catheter is an uncommon finding in adults. When present on CT and/or MR imaging, the findings should raise concern for catheter malfunction and prompt further NM evaluation.

## REFERENCES

1. Bianchi F, Frassanito P, Tamburrini G, et al. **Shunt malfunction mimicking a cystic tumour.** *Br J Neurosurg* 2016 Feb 6. [Epub ahead of print] CrossRef Medline
2. Amans MR, Dillon WP. **Cerebral parenchymal cyst: a rare complication of ventriculoperitoneal shunt malfunction in an adult.** *Radiol Case Rep* 2013;8:784 CrossRef Medline
3. Vajramani GV, Fugleholm K. **Reversible CSF cyst related to a functioning ventriculo-peritoneal shunt.** *Acta Neurochir (Wien)* 2005; 147:1199–202; discussion 1202 CrossRef Medline
4. Balasubramaniam S, Tyagi DK, Sawant HV. **Intraparenchymal pericatheter cyst following disconnection of ventriculoperitoneal shunt system.** *J Postgrad Med* 2013;59:232–34 CrossRef Medline
5. Shekawat JS, Sundar IV, Poonia N, et al. **Intraparenchymal pericatheter cyst following ventriculoperitoneal shunt.** *Neurol India* 2012; 60:341–42 CrossRef Medline
6. Iqbal J, Hassounah M, Sheikh B. **Intraparenchymal pericatheter cyst: a rare complication of ventriculoperitoneal shunt for hydrocephalus.** *Br J Neurosurg* 2000;14:255–58 CrossRef Medline
7. Sinha AK, Lall R, Benson R, et al. **Intraparenchymal pericatheter cyst following ventriculoperitoneal shunt insertion: does it always merit shunt revision?** *Zentralbl Neurochir* 2008;69:152–54; discussion 154 CrossRef Medline
8. H. Sakamoto, K. Fujitani, S. Kitano, K. et al. **Cerebrospinal fluid edema associated with shunt obstruction.** *J Neurosurg* 1994;81: 179–83 CrossRef Medline
9. Chiba Y, Takagi H, Nakajima F, et al. **Cerebrospinal fluid edema: a rare complication of shunt operations for hydrocephalus—report of three cases.** *J Neurosurg* 1982;57:697–700 CrossRef Medline
10. Rim HR, Hwang SK, Kwon SH, et al. **Intraparenchymal pericatheter cyst as a complication of a ventriculo-peritoneal shunt in a premature infant.** *J Korean Neurosurg Soc* 2011;50:143–46 CrossRef Medline
11. Wallace AN, McConathy J, Menias CO, et al. **Imaging evaluation of CSF shunts.** *AJR Am J Roentgenol* 2014;202:38–53 CrossRef Medline
12. Goeser CD, McLeary MS, Young LW. **Diagnostic imaging of ventriculoperitoneal shunt malfunctions and complications.** *Radiographics* 1998;18:635–51 CrossRef Medline
13. Blount JP, Campbell JA, Haines SJ. **Complications in ventricular cerebrospinal fluid shunting.** *Neurosurg Clin N Am* 1993;4:633–56 Medline
14. Sainte-Rose C, Hoffman HJ, Hirsch JF. **Shunt failure.** *Concepts Pediatr Neurosurg* 1989;9:7–20
15. Wall M. **Idiopathic intracranial hypertension.** *Neurol Clin* 2010;28: 593–617 CrossRef Medline
16. Thurtell MJ, Wall M. **Idiopathic intracranial hypertension (pseudotumor cerebri): recognition, treatment, and ongoing management.** *Curr Treat Options Neurol* 2013;15:1–12 CrossRef Medline
17. Curry WT Jr, Butler WE, Barker FG. **Rapidly rising incidence of cerebrospinal fluid shunting procedures for idiopathic intracranial hypertension in the United States, 1988–2002.** *Neurosurgery* 2005; 57:97–108; discussion 97–108 CrossRef Medline

# Value of Thrombus CT Characteristics in Patients with Acute Ischemic Stroke

J. Borst, O.A. Berkhemer, E.M.M. Santos, A.J. Yoo, M. den Blanken, Y.B.W.E.M. Roos, E. van Bavel, W.H. van Zwam, R.J. van Oostenbrugge, H.F. Lingsma, A. van der Lugt, D.W.J. Dippel, H.A. Marquering, and C.B.L.M. Majoie; on behalf of the MR CLEAN investigators



## ABSTRACT

**BACKGROUND AND PURPOSE:** Thrombus CT characteristics might be useful for patient selection for intra-arterial treatment. Our objective was to study the association of thrombus CT characteristics with outcome and treatment effect in patients with acute ischemic stroke.

**MATERIALS AND METHODS:** We included 199 patients for whom thin-section NCCT and CTA within 30 minutes from each other were available in the Multicenter Randomized Clinical Trial of Endovascular Treatment for Acute ischemic stroke in the Netherlands (MR CLEAN) study. We assessed the following thrombus characteristics: location, distance from ICA terminus to thrombus, length, volume, absolute and relative density on NCCT, and perviousness. Associations of thrombus characteristics with outcome were estimated with univariable and multivariable ordinal logistic regression as an OR for a shift toward better outcome on the mRS. Interaction terms were used to investigate treatment-effect modification by thrombus characteristics.

**RESULTS:** In univariate analysis, only the distance from the ICA terminus to the thrombus, length of >8 mm, and perviousness were associated with functional outcome. Relative thrombus density on CTA was independently associated with functional outcome with an adjusted common OR of 1.21 per 10% (95% CI, 1.02–1.43;  $P = .029$ ). There was no treatment-effect modification by any of the thrombus CT characteristics.

**CONCLUSIONS:** In our study on patients with large-vessel occlusion of the anterior circulation, CT thrombus characteristics appear useful for predicting functional outcome. However, in our study cohort, the effect of intra-arterial treatment was independent of the thrombus CT characteristics. Therefore, no arguments were provided to select patients for intra-arterial treatment using thrombus CT characteristics.

**ABBREVIATIONS:** DT = distance from the ICA terminus to the thrombus; IAT = intra-arterial treatment; ICA-T = ICA terminus; IQR = interquartile range; MR CLEAN = Multicenter Randomized Clinical Trial of Endovascular Treatment for Acute ischemic stroke in the Netherlands

Intra-arterial treatment (IAT) of acute ischemic stroke with retrievable stents for patients with a confirmed intracranial arterial occlusion of the anterior circulation has proved beneficial and

safe in multiple randomized controlled trials.<sup>1–5</sup> Several studies have found a relation between radiologic imaging characteristics of the thrombus and functional outcome, which might have value in the prediction of the efficacy of IAT. For example, multiple studies have suggested that patients with a clot longer than 8 mm on NCCT do not respond well to IV alteplase but might profit from IAT.<sup>6,7</sup> Furthermore, a previous study observed that com-

Received September 19, 2016; accepted after revision May 6, 2017.

From the Departments of Radiology (J.B., O.A.B., E.M.M.S., H.A.M., C.B.L.M.M.), Neurology (Y.B.W.E.M.R.), and Biomedical Engineering and Physics (E.M.M.S., M.d.B., E.v.B., H.A.M.), Academic Medical Center, Amsterdam, the Netherlands; Departments of Radiology (W.H.v.Z.) and Neurology (R.J.v.O.), Cardiovascular Research Institute Maastricht, Maastricht University Medical Center, Maastricht, the Netherlands; Departments of Public Health (H.F.L.), Radiology (E.M.M.S., A.v.d.L.), Medical Informatics (E.M.M.S.), and Neurology (O.A.B., D.W.J.D.), Erasmus MC, University Medical Center, Rotterdam, the Netherlands; and Department of Radiology (A.J.Y.), Texas Stroke Institute, Plano, Texas.

This work was supported by the Information Technology for European Advancement 2 project, label ITEA 10004: Medical Distributed Utilization of Services and Applications. The MR CLEAN trial is supported by the Dutch Heart Foundation and by unrestricted grants from Angiocare BV, Covidien/ev3, Medac/Lamepro, and Penumbra. Philips Healthcare provided a workstation with Brain CT Perfusion software (Philips IntelliSpace, version 7.0, Brain CT Perfusion Package); Hester F. Lingsma receives funding from the European Union Seventh Framework Programme

(FP7/2007–2013) under grant agreement No. 602150 (CENTER-TBI); <https://www.center-tbieu/>.

Jordi Borst, Olvert A. Berkhemer, Emile M.M. Santos contributed equally to this work. Henk A. Marquering and Charles B.L.M. Majoie contributed equally to this work.

Please address correspondence to Jordi Borst, MD, Department of Radiology, GI-229, Academic Medical Center Amsterdam, Meibergdreef 9, 1105AZ Amsterdam, the Netherlands; e-mail: [j.borst@amc.uva.nl](mailto:j.borst@amc.uva.nl)

Indicates open access to non-subscribers at [www.ajnr.org](http://www.ajnr.org)

Indicates article with supplemental on-line tables.

<http://dx.doi.org/10.3174/ajnr.A5331>

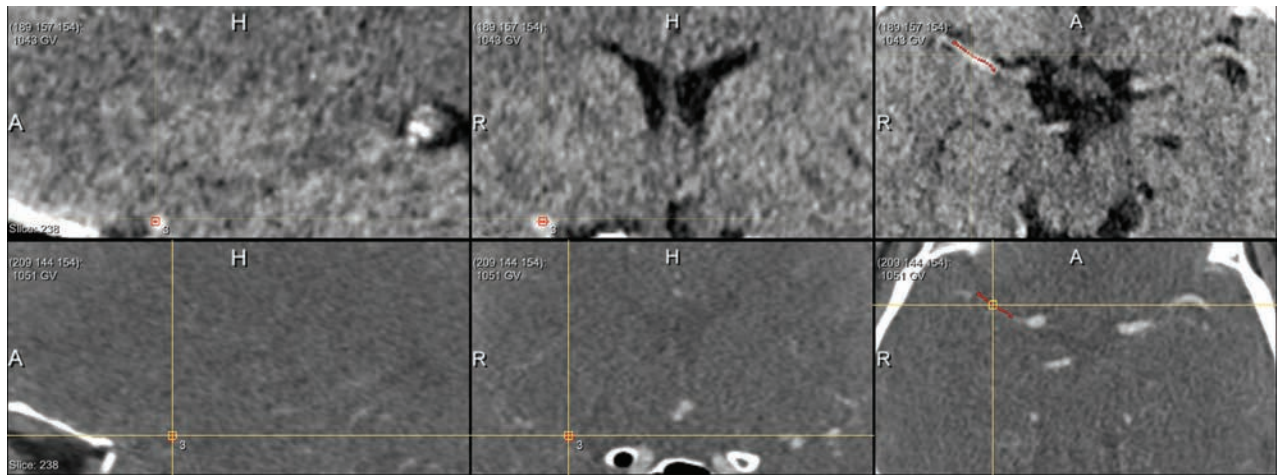


**FIG 1.** Length measurement. Placement of seed points in the thrombus by the observer. Subsequently, the software determined the centerline through the thrombus, which represents the length of the thrombus. Top row from left to right: sagittal view NCCT, coronal view NCCT, axial view NCCT. Bottom row from left to right: sagittal view CTA, coronal view CTA, axial view CTA.

pared with IV alteplase alone, IAT after IV alteplase leads to better outcomes in patients with a distance from the ICA terminus (ICA-T) to the thrombus (DT) shorter than 16 mm.<sup>8</sup> Also, it was found that a thrombus with higher absolute or relative Hounsfield units on NCCT is predictive of successful recanalization with mechanical thrombectomy or intravenous alteplase.<sup>9-12</sup> Moreover, it was recently shown that thrombus perviousness, which is a measure of the amount of contrast penetration in the thrombus on CTA, is strongly associated with functional outcome.<sup>13</sup> On the basis of these observations, we hypothesized that thrombus CT characteristics have the potential to be used for selection of patients who are likely to benefit from IAT. We aimed to determine which thrombus CT characteristics are associated with functional outcome in patients with acute ischemic stroke due to a proximal intracranial occlusion enrolled in the Multi-center Randomized Clinical Trial of Endovascular Treatment for Acute ischemic stroke in the Netherlands (MR CLEAN) study. Moreover, we aimed to determine whether the efficacy of IAT on functional outcome was modified by the thrombus CT characteristics.

## MATERIALS AND METHODS

### Patient Selection

All patients enrolled in MR CLEAN with thin-section ( $\leq 2.5$  mm) baseline NCCT and CTA acquired within 30 minutes from each other on the same scanner were included in this study ( $n = 233$ ). CT data with too much noise ( $n = 8$ ), severe motion artifacts ( $n = 22$ ), insufficient contrast on CTA ( $n = 1$ ), and incomplete ROI ( $n = 3$ ) were excluded; thus, data from 199 patients were available for further analysis. In MR CLEAN, the effect of IAT versus best medical treatment, including IV alteplase, was investigated in patients with acute ischemic stroke. Patients enrolled in MR CLEAN had a proximal intracranial arterial occlusion of the anterior circulation confirmed on vessel imaging. Permission of the ethics committee and institutional review board was given, and patients or their legal representatives signed informed consents. The protocol and a detailed description of the methods of MR CLEAN have been published previously.<sup>14</sup>

### Image Analysis

We determined the following thrombus characteristics on baseline NCCT and CTA imaging: location, DT, length, volume, absolute and relative attenuation on NCCT, and thrombus perviousness measures: absolute and relative density on CTA, attenuation increase, and void fraction.<sup>13</sup> Location of the thrombus (M1, M2, A1, A2, ICA, or ICA-T) was determined on CTA by expert neuroradiologists.<sup>1</sup> The length of the thrombus was measured on NCCT with the aid of coregistered CTA, with an in-house-developed MeVisLab interface ([www.mevislab.de](http://www.mevislab.de)).<sup>15</sup> A trained user (J.B., with 3 years of experience in neuroimaging research), blinded to clinical information, placed several seed points in the thrombus (Fig 1). Subsequently, the software determined the centerline through the thrombus. If needed, the user could adapt the centerline on multiplanar reformations. The length of the thrombus was represented by the length of this centerline. With the same program, the DT was measured by placing several seed points starting in the ICA-T to the proximal border of the thrombus (Fig 2). The volume of the thrombus was calculated with a semiautomated segmentation method adapted from Santos et al.<sup>15</sup> The centerline already determined for the length measurement was subsequently used in the volume calculation.

Density measurement of the thrombus and contralateral vessel segment was performed on NCCT and coregistered CTA by a trained observer (M.d.B., with 1 year of experience), blinded to clinical information, with the in-house-developed MeVisLab interface.<sup>13</sup> The mean thrombus density was calculated by averaging the Hounsfield units of 3 manually placed ROIs of the thrombus. Relative density was calculated by dividing the mean Hounsfield unit of the thrombus by the mean Hounsfield unit of the contralateral vessel segment.<sup>11</sup>

We included thrombus perviousness measures estimating the permeability by quantifying the contrast agent penetration in the thrombus on CTA. Absolute and relative thrombus densities on CTA were derived in a manner similar to that of the density measurement on NCCT. Attenuation increase was determined by subtracting the mean density of the thrombus on NCCT from the

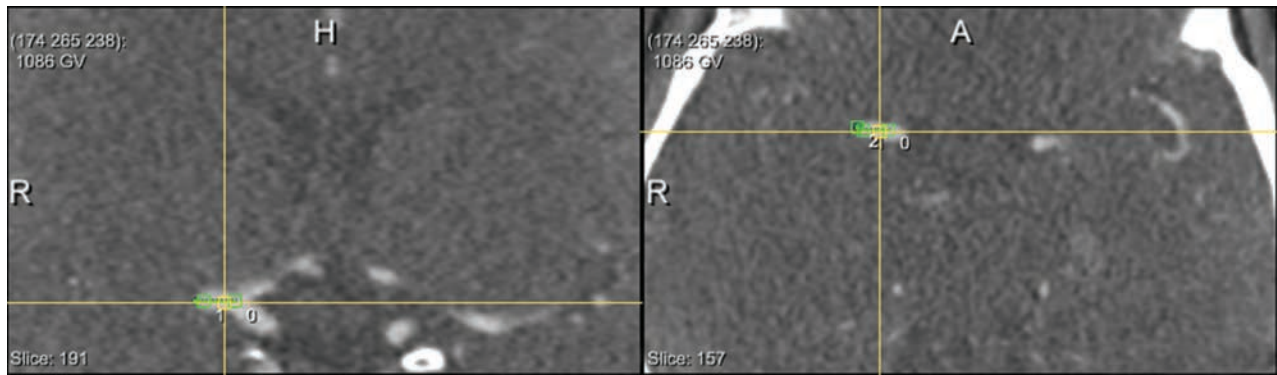


**FIG 2.** Distance from the ICA-T to the thrombus. Placement of seed points in the vessel from the ICA-T to the thrombus by the observer. Subsequently, the software determined the centerline through the vessel, which represents the distance from the ICA-T to the thrombus. Left: coronal view CTA. Right: axial view CTA.

mean density on CTA. Void fraction was the ratio between the attenuation increase of the thrombus and the attenuation increase of the contralateral vessel segment.<sup>13</sup>

### Statistical Analysis

**Association with Outcome.** The primary outcome measure was the full modified Rankin Scale score at 90 days. The mRS is an ordered categorical scale to measure functional disability, ranging from 0 (no symptoms) to 6 (death). A score of  $\leq 2$  indicates functional independence.<sup>16</sup> The association of thrombus characteristics with functional outcome was estimated with univariable and multivariable ordinal logistic regression and was presented as a common OR for a shift in the direction of a better outcome on the mRS.<sup>16,17</sup> The common odds ratio measured the likelihood that the presence of a certain thrombus characteristic would lead to lower modified Rankin Scale scores, compared with the absence of this thrombus characteristic (shift analysis).<sup>17</sup>

If one analyzes the mRS on an ordinal scale, the ordinal nature of the mRS is preserved; therefore, the statistical power is increased compared with dichotomized analyses.<sup>18</sup>

We adjusted for differences in patient characteristics by including the following baseline characteristics as covariates in the multivariable analysis: age, sex, atrial fibrillation, diabetes mellitus, time from onset to randomization, previous stroke, and stroke severity assessed by the NIHSS. We included all thrombus characteristics with a  $P$  value  $< .10$  (in the univariable analysis) in the multivariable analysis.

To avoid multicollinearity, we implemented thrombus characteristics that were more than moderately correlated with each other (Spearman correlation or point-biserial correlation of  $>0.5$ ) in separate models. Of the correlated characteristics, we first included the characteristics with the lowest univariable  $P$  value in the multivariable model. Subsequently, we alternately replaced a correlated characteristic for the others in the multivariable model.

Location of the thrombus (ICA-T,  $n = 46$ ; M1,  $n = 131$ ; M2,  $n = 22$ ) was dichotomized as an ICA-T occlusion versus a non-ICA-T occlusion. Because it has been suggested that patients with a thrombus of  $>8$  mm or a DT of  $<16$  mm do not respond well to intravenous alteplase,<sup>6-8</sup> we have also introduced the dichotomized thrombus length of  $>8$  mm and the DT of  $<16$  mm in the analysis.

Secondary outcome measures were the following: the absence of an intracranial occlusion on follow-up CTA and final infarct volume on follow-up NCCT.<sup>19</sup> For the patients who underwent successful IAT reperfusion, modified Thrombolysis in Cerebral Infarction 2B or 3<sup>20</sup> was also used as a secondary outcome measure. For dichotomized outcome measures, univariable logistic regression analysis was performed, and the association was presented as an OR. For final infarct volume, univariable linear regression was performed, and the association was reported as  $B$  coefficients. The multivariable analysis to determine the association of the thrombus characteristics with final infarct volume or absence of occlusion on follow-up CTA was performed, similar to the multivariable analysis for the mRS.

**Treatment-Effect Modification.** We investigated whether thrombus characteristics had a treatment-effect modification by analyzing whether there was interaction with treatment allocation in the prediction of functional outcome, using a multivariable ordinal logistic regression model, including the thrombus characteristic of interest, treatment allocation, and the multiplicative interaction term of these variables. We also included the baseline characteristics and thrombus characteristics with a univariable  $P$  value  $< .1$  in a multivariable ordinal logistic regression model. Of the correlated characteristics, we included only the thrombus characteristics with the lowest univariable  $P$  value in the multivariable model.

The effect of outliers was minimized by truncation of continuous CT thrombus characteristics (length, volume, DT, absolute and relative density on NCCT, and perviousness) at the 2.5th and 97.5th percentiles.<sup>21</sup> STATA/SE 13.1 (StataCorp, College Station Texas) was used for all statistical analyses.

**RESULTS**

The mean age was 65 years (range, 31–93 years), and 62% (124/199) were men. Table 1 shows the baseline characteristics of the study cohort, and Table 2 shows the baseline characteristics stratified by treatment. Except for the percentage of patients allocated to IAT, the baseline characteristics of the full MR CLEAN cohort and this study cohort were similar. In our study cohort, 39%

**Table 1: Baseline characteristics of the full MR CLEAN cohort and subgroups included and not included in this study**

	MR CLEAN Subgroup Included (n = 199)	MR CLEAN Not Included (n = 301)	MR CLEAN Full Cohort (n = 500)
Mean age (yr)	65 (range, 31–93)	66 (range, 23–96)	65 (range, 23–96)
Male sex (%)	62 (124/199)	56 (168/301)	58 (292/500)
Median NIHSS score	18 (IQR, 14–22)	17 (IQR, 15–21)	18 (IQR, 14–22)
Median ASPECTS	9 (IQR, 8–10)	9 (IQR, 7–10)	9 (IQR, 8–10)
Diabetes mellitus (%)	11 (21/199)	16 (47/301)	14 (68/500)
Atrial fibrillation (%)	27 (54/199)	27 (81/301)	27 (135/500)
Previous stroke (%)	10 (20/199)	11 (34/301)	11 (54/500)
IAT (%)	39 (78/199)	51 (155/301)	47 (233/500)
Median thrombus length (mm) (n = 186)	15.6 (IQR, 10.3–22.2) (range, 4.8–39.5)		
Median thrombus volume (mm <sup>3</sup> ) (n = 186)	70.1 (IQR, 49.3–113.3) (range, 6.1–456.7)		
Median distance to thrombus (mm)	6.4 (IQR, 0.0–13.5) (range, 0.0–38.2)		
T-occlusion (%)	23 (46/199)	29 (88/301)	27 (134/500)
Median density thrombus NCCT (HU)	49.0 (IQR, 44.5–55.4) (range, 33.1–67.8)		
Median relative density thrombus NCCT (%)	134.4 (IQR, 116.8–151.7) (range, 65.8–274.4)		
Median density thrombus CTA (HU)	61.4 (IQR, 52.6–72.1) (range, 38.5–134.3)		
Median relative density thrombus CTA (%)	29.8 (IQR, 21.4–40.8) (range, 12.2–94.7)		
Median thrombus attenuation increase (HU)	11.4 (IQR, 0.1–22.5) (range, –9.9–80.0)		
Median thrombus void fraction (%)	6.0 (IQR, 0.08–15.4) (range, –8.9–61.8)		

**Table 2: Baseline characteristics of the full MR CLEAN subgroups included in this study stratified by treatment**

	IAT (n = 78)	Control (n = 121)
Mean age (yr)	63 (range, 43–87)	66 (range, 31–93)
Male sex (%)	67 (52/78)	56 (72/121)
Median NIHSS	17 (IQR, 13–21)	19 (IQR, 14–23)
Median ASPECTS	9 (IQR, 8–10)	9 (IQR, 8–10)
Diabetes mellitus (%)	9 (7/78)	12 (14/121)
Atrial fibrillation (%)	22 (17/78)	31 (37/121)
Previous stroke (%)	14 (11/78)	7 (9/121)
Median thrombus length (mm) (n = 186)	16.2 (IQR, 11.6–22.0) (range, 4.8–39.5)	15.2 (IQR, 10.3–22.3) (range, 4.8–39.5)
Median thrombus volume (mm <sup>3</sup> ) (n = 186)	69.3 (IQR, 51.7–111.9) (range, 6.1–329.0)	70.9 (IQR, 43.8–115.5) (range, 11.4–456.7)
Median distance to thrombus (mm)	6.8 (IQR, 0.0–12.8) (range, 0.0–38.2)	6.4 (IQR, 0.0–13.5) (range, 0.0–38.2)
T-occlusion (%)	26 (20/78)	21 (26/121)
Median density thrombus NCCT (HU)	49.0 (IQR, 45.2–55.2) (range, 33.1–67.8)	48.9 (IQR, 44.1–55.4) (range, 33.1–67.8)
Median relative density thrombus NCCT (%)	137.4 (IQR, 116.0–151.4) (range, 84.8–213.0)	131.2 (IQR, 117.7–151.7) (range, 65.8–274.4)
Median density thrombus CTA (HU)	61.2 (IQR, 53.3–68.7) (range, 38.5–134.3)	61.9 (IQR, 52.5–75.1) (range, 38.5–134.3)
Median relative density thrombus CTA (%)	29.6 (IQR, 23.2–37.9) (range, 12.2–94.7)	29.8 (IQR, 20.5–43.9) (range, 12.5–88.7)
Median thrombus attenuation increase (HU)	12.3 (IQR, 0.74–19.6) (range, –9.9–80.0)	11.2 (IQR, –0.9–28.5) (range, –9.9–80.0)
Median thrombus void fraction (%)	5.8 (IQR, 0.99–12.3) (range, –8.9–61.8)	6.1 (IQR, –0.47–16.8) (range, –8.9–61.8)

(78/199) of the patients underwent IAT compared with 47% (233/500) in the MR CLEAN cohort. The successful reperfusion rate was 59% (115/194). The median thrombus length was 15.6 mm (interquartile range [IQR], 10.3–22.2 mm), the median DT was 6.4 mm (IQR, 0.0–13.5 mm), and the median density on NCCT was 49.0 HU (IQR, 44.5–55.4 HU). If the thrombus was located in the ICA-T, the DT was 0 mm. In 13 patients, we were unable to determine the length of the thrombus due to lack of contrast in the extracranial ICA.

In this study cohort, 15% (30/199) of the thrombi were <8 mm and 18% (35/199) had a DT ≥ 16 mm. The median relative CTA thrombus density was 29.8% (IQR, 21.4%–40.8%), the median thrombus attenuation increase was 11.4 HU (IQR, 0.1–22.5 HU), and the median thrombus void fraction was 6.0% (IQR, 0.08%–15.4%).

### Associations with Outcome

DT, length of >8 mm, and the perviousness measures (ie, absolute and relative CTA density, attenuation increase, and void fraction) were associated with functional outcome in the univariable

analysis ( $P < .05$ ) (On-line Table 1). Length and length of >8 mm, volume and length, DT and DT < 16 mm, DT and the presence of an ICA-T, and the perviousness measures were correlated with each other (see On-line Table 2 for the correlation coefficients). Only relative thrombus density on CTA was an independent predictor of functional outcome in the multivariable analysis, with an adjusted common OR of 1.21 per 10% (95% CI, 1.02–1.43) ( $P = .029$ ) (see On-line Table 1 for adjusted common ORs). Thrombus volume, DT, DT < 16 mm, NCCT thrombus density, and CTA attenuation increase were associated with the absence of an intracranial occlusion on follow-up CTA (On-line Table 1). In the multivariable analysis, none of the thrombus CT characteristics were associated with the absence of intracranial occlusion on follow-up CTA ( $P > .05$ ) (On-line Table 1). Length of >8 mm, thrombus volume, DT, DT < 16 mm, the presence of ICA-T, NCCT thrombus density, CTA attenuation increase, and void fraction were associated with final infarct volume (On-line Table 1). In the multivariable analysis, none of the thrombus CT characteristics were associated with final infarct volume (On-line Table 1).

### Treatment-Effect Modification

We observed no significant treatment-effect modification of IAT with any of the thrombus CT characteristics.

### DISCUSSION

In this study cohort of patients with a large-vessel occlusion of the anterior circulation, DT, length of  $>8$  mm, and the perviousness measures were associated with functional outcome. In our study, only relative density on CTA was associated with functional outcome after adjustment for the baseline patient characteristics and the other thrombus characteristics. We observed that patients with a higher relative thrombus density on CTA had better functional outcome compared with patients with a lower relative thrombus density on CTA. We observed no treatment-effect modification by any of the thrombus CT characteristics. Therefore, this study provides no arguments to select patients for IAT using thrombus CT characteristics.

Our study confirms that DT is associated with functional outcome in univariable analysis.<sup>8</sup> In this study cohort, the dichotomized thrombus length of  $>8$  mm was associated with functional outcome, which is in line with a previous study demonstrating that patients with a thrombus of  $\leq 8$  mm have a better outcome after IV alteplase.<sup>7</sup> We observed that increasing thrombus density on NCCT was associated with persistent occlusion. In contrast, previous studies have shown that lower absolute and relative thrombus densities are associated with persistent occlusion in patients with anterior circulation occlusion (primarily distal M1 and M2) treated with IV alteplase.<sup>11,12</sup>

We observed that the outcome of patients who underwent IAT was not affected by the density of the thrombus, which is in line with the findings of previous studies in which there was no difference in the NCCT density of the thrombus between patients with and without recanalization after thrombectomy.<sup>22,23</sup> However, several studies using mechanical thrombectomy in a population of patients with large-vessel occlusion observed that recanalization rates were higher for patients with denser thrombi.<sup>10,9</sup>

We measured CT thrombus characteristics on NCCT with the aid of CTA because it was suggested that it is more accurate for low-density thrombi and for patients with high hematocrit levels, which might cause overestimation of the length of the thrombus.<sup>24</sup> DT was determined on multiplanar reformations; this process gives the user a better impression of the 3D anatomy of the vasculature compared with previous measurements on transversal maximum intensity projections.<sup>25</sup>

There are several limitations. We excluded many patients due to the unavailability of thin-section NCCT ( $n = 252$ ), which is needed for accurate measurement of the thrombus characteristics.<sup>26</sup> In 19% of the patients, IV alteplase was administered before CTA; this order could have affected the perviousness measures. However, there was no difference ( $P = .26$ ) in average perviousness between patients in whom IV alteplase was administered before or after the CTA. Due to pragmatic reasons, thrombus density was measured by a trained observer and not by a radiologist. However, a previous study showed that the density measurements by the trained observers were reproducible and showed very good agreement with those of the experienced radiologists.<sup>27</sup> In this study, multiple tests were performed without adjusting the

$P$  values. This choice could have resulted in a false significant association between thrombus characteristics and outcome measures or a false significant treatment-effect modification by the thrombus characteristics. However, this study found only a significant independent association between relative thrombus density on CTA and the mRS, which was also significant ( $P < .001$ ) in the univariable analysis. This makes it less likely that we have falsely rejected a true null hypothesis. Furthermore, all the interaction terms had a  $P$  value  $> .05$  in the adjusted analysis; therefore, on the basis of a  $P$  value of  $.05$ , none of the null hypotheses were rejected. Adjusting the  $P$  values would not change our conclusions.

The confidence intervals of the interaction terms between the thrombus characteristics and treatment effect are wide, thus limiting the generalizability of our observation regarding the absence of significant effect modification.

In this study, relative thrombus density on CTA was independently associated with functional outcome. A higher relative thrombus density on CTA means that the contrast penetration in the thrombus is higher; this feature might be a sign of flow through a thrombus and is related to early reperfusion.<sup>28,29</sup>

### CONCLUSIONS

In this study cohort, a higher relative density of the thrombus on CTA was independently associated with better functional outcome in patients with acute ischemic stroke caused by a large-vessel occlusion in the anterior circulation. Therefore, CT thrombus characteristics appear useful for predicting functional outcome. However, in patients with a large vessel occlusion of the anterior circulation, the treatment effect of IAT was independent of the thrombus CT characteristics. Therefore, no arguments were provided to select patients for IAT using thrombus CT characteristics.

### ACKNOWLEDGMENTS

List of MR CLEAN investigators and affiliations:

Olvert A. Berkhemer, MD,<sup>1,2</sup> Puck S.S. Fransen, MD,<sup>2,3</sup> Debbie Beumer, MD<sup>2,4</sup> Lucie A. van den Berg, MD,<sup>5</sup> Hester F. Lingsma, MD, PhD,<sup>7</sup> Albert J. Yoo, MD,<sup>8</sup> Wouter J. Schonewille, MD,<sup>9</sup> Jan Albert Vos, MD, PhD,<sup>10</sup> Paul J. Nederkoorn, MD, PhD,<sup>5</sup> Marieke J.H. Wermer, MD, PhD,<sup>11</sup> Marianne A.A. van Walderveen, MD, PhD,<sup>12</sup> Julie Staals, MD, PhD,<sup>4</sup> Jeannette Hofmeijer, MD, PhD,<sup>13</sup> Jacques A. van Oostayen, MD, PhD,<sup>14</sup> Geert J. Lycklama à Nijeholt, MD, PhD,<sup>15</sup> Jelis Boiten, MD, PhD,<sup>16</sup> Patrick A. Brouwer, MD,<sup>3</sup> Bart J. Emmer, MD, PhD,<sup>3</sup> Sebastiaan F. de Bruijn, MD, PhD,<sup>17</sup> Lukas C. van Dijk, MD,<sup>18</sup> L. Jaap Kappelle, MD, PhD,<sup>19</sup> Rob H. Lo, MD,<sup>20</sup> Ewoud J. van Dijk, MD, PhD,<sup>21</sup> Joost de Vries, MD, PhD,<sup>22</sup> Paul L.M. de Kort, MD, PhD,<sup>23</sup> Jan S.P. van den Berg, MD, PhD,<sup>24</sup> Boudewijn A.A.M. van Hasselt, MD,<sup>25</sup> Leo A.M. Aerden, MD, PhD,<sup>26</sup> René J. Dallinga, MD,<sup>27</sup> Marieke C. Visser, MD, PhD,<sup>28</sup> Joseph C.J. Bot, MD, PhD,<sup>29</sup> Patrick C. Vroomen, MD, PhD,<sup>30</sup> Omid Eshghi, MD,<sup>31</sup> Tobien H.C.M.L. Schreuder, MD,<sup>32</sup> Roel J.J. Heijboer, MD,<sup>33</sup> Koos Keizer, MD, PhD,<sup>34</sup> Alexander V. Tielbeek, MD, PhD,<sup>35</sup> Heleen M. den Hertog, MD, PhD,<sup>36</sup> Dick G. Gerrits, MD,<sup>37</sup> Renske M. van den Berg-Vos, MD, PhD,<sup>38</sup> Giorgos B. Karas, MD,<sup>39</sup> Ewout W. Steyerberg, MD, PhD,<sup>7</sup> H. Zwenneke Flach, MD,<sup>26</sup>

Henk A. Marquering, PhD,<sup>40,1</sup> Marieke E.S. Sprengers, MD, PhD,<sup>1</sup> Sjoerd F.M. Jenniskens, MD, PhD,<sup>41</sup> Ludo F.M. Beenen, MD,<sup>1</sup> René van den Berg, MD, PhD,<sup>1</sup> Peter J. Koudstaal, MD, PhD,<sup>2</sup> Wim H. van Zwam, MD, PhD,<sup>6</sup> Yvo B.W.E.M. Roos, MD, PhD,<sup>5</sup> Aad van der Lugt, MD, PhD,<sup>3</sup> Robert J. van Oostenbrugge, MD, PhD,<sup>4</sup> Charles B.L.M. Majoie, MD, PhD,<sup>1</sup> and Diederik W.J. Dippel, MD, PhD<sup>2</sup>.

1) Department of Radiology, Academic Medical Center Amsterdam, the Netherlands; 2) Department of Neurology, Erasmus MC University Medical Center Rotterdam, the Netherlands; 3) Department of Radiology, Erasmus MC University Medical Center Rotterdam, the Netherlands; 4) Department of Neurology, Maastricht University Medical Center and Cardiovascular Research Institute Maastricht, the Netherlands; 5) Department of Neurology, Academic Medical Center Amsterdam, the Netherlands; 6) Department of Radiology, Maastricht University Medical Center, the Netherlands; 7) Department of Public Health, Erasmus MC University Medical Center Rotterdam, the Netherlands; 8) Department of Radiology, Texas Stroke Institute, Plano, Texas; 9) Department of Neurology, Sint Antonius Hospital, Nieuwegein, the Netherlands; 10) Department of Radiology, Sint Antonius Hospital, Nieuwegein, the Netherlands; 11) Department of Neurology, Leiden University Medical Center, Leiden, the Netherlands; 12) Department of Radiology, Leiden University Medical Center, Leiden, the Netherlands; 13) Department of Neurology, Rijnstate Hospital, Arnhem, the Netherlands; 14) Department of Radiology, Rijnstate Hospital, Arnhem, the Netherlands; 15) Department of Radiology, MC Haaglanden, the Hague, the Netherlands; 16) Department of Neurology, MC Haaglanden, the Hague, the Netherlands; 17) Department of Neurology, Haga Hospital, the Hague, the Netherlands; 18) Department of Radiology, Haga Hospital, the Hague, the Netherlands; 19) Department of Neurology, University Medical Center Utrecht, Utrecht, the Netherlands; 20) Department of Radiology, University Medical Center Utrecht, Utrecht, the Netherlands; 21) Department of Neurology, Radboud University Medical Center, Nijmegen, the Netherlands; 22) Department of Neurosurgery, Radboud University Medical Center, Nijmegen, the Netherlands; 23) Department of Neurology, Sint Elisabeth Hospital, Tilburg, the Netherlands; 24) Department of Neurology, Isala Klinieken, Zwolle, the Netherlands; 25) Department of Radiology, Isala Klinieken, Zwolle, the Netherlands; 26) Department of Neurology, Reinier de Graaf Gasthuis, Delft, the Netherlands; 27) Department of Radiology, Reinier de Graaf Gasthuis, Delft, the Netherlands; 28) Department of Neurology, VU Medical Center, Amsterdam, the Netherlands; 29) Department of Radiology, VU Medical Center, Amsterdam, the Netherlands; 30) Department of Neurology, University Medical Center Groningen, Groningen, the Netherlands; 31) Department of Radiology, University Medical Center Groningen, Groningen, the Netherlands; 32) Department of Neurology, Atrium Medical Center, Heerlen, the Netherlands; 33) Department of Radiology, Atrium Medical Center, Heerlen, the Netherlands; 34) Department of Neurology, Catharina Hospital, Eindhoven, the Netherlands; 35) Department of Radiology, Catharina Hospital, Eindhoven, the Netherlands; 36) Department of Neurology, Medical Spectrum Twente, Enschede, the Netherlands; 37) Department of Radiology, Medical Spec-

trum Twente, Enschede, the Netherlands; 38) Department of Neurology, Sint Lucas Andreas Hospital, Amsterdam, the Netherlands; 39) Department of Radiology, Sint Lucas Andreas Hospital, Amsterdam, the Netherlands; 40) Department of Biomedical Engineering and Physics, Academic Medical Center Amsterdam, the Netherlands; 41) Department of Radiology, Radboud University Medical Center, Nijmegen, the Netherlands.

Disclosures: Olvert A. Berkhemer—UNRELATED: Payment for Lectures Including Service on Speakers Bureaus: The Academic Medical Center received funds from Stryker for consultations by O.A.B.\* Emilie M.M. Santos—UNRELATED: Grant: Stichting voor de technische wetenschappen (STW), Comments: 11632.\* Albert J. Yoo—UNRELATED: Consultancy: Neuravi, Comments: core imaging lab activities and directorship; Grants/Grants Pending: Penumbra, Comments: core imaging lab activities.\* Wim H. van Zwam—UNRELATED: Consulting Fee or Honorarium: Stryker, Codman Neuro, Comments: modest speaker fees.\* Robert J. van Oostenbrugge—UNRELATED: Board Membership: Medtronic, Comments: member of Data and Safety Monitoring Board of SURTAVI, a cardiointervention trial of valve replacement.\* Aad van der Lugt—RELATED: Grant: Dutch Heart Foundation, Angiocare BV, Covidien/ev3 (Medtronic), Medac/Lamepro, Penumbra, Stryker.\* Diederik W.J. Dippel—UNRELATED: Board Membership: The MR CLEAN trial was partly funded by the Dutch Heart Foundation and by unrestricted grants from Angiocare BV, Medtronic/Covidien/ev3, Medac/Lamepro, Penumbra, Stryker, and Top Medical/Concentric\*; Consultancy: Erasmus MC received funds from Stryker and Bracco for consultations by D.W.J.D.\* Henk A. Marquering—RELATED: Grant: Information Technology for European Advancement 3\*; OTHER: cofounder and shareholder of Nico-Lab. Charles B.L.M. Majoie—RELATED: Grant: Dutch Heart Foundation\*; Consulting Fee or Honorarium: Dr Majoie's institution (Academic Medical Center) received funds from Stryker for consultations by C.B.L.M.M.\*; UNRELATED: Grants/Grants Pending: TWIN Foundation\*; Payment for Lectures Including Service on Speakers Bureaus: Stryker\*. \*Money paid to the institution.

## REFERENCES

- Berkhemer OA, Fransen PS, Beumer D, et al; MR CLEAN Investigators. **A randomized trial of intraarterial treatment for acute ischemic stroke.** *N Engl J Med* 2015;372:11–20 CrossRef Medline
- Campbell BC, Mitchell PJ, Kleinig TJ, et al; EXTEND-IA Investigators. **Endovascular therapy for ischemic stroke with perfusion-imaging selection.** *N Engl J Med* 2015;372:1009–18 CrossRef Medline
- Goyal M, Demchuk AM, Menon BK, et al; ESCAPE Trial Investigators. **Randomized assessment of rapid endovascular treatment of ischemic stroke.** *N Engl J Med* 2015;372:1019–30 CrossRef Medline
- Saver JL, Goyal M, Bonafe A, et al; SWIFT PRIME Investigators. **Stent-retriever thrombectomy after intravenous t-PA vs. t-PA alone in stroke.** *N Engl J Med* 2015;372:2285–95 CrossRef Medline
- Jovin TG, Chamorro A, Cobo E, et al; REVASCAT Trial Investigators. **Thrombectomy within 8 hours after symptom onset in ischemic stroke.** *N Engl J Med* 2015;372:2296–306 CrossRef Medline
- Kamalian S, Morais LT, Pomerantz SR, et al. **Clot length distribution and predictors in anterior circulation stroke: implications for intra-arterial therapy.** *Stroke* 2013;44:3553–56 CrossRef Medline
- Riedel CH, Zimmermann P, Jensen-Kondering U, et al. **The importance of size: successful recanalization by intravenous thrombolysis in acute anterior stroke depends on thrombus length.** *Stroke* 2011;42:1775–77 CrossRef Medline
- Lobsien D, Gawlitza M, Schaudinn A, et al. **Mechanical thrombectomy versus systemic thrombolysis in MCA stroke: a distance to thrombus-based outcome analysis.** *J Neurointerv Surg* 2016;8: 878–82 CrossRef Medline
- Mokin M, Morr S, Natarajan SK, et al. **Thrombus density predicts successful recanalization with Solitaire stent retriever thrombectomy in acute ischemic stroke.** *J Neurointerv Surg* 2015;7:104–07 CrossRef Medline
- Moftakhar P, English JD, Cooke DL, et al. **Density of thrombus on admission CT predicts revascularization efficacy in large vessel occlusion acute ischemic stroke.** *Stroke* 2013;44:243–45 CrossRef Medline
- Puig J, Pedraza S, Demchuk A, et al. **Quantification of thrombus**

- Hounsfield units on noncontrast CT predicts stroke subtype and early recanalization after intravenous recombinant tissue plasminogen activator. *AJNR Am J Neuroradiol* 2012;33:90–96 CrossRef Medline
12. Niesten JM, van der Schaaf IC, van der Graaf Y, et al. **Predictive value of thrombus attenuation on thin-slice non-contrast CT for persistent occlusion after intravenous thrombolysis.** *Cerebrovasc Dis* 2014;37:116–22 CrossRef Medline
  13. Santos EM, Marquering HA, den Blanken MD, et al; MR CLEAN Investigators. **Thrombus permeability is associated with improved functional outcome and recanalization in patients with ischemic stroke.** *Stroke* 2016;47:732–41 CrossRef Medline
  14. Fransen PSS, Beumer D, Berkhemer OA, et al; MR CLEAN Investigators. **MR CLEAN, a multicenter randomized clinical trial of endovascular treatment for acute ischemic stroke in the Netherlands: study protocol for a randomized controlled trial.** *Trials* 2014;15:343 CrossRef Medline
  15. Santos EM, Marquering HA, Berkhemer OA, et al; MR CLEAN Investigators. **Development and validation of intracranial thrombus segmentation on CT angiography in patients with acute ischemic stroke.** *PLoS One* 2014;9:e101985 CrossRef Medline
  16. van Swieten JC, Koudstaal PJ, Visser MC, et al. **Interobserver agreement for the assessment of handicap in stroke patients.** *Stroke* 1988; 19:604–07 CrossRef Medline
  17. Saver JL. **Novel end point analytic techniques and interpreting shifts across the entire range of outcome scales in acute stroke trials.** *Stroke* 2007;38:3055–62 CrossRef Medline
  18. Nunn A, Bath PM, Gray LJ. **Analysis of the modified Rankin scale in randomised controlled trials of acute ischaemic stroke: a systematic review.** *Stroke Res Treat* 2016;2016:9482876 CrossRef Medline
  19. Boers AM, Marquering HA, Jochem JJ, et al; MR CLEAN Investigators. **Automated cerebral infarct volume measurement in follow-up noncontrast CT scans of patients with acute ischemic stroke.** *AJNR Am J Neuroradiol* 2013;34:1522–27 CrossRef Medline
  20. Zaidat OO, Yoo AJ, Khatri P, et al; Cerebral Angiographic Revascularization Grading (CARG) Collaborators, STIR Revascularization Working Group, STIR Thrombolysis in Cerebral Infarction (TICI) Task Force. **Recommendations on angiographic revascularization grading standards for acute ischemic stroke: a consensus statement.** *Stroke* 2013;44:2650–63 CrossRef Medline
  21. Steyerberg EW. **Coding of categorical and continuous predictors.** In: Gail M, Krickeberg K, Samet J, et al, eds. *Clinical Prediction Models: A Practical Approach to Development, Validation, and Updating (Statistics for Biology and Health)*. New York: Springer-Verlag; 2009:159–73 CrossRef
  22. Yilmaz U, Roth C, Reith W, et al. **Thrombus attenuation does not predict angiographic results of mechanical thrombectomy with stent retrievers.** *AJNR Am J Neuroradiol* 2013;34:2184–86 CrossRef Medline
  23. Spiotta AM, Vargas J, Hawk H, et al. **Hounsfield unit value and clot length in the acutely occluded vessel and time required to achieve thrombectomy: complications and outcome.** *J Neurointervent Surg* 2014;6:423–27 CrossRef Medline
  24. New PF, Aronow S. **Attenuation measurements of whole blood and blood fractions in computed tomography.** *Radiology* 1976;121: 635–40 CrossRef Medline
  25. Friedrich B, Gawlitzka M, Schob S, et al. **Distance to thrombus in acute middle cerebral artery occlusion: a predictor of outcome after intravenous thrombolysis for acute ischemic stroke.** *Stroke* 2015;46: 692–96 CrossRef Medline
  26. Riedel CH, Jensen U, Rohr A, et al. **Assessment of thrombus in acute middle cerebral artery occlusion using thin-slice nonenhanced computed tomography reconstructions.** *Stroke* 2010;41:1659–64 CrossRef Medline
  27. Santos EM, Yoo AJ, Beenen LF, et al; MR CLEAN Investigators. **Observer variability of absolute and relative thrombus density measurements in patients with acute ischemic stroke.** *Neuroradiology* 2016;58:133–39 CrossRef Medline
  28. Mishra SM, Dykeman J, Sajobi TT, et al. **Early reperfusion rates with IV tPA are determined by CTA clot characteristics.** *AJNR Am J Neuroradiol* 2014;35:2265–72 CrossRef Medline
  29. Frölich AM, Psychogios MN, Klotz E, et al. **Antegrade flow across incomplete vessel occlusions can be distinguished from retrograde collateral flow using 4-dimensional computed tomographic angiography.** *Stroke* 2012;43:2974–79 CrossRef Medline

# Risk Factor Analysis of Recanalization Timing in Coiled Aneurysms: Early versus Late Recanalization

 J.P. Jeon,  Y.D. Cho,  D.H. Yoo,  J. Moon,  J. Lee,  W.-S. Cho,  H.-S. Kang,  J.E. Kim, and  M.H. Han



## ABSTRACT

**BACKGROUND AND PURPOSE:** Long-term documentation of anatomic and angiographic characteristics pertaining to the timing of recanalization in coiled aneurysms has been insufficient. Our intent was to analyze and compare early and late-phase recanalization after coiling, identifying respective risk factors.

**MATERIALS AND METHODS:** A total of 870 coiled saccular aneurysms were monitored for extended periods (mean,  $30.8 \pm 8.3$  months). Medical records and radiologic data were also reviewed, stratifying patients as either early ( $n = 128$ ) or late ( $n = 52$ ) recanalization or as complete occlusion ( $n = 690$ ). Early recanalization was equated with confirmed recanalization within 6 months after the procedure, whereas late recanalization was defined as verifiable recanalization after imaging confirmation of complete occlusion at 6 months. A multinomial regression model served to assess potential risk factors, the reference point being early recanalization.

**RESULTS:** Posterior circulation ( $P = .009$ ), subarachnoid hemorrhage at presentation ( $P = .011$ ), second attempt for recanalized aneurysm ( $P < .001$ ), and aneurysm size  $>7$  mm ( $P < .001$ ) emerged as variables significantly linked with early recanalization (versus complete occlusion). Late (versus early) recanalization corresponded with aneurysms  $\leq 7$  mm ( $P = .013$ ), and in a separate subanalysis of lesions  $\leq 7$  mm, aneurysms 4–7 mm showed a significant predilection for late recanalization ( $P = .008$ ). However, the propensity for complete occlusion in smaller lesions ( $\leq 7$  mm) increased as the size diminished.

**CONCLUSIONS:** Although long-term complete occlusion after coiling was more likely in aneurysms  $\leq 7$  mm, such lesions were more prone to late (versus early) recanalization, particularly those of 4–7 mm in size. Long-term follow-up imaging is thus appropriate in aneurysms  $>4$  mm to detect late recanalization of those formerly demonstrating complete occlusion.

Endovascular coiling is widely used in treating intracranial aneurysms. Despite continued improvement in related techniques and devices, the potential for recanalization remains. Risk factors linked to recanalization have been studied widely through comparative analysis, examining SAH at presentation, larger aneurysms, posterior locations, and other variables.<sup>1,2</sup> Coiled aneurysms showing major recanalization are subsequently in need of additional coiling, given the odds of rebleeding. Raymond et al<sup>3</sup> found that 46.9% of all recanalizations occurred within 6 months

of procedures, with nearly 40% showing major recanalization.<sup>4</sup> As a function of the follow-up duration, aneurysm size and neck diameter and initial postembolization status were associated with the recanalization of coiled aneurysms monitored for 17 months.<sup>3</sup> However, in coiled aneurysms followed for  $<17$  months, the initial postembolization status emerged as the sole significant risk factor for recanalization. Such a discrepancy may imply that risk factors inherent in aneurysm configuration have a greater long-term impact on recanalization.<sup>4,5</sup> Therefore, an association between the timing of recanalization and related risk factors is feasible. Most previous studies in this setting have limited risk factor analysis to patients showing either recanalization or complete occlusion, without considering time to recanalization. In this study, coiled saccular aneurysms were monitored over a longer term to analyze and compare early and late-phase recanalization, thereby identifying respective risk factors.

## MATERIALS AND METHODS

A retrospective analysis of 898 patients (1035 aneurysms) took place, each patient having undergone coil embolization between

Received January 9, 2017; accepted after revision April 10.

From the Department of Neurosurgery (J.P.J.), Hallym University College of Medicine, Chuncheon, Korea; and Departments of Radiology (Y.D.C., D.H.Y., J.M.) and Neurosurgery (J.L., W.-S.C., H.-S.K., J.E.K., M.H.H.), Seoul National University College of Medicine, Seoul, Korea.

Please address correspondence to Young Dae Cho, MD, Department of Radiology, Seoul National University Hospital, Seoul National University College of Medicine, 28 Yongon-dong, Jongno-gu, Seoul, Korea 110-744; e-mail: aronnn@naver.com

 Indicates article with supplemental on-line table.

 Indicates article with supplemental on-line photo.

<http://dx.doi.org/10.3174/ajnr.A5267>

January 2008 and December 2010 at a single institution. Nonsaccular aneurysms ( $n = 70$ ), specifically the fusiform/dissection, traumatic, or infectious types, were excluded from this analysis. The study end point was the timing of recanalization (early versus late) during follow-up. Another 66 patients lacking 6-month imaging data (lost to follow-up, 40; vegetative states, 16; deaths, 10) and 29 aneurysms followed for 6 months only were secondarily excluded. Ultimately, 746 patients with 870 saccular intracranial aneurysms who were monitored for more than 12 months met criteria for study enrollment.

In reviewing the medical records, sex, age, clinical presentation (unruptured intracranial aneurysm or SAH), and attempt at embolization (first versus second) were recorded, in addition to histories of hypertension, current smoking, and antiplatelet regimens. Patient angiographic variables included size of aneurysm (overall and at neck)<sup>5</sup>; circulatory location (anterior [including posterior communicating artery] versus posterior)<sup>6</sup>; aneurysm type (sidewall versus bifurcation) and depth-to-neck ratio; confirmed stent placement; initial postembolization status (successful occlusion versus residual sac)<sup>4</sup>; and coil technology (hydrogel-modified [HydroSoft; MicroVention, Tustin, California] or polyglycolic acid/lactide copolymer-coated [Matrix; Boston Scientific, Natick, Massachusetts]). Aneurysms were also grouped according to the extent of bioactive coil used (relative to the collective length of inserted coil) as bare ( $\leq 50\%$ ) or bioactive ( $> 50\%$ ). This study was conducted with the approval of our institutional review boards. The requirement to obtain written informed consent for study participation was waived.

### **Endovascular Procedure and Angiographic Follow-Up**

Most endovascular procedures were conducted under general anesthesia using an Integris V (Philips Healthcare, Best, the Netherlands) scanner in each instance.<sup>4</sup> Dual-agent antiplatelet therapy (loading doses [ie, 300 mg each] of clopidogrel and aspirin), given 1 day before procedures, plus additional clopidogrel (75 mg) and aspirin (100 mg) dosing on the mornings of procedures, were administered to patients with unruptured aneurysms for anticipated stent protection.<sup>7</sup> In poor responders to clopidogrel, signaled by the VerifyNow P2Y12 assay (Accumetrics, San Diego, California), cilostazol was added. If stent placement was unlikely, antiplatelet medications were not routinely used except in patients receiving such agents for other medical conditions. A bolus of heparin (3000 IU), given upon placement of the femoral arterial sheath, was thereafter sustained by hourly doses (1000 IU), and the activated clotting time was monitored each hour. Continuation of dual antiplatelet therapy was advised for at least 3 months postoperatively, followed by single-agent maintenance for at least 1 year in patients with stents deployed. In the absence of stent placement, antiplatelet therapy was selectively dispensed in instances of prior antiplatelet medication use, coil protrusion, or procedural thromboembolism.

Immediate postembolization angiographic results were graded as follows by using the 3-point Raymond scale: complete occlusion, residual neck, or residual sac. Complete occlusion and small residual neck were considered successful occlusive attempts.<sup>4</sup> Follow-up radiologic examinations, performed at 6, 12, 24, and 36 months post-procedure, relied on TOF-MRA, with 3D reconstruction and source

images. Additional plain radiography was recommended at postembolization months 1 and 3 in patients presenting with hemorrhage. Conventional angiography was advised if MRA assessment of treated aneurysms was not feasible or if recanalization was suspected by non-invasive diagnostics (such as MRA or plain radiography) to gauge the need for further treatment. Anatomic outcomes in follow-up were categorized by the Raymond scale as follows: complete occlusion and recanalization (minor or major). Early recanalization was equated with confirmed recanalization within 6 months or upon postembolization follow-up imaging at 6 months, whereas late recanalization was defined as verifiable recanalization after imaging confirmation of complete occlusion at 6 months. Two qualified neurointerventionists (Y.D.C. [10 years' experience] and H.-S.K. [15 years' experience]) reviewed the radiologic data. In cases of discrepancy, a consensus was reached by the third interventional neuroradiologist (M.H.H. [ $> 25$  years' experience]).

### **Statistical Analyses**

Continuous data are expressed as mean  $\pm$  standard deviation by using  $\chi^2$  or Fisher exact test and unpaired  $t$  test to assess categorical and continuous variables, respectively. Univariate analysis was applied to evaluate between-group differences (early or late recanalization and stable occlusion). To examine the interrelationships of risk factors, a multinomial regression model was engaged, with early recanalization serving as the reference point. Risk factors differing by group at the  $P < .10$  level were entered into the model. Nagelkerke  $R^2$  was measured for explaining variation, which is estimated on the log-likelihood scale. A Kaplan-Meier estimate of cumulative survival (without recanalization) in coiled aneurysms according to aneurysm size was performed. All calculations relied on standard statistical software (SPSS v19; IBM, Armonk, New York), setting significance at  $P < .05$ .

## **RESULTS**

### **Characteristics of Patient Enrollees**

A total of 870 coiled saccular aneurysms were monitored for a mean period of  $30.8 \pm 8.3$  months. Female patients accounted for 68.4% (595/870) of the aneurysms, and the mean age of all patients was  $57.9 \pm 11.0$  years. Anterior circulation ( $n = 802$ ; 92.2%) and bifurcation aneurysms ( $n = 388$ ; 44.6%) predominated. Successful occlusion as an initial angiographic outcome was achieved in 657 coiled aneurysms (75.5%), with mean aneurysm size estimated at  $5.3 \pm 3.3$  mm. Overall, 712 (81.8%) aneurysms were  $\leq 7$  mm. SAH was evident at presentation in 138 cases (15.9%), including 74 recanalized aneurysms (8.5%). In 707 aneurysms (81.3%), the coil inserted qualified as bare ( $\leq 50\%$  bioactive). Stents were deployed in 222 instances (25.5%). During the follow-up period, 690 coiled aneurysms displayed complete occlusion, early recanalization was observed in 128 (minor recanalization,  $n = 45$ ; major recanalization,  $n = 83$ ), and late recanalization developed in 52 (minor recanalization,  $n = 34$ ; major recanalization,  $n = 18$ ). In terms of late recanalization, 31 (59.6%) instances were evident within 6–12 months, 19 (36.5%) within 12–24 months, and 2 (3.9%) within 24–36 months after procedures. Retreatment was recommended for major recanalized aneurysms and was actually performed as follows: 48 (57.8%) occurring early and 11 (61.1%) occurring late. During the follow-

up, no patients included in this study experienced SAH or rebleeding. Detailed data on characteristics of the aneurysms in this cohort are shown in Table 1.

### Risk Factors of Late Recanalization and Complete Occlusion

In between-group comparisons, female sex, age, history of hypertension, hyperlipidemia, smoking, aneurysm type, depth-to-neck ratio >1, initial postembolization status, and >50% bioactive coil usage did not reach statistical significance. However, aneurysm location, clinical presentation, second embolization for recanalization, aneurysm size >7 mm, and stent deployment differed significantly by group in the univariate analysis (Table 1).

The multinomial regression model further disclosed that posterior circulation ( $P = .009$ ), SAH presentation ( $P = .011$ ), required second embolization ( $P < .001$ ), and aneurysm size >7 mm ( $P < .001$ ) showed stronger associations with the early recanalization (versus complete occlusion) group (Table 2).

In comparing early and late recanalization, a link between aneurysm size >7 mm and early recanalization was apparent, whereas smaller lesions ( $\leq 7$  mm) were associated with late recan-

alization ( $P = .013$ ). Other group variables, such as posterior circulation, SAH presentation, second attempt (in recanalized lesions), antiplatelet agent use, and stent deployment did not differ significantly (Table 2). Further subanalysis of aneurysms  $\leq 7$  mm showed a significant relationship between aneurysms 4–7 mm in size and late recanalization (odds ratio, 3.00;  $P = .008$ ). However, of those aneurysms  $\leq 7$  mm, diminishing size and stable occlusion were increasingly linked (On-line Table).

According to the Kaplan-Meier method, the cumulative survival rate without recanalization at 6 months was 90.7% in aneurysms  $\leq 7$  mm and 60.8% in aneurysms >7 mm. At 30 months after the procedure, the cumulative survival rate was 84.8% for aneurysms  $\leq 7$  mm and 52.8% for aneurysms >7 mm ( $P < .001$ ) (On-line Fig).

### DISCUSSION

Our findings indicate that small-sized aneurysms ( $\leq 7$  mm) are relatively more susceptible to late (versus early) recanalization, despite a stronger association with complete occlusion. On the other hand, early recanalization correlated with locations in the posterior circulation, SAH presentation, second coiling for recanalization, and aneurysm size >7 mm. In particular, aneurysms ranging from 4–7 mm were more prone to late recanalization. Consequently, small-sized aneurysms >4 mm should be followed long-term for potential delayed recanalization, despite any proof of complete occlusion at midterm follow-up.

Patients presenting with SAH are also more likely to develop recanalization after coiling procedures.<sup>3,8</sup> The dynamic nature of ruptured aneurysms and clot lysis appears to promote recanalization. Wardlaw et al<sup>9</sup> reported that such aneurysms showed increased cross-sectional area expansibility (mean, 53%) during the cardiac cycle relative to adjacent normal arteries (mean, 20%). Recently, higher saccular pulsatile pressures have also been recorded in ruptured (versus unruptured) lesions,<sup>10</sup> and thinner, degenerative arterial walls, with significant macrophage infiltration, have been documented in histologic sections of ruptured aneurysms.<sup>11</sup> Mural instability and the increased pulsatile pressure of ruptured aneurysms may thus encourage greater coil compaction than that encountered in unruptured counterparts.<sup>12</sup> Lysis of clot may take place as well within thrombus or at rupture sites once related hypercoagulability subsides.<sup>8</sup>

Of particular importance, an increase in packing attenuation of near 30% may reduce intra-aneurysmal wall shear stress, promoting recanalization.<sup>13</sup> The probability of coil compaction declines if aneurysms are more densely packed (>20% in aneurysms <200 mm<sup>3</sup>; >24% in aneurysms <600 mm<sup>3</sup>).<sup>14</sup> Packing attenuation in our cohort (when excluding recanalized aneurysms) did not differ significantly in patients presenting with ( $36.3 \pm 10.9$ ) or without ( $36.1 \pm 8.8$ ) SAH ( $P = .859$ ). Nevertheless, SAH proved significantly more frequent in aneurysms marked by early recanalization (versus complete occlusion) ( $P = .011$ ). Further studies on the mechanism of recanalization in ruptured aneurysms are clearly needed.

**Table 1: Baseline characteristics of study enrollees**

Variables	Early (n = 128)	Late (n = 52)	Complete (n = 690)	P Value <sup>a</sup>
Female	94 (73.4%)	34 (65.4%)	467 (67.7%)	.389
Age, yr	58.0 $\pm$ 11.1	55.3 $\pm$ 12.1	58.1 $\pm$ 10.5	.330
HTN	80 (62.5%)	25 (48.1%)	375 (54.3%)	.134
Hyperlipidemia	15 (11.7%)	12 (23.1%)	123 (17.8%)	.126
Smoking	19 (14.8%)	6 (11.5%)	91 (13.2%)	.815
Location				
Anterior	104 (81.2%)	48 (92.3%)	650 (94.2%)	
Posterior	24 (18.8%)	4 (7.7%)	40 (5.8%)	<.001
Presentations				
UIA	99 (77.3%)	38 (73.1%)	595 (86.2%)	
SAH	29 (22.7%)	14 (26.9%)	95 (13.8%)	<.001
Second attempt	33 (25.8%)	7 (13.5%)	34 (4.9%)	<.001
Type				
Sidewall	66 (51.6%)	28 (53.9%)	388 (56.2%)	
Bifurcation	62 (48.4%)	24 (46.1%)	302 (43.8%)	.604
Maximum size, mm	8.3 $\pm$ 5.1	5.7 $\pm$ 2.2	4.6 $\pm$ 2.6	
Aneurysm size >7 mm	62 (48.4%)	12 (23.1%)	84 (12.2%)	<.001
D/N ratio (>1)	69 (53.9%)	35 (67.3%)	391 (56.7%)	.249
Balloon	22 (17.2%)	8 (15.4%)	162 (23.5%)	.141
Stent	45 (35.2%)	8 (15.4%)	169 (24.5%)	.009
Antiplatelet medication	48 (37.5%)	19 (36.5%)	183 (26.5%)	.018
Initial occlusion				
Successful occlusion	96 (75.0%)	42 (80.8%)	519 (75.2%)	
Residual sac	32 (25.0%)	10 (19.2%)	171 (24.8%)	.661
Bioactive coil (>50%)	26 (20.3%)	8 (15.4%)	129 (18.7%)	.743

**Note:**—D/N ratio indicates depth-to-neck ratio; HTN, hypertension; UIA, unruptured intracranial aneurysm.

<sup>a</sup>  $P < .05$  is significant.

**Table 2: Multinomial logistic regression; late recanalization versus complete occlusion (early recanalization serving as reference)<sup>a</sup>**

Variables	Late Recanalization		Complete Occlusion	
	Odds Ratio (95% CI)	P Value <sup>b</sup>	Odds Ratio (95% CI)	P Value <sup>b</sup>
Posterior circulation	0.54 (0.17–1.72)	.301	0.42 (0.22–0.80)	.009
SAH presentation	1.16 (0.53–2.56)	.710	0.51 (0.30–0.86)	.011
Second attempt	0.65 (0.24–1.73)	.39	0.15 (0.08–0.27)	<.001
Stent	0.53 (0.21–1.32)	.172	1.39 (0.84–2.31)	.197
Antiplatelet medication	1.15 (0.58–2.30)	.689	0.73 (0.47–1.14)	.167
Aneurysm size >7 mm	0.38 (0.18–0.82)	.013	0.17 (0.10–0.26)	<.001

<sup>a</sup> Reference category: early recanalization. Nagelkerke  $R^2 = 0.214$ .

<sup>b</sup>  $P < .05$  is significant.

Outcomes of the Unruptured Cerebral Aneurysm Study<sup>15</sup> have shown an association between aneurysms >7 mm in size and rupture. Relative to aneurysms 3–4 mm in size, larger lesions were at significantly greater risk (5–6 mm: hazard ratio = 1.13,  $P = .71$ ; 7–9 mm: hazard ratio = 3.35,  $P < .001$ ; 10–24 mm: hazard ratio = 9.09,  $P < .001$ ). According to the International Study of Unruptured Intracranial Aneurysms,<sup>16</sup> 5-year cumulative rupture rates in anterior circulation aneurysms without previous SAH also varied decisively by lesion size (<7 mm, 0%; 7–12 mm, 2.6%; 13–24 mm, 14.5%). Larger aneurysms also are more likely to recanalize. Cognard et al<sup>8</sup> earlier determined that recanalization rates indeed are a function of aneurysm size (2–3 mm, 8.7%; 4–5 mm, 9.0%; and 6–8 mm, 22.0%). In addition, Jeon et al<sup>5</sup> have shown an association between large aneurysms (>7 mm) completely occluded in 6-month follow-up images and late recanalization, and reports by Ogilvy et al<sup>17</sup> and Niimi et al<sup>18</sup> similarly maintain that larger aneurysms ( $\geq 10$  mm) are prone to recanalization. It is thus evident that large aneurysms are at peril of rupture and postprocedural recanalization. However, recanalization rates in small aneurysms have not been fully detailed, though they are considered to be low. Murayama et al<sup>19</sup> have cited a 5.1% overall recanalization rate for small aneurysms 4–10 mm in size with small necks, which was much lower than the 35.3% rate for larger aneurysms. The reported annual recanalization rate in aneurysms  $\leq 7$  mm showing complete occlusion at 6-month follow-up is 2.57%.<sup>5</sup> After some reflection, a subgroup analysis of our data was performed, examining recanalization rates in lesions <4 mm and in those 4–7 mm. Our findings showed that aneurysms 4–7 mm were more prone to late recanalization. Consequently, small-sized aneurysms >4 mm should be followed long-term for potential delayed recanalization despite confirming complete occlusion at midterm follow-up.

Stents are increasingly used in this setting if greater coil packing and flow diversion are anticipated.<sup>20–23</sup> Recanalization rates registered after stent-assisted coil embolization (6.6%–13%)<sup>4,24,25</sup> are notably lower than those encountered after simple coil embolization (10.7%–33.6%).<sup>3,26</sup> In our investigation, stent deployment differed significantly among 3 groups (early recanalization,  $n = 45$  [45/128, 35.2%]; late recanalization,  $n = 8$  [8/52, 15.4%]; and complete occlusion,  $n = 169$  [169/690, 24.5%] [ $P = .009$ ]) through univariate analysis. However, stent deployment held no significant association with complete occlusion or late recanalization in a multinomial logistic regression analysis using early recanalization as a reference. Although potential confounding factors related to the high probability of stent deployment in wide-neck aneurysms and the incorporation of arterial branches by aneurysms may have skewed our assessment of this presumptive benefit, Jeon et al<sup>20</sup> found that stents conferred no protective effects relative to progressive occlusion in small unruptured aneurysms with residual sac filling ( $P = .78$ ). Still, after various corrections in the propensity score analysis, stent placement did promote progressive occlusion in coiled aneurysms.<sup>20</sup> In our opinion, the impact of stents is better investigated by considering the probability of stent deployment.

Hemodynamic force is another reputed factor in aneurysm recanalization and growth.<sup>2</sup> In recanalized aneurysms, maximum

wall shear stress and spatially averaged wall shear stress exceed corresponding pretreatment values.<sup>27</sup> In addition, completely occluded aneurysms show diminished wall shear stress and flow velocity.<sup>28</sup> The efforts of Ortega et al<sup>29</sup> indicate that maximum wall shear stress increases at sites of blood flow impingement near remnant necks. Repetitive flow impingement and subsequent wall shear stress increments may thus lead to recanalization,<sup>4</sup> particularly in recanalized aneurysms. Our results also show that second attempts for recanalization were done with significantly greater frequency in early recanalized versus completely occluded aneurysms ( $P < .001$ ), with no statistical difference between the early and late recanalization groups.

The HydroSoft coil was constructed as a platinum coil with an inner core of hydrogel and was designed to improve packing attenuation with low stiffness.<sup>30</sup> Lee et al<sup>31</sup> reported that the mean packing attenuation of the aneurysms treated with the HydroSoft coil was significantly higher than of those treated with a bare platinum coil (36.0% versus 32.1%;  $P < .001$ ) without a difference in procedure-related complications. The use of the HydroSoft coil significantly lowered the retreatment rate at 12-month follow-up (adjusted risk ratio, 0.21; 95% CI: 0.07–0.64). Matrix detachable coils are covered with polyglycolic and polylactic acid and designed to enhance clot formation and fibrosis within the aneurysm sac.<sup>32</sup> A histology study showed a thick connective tissue formation that demarcated the aneurysm sac from the parent artery.<sup>33,34</sup> In our cohort, the number of treated aneurysms using bioactive coil (>50%) was 26/128 (20.3%) in early recanalization, 8/52 (15.4%) in late recanalization, and 129/690 (18.7%) in complete occlusion ( $P = .743$ ). We speculate that the relative low proportion of bioactive coil (>50%) might lead to insignificant association among the 3 groups.

Although risk factors in recanalization have been well described through comparative studies of stably occluded and recanalized aneurysms, the potential difference between early and late recanalization is perhaps another issue to pursue in devising strategies for patient management. Herein, we have focused on analyzing risk factors with respect to the timing of recanalization. Our findings indicate that aneurysms of 4–7 mm are at significant risk of late recanalization, thereby mandating long-term follow-up.

Unfortunately, selection bias in this large ( $n = 870$ ) and closely monitored sampling of aneurysms cannot be excluded, given the retrospective nature of this study. Furthermore, use of TOF-MRA in follow-up testing may entail some artifact because of stents obscuring recanalization.<sup>20</sup> Although the use of MIP in source images obtained by TOF-MRA has proved effective in estimating recanalization,<sup>35</sup> stent artifacts may still obscure instances of minor recanalizations, impacting calculated recanalization rates.<sup>20</sup> In addition, coil compaction and recanalization could be more pronounced in patients with small aneurysms who underwent MRA follow-up. On another note, anterior circulatory and unruptured aneurysms in our cohort accounted for 92.2% and 84.1% of lesions, respectively. Thus, lesions of the posterior circulation and ruptured aneurysms were not well represented.<sup>5</sup> Finally, and more specifically, recanalization of aneurysms may occur through growth of the lesions themselves, through poorly formed/degraded thrombus, or through failed

attempts at reconfiguring the saccular dome or neck.<sup>36</sup> More detailed investigations of recanalization are needed to better correlate angiographic outcomes with reciprocating effects of the healing process.

## CONCLUSIONS

Risk factors related to early recanalization in this study were posterior circulatory location, SAH presentation, second coiling for recanalization, and aneurysm size >7 mm. Although aneurysms ≤7 mm in size were more prone to complete occlusion in long-term follow-up, a relative predisposition to late (versus early) recanalization was apparent, particularly in aneurysms of 4–7 mm. Long-term follow-up imaging is thus advisable in aneurysms >4 mm to exclude progression to recanalization, despite complete occlusion at midterm monitoring.

Disclosures: Moon Hee Han—UNRELATED: Consultancy: Microvention\*. \*Money paid to the institution.

## REFERENCES

1. Ries T, Siemonsen S, Thomalla G, et al. **Long-term follow-up of cerebral aneurysms after endovascular therapy prediction and outcome of retreatment.** *AJNR Am J Neuroradiol* 2007;28:1755–61 CrossRef Medline
2. Park W, Song Y, Park KJ, et al. **Hemodynamic characteristics regarding recanalization of completely coiled aneurysms: computational fluid dynamic analysis using virtual models comparison.** *Neurointervention* 2016;11:30–36 CrossRef Medline
3. Raymond J, Guilbert F, Weill A, et al. **Long-term angiographic recurrences after selective endovascular treatment of aneurysms with detachable coils.** *Stroke* 2003;34:1398–403 CrossRef Medline
4. Jeon JP, Cho YD, Rhim JK, et al. **Fate of coiled aneurysms with minor recanalization at 6 months: rate of progression to further recanalization and related risk factors.** *AJNR Am J Neuroradiol* 2016;37:1490–95 CrossRef Medline
5. Jeon JP, Cho YD, Rhim JK, et al. **Extended monitoring of coiled aneurysms completely occluded at 6-month follow-up: late recanalization rate and related risk factors.** *Eur Radiol* 2016;26:3319–26 CrossRef Medline
6. Cho YD, Jeon JP, Rhim JK, et al. **Progressive thrombosis of small saccular aneurysms filled with contrast immediately after coil embolization: analysis of related factors and long-term follow-up.** *Neuroradiology* 2015;57:615–23 CrossRef Medline
7. Cho YD, Lee WJ, Kim KM, et al. **Stent-assisted coil embolization of posterior communicating artery aneurysms.** *AJNR Am J Neuroradiol* 2013;34:2171–76 CrossRef Medline
8. Cognard C, Weill A, Spelle L, et al. **Long-term angiographic follow-up of 169 intracranial berry aneurysms occluded with detachable coils.** *Radiology* 1999;212:348–56 CrossRef Medline
9. Wardlaw JM, Cannon JC. **Color transcranial “power” Doppler ultrasound of intracranial aneurysms.** *J Neurosurg* 1996;84:459–61 CrossRef Medline
10. Wardlaw JM, Cannon J, Statham PF, et al. **Does the size of intracranial aneurysms change with intracranial pressure? Observations based on color “power” transcranial Doppler ultrasound.** *J Neurosurg* 1998;88:846–50 CrossRef Medline
11. Kataoka K, Taneda M, Asai T, et al. **Structural fragility and inflammatory response of ruptured cerebral aneurysms. A comparative study between ruptured and unruptured cerebral aneurysms.** *Stroke* 1999;30:1396–401 CrossRef Medline
12. Tan IY, Agid RF, Willinsky RA. **Recanalization rates after endovascular coil embolization in a cohort of matched ruptured and unruptured cerebral aneurysms.** *Interv Neuroradiol* 2011;17:27–35 CrossRef Medline
13. Morales HG, Kim M, Vivas EE, et al. **How do coil configuration and packing density influence intra-aneurysmal hemodynamics?** *AJNR Am J Neuroradiol* 2011;32:1935–41 CrossRef Medline
14. Sluzewski M, van Rooij WJ, Slob MJ, et al. **Relation between aneurysm volume, packing, and compaction in 145 cerebral aneurysms treated with coils.** *Radiology* 2004;231:653–58 CrossRef Medline
15. UCAS Japan Investigators, Morita A, Kirino T, et al. **The natural course of unruptured cerebral aneurysms in a Japanese cohort.** *N Engl J Med* 2012;366:2474–82 CrossRef Medline
16. Wiebers DO, Whisnant JP, Huston J, 3rd, et al. **Unruptured intracranial aneurysms: natural history, clinical outcome, and risks of surgical and endovascular treatment.** *Lancet* 2003;362:103–10 CrossRef Medline
17. Ogilvy CS, Chua MH, Fusco MR, et al. **Validation of a system to predict recanalization after endovascular treatment of intracranial aneurysms.** *Neurosurgery* 2015;77:168–73; discussion 173–74 CrossRef Medline
18. Niimi Y, Song J, Madrid M, et al. **Endosaccular treatment of intracranial aneurysms using Matrix coils: early experience and mid-term follow-up.** *Stroke* 2006;37:1028–32 CrossRef Medline
19. Murayama Y, Nien YL, Duckwiler G, et al. **Guglielmi detachable coil embolization of cerebral aneurysms: 11 years’ experience.** *J Neurosurg* 2003;98:959–66 CrossRef Medline
20. Jeon JP, Cho YD, Rhim JK, et al. **Effect of stenting on progressive occlusion of small unruptured saccular intracranial aneurysms with residual sac immediately after coil embolization: a propensity score analysis.** *J Neurointerv Surg* 2016;8:1025–29 CrossRef Medline
21. Lawson MF, Newman WC, Chi YY, et al. **Stent-associated flow remodeling causes further occlusion of incompletely coiled aneurysms.** *Neurosurgery* 2011;69:598–603; discussion 603–04 CrossRef Medline
22. Park KY, Kim BM, Kim DJ. **Comparison between balloon-assisted and stent-assisted technique for treatment of unruptured internal carotid artery aneurysms.** *Neurointervention* 2016;11:99–104 CrossRef Medline
23. Liu H, Choe J, Jung SC, et al. **Does a low-wall coverage stent have a flow diverting effect in small aneurysms?** *Neurointervention* 2015;10:89–93 CrossRef Medline
24. Hwang SK, Hwang G, Bang JS, et al. **Endovascular Enterprise stent-assisted coil embolization for wide-necked unruptured intracranial aneurysms.** *J Clin Neurosci* 2013;20:1276–79 CrossRef Medline
25. Luo CB, Teng MM, Chang FC, et al. **Stent-assisted coil embolization of intracranial aneurysms: a single center experience.** *J Chin Med Assoc* 2012;75:322–28 CrossRef Medline
26. Kwon SC, Kwon OK, Korean Unruptured Cerebral Aneurysm Coiling (KUCAC) Investigators. **Endovascular coil embolization of unruptured intracranial aneurysms: a Korean multicenter study.** *Acta Neurochir (Wien)* 2014;156:847–54 CrossRef Medline
27. Li C, Wang S, Chen J, et al. **Influence of hemodynamics on recanalization of totally occluded intracranial aneurysms: A patient-specific computational fluid dynamic simulation study.** *Neurosurg* 2012;117:276–83 CrossRef
28. Luo B, Yang X, Wang S, et al. **High shear stress and flow velocity in partially occluded aneurysms prone to recanalization.** *Stroke* 2011;42:745–53 CrossRef Medline
29. Ortega J, Hartman J, Rodriguez J, et al. **Post-treatment hemodynamics of a basilar aneurysm and bifurcation.** *Ann Biomed Eng* 2008;36:1531–46 CrossRef Medline
30. Guo XB, Fan YM, Zhang JN. **HydroSoft coil versus HydroCoil for endovascular aneurysm occlusion study: a single center experience.** *Eur J Radiol* 2011;79:e42–46 CrossRef Medline
31. Lee JY, Seo JH, Lee SJ, et al. **Mid-term outcome of intracranial aneurysms treated with HydroSoft coils compared to historical controls treated with bare platinum coils: a single-center experience.** *Acta Neurochir (Wien)* 2014;156:1687–94 CrossRef Medline
32. Rossitti S. **Endovascular coiling of intracranial aneurysms using bioactive coils: a single-center study.** *Acta Radiol* 2007;48:565–76 CrossRef Medline
33. Szikora I, Seifert P, Hanzely Z, et al. **Histopathologic evaluation of aneurysms treated with Guglielmi detachable coils or Matrix**

- detachable microcoils.** *AJNR Am J Neuroradiol* 2006;27:283–88 Medline
34. Gonzalez NR, Patel AB, Murayama Y, et al. **Angiographic evidence of aneurysm neck healing following endovascular treatment with bio-active coils.** *AJNR Am J Neuroradiol* 2005;26:912–14 Medline
35. Cho YD, Kim KM, Lee WJ, et al. **Time-of-flight magnetic resonance angiography for follow-up of coil embolization with Enterprise stent for intracranial aneurysm: usefulness of source images.** *Korean J Radiol* 2014;15:161–68 CrossRef Medline
36. Brinjikji W, Kallmes DF, Kadirvel R. **Mechanisms of healing in coiled intracranial aneurysms: a review of the literature.** *AJNR Am J Neuroradiol* 2015;36:1216–22 CrossRef Medline

# Influence of Carotid Siphon Anatomy on Brain Aneurysm Presentation

 E. Waihrich,  P. Clavel,  G.A.C. Mendes,  C. Iosif,  I. Moraes Kessler, and  C. Mounayer



## ABSTRACT

**BACKGROUND AND PURPOSE:** Intracranial aneurysm is a devastating disease of complex etiology that is not fully understood. The purpose of this study was to assess the implications of carotid siphon anatomy for the formation and development of intracranial aneurysms.

**MATERIALS AND METHODS:** Between January 2007 and May 2015, lateral view digital subtraction angiographic images of 692 consecutive patients with intracranial aneurysms treated in our department of interventional neuroradiology were reviewed and had their angles measured. Data on the location, presentation, and size of the lesions were collected and evaluated by multivariate analysis in relation to the measured angles.

**RESULTS:** Of 692 aneurysms, 225 (32.51%) ruptured and 467 (67.49%) unruptured, 218 (31.50%) were in the carotid siphon and 474 (68.50%) were distal to the siphon, and the mean aneurysm size was  $7.99 \pm 6.95$  mm. Multivariate analysis showed an association between angles of  $>15.40^\circ$  and rupture ( $P = .005$ ), postsiphon location ( $P = .034$ ), and aneurysm size of  $>1.001$  mm ( $P = .015$ ). Multivariate analysis also showed that every 1-year increase in patient age produced an increase of 1.002 mm in aneurysm size ( $P = .015$ ).

**CONCLUSIONS:** There was a significant independent direct relation of greater anterior knee angle with intracranial aneurysms located distal to the carotid siphon, larger aneurysms, and greater risk of rupture. These findings may be associated with the hemodynamic interactions of blood flow and the curvature of the carotid siphon.

Intracranial aneurysms affect approximately 6%–10% of the world population. Fortunately, only 0.05% of patients progress to rupture, but they face a devastating consequence, subarachnoid hemorrhage, with mortality rates ranging from 56% to 80%.<sup>1,2</sup>

Several factors are related to the formation, development, and rupture of intracranial aneurysms. Among these, the hemodynamic interactions of blood flow and vessel wall have received special attention in recent years. The balance between hemodynamic stress secondary to blood flow in the water hammer pulse and parallel shear stress caused by blood viscosity and friction between blood and the arterial wall appears to be related to the origin and development of aneurysms. That hemodynamic contribution can be exemplified by the preferred location of aneurysms at arterial bifurcations and curvatures.<sup>3–6</sup> Thus, the carotid

siphon is of particular importance because it is a tortuous vessel segment with sharp bends through which blood enters the anterior cerebral circulation.<sup>7–9</sup>

The aim of this study was to investigate the morphologic characteristics of the carotid siphon and their possible association with the formation, development, and occurrence of intracranial aneurysms at this site.

## MATERIALS AND METHODS

The study was approved by the ethics committee of our institution, Dupuytren University Hospital, and written informed consent was obtained from each patient. Data were retrospectively and prospectively collected for all patients with intracranial aneurysms who underwent endovascular treatment between January 2007 and May 2015. Patients with posterior circulation aneurysms, poor-quality digital subtraction angiographic images preventing angle measurement, incomplete documentation, or conditions (medical or other) precluding follow-up were excluded.

Demographic data (age and sex), type of aneurysm, and angiographic features were evaluated. The following angiographic features were considered for analysis: aneurysm size (maximum aneurysm sac diameter), location of the aneurysm in the carotid

Received February 8, 2017; accepted after revision May 4.

From the Department of Interventional Neuroradiology (E.W., P.C., G.A.C.M., C.I., C.M.), Dupuytren University Hospital, Limoges, France; and Department of Neurosurgery (E.W., I.M.K.), Universidade de Brasília, Brasília, DF, Brazil.

Please address correspondence to Eduardo Siqueira Waihrich, MD, MSc, SHIS QI 15, Centro Médico Brasília - Brasília - DF 71635-550; e-mail: eduwaihrich@gmail.com

<http://dx.doi.org/10.3174/ajnr.A5285>

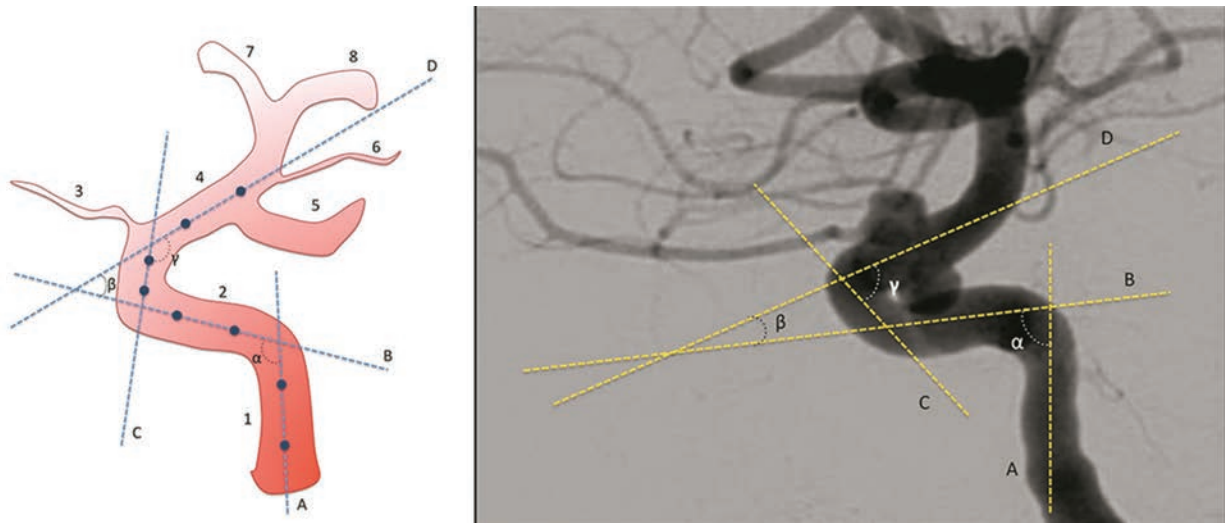


**FIG 1.** Technique for measurement of carotid siphon angles. On the left, an illustration of a carotid siphon with lines traced to cross the midpoints of the diameters of the straight segments of the siphon. On the right, an example of an actual measurement process. A, Line through the vertical petrous segment. B, Line through the horizontal cavernous segment. C, Line through the vertical cavernous segment. D, Line through the supraclinoid segment.  $\alpha$ , Posterior bend angle.  $\beta$ , Anterior bend angle.  $\gamma$ , Anterosuperior bend angle. 1, Ascending petrous segment. 2, Intracavernous segment. 3, Ophthalmic artery. 4, Supraclinoid segment. 5, Posterior communicating artery. 6, Anterior choroidal artery. 7, Anterior cerebral artery. 8, Middle cerebral artery.

siphon (cavernous or supraclinoid segment) or distal to it, and angle of the posterior and anterior knees of the carotid siphon.

Pretreatment intraoperative DSA images obtained after contrast injection into the affected carotid artery (lateral view with the external acoustic meatus at the same level) were assessed by 2 blinded neuroradiologists. Carotid siphon angles were measured at the intersection of 2 lines traced through the midpoints of the diameters of each straight segment of the siphon (Fig 1).<sup>10</sup> If the lines of the cavernous and supraclinoid segments crossed posterior to the siphon due to its tortuosity, the angle of the anterior knee of the carotid siphon received a negative value.<sup>10</sup>

### Statistical Analysis

Multivariate Poisson and logistic regression and multiple linear regression models were used to explore the relationship between demographic and angiographic data with respect to the measured angles.<sup>11-13</sup> Categorical independent variables were divided according to their classification, and continuous independent variables were divided with the median as the cutoff value, as long as a linearity correlation was not observed, as follows: sex (male or female), age (55 years or younger or 55 years and older), aneurysm rupture (yes or no), location (cavernous segment, supraclinoid segment, or distal to the carotid siphon), and size ( $\leq 5$  mm, 6–10 mm, 10–25 mm, or  $>25$  mm), anterior angle ( $\leq 15.40^\circ$  or  $>15.40^\circ$ ), and posterior angle ( $\leq 88.15^\circ$  or  $>88.15^\circ$ ). The cavernous location begins at the petrolingual ligament and extends to the proximal dural ring, which is formed by the medial and inferior periosteum of the anterior clinoid process; the supraclinoid location extended until carotid bifurcation and the postsiphon location comprised the bifurcation onwards. We decided to use the median as a cutoff value to have 2 groups with similar numbers of patients for multivariate analysis. In analysis between the angles and a single other numeric variable, the variables were also analyzed as continuous whenever feasible. Bivariate and multi-

variate analyses were performed, and in both, prevalence ratios and their respective 95% confidence intervals were calculated. The bivariate analysis was used to examine the association between each independent variable and the occurrence of ruptured intracranial aneurysms, followed by multivariate analysis. Statistical analysis was performed with SPSS, Version 22.0 (IBM, Armonk, New York).  $P < .05$  was considered significant.

### RESULTS

Between January 2007 and May 2015, 703 patients with a diagnosis of intracranial aneurysm were treated at the department of interventional neuroradiology of the institution. Of these, 640 patients were eligible and agreed to participate in the study, for a total of 692 intracranial aneurysms.

Of 692 aneurysms, 457 occurred in women (66.04%) and 235 in men (33.96%). The mean patient age was  $54.75 \pm 13.13$  years (men,  $54.70 \pm 13.16$  years; women,  $54.66 \pm 13.13$  years). There were 225 (32.51%) ruptured aneurysms and 467 (67.49%) unruptured aneurysms. Regarding aneurysm location, 218 (31.50%) were in the carotid siphon and 474 (68.50%) were distal to the siphon. Mean aneurysm size was  $7.99 \pm 6.95$  mm (Table 1).

### Aneurysm Rupture

The bivariate analysis showed a statistically significant association between a ruptured intracranial aneurysm and an anterior knee angle of  $>15.40^\circ$  (prevalence ratio = 1.45; 95% CI, 1.16–1.80). Subsequently, sex, age, location, size, and posterior and anterior knee angles were included in the Poisson regression model, but only an anterior knee angle of  $>15.40^\circ$  showed a significant association with ruptured intracranial aneurysms. After we adjusted for the variables mentioned above, there was an increased association (prevalence ratio = 1.36; 95% CI, 1.09–1.69)—that is, patients with aneurysms and an anterior knee angle of  $>15.40^\circ$  showed a 36% higher prevalence of rupture than patients with an anterior knee angle of  $\leq 15.40^\circ$  (Table 2).

In the stratified subgroup analysis by location, only aneurysms located in the anterior communicating artery showed a greater statistical risk of rupture in patients with an anterior angle of  $>15.40^\circ$  ( $P = .049$ ). The risk of rupture was 84% greater in patients with an anterior angle of  $>15.40^\circ$  than in those with an angle of  $\leq 15.40^\circ$  at this location (Table 3).

**Table 1: Epidemiologic data**

Variables	
Total No. of IAs (%)	692 (100)
Mean age (yr)	(54.75 $\pm$ 13.13)
Sex	
Women with IAs (No.) (%)	457 (66.04)
Mean age (yr)	(54.66 $\pm$ 13.13)
Men with IAs (No.) (%)	235 (33.96)
Mean age (yr)	(54.70 $\pm$ 13.16)
Rupture (No.) (%)	
Ruptured IAs	225 (32.51)
Unruptured IAs	467 (67.49)
IA location (No.) (%)	
Siphon	218 (31.50)
Cavernous segment	45 (6.50)
Supraclinoid segment	173 (25.00)
Ophthalmic	67 (9.68)
PcomA	96 (13.87)
Ant. chor	10 (1.45)
Postsiphon (No.) (%)	474 (68.50)
Bifurcation	35 (5.06)
MCA	237 (34.25)
AcomA	170 (24.57)
ACA/pericallosal	32 (4.62)
IA size (No.) (%)	
$\leq 5$ mm	334 (48.27)
6–10 mm	233 (33.67)
11–25 mm	97 (14.02)
$> 25$ mm	28 (4.05)

**Note:**—IA indicates intracranial aneurysm; PcomA, posterior communicating segment; Ant. chor, anterior choroidal segment; ACA, anterior cerebral artery; AcomA, anterior communicating artery.

**Table 2: Distribution of the study variables and association with aneurysm rupture based on crude and adjusted prevalence ratios according to the Poisson regression model with robust variance and their respective 95% CIs**

Variables	Crude PR		Adjusted PR	
	PR (95% CI)	P Value	PR (95% CI)	P Value
Sex		.428		.938
Female	1	–	1	–
Male	1.09 (0.88–1.37)	.428	1.01 (0.81–1.25)	.938
Age		.413		.640
55 yr or younger	1.09 (0.88–1.36)	.413	1.05 (0.83–1.31)	.640
Older than 55 yr	1	–	1	–
Aneurysm location		.009		.022
Postsiphon	1.18 (0.91–1.52)	.208	1.11 (0.86–1.44)	.416
Supraclinoid segment	1	–	1	–
Aneurysm size		.134		.445
$\leq 5$ mm	3.92 (1.04–14.81)	.044	2.18 (0.57–8.27)	.252
6–10 mm	3.49 (0.92–13.27)	.066	1.96 (0.51–7.52)	.326
11–25 mm	3.20 (0.83–12.42)	.092	1.91 (0.49–7.40)	.350
$> 25$ mm	1	–	1	–
Anterior knee angle		.001		.005
$\leq 15.40^\circ$	1	–	1	–
$> 15.40^\circ$	1.45 (1.16–1.80)	.001	1.36 (1.09–1.69)	.005
Posterior knee angle		.685		.773
$\leq 88.15^\circ$	1	–	1	–
$> 88.15^\circ$	1.05 (0.84–1.30)	.685	1.03 (0.84–1.27)	.773

**Note:**—PR indicates prevalence ratio.

### Aneurysm Location

The bivariate analysis showed a statistically significant association between postsiphon location of the intracranial aneurysm and the following variables: male sex (odds ratio = 2.38; 95% CI, 1.59–3.56), age 55 years or younger (OR = 1.46; 95% CI, 1.03–2.06), size  $\leq 5$  mm (OR = 1.92; 95% CI, 1.20–3.06), size 6–10 mm (OR = 2.09; 95% CI, 1.27–3.45), and an anterior knee angle of  $>15.40^\circ$  (OR = 1.55; 95% CI, 1.09–2.20). For the multivariate analysis, sex, age, rupture, size, and anterior and posterior knee angles were included in the logistic regression model.

When the postsiphon and siphon locations were compared, being male and having an anterior knee angle of  $>15.40^\circ$  were significantly associated with the postsiphon location. Regarding sex, after we adjusted for the variables mentioned above, there was a decreased association (OR = 2.23; 95% CI, 1.48–3.37)—that is, men were 2.23 times more likely to have an aneurysm located distal to the siphon than women. Regarding the anterior knee angle, after we adjusted for the variables mentioned above, there was an increased association (OR = 1.48; 95% CI, 1.03–2.13)—that is, patients with an anterior knee angle of  $>15.40^\circ$  had a 48% greater chance of having an aneurysm in the postsiphon location than patients with an anterior knee angle of  $\leq 15.40^\circ$ .

When the cavernous and supraclinoid segment locations were compared, only aneurysms of  $< 25$  mm were associated with the cavernous segment. After adjustment for the variables mentioned above and comparison with aneurysms of  $> 25$  mm, aneurysms of  $\leq 5$  mm had a 92% lower chance (OR = 0.08; 95% CI, 0.02–0.28), aneurysms of 6–10 mm had a 91% lower chance (OR = 0.09; 95% CI, 0.03–0.35), and aneurysms of 11–25 mm had an 88% lower chance (OR = 0.12; 95% CI, 0.03–0.45) of occurring in the cavernous segment (Table 4).

### Aneurysm Size

Multiple linear regression analysis showed that the following variables were predictors significantly associated with aneurysm size: 1) supraclinoid versus postsiphon location: patients with aneurysms located in the supraclinoid segment had mean aneurysm size values 1.06 mm higher than those with aneurysms in the postsiphon location ( $P = .016$ ); 2) cavernous versus supraclinoid location: patients with aneurysms located in the cavernous segment had mean aneurysm size values 1.24 mm higher than those with aneurysms located in the supraclinoid segment ( $P < .001$ ); 3) aneurysm rupture: patients with unruptured aneurysms had mean aneurysm size values 1.05 mm higher than those with ruptured aneurysms ( $P = .026$ ); 4) anterior knee angle: every  $1^\circ$  increase in the anterior angle produced an increase of 1.001 mm in aneurysm size ( $P = .015$ ); and 5) age: every 1-year increase in age produced an average increase of 1.002 mm in aneurysm size ( $P = .003$ ) (Table 5).

## DISCUSSION

Ruptured intracranial aneurysms remain one of the neurosurgical diseases with the highest morbidity and mortality. Despite advances in the knowledge of causes and progression of aneurysms, an understanding of the etiologic mechanisms underlying this disorder is still a challenge in modern neurosurgery.

Recently, hemodynamic studies of the interaction of blood flow and the endothelial wall have received increased attention as an important element in the origin, development, and rupture of intracranial aneurysms.<sup>14-16</sup> Thus, studies of interactions at the level of the carotid siphon are particularly important because of the anatomic peculiarities of this region and approximately one-third of all intracranial aneurysms being located at this site.<sup>1,7,8</sup>

Studies such as those conducted by Lin et al,<sup>8</sup> Bogunović et al,<sup>9</sup> and Takeuchi and Karino<sup>3</sup> have shown that vessels anatomically characterized by sharper bends are associated with higher wall

shear oscillations and lower wall shear stress. Changes in the direction of blood flow due to the curvature of the carotid siphon would be related to the transition from laminar to turbulent flow. These changes in blood flow patterns would lead to decreased and oscillating wall shear stress, thus triggering the first endothelial changes in the genesis of aneurysm and stenosis formation.<sup>4,5</sup>

Jou et al,<sup>16</sup> using 3D images from 25 patients with paraclinoid aneurysms, reported that mean wall shear stress is inversely dependent on aneurysm sac size and that ruptured aneurysms have lower mean wall shear stress when they are close to the aneurysm neck. Zhang et al,<sup>17</sup> also using 3D images, hemodynamic studies, and the anatomic classification in V, U, C, and S shape, showed that stenotic lesions tend to occur right after the sharp bends of the carotid siphon and that siphons with sharper bends, such as the type C shape, have statistically more stenoses than siphons with softer bends. Piccinelli et al<sup>18</sup> individually analyzed the carotid siphon bends with aneurysms and showed that ruptured aneurysms occur statistically more often in carotid siphon bends of smaller diameter and shorter length, and along the outer wall of the curvature. In a recent study, Lauric et al,<sup>19</sup> comparing demographic data and 3D DSA images, showed that women have carotid siphons with higher curvatures than men and that patients with siphons with aneurysms also have higher mean curvatures.

In the present study, we used a simple and reproducible method to analyze the sharpness of the 2 main curvatures through which blood enters the cerebral circulation—that is, the posterior and anterior knee angles of the carotid siphon, associated with a refined statistical analysis to identify independent variables resulting from angle variation. We first performed a 2D analysis of each variable, followed by several multivariate regression analyses to isolate, from all other potentially correlated factors, the consequences of the variation of these angles in relation to intracranial aneurysm rupture, location, and size.

We found that anterior angle values above the median of the study sample (15.40°) were directly and independently associated with a 36% higher incidence of ruptured aneurysms ( $P = .005$ , prevalence ratio = 1.36; 95% CI, 1.09–1.69), with a 48% greater chance of having an aneurysm in the postsiphon location ( $P = .034$ , OR = 1.48; 95% CI, 1.03–2.13), and with larger aneurysms, in which every 1° increase in the anterior angle produced an increase of 1.001 mm in aneurysm size ( $P = .015$ ).

We believe that the change in the blood flow direction at the curvature points of the carotid siphon would occur by a deceleration of the linear velocity of blood flow and loss of the linear vector force of the water hammer pulse. This deceleration would occur with a change of laminar-to-turbulent flow in the vicinity of curvatures, with higher wall shear oscillations and lower wall shear stress. On the one hand, the decrease in the linear vector force toward the aneurys-

**Table 3: Analysis of rupture odds ratio by location subgroups according to anterior angles above or below the median and their respective 95% CIs**

Location/ Angle	Unruptured (%)	Ruptured (%)	P Value	OR (95% CI)
Supraclinoid			.091	1.75 (0.91–3.36)
≤15.40°	71 (74.74)	24 (25.26)		
>15.40°	49 (62.82)	29 (37.18)		
MCA			.354	1.32 (0.73–2.40)
≤15.40°	83 (77.57)	24 (22.43)		
>15.40°	94 (72.31)	36 (27.69)		
AcomA			.049	1.84 (1.00–3.38)
≤15.40°	45 (55.56)	36 (59.55)		
>15.40°	36 (40.45)	53 (59.55)		
Bifurcation			.470	1.90 (0.43–8.48)
≤15.40°	14 (77.78)	4 (22.22)		
>15.40°	11 (64.71)	6 (35.29)		

**Note:**—Supraclinoid indicates supraclinoid segments, including the ophthalmic, posterior communicating, and anterior choroidal segments; Bifurcation, internal carotid artery bifurcation; AcomA, anterior communicating artery.

**Table 4: Distribution of the study variables and association with aneurysm location based on crude and adjusted odds ratios according to the generalized logistic regression model and their respective 95% CIs**

Variables	Crude OR (Postsiphon/Siphon)		Adjusted OR (Cavernous/Supraclinoid)	
	OR (95% CI)	P Value	OR (95% CI)	P Value
Sex		<.001		.427
Male	2.23 (1.48–3.37)	<.001	0.69 (0.27–1.74)	.427
Female	1	–	1	–
Age		.184		.684
55 yr or younger	1.28 (0.89–1.84)	.184	1.16 (0.57–2.38)	.684
Older than 55 yr	1	–	1	–
Rupture		.423		
No	1	–		
Yes	1.17 (0.80–1.72)	.423		
Aneurysm size				
≤5 mm	2.38 (0.69–8.20)	.169	0.08 (0.02–0.28)	<.001
6–10 mm	2.54 (0.73–8.85)	.143	0.09 (0.03–0.35)	<.001
11–25 mm	1.34 (0.37–4.81)	.652	0.12 (0.03–0.45)	.002
>25 mm	1	–	1	–
Anterior knee angle		.034		.066
≤15.40°	1	–	1	–
>15.40°	1.48 (1.03–2.13)	.034	0.48 (0.22–1.05)	.066
Posterior knee angle		.122		.093
≤88.15°	1	–	1	–
>88.15°	1.33 (0.93–1.91)	.122	1.84 (0.90–3.73)	.093

**Table 5: Results of multiple linear regression analysis in relation to aneurysm size**

Variables Associated with Larger Aneurysms	P Value	95% CI
Aneurysm location		
Postsiphon/supraclinoid	.016	0.901–0.989
Cavernous/supraclinoid	<.001	1.133–1.350
Sex		
Male/female	.103	0.993–1.081
Rupture		
Yes/no	.026	0.913–0.994
Anterior knee angle	.015	1.000–1.002
Posterior knee angle	.804	1.000–1.000
Age	.003	1.000–1.003

mal sac would reduce the aneurysm size and risk of rupture; on the other hand, a greater turbulent flow would lead to a greater initial endothelial lesion for aneurysmal formations. Thus, more obtuse anterior angles with less laminar flow deceleration and less generation of turbulent flow in the vicinity of the carotid siphon were statistically associated with larger aneurysms, greater risk of rupture and a higher incidence of aneurysms distal to the carotid siphon. In turn, more acute anterior angles with greater deceleration of laminar flow and greater generation of turbulent flow in the siphon were shown to be associated with smaller aneurysms, a lower risk of rupture, and a higher incidence of aneurysms in the carotid siphon.

High-speed laminar flow due to a low tortuous carotid siphon would lead to hemodynamic effects for other circulation bends and bifurcations distal to the carotid siphon, explaining the higher incidence of postsiphon aneurysms and the greater risk of rupture in these locations in patients with higher anterior angles. The stratified analysis of subgroups by location revealed that aneurysms located in the anterior communicating artery in patients with an anterior angle of  $>15.40^\circ$  had an 84% greater chance of rupture ( $P = .049$ ), suggesting that the hemodynamic effects resulting from carotid siphon anatomy persist distal to the siphon.

We also expected to observe a higher incidence of cavernous segment aneurysms in patients with more acute posterior angles. However, we did not observe any statistical relationship between the posterior angle measures and the studied variables. When comparing the values of anterior and posterior angles, we observed that posterior angle measures were more homogeneous, with a lower SD ( $14.63^\circ \pm 26.13^\circ$  versus  $83.37^\circ \pm 37.54^\circ$ ), and perhaps this lower variability was the reason for the lack of a statistical relationship using our method. In addition, other anatomic obstacles could be related to cavernous aneurysm genesis, such as the angles of the petrous segment, which unfortunately are not the focus of our study.

A relevant finding was the independent statistical relationship between aneurysm size and patient age, in which every 1-year increase in age produced an average increase of 1.002 mm in aneurysm size.

As a partially retrospective review, this study has some limitations related to the quality of the data collected from the available medical records. However, the use of 2 blinded assessors for angle measurement and a large sample were contributing factors to improve the level of information.

## CONCLUSIONS

There was a significant independent direct relation of greater anterior knee angle with intracranial aneurysms located distal to the carotid siphon, larger aneurysms, and greater risk of rupture. These findings may be associated with the hemodynamic interactions of blood flow and the curvature of the carotid siphon.

## REFERENCES

- Caranci F, Briganti F, Cirillo L, et al. **Epidemiology and genetics of intracranial aneurysms.** *Eur J Radiol* 2013;82:1598–605 CrossRef Medline
- King JT Jr. **Epidemiology of aneurysmal subarachnoid hemorrhage.** *Neuroimaging Clin N Am* 1997;7:659–68 Medline
- Takeuchi S, Karino T. **Flow patterns and distributions of fluid velocity and wall shear stress in the human internal carotid and middle cerebral arteries.** *World Neurosurg* 2010;73:174–85; discussion e27 CrossRef Medline
- Sforza DM, Putman CM, Cebra JR. **Hemodynamics of cerebral aneurysms.** *Annu Rev Fluid Mech* 2009;41:91–107 CrossRef Medline
- Malek AM, Alper SL, Izumo S. **Hemodynamic shear stress and its role in atherosclerosis.** *JAMA* 1999;282:2035–42 CrossRef Medline
- Naruse T, Tanishita K. **Large curvature effect on pulsatile entrance flow in a curved tube: model experiment simulating blood flow in an aortic arch.** *J Biomech Eng* 1996;118:180–86 CrossRef Medline
- Griessenauer CJ, Yalcin B, Matusz P, et al. **Analysis of the tortuosity of the internal carotid artery in the cavernous sinus.** *Childs Nerv Syst* 2015;31:941–44 CrossRef Medline
- Lin LM, Colby GP, Jiang B, et al. **Classification of cavernous internal carotid artery tortuosity: a predictor of procedural complexity in Pipeline embolization.** *J Neurointerv Surg* 2015;7:628–33 CrossRef Medline
- Bogunović H, Pozo JM, Cárdenas R, et al. **Automated landmarking and geometric characterization of the carotid siphon.** *Med Image Anal* 2012;16:889–903 CrossRef Medline
- Silva Neto ÂR, Câmara RL, Valença MM. **Carotid siphon geometry and variants of the circle of Willis in the origin of carotid aneurysms.** *Arq Neuropsiquiatr* 2012;70:917–21 CrossRef Medline
- Barros AJ, Hirakata VN. **Alternatives for logistic regression in cross-sectional studies: an empirical comparison of models that directly estimate the prevalence ratio.** *BMC Med Res Methodol* 2003;3:21 CrossRef Medline
- Allison PD. **Binary logit analysis: details and options.** In: *Logistic Regression Using SAS: Theory and Application*. 2nd ed. Cary: SAS Institute; 1999:48–51
- Hosmer DW, Lemeshow S. **Special topics.** In: *Applied Logistic Regression*. 2nd ed. Hoboken: John Wiley & Sons; 2000:260–73
- Brisman JL, Song JK, Newell DW. **Cerebral aneurysms.** *N Engl J Med* 2006;355:928–39 CrossRef Medline
- Thomas JB, Antiga L, Che SL, et al. **Variation in the carotid bifurcation geometry of young versus older adults: implications for geometric risk of atherosclerosis.** *Stroke* 2005;36:2450–56 CrossRef Medline
- Jou LD, Lee DH, Morsi H, et al. **Wall shear stress on ruptured and unruptured intracranial aneurysms at the internal carotid artery.** *AJNR Am J Neuroradiol* 2008;29:1761–67 CrossRef Medline
- Zhang C, Pu F, Li S, et al. **Geometric classification of the carotid siphon: association between geometry and stenoses.** *Surg Radiol Anat* 2013;35:385–94 CrossRef Medline
- Piccinelli M, Bacigaluppi S, Boccardi E, et al. **Geometry of the internal carotid artery and recurrent patterns in location, orientation, and rupture status of lateral aneurysms: an image-based computational study.** *Neurosurgery* 2011;68:1270–85; discussion 1285 CrossRef Medline
- Lauric A, Safain MG, Hippelheuser J, et al. **High curvature of the internal carotid artery is associated with the presence of intracranial aneurysms.** *J Neurointerv Surg* 2014;6:733–39 CrossRef Medline

# Carotid Plaque Morphology and Ischemic Vascular Brain Disease on MRI

 Q.J.A. van den Bouwhuisen,  M.W. Vernooij,  B.F.J. Verhaaren,  H.A. Vrooman,  W.J. Niessen,  G.P. Krestin,  M.A. Ikram,  O.H. Franco, and  A. van der Lugt



## ABSTRACT

**BACKGROUND AND PURPOSE:** Vulnerable carotid plaque components are reported to increase the risk of cerebrovascular events. Yet, the relation between plaque composition and subclinical ischemic brain disease is not known. We studied, in the general population, the association between carotid atherosclerotic plaque characteristics and ischemic brain disease on MR imaging.

**MATERIALS AND METHODS:** From the population-based Rotterdam Study, 951 participants underwent both carotid MR imaging and brain MR imaging. The presence of intraplaque hemorrhage, lipid core, and calcification and measures of plaque size was assessed in both carotid arteries. The presence of plaque characteristics in relation to lacunar and cortical infarcts and white matter lesion volume was investigated and adjusted for cardiovascular risk factors. Stratified analyses were conducted to explore effect modification by sex. Additional analyses were conducted per carotid artery in relation to vascular brain disease in the ipsilateral hemisphere.

**RESULTS:** Carotid intraplaque hemorrhage was significantly associated with the presence of cortical infarcts (OR, 1.9; 95% confidence interval, 1.1–3.3). None of the plaque characteristics were related to the presence of lacunar infarcts. Calcification was the only characteristic that was associated with higher white matter lesion volume. There was no significant interaction by sex.

**CONCLUSIONS:** The presence of carotid intraplaque hemorrhage on MR imaging is independently associated with MR imaging–defined cortical infarcts, but not with lacunar infarcts. Plaque calcification, but not vulnerable plaque components, is related to white matter lesion volume.

**ABBREVIATIONS:** PD = proton density; WML = white matter lesion

Identification of individuals who are at high risk for cerebrovascular events is an important goal in the prevention of cerebrovascular disease. There is growing awareness that the risk of a cerebrovascular event depends on not only the severity of carotid stenosis but also the morphology and composition of the athero-

sclerotic plaque.<sup>1,2</sup> Histologic studies indicate that specific “vulnerable” plaque characteristics, such as a large lipid core, thin fibrous cap, and intraplaque hemorrhage, are key elements to atherosclerotic plaque instability.<sup>3,4</sup> Destabilization of plaque can lead to plaque rupture, with thrombus formation on the disrupted plaque surface and subsequent embolization of thrombus and/or plaque material into the distal vessels. Currently, MR imaging can accurately detect plaque components in the carotid arteries.<sup>5–7</sup>

Ischemic vascular brain disease, manifesting as brain infarcts and white matter lesions (WMLs), is highly prevalent in the elderly, often occurs subclinically, and is associated with an increased risk of adverse neurologic events.<sup>8,9</sup> It is, however, unknown whether atherosclerotic plaque composition also relates to these vascular brain lesions in the general population. Morphologically, brain infarcts can be divided into lacunar infarcts and cortical infarcts. Whereas lacunar infarcts are associated with local occlusive disease of deep perforating arteries,<sup>10</sup> cortical infarcts are primarily caused by thrombo-embolism from extracranial arteries or the heart.<sup>11</sup> For WMLs, cerebral small-vessel disease is considered the main contributory factor. Therefore, we

Received April 6, 2017; accepted April 27.

From the Departments of Epidemiology (Q.J.A.v.d.B., M.W.V., B.F.J.V., M.A.I., O.H.F.), Radiology (Q.J.A.v.d.B., M.W.V., H.A.V., W.J.N., G.P.K., M.A.I., A.v.d.L.), and Medical Informatics (H.A.V., W.J.N.), Erasmus MC, Rotterdam, the Netherlands.

The Rotterdam Study is funded by Erasmus Medical Center and Erasmus University Rotterdam, the Netherlands; the Research Institute for Diseases in the Elderly; the Ministry of Education, Culture and Science; the Ministry for Health, Welfare and Sports; the European Commission (DG XII); and the Municipality of Rotterdam. This study was supported by grants from the Netherlands (Dutch) Heart Foundation (2006B206, 2009B044, and 2009B102), the Netherlands Organization for Scientific Research/the Netherlands Organization for Health Research and Development ZonMw (Vici grant 918.76.619), and the Netherlands Consortium for Healthy Ageing.

Please address correspondence to Aad van der Lugt, MD, PhD, 's-Gravendijkwal 230, PO Box 2040, 3000CA Rotterdam, the Netherlands; e-mail: a.vanderlugt@erasmusmc.nl

 Indicates open access to non-subscribers at [www.ajnr.org](http://www.ajnr.org)

 Indicates article with supplemental on-line tables.

<http://dx.doi.org/10.3174/ajnr.A5288>

hypothesized that vulnerable carotid plaque components as assessed on MR imaging are associated with cortical infarcts rather than with lacunar infarcts or WMLs.

In 951 individuals from the population-based Rotterdam Study,<sup>12</sup> we studied the association of carotid atherosclerotic plaque components, intraplaque hemorrhage, and lipid core, with markers of ischemic brain disease on MR imaging.

## **MATERIALS AND METHODS**

### **Study Population**

The current study was embedded in the Rotterdam Study, a prospective, population-based study among middle-aged and elderly participants (>95% of white descent), aimed at investigating determinants of various diseases among middle-aged and elderly individuals (45 years of age or older).<sup>12</sup> All participants are invited at regular time intervals, every 3–4 years, to the research center for follow-up examinations, including carotid ultrasonography.<sup>13</sup> From October 2007 onward, participants with carotid wall thickening (maximum thickness,  $\geq 2.5$  mm on sonography) in the left, right, or both carotid arteries were invited for MR imaging of the carotid arteries. Until August 2010, 7151 participants of the Rotterdam Study cohort had undergone ultrasonography and were still alive. In 26.3% of these participants ( $n = 1882$ ), carotid wall thickening was present on sonography. We excluded individuals who had MR imaging contraindications ( $n = 43$ ), had dementia ( $n = 12$ ), had physical immobility ( $n = 50$ ), lived in nursing homes ( $n = 60$ ), had moved outside the area ( $n = 54$ ), or had undergone a carotid endarterectomy procedure ( $n = 4$ ). Of the 1659 subjects eligible for carotid MR imaging, 1451 agreed to participate (response, 87.5%). Due to physical inabilities (eg, back pain) or claustrophobia, imaging could not be performed or completed in 85 individuals (5.9%), so, in total, 1366 participants underwent complete carotid MR imaging. The quality of all sequences in each carotid MR imaging was rated on a 5-point scale (1 = worst, 5 = best).<sup>14</sup> Scans were included in the analyses if the image quality was scored  $\geq 3$  ( $n = 1289$ , 94.4%) in all carotid MR imaging sequences. Exclusion ( $n = 77$ ) was mainly due to susceptibility artifacts from dental implants and motion artifacts.

For the current study, we selected participants with carotid MR imaging of sufficient quality who had also undergone an MR imaging examination of their brains as a part of the Rotterdam Scan Study,<sup>15</sup> an ongoing study investigating age-related brain changes on MR imaging. Invitation to the Rotterdam Scan Study was independent of participation in the carotid MR imaging study. The objectives and design of the Rotterdam Scan Study have been described in detail elsewhere.<sup>16</sup> Until August 2010, in total, 951 participants underwent complete MR imaging examinations of both carotid arteries and brain and were included in the current study. The median time interval between the brain and carotid MR imaging was 9 (25th–75th percentile, 2–21) months, with the brain MR imaging preceding the carotid MR imaging in 88.5% of the subjects.

The Rotterdam Study has been approved by the medical ethics committee according to the Population Study Act Rotterdam Study, executed by the Ministry of Health, Welfare and Sports of the Netherlands. Written informed consent was obtained from all participants.

### **Carotid MR Imaging**

Imaging of the carotid arteries was performed on a 1.5T scanner (Signa HD; GE Healthcare, Milwaukee, Wisconsin) with a bilateral phased array surface coil (Machnet, Eelde, the Netherlands). We planned the high-resolution MR imaging sequences so that the carotid plaques were imaged completely on both sides, with a previously described standardized protocol.<sup>17</sup> First, both carotid bifurcations were identified by means of 2D time-of-flight MR angiography. Thereafter, high-resolution MR imaging sequences were planned to image the carotid bifurcations on both sides: a proton density (PD)-weighted FSE black-blood sequence; a PD-weighted FSE black-blood sequence with an increased in-plane resolution; a PD-weighted EPI sequence; a T2WI EPI sequence; a 3D-T1WI gradient-echo sequence; and, finally, a 3D phased-contrast MR angiography.<sup>17</sup>

### **Assessment of Plaque Composition on Carotid MR Imaging**

Carotid plaques were analyzed by a single observer with >3 years' experience in rating carotid MR imaging, as previously described.<sup>17</sup> Analysis involved examination of both carotid arteries. The presence of atherosclerotic plaque was defined as carotid wall thickness of  $\geq 2.0$  mm, and carotid plaque was quantified by measuring maximum carotid wall thickness in the PD-weighted FSE images and by calculation of luminal stenosis with the NASCET criteria.<sup>18</sup> In all carotid arteries with atherosclerotic plaque on MR imaging ( $n = 1752$  carotids in 951 participants), the presence or absence of 3 different plaque components (calcification, intraplaque hemorrhage, and lipid core) was assessed with criteria described elsewhere.<sup>17</sup> For examples of assessment of vulnerable plaque components, see Fig 1.

### **Brain MR Imaging**

Brain MR imaging, details of which are described elsewhere,<sup>16</sup> was performed on the same 1.5T scanner. In short, the imaging protocol included 3 high-resolution axial scans used for assessment of infarcts and white matter lesions (ie, a T1WI sequence, a PD-weighted sequence, and a FLAIR sequence).

Lacunar and cortical infarcts were rated on FLAIR, PD-weighted, and T1WI sequences by 1 of 5 trained raters according to criteria described previously.<sup>16</sup> The presence of infarcts and location (left or right hemisphere) were recorded. WMLs and intracranial volume were segmented with a validated fully automated tissue-classification technique,<sup>19,20</sup> and total WML volume was calculated by summing all WML voxels across the whole brain and per hemisphere. Quantification of WML volume was not possible in 41 brain scans because of susceptibility or motion artifacts. Therefore, 1670 of 1752 carotid arteries were used to study associations between carotid plaque characteristics and WML volumes. Readers who interpreted the brain MR imaging were blinded to the carotid MR imaging findings, and vice versa.

### **Cardiovascular Risk Factors**

Cardiovascular covariates were ascertained with standard procedures as described previously.<sup>21</sup> Risk factors used as covariates in the current study were hypertension (defined as grade 2

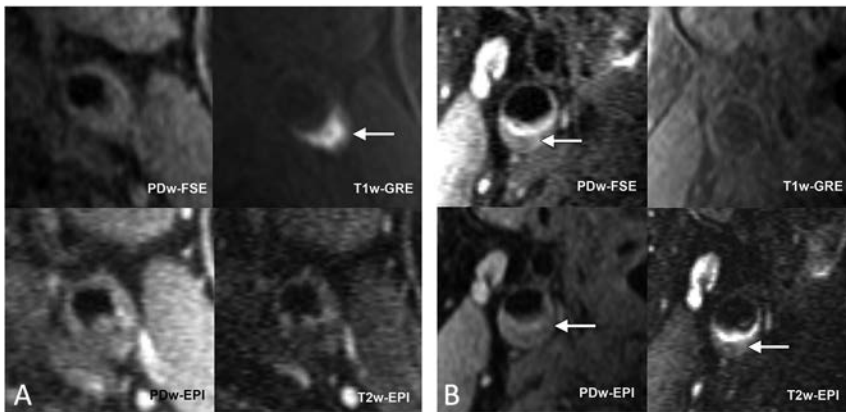


**FIG1.** MR imaging of the carotid artery with atherosclerotic plaque containing vulnerable plaque components. Examples of the presence of intraplaque hemorrhage and lipid core in a carotid plaque. **A,** Axial images of the left carotid artery of a 72-year-old subject with carotid plaque formation in the carotid bifurcation. On the T1-weighted gradient-echo image (T1w-GRE), the carotid plaque has a high signal intensity, identifying intraplaque hemorrhage (*white arrow*). **B,** Axial images of the right carotid artery of a 67-year-old subject with carotid plaque formation in the proximal internal carotid artery. There is no high signal intensity in the carotid plaque on the T1-weighted gradient-echo image. There is a region of low signal intensity in the plaque burden on both PD-weighted (PDw)-EPI and T2-weighted (T2w)-EPI images in the absence of high signal on the T1-weighted gradient-echo image, identifying the presence of a lipid core (*white arrows*).

**Table 1: Characteristics of the study population (n = 951)<sup>a</sup>**

Characteristics	
Age (mean) (yr)	71.2 ± 10.3
Women (No.) (%)	444 (46.7)
Cardiovascular risk factors (No.) (%)	
Hypertension, grade 2 <sup>22</sup>	489 (51.4)
Smoking	
Past	474 (49.8)
Current	233 (24.5)
Diabetes mellitus	142 (14.9)
Hypercholesterolemia	307 (32.3)
Cerebrovascular disease	
History of clinical stroke	57 (6.0)
MRI carotid characteristics	
Intraplaque hemorrhage (No.) (%)	306 (32.2)
Lipid core (No.) (%)	359 (37.7)
Calcifications (No.) (%)	769 (80.9)
Maximum plaque thickness (mean) (mm)	3.6 ± 1.0
Carotid stenosis of 0%–29% (No.) (%)	766 (80.5)
Carotid stenosis of 30%–49% (No.) (%)	114 (12.0)
Carotid stenosis of 50%–69% (No.) (%)	51 (5.4)
Carotid stenosis of 70%–99% (No.) (%)	20 (2.1)
MRI brain characteristics	
Cortical infarct on MRI (No.) (%)	62 (6.5)
Lacunar infarct on MRI (No.) (%)	125 (13.1)
WML volume (median) <sup>b</sup> (interquartile range) (mL)	4.66 (2.24–12.49)

<sup>a</sup> Categorical variables are presented as numbers. Continuous values are expressed as means.

<sup>b</sup> WML volume measurements were possible in 910 of 951 subjects because of susceptibility or motion artifacts.

according to European Society of Cardiology criteria<sup>22</sup>), smoking (classified as current, past, and never), diabetes mellitus (defined as the use of blood glucose-lowering medication and/or a nonfasting serum glucose level of 11.1 mmol/L or higher and/or a fasting serum glucose level of ≥7 mmol/L [≥126 mg/dL]), and hypercholesterolemia (defined as a serum total cholesterol above 6.2 mmol/L [≥239 mg/dL]).

### Prevalent Stroke

A history of stroke was based on the definition in the World Health Organization criteria, including a syndrome of rapidly developing symptoms, with an apparent vascular cause, of focal or global cerebral dysfunction lasting 24 hours or longer or leading to death. We assessed prevalent stroke at baseline during an interview and verified these data with medical records.<sup>23</sup>

### Statistical Analysis

We assessed the relation of carotid plaque characteristics with ischemic vascular brain disease (cortical infarcts, lacunar infarcts, and WML volume) per participant (in both hemispheres). In addition, for infarcts, we also assessed the relation of carotid plaque characteristics per carotid artery (left/right) to brain infarcts in the ipsilateral hemisphere. For the participant-based analysis,

each carotid plaque component was scored positive if present in 1 or both carotid arteries. For the artery-based analysis, only brain infarcts in the hemisphere ipsilateral to the examined carotid artery were taken into account. Associations between carotid plaque characteristics and brain infarcts were analyzed with logistic regression models, and the associations with WML volume were analyzed with linear regression models. WML volume was natural log-transformed because of skewness of the untransformed measure. For the analyses with WML volume as a dependent variable, persons with cortical infarcts were excluded to avoid misclassification from gliosis around the infarct area.

All analyses were adjusted for age, sex, and time interval between brain MR imaging and carotid MR imaging (model A). Associations with WML volumes were also adjusted for intracranial volume to take differences in head size into account. In addition, all analyses were adjusted for major cardiovascular risk factors (model B) and were adjusted for carotid luminal stenosis (model C). Additional stratified analyses were performed to assess effect modification by sex. Also, analyses were repeated after exclusion of individuals with a history of clinical stroke at baseline to compare associations with individuals with and without a history of stroke. To correct for within-person correlated carotid plaque data in the artery-based analyses, we followed the generalized estimation equation approach with an unstructured working correlation matrix. The unit in the analysis was the presence of ischemic brain disease in the left and/or right hemisphere. Each participant yielded a maximum of 2 U in the dataset. In case of missing values for the cardiovascular risk factors, values were imputed by using the expectation-maximization method (<1% of the data). Analyses were performed with SPSS for Windows, Version 22.0 (IBM, Armonk, New York). The *P* value threshold used for significance was .05.

**Table 2: Associations between carotid characteristics and cortical infarcts<sup>a</sup>**

	Per Participant (n = 951)						Per Carotid Artery (n = 1752)					
	Model A <sup>b</sup>	P Value	Model B <sup>c</sup>	P Value	Model C <sup>d</sup>	P Value	Model A <sup>b</sup>	P Value	Model B <sup>c</sup>	P Value	Model C <sup>d</sup>	P Value
Plaque components												
Intraplaque hemorrhage	2.0 (1.2–3.5)	.012	1.9 (1.1–3.3)	.019	1.7 (1.0–3.2)	.059	2.0 (1.1–3.6)	.033	1.9 (1.0–3.6)	.052	1.2 (0.6–2.4)	.633
Lipid core	1.3 (0.8–2.2)	.337	1.3 (0.8–2.2)	.318	1.1 (0.6–1.9)	.697	1.6 (0.9–2.8)	.076	1.6 (0.9–2.8)	.077	1.0 (0.6–1.9)	.881
Calcification	1.1 (0.5–2.3)	.863	1.0 (0.5–2.2)	.977	1.0 (0.5–2.0)	.911	1.6 (0.8–3.1)	.162	1.6 (0.8–3.0)	.177	1.2 (0.6–2.5)	.552
Measures of plaque size												
Maximum carotid wall thickness <sup>e</sup>	1.3 (1.1–1.6)	.006	1.3 (1.1–1.6)	.009	1.2 (1.0–1.6)	.090	1.6 (1.3–1.9)	<.001	1.6 (1.3–1.9)	<.001	0.8 (0.6–1.2)	.320
≥30% stenosis <sup>f</sup>	1.9 (1.1–3.3)	.033	1.8 (1.0–3.2)	.048	NA	NA	3.1 (1.6–6.0)	.001	3.1 (1.6–6.1)	.001	NA	NA

**Note:**—NA indicates not applicable.

<sup>a</sup> Values represent odds ratios (95% confidence intervals).

<sup>b</sup> Model A is adjusted for age, sex, and time interval between brain MRI and carotid MRI.

<sup>c</sup> Model B is adjusted for age, sex, time interval between brain MRI and carotid MRI, and major cardiovascular risk factors (hypertension, smoking, diabetes mellitus, and hypercholesterolemia).

<sup>d</sup> Model C is adjusted for age, sex, carotid stenosis (when appropriate), and time interval between brain MRI and carotid MRI.

<sup>e</sup> Odds ratio per millimeter increase.

<sup>f</sup> Odds ratio of carotid stenosis of ≥30%.

## RESULTS

Table 1 shows baseline variables for the 951 participants. Mean age was  $71.2 \pm 10.3$  years, and 444 (46.7%) were women. Intraplaque hemorrhage was present in 306 (32.2%); lipid core, in 359 (37.7%); and calcification, in 769 (80.9%) participants. Cortical infarcts were present in 62 subjects (6.5%), and lacunar infarcts, in 125 subjects (13.1%). Median WML volume was 4.66 mL (interquartile range, 2.24–12.49). In 1752 carotid arteries with wall thickening, 57 cortical infarcts (3.3%) and 85 lacunar infarcts (4.9%) were present in the ipsilateral hemisphere.

Results of the multivariate adjusted analysis on the association between carotid plaque characteristics and cortical infarcts are presented in Table 2. The presence of intraplaque hemorrhage (OR, 1.9; 95% CI, 1.1–3.3), maximum carotid wall thickness (OR per millimeter increase, 1.3; 95% CI, 1.1–1.6), and carotid stenosis of ≥30% (OR, 1.8; 95% CI, 1.0–3.2) was all significantly associated with cortical infarcts in the subject-based multivariate analysis. When the association between intraplaque hemorrhage and cortical infarcts was adjusted for carotid stenosis, the estimate barely changed (OR, 1.7; 95% CI, 1.0–3.2;  $P = .059$ ), though the association became borderline significant. When we excluded participants with a history of clinical stroke at baseline from the analyses ( $n = 57$ ), the association between intraplaque hemorrhage and cortical infarcts became stronger (OR, 2.4; 95% CI, 1.2–4.6;  $P = .01$ , model B), whereas it did not change for maximum wall thickness (OR, 1.3; 95% CI, 1.0–1.6;  $P = .05$ ) and became nonsignificant for >30% stenosis (OR, 1.5; 0.7–3.0;  $P = .29$ ).

In the carotid-based analysis, intraplaque hemorrhage was also significantly associated with the presence of ipsilateral cortical infarcts (Table 2). Lipid core presence and plaque calcification were not associated with cortical infarcts in the subject-based analyses, though the association for the lipid core was borderline significant in the carotid-based analysis (OR, 1.6; 95% CI, 0.9–2.8;  $P = .08$ ) (Table 2). After additional adjustments for carotid luminal stenosis, the association for intraplaque hemorrhage was nonsignificant (OR, 1.2; 95% CI, 0.6–2.4;  $P = .633$ ).

In Table 3, the relation between carotid characteristics and lacunar infarcts on MR imaging is shown. There were no associations between any of the carotid plaque characteristics and the presence of lacunar infarcts. These results did not change

after additional adjustment for carotid stenosis or exclusion of persons with clinical stroke or when performing artery-based analysis.

The association between carotid characteristics and WML volume is shown in Table 4. Subjects with calcifications had significantly larger WML volume (regression estimate, 0.21; 95% CI, 0.05–0.38). The presence of intraplaque hemorrhage was borderline significantly associated with higher WML volume (regression estimate, 0.13; 95% CI, –0.01–0.28;  $P = .07$ ), but this was further attenuated when adjusting for cardiovascular risk factors ( $P = .145$ ). These results did not change after additional adjustment for carotid stenosis or exclusion of those with clinical stroke. Maximum carotid wall thickness was significantly associated with higher WML volume (regression estimate, 0.08; 95% CI, 0.01–0.15;  $P = .032$ ) when adjusting for carotid stenosis. This result was not present without adjustments for carotid stenosis.

In a sensitivity analysis in 311 subjects, excluding subjects with a time interval of >1 month between carotid and brain MR imaging, the estimates of the associations did not change (On-line Tables 1 and 2).

Stratification for sex did not show significant interaction by sex in any of the analyses (data not shown).

## DISCUSSION

In a large sample of the general population of predominantly white descent, we studied, with MR imaging, the association between vulnerable carotid plaque components and ischemic vascular brain disease. We found that carotid intraplaque hemorrhage was associated with the presence of cortical infarcts, but not with lacunar infarcts. Plaque calcification and carotid wall thickness but not vulnerable plaque components were related to higher WML volume.

One of the major strengths of our study is the large sample of middle-aged and elderly subjects from the general population. Compared with small clinical studies of patients with symptomatic brain ischemia, the use of a community-dwelling population provides information on associations between carotid plaque characteristics and ischemic brain disease that are less biased by the effects of medical intervention or lifestyle modifications. Furthermore, apart from participant-based analyses, we also assessed

**Table 3: Associations between carotid characteristics and lacunar infarcts<sup>a</sup>**

	Per Participant (n = 951)						Per Carotid Artery (n = 1752)					
	Model A <sup>b</sup>	P Value	Model B <sup>c</sup>	P Value	Model C <sup>d</sup>	P Value	Model A <sup>b</sup>	P Value	Model B <sup>c</sup>	P Value	Model C <sup>d</sup>	P Value
Plaque components												
Intraplaque hemorrhage	1.0 (0.6–1.4)	.922	1.0 (0.6–1.5)	.855	1.1 (0.7–1.7)	.562	1.1 (0.6–1.7)	.412	1.1 (0.7–1.9)	.464	1.1 (0.6–1.8)	.856
Lipid core	0.9 (0.6–1.4)	.782	1.0 (0.7–1.5)	.974	1.0 (0.7–1.6)	.832	1.1 (0.6–1.8)	.815	1.0 (0.6–1.8)	.766	1.0 (0.6–1.7)	.946
Calcification	1.0 (0.6–1.8)	.885	1.0 (0.6–1.7)	.992	1.1 (0.6–1.9)	.705	1.0 (0.6–1.6)	.890	1.1 (0.6–1.5)	.773	0.9 (0.5–1.4)	.573
Measures of plaque size												
Maximum carotid wall thickness <sup>e</sup>	1.0 (0.8–1.2)	.815	1.0 (0.8–1.1)	.605	1.1 (0.9–1.4)	.307	1.1 (0.9–1.3)	.581	1.0 (0.8–1.2)	.771	1.0 (0.8–1.4)	.825
≥30% stenosis <sup>f</sup>	0.7 (0.4–1.2)	.168	0.7 (0.4–1.2)	.166	NA	NA	0.8 (0.4–1.6)	.582	0.8 (0.4–1.5)	.450	NA	NA

**Note:**—NA indicates not applicable.

<sup>a</sup> Values represent odds ratios (95% confidence intervals).

<sup>b</sup> Model A is adjusted for age, sex, and time interval between brain MRI and carotid MRI.

<sup>c</sup> Model B is adjusted for age, sex, time interval between brain MRI and carotid MRI, and major cardiovascular risk factors (hypertension, smoking, diabetes mellitus, and hypercholesterolemia).

<sup>d</sup> Model C is adjusted for age, sex, carotid stenosis (when appropriate), and time interval between brain MRI and carotid MRI.

<sup>e</sup> Odds ratio per millimeter increase.

<sup>f</sup> Odds ratio of carotid stenosis of ≥30%.

**Table 4: Associations between subjects' carotid plaque characteristics and WML load (n = 887)<sup>a</sup>**

	Model A <sup>b</sup>	P Value	Model B <sup>c</sup>	P Value	Model C <sup>d</sup>	P Value
Plaque components						
Intraplaque hemorrhage	0.13 (−0.01–0.28)	.070	0.11 (−0.04–0.25)	.145	0.13 (−0.02–0.27)	.083
Lipid core	−0.09 (−0.22–0.05)	.203	−0.06 (−0.19–0.07)	.353	−0.08 (−0.20–0.05)	.277
Calcification	0.23 (0.06–0.39)	.007	0.21 (0.05–0.38)	.010	0.21 (0.05–0.37)	.008
Measures of plaque size						
Maximum carotid wall thickness <sup>e</sup>	0.05 (−0.02–0.12)	.131	0.04 (−0.03–0.10)	.235	0.08 (0.01–0.15)	.032
≥30% stenosis	−0.10 (−0.26–0.07)	.241	−0.11 (−0.27–0.05)	.181	NA	NA

**Note:**—NA indicates not applicable.

<sup>a</sup> Values represent increase in white matter lesion load (natural log-transformed) (95% confidence intervals) for the presence of plaque components, the presence of carotid stenosis of ≥30%, or per-millimeter increase in maximum wall thickness.

<sup>b</sup> Model A is adjusted for age, sex, and time interval between brain MRI and carotid MRI.

<sup>c</sup> Model B is adjusted for age, sex, time interval between brain MRI and carotid MRI, and major cardiovascular risk factors (hypertension, smoking, diabetes mellitus and hypercholesterolemia).

<sup>d</sup> Model C is adjusted for age, sex, carotid stenosis (when appropriate), and time interval between brain MRI and carotid MRI.

<sup>e</sup> Regression coefficients per millimeter increase.

the relation between left/right carotid plaque and ipsilateral ischemic brain disease, enabling us to investigate vascular brain disease in the corresponding vascular territory.

A potential limitation of our study is that a lipid core is best detected with contrast-enhanced MR imaging.<sup>24</sup> Although we did not administer a contrast agent in our population-based sample, the non-contrast-enhanced sequences we used were shown to have good accuracy in validation studies.<sup>5,6,14</sup> Furthermore, we assessed the presence of hemorrhage and lipid core but did not measure the size of each plaque component, which may have affected our sensitivity to detect relevant associations. Another potential limitation is the time interval between brain MR imaging and carotid MR imaging, which was, on average, 9 months, with brain MR imaging preceding carotid MR imaging in 89% of participants. Thus, brain infarcts could potentially have preceded plaque abnormalities in time, influencing our results. However, because the main aim of our study was not risk prediction but investigating etiologic parallels between plaque vulnerability and stroke, we believe that this sequencing will not have seriously influenced our results. Also, adjustment for time interval and sensitivity analysis in subjects with short time intervals between carotid and brain MR imaging did not change our results. Last, our cross-sectional study design makes it difficult to interpret cause and effect of the associations found.

In our study, the presence of intraplaque hemorrhage was related to cortical infarcts, and this seemed primarily true for men.

A small cross-sectional study in patients with recent ischemic events and carotid stenosis found that the size of intraplaque hemorrhage and not the presence of a lipid core was associated with symptomatic plaques.<sup>25</sup> On the other hand, in a prospective MR imaging study in subjects with 50%–79% carotid stenosis, both intraplaque hemorrhage and the size of the lipid core were related to the risk of a cerebrovascular event, albeit not the presence of a lipid core itself.<sup>1</sup> In our study, we only found a borderline significant association between the presence of a lipid core and cortical infarcts, and only for the ipsilateral hemisphere. Thus, on the basis of our findings and those of others, it may be hypothesized that carotid intraplaque hemorrhage, rather than the presence of a lipid core, is a more relevant indicator of plaque vulnerability. However, other studies with a more sensitive measure of lipid core and assessing lipid core size should further explore the relation between lipid core and cortical infarcts.

The association we found between intraplaque hemorrhage and the presence of cortical infarcts is in line with the presumed etiology of cortical infarcts, which are primarily regarded as being caused by large-vessel disease. In contrast, lesions in subcortical brain regions, such as lacunar infarcts and white matter lesions, are considered the sequelae of cerebral small-vessel disease.<sup>26</sup> In our study, none of the vulnerable plaque characteristics—intraplaque hemorrhage and lipid core—or measures of plaque size were associated with the presence of lacunar infarcts, supporting

extracranial carotid embolic disease not being an important factor in the development of lacunar infarcts.

We did not find important differences between the participant-based analyses and the analyses restricted to the ipsilateral hemisphere of each carotid artery, though the degree of carotid stenosis was a confounder for the association between intraplaque hemorrhage and ipsilateral cortical infarcts. Previously, a relationship between plaque burden expressed as severity of stenosis and the presence of intraplaque hemorrhage has been demonstrated.<sup>27</sup> Intraplaque hemorrhage instead of the severity of stenosis must be considered as the link between atherosclerotic disease and brain infarcts. The predictive power of intraplaque hemorrhage versus stenosis should be evaluated in future studies. In addition, atherosclerosis in one vessel bed is known to reflect atherosclerotic activity in other vascular regions.<sup>28</sup> Thus, carotid plaques are not per se only related to ischemic disease in the ipsilateral vascular territory. If we extended this concept of atherosclerosis as a generalized disease, intraplaque hemorrhage could be regarded as a focal manifestation of an underlying systemic disease process that includes several vulnerable lesions.<sup>29</sup>

In the ongoing discussion on the pathogenesis of WMLs, the most generally accepted concept is that they reflect a process of ischemic demyelination, predominantly with small-vessel disease as the etiologic factor.<sup>30</sup> There is, however, also some evidence that large-vessel disease may contribute to the development of WMLs,<sup>31</sup> especially via embolic events from unstable carotid plaques (ie, those with intraplaque hemorrhage).<sup>32</sup> Although we found a borderline significant relation between carotid intraplaque hemorrhage and WML volume, this association attenuated when adjusting for cardiovascular risk factors. This finding may suggest that there is a shared etiology for atherosclerosis and the development of WMLs, rather than a direct causal connection between intraplaque hemorrhage and WML development.

In the current literature, all available data on this topic are from small studies in clinical patients, with 2 thoughts being put forward. Altaf et al<sup>32</sup> found, in 187 symptomatic subjects, an association between carotid intraplaque hemorrhage and WML volume, supporting the large-vessel disease and unstable plaque concept. Kwee et al<sup>33</sup> found, in 50 patients with symptomatic carotid stenosis, that carotid plaque burden was significantly associated with WML severity but that there was no causal relationship between carotid plaque vulnerability and the occurrence of WMLs. In contrast, Patterson et al<sup>34</sup> found MR imaging plaque morphology (ie, plaque size, the presence of intraplaque hemorrhage, or lipid core) in 80 carotid arteries to be not independently predictive of the severity of WMLs, refuting the large-vessel disease and unstable plaque concept. Our results suggest no significant relation between intraplaque hemorrhage or lipid component and WML volume; therefore, our results contribute to this discussion in that they do not support the hypothesis of a role of vulnerable large-vessel atherosclerotic plaque in the development of WMLs. In the current study, carotid plaque calcification is associated with WMLs, also demonstrated in a previous CT-based study by Bos et al.<sup>35</sup> This is possibly the association between luminal stenosis and brain MR imaging markers of ischemia rather

than vulnerable plaque, because previous studies have suggested that for a given volume of plaque, the greater the proportion of calcification, the more “stable” the plaque is.<sup>36,37</sup>

## CONCLUSIONS

The presence of carotid intraplaque hemorrhage and measures of carotid plaque size, as defined with MR imaging, are associated with MR imaging–defined cortical infarcts, but not with lacunar infarcts. Plaque instability does not seem to play a role in WML development.

Disclosures: Quirijn J.A. van den Bouwhuisen—RELATED: Grant: Netherlands Heart Foundation, Comments: grants 2006B206 and 2009B044.\* Benjamin F.J. Verhaaren—RELATED: Grant: Dutch Heart Foundation, Comments: grant No. 2009B102.\* Wiro J. Niessen—UNRELATED: Consultancy: Quantib BV, Comments: I am advisor (chief scientific officer) of Quantib BV\*; Stock/Stock Options: Quantib BV, Comments: I am cofounder and shareholder of Quantib BV. Gabriel P. Krestin—UNRELATED: Consultancy: Bracco\*; Grants/Grants Pending: Siemens, Bayer, GE Healthcare, Bracco\*. \*Money paid to the institution.

## REFERENCES

1. Takaya N, Yuan C, Chu B, et al. **Association between carotid plaque characteristics and subsequent ischemic cerebrovascular events: a prospective assessment with MRI—initial results.** *Stroke* 2006;37:818–23 CrossRef Medline
2. Saam T, Hatsukami TS, Takaya N, et al. **The vulnerable, or high-risk, atherosclerotic plaque: noninvasive MR imaging for characterization and assessment.** *Radiology* 2007;244:64–77 CrossRef Medline
3. Sary HC, Chandler AB, Dinsmore RE, et al. **A definition of advanced types of atherosclerotic lesions and a histological classification of atherosclerosis: a report from the Committee on Vascular Lesions of the Council on Arteriosclerosis, American Heart Association.** *Circulation* 1995;92:1355–74 CrossRef Medline
4. Redgrave JN, Lovett JK, Gallagher PJ, et al. **Histological assessment of 526 symptomatic carotid plaques in relation to the nature and timing of ischemic symptoms: the Oxford plaque study.** *Circulation* 2006;113:2320–28 CrossRef Medline
5. Cappendijk VC, Cleutjens KB, Kessels AG, et al. **Assessment of human atherosclerotic carotid plaque components with multisequence MR imaging: initial experience.** *Radiology* 2005;234:487–92 CrossRef Medline
6. Saam T, Ferguson MS, Yarnykh VL, et al. **Quantitative evaluation of carotid plaque composition by in vivo MRI.** *Arterioscler Thromb Vasc Biol* 2005;25:234–39 Medline
7. Moody AR. **Magnetic resonance direct thrombus imaging.** *J Thromb Haemost* 2003;1:1403–09 CrossRef Medline
8. Vermeer SE, Hollander M, van Dijk EJ, et al; Rotterdam Scan Study. **Silent brain infarcts and white matter lesions increase stroke risk in the general population: the Rotterdam Scan Study.** *Stroke* 2003;34:1126–29 CrossRef Medline
9. van Dijk EJ, Prins ND, Vermeer SE, et al. **Frequency of white matter lesions and silent lacunar infarcts.** *J Neural Transm Suppl* 2002; 25–39 Medline
10. Fisher CM. **Lacunar strokes and infarcts: a review.** *Neurology* 1982; 32:871–76 CrossRef Medline
11. Warlow C, Sudlow C, Dennis M, et al. **Stroke.** *Lancet* 2003;362: 1211–24 CrossRef Medline
12. Hofman A, Darwish Murad S, van Duijn CM, et al. **The Rotterdam Study: 2014 objectives and design update.** *Eur J Epidemiol* 2013;28: 889–926 CrossRef Medline
13. Iglesias del Sol A, Bots ML, Grobbee DE, et al. **Carotid intima-media thickness at different sites: relation to incident myocardial infarction—the Rotterdam Study.** *Eur Heart J* 2002;23:934–40 CrossRef Medline
14. Yuan C, Mitsumori LM, Ferguson MS, et al. **In vivo accuracy of multispectral magnetic resonance imaging for identifying lipid-rich**

- necrotic cores and intraplaque hemorrhage in advanced human carotid plaques. *Circulation* 2001;104:2051–56 CrossRef Medline
15. Ikram MA, van der Lugt A, Niessen WJ, et al. **The Rotterdam Scan Study: design update 2016 and main findings.** *Eur J Epidemiol* 2015; 30:1299–315 CrossRef Medline
  16. Vernooij MW, van der Lugt A, Ikram MA, et al. **Prevalence and risk factors of cerebral microbleeds: the Rotterdam Scan Study.** *Neurology* 2008;70:1208–14 CrossRef Medline
  17. van den Bouwhuisen QJ, Vernooij MW, Hofman A, et al. **Determinants of magnetic resonance imaging detected carotid plaque components: the Rotterdam Study.** *Eur Heart J* 2012;33:221–29 CrossRef Medline
  18. **North American Symptomatic Carotid Endarterectomy Trial: methods, patient characteristics, and progress.** *Stroke* 1991;22: 711–20 CrossRef Medline
  19. Vrooman HA, Cocosco CA, van der Lijn F, et al. **Multi-spectral brain tissue segmentation using automatically trained k-nearest-neighbor classification.** *Neuroimage* 2007;37:71–81 CrossRef Medline
  20. de Boer R, Vrooman HA, van der Lijn F, et al. **White matter lesion extension to automatic brain tissue segmentation on MRI.** *Neuroimage* 2009;45:1151–61 CrossRef Medline
  21. Vliethart R, Oudkerk M, Hofman A, et al. **Coronary calcification improves cardiovascular risk prediction in the elderly.** *Circulation* 2005;112:572–77 CrossRef Medline
  22. European Society of Hypertension-European Society of Cardiology Guidelines Committee. **2003 European Society of Hypertension-European Society of Cardiology guidelines for the management of arterial hypertension.** *J Hypertens* 2003;21:1011–53 CrossRef Medline
  23. Wieberdink RG, van Schie MC, Koudstaal PJ, et al. **High von Willebrand factor levels increase the risk of stroke: the Rotterdam study.** *Stroke* 2010;41:2151–56 Medline
  24. Cai J, Hatsukami TS, Ferguson MS, et al. **In vivo quantitative measurement of intact fibrous cap and lipid-rich necrotic core size in atherosclerotic carotid plaque: comparison of high-resolution, contrast-enhanced magnetic resonance imaging and histology.** *Circulation* 2005;112:3437–44 CrossRef Medline
  25. Saam T, Cai J, Ma L, et al. **Comparison of symptomatic and asymptomatic atherosclerotic carotid plaque features with in vivo MR imaging.** *Radiology* 2006;240:464–72 CrossRef Medline
  26. Pantoni L. **Cerebral small vessel disease: from pathogenesis and clinical characteristics to therapeutic challenges.** *Lancet Neurol* 2010;9:689–701 CrossRef Medline
  27. Selwaness M, Hameeteman R, Van 't Klooster R, et al. **Determinants of carotid atherosclerotic plaque burden in a stroke-free population.** *Atherosclerosis* 2016;255:186–92 CrossRef Medline
  28. Odink AE, van der Lugt A, Hofman A, et al. **Association between calcification in the coronary arteries, aortic arch and carotid arteries: the Rotterdam study.** *Atherosclerosis* 2007;193:408–13 CrossRef Medline
  29. Lutgens E, van Suylen RJ, Faber BC, et al. **Atherosclerotic plaque rupture: local or systemic process?** *Arterioscler Thromb Vasc Biol* 2003;23:2123–30 CrossRef Medline
  30. Pantoni L, Garcia JH. **Pathogenesis of leukoaraiosis: a review.** *Stroke* 1997;28:652–59 CrossRef Medline
  31. de Leeuw FE, de Groot JC, Bots ML, et al. **Carotid atherosclerosis and cerebral white matter lesions in a population based magnetic resonance imaging study.** *J Neurol* 2000;247:291–96 CrossRef Medline
  32. Altaf N, Morgan PS, Moody A, et al. **Brain white matter hyperintensities are associated with carotid intraplaque hemorrhage.** *Radiology* 2008;248:202–09 CrossRef Medline
  33. Kwee RM, Hofman PA, Gronenschild EH, et al. **Association between carotid plaque characteristics and cerebral white matter lesions: one-year follow-up study by MRI.** *PLoS One* 2011;6:e17070 CrossRef Medline
  34. Patterson AJ, UK-Im JM, Tang TY, et al. **Association between white matter ischaemia and carotid plaque morphology as defined by high-resolution in vivo MRI.** *Eur J Vasc Endovasc Surg* 2009;38: 149–54 CrossRef Medline
  35. Bos D, Ikram MA, Elias-Smale SE, et al. **Calcification in major vessel beds relates to vascular brain disease.** *Arterioscler Thromb Vasc Biol* 2011;31:2331–37 CrossRef Medline
  36. Kwee RM. **Systematic review on the association between calcification in carotid plaques and clinical ischemic symptoms.** *J Vasc Surg* 2010;51:1015–25 CrossRef Medline
  37. Gupta A, Baradaran H, Kamel H, et al. **Evaluation of computed tomography angiography plaque thickness measurements in high-grade carotid artery stenosis.** *Stroke* 2014;45:740–45 CrossRef Medline

# Sigmoid Sinus Diverticulum, Dehiscence, and Venous Sinus Stenosis: Potential Causes of Pulsatile Tinnitus in Patients with Idiopathic Intracranial Hypertension?

J.A. Lansley, W. Tucker, M.R. Eriksen, P. Riordan-Eva, and S.E.J. Connor

## ABSTRACT

**BACKGROUND AND PURPOSE:** Pulsatile tinnitus is experienced by most patients with idiopathic intracranial hypertension. The pathophysiology remains uncertain; however, transverse sinus stenosis and sigmoid sinus diverticulum/dehiscence have been proposed as potential etiologies. We aimed to determine whether the prevalence of transverse sinus stenosis and sigmoid sinus diverticulum/dehiscence was increased in patients with idiopathic intracranial hypertension and pulsatile tinnitus relative to those without pulsatile tinnitus and a control group.

**MATERIALS AND METHODS:** CT vascular studies of patients with idiopathic intracranial hypertension with pulsatile tinnitus ( $n = 42$ ), without pulsatile tinnitus ( $n = 37$ ), and controls ( $n = 75$ ) were independently reviewed for the presence of severe transverse sinus stenosis and sigmoid sinus diverticulum/dehiscence according to published criteria. The prevalence of transverse sinus stenosis and sigmoid sinus diverticulum/dehiscence in patients with idiopathic intracranial hypertension with pulsatile tinnitus was compared with that in the nonpulsatile tinnitus idiopathic intracranial hypertension group and the control group. Further comparisons included differing degrees of transverse sinus stenosis (50% and 75%), laterality of transverse sinus stenosis/sigmoid sinus diverticulum/dehiscence, and ipsilateral transverse sinus stenosis combined with sigmoid sinus diverticulum/dehiscence.

**RESULTS:** Severe bilateral transverse sinus stenoses were more frequent in patients with idiopathic intracranial hypertension than in controls ( $P < .001$ ), but there was no significant association between transverse sinus stenosis and pulsatile tinnitus within the idiopathic intracranial hypertension group. Sigmoid sinus dehiscence (right- or left-sided) was also more common in patients with idiopathic intracranial hypertension compared with controls ( $P = .01$ ), but there was no significant association with pulsatile tinnitus within the idiopathic intracranial hypertension group.

**CONCLUSIONS:** While our data corroborate previous studies demonstrating increased prevalence of sigmoid sinus diverticulum/dehiscence and transverse sinus stenosis in idiopathic intracranial hypertension, we did not establish an increased prevalence in patients with idiopathic intracranial hypertension with pulsatile tinnitus compared with those without. It is therefore unlikely that these entities represent a direct structural correlate of pulsatile tinnitus in patients with idiopathic intracranial hypertension.

**ABBREVIATIONS:** IIH = idiopathic intracranial hypertension; PT = pulsatile tinnitus; SSDD = sigmoid sinus diverticulum/dehiscence; TSS = transverse sinus stenosis

**P**ulsatile tinnitus (PT) is the perception of an abnormal sound that is synchronous with the heartbeat. The phenomenon may result from abnormal mechanical somatosound production

(due to abnormal turbulence or location of vascular flow) or enhanced perception (due to increased transmission of the somatosound or reduced conduction of normal sound).<sup>1</sup> PT is a well-recognized feature of idiopathic intracranial hypertension (IIH), being present in approximately 60% of patients.<sup>2-4</sup> The pathophysiology of PT in these patients is unknown; however, observed variations in transverse and sigmoid sinus anatomy seen in IIH have been proposed as a possible underlying cause.

Transverse sinus stenosis (TSS) is well-described as a cause of PT, and resolution of symptoms has been reported following successful venous sinus stent placement.<sup>5-8</sup> Venous sinus stent placement performed as a treatment for IIH has also resulted in resolution of PT in affected patients,<sup>7,8</sup> which lends support to the

Received September 22, 2016; accepted after revision April 29, 2017.

From the Barts Health National Health Service Trust (J.A.L.), London, UK; King's College Hospital (W.T., M.R.E., P.R.-E., S.E.J.C.), Denmark Hill, London, UK; Aleris Roentgen Institute Stavanger (M.R.E.), Stavanger, Norway; and Guy's and St Thomas' Hospital (S.E.J.C.), London, UK.

Paper previously presented at: Annual Meeting and Refresher Course of the European Society of Head and Neck Radiology, September 22–24, 2016; Leiden, the Netherlands.

Please address correspondence to Joseph A. Lansley, MBBS, Neuroradiology Department, Royal London Hospital, Whitechapel Rd, London, E1 1BB, UK; e-mail: dr.joseph.lansley@gmail.com

<http://dx.doi.org/10.3174/ajnr.A5277>

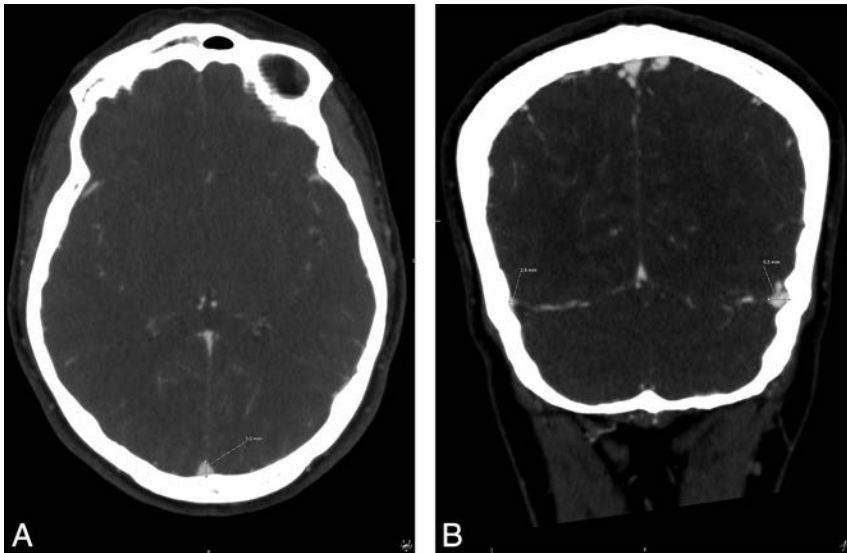


**FIG 1.** A, Superior sagittal sinus height measurement (2 cm above the torcula). B, Transverse sinus stenosis measurement.

proposal that the resulting turbulent venous flow may be the somatosound responsible for PT in IIH.<sup>9,10</sup> However, PT is not seen in all patients with IIH with TSS, and other factors may be required for the symptom to manifest.

More recently, sigmoid sinus diverticulum and/or dehiscence (SSDD) has been shown to be associated with PT.<sup>1,11-16</sup> This association has been noted to be particularly frequent in patients with elevated body mass indices and those with imaging features of IIH,<sup>1,14,15</sup> leading some authors to suggest that SSDD may reflect a manifestation of subclinical IIH.<sup>2,14</sup>

Interventional studies have revealed that endovascular stenting of TSS or surgical correction of SSDD may resolve PT<sup>5,7,8,13,17-19</sup>; however, these procedures are not without complications.<sup>12</sup> Understanding the underlying mechanism is therefore essential to enable appropriate targeting of therapy.

We aimed to determine whether the prevalence of TSS and SSDD was increased in patients with IIH with PT relative to patients with IIH without PT and a control group without IIH.

## MATERIALS AND METHODS

### Subjects

One hundred seventy consecutive patients diagnosed with IIH were identified from a clinical data base at our institution and selected for retrospective review. IIH diagnosis was made with the support of CSF pressure measurements and according to the modified Dandy criteria<sup>20</sup> in all except 1 patient in whom lumbar puncture was precluded due to cerebellar tonsillar herniation. Case notes were reviewed for demographic and clinical details, including a history of pulsatile tinnitus. Laterality of PT was not consistently recorded and hence not documented. Patients were excluded if there was no CT venogram available for evaluation. When >1 CT venogram had been obtained on the same patient, the examination closest to the diagnosis of IIH was selected for analysis. Seventy-nine patients with IIH (mean, 32 ± 5.8 years of age; male/female ratio, 4:75) were available for evaluation.

A cohort of control subjects was generated by using contemporaneous CT angiograms obtained on the same CT scanner for reasons other than suspected venous pathology or pulsatile tinnitus. A list of CTA examinations was generated by searching the PACS archive for intracranial CTAs performed in the study period (January 1, 2005, to May 22, 2015) that contained the text “normal” in the body of the report. The resulting 1250 studies were ranked by age with subjects younger than 16 and older than 45 years of age excluded to closely model the IIH cohort. The report text of the remaining scans was manually screened, and studies with abnormal findings were excluded. The resulting 183 CTAs were reviewed, and further exclusions were made if there was confounding pathology or if venous opacification was insufficient (defined as <160 HU measured at the torcula). After this process, 75 control subjects were available for evaluation.

The study was reviewed by the local National Health Service Research Ethics Committee and was considered to represent “service evaluation.”

### Radiologic Assessment

CTAs and CT venograms were obtained with a LightSpeed 16 scanner (GE Healthcare, Milwaukee, Wisconsin). Scanning parameters were 0.625-mm collimation; pitch, 0.938:1; noise index, 2.2; automilliamperage limit, 380.

The presence of venous sinus stenosis, sigmoid plate dehiscence, and diverticula was assessed by 2 neuroradiologists independently (J.A.L. and M.R.E., with 9 and 15 years of radiology experience, respectively). Venous sinus luminal dimensions were first evaluated with maximum-intensity-projection reconstructions to provide an overview of the narrowest portion of the sinus encountered from the torcula to the distal sigmoid sinus. Multiplanar reformats (0.6 mm thick) at standard magnifications and perpendicular to the plane of the skull vault were then used to assess the height of the sinuses. Percentage stenoses were calculated as the ratio of the maximal narrowing relative to the maximal height of the superior sagittal sinus (measured 2 cm above the torcula, Fig 1). Stenoses were categorized as >50% and >75% relative to the superior sagittal sinus according to previously published criteria.<sup>21</sup>

A rigorous, objective radiographic classification of SSDDs is yet to be established. For this study, we adapted a previously described methodology,<sup>1</sup> using MPR reconstructions and an edge-sharpening tool available on our PACS. Assessments were made with standard bone windows (width, 4000 HU centered at 400 HU). Dehiscence was characterized as complete absence of cortical bone adjacent to the sigmoid sinus (air-on-sinus sign) evident on at least 2 consecutive 0.6-mm sections in 2 orthogonal planes (Fig 2). “Sigmoid sinus diverticulum” was defined as a focal out-pouching of the normal semicircular sigmoid sinus groove ex-

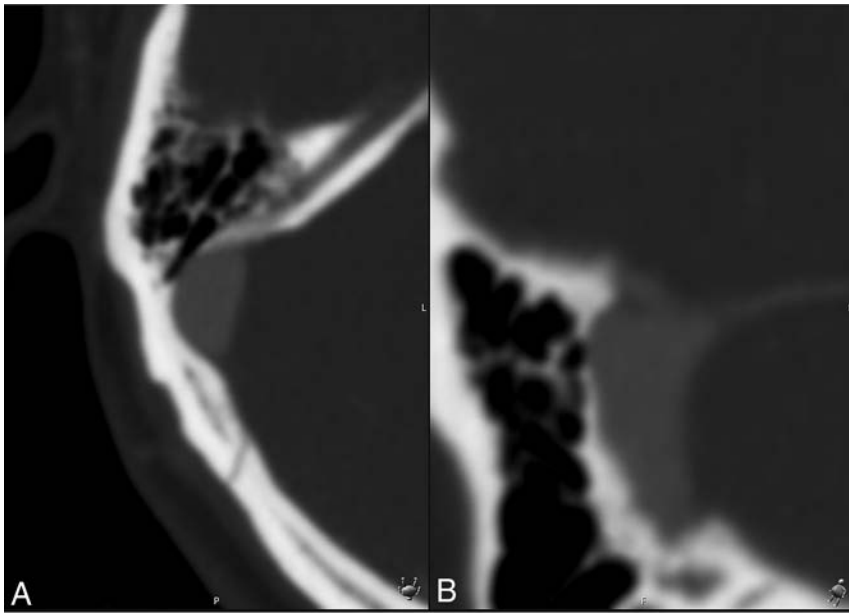


**FIG 2.** Dehiscence of the sigmoid sinus wall: “air-on-sinus” sign in the axial (A) and sagittal planes (B).

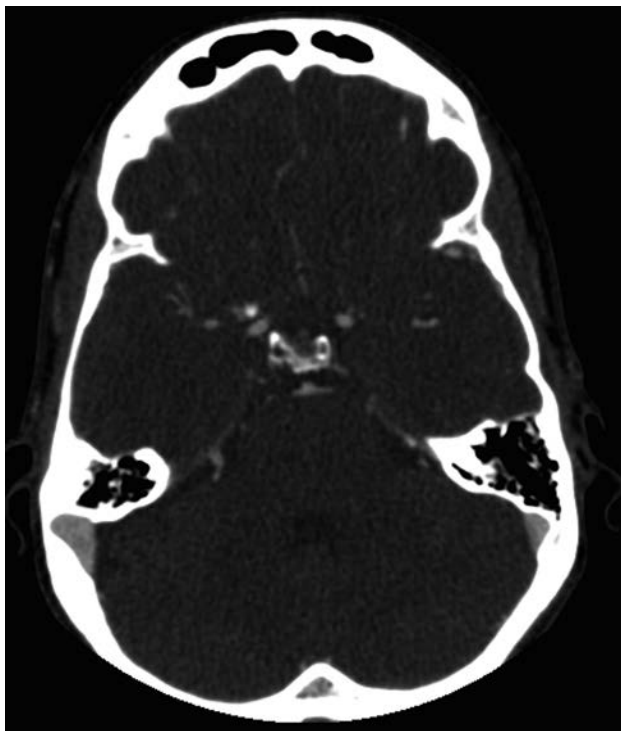


**FIG 3.** Example of a right sigmoid diverticulum.

panding into the mastoid air cells and/or temporal bone cortex (Fig 3).<sup>18</sup>

Consensus review was undertaken for all discrepant cases derived from the initial independent readings.

### Statistical Analysis

Data were entered into an Excel spreadsheet (Excel for Mac, 2011; Microsoft, Redmond, Washington). The statistical package Stat-Plus (AnalystSoft, Walnut, California) was used for descriptive statistics.

The prevalence of TSS (>75% and >50%), sigmoid sinus dehiscence, and sigmoid sinus diverticulum in patients with IIH was compared with that in the control group to see whether the previously reported associations were replicated in our cohort. Further subgroup analyses were performed to compare the PT-IIH group with the controls and the non-PT IIH group. Group comparisons were also performed to compare the prevalence of ipsilateral TSS and SSDD in the cohorts in case simultaneous abnormalities were needed for PT to manifest. Statistical comparison was performed with  $\chi^2$  or Fisher exact tests as appropriate, with  $P < .05$  being required for significance.

We performed further exploratory between-group comparisons, taking into account variations in the laterality of TSS and SSDD (ie, left, right, unilateral, bilateral, and either unilateral or bilateral).

### RESULTS

There was no significant difference in the average age of the IIH group ( $32 \pm 5.8$  years) and control group ( $32 \pm 10.2$  years). Of the 79 patients with IIH, 42 had PT. The average body mass index in the IIH group was 37, and there was no significant difference in body mass indices between patients with IIH with and without PT. The IIH group was almost exclusively female (75:4), whereas the control group comprised 35 men and 40 women.

The characteristics and imaging analysis results of the groups are summarized in the Table.

Patients with IIH were significantly more likely to have a severe grade of venous sinus stenosis (>50% and >75%) compared with controls. When both left and right transverse sigmoid sinus drainage pathways were considered together, 49% of patients with IIH had >75% stenosis affecting 1 side compared with just 7% of controls ( $P < .001$ ). This significance was maintained for the PT-IIH subgroup analysis, but there was no significant association between severe dural venous sinus stenosis and PT within the IIH group.

Dehiscence, as defined by the “air-on-sinus” sign, was more common on the right in all groups. In the IIH group, 41% of all temporal bones were dehiscence, compared with 27% of controls ( $P = .01$ ). The significance of this difference was retained when controls were compared with the PT-IIH subgroup, but there was no significant difference between patients with and without PT in the IIH group.

Sigmoid sinus diverticula were twice as common in patients with IIH compared with controls (8% versus 4%); however, the difference was not significant, and no other significant differences were found in the subgroup analyses.

There was no significant difference in the prevalence of ipsi-

## Characteristics and imaging analysis results of the groups

	Subgroup 1 (IIH with PT) (n = 42)	Subgroup 2 (IIH without PT) (n = 37)	Patients with IIH (Combined) (n = 79)	Controls (n = 75)	P	P1	P2
Rt stenosis >75%	21 (50%)	14 (38%)	35 (44%)	3 (4%)	.28	<.001 <sup>a</sup>	<.001 <sup>a</sup>
Lt stenosis >75%	21 (50%)	21 (57%)	42 (53%)	7 (9%)	.55	<.001 <sup>a</sup>	<.001 <sup>a</sup>
Rt or Lt stenosis >75%	42 (50%)	35 (47%)	77 (49%)	10 (7%)	.73	<.001	<.001 <sup>a</sup>
Unilateral >75% stenosis	16 (38%)	15 (41%)	33 (42%)	10 (13%)	.82	.002 <sup>a</sup>	<.001 <sup>a</sup>
Bilateral >75% stenoses	13 (31%)	9 (24%)	22 (28%)	0	.51	<.001 <sup>a</sup>	<.001 <sup>a</sup>
Unilateral or bilateral >75% stenosis	29 (69%)	24 (65%)	55 (70%)	10 (13%)	.69	<.001 <sup>a</sup>	<.001 <sup>a</sup>
Rt stenosis >50%	30 (71%)	28 (76%)	58 (73%)	6 (8%)	.67	<.001 <sup>a</sup>	<.001 <sup>a</sup>
Lt stenosis >50%	33 (78%)	32 (86%)	65 (82%)	19 (25%)	.36	<.001 <sup>a</sup>	<.001 <sup>a</sup>
Rt or Lt stenosis >50%	63 (75%)	60 (81%)	123 (78%)	25 (16%)	.36	<.001 <sup>a</sup>	<.001 <sup>a</sup>
Unilateral >50% stenosis	7 (17%)	10 (27%)	17 (22%)	21 (28%)	.26	.17	.35
Bilateral >50% stenoses	28 (67%)	25 (68%)	53 (67%)	2 (3%)	.93	<.001 <sup>a</sup>	<.001 <sup>a</sup>
Unilateral or bilateral >50% stenoses	35 (83%)	35 (94%)	70 (89%)	23 (31%)	.12	<.001 <sup>a</sup>	<.001 <sup>a</sup>
Rt diverticulum	5 (12%)	3 (8%)	8 (10%)	6 (8%)	.72	.48	.65
Lt diverticulum	2 (5%)	2 (5%)	4 (5%)	0	1	.13	.12
Rt or Lt diverticulum	7 (8%)	5 (7%)	12 (8%)	6 (4%)	.71	.17	.18
Unilateral diverticulum	5 (12%)	5 (14%)	10 (13%)	6 (8%)	.83	.49	.34
Bilateral diverticula	1 (2%)	0	1 (1%)	0	1	.36	1
Unilateral or bilateral diverticula	6 (14%)	5 (14%)	11 (14%)	6 (8%)	.92	.28	.24
Rt dehiscence	24 (57%)	16 (43%)	40 (51%)	28 (37%)	.22	.04 <sup>a</sup>	.10
Lt dehiscence	12 (29%)	12 (32%)	24 (30%)	12 (16%)	.71	.11	.04 <sup>a</sup>
Rt or Lt dehiscence	36 (42%)	28 (38%)	64 (41%)	40 (27%)	.52	.01 <sup>a</sup>	.01 <sup>a</sup>
Unilateral dehiscence	18 (43%)	12 (32%)	30 (38%)	26 (35%)	.34	.38	.70
Bilateral dehiscence	9 (21%)	8 (22%)	17 (22%)	7 (9%)	.98	.07	.04 <sup>a</sup>
Unilateral or bilateral dehiscence	27 (64%)	20 (54%)	47 (60%)	33 (44%)	.36	.04 <sup>a</sup>	.05 <sup>a</sup>

Note:—P indicates IIH with PT vs IIH without PT; P1, IIH with PT vs controls; P2, IIH (combined) vs controls; Rt, right; Lt, left.

<sup>a</sup> Significant.

lateral stenosis and dehiscence or ipsilateral stenosis and diverticulum between IIH patients with PT and those without PT.

## DISCUSSION

Venous tinnitus in IIH has been determined to be the most frequent cause of PT in some series,<sup>4</sup> and it is proposed that this may have a direct anatomic correlate with either TSS or SSDD. An increased prevalence of TSS and SSDD has been noted in patients with PT,<sup>12,22</sup> and the symptoms of PT have responded to previous targeted treatments to the transverse sigmoid sinus in patients with and without IIH.<sup>5,7,8,17-19</sup>

Although both TSS and SSDD have been linked to IIH, to the best of our knowledge, no previous studies have investigated the frequency in patients with IIH with and without PT. We aimed to evaluate whether the prevalence of either entity could explain the occurrence of PT in a cohort of patients with confirmed IIH. Alternatively, TSS and SSDD may have a noncausal association with PT and CSF, or brain pulsation may be transmitted to the inner ear structures by alternative mechanisms.<sup>22,23</sup>

TSS is present in most patients with IIH<sup>21,24,25</sup>; however, the etiology remains controversial. Pre-existing areas of TSS may be implicated in the development of IIH<sup>7,26</sup>; however, it is also postulated that they occur secondary to raised CSF pressure, and reversibility of stenoses has been demonstrated by lowering CSF pressure.<sup>27</sup> Patients with TSS secondary to IIH may experience PT due to turbulent venous flow directly related to the venous stenoses or due to periodic narrowing caused by arterial pulsations transmitted to the venous sinuses across the CSF.<sup>28</sup>

Patients with PT and SSDD have been found to have clinical and imaging characteristics of IIH.<sup>1,12,15</sup> A number of mechanisms have been proposed to explain this association. It is possible

that the impact of pulsatile, turbulent blood flow on the sinus wall could cause the formation of SSDD.<sup>15,18</sup> Alternatively the presence of SSDD may be a direct result of raised CSF pressures.<sup>12,16,29</sup> It has also been postulated that sigmoid sinus dehiscence could cause PT in these patients due to increased transmission of turbulent flow to the inner ear after loss of the insulating properties afforded by cortical bone.<sup>1,16,30</sup> Although our findings did demonstrate an association between dehiscence and IIH, there was no association within the IIH group to support a direct causal relationship. We also investigated the suggestion that a combination of TSS and SSDD may be required to cause PT,<sup>1</sup> but we found no increased frequency of ipsilateral TSS and SSDD in our PT cohort with IIH to support this.

It is possible that dehiscence involving specific locations on the curve of the sigmoid sinus results in PT symptoms.<sup>13</sup> We did not categorize dehiscence in this way; this choice could have reduced our ability to detect a significant association. We also found that tiny focal areas of dehiscence were commonly present, even in control subjects, which casts some doubt about their clinical significance.

We did not distinguish different types of stenosis: tapered “extraluminal” narrowing versus “intraluminal” narrowing typified by arachnoid granulations.<sup>21</sup> This could also have limited our ability to detect a significant association between stenosis and PT.

It is unclear whether sigmoid sinus diverticula and dehiscence represent separate entities or whether there is an underlying pathophysiologic spectrum of disease.<sup>1,15</sup> Diverticula may cause turbulent venous flow and lead to symptomatic PT when coexisting with elevated intracranial pressure, independent of TSS; how-

ever, our IIH cohort did not reveal any association between PT and diverticula to lend support to this theory.

We explored the combined effect of TSS and ipsilateral SSDD, but it is possible that a more complex combination of anatomic features is required to cause PT or that the pathophysiology differs between patients. It has been shown that ipsilateral venous outflow dominance, high jugular bulb, and temporal bone hyperpneumatization may also be important in the manifestation of SSDD as PT.<sup>13,16</sup> Complex interactions with venous dominance, the site and size of dehiscence, and the type of stenosis (intraluminal versus extraluminal) were not fully evaluated in our study. Although we did not document venous dominance directly, diverticula and dehiscence were observed more frequently on the right; this feature is of interest because this is more likely to be the dominant sinus.<sup>31</sup>

Our findings reveal a high prevalence of PT in IIH, which is in line with previous studies.<sup>3</sup> The data also corroborate previous research indicating a high frequency of transverse sinus stenosis and sigmoid sinus wall abnormalities in IIH. However, we found no significant association between PT and venous sinus or sinus wall abnormalities within the IIH group, suggesting that a direct causal link is unlikely. Furthermore, ipsilateral dehiscence and TSS abnormalities were not significantly more frequent in the PT group; this finding suggests that even when combined, these factors are not sufficient to cause PT.

Our dataset contained a large validated cohort of patients diagnosed with IIH, corroborated by CSF pressure measurements; however, the study design has some important limitations. First, the retrospective nature meant that there was nonuniformity of data. Most important, we had limited information on the laterality of PT. It is recognized that PT in IIH is most commonly unilateral,<sup>32</sup> and this information would have allowed a greater confidence in relating PT to the venous correlates. The lack of well-defined criteria and the subjective nature of the scoring for SSDD are also potential drawbacks; however, these were similarly applied across groups with standardized viewing parameters, and a consensus review was undertaken in cases of disagreement.

Another potential bias was introduced by including only patients with IIH who had undergone CT venography, which a large number of patients in the data base had not undertaken. The use of CTAs for the control group meant that observer blinding was not possible, and cases could be distinguished from controls. Nevertheless, observers were blinded to the presence of PT within the IIH group, and the question of this association was the primary aim of this study.

No previous studies describe the incidence of SSDD/TSS in confirmed IIH cases, to our knowledge; therefore, we were unable to perform a power calculation, and the sample size was determined by the size of the clinical data base.

Finally, the control group was not matched for sex, resulting in a female bias for the IIH cohort. Previous control cohorts have comprised subjects with middle ear symptoms referred for ear, nose, and throat investigations. The relatively high proportion of SSDD abnormalities found in these subjects (up to 18%) may misrepresent the general population.<sup>14</sup> We thought it was important to know the prevalence of SSDD in the general population to better understand the likelihood of SSDD as a coincidental find-

ing. A mixed-sex control group was therefore used to provide data about the incidence of SSDD.

Four percent of controls in our cohort had a combined conduit score of <5, in line with the 7% of controls in the study by Farb et al.<sup>21</sup> Sigmoid sinus dehiscence was more common in our control cohort (44% of patients, 53% of ears) compared with 1.2% and 18% of incidental SSDD reported in previous studies.<sup>12,14</sup> This discrepancy is likely to reflect shortcomings of CT assessment. Only tiny focal areas of apparent bone loss were required to be categorized as dehiscence; however, as previously shown in temporal bone histologic studies, bone thickness of <0.1 mm can be falsely read as dehiscence.<sup>33,34</sup> We also found a higher incidence of sigmoid sinus diverticula in our control cohort than described in previous studies: 8% compared with 0.5% reported by Grewal et al,<sup>14</sup> which may reflect differences in the demographic studied or possibly be due to sampling bias inherent in our smaller sample size.

## CONCLUSIONS

Although TSS and sigmoid sinus dehiscence were shown to be more frequently present in patients with IIH compared with controls, our findings do not support the proposed pathophysiologic mechanism that SSDD or TSS are directly responsible for PT in IIH. The finding of SSDD in a patient with PT may be coincidental, and patients considering surgical intervention should be counseled accordingly.

Disclosures: Marianna R. Eriksen—UNRELATED: Employment: Aleris Roentgen Institut Stavanger, Norway.

## REFERENCES

1. Harvey RS, Hertzano R, Kelman SE, et al. **Pulse-synchronous tinnitus and sigmoid sinus wall anomalies: descriptive epidemiology and the idiopathic intracranial hypertension patient population.** *Otol Neurotol* 2014;35:7–15 CrossRef Medline
2. Shaw GY, Million SK. **Benign intracranial hypertension: a diagnostic dilemma.** *Case Rep Otolaryngol* 2012;2012:814696 CrossRef Medline
3. Markey KA, Mollan SP, Jensen RH, et al. **Understanding idiopathic intracranial hypertension: mechanisms, management, and future directions.** *Lancet Neurol* 2016;15:78–91 CrossRef Medline
4. Sismanis A. **Pulsatile tinnitus: a 15-year experience.** *Am J Otol* 1998;19:472–77 Medline
5. Baomin L, Yongbing S, Xiangyu C. **Angioplasty and stenting for intractable pulsatile tinnitus caused by dural venous sinus stenosis: a case series report.** *Otol Neurotol* 2014;35:366–70 CrossRef Medline
6. Russell EJ, De Michaelis BJ, Wiet R, et al. **Objective pulse-synchronous “essential” tinnitus due to narrowing of the transverse dural venous sinus.** *Int Tinnitus J* 1995;1:127–37 Medline
7. Donnet A, Metellus P, Levrier O, et al. **Endovascular treatment of idiopathic intracranial hypertension: clinical and radiologic outcome of 10 consecutive patients.** *Neurology* 2008;70:641–47 CrossRef Medline
8. Ahmed RM, Wilkinson M, Parker GD, et al. **Transverse sinus stenting for idiopathic intracranial hypertension: a review of 52 patients and of model predictions.** *AJNR Am J Neuroradiol* 2011;32:1408–14 CrossRef Medline
9. Sismanis A. **Pulsatile tinnitus: contemporary assessment and management.** *Curr Opin Otolaryngol Head Neck Surg* 2011;19:348–57 CrossRef Medline
10. Jindal M, Hiam L, Raman A, et al. **Idiopathic intracranial hypertension in otolaryngology.** *Eur Arch Otorhinolaryngol* 2009;266:803–06 CrossRef Medline

11. Mattox DE, Hudgins P. **Algorithm for evaluation of pulsatile tinnitus.** *Acta Otolaryngol* 2008;128:427–31 CrossRef Medline
12. Schoeff S, Nicholas B, Mukherjee S, et al. **Imaging prevalence of sigmoid sinus dehiscence among patients with and without pulsatile tinnitus.** *Otolaryngol Head Neck Surg* 2014;150:841–46 CrossRef Medline
13. Geng W, Liu Z, Fan Z. **CT characteristics of dehiscent sigmoid plates presenting as pulsatile tinnitus: a study of 23 patients.** *Acta Radiol* 2015;56:1404–08 CrossRef Medline
14. Grewal AK, Kim HY, Comstock RH 3rd, et al. **Clinical presentation and imaging findings in patients with pulsatile tinnitus and sigmoid sinus diverticulum/dehiscence.** *Otol Neurotol* 2014;35:16–21 CrossRef Medline
15. Liu Z, Dong C, Wang X, et al. **Association between idiopathic intracranial hypertension and sigmoid sinus dehiscence/diverticulum with pulsatile tinnitus: a retrospective imaging study.** *Neuroradiology* 2015;57:747–53 CrossRef Medline
16. Zhao P, Lv H, Dong C, et al. **CT evaluation of sigmoid plate dehiscence causing pulsatile tinnitus.** *Eur Radiol* 2016;26:9–14 CrossRef Medline
17. Sanchez TG, Murao M, de Medeiros IR, et al. **A new therapeutic procedure for treatment of objective venous pulsatile tinnitus.** *Int Tinnitus J* 2002;8:54–57 Medline
18. Eisenman DJ. **Sinus wall reconstruction for sigmoid sinus diverticulum and dehiscence: a standardized surgical procedure for a range of radiographic findings.** *Otol Neurotol* 2011;32:1116–19 CrossRef Medline
19. Otto KJ, Hudgins PA, Abdelkafy W, et al. **Sigmoid sinus diverticulum: a new surgical approach to the correction of pulsatile tinnitus.** *Otol Neurotol* 2007;28:48–53 CrossRef Medline
20. Friedman DI, Jacobson DM. **Diagnostic criteria for idiopathic intracranial hypertension.** *Neurology* 2002;59:1492–95 CrossRef Medline
21. Farb RI, Vanek I, Scott JN, et al. **Idiopathic intracranial hypertension: the prevalence and morphology of sinovenous stenosis.** *Neurology* 2003;60:1418–24 CrossRef Medline
22. Chiarella G, Bono F, Cassandro C, et al. **Bilateral transverse sinus stenosis in patients with tinnitus.** *Acta Otorhinolaryngol Ital* 2012;32:238–43 Medline
23. Shulman A. **Brain pulsatility and pulsatile tinnitus: clinical types.** *Int Tinnitus J* 2012;17:2–3 Medline
24. Higgins JN, Gillard JH, Owler BK, et al. **MR venography in idiopathic intracranial hypertension: unappreciated and misunderstood.** *J Neurol Neurosurg Psychiatry* 2004;75:621–25 CrossRef Medline
25. Johnston I, Kollar C, Dunkley S, et al. **Cranial venous outflow obstruction in the pseudotumour syndrome: incidence, nature and relevance.** *J Clin Neurosci* 2002;9:273–78 CrossRef Medline
26. Higgins JN, Owler BK, Cousins C, et al. **Venous sinus stenting for refractory benign intracranial hypertension.** *Lancet* 2002;359:228–30 CrossRef Medline
27. Scoffings DJ, Pickard JD, Higgins JN. **Resolution of transverse sinus stenoses immediately after CSF withdrawal in idiopathic intracranial hypertension.** *J Neurol Neurosurg Psychiatry* 2007;78:911–12 CrossRef Medline
28. Sismanis A. **Otologic manifestations of benign intracranial hypertension syndrome: diagnosis and management.** *Laryngoscope* 1987;97(8 pt 2 suppl 42):1–17 Medline
29. Butros SR, Goncalves LF, Thompson D, et al. **Imaging features of idiopathic intracranial hypertension, including a new finding: widening of the foramen ovale.** *Acta Radiol* 2012;53:682–88 CrossRef Medline
30. Topal O, Erbek SS, Erbek S, et al. **Subjective pulsatile tinnitus associated with extensive pneumatization of temporal bone.** *Eur Arch Otorhinolaryngol* 2008;265:123–25 Medline
31. Durgun B, Ilglt ET, Cizmeli MO, et al. **Evaluation by angiography of the lateral dominance of the drainage of the dural venous sinuses.** *Surg Radiol Anat* 1993;15:125–30 CrossRef Medline
32. Hofmann E, Behr R, Neumann-Haefelin T, et al. **Pulsatile tinnitus: imaging and differential diagnosis.** *Dtsch Arztebl Int* 2013;110:451–58 CrossRef Medline
33. Carey JP, Minor LB, Nager GT. **Dehiscence or thinning of bone overlying the superior semicircular canal in a temporal bone survey.** *Arch Otolaryngol Head Neck Surg* 2000;126:137–47 CrossRef Medline
34. Mondina M, Bonnard D, Barreau X, et al. **Anatomo-radiological study of the superior semicircular canal dehiscence of 37 cadaver temporal bones.** *Surg Radiol Anat* 2013;35:55–59 CrossRef Medline

# Increased Curvature of the Tentorium Cerebelli in Idiopathic Intracranial Hypertension

 P.P. Morris,  N. Lachman,  D.F. Black,  R.A. Carter,  J. Port, and  N. Campeau

## ABSTRACT

**BACKGROUND AND PURPOSE:** Transverse sinus effacement is detectable on MRV examinations in almost all patients with idiopathic intracranial hypertension. This effacement of the transverse sinus is presumed to be mediated by elevation of intracranial pressure, resulting in compression and inward collapse of the dural margins of the sinus. We sought to establish whether supratentorial broad-based downward deformity of the tentorium might explain transverse sinus effacement in idiopathic intracranial hypertension.

**MATERIALS AND METHODS:** MRV examinations of 53 adult patients with idiopathic intracranial hypertension were reviewed retrospectively and compared with 58 contemporaneously acquired controls. The curvature of the tentorium with reference to a line connecting the transverse sinus laterally with the confluence of the tentorial leaves medially was calculated as a segment of a circle. The height and area of the segment and the angle subtended by the midpoint of the tentorium from the falx were calculated.

**RESULTS:** The height and area of the segment described by the chord connecting the transverse sinus with the apex of the tentorial confluence and subtended midtentorial angle were greater in the idiopathic intracranial hypertension group; this finding supports the hypothesis that increased tentorial bowing is present in idiopathic intracranial hypertension.

**CONCLUSIONS:** Increased bowing of the tentorium in patients with idiopathic intracranial hypertension compared with controls is a new observation, lending itself to new hypotheses on the nature and localization of elevated intracranial pressure in idiopathic intracranial hypertension. Bowing of the tentorium may play a part in distorting the contour of the transverse sinuses, resulting, at least in part, in the effacement of the transverse sinuses in idiopathic intracranial hypertension.

**ABBREVIATIONS:** ICP = intracranial pressure; IIH = idiopathic intracranial hypertension

Idiopathic intracranial hypertension (IIH), alternatively known as pseudotumor cerebri, is a poorly understood condition characterized by elevation of intracranial pressure (ICP) in the absence of a definable intracranial mass or other anatomic explanation.<sup>1,2</sup> The diagnosis is established by the Modified Dandy criteria, revised in 2013 to incorporate imaging findings, but the essence of the diagnosis is an opening CSF pressure of >250 mm H<sub>2</sub>O in adults or 280 mm H<sub>2</sub>O in children without obvious cause.<sup>3,4</sup> The diagnosis can be elusive on clinical grounds due to the nonspecific and fluctuating nature of the clinical symptoms. Neuroradiologic diagnosis of IIH can also be difficult on MR imaging because it relies on inconsistently present anatomic corre-

lates of chronically elevated ICP, such as flattening of the diaphragm sellae, distension of the optic nerves sheaths, flattening of the posterior sclera, or signs of papilledema.<sup>5,6</sup> Remodelling of the pituitary gland contour or of the sella turcica itself may be seen in 40%–60% of patients, and ocular findings, though reportedly present in 88% of pediatric patients under anesthesia, are less consistently perceived in adult patients.<sup>7</sup> Vascular studies, specifically gadolinium-bolused MR venography, have shown that 94% of adult patients with IIH demonstrate a very characteristic appearance of bilateral effacement/attenuation of the contours of the transverse sinuses, so-called “transverse sinus stenosis.”<sup>8–10</sup> This finding has been the subject of potential therapeutic focus in some patients with IIH refractory to medical therapy alone, with clinical improvement or stabilization reported in most severely ill patients treated with transvenous stent placement. It is a curious observation that this dural sinus effacement is consistently and exclusively confined to the lateral margins of the transverse sinuses where the upward sweep of the sinus is maximal on a sagittal view and the scope of the suspension curve or “hammock-sling” of the tentorial cerebelli is maximal on a coronal view.

Received September 13, 2016; accepted after revision May 6, 2017.

From the Departments of Radiology (P.P.M., D.F.B., R.A.C., J.P., N.C.) and Anatomy (N.L.), Mayo Clinic, Rochester, Minnesota.

Please address correspondence to Pearce Morris, MB, BCH, Department of Radiology, Mayo Clinic, 200 First St SW, Rochester, MN 55905; e-mail: morris.ppearce@mayo.edu

<http://dx.doi.org/10.3174/ajnr.A5289>

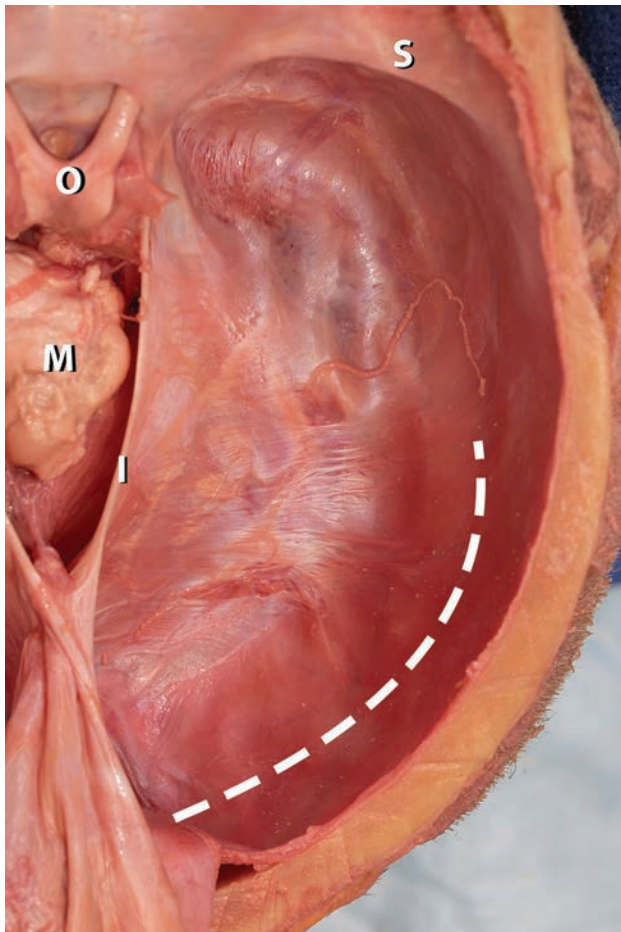


**FIG 1.** Image from an anatomic dissection of a human cadaver viewed from above and behind. The cerebral hemispheres and diencephalon have been removed, exposing the tentorial margin and cut surface of the midbrain (M). The lesser wing of the sphenoid (S) and optic chiasm (O) lie on the upper aspect of the image. The falx cerebri is folded posteriorly in the midline, causing retraction of the tentorial incisura (I). The approximate course of the hidden transverse sinus is represented by the *broken line*. The point of the image is to emphasize the smooth, featureless sweep of the tentorium as it splits around the margins of the transverse sinus and continues laterally as the dural margin of the right hemicranium. The transition is so featureless that the margins of the transverse sinus cannot be either visualized or easily palpated in this example, raising the question of how even mildly elevated intracranial pressure could cause a focal indentation on this featureless span of “tough” tissue to bring about effacement of the buried transverse sinus.

During anatomic brain dissection, the sweep of the tentorium cerebelli blends so seamlessly with the margins of the transverse sinus (Fig 1) that it becomes difficult to envision how moderately elevated ICP could efface the transverse sinus in such a focal manner. This force would have to exert a focal indentation on the margins of the transverse sinus and create a definable furrow along the sinus, thus requiring a marked degree of local dural stretching. It is more cogent to invoke the Laplace Law pertaining to tension along a curved surface and to suggest that supratentorial pressure would be more likely to exert a generalized effect on the broad expanse of the tentorium. If such an effect were present, it should be most robustly detectable where the sweep of the tentorium is at its widest, which, coincidentally or otherwise, also corresponds with the characteristic location of the effacement of



**FIG 2.** A midline sagittal view from the source image data was used for orientation of the oblique coronal plane and then for measurements. The oblique coronal plane (*continuous line*) intersects the junction of the great vein of Galen and the straight sinus and runs in a plane orthogonal to the subcallosal line (*dotted line*).

the transverse sinus seen in IIH. To advance this hypothesis, that the effacement of the transverse sinus in IIH may be, in some part, secondary to diffusely distributed ICP effects on the tentorium rather than a focal effect on the margins of the transverse sinus, we sought to determine whether a greater degree of curvature of the tentorium could be detected in patients with IIH compared with a control group.

## MATERIALS AND METHODS

A retrospective review of MR images and clinical records with institutional review board approval was conducted on 53 patients with IIH and 58 adult controls. Subjects were identified through a key word search of the electronic medical records spanning a 5-year period, 2010–2015. Patients with IIH ( $n = 53$ ; 16–60 years of age) were diagnosed by meeting the Modified Dandy diagnostic criteria in the absence of other identifiable explanations for their symptoms or elevated ICP. Control subjects ( $n = 58$ ; 16–60 years of age) were all diagnosed with migraine-type headache or other nonspecific headaches and were gathered sequentially in chronologic order from a list of non-IIH subjects with MR imaging and MRV during the same period. Controls did not demonstrate identifiable intracranial pathology, elevation of ICP, dural sinus thrombosis, or other anatomic causes for headache.

### Image Review

Source images from 3D gadolinium-bolused MRV examinations were used for analysis. Data files were imported into an independent Advantage Windows Workstation (GE Healthcare, Milwaukee, Wisconsin) and reformatted in multiplanar reconstructions at a resolution of 0.6 mm per pixel.

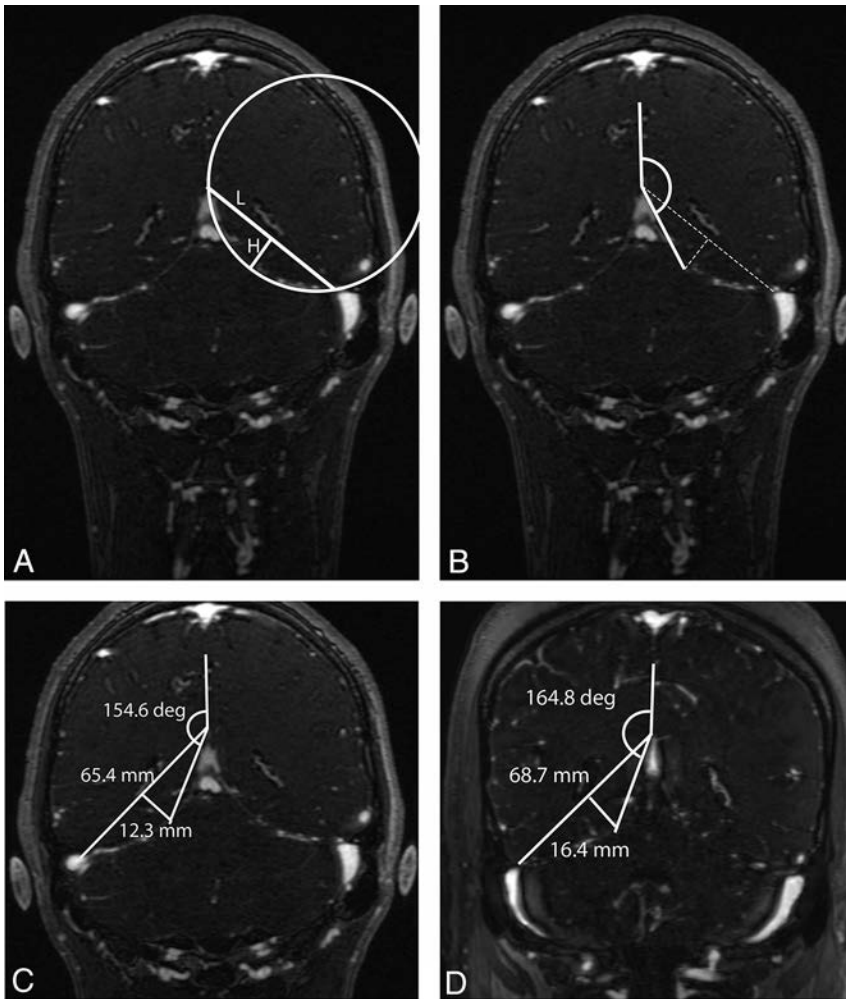


**FIG 3.** Illustration of the geometric landmarks used to calculate the curvature of the tentorium. A, A segment of a theoretic circle of chord length (L) and height (H) is constructed by using landmarks for the insertion points of the tentorium cerebelli, as described in the text. The conformity of the circle perimeter to the actual sweep of the tentorial curve may be imperfect, but this is of no consequence because its role is primarily illustrative, to help envision the geometric relationship of the primary anatomic points. B, With the same anatomic points illustrated in A, an angle subtended by the midpoint of the tentorium is calculated with the midline tentorial convergence as an apex and the vertical falx cerebri as a baseline. C, Illustration of these measurements in a control subject, a 22-year-old male patient with an ultimate diagnosis of migraine headaches. D, Illustration of same measurements in a patient with IIH, a 22-year-old female patient with a body mass index of 48.2 and an opening CSF pressure of 338 mm H<sub>2</sub>O.

**Table 1: Characteristics of patients with idiopathic intracranial hypertension and controls**

Variable	Controls (n = 58)	IIH (n = 53)	P
Age (mean) (yr)	34.8 ± 9.7	31.3 ± 10.3	.06
Sex (male/female)	44:14	50:3	.008
BMI (mean) (kg/m <sup>2</sup> )	28.1 ± 7.6	36.9 ± 8.9	<.0001
Weight (mean) (Kg)	80.4 ± 28.4	101.7 ± 28.7	.0002
Opening CSF pressure (mean) (mm H <sub>2</sub> O)	NA	363.2 ± 84	NA

**Note:**—BMI indicates body mass index; NA, not applicable.

### Measurements

**Tentorial Radius of Curvature.** The apex of the tentorial convergence in the midline was selected by finding the midline sagittal image showing the confluence of the great vein of Galen and the straight sinus. An oblique coronal plane passing through this point and lying orthogonal to the subcallosal line<sup>11</sup> on the midline

sagittal view passes at or near the widest transverse diameter of the cerebellar tentorium and was used to define the measurement landmarks of the tentorium (Fig 2). The curvature of the tentorium was determined from the theoretic chord segment length and height of an imperfect circle inscribing the curvature of the tentorium (Fig 3A). Specifically, the chord length of the circle segment passing between the midline apposition points of the tentorial leaves above the venous confluence and the lateral point where the tentorium splits to enfold the transverse sinus was measured with workstation tools. The height of the segment was measured orthogonal to and at the midpoint of segment length. With the segment of a circle defined by segment length and height, it is thus possible to calculate the radius of curvature of this theoretic circle and the area of the segment. These measurements were performed bilaterally.

**Falx-to-Midtentorium Angle.** To circumvent potential bias in defining the lateral point of the chord segment length, we devised a second index of tentorial curvature (Fig 3B). With the same oblique coronal image defined above, the angle defined with the vertex at the midline confluence of the tentorial leaves and rays subtending the midpoint of the tentorial curve and the midline falx cerebri was measured bilaterally in all cases. An increase in this angle was expected to indicate a greater degree of bowing of the tentorium in the patients with IIH group, independent of the measurement technique described in “Tentorial Radius of Curvature” above (Fig 3C, -D).

### Statistics

Summarized data are presented as mean (± SD) or frequency (percentage). Two-sample *t* tests and Fisher exact tests were used for differences in demographic and imaging findings between controls and subjects with IIH. Multiple linear regression was used to adjust for the effects of age, body mass index, and sex. Two-sided *P* values < .05 were considered statistically significant. Statistical analysis was conducted with JMP Pro 11.2 for Mac (SAS Institute, Cary, North Carolina).

### RESULTS

Group comparisons are presented in Table 1. A greater representation of male subjects was present in the control group compared with patients with IIH, but mean ages were comparable. Body

**Table 2: Measurement of the tentorial curvature**

	Height Right (Mean) (mm)	Height Left (Mean) (mm)	Area of Segment Right (Mean) (mm <sup>2</sup> )	Area of Segment Left (Mean) (mm <sup>2</sup> )	Falx-Tentorium Angle (Mean) (mm)
Controls (n = 58)	11.6 ± 1.7	11.5 ± 1.8	515.6 ± 104.2	515.6 ± 113.3	151.5 ± 4.4
IIH (n = 53)	14.6 ± 2.2	14.2 ± 2.1	676.1 ± 130.5	688.2 ± 131.4	154.1 ± 3.4
R <sup>2</sup>	.31	.33	.32	.33	.091
P <sup>a</sup>	<.0001	<.0001	<.0001	<.00001	<.0007

<sup>a</sup> P values are significant.

**Table 3: Regression analysis controlling for the effect of BMI, age, and sex**

	Controls (Mean) (n = 58)	IIH (Mean) (n = 53)	Unadjusted Difference	P	Adjusted Difference	Adjusted P Value
Height right (mm)	11.6 ± 1.7	14.5 ± 2.2	2.64	<.0001	2.21	<.0001
Height left (mm)	11.5 ± 1.7	14.2 ± 1.1	2.69	<.0001	2.60	<.0001
Area of segment right (mm <sup>2</sup> )	515.6 ± 104.2	676.1 ± 130.5	160.48	<.0001	133.92	<.0001
Area of segment left (mm <sup>2</sup> )	515.6 ± 113.3	688.2 ± 131.4	172.24	<.0001	161.98	<.0001
Falx-tentorium angle	151.5 ± 4.4	154.1 ± 3.4	2.62	<.0007	2.22	<.023

mass index levels were significantly higher in the IIH group as expected.

All parameters of tentorial curvature, height of the segment, area of the segment, and the angle subtended by the midpoint of the tentorium showed a consistent indication of greater bowing in the IIH group compared with controls (Table 2). The distance from the baseline defined by the medial and lateral tentorial insertion points to the tentorial curvature itself was significantly greater in the IIH group. The angle subtended by the tentorial midpoint and the falx cerebri was also demonstrably greater, indicating a deeper degree of curvature compared with controls. With multiple linear regression analysis, this effect persisted after adjustment for sex, age, and body mass index (Table 3).

## DISCUSSION

Our observations appear to be in agreement with our initial hypothesis that a downward deflection of the tentorium cerebelli is detectable in patients with IIH. This leads us to the hypothesis that this deflection could explain, in part or in whole, the distortion or effacement of the transverse sinuses seen in IIH.

From a mechanical point of view, this hypothesis is reasonable in that a diffuse supratentorial mass effect, likely mediated through a broad-based change in brain volume in patients with IIH, would be more likely to exert a deflection on the entire span of the tentorium rather than on a focal indentation along a segment of the transverse sinus. A broad-based mass effect of this nature would be expected to show itself where the “suspension bridge” configuration or hammock-like span of the tentorium is at its greatest. The secondary distortion of the anatomic structures (ie, dural leaves of the transverse sinus) at the insertion of the tentorial span would also be most prominent at this point of maximal span. This feature is consistent with the observed transverse sinus stenosis seen in patients with IIH, which is characterized by its location at the widest point of the tentorium in almost all patients, where surface tension of the dura would be predicted to be maximal. Simple generalized venous compression of the transverse sinuses does not appear to explain such a phenomenon, because venous compression/effacement of the dural sinuses elsewhere does not appear to be a variant expression of this pathologic epiphenomenon, at least not prominently.

Our observations raise intriguing questions as to the nature of

the intracranial volumetric changes associated with IIH. Volumetric changes in CSF content of the intracranial cavity have been previously suggested as instrumental to the genesis of elevated ICP in this condition,<sup>12</sup> but these results have been inconsistent.<sup>13</sup> Oversecretion of CSF on the one hand or impaired absorption of CSF<sup>14</sup> on the other do not seem to furnish satisfactory explanations for the observations made in IIH because oversecretion of CSF in cases of choroid plexus papilloma in the first instance or underabsorption of CSF following subarachnoid hemorrhage in the second do not give the same clinical or imaging appearance as IIH.<sup>15,16</sup> Greater interest has focused on brain parenchymal changes, with hypothesized alterations in extracellular or intracellular fluid shifts in IIH<sup>17,18</sup> and possibly more unexplored dynamic changes of the posited brain “glymphatic” system.<sup>19,20</sup> Our results would seem to point to a supratentorial compartmental predilection for such changes, but this is not necessarily the only interpretation of these data. A supratentorial mass effect in IIH, suggested by this study, could be simply a reflection of the greater magnitude of brain parenchymal volumetric change expressed in the supratentorial structures based on innate volume, compared with the intratentorial space.

Our study is limited on several counts. The characteristic effacement of the transverse sinuses, universally present in the patients with IIH group, prevented the use of a blinded process for measuring the geometry of the tentorium of interest in this study. The technique used is relatively simple and rudimentary and warrants confirmation with an automated technique if possible. A difficulty with consistent measurement of the landmarks of the transverse sinus between patients with IIH and controls is inevitable, with manual or automated techniques, by virtue of the necessity to measure a structure that is distorted and displaced by the disease process. The conformity of the tentorial curvature to the geometric circle construed in our measurements is variable and imperfect within both patient groups. However, the use of the geometric circle is conceptually illustrative, and variations of anatomic curvature away from a theoretic circle do not affect the core observations pertaining to the bowing of the tentorium. An additional potential limitation is that the controls were not matched for the subjects as to sex or body mass index.

The significance of our observations is 2-fold. First, the hy-

pothesis advanced in this article answers many of the questions previously posed as to the genesis of the transverse sinus effacement seen in patients with IIH and explains its characteristic location. A mechanical distortion of the transverse sinus by a deflection of the tentorium, rather than exclusively by venous compression of the transverse sinus by elevated ICP, makes more sense in view of many of the clinical observations made during transvenous manometry in patients with IIH, such as incongruity between fluctuating ICP readings and elevated venous pressures. Elevated ICP alone does not seem to explain adequately the degree of venous effacement seen in many patients. Second, these results could suggest why some patients with IIH are more vulnerable to the development of secondary venous obstruction and hypertension if, for instance, the transverse sinus is innately narrowed by a pre-existing arachnoid granulation. Innate elasticity of the dura mater would also explain the reversibility of this venous stenotic phenomenon seen with effective medical or CSF diversionary procedures in IIH.<sup>21</sup> Last, it behooves us to better understand the mechanical basis for venous stenoses in IIH, particularly if the transvenous stent treatment of this disorder continues its advance as a potential intervention for patients with medically refractory conditions.<sup>22-28</sup>

## CONCLUSIONS

Our data support the original hypothesis that a downward bowing or deflection of the tentorium cerebelli is detectable in patients with IIH compared with similarly aged controls. This observation points to a supratentorial mass effect of the disease or at least a preferential expression in that location. It also suggests that deformity of the tentorial insertion around the transverse sinus could be a fundamental mechanism for the genesis of venous stenotic changes that are well-recognized in this condition.

Disclosures: Pearse Morris—UNRELATED: Royalties: Lippincott, Williams & Wilkins (textbook royalties).

## REFERENCES

- Friedman DI, Jacobson DM. **Idiopathic intracranial hypertension.** *J Neuroophthalmol* 2004;24:138–45 CrossRef Medline
- Markey KA, Mollan SP, Jensen RH, et al. **Understanding idiopathic intracranial hypertension: mechanisms, management, and future directions.** *Lancet Neurol* 2016;15:78–91 CrossRef Medline
- Friedman DI, Jacobson DM. **Diagnostic criteria for idiopathic intracranial hypertension.** *Neurology* 2002;59:1492–95 CrossRef Medline
- Friedman DI, Liu GT, Digre KB. **Revised diagnostic criteria for the pseudotumor cerebri syndrome in adults and children.** *Neurology* 2013;81:1159–65 CrossRef Medline
- Agid R, Farb RI, Willinsky RA, et al. **Idiopathic intracranial hypertension: the validity of cross-sectional neuroimaging signs.** *Neuroradiology* 2006;48:521–27 CrossRef Medline
- Ridha MA, Saindane AM, Bruce BB, et al. **MRI findings of elevated intracranial pressure in cerebral venous thrombosis versus idiopathic intracranial hypertension with transverse sinus stenosis.** *Neuroophthalmology* 2013;37:1–6 CrossRef Medline
- Maralani PJ, Hassanlou M, Torres C, et al. **Accuracy of brain imaging in the diagnosis of idiopathic intracranial hypertension.** *Clin Radiol* 2012;67:656–63 CrossRef Medline
- Higgins JN, Gillard JH, Owler BK, et al. **MR venography in idiopathic intracranial hypertension: unappreciated and misunderstood.** *J Neurol Neurosurg Psychiatry* 2004;75:621–25 CrossRef Medline
- Farb RI, Vanek I, Scott JN, et al. **Idiopathic intracranial hypertension: the prevalence and morphology of sinovenous stenosis.** *Neurology* 2003;60:1418–24 CrossRef Medline
- Morris PP, Black DF, Port J, et al. **Transverse sinus stenosis is the most sensitive MR imaging correlate of idiopathic intracranial hypertension.** *AJNR Am J Neuroradiol* 2017;38:471–77 CrossRef Medline
- Traboulsee A, Simon JH, Stone L, et al. **Revised recommendations of the Consortium of MS Centers Task Force for a Standardized MRI Protocol and clinical guidelines for the diagnosis and follow-up of multiple sclerosis.** *AJNR Am J Neuroradiol* 2016;37:394–401 CrossRef Medline
- Donaldson JO. **Cerebrospinal fluid hypersecretion in pseudotumor cerebri.** *Trans Am Neurol Assoc* 1979;104:196–98 Medline
- Malm J, Kristensen B, Markgren P, et al. **CSF hydrodynamics in idiopathic intracranial hypertension: a long-term study.** *Neurology* 1992;42:851–58 CrossRef Medline
- Johnston I. **Reduced C.S.F. absorption syndrome: reappraisal of benign intracranial hypertension and related conditions.** *Lancet* 1973;2:418–21 Medline
- Eisenberg HM, McComb JG, Lorenzo AV. **Cerebrospinal fluid overproduction and hydrocephalus associated with choroid plexus papilloma.** *J Neurosurg* 1974;40:381–85 CrossRef Medline
- Damkier HH, Brown PD, Praetorius J. **Cerebrospinal fluid secretion by the choroid plexus.** *Physiol Rev* 2013;93:1847–92 CrossRef Medline
- Gideon P, Sørensen PS, Thomsen C, et al. **Increased brain water self-diffusion in patients with idiopathic intracranial hypertension.** *AJNR Am J Neuroradiol* 1995;16:381–87 Medline
- Bastin ME, Sinha S, Farrall AJ, et al. **Diffuse brain oedema in idiopathic intracranial hypertension: a quantitative magnetic resonance imaging study.** *J Neurol Neurosurg Psychiatry* 2003;74:1693–96 CrossRef Medline
- Iliff JJ, Nedergaard M. **Is there a cerebral lymphatic system?** *Stroke* 2013;44:S93–95 CrossRef Medline
- Ueno M, Chiba Y, Murakami R, et al. **Blood-brain barrier and blood-cerebrospinal fluid barrier in normal and pathological conditions.** *Brain Tumor Pathol* 2016;33:89–96 CrossRef Medline
- King JO, Mitchell PJ, Thomson KR, et al. **Cerebral venography and manometry in idiopathic intracranial hypertension.** *Neurology* 1995;45:2224–28 CrossRef Medline
- Higgins JN, Owler BK, Cousins C, et al. **Venous sinus stenting for refractory benign intracranial hypertension.** *Lancet* 2002;359:228–30 CrossRef Medline
- Higgins JN, Pickard JD. **Lateral sinus stenoses in idiopathic intracranial hypertension resolving after CSF diversion.** *Neurology* 2004;62:1907–08 CrossRef Medline
- Higgins JN, Tipper G, Varley M, et al. **Transverse sinus stenoses in benign intracranial hypertension demonstrated on CT venography.** *Br J Neurosurg* 2005;19:137–40 CrossRef Medline
- De Simone R, Ranieri A, Montella S, et al. **The role of dural sinus stenosis in idiopathic intracranial hypertension pathogenesis: the self-limiting venous collapse feedback-loop model.** *Panminerva Med* 2014;56:201–09 Medline
- Elder BD, Goodwin CR, Kosztowski TA, et al. **Venous sinus stenting is a valuable treatment for fulminant idiopathic intracranial hypertension.** *J Clin Neurosci* 2015;22:685–89 CrossRef Medline
- Satti SR, Leishangthem L, Chaudry MI. **Meta-analysis of CSF diversion procedures and dural venous sinus stenting in the setting of medically refractory idiopathic intracranial hypertension.** *AJNR Am J Neuroradiol* 2015;36:1899–904 CrossRef Medline
- Starke RM, Wang T, Ding D, et al. **Endovascular treatment of venous sinus stenosis in idiopathic intracranial hypertension: complications, neurological outcomes, and radiographic results.** *ScientificWorldJournal* 2015;2015:14040 CrossRef Medline

# Ethanol Ablation of Ranulas: Short-Term Follow-Up Results and Clinicoradiologic Factors for Successful Outcome

 K.H. Ryu,  J.H. Lee,  J.Y. Lee,  S.R. Chung,  M.S. Chung,  H.W. Kim,  Y.J. Choi, and  J.H. Baek

## ABSTRACT

**BACKGROUND AND PURPOSE:** Surgical excision of an affected sublingual gland for treatment of a ranula can carry a potential of a nerve damage or postoperative complications. However, there have been little studies about effective minimally invasive therapeutic method, yet. Our aim was to evaluate the efficacy and safety of ethanol ablation of ranulas and the clinicoradiologic factors that can predict outcome.

**MATERIALS AND METHODS:** This retrospective study evaluated 23 patients with ranulas treated by percutaneous ethanol ablation. Treatment outcome was assessed in 20 patients followed for at least 6 months. The duration of symptoms before ethanol ablation, pretreatment volume, and parapharyngeal extension on sonography and/or CT were correlated with the outcome. The Mann-Whitney *U* test and Fisher exact test were used for comparison of the factors according to the outcome.

**RESULTS:** The study evaluated 14 males and 9 females with a median age of 26 years (range, 3–41 years). Among 20 patients who were followed for at least 6 months (median, 20 months; range, 6–73 months), 9 patients (45%) demonstrated complete disappearance of the ranulas and 11 (55%) showed an incomplete response. When the patients were divided according to the duration of symptoms before ethanol ablation, the complete response rate was significantly higher in patients with  $\leq 12$  months of symptoms (73%, 8/11) than that in others (11%, 1/9) ( $P = .010$ ). Pretreatment volume and parapharyngeal extension were not significantly different between the 2 groups.

**CONCLUSIONS:** Ethanol ablation is a safe and noninvasive treatment technique for ranulas with a significantly better outcome in patients with  $\leq 12$  months of symptoms. Therefore, it could be considered an alternative nonsurgical approach for ranulas with recent onset of symptoms.

**ABBREVIATION:** EA = ethanol ablation

A ranula is a pseudocyst or mucous-retention cyst that arises from leakage of saliva from the sublingual or minor salivary gland.<sup>1</sup> Ranulas have traditionally been surgically treated by excision of the affected sublingual gland with or without the excision of the ranula.<sup>1,2</sup> Surgical excision is a definitive treatment with

very low recurrence rates, ranging from 0% to 2%.<sup>3,4</sup> However, excision of the sublingual gland can be technically difficult and carries a potential risk of damage to the surrounding vital structures, including the lingual nerve and the submandibular duct, with postoperative complication rates ranging from 11% to 29%.<sup>3,4</sup> Therefore, there is a need for a nonsurgical minimally invasive treatment of ranulas.

Among chemical ablation agents, picibanil (OK-432; Chugai Pharmaceutical Co, Tokyo, Japan) has been most commonly reported for minimally invasive treatment of ranulas.<sup>1,3,5-9</sup> Intracystic injection of OK-432 is safe without serious complications, but the recurrence rate is relatively high, from 23% to 48%.<sup>1,3,8</sup> Therefore, more effective sclerosing agents are necessary for successful minimally invasive treatment of ranulas.

Ethanol is an effective sclerosing agent<sup>2,10</sup>; its effects include instantaneous cellular dehydration and protein denaturation that result in the clumping of blood cells and vessel wall necrosis, followed

Received December 27, 2016; accepted after revision May 9, 2017.

From the Department of Radiology and Research Institute of Radiology (K.H.R., J.H.L., J.Y.L., S.R.C., M.S.C., H.W.K., Y.J.C., J.H.B.), University of Ulsan College of Medicine, Asan Medical Center, Seoul, Republic of Korea; Department of Radiology (K.H.R.), Gyeongsang National University School of Medicine and Gyeongsang National University Changwon Hospital, Changwon, Republic of Korea; Department of Radiology (J.Y.L.), Soonchunhyang University College of Medicine, Soonchunhyang University Bucheon Hospital, Bucheon, Republic of Korea; and Department of Radiology (M.S.C.), Chung-Ang University College of Medicine, Chung-Ang University Medical Center, Seoul, Republic of Korea.

Please address correspondence to Jeong Hyun Lee, MD, PhD, Head & Neck Division, Department of Radiology and Research Institute of Radiology, University of Ulsan College of Medicine, Asan Medical Center, 88 Olympic-ro-43-gil, Songpa-gu, 05505, Seoul, Republic of Korea; e-mail: jeonghlee@amc.seoul.kr

<http://dx.doi.org/10.3174/ajnr.A5292>

by thrombosis and occlusion of vessels.<sup>10,11</sup> It has been reported that ethanol ablation (EA) is effective and safe for the treatment of benign cervical cystic lesions, including cystic thyroid nodules, thyroglossal duct cysts, and lymphatic malformations.<sup>12-18</sup>

To the best of our knowledge, no previous studies have examined the treatment efficacy and safety of EA for ranulas. The purpose of this study was to evaluate these features and the clinicoradiologic factors that can predict its outcome in a retrospective cohort.

## MATERIALS AND METHODS

### Patients

This study was approved by the institutional review board of our institution (University of Ulsan College of Medicine, Asan Medical Center), and written informed consent for EA was obtained from all patients before the procedure. We searched the electronic medical records from 2010 to 2015 to find consecutive patients treated with EA after confirmation of a ranula by aspiration of thick mucus fluid.

### Preprocedural Evaluation

In addition to basic demographic data, we also evaluated the duration of symptoms before EA and the history of prior treatment. In all patients, the preprocedural sonography was performed by 1 radiologist (J.H.L., with 14 years of experience in performing sonography-guided procedures of the head and neck regions) with 1 of 2 sonographic systems: an Acuson S3000 Ultrasound System (Siemens, Erlangen, Germany) or an EUB-7500 unit (Hitachi Medical Systems, Tokyo, Japan) equipped with a linear, high-frequency probe (6–18 or 5–14 MHz). The sonographic examination was performed to determine the location of the ranula, the presence of direct contact with the sublingual gland, and the volume of the cystic lesion. If available, contrast-enhanced CT was also evaluated for the aforementioned imaging findings.

### Ethanol Ablation and Follow-Up

All EAs were performed by the same radiologist (J.H.L.), with the patient in a supine position and the neck extended under local anesthesia with 2% lidocaine. Moderate sedation was used for an uncooperative child. A 16- to 18-gauge needle was inserted into the ranula to aspirate the thick mucus fluid with a 30-mL syringe via a short connector. Internal debris and residual thick mucus material were cleared by irrigation with saline. Before the ethanol injection, 2% lidocaine was injected and retained inside the pseudocyst for 30 seconds to check for any sensory or motor changes induced by the lidocaine anesthesia and for pain control. After re-aspiration of the lidocaine, 100% ethanol was slowly injected into the ranula. The amount injected was determined to be approximately 50% of the volume of the aspirate. The injected ethanol was completely re-aspirated after remaining in the ranula for 10 minutes.

Patients were re-evaluated at 1-, 6-, and 12-month intervals after EA and then annually with sonography and/or CT examination to check for the recurrence of the lesion or of symptoms. EA was re-performed if there was a cystic cavity of >50% of the initial volume at the 1-month follow-up or if there was a recurrence of a cystic lesion with an estimated volume of >1–2 mL during the

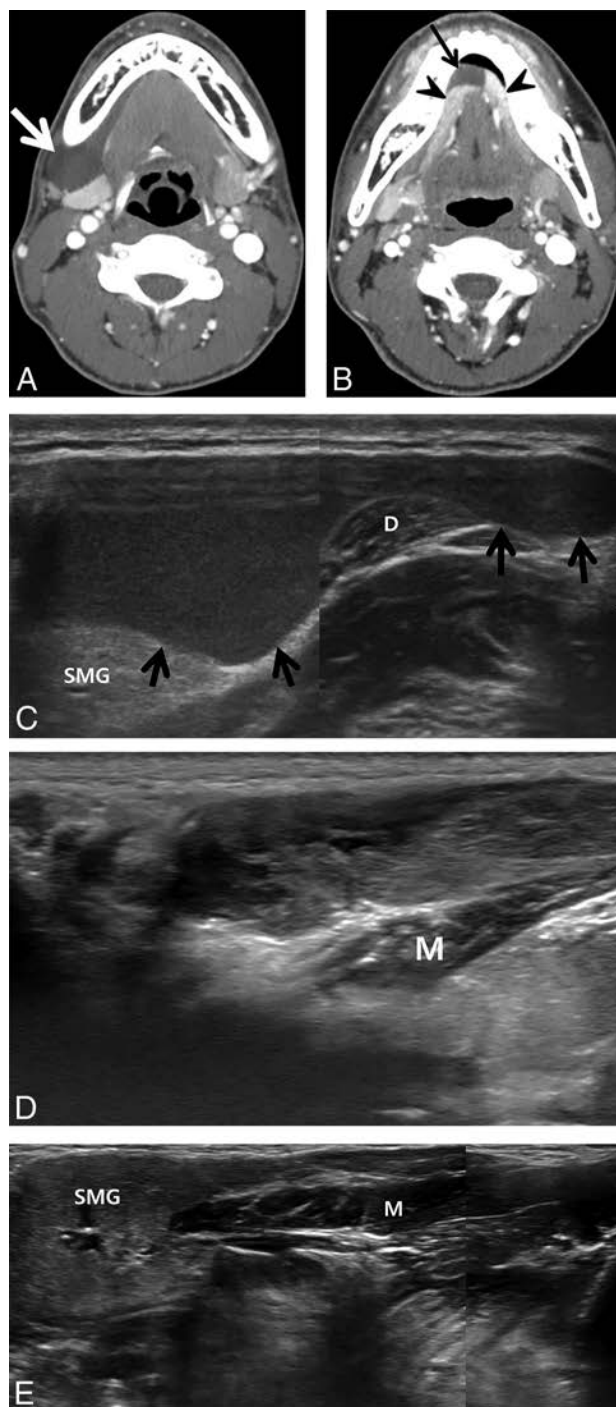


**FIG 1.** A 19-year-old man with a plunging ranula in the right submandibular space developed 1 month previously. *A* and *B*, Pretreatment contrast-enhanced axial CT images. *A*, Axial CT image shows a well-defined cystic mass in the right submandibular (thick arrow) space. *B*, Another CT image demonstrates the cystic mass continuing into the sublingual space (thin arrow), showing direct contact with bilateral sublingual glands (arrowheads). *C*, Pretreatment oblique sonogram shows a fluid collection with internal debris in the right submandibular space (arrows). *D*, Sonogram 1 month after 2 sessions of ethanol ablation in the same plane as *C* shows complete disappearance of the ranula in the submandibular space. *E*, A sonogram 12 months after *D* in the same plane shows complete disappearance of the ranula in the submandibular and sublingual spaces. SMG indicates submandibular gland; M, mylohyoid muscle; D, anterior belly of the digastric muscle.

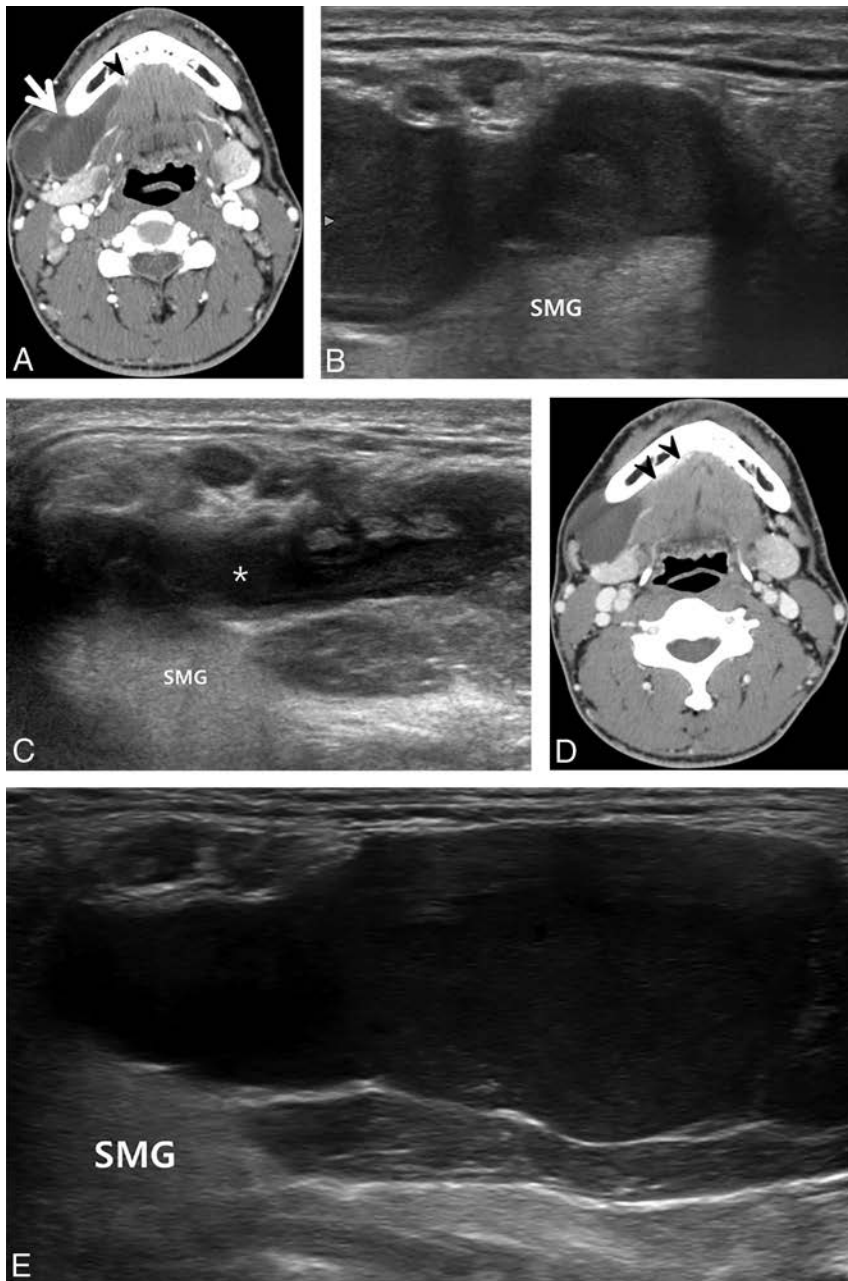


**FIG 2.** A 32-year-old man with a plunging ranula in the right submandibular space for the past 16 months. *A*, Pretreatment contrast-enhanced axial CT image shows a well-defined lobulated cystic mass (*arrow*) in the right submandibular space showing direct contact with the herniated right sublingual gland (*arrowhead*). *B*, Pretreatment oblique sonogram shows a fluid collection in the right submandibular space. *C*, Sonogram 1 month after ethanol ablation demonstrates the remaining fluid in the same space (*asterisk*). *D*, Contrast-enhanced axial CT image 34 months after ethanol ablation shows the cystic mass in the right submandibular space, adjacent to the herniated right sublingual gland (*arrowheads*). *E*, Oblique sonogram 34 months after ethanol ablation also demonstrates a cystic mass in the same space, showing an increase in size compared with *C*. SMG indicates submandibular gland.

remainder of the follow-up period. However, none of the patients were treated with EA >3 times.

### Statistical Analysis

The final treatment outcome was assessed at the last follow-up as a complete response (complete disappearance of the cystic cavity), an incomplete response (decreased volume of the cystic cavity), or no response (unchanged cystic cavity). Treatment re-

sponse was only assessed in patients who were followed up for at least for 6 months after the last EA. We tested for an association between the final outcome and the duration of symptoms before EA, pretreatment volume, and extension to the parapharyngeal space on sonography or CT with a Mann-Whitney *U* test and Fisher exact test.

All statistical analyses were performed with the SPSS, Version 12.0 (IBM, Armonk, New York). The Mann-Whitney *U* test and Fisher exact test were used for comparison of the factors according to the outcome. A *P* value < .05 was considered statistically significant.

### RESULTS

Twenty-three patients were treated with EA, including 14 males and 9 females with a median age of 26 years (range, 3–41 years). Among the 23 patients, 19 had a plunging ranula continuous with a herniated sublingual gland in the submandibular space, 2 had simple ranulas, and 2 had ranulas with direct contact with the submandibular gland instead of the sublingual gland.

Seven of the 23 patients had a history of prior treatment, including 5 patients who had been treated with chemical ablation with OK-432 and 2 patients who had been surgically treated (one via intraoral excision of the ranula and the other via excision of the submandibular gland). The number of EA sessions was 1 in 11 patients, 2 in 10 patients, and 3 in 2 patients. There were no procedure-related complications in any patients.

Twenty of the 23 patients were followed up for at least 6 months after EA and were assessed for the final treatment outcome at the last follow-up. The median follow-up time after the last EA was 20 months (range, 6–73 months). Nine of 20 (45%) patients demonstrated complete disappearance of the ranula (Fig 1), but 11 (55%) demonstrated an incomplete response (Fig 2). Four of 11 patients with an incomplete response

underwent surgical excision of the sublingual gland after recurrence. The clinicoradiologic characteristics and outcome of all patients are summarized in the Table.

Among the 9 patients with complete response, EA was performed once in 7 patients and twice in 2 patients. Both patients with simple ranulas showed a complete response after a single session of EA. Among the 11 patients with incomplete responses, the number of EA sessions was 1 in 2 patients, 2 in 7 patients, and

## Summary of clinicoradiologic factors and outcome after ethanol ablation

No	Sex	Age (yr)	Prior Treatment			Pretreatment Characteristics of Ranulas			No. of EAs	Outcome	F/U Duration (mo)	Imaging F/U
			OK-432	Surgery	Symptom Duration (mo)	Type	PPS Extension	Volume (mL)				
1	M	22	Yes		1	Plunging	Yes	4.5	1	Complete	73	US
2	F	7			1	Plunging	Yes	10.5	1	Complete	25	US
3	M	19			1	Plunging		15.0	2	Complete	13	US
4	F	34		SLG excision	2	Simple		7.1	1	Complete	27	—
5	F	18			2	Plunging		9.4	1	Complete	15	US
6	F	32			2	Simple		6.5	1	Complete	19	US
7	M	27			3	Plunging <sup>a</sup>	Yes	30.0	2	Complete	29	US
8	M	3			8	Plunging		3.0	1	Complete	6	US
9	M	28			12	Plunging	Yes	19.6	1	Complete	32	US
10	M	32			16	Plunging		30.0	1	Incomplete	34	US/CT
11	F	25			2	Plunging		20.0	2	Incomplete	8	US
12	M	23			4	Plunging	Yes	8.8	2	Incomplete	21	US
13	F	31	Yes		7	Plunging	Yes	3.1	1	Incomplete	32	US
14	F	28			12	Plunging	Yes	14.4	3	Incomplete	7	US
15	M	17			12	Plunging	Yes	8.2	1	Incomplete	15	—
16	M	23			13	Plunging		3.3	2	Incomplete	6	US
17	M	38	Yes	SMG excision	36	Plunging		45.1	2	Incomplete	46	US
18	M	41			36	Plunging		2.1	2	Incomplete	22	US
19	F	13			42	Plunging <sup>a</sup>		8.9	2	Incomplete	16	US/CT
20	M	37	Yes		240	Plunging		9.4	2	Incomplete	8	US
21	M	27	Yes		13	Plunging	Yes	27.0	3	Incomplete	1	US/CT
22	F	32			13	Plunging	Yes	9.0	1	Incomplete	1	US
23	M	16			24	Plunging		11.0	2	Complete	1	US

**Note:**—F/U indicates follow-up; PPS, parapharyngeal space; SLG, sublingual gland; SMG, submandibular gland; US, ultrasound.

<sup>a</sup> The ranula was in contact with the hilum of the submandibular gland.

3 in 2 patients, which was significantly different from that in those with complete responses ( $P = .026$ ).

When the clinical and radiologic factors were compared between the complete and incomplete response groups, the duration of symptoms before EA was significantly shorter in the complete response group (median, 2 months; range, 1–12 months) than in the incomplete response group (median, 13 months; range, 2–240 months;  $P = .001$ ). When the patients were divided according to the duration of symptoms, the complete response rate was significantly higher in patients with  $\leq 12$  months of symptoms (73%, 8/11) than in those with  $> 12$  months of symptoms (11%, 1/9) ( $P = .010$ ). The complete response rate was not significantly different between pediatric (3/5, 60%) and nonpediatric (6/15, 40%) patients ( $P > .05$ ). The other factors, including pretreatment volume and the presence of a parapharyngeal extension, were not significantly different between the complete (median, 9 mL; range, 3–30 mL;  $n = 4$ , 44%) and the incomplete (median, 9 mL; range, 3–45 mL;  $n = 4$ , 36%) response groups ( $P > .05$ ).

## DISCUSSION

In this study, we demonstrated that EA could be safely performed without any adverse events and could achieve complete disappearance of ranulas in 45% of patients at the 6-month follow-up. We also found that EA was significantly more effective and had a significantly higher complete response rate in patients with  $\leq 12$  months of symptoms, compared with those with a longer duration of symptoms (73% versus 11%, respectively). Although long-term follow-up results are still unknown, EA could be an alternative nonsurgical approach for patients experiencing symptoms for  $\leq 12$  months, given the potential risk of damage to the lingual nerve and the submandibular duct in an operation.

Two studies have previously reported a complete response rate of 52%–77%<sup>1,8</sup> after chemical ablation of ranulas with OK-432 at a median follow-up of 10–12 months. The studies reported ad-

verse events such as early rupture of the ranula (37%), fever lasting 2–3 days after injection (57%), injection site swelling for 1 week (47%), mild odynophagia (33%), and 1 incident of severe swallowing difficulty, which required admission for treatment.<sup>1,8</sup> Neither of the previous studies correlated the clinical or radiologic characteristics with the treatment outcome or reported the pretreatment duration of symptoms among the enrolled patients.

OK-432 is a lyophilized mixture of a low-virulence strain of group-A *Streptococcus pyogenes* incubated with benzylpenicillin.<sup>2</sup> The sclerosing effect of OK-432 retained in the cystic cavity is due to a strong local inflammatory reaction by activated neutrophils and monocytes, which secondarily produce cytokines and induce transient flulike symptoms or early rupture of the treated ranula. In addition, the use of OK-432 is contraindicated in those with penicillin allergy.<sup>5,8</sup> On the other hand, ethanol acts as a sclerosing agent by instantaneous dehydration of the cyst wall, protein denaturation, clumping of blood cells, and vessel wall necrosis,<sup>2</sup> which allow us to re-aspirate the injected ethanol after 5–10 minutes of retention. We believe that re-aspiration of the ethanol may reduce the potential for adverse events, such as facial flushing or dizziness, due to systemic absorption of the chemical ablation agent or site swelling or odynophagia from leakage at the injection site.

Another technique that may minimize local complications is the injection of lidocaine into the ranula after aspiration of the thick mucus fluid. We used 2% lidocaine at half the volume of the aspirate for 30 seconds before the ethanol injection in all cases, first, to check for the presence of the hypoglossal or the lingual nerve and, second, to locally anesthetize the surrounding soft tissues. No motor or sensory changes were noted in any of the patients after lidocaine injection in this study.

To our knowledge, this is the first report to evaluate the efficacy of EA in the treatment of ranulas. Although the overall complete response rate at 6-month follow-up was lower than anti-

pated, we were able to determine that the duration of symptoms was the only clinicoradiologic factor predicting a better outcome after EA in patients with ranulas. Neither the pretreatment volume nor the parapharyngeal extension was associated with the treatment outcome. Given that ductal disruption by trauma is a major causative factor of ranulas, persistent leakage of mucus fluid might hinder the sealing off of the leaking point with ethanol.

This study has several limitations in addition to its retrospective nature. First, we did not evaluate the long-term follow-up outcome after EA. However, we demonstrated the safety of EA for treating ranulas and described some techniques that may improve its safety. We believe our results could be the basis of promoting further studies with larger groups of patients and longer follow-up periods. Second, our study included 7 patients with a history of prior treatment, including surgery or chemical ablation with OK-432. Because the number of enrolled patients was small, we could not evaluate the potential confounding effects of previous treatments. This should be further investigated in future studies. Last, the sample size of this study was too small to generalize our results, which should be proved with further larger studies.

## CONCLUSIONS

EA is a safe noninvasive treatment technique for ranulas, showing significantly better outcomes in patients with  $\leq 12$  months of symptoms. Given the potential risk of damage to the lingual nerve and the submandibular duct during an operation, EA could be considered an alternative nonsurgical approach for patients with symptoms for  $\leq 12$  months.

## REFERENCES

1. Roh JL. **Primary treatment of ranula with intracystic injection of OK-432.** *Laryngoscope* 2006;116:169–72 CrossRef Medline
2. Kim JH. **Ultrasound-guided sclerotherapy for benign non-thyroid cystic mass in the neck.** *Ultrasonography* 2014;33:83–90 CrossRef Medline
3. Patel MR, Deal AM, Shockley WW. **Oral and plunging ranulas: what is the most effective treatment?** *Laryngoscope* 2009;119:1501–09 CrossRef Medline
4. Zhao YF, Jia J, Jia Y. **Complications associated with surgical management of ranulas.** *J Oral Maxillofac Surg* 2005;63:51–54 Medline
5. Fukase S, Ohta N, Inamura K, et al. **Treatment of ranula with intracystic injection of the streptococcal preparation OK-432.** *Ann Otol Rhinol Laryngol* 2003;112:214–20 CrossRef Medline
6. Woo JS, Hwang SJ, Lee HM. **Recurrent plunging ranula treated with OK-432.** *Eur Arch Otorhinolaryngol* 2003;260:226–28 Medline
7. Lee HM, Lim HW, Kang HJ, et al. **Treatment of ranula in pediatric patients with intralesional injection of OK-432.** *Laryngoscope* 2006;116:966–69 Medline
8. Rho MH, Kim DW, Kwon JS, et al. **OK-432 sclerotherapy of plunging ranula in 21 patients: it can be a substitute for surgery.** *AJNR Am J Neuroradiol* 2006;27:1090–95 Medline
9. Roh JL, Kim HS. **Primary treatment of pediatric plunging ranula with nonsurgical sclerotherapy using OK-432 (picibanil).** *Int J Pediatr Otorhinolaryngol* 2008;72:1405–10 CrossRef Medline
10. Mason KP, Michna E, Zurakowski D, et al. **Serum ethanol levels in children and adults after ethanol embolization or sclerotherapy for vascular anomalies.** *Radiology* 2000;217:127–32 CrossRef Medline
11. Gelczer RK, Charboneau JW, Hussain S, et al. **Complications of percutaneous ethanol ablation.** *J Ultrasound Med* 1998;17:531–33 CrossRef Medline
12. Kim SM, Baek JH, Kim YS, et al. **Efficacy and safety of ethanol ablation for thyroglossal duct cysts.** *AJNR Am J Neuroradiol* 2011;32:306–09 CrossRef Medline
13. Lee SJ, Ahn IM. **Effectiveness of percutaneous ethanol injection therapy in benign nodular and cystic thyroid diseases: long-term follow-up experience.** *Endocr J* 2005;52:455–62 CrossRef Medline
14. Zingrillo M, Torlontano M, Chiarella R, et al. **Percutaneous ethanol injection may be a definitive treatment for symptomatic thyroid cystic nodules not treatable by surgery: five-year follow-up study.** *Thyroid* 1999;9:763–67 CrossRef Medline
15. Impellizzeri P, Romeo C, Borruto FA, et al. **Sclerotherapy for cervical cystic lymphatic malformations in children: our experience with computed tomography-guided 98% sterile ethanol insertion and a review of the literature.** *J Pediatr Surg* 2010;45:2473–78 CrossRef Medline
16. Baek JH, Ha EJ, Choi YJ, et al. **Radiofrequency versus ethanol ablation for treating predominantly cystic thyroid nodules: a randomized clinical trial.** *Korean J Radiol* 2015;16:1332–40 CrossRef Medline
17. In HS, Kim DW, Choo HJ, et al. **Ethanol ablation of benign thyroid cysts and predominantly cystic thyroid nodules: factors that predict outcome.** *Endocrine* 2014;46:107–13 CrossRef Medline
18. Koo HJ, Lee JH, Kim GY, et al. **Ethanol and/or radiofrequency ablation to treat venolymphatic malformations that manifest as a bulging mass in the head and neck.** *Clin Radiol* 2016;71:1070.e1–7 CrossRef Medline

# T1 Signal Measurements in Pediatric Brain: Findings after Multiple Exposures to Gadobenate Dimeglumine for Imaging of Nonneurologic Disease

G.K. Schneider, J. Stroeder, G. Roditi, C. Colosimo, P. Armstrong, M. Martucci, A. Buecker, and P. Raczeck

## ABSTRACT

**BACKGROUND AND PURPOSE:** Signal intensity increases possibly suggestive of gadolinium retention have recently been reported on unenhanced T1-weighted images of the pediatric brain following multiple exposures to gadolinium-based MR contrast agents. Our aim was to determine whether T1 signal changes suggestive of gadolinium deposition occur in the brains of pediatric nonneurologic patients after multiple exposures to gadobenate dimeglumine.

**MATERIALS AND METHODS:** Thirty-four nonneurologic patients (group 1; 17 males/17 females; mean age, 7.18 years) who received between 5 and 15 injections (mean, 7.8 injections) of 0.05 mmol/kg of gadobenate during a mean of 2.24 years were compared with 24 control patients (group 2; 16 males/8 females; mean age, 8.78 years) who had never received gadolinium-based contrast agents. Exposure to gadobenate was for diagnosis and therapy monitoring. Five blinded readers independently determined the signal intensity at ROIs in the dentate nucleus, globus pallidus, pons, and thalamus on unenhanced T1-weighted spin-echo images from both groups. Unpaired *t* tests were used to compare signal-intensity values and dentate nucleus–pons and globus pallidus–thalamus signal-intensity ratios between groups 1 and 2.

**RESULTS:** Mean signal-intensity values in the dentate nucleus, globus pallidus, pons, and thalamus of gadobenate-exposed patients ranged from 366.4 to 389.2, 360.5 to 392.9, 370.5 to 374.9, and 356.9 to 371.0, respectively. Corresponding values in gadolinium-based contrast agent–naïve subjects were not significantly different ( $P > .05$ ). Similarly, no significant differences were noted by any reader for comparisons of the dentate nucleus–pons signal-intensity ratios. One reader noted a difference in the mean globus pallidus–thalamus signal-intensity ratios ( $1.06 \pm 0.006$  versus  $1.02 \pm 0.009$ ,  $P = .002$ ), but this reflected nonsignificantly higher T1 signal in the thalamus of control subjects. The number of exposures and the interval between the first and last exposures did not influence signal-intensity values.

**CONCLUSIONS:** Signal-intensity increases potentially indicative of gadolinium deposition are not seen in pediatric nonneurologic patients after multiple exposures to low-dose gadobenate.

**ABBREVIATIONS:** DN = dentate nucleus; GBCA = gadolinium-based contrast agent; Gd = gadolinium; GP = globus pallidus; NSF = nephrogenic systemic fibrosis; SI = signal intensity

Recent reports have detailed high signal intensity (SI) in certain brain areas (primarily the dentate nucleus [DN] and globus pallidus [GP]) on unenhanced T1-weighted images following multiple exposures to gadolinium-based contrast agents

(GBCAs).<sup>1–20</sup> Many of these reports have focused on apparent differences between macrocyclic and open-chain “linear” GBCAs,<sup>4–13</sup> invariably associating progressive T1 hyperintensity with multiple exposures to linear GBCAs and concluding that observed T1 signal reflects the lower stability of these agents and thus a greater propensity for gadolinium (Gd) release and, subsequently, deposition in the brain. Among the more recent reports are several that describe retrospective assessments in pediatric patients.<sup>15–19</sup> Although each patient evaluated received just 1 specific linear GBCA (gadopentetate dimeglumine; Magnevist; Bayer HealthCare, Wayne, New Jersey), the study-based recommendations in each case were to consider carefully the use of all linear agents in pediatric subjects.

Gadobenate dimeglumine (MultiHance; Bracco Diagnostics, Monroe, New Jersey) is an ionic open-chain, linear GBCA that

Received January 6, 2017; accepted after revision April 24.

From the Department of Diagnostic and Interventional Radiology (G.K.S., J.S., A.B., P.R.), Saarland University Medical Center, Homburg/Saar, Germany; Department of Radiology (G.R., P.A.), National Health Service Greater Glasgow and Clyde, Glasgow Royal Infirmary, Glasgow, Scotland, UK; and Institute of Radiology (C.C., M.M.), Radiodiagnostica e Neuroradiologia, Fondazione Policlinico Universitario ‘A. Gemelli’, Università Cattolica del Sacro Cuore, Rome, Italy.

Please address correspondence to Guenther Schneider, MD, PhD, Department of Diagnostic and Interventional Radiology, Saarland University Medical Center, Kirrberger Str 1, 66421 Homburg/Saar, Germany; e-mail: dr.guenther.schneider@uniklinikum-saarland.de

<http://dx.doi.org/10.3174/ajnr.A5270>

differs fundamentally from gadopentetate and other extracellular GBCAs in having an aromatic substituent on the chelating molecule.<sup>21</sup> Unique properties conferred by this substituent include increased R1-relaxivity,<sup>22</sup> which permits the acquisition of diagnostically valid images with a reduced dose,<sup>23</sup> and liver-specificity, which permits gadobenate use for hepatobiliary-phase liver applications.<sup>24</sup> An additional benefit is increased molecular stability compared with gadopentetate, other linear agents, and certain macrocyclic agents.<sup>25</sup> Studies that have evaluated brain T1 signal intensities after multiple exposures to gadobenate have yielded conflicting results with one report demonstrating T1 signal increases, albeit to a lesser extent than with gadopentetate,<sup>10</sup> and others demonstrating no direct changes.<sup>11,12</sup>

We aimed to determine whether multiple exposures to low-dose gadobenate for nonneurologic pathology results in T1 signal changes in the DN and GP of pediatric patients relative to that in age- and weight-matched GBCA-naïve control subjects.

## MATERIALS AND METHODS

### Participants

This single-center (Saarland University Medical Center, Homburg/Saar, Germany) prospective study was approved by the institutional review board. Written informed consent for the use of imaging data was obtained routinely from all parents or legal guardians at the time of the first examination. Pediatric (younger than 18 years of age), mainly oncologic patients referred for diagnosis and subsequent therapy monitoring who had undergone at least 5 MR imaging examinations enhanced solely with gadobenate and who had no known neurologic disease or symptoms were identified from our electronic data base. Initial exposure to the first patient meeting these criteria was in August 2008. Patients with unsatisfactory images because of motion artifacts, an unknown history of GBCA administration, or severely impaired renal function (glomerular filtration rate < 30 mL/min) were excluded. All eligible patients underwent unenhanced T1-weighted imaging of the brain as a prospective adjunctive acquisition immediately before the next scheduled routine follow-up examination (performed in all cases between September 2015 and March 2016). Thirty-four patients met the inclusion criteria (group 1). A further 24 age- and weight-matched subjects with no known neurologic disease or symptoms who had never been administered any GBCA composed a GBCA-naïve control group (group 2). Patients in group 1 received 5 ( $n = 9$ ), 6 ( $n = 7$ ), 7 ( $n = 3$ ), 8 ( $n = 4$ ), 9 ( $n = 2$ ), 10 ( $n = 3$ ), 11 ( $n = 1$ ), 12 ( $n = 2$ ), 13 ( $n = 1$ ), 14 ( $n = 1$ ), and 15 ( $n = 1$ ) injections of gadobenate each at a dose of 0.05 mmol/kg of body weight (0.1 mL/kg of body weight).

### Imaging Protocol

All brain MR imaging examinations were performed on 1.5T whole-body MR imaging systems (Magnetom Aera or Magnetom Symphony, Siemens, Erlangen, Germany). All examinations used an unenhanced axial T1-weighted spin-echo sequence (TR/TE, 450–650/7–12 ms; section thickness, 5 mm with a 1.5-mm gap). Unenhanced axial T2-weighted images were acquired with TR/TE, 4000–5400/80–100 ms; section thickness, 5 mm; FOV, 230 mm).

### Data Collection

Four general consultant radiologists (A.B., P.R., G.R., and P.A., with 25, 4, 20, and 3 years' experience, respectively) and 2 neuro-radiologists in consensus (C.C., M.M., with 35 and 5 years' experience, respectively; considered reader 5), who were all blinded to patient diagnoses and details of all contrast administrations, determined SI values in operator-defined oval ROIs positioned within the DN, GP, thalamus, and pons of all patients and control subjects, as described by Kanda et al.<sup>1</sup> Each reader was instructed to make ROIs as large as possible (mean size, 10 mm<sup>2</sup>; range, 6–18 mm<sup>2</sup>). ROIs in the DN were placed on the right side whenever possible and were positioned as far as possible from pulsating vessels (if present), without including rim aspects. ROIs in the GP were placed in the capsula interna; ROIs in the central pons and thalamus were adjusted as appropriate to ensure homogeneity. If T1-weighted images were considered inconclusive for visualization, T2-weighted images were available to each reader for correlation, with ROIs then placed on the corresponding T1-weighted image.

Image sets for gadobenate-exposed and GBCA-naïve subjects were randomized, transcribed to a CD-ROM, and sent by mail to each blinded reader for viewing and independent evaluation on each reader's personal PACS workstation.

### Statistical Analysis

Comparison of demographic characteristics between groups 1 and 2 was performed by using a Student *t* test for age and weight and a Fisher exact test for sex. The primary outcome measure was whether repeat exposure to gadobenate (group 1) resulted in statistically significant increases in brain intraparenchymal SI relative to that in age- and weight-matched GBCA-naïve control subjects (group 2). To evaluate the primary outcome measure, we calculated DN-pons and GP-thalamus SI ratios for all subjects. SI values determined in the DN, GP, thalamus, and pons as well as DN-pons and GP-thalamus SI ratios were compared between groups 1 and 2 with unpaired *t* tests. Differences were considered significant for  $P < .05$ . Generalized multivariate linear regression was used to determine whether SI ratios were influenced by the number of gadobenate injections (control group considered as zero injections), age, sex, or weight. The interreader reliability of SI measurements was determined from the intraclass correlation coefficient, obtained from the generalized random effects regression model.

## RESULTS

Demographic details of patients in groups 1 and 2 are presented in Table 1. The gadobenate-exposed subjects included 6 infants (2 years of age or younger at first exposure), 11 subjects from 2 to 8 years of age at first exposure, and 17 subjects 9 years of age or older at first exposure. No significant differences were noted for age, weight, or sex distribution between groups 1 and 2. Each patient in group 1 was administered MultiHance at a dose of 0.05 mmol/kg of body weight. Given that 1 mL of MultiHance solution for injection contains 334 mg of gadobenate,<sup>26</sup> this corresponds to 33.4 mg of gadobenate/kg of body weight. On the basis of patient weight at each examination, a mean total accumulated dose of  $9.8 \pm 8.33$  g of gadobenate (range, 1.67–37.41 g) was adminis-

**Table 1: Summary of group characteristics<sup>a</sup>**

Characteristic	Gadobenate-Exposed (n = 34)	GBCA-Naïve Control (n = 24)	P Value
Age	7.18 ± 5.93 yr 9 mo to 17 yr	8.78 ± 5.78 yr 7 mo to 17 yr	.31
Sex (M/F)	17:17	16:8	.28
Body weight (kg)	30.55 ± 18.57 7.8–68	26.71 ± 17.23 8.1–64	.43
No. of administrations	7.8 ± 2.9 5–15	NA	NA
Interval between first and last administrations	2.24 ± 1.97 yr 9 mo to 7 yr	NA	NA
Accumulated volume of gadobenate administered (mL)	29.35 ± 24.95 5–112	NA	NA
Accumulated gadobenate dose (g) <sup>b</sup>	9.8 ± 8.33 1.67–37.41	NA	NA

**Note:**—NA indicates not applicable.

<sup>a</sup>Data are mean ± SD and range.

<sup>b</sup>One milliliter of MultiHance solution for injection contains 334 mg of gadobenamic acid as the meglumine salt.<sup>39</sup>

**Table 2: Summary of patient diagnoses<sup>a</sup>**

Group 1 (Gadobenate-Exposed)		Group 2 (GBCA-Naïve Controls)	
Diagnosis	No.	Diagnosis	No.
T-cell non-Hodgkin lymphoma	1	Chronic recurrent osteomyelitis	3
Hodgkin lymphoma	3	Pelvic trauma	1
Coccygeal teratoma	1	Cystic fibrosis	2
Nephroblastoma	4	DORV/VSD	1
Neuroblastoma	3	Polycystic kidney disease	1
Chronic recurrent osteomyelitis	2	Melanoma	1
Hepatoblastoma	2	Non-Hodgkin lymphoma	2
Mesoblastic nephroma	1	Skull base osteoid osteoma	1
ALL	1	Germ cell tumor	1
Paravertebral schwannoma	1	Polytrauma, knee distortion, ACL rupture	1
Angioma of the spleen	1	Myocarditis	2
Germ cell tumor	2	Hemophilia A	1
Renal clear cell sarcoma	1	Blunt head trauma	2
Ewing sarcoma	3	Osler disease	1
Osteosarcoma	2	Multiple osteochondroma, whole-body staging	1
Rhabdoid tumor of the kidney	1	Congenital aortic malformation, whole-body imaging	1
Dermatofibrosarcoma	1	Persistent left superior vena cava, thoracic and head/neck imaging	1
ARVD/ARVC	1	Hypertension work-up	1
Hemangioendothelioma	1		
Renal leiomyosarcoma	1		
Focal nodular hyperplasia	1		

**Note:**—ALL indicates acute lymphoblastic leukemia; DORV, double outlet right ventricle; VSD, ventricula septal defect; ACL, anterior cruciate ligament; ARVD, arrhythmogenic right ventricular dysplasia; ARVC, arrhythmogenic right ventricular cardiomyopathy.

<sup>a</sup>Patients in group 1 underwent multiple gadobenate-enhanced MR imaging studies for therapy follow-up or remission control. Patients in group 2 underwent preliminary unenhanced imaging as part of the initial work-up at the first visit.

tered per patient at a mean volume of 3.85 ± 3.14 mL/examination (1.27 ± 1.05 g gadobenate/examination). Patient diagnoses and reasons for follow-up imaging of patients in group 1 are given in Table 2.

SI values determined in the DN, GP, pons, and thalamus as well as the DN-pons and GP-thalamus SI ratios are reported in Table 3. No significant differences ( $P > .05$ ) in T1 signal intensity between gadobenate-exposed and GBCA-naïve control subjects were noted in any brain region by any reader. Similarly, no significant differences between gadobenate-exposed and GBCA-naïve control subjects were noted by any reader for DN-pons SI ratios. A significant difference in GP-thalamus SI ratios was noted by 1 of 5 readers (reader 5), but this was considered anomalous due in

part to nonsignificantly higher mean T1 signal intensity in the thalamus of control subjects. Generalized multivariate linear regression confirmed no influence of the number of gadobenate exposures on SI ratios across readers after adjusting for age, sex, and weight. Strong agreement among all readers was noted for SI assessments in the DN, GP, pons, and thalamus with intraclass correlation coefficient values ranging from 0.84 to 0.97 for gadobenate-exposed subjects and from 0.86 to 0.92 for GBCA-naïve control subjects.

Figures 1 and 2 show representative T1- and T2-weighted images of pediatric brain regions after multiple injections of 0.05 mmol/kg of gadobenate in patients younger than 2 years of age (8 injections; total, 3.34 g of gadobenate) and ~7 years of age (14 injections; total, 27.39 g of gadobenate), respectively.

## DISCUSSION

To date, no clinical signs or symptoms associated with T1 signal increases in the brain have been reported and no consequences for patient health, including neurologic function, have been identified. Nevertheless, the latest version of the American College of Radiology *Manual on Contrast Media*<sup>27</sup> recommends careful consideration of the clinical benefit versus the unknown potential risk of Gd deposition when deciding to perform a Gd-enhanced MR imaging study and particular attention paid to pediatric and other patients who may receive many GBCA-enhanced MR imaging studies during their lifetime. It further recommends taking into account multiple factors when selecting a GBCA, including diagnostic efficacy, relaxivity, rate of adverse reactions, dosing/con-

centration, and propensity to deposit in more sensitive organs such as the brain. Our findings in 34 nonneurologic pediatric patients who received between 5 and 15 administrations of low-dose (0.05 mmol/kg of body weight) gadobenate revealed no differences in T1 signal intensity in the DN, GP, pons, and thalamus relative to the SI measurements in 24 age- and weight-matched control subjects who had never been exposed to GBCA. Likewise, no significant differences in DN-pons SI ratios were noted, while just 1 of 5 blinded readers reported a significantly higher GP-thalamus SI ratio, which could be ascribed to higher T1 signal intensity in the thalamus of control subjects.

Our findings are in contrast to those of Flood et al,<sup>18</sup> who found an increased DN-pons SI ratio in patients exposed to gado-

**Table 3: Comparison of brain SI values and DN-pons and GP-thalamus SI ratios between gadobenate-exposed and GBCA-naïve control subjects<sup>a</sup>**

Reader/Patient Group	DN	Pons	GP	Thalamus	DN-Pons Ratio	GP-Thalamus Ratio
Reader 1						
Exposed	366.4 ± 8.62	370.5 ± 8.59	360.5 ± 10.2	360.3 ± 9.99	0.989 ± 0.004	1.0 ± 0.003
Control	374.3 ± 8.12	377.0 ± 8.65	364.4 ± 10.3	363.2 ± 9.88	0.994 ± 0.004	1.0 ± 0.002
P value	.526	.609	0.796	.842	.383	.572
Reader 2						
Exposed	367.8 ± 9.33	373.6 ± 8.84	392.3 ± 11.17	370.5 ± 10.66	0.984 ± 0.006	1.06 ± 0.009
Control	370.9 ± 9.70	381.9 ± 10.25	380.5 ± 11.59	373.3 ± 11.1	0.972 ± 0.007	1.02 ± 0.009
P value	.826	.547	.476	.859	.217	.185
Reader 3						
Exposed	389.2 ± 9.79	374.5 ± 8.63	383.6 ± 10.68	356.9 ± 9.06	1.04 ± 0.009	1.07 ± 0.012
Control	386.3 ± 10.14	380.9 ± 10.73	383.5 ± 12.98	365.6 ± 11.67	1.02 ± 0.009	1.05 ± 0.011
P value	.839	.642	.996	.555	.101	.134
Reader 4						
Exposed	365.3 ± 8.40	372.6 ± 8.71	381.1 ± 9.95	369.9 ± 9.54	0.98 ± 0.006	1.03 ± 0.006
Control	368.3 ± 9.47	378.5 ± 10.28	381.8 ± 10.57	376.3 ± 9.28	0.97 ± 0.005	1.01 ± 0.007
P value	.816	.661	.959	.644	.388	.083
Reader 5						
Exposed	386.5 ± 9.82	374.9 ± 9.04	392.9 ± 10.64	371.0 ± 9.68	1.03 ± 0.013	1.06 ± 0.006
Control	386.3 ± 10.85	383.4 ± 10.71	385.4 ± 12.47	376.8 ± 11.17	1.01 ± 0.007	1.02 ± 0.009
P value	.987	.547	.647	.699	.147	.002

<sup>a</sup> Values are mean ± standard error of the mean.

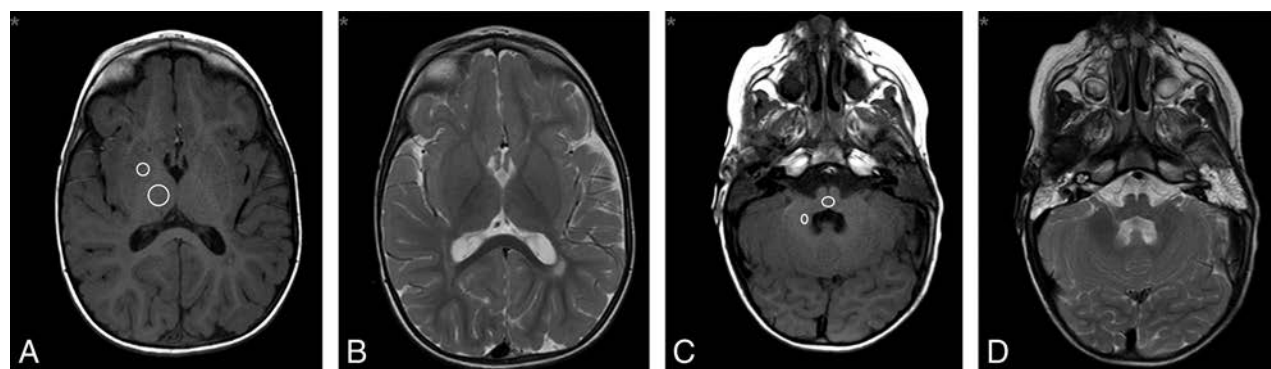


**FIG 1.** Oncologic male patient (1 year 9 months of age at his first visit) undergoing follow-up imaging for cervical neuroblastoma in remission. Unenhanced T1- and T2-weighted transverse images of the DN-pons (A and B) and GP-thalamus (C and D) after 8 injections of 0.05 mmol/kg of gadobenate reveal no evidence of SI changes.

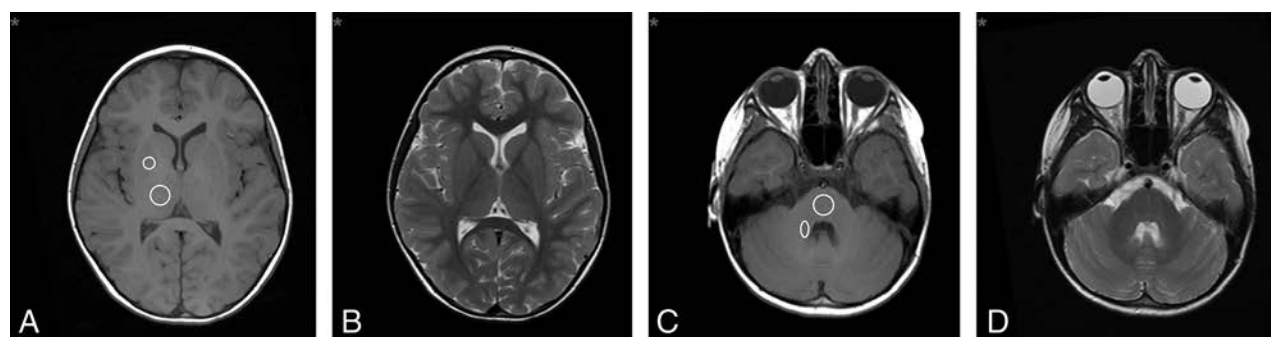


**FIG 2.** Oncologic female patient (7 years 2 months of age at her first visit) undergoing follow-up imaging for non-Hodgkin lymphoma in remission. Unenhanced T1- and T2-weighted transverse images of the DN-pons (A and B) and GP-thalamus (C and D) after 14 injections of 0.05 mmol/kg of gadobenate reveal no evidence of SI changes.

pentetate relative to GBCA-naïve control subjects (though no differences in GP-thalamus SI ratio were found) and in contrast to those of Hu et al,<sup>19</sup> who found significantly higher T1 signal in the DN and GP of patients after serial exposure to gadopentetate than in the DN and GP of control subjects.

There are at least 2 possible reasons for the different findings.

First, our patient population was different. Whereas Flood et al<sup>18</sup> and Hu et al<sup>19</sup> evaluated patients who had undergone multiple brain examinations, our patient cohort comprised mainly oncologic patients with no known brain abnormalities. It is thus possible that the patients evaluated by Flood et al and Hu et al were more prone to brain Gd deposition due to a more compromised

blood-brain barrier. On the other hand, studies have demonstrated T1-signal increases in the DN and GP even in the presence of a seemingly intact BBB,<sup>14,28</sup> implying that the potential for T1-hyperintensity may be independent of the patient's clinical status and dependent solely on the amount of Gd administered. However, most of the Gd found deposited in the brain is actually in the perivascular space and has not passed the BBB,<sup>29,30</sup> while Gd that does appear to have crossed an intact BBB is found primarily in the neural tissue interstitium rather than in neural cells.<sup>14</sup>

Second, whereas gadobenate and gadopentetate are both ionic open-chain GBCAs, they differ fundamentally in that an aromatic substituent is present on the gadobenate molecule. On the one hand, this substituent influences the elimination profile of gadobenate, facilitating its excretion in part (typically up to 5% of the injected dose in subjects with normal renal function) via the hepatobiliary route.<sup>31</sup> More pertinently, it also leads to markedly higher R1-relaxivity *in vivo*,<sup>22</sup> which, in turn, leads to markedly increased SI enhancement on T1-weighted images for equivalent administered doses. A proven benefit of this higher relaxivity is that a lower gadobenate dose can be used to obtain diagnostically valid images.<sup>23,24</sup> In our study, the mean accumulated dose across all patients was  $9.8 \pm 8.33$  g, administered across a mean of  $7.8 \pm 2.9$  examinations (mean,  $3.85 \pm 3.14$  mL of MultiHance/examination, corresponding to  $1.27 \pm 1.05$  g of gadobenate/examination). This is considerably lower than the mean accumulated gadopentetate dose of  $16.2 \pm 10.1$  g across a mean of  $5.9 \pm 2.7$  examinations (mean, 2.75 g gadopentetate/examination) given by Flood et al<sup>18</sup> and would similarly be lower than that administered by Hu et al,<sup>19</sup> given that they injected a standard dose of 0.1 mmol/kg of gadopentetate/examination. At our institution, we routinely administer 0.05 mmol/kg of gadobenate for pediatric oncologic imaging.

An additional feature conferred by the aromatic substituent, which is invariably overlooked when simplistic comparisons are made between "linear" and macrocyclic GBCAs,<sup>4-10,32</sup> is improved steric hindrance and thus increased kinetic inertia. An increased steric effect conferred by a bulky substituent potentially hinders unwrapping of the ligand around the gadolinium, thereby increasing molecular stability.<sup>33</sup> Improved kinetic inertia due to an aromatic substituent has previously been demonstrated for gadofosveset.<sup>34</sup> Unfortunately, accurate *in vivo* measurements of the kinetic stability of gadobenate are currently lacking, though its thermodynamic and conditional stability constants *in vitro* are the highest of all open-chain GBCAs and higher also than the macrocyclic agent gadobutrol.<sup>25</sup> Further evidence of the inherent stability of gadobenate comes from the fact that this GBCA, unlike all other GBCAs except gadoterate meglumine (Dotarem; Guerbet, Aulnay-sous-Bois, France), does not contain any excess chelating agent in its formulation.<sup>25</sup> Excess chelating agent is an indirect indicator of the potential of a GBCA to release Gd; that the gadobenate formulation does not contain excess chelate implies that it does not release Gd to the same extent as other GBCAs.

Our findings are in stark contrast to those of Weberling et al,<sup>10</sup> who found significantly increased DN-pons and DN-CSF SI ratios after serial exposures of gadobenate to adults. However, several factors should be borne in mind when evaluating the results

of Weberling et al. First, the patients evaluated were only required to have had a minimum of 5 consecutive gadobenate-enhanced MR imaging scans; each patient's first included scan was not necessarily the first scan the patient received, and prior scans with other GBCAs might have been performed. The likelihood that patients might have had prior MR imaging exams with other GBCAs is clearly a major confounding factor. Ramalho et al<sup>12</sup> showed that significant T1 hyperintensity in deep brain nuclei occurred after the use of gadobenate in patients who had received prior administration of gadodiamide (Omniscan; GE Healthcare, Piscataway, New Jersey), but not in patients who had not previously received gadodiamide. An earlier report by Ramalho et al<sup>11</sup> demonstrated significant SI increases in the DN and GP of patients who had received gadodiamide but not in patients who had received gadobenate. The lack of adequate patient screening by Weberling et al<sup>10</sup> means that possible potentiating effects of prior exposure to other GBCAs could not be excluded.

Second, each patient evaluated by Weberling et al<sup>10</sup> received a standardized volume of 15 or 20 mL of gadobenate per examination irrespective of body weight, resulting in a mean accumulated volume of  $136.9 \pm 57.6$  mL (ie, a mean accumulated dose of 45.72 g of gadobenate) between the first and last MR imaging examinations. Given that an approved gadobenate dose for all indications other than the liver, kidneys, urinary tract, and adrenal glands is 0.1 mmol/kg of body weight,<sup>26</sup> which corresponds to 15 mL for a 75-kg patient, any patient below 75 kg in weight would have received more than the approved dose (ie, more than the approved amount of Gd). Third, all except 1 of the patients evaluated by Weberling et al had brain metastases from melanoma, with many undergoing radiation therapy. These patients would certainly have had a more severely compromised BBB, potentially allowing easier GBCA access to deep brain nuclei.

Weberling et al<sup>10</sup> ascribed their observed SI increases to Gd retention, speculating that their findings reflect the specific potential of gadobenate to release Gd. In drawing parallels with the postulated causative role of GBCAs in nephrogenic systemic fibrosis (NSF), they noted that gadobenate is classified as being of intermediate risk for NSF by the European Medicines Agency<sup>35</sup>; and in referring to 1 *in vitro* determination of kinetic stability conducted by a competitor to the manufacturer of gadobenate,<sup>36</sup> they suggested that the potential for Gd release is similar for gadobenate and gadopentetate. Unfortunately, *in vitro* determinations of kinetic stability are inherently limited in that they cannot replicate normal physiologic conditions *in vivo* and cannot account for differing and unique routes of elimination among GBCAs. Although Weberling et al<sup>10</sup> acknowledged that no unconfounded cases of NSF have been reported for gadobenate,<sup>37</sup> they failed to point out that other relevant regulatory authorities, including the US Food and Drug Administration, classify gadobenate as having a low risk of NSF.<sup>38,39</sup> In this regard, most (73%) of the unconfounded published NSF cases were reported in the United States,<sup>40</sup> and at the height of the NSF crisis (2006–2010), just 1 macrocyclic GBCA (gadoteridol, ProHance; Bracco Diagnostics) had FDA approval for commercial use. Gadobutrol (Gadavist; Bayer Healthcare) and gadoterate (Guerbet) were approved in 2011 and 2013, respectively. The other approved GBCAs besides gadobenate were gadodiamide (GE Healthcare), gadoversetamide

(OptiMARK; Covidien), and gadopentetate (Bayer Healthcare), which were avoided and subsequently contraindicated in patients with severe renal impairment,<sup>38</sup> leaving only gadobenate as an approved open-chain GBCA for routine applications in this population.

If, as is widely accepted, NSF occurs because of Gd release from the chelating molecule,<sup>35</sup> then at least 1 unconfounded case might have been expected for gadobenate if, as postulated by Weberling et al,<sup>10</sup> Gd is released in vivo to an extent similar to that seen with gadopentetate. That no unconfounded cases have been reported despite exhaustive investigation<sup>41-43</sup> suggests that Gd is not released from gadobenate to the same extent and that any observed T1 hyperintensity reflects retention of the intact molecule. Roberts et al<sup>44</sup> recently reported high levels of Gd in the skin of a patient who underwent 61 enhanced brain examinations with a variety of GBCAs and that speciation analysis revealed intact gadobenate.

Further studies are required to determine whether T1 hyperintensity is seen in some patients after serial gadobenate exposure, and if so, whether this reflects accumulation of intact gadobenate or released Gd bound to macromolecules (eg, neuromelanin). In this regard, it is possible that Gd released from less stable GBCAs binds to macromolecules and that the observed T1 hyperintensity reflects elevated T1-signal due to slowing of the molecular tumbling rate of these Gd-macromolecule complexes.<sup>30</sup> This hypothesis might explain why elevated T1 signal is observed with less stable GBCAs despite the very small Gd concentrations shown to be retained<sup>20</sup> and, conceivably, why detectable high signal is less evident with more stable GBCAs if these are retained as fully intact molecules rather than as Gd-macromolecular complexes.<sup>45</sup> Of note, however, is the study by Stojanov<sup>13</sup> and a recent study in pediatric subjects by Rossi Espagnet et al.<sup>46</sup> that demonstrate quantifiable T1 signal increases after multiple exposures to the macrocyclic GBCAs gadobutrol and gadoterate, respectively.

Also worthy of study is the possible differential impact of GBCA R1-relaxivity on T1 hyperintensity if GBCAs are retained as intact molecules; it is likely that retained GBCAs that have low R1-relaxivity may be less detectable than retained intact GBCAs that have higher R1-relaxivity. Finally, T1 signal increases are merely suggestive of Gd retention, and T1 hyperintensity might alternatively reflect various disease-related processes.<sup>47-49</sup> While imaging studies can be considered, at best, an indirect second-level marker of Gd deposition, a true picture can only come from direct tissue analysis. In this regard, studies have demonstrated measurable Gd not only in the DN and GP but also in other brain areas and body organs.<sup>14,20,28</sup> Most important, Murata et al<sup>20</sup> have shown that deposition occurs with both linear and macrocyclic GBCAs and that it is up to 23 times higher in organs such as bone than in the brain.

Despite excellent interreader agreement regarding the reproducibility of SI measurements and despite the absence of significant differences in SI values between gadobenate-exposed and GBCA-naïve control subjects across any of the 4 evaluated brain regions, a significant difference in the GP-thalamus SI ratio was nevertheless still observed in 1 of the 5 blinded assessments. Although this can be explained by higher T1 signal in the thalamus of control subjects, it highlights the potential impact of even min-

imal differences in SI measurements on study interpretation. This, in turn, points to the importance of multiple readers when performing quantitative evaluations and to the dangers of drawing conclusions based on evaluations performed by just 1 or 2 readers, particularly if such readers are not blinded to information regarding the images under evaluation. Accurate placing of ROIs for quantitative assessment is a highly subjective procedure, which is susceptible to considerable interreader variation.

Our study has some limitations. First, this was a single-center study. Second, because we assessed nonneurologic patients who had not previously undergone MR imaging of the brain, it was not possible to compare unenhanced T1-weighted images after multiple gadobenate administrations with baseline unenhanced images acquired before the first gadobenate administration. However, the lack of significant SI differences between gadobenate-exposed and GBCA-naïve control subjects suggests that no differences would have been seen. Third, we determined DN-pons and GP-thalamus SI ratios despite Gd retention being observed in both the pons and thalamus.<sup>14,20</sup> However, the T1 signal changes in these brain areas are much lower than in the DN and GP, and these ratios are commonly calculated parameters.<sup>1-4,8-13,16-18</sup> Finally, we did not normalize the SI values of the DN and GP against the SI of the CSF to account for possible intra- and intersequence signal-intensity differences, differences between MR units, and magnetic field inhomogeneity as described by McDonald et al.<sup>14</sup> SI normalization might be appropriate for future studies.

## CONCLUSIONS

Our study of 34 pediatric patients who received between 5 and 15 administrations of 0.05 mmol/kg of body weight gadobenate revealed no differences in T1 signal in the DN, GP, pons, and thalamus relative to measurements in 24 age- and weight-matched control subjects who had never been exposed to any GBCA. Likewise, no meaningful differences were seen in the DN-pons and GP-thalamus SI ratios. If T1 hyperintensity and Gd retention in deep brain nuclei occur in an exposure-dependent fashion, with greater T1 shortening observed following greater prior exposure to GBCAs,<sup>1</sup> it would seem prudent to administer the lowest possible dose of a GBCA to achieve diagnostically valid studies, particularly when repeat MR imaging studies are required for follow-up or screening purposes. To this end, a recent intraindividual crossover study in which patients received 2 MR imaging contrast agents in 2 otherwise identical MR imaging examinations has demonstrated similar diagnostic imaging performances for a half-dose (0.05 mmol/kg of body weight) of gadobenate relative to a full dose (0.1 mmol/kg of body weight) of the standard relaxivity macrocyclic GBCA, gadoterate, for morphologic imaging of brain tumors.<sup>23</sup> Similarly, a prior study<sup>50</sup> demonstrated significant superiority for a three-quarter dose (0.075 mmol/kg of body weight) of gadobenate relative to a full dose (0.1 mmol/kg of body weight) of gadoterate for cranial MR imaging. In both studies, similar or improved imaging performance was achieved with a lower total administered dose of gadolinium when gadobenate was used. We consider half-dose gadobenate safe and effective for diagnosis and routine follow-up of pediatric oncologic patients.

Disclosures: Guenther K. Schneider—UNRELATED: Grants/Grants Pending: Bracco, Siemens, Bayer, Comments: research/clinical studies\*; Payment for Lectures Including Service on Speakers Bureaus: Bracco, Siemens. Jonas Stroeder—UNRELATED: Payment for Lectures Including Service on Speakers Bureaus: Bracco, Comments: allowance for lecture given in June 2014. Giles Roditi—UNRELATED: Payment for Lectures Including Service on Speakers Bureaus: Bayer, Bracco, Comments: speaker honoraria once for each company for lecturing in educational courses. Cesare Colosimo—UNRELATED: Consultancy: Bracco, Bayer. Arno Buecker—UNRELATED: Payment for Lectures Including Service on Speakers Bureaus: Bracco. \*Money paid to the institution.

## REFERENCES

- Kanda T, Ishii K, Kawaguchi H, et al. **High signal intensity in the dentate nucleus and globus pallidus on unenhanced T1-weighted MR images: relationship with increasing cumulative dose of gadolinium-based contrast material.** *Radiology* 2014;270:834–41 CrossRef Medline
- Errante Y, Cirimele V, Mallio CA, et al. **Progressive increase of T1 signal intensity of the dentate nucleus on unenhanced magnetic resonance images is associated with cumulative doses of intravenously administered gadodiamide in patients with normal renal function, suggesting dechelation.** *Invest Radiol* 2014;49:685–90 CrossRef Medline
- Quattrocchi CC, Mallio CA, Errante Y, et al. **Gadodiamide and dentate nucleus T1 hyperintensity in patients with meningioma evaluated by multiple follow-up contrast enhanced magnetic resonance examinations with no systemic interval therapy.** *Invest Radiol* 2015;50:470–72 CrossRef Medline
- Radbruch A, Weberling LD, Kieslich PJ, et al. **Gadolinium retention in the dentate nucleus and globus pallidus is dependent on the class of contrast agent.** *Radiology* 2015;275:783–91 CrossRef Medline
- Quattrocchi CC, Mallio CA, Errante Y, et al. **High T1 signal intensity in dentate nucleus after multiple injections of linear gadolinium chelates.** *Radiology* 2015;276:616–17 CrossRef Medline
- Kanda T, Osawa M, Oba H, et al. **High signal intensity in dentate nucleus on unenhanced T1-weighted MR images: association with linear versus macrocyclic gadolinium chelate administration.** *Radiology* 2015;275:803–09 CrossRef Medline
- Cao Y, Huang DQ, Shih G, et al. **Signal change in the dentate nucleus on T1-weighted MR images after multiple administrations of gadopentetate dimeglumine versus gadobutrol.** *AJR Am J Roentgenol* 2016;206:414–19 CrossRef Medline
- Radbruch A, Weberling LD, Kieslich PJ, et al. **Intraindividual analysis of signal intensity changes in the dentate nucleus after consecutive serial applications of linear and macrocyclic gadolinium-based contrast agents.** *Invest Radiol* 2016;51:683–90 CrossRef Medline
- Radbruch A, Weberling LD, Kieslich PJ, et al. **High-signal intensity in the dentate nucleus and globus pallidus on unenhanced T1-weighted images: evaluation of the macrocyclic gadolinium-based contrast agent gadobutrol.** *Invest Radiol* 2015;50:805–10 CrossRef Medline
- Weberling LD, Kieslich PJ, Kickingereder P, et al. **Increased signal intensity in the dentate nucleus on unenhanced T1-weighted images after gadobenate dimeglumine administration.** *Invest Radiol* 2015;50:743–48 CrossRef Medline
- Ramalho J, Castillo M, AIObaidy M, et al. **High signal intensity in globus pallidus and dentate nucleus on unenhanced T1-weighted MR images: evaluation of two linear gadolinium-based contrast agents.** *Radiology* 2015;276:836–44 CrossRef Medline
- Ramalho J, Semelka RC, AIObaidy M, et al. **Signal intensity change on unenhanced T1-weighted images in dentate nucleus following gadobenate dimeglumine in patients with and without previous multiple administrations of gadodiamide.** *Eur Radiol* 2016;26:4080–88 CrossRef Medline
- Stojanov DA, Aracki-Trenkic A, Vojinovic S, et al. **Increasing signal intensity within the dentate nucleus and globus pallidus on unenhanced T1W magnetic resonance images in patients with relapsing-remitting multiple sclerosis: correlation with cumulative dose of a macrocyclic gadolinium-based contrast agent, gadobutrol.** *Eur Radiol* 2016;26:807–15 CrossRef Medline
- McDonald RJ, McDonald JS, Kallmes DF, et al. **Intracranial gadolinium deposition after contrast-enhanced MR imaging.** *Radiology* 2015;275:772–82 CrossRef Medline
- Miller JH, Hu HH, Pokorney A, et al. **MRI brain signal intensity changes of a child during the course of 35 gadolinium contrast examinations.** *Pediatrics* 2015;136:e1637–40 CrossRef Medline
- Roberts DR, Holden KR. **Progressive increase of T1 signal intensity in the dentate nucleus and globus pallidus on unenhanced T1-weighted MR images in the pediatric brain exposed to multiple doses of gadolinium contrast.** *Brain Dev* 2016;38:331–36 CrossRef Medline
- Roberts DR, Chatterjee AR, Yazdani M, et al. **Pediatric patients demonstrate progressive T1-weighted hyperintensity in the dentate nucleus following multiple doses of gadolinium-based contrast agent.** *AJNR Am J Neuroradiol* 2016;37:2340–47 CrossRef Medline
- Flood TF, Stence NV, Maloney JA, et al. **Pediatric brain: repeated exposure to linear gadolinium-based contrast material is associated with increased signal intensity at unenhanced T1-weighted MR imaging.** *Radiology* 2017;282:222–28 CrossRef Medline
- Hu HH, Pokorney A, Towbin RB, et al. **Increased signal intensities in the dentate nucleus and globus pallidus on unenhanced T1-weighted images: evidence in children undergoing multiple gadolinium MRI exams.** *Pediatr Radiol* 2016;46:1590–98 CrossRef Medline
- Murata N, Gonzalez-Cuyar LF, Murata K, et al. **Macrocyclic and other non-group 1 gadolinium contrast agents deposit low levels of gadolinium in brain and bone tissue: preliminary results from 9 patients with normal renal function.** *Invest Radiol* 2016;51:447–53 CrossRef Medline
- Laurent S, Elst LV, Muller RN. **Comparative study of the physico-chemical properties of six clinical low molecular weight gadolinium contrast agents.** *Contrast Media Mol Imaging* 2006;1:128–37 CrossRef Medline
- Shen Y, Goerner FL, Snyder C, et al. **T1 relaxivities of gadolinium-based magnetic resonance contrast agents in human whole blood at 1.5, 3, and 7 T.** *Invest Radiol* 2015;50:330–38 CrossRef Medline
- Vaneckova M, Herman M, Smith MP, et al. **The benefits of high relaxivity for brain tumor imaging: results of a multicenter intraindividual crossover comparison of gadobenate dimeglumine with gadoterate meglumine (The BENEFIT Study).** *AJNR Am J Neuroradiol* 2015;36:1589–98 CrossRef Medline
- Morana G, Grazioli L, Kirchin MA, et al. **Solid hypervascular liver lesions: accurate identification of true benign lesions on enhanced dynamic and hepatobiliary phase magnetic resonance imaging after gadobenate dimeglumine administration.** *Invest Radiol* 2011;46:225–39 CrossRef Medline
- van der Molen AJ. **Nephrogenic systemic fibrosis and the role of gadolinium contrast media.** *J Med Imaging Radiat Oncol* 2008;52:339–50 CrossRef Medline
- MultiHance Summary of Product Characteristics. Updated September 29, 2016. <https://www.medicines.org.uk/emc/medicine/6132>. Accessed May 26, 2017
- American College of Radiology. *ACR Manual on Contrast Media*. Version 10.2; 2016. <http://www.acr.org/quality-safety/resources/contrast-manual>. Accessed August 29, 2016
- Kanda T, Fukusato T, Matsuda M, et al. **Gadolinium-based contrast agent accumulates in the brain even in subjects without severe renal dysfunction: evaluation of autopsy brain specimens with inductively coupled plasma mass spectroscopy.** *Radiology* 2015;276:228–32 CrossRef Medline
- Naganawa S, Nakane T, Kawai H, et al. **Gd-based contrast enhancement of the perivascular spaces in the basal ganglia.** *Magn Reson Med* 2017;16:61–65
- Hoggard N, Roditi GH. **T1 hyperintensity on brain imaging subsequent to gadolinium-based contrast agent administration: what do we know about intracranial gadolinium deposition?** *Br J Radiol* 2017;90:20160590 CrossRef Medline
- Spinazzi A, Lorusso V, Pirovano G, et al. **Safety, tolerance, biodistribution, and MR imaging enhancement of the liver with gadobenate**

- dimeglumine: results of clinical pharmacologic and pilot imaging studies in nonpatient and patient volunteers. *Acad Radiol* 1999;6:282–91 CrossRef Medline
32. Malayeri AA, Brooks KM, Bryant LH, et al. **National Institutes of Health perspective on reports of gadolinium deposition in the brain.** *J Am Coll Radiol* 2016;13:237–41 CrossRef Medline
  33. Idée JM, Port M, Robic C, et al. **Role of thermodynamic and kinetic parameters in gadolinium chelate stability.** *J Magn Reson Imaging*. 2009;30:1249–58 CrossRef Medline
  34. Caravan P, Comuzzi C, Crooks W, et al. **Thermodynamic stability and kinetic inertness of MS-325, a new blood pool agent for magnetic resonance imaging.** *Inorg Chem* 2001;40:2170–76 CrossRef Medline
  35. Thomsen HS, Morcos SK, Almén T, et al; ESUR Contrast Medium Safety Committee. **Nephrogenic systemic fibrosis and gadolinium-based contrast media: updated ESUR Contrast Medium Safety Committee guidelines.** *Eur Radiol* 2013;23:307–18 CrossRef Medline
  36. Frenzel T, Lengsfeld P, Schirmer H, et al. **Stability of gadolinium-based magnetic resonance imaging contrast agents in human serum at 37 degrees C.** *Invest Radiol* 2008;43:817–28 CrossRef Medline
  37. Heverhagen JT, Krombach GA, Gizewski E. **Application of extracellular gadolinium-based MRI contrast agents and the risk of nephrogenic systemic fibrosis.** *Rofa* 2014;186:661–69 CrossRef Medline
  38. Yang L, Krefting I, Gorovets A, et al. **Nephrogenic systemic fibrosis and class labeling of gadolinium-based contrast agents by the Food and Drug Administration.** *Radiology* 2012;265:248–53 CrossRef Medline
  39. Guideline on the use of gadolinium-containing MRI contrast agents in patients with renal impairment. V2. <https://www.ranzcr.com/search/gadolinium-containing-mri-contrast-agents-guidelines>. Accessed May 26, 2017
  40. Spinazzi A. **MRI contrast agents and nephrogenic systemic fibrosis.** In: Shellock FG, Crues JV, Karacozoff AM, eds. *MRI Bioeffects, Safety, and Patient Management*. Los Angeles: Biomedical Research Publishing Group; 2014:chap 11:256–81
  41. Nandwana SB, Moreno CC, Osipow MT, et al. **Gadobenate dimeglumine administration and nephrogenic systemic fibrosis: is there a real risk in patients with impaired renal function?** *Radiology* 2015;276:741–47 CrossRef Medline
  42. Soulez G, Bloomgarden DC, Rofsky NM, et al. **Prospective cohort study of nephrogenic systemic fibrosis in patients with stage 3–5 chronic kidney disease undergoing MRI with injected gadobenate dimeglumine or gadoteridol.** *AJR Am J Roentgenol* 2015;205:469–78 CrossRef Medline
  43. Bruce R, Wentland AL, Haemel AK, et al. **Incidence of nephrogenic systemic fibrosis using gadobenate dimeglumine in 1423 patients with renal insufficiency compared with gadodiamide.** *Invest Radiol* 2016;51:701–05 CrossRef Medline
  44. Roberts DR, Lindhorst SM, Welsh CT, et al. **High levels of gadolinium deposition in the skin of a patient with normal renal function.** *Invest Radiol* 2016;51:280–89 CrossRef Medline
  45. Jost G, Lenhard DC, Sieber MA, et al. **Signal increase on unenhanced T1-weighted images in the rat brain after repeated, extended doses of gadolinium-based contrast agents: comparison of linear and macrocyclic agents.** *Invest Radiol* 2016;51:83–89
  46. Rossi Espagnet MC, Bernardi B, Pasquini L, Figà-Talamanca L, et al. **Signal intensity at unenhanced T1-weighted magnetic resonance in the globus pallidus and dentate nucleus after serial administrations of a macrocyclic gadolinium-based contrast agent in children.** *Pediatr Radiol* 2017 May 19. [Epub ahead of print] CrossRef
  47. Prosch H, Grois N, Wnorowski M, et al. **Long-term MR imaging course of neurodegenerative Langerhans cell histiocytosis.** *AJNR Am J Neuroradiol* 2007;28:1022–28 CrossRef Medline
  48. Maeda H, Sato M, Yoshikawa A, et al. **Brain MR imaging in patients with hepatic cirrhosis: relationship between high intensity signal in basal ganglia on T1-weighted images and elemental concentrations in brain.** *Neuroradiology* 1997;39:546–50 CrossRef Medline
  49. Mochizuki H, Kamakura K, Masaki T, et al. **Atypical MRI features of Wilson's disease: high signal in globus pallidus on T1-weighted images.** *Neuroradiology* 1997;39:171–74 CrossRef Medline
  50. Khouri Chalouhi K, Papini GD, Bandirali M, et al. **Less is better? Intraindividual and interindividual comparison between 0.075 mmol/kg of gadobenate dimeglumine and 0.1 mmol/kg of gadoterate meglumine for cranial MRI.** *Eur J Radiol* 2014;83:1245–49 CrossRef Medline

# New Ultrasound Measurements to Bridge the Gap between Prenatal and Neonatal Brain Growth Assessment

<sup>1</sup>I.V. Koning, <sup>2</sup>J.A. Roelants, <sup>3</sup>I.A.L. Groenenberg, <sup>4</sup>M.J. Vermeulen, <sup>5</sup>S.P. Willemsen, <sup>6</sup>I.K.M. Reiss, <sup>7</sup>P.P. Govaert, <sup>8</sup>R.P.M. Steegers-Theunissen, and <sup>9</sup>J. Dudink

## ABSTRACT

**BACKGROUND AND PURPOSE:** Most ultrasound markers for monitoring brain growth can only be used in either the prenatal or the postnatal period. We investigated whether corpus callosum length and corpus callosum–fastigium length could be used as markers for both prenatal and postnatal brain growth.

**MATERIALS AND METHODS:** A 3D ultrasound study embedded in the prospective Rotterdam Periconception Cohort was performed at 22, 26 and 32 weeks' gestational age in fetuses with fetal growth restriction, congenital heart defects, and controls. Postnatally, cranial ultrasound was performed at 42 weeks' postmenstrual age. First, reliability was evaluated. Second, associations between prenatal and postnatal corpus callosum and corpus callosum–fastigium length were investigated. Third, we created reference curves and compared corpus callosum and corpus callosum–fastigium length growth trajectories of controls with growth trajectories of fetuses with fetal growth retardation and congenital heart defects.

**RESULTS:** We included 199 fetuses; 22 with fetal growth retardation, 20 with congenital heart defects, and 157 controls. Reliability of both measurements was excellent (intraclass correlation coefficient  $\geq 0.97$ ). Corpus callosum growth trajectories were significantly decreased in fetuses with fetal growth restriction and congenital heart defects ( $\beta = -2.295$ ; 95% CI,  $-3.320$ – $-1.270$ ;  $P < .01$ ;  $\beta = -1.267$ ; 95% CI,  $-0.972$ – $0.562$ ;  $P < .01$ , respectively) compared with growth trajectories of controls. Corpus callosum–fastigium growth trajectories were decreased in fetuses with fetal growth restriction ( $\beta = -1.295$ ; 95% CI,  $-2.595$ – $0.003$ ;  $P = .05$ ).

**CONCLUSIONS:** Corpus callosum and corpus callosum–fastigium length may serve as reliable markers for monitoring brain growth from the prenatal into the postnatal period. The clinical applicability of these markers was established by the significantly different corpus callosum and corpus callosum–fastigium growth trajectories in fetuses at risk for abnormal brain growth compared with those of controls.

**ABBREVIATIONS:** CC = corpus callosum; CCF = corpus callosum–fastigium; CHD = congenital heart defect; FGR = fetal growth restriction; GA = gestational age; US = ultrasound

In preterm infants and those small-for-gestational age, brain growth is an important predictor of neurodevelopmental outcome.<sup>1–4</sup> Although prenatal growth often predicts postnatal growth, there is a traditional division between fetal and neonatal

growth charts.<sup>5</sup> This is mainly due to the lack of consistent measures of brain growth that can be used in both the prenatal and postnatal periods.

Markers of brain growth that can theoretically be used in both the prenatal and postnatal periods include head circumference and a few ultrasound (US) and MR imaging measures. Head circumference measured postnatally, however, lacks precision and does not correspond well with neurodevelopmental outcome.<sup>6,7</sup> Prenatal and postnatal US markers are largely based on individual brain structures, only reflecting growth of a specific part of the brain.<sup>8–12</sup> Moreover, these brain structures are not measured consistently during the prenatal and postnatal periods due to the absence of corresponding standard US planes. Although MR imaging provides more precise measures of brain growth, volume, and development, this technique is expensive and therefore not suitable for serial measurements.

Recently, we demonstrated that corpus callosum–fastigium

Received December 23, 2016; accepted after revision April 24, 2017.

From the Department of Obstetrics and Gynecology (I.V.K., J.A.R., I.A.L.G., S.P.W., R.P.M.S.-T.), Division of Obstetrics and Prenatal Medicine, and Department of Biostatistics (S.P.W.), Erasmus MC, University Medical Center, Rotterdam, the Netherlands; Department of Pediatrics (I.V.K., J.A.R., M.J.V., I.K.M.R., P.P.G., R.P.M.S.-T., J.D.), Division of Neonatology, Erasmus MC–Sophia Children's Hospital, Rotterdam, the Netherlands; Department of Neonatology (P.P.G.), ZNA Koningin Paola Ziekenhuis, Antwerp, Belgium; and Department of Neonatology (J.D.), Wilhelmina's Children's Hospital, University Medical Center Utrecht, Utrecht, the Netherlands.

This work was supported by a grant of the Sophia Children's Hospital Fund, Rotterdam, the Netherlands (Sophia Foundation for Medical Research, grant No. 644).

Please address correspondence to J. Dudink, MD, PhD, Department of Pediatrics, Division of Neonatology, Erasmus MC–Sophia Children's Hospital, Wytemaweg 80, 3015 CN, Rotterdam, the Netherlands; e-mail: j.dudink@umcutrecht.nl

<http://dx.doi.org/10.3174/ajnr.A5278>

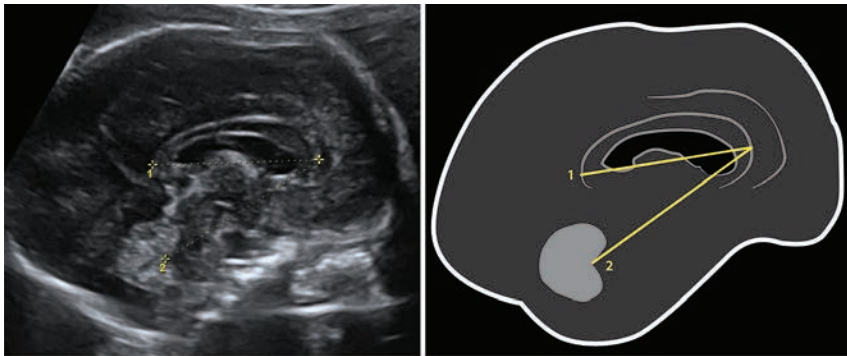


**FIG 1.** Prenatal measurement of CC and CCF lengths. 1, Corpus callosum length, outer-outer border. 2, Corpus callosum–fastigium length, from the genu of the corpus callosum to the fastigium (roof of the fourth ventricle).

(CCF) length is a reliable bedside-available US marker that can be used to monitor brain growth in preterm infants during neonatal intensive care unit stays.<sup>13</sup> CCF length is considered a composite marker of diencephalon and mesencephalon size and thereby adds information to the more widely used corpus callosum (CC) length.<sup>13</sup> We hypothesized that these 2 cranial ultrasound measures are feasible for use during prenatal US examinations. Thereby, these markers would provide a continuum for monitoring brain growth, bridging the period before and after birth.

Our main aim was to investigate whether CC and CCF lengths can be used as reliable US markers for monitoring fetal and neonatal brain growth. First, we assessed the reliability of the measurements. Second, we created reference curves from 22 to 42 weeks' gestational age (GA) by combining fetal and neonatal measurements. Finally, as a first step to evaluate the clinical applicability of these US markers, we investigated CC and CCF growth trajectories in fetuses at risk of abnormal brain growth and compared them with those of control fetuses.

## MATERIALS AND METHODS

### Study Design

This 3D-US study was embedded in the Rotterdam Periconceptional Cohort (Predict Study), an ongoing prospective cohort study at the Department of Obstetrics and Gynecology, Erasmus MC, University Medical Center, Rotterdam, the Netherlands.<sup>14</sup> At enrollment, all participating women and their partners gave written informed consent on behalf of themselves and their unborn child. This study was approved by the regional medical ethical committee and institutional review board of the Erasmus MC, University Medical Center in Rotterdam (MEC 2004-227; date of approval, January 25, 2013).

Pregnant women were enrolled between November 2013 and July 2015. They were either enrolled before 12 weeks' GA or between 22 and 32 weeks' GA. Controls were enrolled before 12 weeks' GA and were defined as fetuses without fetal growth restriction (FGR) before 32 weeks' GA, born after 37 weeks' GA, and without congenital anomalies. Cases included those pregnancies referred to our outpatient clinic with FGR or an isolated fetal congenital heart defect (CHD) between 22 and 32 weeks' GA. The diagnosis was confirmed by an extended structural US examination at our hospital. FGR was defined as abdominal circumference

or estimated fetal weight percentile of  $<5$  according to Hadlock et al.<sup>15</sup>

For this analysis, we excluded pregnancies ending in intrauterine fetal death, termination of pregnancy, or only preterm birth (without FGR or CHD). We also excluded fetuses with congenital anomalies other than CHD, with trisomy 21, and without US images.

### Study Parameters

According to Dutch clinical practice, GA in spontaneously conceived pregnancies was calculated on the basis of the first trimester crown-rump length measurements before 13 weeks' GA.<sup>16</sup> In pregnancies conceived through in vitro fertilization, with or without intracytoplasmic sperm injection procedures, GA was calculated from the date of oocyte retrieval plus 14 days or from the day of embryo transfer plus 17 or 18 days after cryopreserved embryo transfer, depending on the number of days between oocyte retrieval and cryopreservation.

Data were collected on maternal characteristics, medical and obstetric history, pregnancy course, and neonatal outcome from self-administered questionnaires in the first trimester, second trimester, and around delivery. Follow-up data on pregnancy outcomes were validated on the basis of a US report of the routine second trimester anomaly scan and on obstetric medical records.

### Prenatal Sonography

Prenatal 3D-US examinations were performed on the Voluson E8 system (GE Healthcare, Milwaukee, Wisconsin) by using a 1 to 7 MHz transabdominal transducer or a 6 to 12 MHz transvaginal transducer. Primarily, we used an abdominal approach, but a transvaginal approach was considered when the fetus was in a head-down presentation. Serial prenatal 3D-US examinations and measurements were performed at 22, 26, and 32 weeks of gestation by 1 certified sonographer (I.V.K.). Standard biometry was measured, including biparietal diameter, head circumference, abdominal circumference, and femur length. An estimation of fetal weight was calculated with the Hadlock equation.<sup>15</sup> Biometry was followed by detailed 3D neurosonography. Standard planes were obtained according to the International Society of Ultrasound in Obstetrics and Gynecology guidelines.<sup>17</sup> CC and CCF length measurements were performed off-line in an exact midsagittal plane (Fig 1). CC length is measured from the splenium, outer-outer border. CCF length represents the length between the genu of the CC and the fastigium (roof of the fourth ventricle).<sup>13</sup> CCF length was only measured in images in which CC measurement was performed successfully. Manipulation of the 3D-US volume to ensure an exact midsagittal plane for the measurements was performed in 4D View, Version 5.0 (GE Healthcare).

### Postnatal Assessments

After birth, cranial ultrasound was planned between 42 + 0 and 42 + 6 weeks' postmenstrual age, independent of GA at birth.

**Table 1: Baseline characteristics<sup>a</sup>**

Characteristics	Controls (n = 157)	FGR (n = 22)	CHD (n = 20)	Missing
Maternal				
Age at enrollment (yr)	32.3 (21–44)	29.7 (21–41)	33.0 (22–48)	7
Nulliparous	69 (44)	13 (68)	11 (58)	6
Mode of conception (IVF/ICSI)	48 (31)	2 (10)	2 (11)	3
Geographic background				6
Western	126 (81)	15 (79)	18 (90)	
Non-Western	29 (19)	4 (21)	2 (10)	
Educational level				8
Low	20 (13)	4 (20)	0	
Intermediate	56 (36)	12 (60)	7 (39)	
High	79 (51)	4 (20)	11 (61)	
Prepregnancy BMI (kg/m <sup>2</sup> )	22.9 (15.2–39.7)	22.9 (17.6–43.4)	23.4 (18.0–35.8)	19
Periconception folic acid initiation (yes)	149 (96)	15 (79)	18 (95)	6
Periconception smoking (yes)	25 (16)	3 (16)	3 (16)	8
Periconception alcohol consumption (yes)	44 (29)	4 (21)	10 (53)	9
Neonatal				
Birth weight (g)	3345 (2035–4380)	1400 (400–2900)	3420 (1650–4140)	2
Gestational age at birth (wk)	39 <sup>+1</sup> (37 <sup>+0</sup> –41 <sup>+5</sup> )	34 <sup>+2</sup> (26 <sup>+3</sup> –39 <sup>+3</sup> )	38 <sup>+6</sup> (28 <sup>+4</sup> –41 <sup>+5</sup> )	2
Males	82 (52)	11 (50)	13 (65)	0

**Note:**—BMI indicates body mass index; IVF/ICSI, in vitro fertilization with or without intracytoplasmic sperm injection; ICSI, intracytoplasmic sperm injection.

<sup>a</sup>Data are presented as median and range or number and percentage. Missing data were due to incomplete questionnaires.

Cranial ultrasound was performed by an experienced team of researchers with MyLab 70 (Esaote, Genoa, Italy) with a convex neonatal probe (7.5 MHz). CC and CCF length measurements were performed off-line by 1 researcher (J.A.R.) according to the method described above, with MyLab software.

To enhance precision, we repeated all prenatal and postnatal measurements 3 times. The mean values were used in the statistical analyses.

### Statistical Analysis

For data analyses, we used SPSS (Release 21 for Windows; IBM, Armonk, New York) and R statistical and computing software, Version 3.1.3 (<http://www.r-project.org>). Results with *P* values < .05 were considered statistically significant.

Previously, we demonstrated that postnatal measurements of CC and CCF length had good intra- and interobserver agreement.<sup>13</sup> To evaluate the reliability and reproducibility of prenatal measurements, we randomly selected 30 US examinations of 30 different fetuses, equally divided across the 3 prenatal time points from the whole study population. CC and CCF length measurements were then performed in 3-fold by 2 independent observers (I.V.K. [1] and J.A.R. [2]). We performed analyses for intra- and interobserver reliability, calculating the mean differences with 95% CIs and intraclass correlation coefficients. Moreover, the extent of agreement was examined with the Bland-Altman method.

Generalized Additive Models for Location and Scale were used to create reference ranges of CC and CCF length measurements between 22 and 42 weeks' GA in controls.<sup>18</sup> To investigate whether cases showed deviations in CC and CCF growth, we created growth trajectories for each subject of the serial measurements of CC and CCF lengths between 22 and 42 weeks' GA. A maximum-likelihood approach was used to test whether polynomials of GA contributed to the best model fit. In the same manner, we tested the contribution of random and fixed effects of the intercept and slopes for all included polynomials. A quadratic model of GA with random intercept and slopes was designated as

the best model. We placed the origin of the GA scale at 140 days' GA. In this model, the variable indicating whether a fetus was FGR, CHD, or control was used as the covariate of interest (model 1). Last, the final model (model 2) was adjusted for serial measurements of fetal weight and sex.

## RESULTS

### Study Population

In total, 227 pregnant women were enrolled prenatally. After excluding pregnancies ending in intrauterine fetal death (*n* = 1), termination of pregnancy (*n* = 1), preterm birth (*n* = 14), and those with congenital anomalies other than CHD (*n* = 4), trisomy 21 (*n* = 2), and withdrawals (*n* = 6), the study population consisted of 199 pregnancies. Of these 199 fetuses, 22 had FGR, 20 had CHD, and 157 were controls. The general characteristics of the study populations are listed in Table 1.

### Success Rates and Reliability Analyses

Of 542 prenatal 3D-US scans, 377 contained a high-quality midsagittal plane eligible for CC and CCF length measurements. Means and success rates of CC and CCF length measurements per gestational age are listed in Table 2. Success rates ranged between 61% and 75% for prenatal CC length measurements and between 59% and 72% for prenatal CCF length measurements. Postnatally, CC and CCF length measurements were successful in 97%. In 83% of the subjects, CC length was measured at least at 2 time points during the whole study period, and CCF length, in 65%.

The intra- and interobserver reliability and agreement are shown in Table 3. CC lengths measured by observer 1 were slightly smaller (mean difference, −1.109 mm; mean percentage difference, −3.4%) than those measured by observer 2. Ninety-five percent limits of agreement for all measurements represented excellent agreement when the CC and CCF length measurements were repeated by the same observer and good agreement when repeated by a second observer. Intraclass correlation coefficient

values of both intra- and interobserver were  $\geq 0.97$ , which represents excellent reliability.

### Linear Mixed-Model Analyses

In Fig 2A, -B, the reference curves and individual growth trajectories of CC and CCF lengths are shown. The results of the linear mixed-models estimating differences in the mean growth trajectories of CC and CCF lengths among controls and fetuses with FGR and CHD are shown in Table 4. Growth trajectories of CC length were significantly decreased in fetuses with FGR and CHD compared with growth trajectories of controls. CCF growth trajectories were only significantly decreased in fetuses with FGR compared with those of controls. In Fig 2C, these trajectories are graphically displayed.

### DISCUSSION

Here, we demonstrate that CCF and CC length may serve as reliable markers for monitoring prenatal and postnatal brain growth. Fetuses with FGR showed decreased growth of both CC and CCF length, while in fetuses with CHD, only CC growth was decreased between 22 and 42 weeks' GA.

Our findings suggest that we are able to bridge the traditional division between fetal and neonatal US growth charts. To date, studies that combine fetal and neonatal US markers of brain growth in a single cohort are scarce. One explanation is that standard prenatal US planes containing easily recognizable landmarks of the brain do not correspond well with the standardized planes accessible by cranial ultrasound. This lack of correspondence re-

sults in differences in prenatal and postnatal measures and measuring methods. For example, head circumference assessed prenatally, calculated from the biparietal diameter and occipital frontal diameter, correlates poorly with direct postnatal measurements with a tape measure.<sup>7,19</sup> Furthermore, changes in head shape can be induced by delivery (eg, skull molding, edematous swelling, and hematomas).

In contrast to other prenatal US measurements, excellent reliability was shown for CC and CCF lengths, comparable with the reliability of the postnatal measurements.<sup>13</sup> On the basis of our data, we suggest that CCF length is the most reliable and relevant marker for monitoring brain growth. CCF length can be assumed to be a composite marker of multiple brain structures with different embryologic origins. Therefore, CCF length may be a better representative of global brain growth than previous sonographic markers based on individual brain structures.<sup>8-12</sup>

Growth trajectories of CC and CCF length were decreased in fetuses at risk for abnormal brain growth and impaired long-term neurodevelopmental outcome. While studies using CCF length have not been published in the literature before, CC length findings are in line with those in previous literature. The decreased CC growth trajectories in fetuses with FGR are in accordance with findings of a recent MR imaging study that showed significantly reduced CC length in fetuses with FGR compared with CC length of appropriate-for-gestational-age controls.<sup>20</sup> Results from our previous study in preterm infants demonstrated a similar association between CCF length and birth weight SD score.<sup>13</sup> There are, to the best of our knowledge, no publications on CC length in fetuses with CHD with which to compare our results, though previous studies did report anomalies of the CC and reduction of CC volume in children with CHD.<sup>21,22</sup> The decreased growth trajectory of CC length in fetuses with CHD is, however, supported by accumulating evidence reporting that fetuses with CHD are at risk for abnormal brain growth and development.<sup>23-26</sup>

Brain growth is an important predictor of neurodevelopmental outcome.<sup>1,3,27</sup> We hypothesize that the decreased CC and CCF growth trajectories observed in cases may have consequences for long-term outcome. In preterm infants, a shorter CC length is related to a higher risk of an adverse neurodevelopmental outcome at 2 years' corrected age.<sup>4</sup> Moreover, a significantly smaller corpus callosum was found in individuals with schizophrenia and autism.<sup>28,29</sup> CCF length represents the diencephalon and thus includes thalamus development, which is crucial for cognitive functioning. Derangements in thalamus development are associated with adverse neurodevelopmental outcome.<sup>30</sup> Yet, the clinical rele-

**Table 2: Success rates and means of corpus callosum and corpus callosum-fastigium length per gestational age<sup>a</sup>**

Length (mm)/ GA (wk)	US Scans (No.)	Measurements (No.)	Success Rate (%)	Mean (SD) (mm)
CC				
22	166	124	75	26.35 (1.22)
26	188	138	73	34.33 (1.86)
32	188	115	61	41.56 (2.19)
42	143	138	97	48.09 (3.15)
CCF				
22	124	89	72	33.09 (1.61)
26	138	82	59	39.39 (1.92)
32	115	81	70	45.86 (2.07)
42	143	138	97	52.26 (3.12)

<sup>a</sup> Presented are the success rates, means, and corresponding SD values of the CC and CCF measurements per full week of gestation. The success rates for CC length and postnatal CCF length were calculated by the number of successful measurements divided by the total number of US images. Success rates of prenatal CCF measurements were calculated by dividing the number of successful CCF measurements by the number of midsagittal images eligible for CC length.

**Table 3: Intraobserver and interobserver reliability for prenatal measurements of corpus callosum and corpus callosum-fastigium length<sup>a</sup>**

	Absolute Difference			Relative Difference			ICC
	Mean Difference (mm)	95% CI Mean Difference (mm)	P	95% Limits of Agreement (mm)	Mean Difference (%)	95% Limits of Agreement (%)	
Intraobserver							
CC	0.011	-0.228 to 0.250	.923	-1.373, 1.396	0.1	-4.1, 4.3	>0.99
CCF	0.180	-0.157 to 0.517	.284	-1.711, 2.071	0.4	-4.7, 5.4	>0.99
Interobserver							
CC	-1.109	-1.702 to -0.515	.001	-4.546, 2.329	-3.4	-14.9, 8.1	0.97
CCF	-0.125	-0.741 to 0.492	.684	-3.589, 3.340	-0.4	-9.5, 8.6	0.97

**Note:**—ICC indicates intraclass correlation coefficient.

<sup>a</sup> Intra- and interobserver reliability analyses for prenatal CC and CCF measurements in a random selection of 30 ultrasound scans.

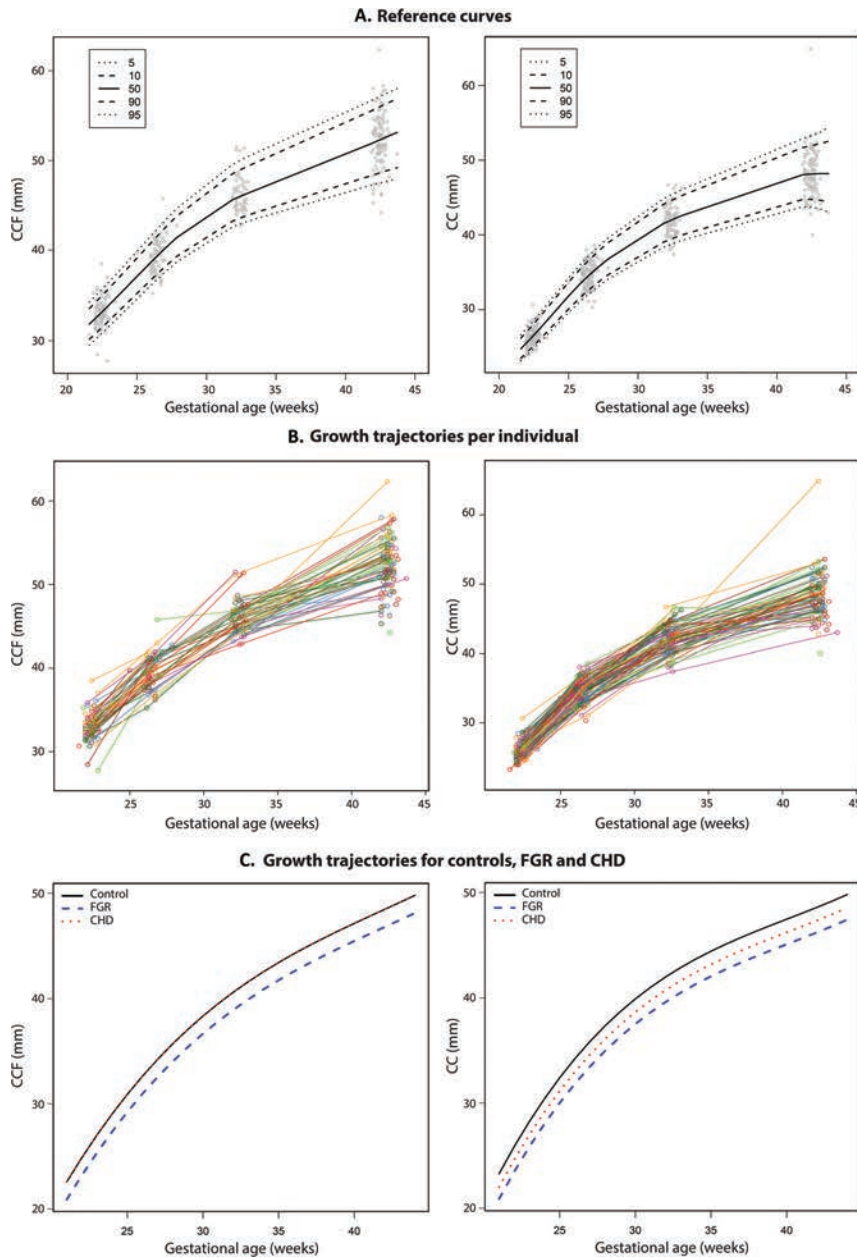


**FIG 2.** Growth curves. A, Reference curves between 22 and 42 weeks of gestation for CCF (left) and CC (right) length, with the 5th, 10th, 50th, 90th, and 95th percentiles. B, Individual growth trajectories of CCF (left) and CC (right) length between 22 and 42 weeks of gestation. C, Growth trajectories for controls (black) and fetuses with FGR (striped blue) and CHD (dotted red).

**Table 4: Linear mixed models—growth trajectories of CC and CCF influenced by the presence of fetal growth restriction and congenital heart defects<sup>a</sup>**

	Model 1			Model 2		
	$\beta$	95% CI	P Value	$\beta$	95% CI	P Value
CC						
FGR	-2.384	-3.26 to -1.505	<.01 <sup>b</sup>	-2.295	-3.320 to -1.270	<.01 <sup>b</sup>
CHD	-1.252	-1.954 to -0.549	<.01 <sup>b</sup>	-1.267	-1.972 to -0.562	<.01 <sup>b</sup>
CCF						
FGR	-1.413	-2.500 to -0.326	.01 <sup>b</sup>	-1.295	-2.595 to 0.003	.05
CHD	0.012	-0.829 to 0.963	.98	0.000	-0.835 to 0.835	.99

<sup>a</sup> Data are presented in  $\beta$  values with corresponding 95% CI and P values, compared with controls. Model 1 represents the crude model with GA and its polynomials as predictor and type of case as covariate of interest. Model 2 is the fully adjusted model for the covariates in model 1 and for serial measurements of fetal weight and sex.

<sup>b</sup> Significant.

vance for neurodevelopmental outcome of differences in CC and CCF growth trajectories needs further investigation.

### Clinical Applicability

The landmarks used for CC and CCF length measurements are relatively easy to distinguish on US images. Prenatally, the main challenge is obtaining an exact midsagittal plane. The prenatal success rates are predominantly influenced by acoustic shadowing and the position of the fetus. 3D-US can enhance precision by manipulating volumes to reconstruct the exact midsagittal plane.<sup>31-33</sup> When a midsagittal plane is obtained, both measurements take <1 minute in experienced hands. Postnatally, a standard midsagittal plane is easy to obtain through the anterior fontanelle; also, the off-line measurements of CC and CCF lengths take <1 minute. Newly developed software that enables the identification of the midline automatically could still improve the measurements for clinical practice.<sup>34</sup>

### Strengths and Limitations

Some considerations should be taken into account. First, our study was conducted in a tertiary hospital population, with a relatively high maternal age, mainly of Western origin, and a high educational level. Therefore, replication of the data is warranted to validate our findings for the general population. Second, the small number of cases limits the conclusions of our study. We cannot exclude that absence of statistically significant findings may be due to lack of power. Third, the growth charts are based on measurements at 4 time points and may improve by including intermediate time points to further smooth the curves. Finally, the US scans and measurements were performed by experienced observers, which potentially enhanced the quality of the midsagittal images and thus success rates and reliability. Clinical applicability may be overestimated as a consequence. Success rates of the measurements were mostly influenced by fetal position, which we assume to be independent of the variables in this study. We consider the prospective and longitudinal study design as a strength of our study. Combining prenatal and postnatal measurements in

1 reference curve is an innovative method to facilitate monitoring of fetuses at risk of impaired brain growth.

### Future Implications for Clinical Care and Research

Tight collaboration between obstetric and neonatal researchers and caregivers is needed for bridging the gap when monitoring fetal and neonatal brain growth. This is of great importance for optimizing neurodevelopmental care in fetuses and infants at risk of abnormal brain growth and neurodevelopmental impairment. Easily applicable US tools that can be used independent of the prenatal or postnatal period will have clinical implications. We consider our reference curves useful for age-equivalent preterm infants because they are largely comparable with the postnatal reference curves between 24 and 32 weeks in preterm infants from Roelants et al.<sup>13</sup> In addition, CC and CCF length measurements may be applicable from midgestation onward and may theoretically be prolonged until closure of the anterior fontanelle in the first year of life. Future research should correlate these measurements to commonly used MR imaging markers and explore the link between the growth measures and functional neurodevelopmental outcome.

### CONCLUSIONS

In this prospective cohort, we demonstrated that CC and CCF length measurements are reliable markers for brain growth from the fetal into the early neonatal period. By combining prenatal and postnatal CC and CCF length measurements in 1 reference curve, we created a continuum for monitoring brain growth, irrespective of the intra- or extra-uterine environment. We demonstrated that fetuses at risk of abnormal brain growth (ie, those with CHD and FGR) showed significantly decreased CC and CCF growth between 22 and 42 weeks' GA. Whether these markers could serve as early predictors of neurodevelopmental outcome in later life warrants further research.

### ACKNOWLEDGMENTS

We thank the Department of Obstetrics and Gynecology, Division of Obstetrics and Prenatal Medicine, Erasmus MC, University Medical Center, and the research group of the Rotterdam Predict study for their contribution to the study.

Disclosures: Irene V. Koning—RELATED: Grant: Sophia Foundation for Medical Research, Comments: grant No. 644.

### REFERENCES

1. Young JM, Powell TL, Morgan BR, et al. **Deep grey matter growth predicts neurodevelopmental outcomes in very preterm children.** *Neuroimage* 2015;111:360–68 CrossRef Medline
2. Lee W, Al-Dossary H, Raybaud C, et al. **Longitudinal cerebellar growth following very preterm birth.** *J Magn Reson Imaging* 2016;43:1462–73 CrossRef Medline
3. Stiles J, Jernigan TL. **The basics of brain development.** *Neuropsychol Rev* 2010;20:327–48 CrossRef Medline
4. Park HW, Yoon HK, Han SB, et al. **Brain MRI measurements at a term-equivalent age and their relationship to neurodevelopmental outcomes.** *AJNR Am J Neuroradiol* 2014;35:599–603 CrossRef Medline
5. van Uitert EM, Exalto N, Burton GJ, et al. **Human embryonic growth trajectories and associations with fetal growth and birthweight.** *Hum Reprod* 2013;28:1753–61 CrossRef Medline
6. Kan E, Roberts G, Anderson PJ, et al. **The association of growth impairment with neurodevelopmental outcome at eight years of age in very preterm children.** *Early Hum Dev* 2008;84:409–16 CrossRef Medline
7. Sutter K, Engstrom JL, Johnson TS, et al. **Reliability of head circumference measurements in preterm infants.** *Pediatr Nurs* 1997;23:485–90 Medline
8. Anderson NG, Laurent I, Cook N, et al. **Growth rate of corpus callosum in very premature infants.** *AJNR Am J Neuroradiol* 2005;26:2685–90 Medline
9. Imamoglu EY, Gursoy T, Ovali F, et al. **Nomograms of cerebellar vermis height and transverse cerebellar diameter in appropriate-for-gestational-age neonates.** *Early Hum Dev* 2013;89:919–23 CrossRef Medline
10. Hagmann CF, Robertson NJ, Acolet D, et al. **Cerebral measurements made using cranial ultrasound in term Ugandan newborns.** *Early Hum Dev* 2011;87:341–47 CrossRef Medline
11. Maunu J, Parkkola R, Rikalainen H, et al. **Brain and ventricles in very low birth weight infants at term: a comparison among head circumference, ultrasound, and magnetic resonance imaging.** *Pediatrics* 2009;123:617–26 CrossRef Medline
12. Rademaker KJ, Lam JN, Van Haastert IC, et al. **Larger corpus callosum size with better motor performance in prematurely born children.** *Semin Perinatol* 2004;28:279–87 CrossRef Medline
13. Roelants JA, Koning IV, Raets MM, et al. **A new ultrasound marker for bedside monitoring of preterm brain growth.** *AJNR Am J Neuroradiol* 2016;37:1516–22 CrossRef Medline
14. Steegers-Theunissen RP, Verheijden-Paulissen JJ, van Uitert EM, et al. **Cohort profile: the Rotterdam Periconceptual Cohort (Predict Study).** *Int J Epidemiol* 2016;45:374–81 CrossRef Medline
15. Hadlock FP, Harrist RB, Sharman RS, et al. **Estimation of fetal weight with the use of head, body, and femur measurements: a prospective study.** *Am J Obstet Gynecol* 1985;151:333–37 CrossRef Medline
16. Robinson HP, Fleming JE. **A critical evaluation of sonar “crown-rump length” measurements.** *Br J Obstet Gynaecol* 1975;82:702–10 CrossRef Medline
17. Merz E, Benoit B, Blaas HG, et al; ISUOG 3D Focus Group. **Standardization of three-dimensional images in obstetrics and gynecology: consensus statement.** *Ultrasound Obstet Gynecol* 2007;29:697–703 CrossRef Medline
18. Rigby RA, Stasinopoulos DM. **Generalized additive models for location, scale and shape (with discussion).** *J R Stat Soc Ser C Appl Stat* 2005;54:507–44 CrossRef
19. Melamed N, Yogev Y, Danon D, et al. **Sonographic estimation of fetal head circumference: how accurate are we?** *Ultrasound Obstet Gynecol* 2011;37:65–71 CrossRef Medline
20. Egaña-Ugrinovic G, Sanz-Cortés M, Couve-Pérez C, et al. **Corpus callosum differences assessed by fetal MRI in late-onset intrauterine growth restriction and its association with neurobehavior.** *Prenat Diagn* 2014;34:843–49 CrossRef Medline
21. Mlczech E, Brugger P, Ulm B, et al. **Structural congenital brain disease in congenital heart disease: results from a fetal MRI program.** *Eur J Paediatr Neurol* 2013;17:153–60 CrossRef Medline
22. von Rhein M, Buchmann A, Hagmann C, et al. **Brain volumes predict neurodevelopment in adolescents after surgery for congenital heart disease.** *Brain* 2014;137:268–76 CrossRef Medline
23. Khalil A, Suff N, Thilaganathan B, et al. **Brain abnormalities and neurodevelopmental delay in congenital heart disease: systematic review and meta-analysis.** *Ultrasound Obstet Gynecol* 2014;43:14–24 CrossRef Medline
24. Jansen FA, Everwijn SM, Scheepjens R, et al. **Fetal brain imaging in isolated congenital heart defects – a systematic review and meta-analysis.** *Prenat Diagn* 2016;36:601–13 CrossRef Medline
25. Masoller N, Martinez JM, Gómez O, et al. **Evidence of second-trimester changes in head biometry and brain perfusion in fetuses with congenital heart disease.** *Ultrasound Obstet Gynecol* 2014;44:182–87 CrossRef Medline
26. Williams IA, Fifer WP, Andrews H. **Fetal growth and neurodevelop-**

- mental outcome in congenital heart disease.** *Pediatr Cardiol* 2015; 36:1135–44 CrossRef Medline
27. Henrichs J, Schenk JJ, Barendregt CS, et al. **Fetal growth from mid- to late pregnancy is associated with infant development: the Generation R Study.** *Dev Med Child Neurol* 2010;52:644–51 CrossRef Medline
  28. Piven J, Bailey J, Ranson BJ, et al. **An MRI study of the corpus callosum in autism.** *Am J Psychiatry* 1997;154:1051–56 CrossRef Medline
  29. Woodruff PW, McManus IC, David AS. **Meta-analysis of corpus callosum size in schizophrenia.** *J Neurol Neurosurg Psychiatry* 1995;58: 457–61 CrossRef Medline
  30. Eaton-Rosen Z, Melbourne A, Orasanu E, et al. **Longitudinal measurement of the developing thalamus in the preterm brain using multi-modal MRI.** *Med Image Comput Comput Assist Interv* 2014;17: 276–83 Medline
  31. Monteagudo A, Timor-Tritsch IE, Mayberry P. **Three-dimensional transvaginal neurosonography of the fetal brain: ‘navigating’ in the volume scan.** *Ultrasound Obstet Gynecol* 2000;16:307–13 CrossRef Medline
  32. Mueller GM, Weiner CP, Yankowitz J. **Three-dimensional ultrasound in the evaluation of fetal head and spine anomalies.** *Obstet Gynecol* 1996;88:372–78 CrossRef Medline
  33. Wang PH, Ying TH, Wang PC, et al. **Obstetrical three-dimensional ultrasound in the visualization of the intracranial midline and corpus callosum of fetuses with cephalic position.** *Prenat Diagn* 2000; 20:518–20 Medline
  34. Yaqub M, Rueda S, Kopuri A, et al. **Plane localization in 3-D fetal neurosonography for longitudinal analysis of the developing brain.** *IEEE J Biomed Health Inform* 2016;20:1120–28 CrossRef Medline

# Analysis of 30 Spinal Angiograms Falsely Reported as Normal in 18 Patients with Subsequently Documented Spinal Vascular Malformations

P. Barreras, D. Heck, B. Greenberg, J.-P. Wolinsky, C.A. Pardo, and P. Gailloud



## ABSTRACT

**BACKGROUND AND PURPOSE:** The early diagnosis of spinal vascular malformations suffers from the nonspecificity of their clinical and radiologic presentations. Spinal angiography requires a methodical approach to offer a high diagnostic yield. The prospect of false-negative studies is particularly distressing when addressing conditions with a narrow therapeutic window. The purpose of this study was to identify factors leading to missed findings or inadequate studies in patients with spinal vascular malformations.

**MATERIALS AND METHODS:** The clinical records, laboratory findings, and imaging features of 18 patients with spinal arteriovenous fistulas and at least 1 prior angiogram read as normal were reviewed. The clinical status was evaluated before and after treatment by using the Aminoff-Logue Disability Scale.

**RESULTS:** Eighteen patients with 19 lesions underwent a total of 30 negative spinal angiograms. The lesions included 9 epidural arteriovenous fistulas, 8 dural arteriovenous fistulas, and 2 perimedullary arteriovenous fistulas. Seventeen patients underwent endovascular (11) or surgical (6) treatment, with a delay ranging between 1 week and 32 months; the Aminoff-Logue score improved in 13 (76.5%). The following factors were identified as the causes of the inadequate results: 1) lesion angiographically documented but not identified (55.6%); 2) region of interest not documented (29.6%); or 3) level investigated but injection technically inadequate (14.8%).

**CONCLUSIONS:** All the angiograms falsely reported as normal were caused by correctible, operator-dependent factors. The nonrecognition of documented lesions was the most common cause of error. The potential for false-negative studies should be reduced by the adoption of rigorous technical and training standards and by second opinion reviews.

**ABBREVIATIONS:** PmAVF = perimedullary arteriovenous fistula; SDAVF = spinal dural arteriovenous fistula; SEAVF = spinal epidural arteriovenous fistula

Spinal vascular malformations can be subdivided into high-flow and low-flow lesions. The high-flow group includes spinal arteriovenous malformations and prominent perimedullary arteriovenous fistulas (PmAVF, Merland type 2 and 3<sup>1</sup>). The low-flow group is principally made of spinal dural (SDAVF) and spinal epidural arteriovenous fistulas (SEAVF) as well as less common small PmAVFs (Merland type 1). Although the detection of fast-flow lesions is generally straightforward with noninvasive imaging because of the large size of the vessels involved, low-flow anomalies—which are more frequent—can represent a major

diagnostic challenge. Low-flow arteriovenous fistulas typically occur in older men presenting with a venous hypertensive myelopathy secondary to the drainage of the fistula into the perimedullary venous system.<sup>2-5</sup> They are characterized by progressive courses and narrow therapeutic windows, yet their diagnoses are often established with considerable delay, if at all.<sup>5</sup> This situation is in large part related to their nonspecific clinical presentations and the ambiguous noninvasive imaging characteristics of venous hypertensive myelopathy. Spinal DSA, the “gold standard” technique for the investigation of spinal vascular anomalies, remains necessary to identify and characterize these lesions. Modern spinal DSA is associated with extremely low risks of neurologic or systemic complications,<sup>6</sup> but it is a technically demanding procedure that requires a methodical approach to offer a high diagnostic yield.

This article analyzes the clinical and imaging characteristics of 18 patients with proved spinal vascular malformations but initial angiographic investigation reported as normal. The purpose of this review was to identify the factors that led to missed findings or

Received December 30, 2016; accepted after revision April 24, 2017.

From the Transverse Myelitis Center, Department of Neurology (P.B., C.A.P.), Division of Interventional Neuroradiology (D.H., P.G.), and Department of Neurosurgery (J.-P.W.), The Johns Hopkins Hospital, Baltimore, Maryland; and Transverse Myelitis Center (B.G.), University of Texas Southwestern Medical Center, Dallas, Texas.

Please address correspondence to Philippe Gailloud, MD, Johns Hopkins University School of Medicine, 1800 E Orleans St, Bloomberg Building Room 7216, Baltimore, MD 21287; e-mail: phg@jhmi.edu

<http://dx.doi.org/10.3174/ajnr.A5275>

inadequate studies and propose strategies aimed at reducing their impact.

## MATERIALS AND METHODS

This is a retrospective study including 18 patients treated at our institution (The Johns Hopkins Hospital) between August 2009 and April 2016 for a vascular malformation and having at least 1 initial spinal angiogram read as normal. The final angiographic study unequivocally documenting the vascular malformation was performed by the senior author (P.G.) in all cases; the procedures were all performed under conscious sedation. The negative studies were reviewed and classified by 2 authors who were both aware of the final angiographic diagnoses (P.B., P.G.). In situations combining multiple sources of error, the visibility of the lesion was used as the dominant criterion to categorize the cause of the erroneous result. In case 15 for example, the quality of the angiographic image was reduced by the nonselective nature of the injection, yet the lesion was documented; this case was classified as a documented but not identified lesion.

Seventeen patients had their vascular malformations treated, including 1 patient with 2 separate anomalies, whereas 1 lesion

**Table 1: Aminoff-Logue Disability Scale**

Disturbances of Gait	
1.	Leg weakness, abnormal stance, or gait without restriction of locomotor activity
2.	Restricted exercise tolerance
3.	Requires stick or some support for walking
4.	Requires crutches or 2 sticks for walking
5.	Unable to stand, confined to bed or wheelchair
Micturition	
1.	Mild: hesitancy, urgency, or frequency
2.	Moderate: occasional incontinence or retention
3.	Severe: total incontinence or persistent retention
Bowel	
1.	Mild: constipation
2.	Moderate: occasional incontinence or severe constipation
3.	Persistent fecal incontinence

spontaneously resolved without intervention. The clinical status of each patient was evaluated before treatment and at the last follow-up visit by using the Aminoff-Logue Disability Scale based on data gathered retrospectively from chart review (Table 1).<sup>7</sup> Updated follow-up information was obtained by telephone interviews. The difference between the mean pre- and posttreatment Aminoff-Logue scores was calculated by using a standard Student *t* test. A *P* value <.05 was used to define statistical significance.

Besides the presence of an abnormal medullary signal on T2-weighted images, 2 additional MR imaging characteristics were recorded: the presence of parenchymal enhancement after gadolinium administration and flow voids on T2-weighted images, categorized as absent (−), subtle (+), focal (++) , or diffuse (+++) (Fig 1).

## RESULTS

### Demographic and Clinical Features

We found 18 patients with 19 angiographically confirmed spinal vascular malformations and at least 1 angiographic study read as normal, for a total of 30 negative angiograms (median, 1; average, 1.7; range, 1–6) (Table 2). The cohort included 15 men and 3 women, aged from 25–89 years. Most patients were men (83%) with an average age of 63 years at the time of presentation. Past medical history—available for all patients—included cardiovascular risk factors, notably arterial hypertension in 12 cases (67%) and smoking in 11 cases (61%).

The following symptoms and clinical features were recorded in the patients' charts: leg weakness (*n* = 17; 94%), leg numbness (*n* = 12; 67%), bladder dysfunction (*n* = 12; 67%), neurogenic claudication (*n* = 7; 39%), abnormal sensory examination (*n* = 16; 89%), and a sensory level noted in 11 cases (61%). Urinary retention and/or decreased rectal tone was noted in 7 cases (39%). The beginning of clinical manifestation according to the chart was greater than 21 days in 15 patients (83%), less than 48 hours in 1 (5%), and acute in 2 (11%).

The CSF—collected in 14 patients—showed elevated protein (>45 mg/dL) in 11 patients (79%) and pleocytosis (>5 cells/mm<sup>3</sup>) in 5 (36%).

The initial diagnosis was transverse myelitis in 15 cases (83%). Of the 13 patients initially treated with IV methylprednisolone, 1 improved (8%), 7 showed no response (54%), and 5 experienced immediate and substantial clinical worsening (38%).

### Noninvasive Imaging Characteristics

MR imaging documented a myelopathy extending over at least 4 vertebral levels, with a central pattern of abnormal signal involving the thoracic and/or lumbar spinal cord in all patients. Enhancement after the gadolinium injection was noted in 15 cases (83%). Flow voids were present in 11 cases (61%). They were focal

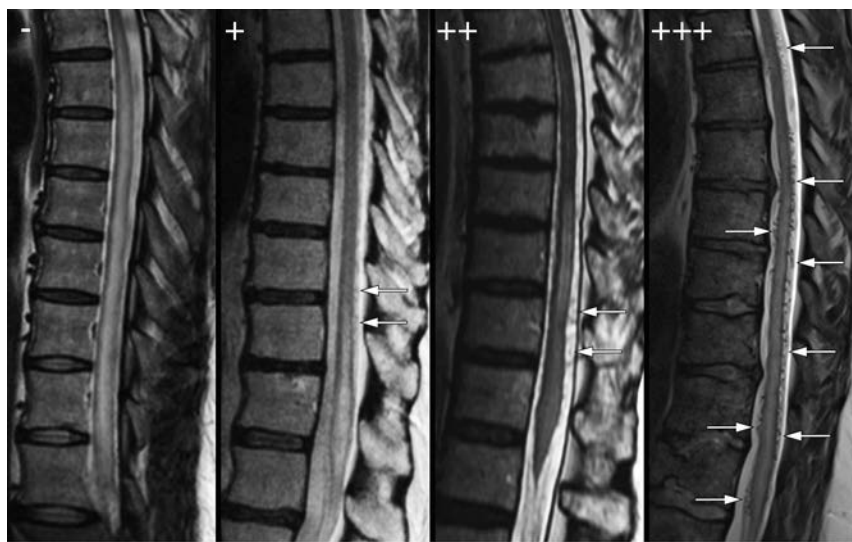


**FIG 1.** Grading of flow voids on sagittal T2-weighted images (−, +, ++, +++). *Left*, 50-year-old man (patient 2) with a left L5 SDAVF. *Center left*, 73-year-old man (patient 8) with a left L4 SEAVF. *Center right*, 75-year-old man (patient 10) with a right T12 SDAVF. *Right*, 49-year-old man (patient 12) with a right S2 SDAVF.

**Table 2: Imaging and treatment characteristics**

Case	Age/Sex	Gad	Flow Voids	Initial Diagnosis	Negative DSA	Final Diagnosis	Loc <sup>a</sup>	Treat	Aminoff-Logue Score	
									Pre	Post
1	40/M	+	—	TM	2	SEAVF	T9	Surg	8	6
2	50/M	+	—	TM	2	SDAVF	L5	Endo	8	8
3	73/M	+	+	TM	1	SDAVF	L4	Endo	8	5
4	80/M	+	++	TM	2	SEAVF	L5	Endo	9	7
5	60/M		+	TM	1	SDAVF	T4	Endo	9	8
6 <sup>b</sup>	56/F	+	+	TM	1	SEAVFs	L2	Endo	10	8
							L4	Endo		
7	89/M		—	Tumor	1	SEAVF	S1	Endo	3	1
8	73/F	+	—	TM	1	SEAVF	L4	Endo	10	5
9	58/M	+	+	TM	1	PmAVF	T10	Surg	10	10
10	75/M	+	++	TM	1	SDAVF	T12	Endo	10	7
11	75/M	+	—	TM	3	SDAVF	L3	Surg	8	9
12	49/M	+	++	TM	6	SDAVF	S2	Endo	6	4
13	69/M		—	TM	2	SEAVF	L5	Endo	11	11
14	56/M	+	++	Syrinx	1	PmAVF	T8	Surg	5	1
15	66/F	+	—	TM	1	SDAVF	T10	Endo	11	7
16	71/M		+	TM	2	SEAVF	S1	None	10	None
17	61/M	+	—	NMO	1	SDAVF	T4	Surg	9	6
18	25/M	+	++	TM	1	SEAVF	T12	Surg	11	4

**Note:**—Endo indicates endovascular; Gad, spinal cord enhancement after gadolinium; Loc, lesion location; NMO, neuromyelitis optica; Pre, pretreatment; Post, posttreatment; Surg, surgery; TM, transverse myelitis; Treat, treatment.

<sup>a</sup> For the 2 PmAVFs, the indicated level corresponds to the feeding artery.

<sup>b</sup> Patient 6 had 2 separate SEAVFs treated in separate endovascular procedures.

(++) in 4 cases (22%) and diffuse (+++) in 2 (11%). Subtle flow voids (+) were retrospectively observed in 5 instances (28%), but reported only once.

### Vascular Malformation Characteristics

All the lesions were low-flow arteriovenous fistulas, including 9 SEAVFs (47%), 8 SDAVFs (42%), and 2 PmAVFs (Merland Type 1; 1%) (Table 2). No spinal arteriovenous malformation or prominent PmAVF (Merland Type 2 or 3) was observed. The delay between presentation and treatment ranged between 1 week and 32 months (median, 9.0; average, 11.1).

Both PmAVFs were located on the anterior aspect of the tip of the conus medullaris and were supplied by the anterior spinal artery via anterior radiculomedullary arteries originating from a thoracic intersegmental artery (T8 and T10, respectively). The SDAVF/SEAVFs were thoracic (T2 through T12) ( $n = 6$ ; 35.3%), lumbar (L1 through L5) ( $n = 8$ ; 47.1%), or sacral (S1 through S2) ( $n = 3$ ; 17.6%). Nine of these 17 lesions (52.9%) were located at L4 or below, including 6 supplied either by an iliolumbar artery ( $n = 3$ ) or by a lateral sacral artery branch ( $n = 3$ ).

Eighteen of the 19 lesions were treated either endovascularly ( $n = 12$ ; 66.7%) or surgically ( $n = 6$ ; 33.3%). One patient had 2 separate SEAVFs; another patient had a pelvic SEAVF that thrombosed spontaneously.

After treatment, the clinical condition measured by the Aminoff-Logue scale improved in 13 of the 17 patients (76.5%), with an average gain of 3 points ( $P = .01$ ) (Table 2). Three patients were unchanged (17.6%), and 1 got worse immediately after surgery, likely as a result of spinal venous thrombosis. Of note, 5 patients reported a subjective improvement in their pain level as well as increased sensation in previously numb areas, 2 elements not captured by the Aminoff-Logue scale. The patient with the spontaneously thrombosed lesion showed no clinical improvement.

### Analysis of Missed Findings or Inadequate Studies

Thirty spinal angiograms falsely reported as normal were obtained in 18 patients (median, 1; average, 1.7; range, 1–6), 26 of them performed in various academic centers (86.7%). Twenty-seven of these angiograms were available for review. The factors identified as the cause of the missed findings or inadequate studies could be categorized as follows:

1) The lesion was angiographically documented but not identified ( $n = 15$ ; 55.6%). In some instances, the anomaly went unnoticed (Fig 2), whereas in others, the abnormal vessel was seen but misinterpreted (Fig 3).

2) The region of interest was not documented ( $n = 8$ ; 29.6%), including: a) the level of interest was not investigated ( $n = 7$ ; 25.9%), the lesion being located at or below L3 in all instances (L3 = 1, L4 = 2, L5 = 3, S2 = 1); or b) the level was accidentally skipped ( $n = 1$ ; 3.7%).

3) The level was investigated, but the injection was technically inadequate ( $n = 4$ ; 14.8%). In 3 cases, the supplying branch was not studied selectively (Fig 4), whereas in 1 of the 2 PmAVFs, the anterior spinal artery was well opacified, but the lesion was not included in the field-of-view.

As noted earlier, in situations combining multiple technical and/or cognitive factors, the lesion's visibility was used as the dominant criterion to categorize the cause of the false-negative study.

## DISCUSSION

### Patient Demographics and Type of Vascular Malformations

This report analyzed 30 spinal angiograms read as normal in 18 patients later diagnosed with a spinal vascular malformation. All of the lesions diagnosed were slow-flow vascular malformations; besides 2 small PmAVFs (Merland Type 1; 10%) located at the conus medullaris, they were either SEAVFs or SDAVFs. This finding is not surprising because the detection of conspicuous anom-

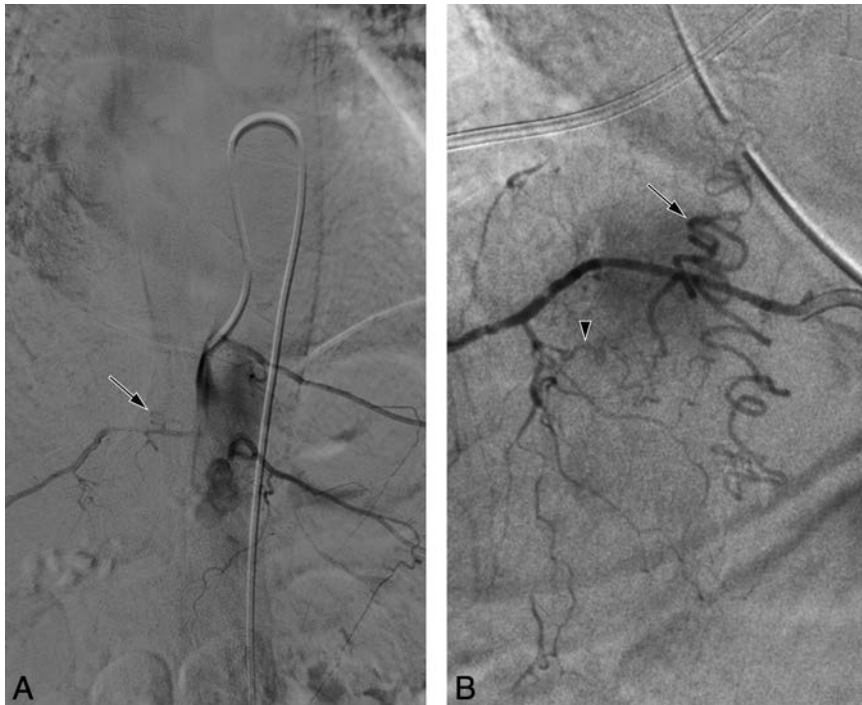


**FIG 2.** 66-year-old woman (patient 15) with a right T10 SDAVF and 1 prior negative spinal angiogram. *A*, DSA, nonselective injection at the T9 level, posteroanterior view, arterial phase (first study). The right T10 intersegmental artery supplies an arteriovenous shunt with early opacification of perimedullary venous structures (*arrow*). The anomaly was not detected. *B*, DSA, right T10 injection, posteroanterior view, arterial phase (second study). Selective angiography confirms the presence of an SDAVF fed by the right T10 radicular artery (*arrowhead*) and documents its extensive perimedullary drainage (*arrow*).



**FIG 3.** 60-year-old man (patient 5) with a right T4 SDAVF and 1 prior negative angiogram. The patient consulted for a second opinion after substantial clinical peioration during intravenous steroid therapy. *A*, DSA, right T4 injection, posteroanterior view, arterial phase (first study). A midline vessel (*arrows*) was noted but interpreted as being the anterior spinal artery. *B*, DSA, right T4 injection, posteroanterior view, arterial phase (second study). A right T4 radiculomeningeal branch (*white arrowhead*) supplies an arteriovenous shunt draining into a posterior radiculomedullary vein (*black arrowhead*) and the posterior-median spinal vein (*black arrows*).

alies such as spinal arteriovenous malformations or PmAVFs (Merland Type 2 or 3) does not usually represent a challenge for noninvasive imaging, spinal DSA being then used to characterize their angioarchitecture and plan their management.

Our patients' demographic characteristics (predominantly older men) are consistent with previously published data on slow-flow vascular malformations.<sup>5</sup> From a diagnostic perspective, the high prevalence of elevated CSF proteins (79%) and gadolinium enhancement on MR imaging (83%) probably explains the frequent misdiagnosis of transverse myelitis (83%).<sup>8</sup> Flow voids, often considered as essential to the diagnosis of vascular malformation, were retrospectively detected in 11 cases (61%) but, because of their subtle nature, were correctly identified at the time of initial MR imaging interpretation in only 7 cases (39%).

Of particular interest is the preponderance of low lumbar and sacral lesions in our cohort; most of the missed SEAVFs/SADVFs (52.9%) were found at or below the L4 level. Besides certain technical considerations discussed separately, this finding seems to correlate with the relatively common misconception that a thoracic myelopathy cannot be accounted for by a pelvic lesion.

In terms of functional outcome, it is important to note that despite the significantly delayed diagnosis (11 months on average) and the clinical worsening caused in some cases by inadequate initial measures (notably steroid therapy), patients did still significantly benefit from the treatment of their vascular malformation. First and foremost, the progressive clinical deterioration typically associated with venous hypertensive myelopathy was stopped in all cases but 1, the exception being a patient who got worse shortly after treatment, likely from spinal venous thrombosis. Besides stopping the disease progression, endovascular or surgical therapy was able to bring a functional improvement in 13 of the 17 patients treated, with a significant difference retrospectively noted between the pre- and posttreatment Aminoff-Logue scores retrospectively (mean follow-up, 20 months;  $P = .012$ ). This finding is consistent with the previously



**FIG 4.** 75-year-old man (patient 11) with a right L3 spinal dural arteriovenous fistula (SDAVF) and 3 prior negative angiograms. *A*, DSA, nonselective injection at the level of L3, posteroanterior view, arterial phase (first study), showing no evidence of vascular malformation. In 1 of the other negative angiograms, L3 was not investigated at all, and the third study was not available for review. *B*, DSA, right L3 injection, posteroanterior view, arterial phase (second study), an arteriovenous shunt supplied by a right L3 radiculomeningeal branch and draining into a right L3 radiculomedullary vein (*arrowheads*). *C*, DSA, right L3 injection, posteroanterior view, arterial phase (second study). The congested perimedullary venous system surrounding the lumbosacral spinal cord is documented by this acquisition with a larger field of view.

held view that even patients with severe disabilities can show significant improvement.<sup>9</sup>

#### **Technical Factors Leading to Missed Findings or Inadequate Studies**

This review identified several factors behind the missed findings or inadequate results. All were operator-dependent and potentially avoidable. The principal cause of missed diagnoses was a documented yet unrecognized lesion (55.6%). In other words, the anomaly was visible in the recorded images, but not identified as a vascular malformation. The same mechanism was responsible for false-negative studies in 3 additional cases of SDAVFs not included in our cohort because of a lack of detailed clinical information. This finding serves as a strong reminder of the complexity of spinal angiographic images, considering notably that most studies (86.7%) were obtained in academic centers.

The vessel of interest not being investigated was the second most frequent cause of inadequate study (29.6%). In 1 case, the vertebral levels were mislabeled and the feeding artery skipped by mistake. In the other 7 instances (25.9%), the intersegmental artery supplying the lesion was not included in the planned angiogram. Interestingly, the lesion was located at or below L3 in all of these cases. This finding has an important implication besides the fact that low lumbar or sacral vascular malformations are frequent; it suggests that low lumbar and pelvic vessels are often ignored during spinal angiography. Although this may be partly attributed to the technically more demanding catheterization of these branches, notably in older patients, the main reason behind this disregard appears to be the misconception that a pelvic flush angiogram supplemented by selective internal iliac injections is not an integral component of a full spinal angiogram. In our practice, spinal DSA performed in older patients with a suspicion of

low-flow vascular malformation starts with a pelvic flush angiogram, which not infrequently establishes the diagnosis during the first few minutes of the procedure. Finally, in 4 cases (14.8%), the vessel of interest was investigated, but the angiograms were technically inadequate. In 1 of the PmAVFs, the feeding artery (left T10) was injected, but considered as normal, and the conus medullaris (site of the lesion) was not included in the field of view. In the other 3 instances, the feeding vessels were studied with nonselective injections, the small amount of contrast passing through the vessel of interest being considered of diagnostic value. In each case, a lesion was subsequently identified by selective angiography.

#### **How to Limit the Risk of Inadequate Spinal Angiograms?**

Our findings suggest that missed findings or inadequate studies might be avoided in most cases by the adoption of a rigorous angiographic protocol. The following recommendations—easily implementable in daily angiographic practices—should significantly reduce the risk of false-negative studies:

1) Carefully identify the vertebral levels investigated at the beginning of the procedure. Although the use of a ruler is in our opinion mandatory, it may not prevent skipping a level if one does not meticulously document the progress of the study and record the explored branches.

2) Avoid, as much as possible, poor angiographic visualization related to nonselective injections.<sup>10</sup> It is also critical to document radiculomedullary arteries in their entirety, as exemplified by the PmAVF left out of the field of view during the injection of the artery of Adamkiewicz in 1 of the negative angiograms.

3) In most instances, it is necessary to perform a complete spinal angiogram—even if a lesion has already been documented—including the pelvis and the cervical region and, in selected cases, the carotid arteries as well. There is no strict correlation between the site of an arteriovenous fistula and the location and extent of the resulting spinal cord damage. A cervical SDAVF can, for example, induce midthoracic or lumbar cord edema with a normal MR imaging appearance of the cervical and upper thoracic spinal parenchyma. The potential for multiple synchronous spinal lesions must also be kept in mind.

4) Finally, the fact that most of the missed lesions were actually documented by the initial “negative” studies emphasizes the importance of a meticulous analysis of angiographic images, optimized by electronic means such as best mask selection and pixel shifting. It also stresses the value of second readings and second opinions. Second opinions also represent an educative tool, in keeping with Pinto and Brunese’s<sup>11</sup> opinion that “a radiology safety culture will only exist when the radiologist who made the

error views such feedback positively as a learning experience.” With angiographic images as complex and findings as subtle as the ones acquired during spinal angiography, no level of proficiency can prove completely immune to faulty interpretation.

### **Spinal Angiography as the “Gold Standard” Spinal Vascular Technique**

Although no imaging technique is exempt from the risk of false-negative studies, it seems that various technical and cognitive factors render spinal angiography more prone to misleading interpretation than, for example, cerebral angiography. This fact directly impacts patient care because there is a justified tendency to rely on a “gold standard” technique. The number of patients with vascular malformations who remain misdiagnosed after a spinal angiogram falsely read as normal is unknown but likely not anecdotal. Spinal angiography should therefore only be considered as a “gold standard” technique when performed by experienced angiographers following strict technical guidelines.

### **CONCLUSIONS**

In the spinal angiograms analyzed for this study, the causes of missed findings or inadequate studies were all avoidable operator-related factors, most notably the nonrecognition of an angiographically documented lesion. The potential for inadequate studies should be reduced by the adoption of rigorous technical and training standards and by second opinion reviews.

Disclosures: Donald Heck—UNRELATED: Consultancy: Stryker; Payment for Lectures (including service on Speakers Bureaus): Stryker. Benjamin Greenberg—UNRELATED: Consultancy: Novartis, Boston Pharmaceuticals, Bayer; Grants/Grants Pending: Chugai, Medimmune, Acorda, Genentech, Patient-Centered Outcomes Research Institute, National Institutes of Health, Guthy Jackson Charitable Foundation\*; Payment for Lectures (including service on Speakers Bureaus): Multiple Sclerosis Association of America. Carlos Pardo—UNRELATED: Expert Testimony, Comments: expert witness for legal purposes and legal deposition; Grants/Grants Pending: Transverse Myelitis Association, Comments: the Transverse Myelitis Association

provides grant support to the Johns Hopkins Transverse Myelitis Center for facilitating patient treatment and research on myelopathies\*. Philippe Gailloud—UNRELATED: Consultancy: Codman Neurovascular; Grants/Grants Pending: Siemens Medical\*; Stock/Stock Options: Artventive Medical. \*Money paid to the institution.

### **REFERENCES**

1. Riche MC, Reizine D, Melki JP, et al. **Classification of spinal cord vascular malformations.** *Radiat Med* 1985;3:17–24 Medline
2. Aminoff MJ, Barnard RO, Logue V. **The pathophysiology of spinal vascular malformations.** *J Neurol Sci* 1974;23:255–63 CrossRef Medline
3. Merland JJ, Riche MC, Chiras J. **Intraspinal extramedullary arteriovenous fistulae draining into the medullary veins.** *J Neuroradiol* 1980;7:271–320 Medline
4. Hurst RW, Kenyon LC, Lavi E, et al. **Spinal dural arteriovenous fistula: the pathology of venous hypertensive myelopathy.** *Neurology* 1995;45:1309–13 CrossRef Medline
5. Jellema K, Canta LR, Tijssen CC, et al. **Spinal dural arteriovenous fistulas: clinical features in 80 patients.** *J Neurol Neurosurg Psychiatry* 2003;74:1438–40 CrossRef Medline
6. Chen J, Gailloud P. **Safety of spinal angiography: complication rate analysis in 302 diagnostic angiograms.** *Neurology* 2011;77:1235–40 CrossRef Medline
7. Aminoff MJ, Logue V. **Clinical features of spinal vascular malformations.** *Brain* 1974;97:197–210 CrossRef Medline
8. Transverse Myelitis Consortium Working Group. **Proposed diagnostic criteria and nosology of acute transverse myelitis.** *Neurology* 2002;59:499–505 CrossRef Medline
9. Merland J, Assouline E, Rüfenacht D, et al. **Dural spinal arteriovenous fistulae draining into medullary veins. Clinical and radiological results of treatment (emboliation and surgery) in 56 cases.** In: Valk J, ed. *Neuroradiology 1985/1986: Proceedings of the XIIIth Congress of the European Society of Neuroradiology, Amsterdam, 11–15 September 1985.* Amsterdam: Elsevier; 1986
10. Gailloud P. **Diagnostic inefficiency of nonselective spinal angiography (flush aortography) in the evaluation of the normal and pathological spinal vasculature.** *Curr Probl Diagn Radiol* 2016;45:180–84 CrossRef Medline
11. Pinto A, Brunese L. **Spectrum of diagnostic errors in radiology.** *World J Radiol* 2010;2:377–83 CrossRef Medline

# Diagnostic Utility of Increased STIR Signal in the Posterior Atlanto-Occipital and Atlantoaxial Membrane Complex on MRI in Acute C1–C2 Fracture

Y.-M. Chang, G. Kim, N. Peri, E. Papavassiliou, R. Rojas, and R.A. Bhadelia

## ABSTRACT

**BACKGROUND AND PURPOSE:** Acute C1–C2 fractures are difficult to detect on MR imaging due to a paucity of associated bone marrow edema. The purpose of this study was to determine the diagnostic utility of increased STIR signal in the posterior atlanto-occipital and atlantoaxial membrane complex (PAOAAM) in the detection of acute C1–C2 fractures on MR imaging.

**MATERIALS AND METHODS:** Eighty-seven patients with C1–C2 fractures, 87 with no fractures, and 87 with other cervical fractures with acute injury who had both CT and MR imaging within 24 hours were included. All MR images were reviewed by 2 neuroradiologists for the presence of increased STIR signal in the PAOAAM and interspinous ligaments at other cervical levels. Sensitivity and specificity of increased signal within the PAOAAM for the presence of a C1–C2 fracture were assessed.

**RESULTS:** Increased PAOAAM STIR signal was seen in 81/87 patients with C1–C2 fractures, 6/87 patients with no fractures, and 51/87 patients with other cervical fractures with 93.1% sensitivity versus those with no fractures, other cervical fractures, and all controls. Specificity was 93.1% versus those with no fractures, 41.4% versus those with other cervical fractures, and 67.2% versus all controls for the detection of acute C1–C2 fractures. Isolated increased PAOAAM STIR signal without increased signal in other cervical interspinous ligaments showed 89.7% sensitivity versus all controls. Specificity was 95.3% versus those with no fractures, 83.7% versus those with other cervical fractures, and 91.4% versus all controls.

**CONCLUSIONS:** Increased PAOAAM signal on STIR is a highly sensitive indicator of an acute C1–C2 fracture on MR imaging. Furthermore, increased PAOAAM STIR signal as an isolated finding is highly specific for the presence of a C1–C2 fracture, making it a useful sign on MR imaging when CT is either unavailable or the findings are equivocal.

**ABBREVIATIONS:** IDEAL = iterative decomposition of water and fat with echo asymmetric and least squares estimation; NF = no fracture; OF = other cervical fracture; PAOAAM = posterior atlanto-occipital and atlantoaxial membrane complex

Injuries at the craniocervical junction occur in approximately 30% of patients presenting with blunt cervical spine trauma resulting in osseous and/or ligamentous injury.<sup>1,2</sup> Given the high potential for neurologic morbidity associated with these injuries, accurate and timely assessment is critical for improved patient outcomes.<sup>3,4</sup> Due to its high sensitivity for detecting acute fractures or dislocations by virtue of its high spatial resolution, ability to obtain multiplanar reformations, and speed, multidetector CT is the established initial imaging technique in patients suspected of having craniocervical and other cervical spine injuries.<sup>5–7</sup> Although MR imaging has superior ability for the evaluation of soft-

tissue and spinal cord injuries and the determination of fracture acuity, its use is generally limited to cases with evidence of severe injuries on CT, abnormal neurologic findings, or equivocal CT findings. This secondary role of MR imaging in screening cervical spine injuries is driven not only by its higher cost, lower speed, and decreased availability compared with CT, but also by its decreased sensitivity for craniocervical junction and posterior element fractures.<sup>8,9</sup>

Recent work has shown that type II odontoid fractures in older patients may not exhibit STIR hyperintense marrow signal at the fracture site, limiting the utility of MR imaging in the evaluation of the presence and acuity of a fracture.<sup>10,11</sup> Nevertheless, because of the potential for concomitant ligamentous and neurologic injuries associated with craniocervical fractures, MR imaging is frequently used as a complementary technique to CT at many tertiary care centers.<sup>12,13</sup> In some of these instances, the initial CT or report obtained at an outside hospital may not be available for review by the radiologist inter-

Received October 30, 2016; accepted after revision May 4, 2017.

From the Departments of Radiology (Y.-M.C., G.K., N.P., R.R., R.A.B.) and Neurosurgery (E.P.), Beth Israel Deaconess Medical Center, Boston, Massachusetts.

Please address correspondence to Yu-Ming Chang, MD, PhD, Department of Radiology, Beth Israel Deaconess Medical Center, WCB90, 330 Brookline Ave, Boston, MA 02115; e-mail: ychang2@bidmc.harvard.edu

<http://dx.doi.org/10.3174/ajnr.A5284>

preparing follow-up MR imaging in a timely fashion, or CT may have equivocal findings, creating a perfect scenario for missing C1–C2 fractures on MR imaging, with the potential for medico-legal implications.

We have observed increased signal on STIR images in the region of the posterior atlanto-occipital and atlantoaxial membranes, considered in the current study as a single complex (PAOAM), in patients with acute C1–C2 fractures. However, this finding is typically not seen in patients presenting with trauma without cervical fractures, leading us to hypothesize that this may be a useful diagnostic indicator of acute C1–C2 fracture on MR imaging. Based on this hypothesis, the purpose of the study was to determine the diagnostic utility of increased PAOAM STIR signal in the detection of acute C1–C2 fractures, the presence of which may prompt the reader to repeat or reinterpret CT cervical spine studies with equivocal findings.

## MATERIALS AND METHODS

### Patients and Control Groups

Following institutional review board approval for this Health Insurance Portability and Accountability Act–compliant study, a retrospective review from 2008 to 2015 of our institutional imaging data base was performed for patients with acute isolated C1–C2 fractures who had both CT and MR imaging of the cervical spine within 24 hours of each other. Per review of the medical records, the CT examinations were performed within 24 hours of trauma. CT performed at an outside hospital before transfer was included if it had been performed within 24 hours. All MR images were obtained at our institution. The presence of acute C1–C2 fractures was determined by the CT report and history/clinical examination documented in the medical records. One hundred two patients with C1–C2 fractures were identified. Nine fractures were determined to be chronic on the basis of review of prior imaging and/or clinical history and were excluded from analysis. Six additional patients were excluded due to the absence of diagnostic STIR images, leaving 87 patients.

Two control groups with CT scans obtained within 24 hours of blunt cervical spine trauma and MR images within 24 hours of the CT were selected consecutively by reviewing the imaging data base from 2013 to 2015 until each group included 87 patients. The controls consisted of a no fracture (NF) group and an other fracture (OF) group. The NF group included patients with a clinical history of blunt cervical spine trauma without reported fractures on CT. The OF group included all fractures isolated in the cervical spine (regardless of fracture morphology), excluding concomitant C1–C2 fractures.

### CT and MR Imaging

Noncontrast CT of the cervical spine was performed on a 128–detector CT scanner (Discovery HD750; GE Healthcare, Milwaukee, Wisconsin). Images were acquired helically with a section thickness of 2.5 mm, a pitch of 0.984, a gantry rotation time of 1 second, at 120 kV with a tube current of 340 mA. All outside CT scans were also helically acquired and obtained on 64– or 128–detector CT scanners.

All MR imaging examinations were performed on one of two 1.5T MR imaging scanners with our standard departmental pro-

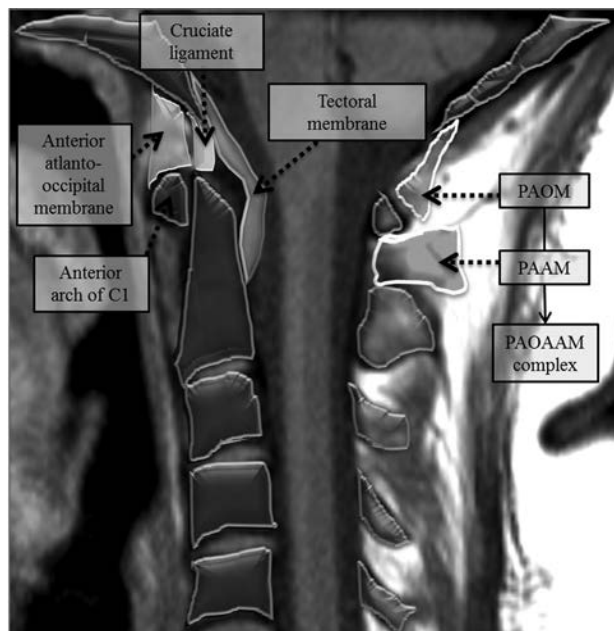


**FIG 1.** Overview of the anatomy at the craniocervical junction. The posterior atlanto-occipital membrane (PAOM) is a thickened band of the ligamentum flavum extending from the posterior arch of the atlas to the posterior occipital bone. The posterior atlantoaxial membrane (PAAM) is a correlate extending from the posterior arch of the atlas to the posterior elements of C2. The PAOM and PAAM are considered a single complex in this article (PAOAM).

tol of T1- and T2-weighted and STIR or STIR-equivalent iterative decomposition of water and fat with echo asymmetric and least squares estimation (IDEAL) sagittal water-selective images and axial T2-weighted and gradient recalled-echo images. On the Signa HDx scanner (GE Healthcare), STIR (2008–2012) imaging parameters were TR/TE = 3750/60 ms and TI = 150 ms, and IDEAL (2012–2015) imaging parameters were TR/TE = 4222/85 ms. For both sequences, the matrix was 320 × 256. For the Magnetom Espree (Siemens, Erlangen, Germany) scanner, the parameters were TR/TE = 5570/64 ms, TI = 150 ms, and matrix = 320 × 224. For both GE Healthcare and Siemens scanners, the FOV was 220 mm and the section thickness was 3 mm.

### Image Analysis

All CT scans obtained in our institution were interpreted by a board-certified radiologist (emergency department radiologist or neuroradiologist). The subspecialty training of outside institution interpreters was not known. The CT studies were not independently re-reviewed by the investigators. For simplicity, STIR and IDEAL images will be collectively referred to as STIR images. STIR images from MR images were independently reviewed by 2 board-certified, fellowship-trained neuroradiologists (with 25 and 2 years of postfellowship experience), blinded to the CT reports and images, for the presence of increased signal on STIR images in the region of the PAOAM. The increased STIR signal in the PAOAM was defined as increased signal in one or both of the posterior atlanto-occipital and the posterior atlantoaxial membranes, which are considered in the current study as a single complex (PAOAM) (Fig 1). STIR images were also used to assess the presence of increased signal in interspinous ligaments at other cervical levels (Figs 1–4).

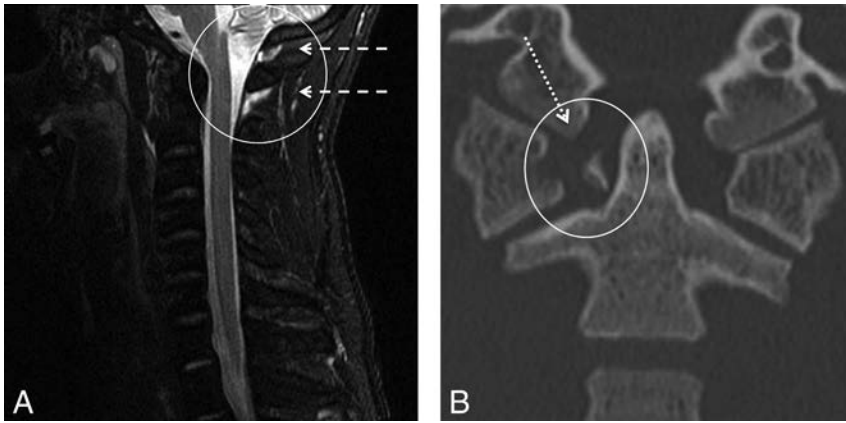


**FIG 2.** Isolated increased PAOAAM signal. *A*, STIR midline sagittal image of a 26-year-old man, presenting after assault. There is an isolated increased STIR signal (circle and dashed arrows) at the PAOAAM and none at the interspinous ligaments. *B*, CT demonstrates the anterior and posterior arches of C1 fractures, with an avulsed transverse ligament (circle and dotted arrow) and lateral subluxation of the lateral masses.

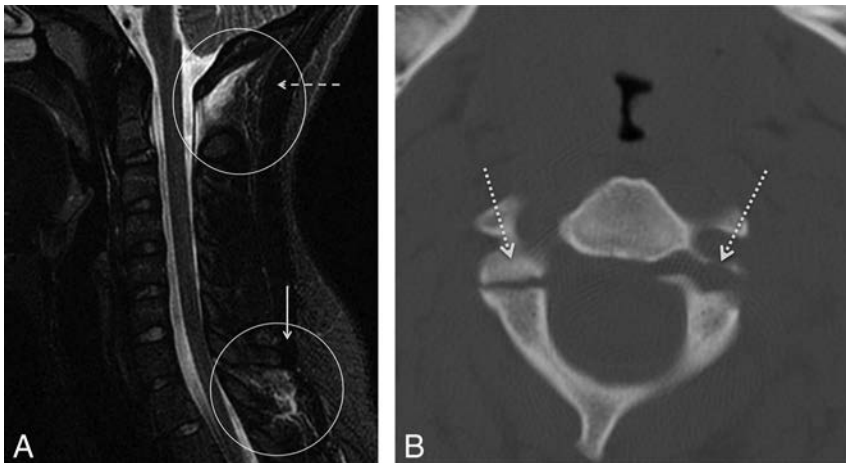


**FIG 3.** Increased PAOAAM signal. *A*, STIR midline sagittal image of a 17-year-old adolescent girl, presenting after a motor vehicle collision. There is an increased STIR signal at the PAOAAM (circle and dashed arrow) and at the interspinous ligaments (circle and solid arrow). *B*, CT demonstrates comminuted fractures of the bilateral C2 pedicles (dotted arrows).

### Data Analysis

Differences in age among C1–C2, NF, and OF groups were assessed by using 1-way ANOVA. Interobserver reliability for both increased PAOAAM and interspinous ligament STIR signal was measured with  $\kappa$  coefficients. Disagreements were resolved by consensus agreement between the 2 interpreters, and the reconciled data were used for subsequent analyses. The frequency of increased STIR signal in the PAOAAM and the presence of increased STIR signal in the interspinous ligaments at other cervical levels were determined for all patients. The sensitivity and specificity of increased STIR signal in the PAOAAM, both isolated to the PAOAAM and in the presence of STIR hyperintensity at other cervical levels, were assessed for the C1–C2, NF + OF (all controls), NF, and OF groups. We also assessed the sensitivity and specificity of isolated increased STIR signal in the PAOAAM associated with C1–C2 fractures by comparing these groups. Subgroup analysis of C1–C2 fracture types separated into odontoid type II, odontoid type III, C2 pars interarticular (hangman), C2 lamina or transverse process, C2 comminuted vertebral body, iso-

lated C1, and combined C1 and C2 fractures with presence of increased STIR signal in the PAOAAM was performed with the  $\chi^2$  test. Additional analysis of patients with NF separated into midcervical (C3 through C4), lower cervical (C5 through C7), and mixed (C3 through C4 and C5 through C7) level fractures with presence of increased STIR signal in the PAOAAM was also performed. Statistical significance was set at  $P \leq .05$ .

### RESULTS

Demographic characteristics of patients with C1–C2 fractures, NF, and OF are shown in Table 1. There were no significant age differences among the C1–C2 fracture, NF, and OF groups ( $P \leq .2$ , Table 1). With terminology established by Landis and Koch,<sup>14</sup> there was “almost perfect” interobserver agreement between readers in the detection of PAOAAM signal ( $\kappa = 0.91$ ; 95% CI, 0.88–0.97) and interspinous ligament signal at other cervical levels ( $\kappa = 0.93$ ; 95% CI, 0.89–0.98).

The 87 C1–C2 fractures were the following: odontoid type II ( $n = 27$ ), odontoid type III ( $n = 19$ ), C2 pars interarticular (hangman) ( $n = 7$ ), C2 lamina or transverse process fractures ( $n = 3$ ), C2 comminuted vertebral body ( $n = 8$ ), isolated C1 ( $n = 20$ ), and combined C1 and C2 ( $n = 3$ ). Twenty-five of 27 odontoid type II, 18/19 odontoid type III, 7/7 hangman, 3/3 C2 lamina or transverse process, 8/8 C2 comminuted vertebral body, 19/20 isolated C1, and 3/3 combined C1 and C2 fractures demonstrated increased PAOAAM STIR signal. No significant difference was found in the presence of PAOAAM signal among the C1–C2 fracture groups ( $\chi^2 = 1.52$ ,  $P = .96$ ).

Fractures at other cervical levels included 16 mid- (C3 through C4), 59 lower- (C5 through C7), and 12 mixed-level fractures. Nine of 16 mid-, 33/59 lower-, and 9/12 mixed-level fractures were associated with increased PAOAAM STIR signal. No significant difference in the presence of PAOAAM signal among fractures involving mid-versus-lower cervical spine was noted ( $\chi^2 = 1.54$ ,  $P = .46$ ).

Two patterns of increased STIR signal were observed in patients with acute C1–C2 fractures: 1) increased STIR signal in the PAOAAM with increased STIR signal in ligaments at other cervical levels (Fig 3), and 2) isolated increased STIR signal localized to the PAOAAM without increased signal in ligaments at other cervical levels (Fig 2).

Increased STIR signal in the PAOAAM was seen in 81/87



**FIG 4.** Other interspinous ligament signal. A, STIR midline sagittal image of a 66-year-old man presenting after a fall secondary to intoxication. There is no STIR signal at the PAOAAM (gray circle and dashed arrow), but only at the interspinous ligaments (white circle and short solid arrow). There is an interruption at the anterior longitudinal ligament at C5–6 (long solid arrow). B, CT demonstrates a fracture of the ossified anterior longitudinal ligament at C5–6 (circle and dotted arrow).

**Table 1: Patient characteristics: sex distribution**

	Male	Female	Age	Mean	SD
			Range (yr)	Age (yr)	
C1–C2 fracture	44	43	18–96	66	21.4
No fracture	57	30	24–96	62	17.5
Other fracture	50	37	21–102	61	21.2

(93.1%) patients with C1–C2 fractures, 6/87 (6.9%) with NFs, and 51/87 (58.6%) with OFs. The sensitivity and specificity of increased STIR signal in the PAOAAM in detecting acute fractures at C1–C2 are shown in Table 2. Isolated increased STIR signal in the PAOAAM was seen in 52/87 (59.8%) patients with C1–C2 fractures, 4/87 (4.6%) with NFs, and 7/87 (8.0%) with OFs. The sensitivity and specificity of isolated increased STIR signal in the PAOAAM in detecting acute fractures at C1–C2 are shown in Table 3.

## DISCUSSION

Our results show that increased STIR signal is observed in most patients with C1–C2 fractures and that this finding is a highly sensitive MR imaging sign of fractures in this area. We also observed that this finding has high specificity when compared with patients without cervical spine fracture (patients with NF). However, the specificity decreases when compared with patients with other cervical fractures (OF group) and all controls (NF + OF). This decreased specificity in relation to all controls and the OF group was due to the presence of increased STIR signal in the PAOAAM in many patients with other cervical spine fractures, suggesting that this structure is frequently affected in any type of cervical spine fracture. We also observed that when increased PAOAAM STIR signal is an isolated finding in patients with cervical spine injury and there is no associated increased signal in ligaments at other cervical levels, this finding has high specificity in indicating the presence of a C1–C2 fracture. On the basis of our observations, we believe that increased STIR

signal in the PAOAAM should make a radiologist suspicious of the presence of a cervical spine fracture when interpreting a cervical spine MR imaging study. Furthermore, when the increased STIR signal in the PAOAAM is an isolated finding, a C1–C2 fracture should be suspected until proved otherwise by CT.

The STIR sequence on MR imaging is known to be very sensitive for the detection of a marrow edema pattern in subtle compression or micro-/insufficiency fractures, particularly of the thoracic and lumbar spines and appendicular skeleton, such as the pelvis and femur.<sup>15–18</sup> Conversely, in the cervical spine, prior work has shown not only the superiority of CT in the detection of bony injuries, but also that STIR imaging is much less sensitive for the detection of acute fractures. Holmes et al,<sup>9</sup> showed that of 66 patients with both

CT and MR imaging examinations, the sensitivity for osseous fractures was 95% on CT versus 50% on MR imaging, with most of the missed lesions involving the lateral and posterior elements, with the caveat that the specific time interval between the CT and MR imaging studies was not reported by the authors.

Limitations of the STIR sequence were first demonstrated by Peri et al in 2009 in type II and III odontoid fractures in which STIR abnormalities were not seen in 22% of acute fractures and were limited to the fracture cleft in 11/18 patients.<sup>10</sup> In addition, a more recent study reported that the sensitivity of STIR signal for demonstrating acute type II odontoid fractures was only 82% in patients younger than 57 years of age and became significantly lower at 54% in patients older than 57 years of age.<sup>11</sup> The mechanism underlying this difference in the sensitivity of MR imaging for the detection of acute fractures in the cervical spine versus the thoracic and lumbar spine is unclear; however, Lensing et al<sup>11</sup> postulated that this issue may be due to a combination of progressive decreased vascularity at the odontoid base and age-related osteopenia.

Our findings also suggest that increased PAOAAM signal associated with C1–C2 fractures is not related to fracture morphology. Of note, prior work in the thoracolumbar spine reports that interspinous ligamentous injuries associated with fracture are correlated with the degree of kyphotic angulation and similar measures rather than fracture type.<sup>19,20</sup> It is likely that the lack of correlation between C1–C2 fracture types and PAOAAM signal is due to the understanding that most cervical fractures are associated with high energy trauma, secondary to extreme flexion, extension, shearing, and rotation forces. Therefore, we believe that the findings outlined on our study can be generalized to any C1–C2 cervical fracture.<sup>21</sup> In further support, cervical trauma associated with whiplash injury, presumably resulting from lower energy trauma than that associ-

**Table 2: Diagnostic utility of increased stir signal<sup>a</sup> at the PAOAAM in detecting the presence of an acute C1–C2 fracture**

	C1–C2 (n = 81/87) vs All Controls (n = 57/174)	C1–C2 (n = 81/87) vs NF (n = 6/87)	C1–C2 (n = 81/87) vs OF (n = 51/87)
Sensitivity (95% CI)	93.1% (85.6%–97.4%)	93.1% (85.6%–97.4%)	93.1% (85.6%–97.4%)
Specificity (95% CI)	67.2% (59.7%–74.2%)	93.1% (85.6%–97.4%)	41.4% (30.9%–52.5%)

**Note:**—C1–C2 indicates all patients with C1–C2 fractures on CT, with or without PAOAAM or another posterior ligament signal; NF, patients with a history of trauma without fracture on CT, with or without PAOAAM or another interspinous ligament signal; OF, patients with cervical spine fracture other than C1–C2 on CT, with or without PAOAAM or another interspinous ligament signal; controls, no cervical fracture plus other cervical fracture with or without PAOAAM or another interspinous ligament signal.

<sup>a</sup> Increased STIR Signal in PAOAAM with or without increased signal in other cervical ligaments.

**Table 3: Diagnostic utility of isolated increased STIR signal<sup>a</sup> at the PAOAAM in detecting the presence of an acute C1–C2 fracture**

	C1–C2 (n = 52/87) vs All Controls (n = 11/174)	C1–C2 (n = 52/87) vs NF (n = 4/87)	C1–C2 (n = 52/87) vs OF (n = 7/87)
Sensitivity (95% CI)	89.7% (78.8%–96.1%)	89.7% (78.8%–96.1%)	89.7% (78.8%–96.1%)
Specificity (95% CI)	91.4% (85.1%–95.6%)	95.3% (78.8%–96.1%)	83.7% (69.3%–93.2%)

<sup>a</sup> Isolated increased STIR signal in the PAOAAM without increased signal in other posterior cervical ligaments.

ated with fractures, is not associated with PAOAAM injury compared with controls.<sup>22</sup>

The study has several limitations. First, we only looked at the STIR hyperintense signal of the PAOAAM and interspinous ligaments at other cervical levels and did not assess the marrow edema pattern or other soft-tissue signal in the current study. Although we specifically chose not to assess the marrow edema pattern in this study given the relatively lower sensitivity for odontoid and other craniocervical fractures on previous reports, such findings parenthetically noted may have resulted in some confirmation bias. Second, given that the OF and NF control groups were chosen consecutively among patients and not randomly, this method may have resulted in unforeseen selection bias. Third, because this report was focused on C1–C2 fractures, we did not analyze whether there were additional fracture types at the level of the craniocervical junction or skull base that may be associated with increased PAOAAM STIR signal. This omission could potentially result in lowered specificity of the findings for C1–C2 fractures. Further work elucidating this question will be required. We also did not independently review CT scans to confirm a diagnosis of cervical spine fracture, potentially resulting in over-/underestimation of the sensitivity and specificity of PAOAAM STIR signal for C1–C2 fractures. Finally, diagnosis of the acuity of the fracture was based on history/clinical findings, and we did not obtain a follow-up MR imaging to confirm whether and when PAOAAM increased signal subsequently resolved.

In our current study, we anecdotally noted 9 patients with a questionable history of prior C2 fracture whose cervical CT findings at the time of the new trauma were equivocal and later were determined to be chronic on the basis of prior imaging and/or clinical history and, therefore, were not included in the study. In these patients, the MR imaging performed within 24 hours of cervical CT did not demonstrate increased PAOAAM signal. Due to the small number of patients in this group, no definite conclusions could be drawn from this observation. Nevertheless, this finding suggests that increased signal at the PAOAAM is correlated with acute injury and is unlikely to be confounded by superimposed subacute-to-chronic injury. However, further study is required to address this issue. Furthermore, 6/87 patients in the C1–C2 fracture group did not demonstrate as-

sociated increased PAOAAM signal. The mechanism underlying this difference is uncertain and likely multifactorial, including mechanism of injury, cervical alignment, and bone density. For example, this subset of patients all demonstrated subjective decreased bone mineralization on CT examinations, though this was not confirmed by bone density examinations in the available medical records. Thus, it is possible that C1–C2 fractures in this false-negative group may occur with lower energy trauma and are less likely to result in ligamentous injury. Correlation with bone density in future studies would help elucidate these findings.

## CONCLUSIONS

The presence of an increased PAOAAM signal on STIR images is a highly sensitive indicator of an acute C1–C2 fracture on MR imaging. As an isolated finding, increased PAOAAM signal is highly specific for the presence of a C1–C2 fracture, making it a diagnostically useful imaging sign for possible re-interpretation of reportedly negative/equivocal CT findings or repeat CT imaging if not available.

Disclosures: Rafael Rojas—UNRELATED: Consultancy: Guerbet, Comments: Guerbet MRI Advisory Board meeting, Chicago, July 2016.

## REFERENCES

1. Riascos R, Bonfante E, Cotes C, et al. **Imaging of atlanto-occipital and atlantoaxial traumatic injuries: what the radiologist needs to know.** *Radiographics* 2015;35:2121–34 CrossRef Medline
2. Bohlman HH. **Acute fractures and dislocations of the cervical spine: an analysis of three hundred hospitalized patients and review of the literature.** *J Bone Joint Surg Am* 1979;61:1119–42 CrossRef Medline
3. Mendenhall SK, Sivaganesan A, Mistry A, et al. **Traumatic atlantooccipital dislocation: comprehensive assessment of mortality, neurologic improvement, and patient-reported outcomes at a level 1 trauma center over 15 years.** *Spine J* 2015;15:2385–95 CrossRef Medline
4. Hall GC, Kinsman MJ, Nazar RG, et al. **Atlanto-occipital dislocation.** *World J Orthop* 2015;6:236–43 CrossRef Medline
5. Berne JD, Velmahos GC, El-Tawil Q, et al. **Value of complete cervical helical computed tomographic scanning in identifying cervical spine injury in the unevaluable blunt trauma patient with multiple injuries: a prospective study.** *J Trauma* 1999;47:896–902; discussion 902–03 CrossRef Medline
6. Acheson MB, Livingston RR, Richardson ML, et al. **High-resolution CT scanning in the evaluation of cervical spine fractures: comparison with plain film examinations.** *AJR Am J Roentgenol* 1987;148:1179–85 CrossRef Medline
7. Barba CA, Taggart J, Morgan AS, et al. **A new cervical spine clearance protocol using computed tomography.** *J Trauma* 2001;51:652–56; discussion 656–57 CrossRef Medline
8. Crim JR, Moore K, Brodke D. **Clearance of the cervical spine in multitrauma patients: the role of advanced imaging.** *Semin Ultrasound CT MR* 2001;22:283–305 CrossRef Medline
9. Holmes JF, Mirvis SE, Panacek EA, et al; NEXUS Group. **Variability in computed tomography and magnetic resonance imaging in pa-**

- tients with cervical spine injuries. *J Trauma* 2002;53:524–29; discussion 530 CrossRef Medline
10. Peri N, Papavassiliou E, Rojas R, et al. **MRI of acute odontoid fractures: is marrow edema helpful in diagnosing “ACUTE” nature of fracture and predicting healing?** In: *Proceedings of the Radiological Society of North America Scientific Assembly and Annual Meeting*; Chicago, Illinois. November 29 to December 4, 2009
  11. Lensing FD, Bisson EF, Wiggins RH 3rd, et al. **Reliability of the STIR sequence for acute type II odontoid fractures.** *AJNR Am J Neuroradiol* 2014;35:1642–46 CrossRef Medline
  12. Adams JM, Cockburn MI, Difazio LT, et al. **Spinal clearance in the difficult trauma patient: a role for screening MRI of the spine.** *Am Surg* 2006;72:101–05 Medline
  13. Chew BG, Swartz C, Quigley MR, et al. **Cervical spine clearance in the traumatically injured patient: is multidetector CT scanning sufficient alone? Clinical article.** *J Neurosurg Spine* 2013;19:576–81 CrossRef Medline
  14. Landis JR, Koch GG. **The measurement of observer agreement for categorical data.** *Biometrics* 1977;33:159–74 CrossRef Medline
  15. Pizones J, Izquierdo E, Alvarez P, et al. **Impact of magnetic resonance imaging on decision making for thoracolumbar traumatic fracture diagnosis and treatment.** *Eur Spine J* 2011;20(suppl 3):390–96 CrossRef Medline
  16. Spiegl UJ, Beisse R, Hauck S, et al. **Value of MRI imaging prior to a kyphoplasty for osteoporotic insufficiency fractures.** *Eur Spine J* 2009;18:1287–92 CrossRef Medline
  17. Winklhofer S, Thekkumthala-Sommer M, Schmidt D, et al. **Magnetic resonance imaging frequently changes classification of acute traumatic thoracolumbar spine injuries.** *Skeletal Radiol* 2013;42:779–86 CrossRef Medline
  18. Cabarrus MC, Ambekar A, Lu Y, et al. **MRI and CT of insufficiency fractures of the pelvis and the proximal femur.** *AJR Am J Roentgenol* 2008;191:995–1001 CrossRef Medline
  19. Chen JX, Goswami A, Xu DL, et al. **The radiologic assessment of posterior ligamentous complex injury in patients with thoracolumbar fracture.** *Eur Spine J* 2017;26:1454–62 CrossRef Medline
  20. Hiyama A, Watanabe M, Katoh H, et al. **Relationships between posterior ligamentous complex injury and radiographic parameters in patients with thoracolumbar burst fractures.** *Injury* 2015;46:392–98 CrossRef Medline
  21. Pratt H, Davies E, King L. **Traumatic injuries of the C1/C2 complex: computed tomographic imaging appearances.** *Curr Probl Diagn Radiol* 2008;37:26–38 CrossRef Medline
  22. Dullerud R, Gjertsen O, Server A. **Magnetic resonance imaging of ligaments and membranes in the craniocervical junction in whiplash-associated injury and in healthy control subjects.** *Acta Radiol* 2010;51:207–12 CrossRef

# Prospective Comparison of Changes in Lumbar Spine MRI Findings over Time between Individuals with Acute Low Back Pain and Controls: An Exploratory Study

J. Panagopoulos, J.S. Magnussen, J. Hush, C.G. Maher, M. Crites-Battie, J.G. Jarvik, T.S. Jensen, and M.J. Hancock



## ABSTRACT

**BACKGROUND AND PURPOSE:** The clinical importance of lumbar MR imaging findings is unclear. This study was an exploratory investigation of whether lumbar spine MR imaging findings change more commonly during a 12-week period in individuals with acute low back pain compared with pain-free controls.

**MATERIALS AND METHODS:** Twenty individuals with recent-onset low back pain and 10 pain-free controls were recruited into an exploratory prospective cohort study. All participants had a lumbar spine MR imaging at baseline and repeat MR imaging scans at 1, 2, 6, and 12 weeks. The proportion of individuals who had MR imaging findings that changed during the 12-week period was compared with the same proportion in the controls.

**RESULTS:** In 85% of subjects, we identified a change in at least 1 MR imaging finding during the 12 weeks; however, the proportion was similar in the controls (80%). A change in disc herniation, annular fissure, and nerve root compromise was reported more than twice as commonly in the subjects as in controls (65% versus 30%, 25% versus 10%, and 15% versus 0%, respectively). Caution is required in interpreting these findings due to wide confidence intervals, including no statistical difference. For all other MR imaging findings, the proportions of subjects and controls in whom MR imaging findings were reported to change during 12 weeks were similar.

**CONCLUSIONS:** Changes in MR imaging findings were observed in a similar proportion of the low back pain and control groups, except for herniations, annular fissures, and nerve root compromise, which were twice as common in subjects with low back pain.

**ABBREVIATIONS:** HIZ = high-intensity zone; LBP = low back pain

Low back pain (LBP) is very common and the leading cause of disability worldwide.<sup>1</sup> Nevertheless, little progress has been made in identifying highly effective treatments.<sup>2,3</sup> Currently >90% of LBP is classified as nonspecific back pain, indicating that it is not possible to identify a specific cause of the pain for most individuals.<sup>4</sup> A better understanding of the nociceptive contribu-

tors to LBP may result in the development of more effective treatments.

MR imaging has the potential to identify pathoanatomic contributors to LBP, yet the importance of these MR imaging findings remains unclear.<sup>5-7</sup> It is possible that certain MR imaging findings are part of the normal aging process, and various studies have highlighted the presence of pathoanatomic lumbar spine findings in the MR images of asymptomatic patients.<sup>5-7</sup> Therefore, it is unclear whether “abnormal” MR imaging findings reflect nociceptive contributors to the experience of back pain or whether they are normal structural variants unrelated to the pain experience.

Most previous MR imaging studies were cross-sectional in design and, thus, provide limited evidence of the clinical importance of MR imaging findings. A recent systematic review and meta-analysis of these studies concluded that while many findings were common in individuals without LBP, several findings were substantially more common in those with LBP.<sup>8</sup>

Relatively few longitudinal studies have investigated the clinical importance of MR imaging findings.<sup>9</sup> There are even fewer

Received February 24, 2017; accepted after revision May 9.

From the Faculty of Medicine and Health Sciences (J.P., M.J.H., J.S.M., J.H.) and Centre for Physical Health (J.S.M., J.H., M.J.H.), Macquarie University, Sydney, New South Wales, Australia; George Institute of Public Health (C.G.M.), University of Sydney, Sydney, New South Wales Australia; Department of Physiotherapy (M.C.-B.), University of Alberta, Edmonton, Alberta, Canada; Departments of Radiology, Neurological Surgery, and Health Services (J.G.J.), University of Washington, Seattle, Washington; Nordic Institute of Clinical Biomechanics (T.S.J.), Odense, Denmark; Spine Centre of Southern Denmark (T.S.J.), Middelfart, Denmark; and Institute for Regional Health Research (T.S.J.), University of Southern Denmark, Odense, Denmark.

This project is supported by funding from Arthritis NSW, Australia.

Please address correspondence to Mark J. Hancock, PhD, Faculty of Medicine and Health Sciences and Centre for Physical Health, Ground floor, 75 Talavera Rd, Macquarie University, Sydney, NSW 2109, Australia; e-mail: mark.hancock@mq.edu.au

Indicates article with supplemental on-line table.

<http://dx.doi.org/10.3174/ajnr.A5357>

studies that have performed repeat MR imaging investigations on the same individuals across time, and those that have reported them had mostly long follow-up periods between scans. Long follow-ups provide little evidence about the clinical importance of MR imaging changes with time. Therefore, there is a need to investigate whether MR imaging findings change during the short-term in individuals with a recent-onset episode of LBP. Change could be either an improvement or worsening of an MR imaging finding with time. Comparison with pain-free participants is required to distinguish whether any changes in MR imaging findings are clinically relevant.

Therefore, the aims of this exploratory study were to determine the following:

1) Whether lumbar spine MR imaging findings change more commonly during a 12-week period in individuals with acute nonspecific LBP compared with a pain-free control group.

2) Which MR imaging findings change most commonly during the 12-week period in individuals with acute nonspecific LBP.

## MATERIALS AND METHODS

This exploratory study followed an inception cohort of 20 individuals with recent-onset LBP and compared them with a cohort of 10 pain-free controls. Subjects were assessed by a physiotherapist and then underwent an MR imaging scan on the same day. Repeat MR imaging scans at 1-, 2-, 6-, and 12-week follow-ups were obtained for all participants. Ethics approval for this study was obtained from Macquarie University Human Research Ethics Committee (reference No. 5201300630).

### Participants

**Subject Participants.** Potential participants were identified by physiotherapists or chiropractors working in primary care. A researcher contacted interested potential participants as soon as possible after their referral to screen them for eligibility. Those who met the inclusion criteria were scheduled for a baseline MR imaging scan as soon as possible.

**Inclusion Criteria.** Individuals were eligible for the study if they met all of the following criteria: presented to a primary care practitioner with recent-onset LBP of <2 weeks' duration, with or without associated leg pain; available to enroll in the study and undergo initial MR imaging within 3 weeks from the onset of the pain episode; average pain intensity of  $\geq 4$  on an 11-point Numerical Pain Rating Scale 24 hours before the initial MR imaging; sudden-onset episode of LBP (pain intensity increased by  $\geq 4$  points on the Numerical Pain Rating Scale during <24 hours); and age younger than 55 years.

**Exclusion Criteria.** Patients were excluded if they had a clinical presentation suggesting the presence of the following conditions: radiculopathy (myotomal weakness/loss of reflexes/paraesthesia), canal stenosis (bilateral leg pain or symptoms, worsened with extension and improved with flexion), fracture, cancer, inflammatory joint diseases, infection, or cauda equina syndrome; contraindication to MR imaging; previous spinal surgery; or lumbar symptoms that could not be reproduced during physical examination.

**Control Participants.** Control participants were a convenience sample recruited from students and staff in the university department where the study was performed. To be eligible, they needed to have had no LBP during the past 12 months. Because we had 20 subjects and 10 controls, we recruited the controls to achieve matching with subjects in terms of average age, sex, and history of previous episodes of LBP.

### MR Imaging Evaluation

All participants were imaged on a high-field-strength system (3T Verio; Siemens, Erlangen, Germany). The study used the spine coil in combination with an anterior phased array coil. A standardized protocol was used for all participants, which commenced with a sagittal short tau inversion recovery sequence (TR, 3000 ms; TE, 35 ms; TI, 215 ms) and a sagittal T2 FSE sequence (TR, 4500 ms; TE, 101 ms). Both sagittal sequences used a 320-mm FOV with a 4-mm section thickness and a 1-mm intersection gap.

After the sagittal scans, the study was reviewed by an experienced radiologist who made a clinical judgment of the spinal level that appeared most involved. The protocol then included ultra-high-resolution focused axial T2 imaging (2-mm sections with an intersection gap of 0.2 mm through the ROI; TR, 3000 ms; TE, 87 ms; in-plane resolution,  $0.54 \times 0.43$  mm).

An axial-volume steady-state sequence was undertaken with the ROI in the midsection of the axial acquisition. This was designed to cover 1 disc above and below the level of interest, with the sequence angled to the disc of interest. The parameters were section thickness, 1 mm with no gap; FOV, 100 mm; TR, 5.58 ms; and TE, 2.41 ms. A sagittal high-resolution acquisition was also acquired, centered on the ROI. The parameters were section thickness, 2 mm; intersection gap, 0.5 mm; FOV, 100 mm; TR, 5800 ms; and TE, 88 ms.

All participants received their baseline MR imaging findings in the form of reported scans at the week 1 follow-up MR imaging appointment. To reduce the likelihood of reported MR imaging findings causing concern in participants,<sup>10</sup> we included, with the report, a letter stating: "Your MR imaging has been reviewed by a specialist radiologist and there is no evidence of any serious cause of your pain such as a fracture or cancer. We have included a full report; however, it is very important that you realize these findings discussed are common in people with and without back pain and it is best to consider them normal age-related findings."

### Repeat Images

Repeat images were obtained with the same MR imaging scanner sequences for both the standard MR imaging and the focused MR imaging at follow-up time points: 1 week, 2 weeks, 6 weeks, and 12 weeks from the baseline scan for all participants. Participants did not receive the images or reports of follow-up MR imaging scans.

### Reporting of Scans

MRIs were evaluated by an experienced radiologist (J.S.M.). All images were de-identified during coding so that the radiologist was blinded to whether a person was a subject or control. The radiologist first reported on the presence of all MR imaging findings of interest (high-intensity zone [HIZ]),<sup>11</sup> Modic change, disc

**Table 1: MRI findings and the method of assessment at each spinal level**

MRI Finding	Method of Scoring at Each Spinal Level
Disc degeneration	Scale of Pfirrmann et al; 1–5 <sup>13</sup>
Signal intensity loss	Hypointense, intermediate, hyperintense <sup>13</sup>
Disc height loss	Absent, mild, moderate, severe <sup>13</sup>
Modic changes	According to Fardon et al <sup>14</sup> combined task force; present or absent
Annular fissure	According to Fardon et al <sup>14</sup> combined task force; present or absent
HIZ	According to April and Bogduk <sup>11</sup> and Fardon et al <sup>14</sup> combined task force; present or absent
Disc herniation	According to Fardon et al <sup>14</sup> combined task force; normal, protrusion, extrusion, sequestration
Canal stenosis	None, mild, moderate, severe <sup>12</sup>
Spondylolisthesis or retrolisthesis	Present or absent <sup>12</sup>
Edema (posterior elements)	Present or absent
Nerve root compression	No contact, contact, contact and deviation, compression <sup>15</sup>
Facet joint arthropathy	None, mild, moderate, severe <sup>12</sup>

**Table 2: Baseline characteristics and MRI findings of participants**

Variable	LBP Participants (n = 20)	Control Participants (n = 10)
Female sex (No.) (%)	9 (45%)	5 (50%)
Age (mean) (SD) (yr)	37.4 (9.4)	39.8 (9.4)
≥2 previous episodes (%)	55%	50%
Pain intensity (mean) (SD) (NPRS)	5.95 (1.47)	0
Duration of current episode (median) (IQR) (day)	6.5 (3.3–9.5)	0
Disc degeneration ≥3 (No.) (%)	16 (80%)	6 (60%)
Signal intensity loss (No.) (%)	12 (60%)	4 (40%)
Disc height loss (No.) (%)	2 (10%)	2 (20%)
Modic changes (No.) (%)	6 (30%)	2 (20%)
Annular fissure (No.) (%)	3 (15%)	1 (10%)
HIZ (No.) (%)	10 (50%)	6 (60%)
Disc herniation total (No.) (%)	20 (100%)	9 (90%)
Canal stenosis (No.) (%)	2 (10%)	0 (0%)
Spondylolisthesis or retrolisthesis (No.) (%)	6 (30%)	4 (40%)
Facet joint arthropathy (No.) (%)	11 (55%)	4 (40%)
Bone edema (posterior elements) (No.) (%)	0 (0%)	1 (10%)
Nerve root compression (No.) (%)	10 (50%)	2 (20%)

**Note:**—IQR indicates interquartile range; NPRD, Numerical Pain Rating Scale.

degeneration, disc height, disc signal intensity, annular fissure, disc herniation [protrusions and extrusions], central canal stenosis, spondylolisthesis or retrolisthesis, facet joint pathology, and nerve root compromise<sup>12–15</sup>) at baseline, following standardized protocols. A description of the MR imaging findings and the methods by which they were scored can be found in Table 1. We reported HIZs when there was an area of high intensity in the outer annulus with no clear connection to the signal of the nucleus pulposus.<sup>11</sup> Each follow-up MR imaging was then compared with the baseline scan to identify whether any change had occurred. All findings were documented on a standardized reporting form, and the radiologist was asked to report whether the change in MR imaging from baseline to follow-up was definite or probable.

To determine the intrarater reliability of the change scores assessed, the same radiologist reported on all images a second time >2 months after the original reporting. He remained blinded to whether the participant was a subject or control, and to the original reports.

### Outcome

We assessed whether each individual had an MR imaging finding (any type) that the radiologist considered a definite or probable change at any time point from baseline. A change could be an appearance, disappearance, improvement, or a

worsening of a pathoanatomic finding on MR imaging. We also assessed definite changes and probable changes separately. For each individual MR imaging finding (eg, HIZ), we determined whether each individual had the following: 1) definite or probable change, 2) definite change, or 3) probable change at any time point.

Each definite or probable MR imaging change that occurred with time was also reported as either an improvement or a worsening compared with baseline MR imaging. If an MR imaging finding both improved and worsened at different follow-up time points (compared with baseline), we reported the change at or closest to the 12-week time point.

### Analysis

Logistic regression models were used to compare the proportion of subjects who had any MR imaging finding that definitely or probably changed to the same proportion in the controls. Similar models were used to compare the proportions of subjects and controls with definite or probable changes of specific MR imaging findings (eg, HIZ). Because this was an exploratory study, we emphasized the magnitude of differences between subjects and controls rather than the statistical significance when presenting and interpreting the results.

The intrarater reliability for MR imaging findings was investigated with the  $\kappa$  statistic. All analyses were conducted with SPSS, Version 22.0 (IBM, Armonk, New York).

### RESULTS

Between March 2014 and May 2015, twenty subject participants and 10 control participants were enrolled into the study. Baseline characteristics of the participants, including baseline MR imaging findings, are shown in Table 2. The groups were well-matched for sex, age, and history of ≥2 previous episodes. All 20 subjects had pain in the lumbar region, and 3 had pain extending below the knee. The median duration of pain in the subjects was 6.5 days. Seventeen of the 20 subjects (85%) reported >50% reduction in pain at the 12-week follow-up (or last follow-up conducted), and 3 of the 20 subjects (15%) reported minimal or no change in their

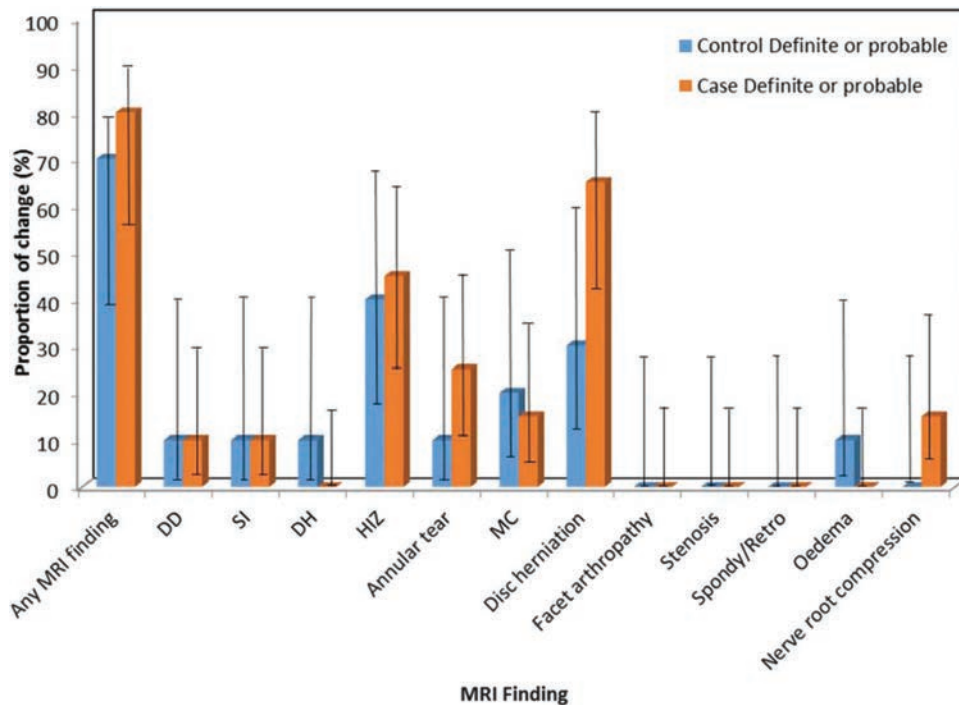


**FIG 1.** Bar chart showing proportions of subjects and controls for whom a definite or probable change occurred in MR imaging findings with time. DD indicates disc degeneration; SI, signal intensity; DH, disc herniation; MC, Modic changes; Spondy/Retro, spondylolisthesis or retrolisthesis.

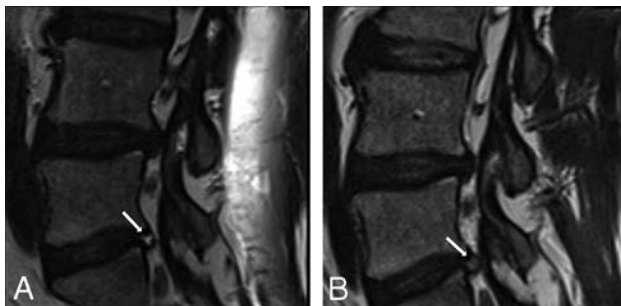


**FIG 2.** Images of an annular fissure from 1 participant with LBP showing an example of definite change.

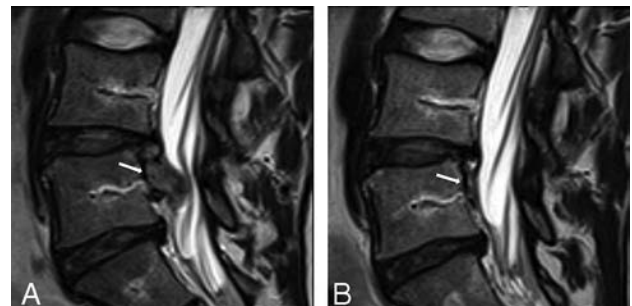


**FIG 3.** Images of disc herniation from 1 participant with LBP showing evidence of definite change.

Visual Analog Scale ( $\leq 1$ -point change). All control participants remained pain-free. The reliability was moderate for identifying change in the HIZ ( $\kappa = 0.60$ ), annular fissures ( $\kappa = 0.51$ ), Modic changes ( $\kappa = 0.53$ ), and disc herniations ( $\kappa = 0.67$ ). For all other findings, there were no findings reported on at least 1 reading, so  $\kappa$  values could not be calculated.

Of the 20 subjects, 17 (85%) completed all 5 MR imaging scans. One participant withdrew after his 2-week scan. Two further subjects and 2 control participants missed 1 scan each. Thus, a total of 144 of a possible 150 (96%) MR imaging scans were performed.

The On-line Table and Fig 1 present the data on definite, probable, and definite or probable change for subjects and controls for each MR imaging finding and any MR imaging finding during the 12-week period. Change was most commonly reported for the MR imaging findings of disc herniations, HIZ, and annular fissures. Examples of definite change in serial MR images are shown in Figs 2 and 3. An example of probable change is shown in Fig 4. For the outcome of definite or probable change in any MR imag-

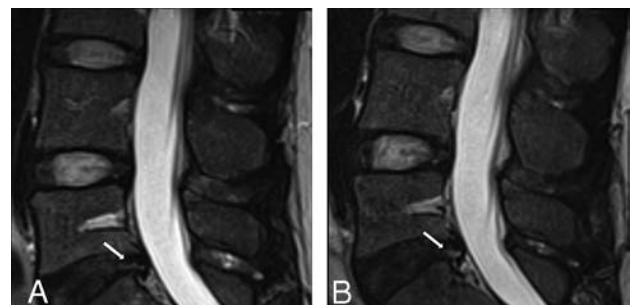


**FIG 4.** Images of a high-intensity zone from 1 participant with LBP showing evidence of probable change.

ing finding during the 12 weeks, similar proportions were found for subjects (85%) and controls (80%) (odds ratio, 1.4; 95% CI, 0.2–10.2). When we investigated specific MR imaging findings, a change in disc herniation, annular fissure, or nerve root compromise was reported more than twice as commonly in subjects as in controls (65% versus 30%; OR, 4.3; 95% CI, 0.8–22.2; and 25%

**Table 3: Proportion of participants in whom MRI findings worsened or improved during a 12-week period<sup>a</sup>**

MRI Findings/Subjective Change	Controls			Subjects with LBP		
	Worsened	Improved	Worsened or Improved	Worsened	Improved	Worsened or Improved
Disc degeneration	1/10 = 10%	0/10 = 0%	1/10 = 10%	2/20 = 10%	0/20 = 0%	2/20 = 10%
Disc signal intensity	1/10 = 10%	0/10 = 0%	1/10 = 10%	2/20 = 10%	0/20 = 0%	2/20 = 10%
Disc height	1/10 = 10%	0/10 = 0%	1/10 = 10%	0/20 = 0%	0/20 = 0%	0/20 = 0%
HIZ	0/10 = 0%	4/10 = 40%	4/10 = 40%	5/20 = 25%	3/20 = 15%	8/20 = 40%
Annular fissure	0/10 = 0%	1/10 = 10%	1/10 = 10%	2/20 = 10%	3/20 = 15%	5/20 = 25%
Modic changes	1/10 = 10%	1/10 = 10%	2/10 = 20%	1/20 = 5%	2/20 = 10%	3/20 = 15%
Disc herniation	0/10 = 0%	3/10 = 30%	3/10 = 30%	7/20 = 35%	6/20 = 30%	13/20 = 65%
Facet joint arthropathy	0/10 = 0%	0/10 = 0%	0/10 = 0%	0/20 = 0%	0/20 = 0%	0/20 = 0%
Central canal stenosis	0/10 = 0%	0/10 = 0%	0/10 = 0%	0/20 = 0%	0/20 = 0%	0/20 = 0%
Spondylolisthesis or retrolisthesis	0/10 = 0%	0/10 = 0%	0/10 = 0%	0/20 = 0%	0/20 = 0%	0/20 = 0%
Edema	0/10 = 0%	1/10 = 10%	1/10 = 10%	0/20 = 0%	0/20 = 0%	0/20 = 0%
Nerve root compromise	0/10 = 0%	0/10 = 0%	0/10 = 0%	2/20 = 20%	1/20 = 10%	3/20 = 15%

<sup>a</sup> If a particular MRI finding both improved and worsened at different follow-up time points (compared with baseline), we reported the change at or closest to the 12-week time point.

versus 10%; OR, 3.0; 95% CI, 0.3–29.9, respectively); however, confidence intervals were very wide, so they must be treated with caution. A change in nerve root compromise was reported in 15% of subjects and no controls. For all other MR imaging findings, the proportions of subjects and controls in whom MR imaging findings were reported to change during 12 weeks were relatively similar. When findings were evaluated separately for definite and probable changes, the results were similar (On-line Table). No MR imaging changes (definite or probable) were reported in either subjects or controls for facet joint arthropathy, canal stenosis, and spondylolisthesis or retrolisthesis.

Table 3 presents the number of MR imaging findings that either improved or worsened during the 12-week follow-up. For the MR imaging findings, such as herniations, annular fissures, HIZs, Modic changes, and nerve root compromise, in which change with time was common, we noted both worsening and improvement during the follow-up period.

## DISCUSSION

### Principal Findings

Changes in most MR imaging findings were observed in a similar proportion of the LBP and control groups, except for herniations, annular fissures, and nerve root compromise, which were more than twice as frequent in the LBP subjects. Caution is required in interpreting these novel findings due to the wide confidence intervals and nonstatistically significant differences. No MR imaging changes were reported in either subjects or controls for facet joint arthropathy, canal stenosis, and spondylolisthesis or retrolisthesis.

### Study Strengths and Weaknesses

One important strength of this study is the prospective design, in which MR imaging changes were tracked longitudinally for 5 serial images, for both those with an acute episode of LBP and a control group. We are not aware of any previous study like this. Furthermore, the control group was well-matched for age, sex, and previous episodes of LBP. Additional strengths include use of the same MR imaging scanner for all imaging and very high rates of follow-up (96% of all possible follow-up occasions).

The use of a subjective evaluation of changes in MR imaging findings could be considered a weakness of the study, despite being made by a highly experienced radiologist with a strict protocol and standardized reporting form. MR imaging reporting was only conducted by 1 radiologist, which is a limitation of the study. The sample size was small because this was an exploratory study, which has likely resulted in our findings being underpowered. The subjects with LBP were selected and were not a consecutive series presenting to care. We aimed to recruit a relatively young sample, with recent sudden-onset pain because we thought that this population provided the best opportunity to identify changes in MR imaging findings during a relatively short time if they occurred. Our findings are unlikely to generalize to a more heterogeneous population of individuals with LBP. Our study also used focused imaging performed on 5 occasions during 12 weeks. This type and frequency of imaging are not representative of, or proposed for, clinical practice. Instead, the study aimed to provide a novel understanding of pathology identifiable on MR imaging.

### Comparison with Other Studies

We are not aware of any study that has compared change in MR imaging findings in subjects with LBP and controls without LBP. Only 1 other study, by Modic et al,<sup>16</sup> has used repeat MR imaging in patients with LBP during the short-term (6 weeks). In the Modic study, it was reported that disc herniations reduced or disappeared in 15% of subjects during the 6-week observation period.<sup>16</sup> In comparison, we report a definite or probable change in disc herniation in 65% (13/20) of subjects during 12 weeks. In our study, 46% of the definite or probable changes (6/13) reported were the result of herniations reducing or disappearing, while in 54% (7/13) of subjects, the herniation appeared or worsened. Modic et al reported that nerve root compromise reduced or disappeared in 17% of patients with LBP. In our study, we found that 15% (3/20) of subjects had a definite or probable change in nerve root compromise. However, in 1 subject, this was a result of the nerve root compromise reducing or disappearing, while in the other 2 subjects, the nerve root compromise worsened.

### Interpretation and Implications

An interesting and somewhat unexpected finding of our study was that some MR imaging findings changed in a relatively high proportion of our controls, as well as our cases. This was particularly the case for disc-based MR imaging findings such as disc herniation. One possible reason for the changes in MR imaging findings in pain-free controls is that they were “true” changes across time occurring despite the controls having no current LBP. Another possibility is that the changes over time in both groups were artifacts of the repeat imaging sectioning being at slightly different points on follow-up scans, so the images looked different, but the appearance was not due to any real change over time. Future studies may choose to compare subjects with acute LBP to a control group with no history of previous LBP to provide a clearer contrast.

Most patients reported substantial clinical improvement in pain during the 12 weeks; however, some MR imaging findings that changed were reported as worsening. This discrepancy questions the clinical importance of the MR imaging findings of worsening or improving, as reported. This study did not aim to investigate the direct relationship between changes in MR imaging findings over time and change in clinical symptoms; very large studies are required to examine this relationship adequately. Although speculative, it is possible that what was reported as a worsening may, in fact, be a marker of the healing process, like bone fractures that can become more evident on x-ray during the first few weeks after a fracture despite healing occurring and pain reducing. This is an important area for future research.

In the past 2 decades, there has been growing understanding that LBP is a complex perceptual experience influenced by environmental and psychological factors, in addition to nociceptive signal generation from peripheral lumbar structures.<sup>17,18</sup> It is possible that the influence of such factors may, at least in part, explain the study finding that changes in some MR imaging findings over time were observed in a similar proportion of subjects with LBP and controls.

The focused imaging protocol used in this study is novel and

may provide insight into important MR imaging changes with time. However, it may also be overly sensitive and identify unimportant changes. Future investigation into the optimal methods of imaging to identify important changes in MR imaging findings is required.

### ACKNOWLEDGMENTS

The authors thank Mr Jeff McIntosh and all the staff at Macquarie Medical Imaging for their administrative assistance and expertise in MR imaging. The authors also wish to thank all the physiotherapy and chiropractic clinics who referred patients for this study and the participants of this study for their time in returning for several follow-up scans.

Disclosures: Julia Hush—UNRELATED: Employment: Macquarie University. Jeffrey G. Jarvik—UNRELATED: Consultancy: HealthHelp, Comments: a radiology benefits management company; Patents (Planned, Pending or Issued): PhysioSonics, Comments: a high-intensity focused ultrasound diagnostic company\*; Stock/Stock Options: PhysioSonics; Travel/Accommodations/Meeting Expenses Unrelated to activities Listed: GE Radiology Research Academic Fellowship, Radiological Society of North America, Comments: member of the academic advisory board for GE Radiology Research Academic Fellowship, Faculty for the Radiological Society of North America, Clinical Trials Workshop. Tue Secher Jensen—UNRELATED: Grants/Grants Pending: Foundation for Chiropractic Research and Post Graduate Education, Comments: salary paid from grants from the Danish Foundation for Chiropractic Research and Post Graduate Education (Sag.nr.108-02/923)\* Mark J. Hancock—RELATED: Grant: Arthritis NSW.\* \*Money paid to the institution.

### REFERENCES

1. Vos T, Flaxman AD, Naghavi M, et al. **Years lived with disability (YLDs) for 1160 sequelae of 289 diseases and injuries 1990–2010: a systematic analysis for the Global Burden of Disease Study 2010.** *Lancet* 2012;380:2163–96 CrossRef Medline
2. Machado LA, Maher CG, Herbert RD, et al. **The effectiveness of the McKenzie method in addition to first-line care for acute low back pain: a randomized controlled trial.** *BMC Med* 2010;8:10 CrossRef Medline
3. UK BEAM Trial Team. **United Kingdom back pain exercise and manipulation (UK BEAM) randomised trial: effectiveness of physical treatments for back pain in primary care.** *BMJ* 2004;329:1377 CrossRef Medline
4. Airaksinen O, Brox J, Cedraschi C, et al. **Chapter 4: European guidelines for the management of chronic nonspecific low back pain.** *Eur Spine J* 2006;15:s192–300 CrossRef Medline
5. Brinjikji W, Luetmer P, Comstock B, et al. **Systematic literature review of imaging features of spinal degeneration in asymptomatic populations.** *AJNR Am J Neuroradiol* 2015;36:811–16 CrossRef Medline
6. Boden SD, Davis D, Dina T, et al. **Abnormal magnetic-resonance scans of the lumbar spine in asymptomatic subjects: a prospective investigation.** *J Bone Joint Surg Am* 1990;72:403–08 CrossRef Medline
7. Jensen MC, Brant-Zawadzki MN, Obuchowski N, et al. **Magnetic resonance imaging of the lumbar spine in people without back pain.** *N Engl J Med* 1994;331:69–73 CrossRef Medline
8. Brinjikji W, Diehn F, Jarvik J, et al. **MRI findings of disc degeneration are more prevalent in adults with low back pain than in asymptomatic controls: a systematic review and meta-analysis.** *AJNR Am J Neuroradiol* 2015;36:2394–99 CrossRef Medline
9. Steffens D, Hancock MJ, Maher CG, et al. **Does magnetic resonance imaging predict future low back pain? A systematic review.** *Eur J Pain* 2014;18:755–65 CrossRef Medline
10. Webster BS, Bauer AZ, Choi Y, et al. **Iatrogenic consequences of early magnetic resonance imaging in acute, work-related, disabling low back pain.** *Spine* 2013;38:1939–46 CrossRef Medline
11. Aprill C, Bogduk N. **High-intensity zone: a diagnostic sign of pain-**

- ful lumbar disc on magnetic resonance imaging.** *Br J Radiol* 1992;65:361–69 CrossRef Medline
12. Carrino JA, Lurie JD, Tosteson ANA, et al. **Lumbar spine: reliability of MR imaging findings.** *Radiology* 2009;250:161–70 CrossRef Medline
  13. Pfirrmann CW, Metzdorf A, Zanetti M, et al. **Magnetic resonance classification of lumbar intervertebral disc degeneration.** *Spine* 2001;26:1873–78 CrossRef Medline
  14. Fardon DF, Williams AL, Dohring EJ, et al. **Lumbar disc nomenclature: version 2.0: recommendations of the combined task forces of the North American Spine Society, the American Society of Spine Radiology and the American Society of Neuroradiology.** *Spine J* 2014;14:2525–45 CrossRef Medline
  15. Pfirrmann CW, Dora C, Schmid MR, et al. **MR image–based grading of lumbar nerve root compromise due to disk herniation: reliability study with surgical correlation.** *Radiology* 2004;230:583–88 CrossRef Medline
  16. Modic MT, Obuchowski NA, Ross JS, et al. **Acute low back pain and radiculopathy: MR imaging findings and their prognostic role and effect on outcome.** *Radiology* 2005;237:597–604 CrossRef Medline
  17. Huijnen IP, Rusu AC, Scholich S, et al. **Subgrouping of low back pain patients for targeting treatments: evidence from genetic, psychological, and activity-related behavioral approaches.** *Clin J Pain* 2015;31:123–32 CrossRef Medline
  18. Hush JM, Stanton TR, Siddall P, et al. **Untangling nociceptive, neuropathic and neuroplastic mechanisms underlying the biological domain of back pain.** *Pain Manag* 2013;3:223–36 CrossRef Medline

# Syringohydromyelia in Patients with Chiari I Malformation: A Retrospective Analysis

K.A. Gad and D.M. Yousem

## ABSTRACT

**BACKGROUND AND PURPOSE:** The association of syringohydromyelia with Chiari I malformation has a wide range, between 23% and 80% of cases in the current literature. In our experience, this range might be overestimated compared with our observations in clinical practice. Because there is an impact of Chiari I malformation–associated syringohydromyelia on morbidity and surgical intervention, its diagnosis is critical in this patient population. Identifying related variables on the basis of imaging would also help identify those patients at risk of syrinx formation during their course of disease.

**MATERIALS AND METHODS:** We performed a retrospective analysis of the MR imaging studies of 108 consecutive cases of Chiari I malformation. A multitude of factors associated with syrinx formation were investigated, including demographic, morphometric, osseous, and dynamic CSF flow evaluation.

**RESULTS:** Thirty-nine of 108 (36.1%) patients with Chiari I malformation had syringohydromyelia. On the basis of receiver operating characteristic curve analysis, a skull base angle (nasion-sella-basion) of 135° was found to be a statistically significant classifier of patients with Chiari I malformation with or without syringohydromyelia. Craniocervical junction osseous anomalies (OR = 4.3,  $P = .001$ ) and a skull base angle of >135° (OR = 4.8,  $P = .0006$ ) were most predictive of syrinx formation. Pediatric patients (younger than 18 years of age) who developed syringohydromyelia were more likely to have associated skull base osseous anomalies than older individuals ( $P = .01$ ).

**CONCLUSIONS:** Our findings support evidence of the role of foramen magnum blockage from osseous factors in the development of syringohydromyelia in patients with Chiari I malformation.

**ABBREVIATION:** CMI = Chiari I malformation

The association of syringohydromyelia with Chiari I malformation (CMI) is estimated in the literature, with a wide range between 23% and 80% of cases.<sup>1-5</sup> The heterogeneity of values may imply either inconsistent methodologic criteria for defining CMI with discrepancy of measurements or a possible overlap among cases with true syrinx and central canal dilation, and those with cord edema and a clinical presyrinx state. Moreover, the true prevalence of syrinx in this population remains poorly defined due to factors related to characteristics of the studied populations. Selecting only patients who have myelopathic symptoms may

falsely increase the prevalence. Similar selection bias can also occur when including only patients who are referred for neurosurgical consultation because of spinal pathology.

A large-scale survey for the Pediatric Section of the American Association of Neurologic Surgeons concluded that syringohydromyelia is considered an indication for surgery in CMI.<sup>6</sup> Recent DTI studies have shown significantly decreased fractional anisotropy values at the level of a syrinx, which appeared more evident in symptomatic patients.<sup>7</sup> The critical association of syringohydromyelia secondary to CMI with regard to surgical intervention makes early diagnosis crucial in choosing the management plan for these patients.

In the current study, we sought to determine the prevalence of syringohydromyelia associated with symptomatic CMI by a retrospective analysis of 108 MR imaging cases diagnosed at our institution with the most widely accepted diagnostic criteria. A multitude of demographic, morphometric, osseous, and functional neuropathologic factors associated with the condition were

Received July 14, 2016; accepted after revision May 6, 2017.

From the Division of Neuroradiology (K.A.G., D.M.Y.), The Russell H. Morgan Department of Radiology and Radiological Science, The Johns Hopkins Medical Institutions, Baltimore, Maryland; and Radiology Department (K.A.G.), Faculty of Medicine, Suez Canal University, Ismailia, Egypt.

Please address correspondence to David M. Yousem, MD, MBA, Johns Hopkins Medical Institutions, 600 N. Wolfe St, Phipps B100F, Baltimore, MD 21287; e-mail: dyousem1@jhmi.edu

<http://dx.doi.org/10.3174/ajnr.A5290>

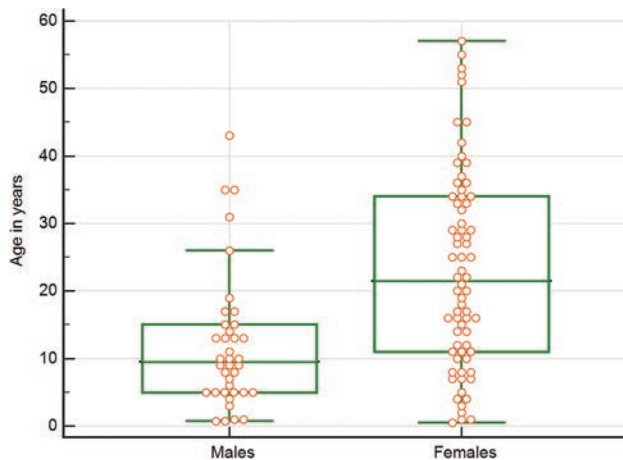


**FIG 1.** A graph plotting age and sex demographics of all study subjects.

investigated to better understand the pathophysiology of CMI-associated syringohydromyelia. We hypothesized that skull base anomalies may be related to syrinx formation in symptomatic patients with CMI.

## MATERIALS AND METHODS

Following institutional review board approval and with Health Insurance Portability and Accountability Act compliance, 108 consecutive patients with the MR imaging diagnosis of CMI were retrospectively identified in radiology records at the Johns Hopkins Medical institution. A request form was submitted to search for patients with CMI in radiology reports with the following keywords: Chiari 1, Chiari I, CM1, and CMI.

Inclusion criteria were herniation of at least 1 cerebellar tonsil  $\geq 5$  mm below the McRae line (basion-to-opisthion) on sagittal T1-weighted images, and supporting clinical findings including the following: 1) posterior headache worse with the Valsalva maneuver, coughing, sneezing, or exercise; 2) neck pain, tingling, numbness, or burning; 3) generalized weakness or unrelenting fatigue; 4) dizziness worse with lying down; 5) peripheral motor/sensory deficit; 6) sleep apnea; or 7) lower cranial neuropathy. Thirty-seven males and 70 females with a median age of 15.5 years (95% CI, 12.3–19.0 years) were included from January 2014 to May 2016 (Fig 1). Any tonsillar herniation secondary to a space-occupying lesion was excluded. Exclusion criteria also included previous decompressive, cranial, or spinal surgeries. MR images were evaluated, including sagittal T1, axial T1, and axial T2 of the brain and T1 (sagittal and axial) and T2 (sagittal and axial) of the spine. Dynamic phase-contrast CSF flow studies were also evaluated when available.

After we excluded 7 studies due to poor technical quality, only 69 patients with technically accepted phase-contrast images at a velocity-encoding threshold of 5 cm/s were analyzed. CSF flow was evaluated qualitatively on the basis of phase-contrast cine images. A normal flow pattern must be a clear bidirectional flow signal: caudal and cranial (black and white with the cardiac cycle) at the ventral and dorsal columns within the foramen magnum. Any deviation from this strict criterion was considered abnormal CSF flow.

Two blinded subspecialty-certified neuroradiologists (with

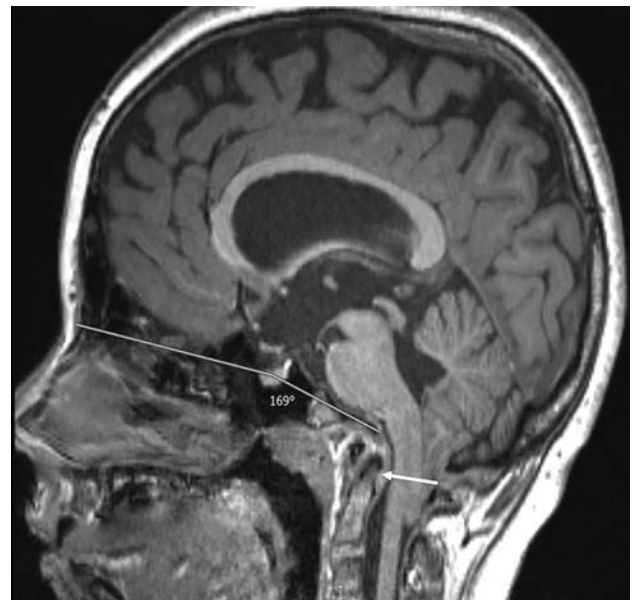


**FIG 2.** A 12-year-old male patient with CMI. The skull base angle from the nasion to the center of the pituitary fossa to the clivus (anterior wall of the foramen magnum) measures  $169^\circ$ . The odontoid tip is retroverted; this feature results in compression on the cervicomedullary junction (arrow).

15 and 11 years of neuroradiology practice) read the cases followed by a third reading by an expert subspecialty-certified neuroradiologist (with 27 years of neuroradiology practice) if there was any interrater discordance. The main dependent variable was the presence of syringohydromyelia. Any measurable intramedullary sharply demarcated fluid cavity of  $>2$ -mm width in the axial plane that followed CSF signal in both T1 and T2 imaging was considered a syrinx. We identified the following independent variables: degree (in millimeters) of tonsillar herniation, the presence of hydrocephalus, the location and size of the syrinx, and associated craniocervical osseous anomalies including the following: 1) platybasia defined as abnormal flattening of the skull base with a basal angle measuring  $>143^\circ$  between intersecting lines from the nasion to the sella (in the center of the pituitary gland and from the sella to the anterior margin of the foramen magnum) (Fig 2)<sup>8</sup>; 2) a retroverted odontoid defined as a posterior inclination of the odontoid relative to the body of C2 with a retroversion angle measuring  $<70^\circ$  (Fig 3)<sup>9</sup>; 3) a short hypoplastic clivus defined as  $<1.5$ -cm clival length measured from the sphenoclivus synchondrosis to the basion<sup>10</sup>; and 4) basilar invagination defined as a protrusion of the odontoid tip of at least 5 mm above the Chamberlain line between the posterior end of the hard palate and the posterior lip of the foramen magnum (Fig 4).<sup>10</sup> All measurements were made with the VitreaView platform 2010–2016 (Vital Images, Minnetonka, Minnesota), with electronic calipers and electronic measurement of angulation.

## Statistical Analysis

We calculated the prevalence of syringohydromyelia in our sample. We examined the likelihood of an association of the variables defined above with the occurrence of syringohydromyelia using  $\chi^2$  analysis. For continuous variables, receiver operating charac-

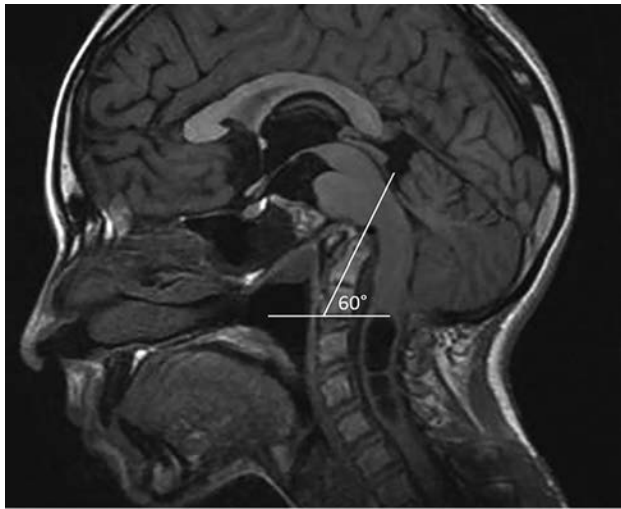


**FIG 3.** Sagittal T1-weighted MR image demonstrating an abnormally small odontoid retroversion angle ( $\sim 60^\circ$ ) between a horizontal line parallel to the inferior endplate of C2 and the long axis of the odontoid process passing through its tip in a child with CMI and associated cervical syrinx.

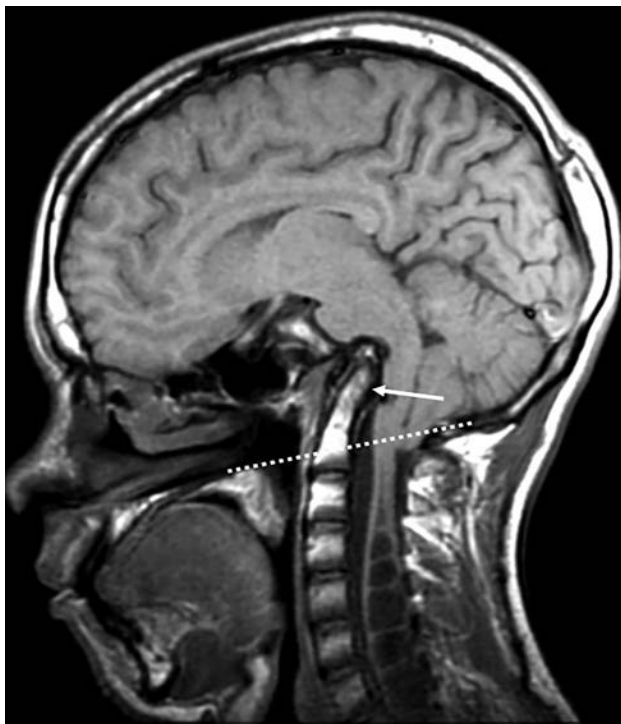


**FIG 4.** Sagittal T1 at the level of craniocervical junction in an 18-year-old male patient with CMI showing a retroverted odontoid (arrow) with its tip protruding into the foramen magnum 22 mm above the Chamberlain line (dotted line), resulting in basilar invagination and anterior brain stem compression. Note multilevel syrinx formation of the upper cord. The clivus (not completely shown) is short and deformed.

teristic curves were generated to identify cutoff points with the best performance of sensitivity and specificity. At these cutoff points, logistic regression analysis was performed to identify the best-fitting model that affects the occurrence of syringomyelia in patients with CMI. Odds ratios were calculated. All statistical tests were performed by using the MedCalc statistical soft-

#### Frequency of syrinx formation according to location

Syrinx Location ( $n = 39$ )	No.
Cervicothoracic	23
Cervical	9
Thoracic	6
Whole cord	1

ware package for Windows, Version 16.4.3–2016, (MedCalc Software, Mariakerke, Belgium).

#### RESULTS

Syringomyelia was present in 39 (36.1%) of 108 symptomatic patients with CMI (Table). Hydrocephalus was present in only 7/108 patients (6.5%); 3 of 7 had no syringomyelia. No statistically significant association was found between the patient age or sex and syrinx formation. Among our total sample of 108 symptomatic patients with CMI, 30 had  $\geq 1$  bony anomaly identified at the craniocervical junction as follows: retroverted odontoid ( $n = 23$ , with the retroversion angle ranging from  $59^\circ$  to  $68^\circ$ ); platybasia ( $n = 15$ , with the skull base angle ranging from  $145^\circ$  to  $164^\circ$ ); short clivus ( $n = 7$ , with clival length ranging from 9 to 43 mm); and basilar invagination ( $n = 6$ , with the protrusion distance above the Chamberlain line ranging from 5 to 22 mm). The presence of any type of craniocervical bony anomaly was statistically associated with syringomyelia ( $P = .001$ ). A skull base angle at a cutoff point of  $135^\circ$  was identified by the receiver operating characteristic curve as having the best performance for the prediction of syringomyelia ( $P = .02$ ) with a sensitivity of 50% and a specificity of 82.6% (Fig 5). Above this cutoff point ( $>135^\circ$ ), there was a strong  $\chi^2$  association with syrinx formation ( $P = .0002$ ). With univariate logistic regression analysis, craniocervical junction osseous anomalies (odds ratio = 4.3,  $P = .001$ ) and a skull base angle of  $>135^\circ$  (odds ratio = 4.8,  $P = .0006$ ) were the most predictive of syrinx formation. With multivariate analysis, the only predictive variable was a skull base angle of  $>135^\circ$ .

Among patients with syringomyelia ( $n = 39$ ), the patient age was associated with craniocervical anomalies based on logistic regression ( $P = .01$ ). Receiver operating characteristic curve analysis showed a cutoff point of 18 years as patients younger than 18 years of age with syringomyelia were more likely to have associated craniocervical bony anomalies compared with older individuals ( $P = .04$ ).

There was no statistically significant association between the degree of tonsillar herniation or abnormal phase-contrast CSF flow at the foramen magnum and syrinx formation.

Of our 39 cases of syringomyelia, 25 had a large syrinx with the widest dimension on axial scans of  $>6$  mm. The smallest syrinx size encountered in 1 case measured 3 mm in width. However, no statistically significant association could be found between the size of syrinx and any of the tested variables.

#### DISCUSSION

##### Prevalence of Syringomyelia

Identifying syrinx formation in patients with symptomatic CMI is critical in working up their management plan. In our descriptive study of 108 symptomatic patients who were clinically diagnosed with CMI, syringomyelia was present in 39 (36.1%) pa-

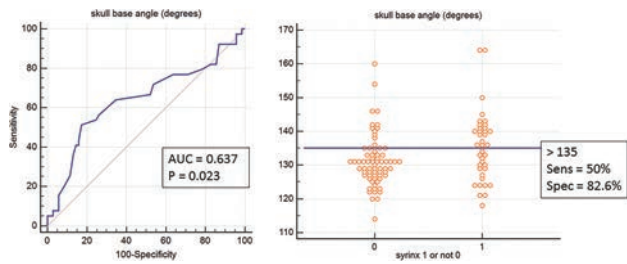


**FIG 5.** Receiver operating characteristic curve (*left*) and plot graph (*right*) demonstrating the skull base angle in the prediction of syrinx formation among our total sample ( $n = 108$ ). AUC indicates area under the curve; Sens, sensitivity; Spec, specificity.

tients. We believe that our prevalence is not affected by any selection bias that may falsely overestimate or underestimate the true figures because our patients were identified by MR imaging as well as clinical criteria in a specific 2014–2016 timeframe, including all referred individuals based on MR imaging findings and clinical assessment. They were not selected from neurosurgical archives or data bases in a trial, to avoid commonly encountered overestimation of syringohydromyelia in studies in which patients were surgical candidates. Our sample also included those patients who were incidentally diagnosed while undergoing MR brain imaging for any other reason and then referred for clinical consultation and diagnosed as having CMI based on confirming clinical signs and symptoms. Patients with secondary CMI such as those with an intracranial space-occupying lesion were also excluded.

Several studies have been attempted, with different criteria, to explore the imaging prevalence of syringohydromyelia among patients with CMI. In a study by Strahle et al,<sup>3</sup> most patients underwent MR imaging of the cervical spine and almost half of them underwent full spine imaging, resulting in 22.9% of patients with CMI having a syrinx detected. Aitken et al<sup>11</sup> identified spinal syringes in 12% of children with CMI in their study; the authors relied on reviewing only radiology reports in many patients without having access to their images.

### Craniocervical Bony Anomalies

In our study, the presence of craniocervical bony anomalies was statistically associated with syringohydromyelia. A retroverted odontoid with an angle of  $<70^\circ$  was found to be the most common developmental osseous anomaly ( $n = 23$ ) of the craniocervical junction among our series, while basilar invagination was present in only 6 cases. With logistic regression, craniocervical junction osseous anomalies and a skull base angle of  $>135^\circ$  were most predictive of syrinx formation. Since 1896, when Arnold Chiari highlighted insufficient bone growth and insufficient enlargement of portions of the skull during development as additional mechanisms that cause increased intracranial pressure and subsequent tonsillar herniation, it has been accepted that developmental morphometric anomalies of the posterior fossa are linked to CMI.

In the classic study on 364 patients with CMI by Milhorat et al,<sup>1</sup> in which syringohydromyelia was found in 65% of patients, the authors highlighted commonly associated problems, including scoliosis (42%), a retroflexed odontoid process (26%), basilar invagination (12%), and varying degrees of bony dysplasia of the

posterior cranial fossa based on volumetric calculations. Vega et al<sup>12</sup> studied 42 patients with CMI compared with 46 controls and found that patients with CMI had shorter clivus lengths and a shorter Chamberlain line. The concept of complex Chiari malformation is being widely accepted in the neurosurgery literature. A complex severe craniocervical anomaly would add more burden to the disease.<sup>13</sup> We believe that a complex Chiari malformation might represent a separate entity of the disease that requires a different surgical approach. Brockmeyer<sup>14</sup> defined the complex Chiari malformation as “cerebellar tonsil herniation combined with one or more of the following radiographic findings: brain stem herniation through the foramen magnum (Chiari 1.5 malformation), medullary kink, retroflexed odontoid, abnormal clival-cervical angle, occipitalization of the atlas, basilar invagination, syringohydromyelia or scoliosis.” The authors differentiated patients with complex Chiari malformation from those with typical CMI as being more likely to require advanced surgical interventions other than standard suboccipital decompression.

In another study by Moore and Moore,<sup>15</sup> odontoid retroflexion, craniocervical junction osseous anomalies, and syringohydromyelia were more often observed in patients with complex Chiari malformation than in those with typical CMI. These observations are in parallel with our findings. Our odds ratios were 4.8 and 4.3 for craniocervical anomalies and a skull base angle of  $>135^\circ$ , respectively, in the prediction of syringohydromyelia. These findings might give importance to the variant of complex Chiari malformation as a special research entity and should be a point of emphasis in the radiology report when these findings are present. The position of the obex was described in the same study by Moore and Moore<sup>15</sup> as a characteristic imaging feature that was present in all complex cases. However, we did not evaluate the obex level in our study due to interobserver variability.

CSF flow studies indicated that the tonsils in CMI partially obstruct the free movement of CSF across the foramen magnum. Normally, the cardiac systole delivers blood to the brain; most of the new volume is absorbed by the venous system of the brain, however, during systole; and about 0.75–1.0 mL of CSF gets rapidly moved from the cisterna magna across the subarachnoid space and into the spinal subarachnoid space at the level of the foramen magnum. This extra amount of spinal CSF should move back to the cranial space during diastole. Blocking this backward rapid movement of CSF partially entraps the spinal intrathecal space, resulting in reduced compliance in the spinal CSF space. The tonsillar movement is against a partially entrapped CSF space with reduced compliance and increased intrathecal pressure. It is the complex interplay between clivus inclination and odontoid angulation that can create a point of mechanical stress and tension leading to anterior brain stem compression.

The presence of associated skull base anomalies makes CMI defined by neurosurgeons a “complex” Chiari malformation, which requires more advanced surgical decompressive approaches. According to Bollo et al,<sup>13</sup> the presence of basilar invagination puts the patient at risk of craniocervical fusion. In our study, we evaluated the presence of craniocervical kyphosis by identifying platybasia and odontoid retroversion and by measuring the skull base angle (intersecting lines from the nasion to the sella and from the sella to the anterior margin of the foramen

magnum). A normal angle lies between 125° and 143°. Although an angle of >143° is required to quantitatively diagnose platybasia, we found that higher angles are more commonly associated with syrinx formation using logistic regression among our cases of CMI. Our findings are in full support of the suggested pathophysiology of CMI, in which an obtuse angle results in an upward tilt of the clivus with a relatively higher location of the opisthion. This aberrant osseous configuration is associated with 2 abnormal morphometric changes: 1) narrowing or ventral compromise to the foramen magnum with corresponding downstream CSF flow resulting in syrinx formation, and 2) a smaller posterior fossa volumetric capacity with corresponding cerebellar herniation and crowding of structures at the already compromised foramen magnum, leading to more blockage.

A cutoff point of 135° was statistically significant, showing a relatively high specificity of 82.6% in predicting an associated syringohydromyelia. Although its sensitivity was not high (50%), there were only 12/69 (17.4%) patients without syrinx who showed a skull base angle above 135°. Sgouros et al<sup>16</sup> noted that skull base angles were larger in 30 patients with CMI compared with controls. The authors used a modified angle with the dorsum sella as a reference midpoint for intersecting lines. Their angle was slightly higher than ours where lines intersect more inferiorly in the pituitary center; however, in their results, the presence of syringohydromyelia was also associated with a larger angle (151°) compared with CMI without syringohydromyelia (145°). We believe that measuring the skull base angle in CMI can help identify those patients at risk of developing syrinx (OR = 4.8, *P* = .0006).

### **Impaired CSF Flow by Tonsillar Herniation**

Disturbed CSF flow dynamics remain a standard phenomenon by which patients with CMI can develop syringohydromyelia. Bunck et al<sup>17</sup> revealed pronounced alteration of CSF flow dynamics with 4D phase-contrast quantitative MR imaging in 12 patients with CMI with syringohydromyelia compared with 8 without it. In our study, we could not establish a statistically significant association between impaired CSF flow in cine phase-contrast MR imaging and syrinx formation. The association between the degree of mechanical blockage and the formation of syrinx has been debatable in the literature. Our finding of the lack of association may shed light on a noncompressive etiology of syringohydromyelia.

Schuster et al<sup>18</sup> presented a systematic review of residual syringohydromyelia after decompressive surgery, in which the rate of postoperative persistent syrinx ranged between 0% and 22%, raising the possibility of a noncompressive etiology in the development of syrinx. We believe that CSF flow dynamics at the foramen magnum is a complicated process that would have been more accurately evaluated if quantitative indicators were considered. Due to this technical limitation of our study besides the relatively small number of cases with available technically acceptable phase-contrast MR images (69/108), a clear interpretation of these findings was not possible.

Clarke et al<sup>19</sup> presented a computational model in CMI, in which the presence and absence of syringohydromyelia were compared. This study introduced an advanced understanding of the pressure gradient and peak pressure timing differences between CMI with or without syringohydromyelia. The authors

found that the dynamic profile of subarachnoid spinal pressure relative to the cardiac cycle (in which intraspinal arteriolar pressure varies) is more critical in regard to the chance of fluid accumulation and the development of a presyrinx or syrinx state.<sup>19</sup>

The association between the degree of mechanical blockage and the formation of syrinx has been debatable in the literature. Although the degree of tonsillar herniation in our results gives an insight into the mechanical perspective of CSF flow compromise at the foramen magnum, it is still insufficient to predict syringohydromyelia on the basis of how far cerebellar tonsils have descended, possibly because of the complex mechanical-versus-nonmechanical algorithms determining the pathogenesis of the condition.

### **Study Limitations**

Our study had a few technical limitations related to the partial inhomogeneity of the data (such as fewer CSF flow studies) as well as the cross-sectional design with a lack of longitudinal follow-up. The development of syringohydromyelia in CMI is a dynamic process. Further longitudinal studies are needed to follow up patients with CMI, trying to identify different trends in relation to syrinx formation in those patients and how these trends could be affected by the degree of mechanical blockage and the age of the patient. Quantitative assessment of CSF flow would also represent a valid parameter compared with the qualitative method we used. Assessment of the obex level by quantitative measurement of its position relative to the foramen magnum would have been an important variable that we recommend in future studies because it might be linked to the diagnosis of complex Chiari malformation besides other craniocervical anomalies.

### **CONCLUSIONS**

Our prevalence of syringohydromyelia associated with CMI (36.1%) lies in the low range compared with existing values in the literature. In view of the statistically significant association between syrinx formation and craniocervical osseous abnormalities, our findings support the role of developmental foramen magnum compromise in the pathophysiology of CMI-related syringohydromyelia.

Disclosures: David M. Yousem—UNRELATED: Expert Testimony: medicolegal cases, self-employed; Payment for Lectures Including Service on Speakers Bureaus: American College of Radiology Education Center course director\*; Royalties: Elsevier for 4 books; Payment for Development of Educational Presentations: CMEInfo.com for Hopkins continuing medical education courses\*. \*Money paid to the institution.

### **REFERENCES**

1. Milhorat TH, Chou MW, Trinidad EM, et al. **Chiari I malformation redefined: clinical and radiographic findings for 364 symptomatic patients.** *Neurosurgery* 1999;44:1005–17 CrossRef Medline
2. Speer MC, Enterline DS, Mehlretter L, et al. **Review article: Chiari type I malformation with or without syringomyelia—prevalence and genetics.** *J Gen Couns* 2003;12:297–311 CrossRef Medline
3. Strahle J, Muraszko KM, Kapurch J, et al. **Chiari malformation type I and syrinx in children undergoing magnetic resonance imaging.** *J Neurosurg Pediatr* 2011;8:205–13 CrossRef Medline
4. Ellenbogen RG, Armonda RA, Shaw DW, et al. **Toward a rational treatment of Chiari I malformation and syringomyelia.** *Neurosurg Focus* 2000;8:1–10 Medline
5. Moriwaka F, Tashiro K, Tachibana S, et al. **Epidemiology of syringo-**

- myelia in Japan: the nationwide survey [in Japanese]. *Rinsho Shinkeigaku* 1995;35:1395–97 Medline
6. Haines SJ, Berger M. **Current treatment of Chiari I malformations types I and II: a survey of the Pediatric Section of the American Association of Neurological Surgeons.** *Neurosurgery* 1991;28:353–57 CrossRef Medline
  7. Yan H, Zhu Z, Liu Z, et al. **Diffusion tensor imaging in cervical syringomyelia secondary to Chiari I malformation: preliminary results.** *Spine (Phila Pa 1976)* 2015;40:E381–87 CrossRef Medline
  8. Koenigsberg RA, Vakil N, Hong TA, et al. **Evaluation of platybasia with MR imaging.** *AJNR Am J Neuroradiol* 2005;26:89–92 Medline
  9. Besachio DA, Khaleel Z, Shah LM. **Odontoid process inclination in normal adults and in an adult population with Chiari malformation type I.** *J Neurosurg Spine* 2015;23:701–06 CrossRef Medline
  10. Pang D, Thompson DN. **Embryology and bony malformations of the craniovertebral junction.** *Childs Nerv Syst* 2011;27:523–64 CrossRef Medline
  11. Aitken LA, Lindan CE, Sidney S, et al. **Chiari type I malformation in a pediatric population.** *Pediatr Neurol* 2009;40:449–54 CrossRef Medline
  12. Vega A, Quintana F, Berciano J. **Basichondrocranium anomalies in adult Chiari type I malformation: a morphometric study.** *J Neurol Sci* 1990;99:137–45 CrossRef Medline
  13. Bollo RJ, Riva-Cambrin J, Brockmeyer MM, et al. **Complex Chiari malformations in children: an analysis of preoperative risk factors for occipitocervical fusion.** *J Neurosurg Pediatr* 2012;10:134–41 CrossRef Medline
  14. Brockmeyer DL. **The complex Chiari I: issues and management strategies.** *Neurol Sci* 2011;32(suppl 3):S345–47 CrossRef Medline
  15. Moore HE, Moore KR. **Magnetic resonance imaging features of complex Chiari malformation variant of Chiari I malformation.** *Pediatr Radiol* 2014;44:1403–11 CrossRef Medline
  16. Sgouros S, Kountouri M, Natarajan K. **Skull base growth in children with Chiari malformation type I.** *J Neurosurg* 2007;107(3 suppl):188–92 Medline
  17. Bunck AC, Kroeger JR, Juettner A, et al. **Magnetic resonance 4D flow analysis of cerebrospinal fluid dynamics in Chiari I malformation with and without syringomyelia.** *Eur Radiol* 2012;22:1860–70 CrossRef Medline
  18. Schuster JM, Zhang F, Norvell DC, et al. **Persistent/recurrent syringomyelia after Chiari decompression: natural history and management strategies—a systematic review.** *Evid Based Spine Care J* 2013;4:116–25 CrossRef Medline
  19. Clarke EC, Fletcher DF, Stoodley MA, et al. **Computational fluid dynamics modelling of cerebrospinal fluid pressure in Chiari malformation and syringomyelia.** *J Biomech* 2013;46:1801–09 CrossRef Medline

# Characteristics of CSF Velocity-Time Profile in Posttraumatic Syringomyelia

J. Yeo, S. Cheng, S. Hemley, B.B. Lee, M. Stoodley, and L. Bilston



## ABSTRACT

**BACKGROUND AND PURPOSE:** The development of syringomyelia has been associated with changes in CSF flow dynamics in the spinal subarachnoid space. However, differences in CSF flow velocity between patients with posttraumatic syringomyelia and healthy participants remains unclear. The aim of this work was to define differences in CSF flow above and below a syrinx in participants with posttraumatic syringomyelia and compare the CSF flow with that in healthy controls.

**MATERIALS AND METHODS:** Six participants with posttraumatic syringomyelia were recruited for this study. Phase-contrast MR imaging was used to measure CSF flow velocity at the base of the skull and above and below the syrinx. Velocity magnitudes and temporal features of the CSF velocity profile were compared with those in healthy controls.

**RESULTS:** CSF flow velocity in the spinal subarachnoid space of participants with syringomyelia was similar at different locations despite differences in syrinx size and locations. Peak cranial and caudal velocities above and below the syrinx were not significantly different (peak cranial velocity,  $P = .9$ ; peak caudal velocity,  $P = 1.0$ ), but the peak velocities were significantly lower ( $P < .001$ ,  $P = .007$ ) in the participants with syringomyelia compared with matched controls. Most notably, the duration of caudal flow was significantly shorter ( $P = .003$ ) in the participants with syringomyelia.

**CONCLUSIONS:** CSF flow within the posttraumatic syringomyelia group was relatively uniform along the spinal canal, but there are differences in the timing of CSF flow compared with that in matched healthy controls. This finding supports the hypothesis that syrinx development may be associated with temporal changes in spinal CSF flow.

Syringomyelia is a neurologic condition characterized by the development of a syrinx, a fluid cyst in the spinal cord. It is commonly associated with conditions that obstruct spinal CSF flow such as spinal cord injury,<sup>1</sup> Chiari type I malformation, and spinal tumors. Syrinxes form and enlarge in either the central canal of the spinal cord or in the cord parenchyma. For a syrinx to enlarge, the laws of mechanics require that the syrinx pressure

exceed the pressure in the surrounding cord tissue and spinal subarachnoid space. However, the mechanism of CSF flow into a syrinx in the presence of this reverse pressure gradient is poorly understood and remains controversial. Computational models suggest that CSF could be driven by cardiac pulsations from the spinal subarachnoid space into the spinal cord via periarterial spaces, including toward a syrinx.<sup>2</sup> Besides CSF, another possible source of syrinx fluid could be extracellular fluid. It has recently been shown that after spinal cord injury, the blood–spinal cord barrier is damaged for an extended time<sup>3</sup> and fluid could hence pass from the vasculature into a syrinx. However, the source of fluid in the syrinx has yet to be identified because the chemical composition of CSF and extracellular fluid is indistinguishable.<sup>4</sup>

Understanding the characteristics of CSF dynamics in the spinal subarachnoid space and the way they change in conditions associated with syringomyelia may help elucidate the mechanism of the disease. Characterizing CSF flow in syringomyelia may also improve clinical management because syrinx morphology from MR anatomic images alone is insufficient to predict disease progression and surgical outcomes. Current treatment techniques for posttraumatic syringomyelia, such as shunting, are associated

Received February 20, 2017; accepted after revision April 24.

From Neuroscience Research Australia (J.Y., B.B.L., L.B.), Randwick, New South Wales, Australia; Department of Engineering (S.C.), Faculty of Science and Engineering, and Australian School of Advance Medicine (S.H., M.S.), Macquarie University, Sydney, New South Wales, Australia; Prince of Wales Hospital (B.B.L.), Sydney, New South Wales, Australia; and Prince of Wales Clinical School (B.B.L., L.B.), University of New South Wales, Kensington, New South Wales, Australia.

This research was supported by the Australian National Health and Medical Research Council (APP1063628). L.B. is supported by National Health and Medical Research fellowship. The authors would also like to acknowledge the Column of Hope for funding part of this project.

Please address correspondence to Shaokoon Cheng, PhD, Department of Engineering, Faculty of Science and Engineering, Balaclava Rd, North Ryde, NSW, 2109, Australia; e-mail: shaokoon.cheng@mq.edu.au

Indicates open access to non-subscribers at [www.ajnr.org](http://www.ajnr.org)

<http://dx.doi.org/10.3174/ajnr.A5304>

with syrinx recurrence. Therefore, understanding the CSF flow characteristics in these patients may help in developing effective techniques to manage this complex condition.

CSF flow in the spinal subarachnoid space consists of pulsatile caudal and rostral flow during systole and diastole, respectively.<sup>5</sup> Caudal flow in the spinal subarachnoid space commences approximately 100 ms after the onset of systole in healthy individuals, and the timing of its onset is affected by age and CSF obstructions in the spinal subarachnoid space. Detailed mechanisms that underpin the earlier onset of peak caudal CSF are not yet well-established and may be influenced by compliance in the cranio-spinal system. In the spinal subarachnoid space of healthy individuals, peak caudal and cranial velocities and their onset vary with spinal level. However, these variables are different in those with Chiari malformation.<sup>6</sup>

Despite numerous studies in the literature of CSF flow in participants with Chiari type I malformation with and without syringes, there is a lack of understanding of spinal CSF dynamics in those who have sustained a spinal cord injury. Therefore, this study aimed to determine the CSF velocity-time profiles adjacent to the syrinx in participants with spinal cord injury and compare them with those in healthy controls. It is hypothesized that the peak CSF velocities and timing of the profile would be significantly altered in patients with posttraumatic syringomyelia.

## MATERIALS AND METHODS

### Participants

This study was approved by the South Eastern Sydney Local Health District Human Research Ethics Committee (Sydney, New South Wales, Australia). Participants were recruited from the spinal injury outpatient clinic at the Prince of Wales Hospital, Sydney, New South Wales, Australia. All patients had an American Spinal Injury Association (ASIA) impairment scale score of A except for 1 participant with no recorded ASIA score.<sup>7</sup> None had past spinal surgery. They were informed about the details of the study on at least 2 separate occasions before their scan, and written informed consent was obtained. They were also carefully screened for MR imaging safety. Six participants (4 men, 2 women; mean age,  $46.5 \pm 13.9$  years) previously diagnosed with posttraumatic syringomyelia were selected for the study.

The participants with syringomyelia were recruited prospectively. Their data were compared with retrospectively reanalyzed scanned data of 6 healthy controls (3 men, 3 women) matched for age (mean age,  $45 \pm 18.1$  years) and weight. On the basis of a statistical power analysis, a sample size of 6 was determined to adequately demonstrate significant differences in the characteristics of the CSF velocity-time profile between the participants with syringomyelia and healthy controls based on a mean difference of  $0.15 \pm 0.09$  cm/s and 80% power in a 2-tailed *t* test.

### Imaging Protocols

MR imaging measurements were performed on a 3T MR imaging scanner (Achieva TX; Philips Healthcare, Best, the Netherlands). Depending on the syrinx location, participants were scanned with a neurovascular coil and/or a 32-channel thoracic coil. Meanwhile, the healthy controls were retrospectively scanned with a neurovascular coil. All participants were scanned without any an-

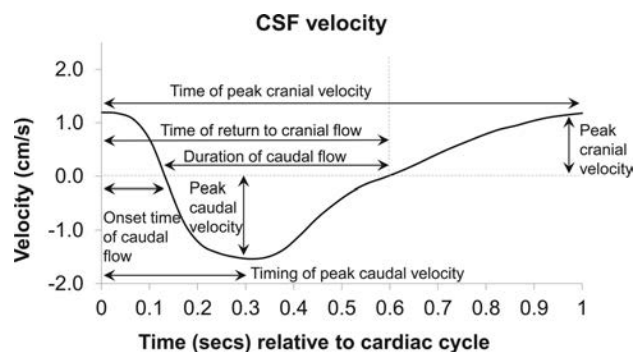


**FIG 1.** Representative CSF velocity profile from a healthy control volunteer showing measurements collected for analysis.

esthesia. A T1-weighted sequence was performed in the midsagittal plane to verify the syrinx location. The parameters of the sequence were the following: flip angle =  $10^\circ$ , FOV =  $200 \times 200$  mm, TR/TE = 21/7.3 ms, and section thickness = 5 mm. Phase-contrast MR imaging was used to measure CSF flow velocity, and cardiac gating was achieved with vector cardiogram leads. Thirty cardiac phase images were obtained from the onset of the R wave. CSF flow velocities at the base of the skull and above and below the syrinx spinal level were measured with an axial imaging plane aligned perpendicular to the spinal cord. The encoding velocities for the scans were 10 cm/s for the base of the skull and 12–14 cm/s for other spinal levels. Control flows were measured at the base of skull and the C5 spinal level. The imaging parameters for this sequence were the following: flip angle =  $10^\circ$ , matrix =  $240 \times 176$ , FOV =  $250 \times 250$  mm, TR = 21 ms, TE = 6.8 ms, and section thickness = 5 mm. The duration of each scan session, including setup and subject positioning, varied among participants and ranged from 1 to 1.5 hours. The heart rates of the participants with syrinx and the controls during the scan were  $64.3 \pm 4.6$  beats per minute and  $69.0 \pm 15.0$  beats per minute, respectively, and they were not significantly different ( $P = .4$ ).

### Data Analysis

CSF velocity-time profiles were measured from phase-contrast MR images with Segment.<sup>8</sup> ROIs were defined (2 lateral, 1 anterior, 1 posterior) with circular monitoring points of approximately 2 mm in diameter. The average CSF velocity-time profiles of the 4 ROIs were obtained at the 3 spinal levels (base of the skull and above and below the syrinx), and features of the profile were analyzed with the same protocol as that of Clarke et al.<sup>9</sup> The features measured were maximum velocities in the cranial and caudal direction and their timing, onset time and duration of caudal flow, and time of return to cranial flow. A representative CSF velocity-time profile from a healthy control is shown in Fig 1.

Features of the velocity-time profiles were compared for the following: 1) above and below the syrinx in participants with syringomyelia, 2) the base of the skull in participants with syringomyelia and healthy controls, and 3) the spinal level near the syrinx in participants with syringomyelia (between C4 and T12) and healthy controls (C5). A paired *t* test was used to analyze differences in CSF flow above and below the syrinx, and an unpaired *t*

test was used for all other statistical analyses. A Bonferroni post hoc correction was performed by adjusting the significance level of the *t* tests from .05 to .007. This was obtained by dividing .05 by 7 because there were 7 hypotheses (representing the 7 features of the CSF velocity-time profile) that would be tested using the average velocity-time profile.

**Table 1: Syring maximum transverse diameter and location in participants<sup>a</sup>**

Patients with Syring	Syrinx Location	Spinal Injury	Maximum Syring Diameter (mm)	Flow Measurements
SP1	T6–T7	T6	4.2	BOS, T5 <sup>b</sup> (AS), T7 (BS)
SP2	C6–T1	C6	17.1	BOS, C4 <sup>b</sup> (AS), T2 (BS)
SP3	C1–C6	C6	23.4	BOS (AS), C4, T1 (BS)
SP4	T2–T6	T5	8.2	BOS, T1 <sup>b</sup> (AS), T7 (BS)
SP5	T1–T4	T3	15.0	C7 <sup>b</sup> (AS), T5 (BS)
SP6	L1–L2	L1	9.2	BOS, T12 <sup>b</sup> (AS), L2 (BS)

**Note:**—AS indicates above the syrinx; BS, below the syrinx; BOS, base of skull.

<sup>a</sup> Data obtained at these levels were used to compare flow in the participants with syrinx (Fig 2).

<sup>b</sup> CSF flow measurements obtained at this spinal level were used to compare flow with that of controls at C5 (Fig 3).

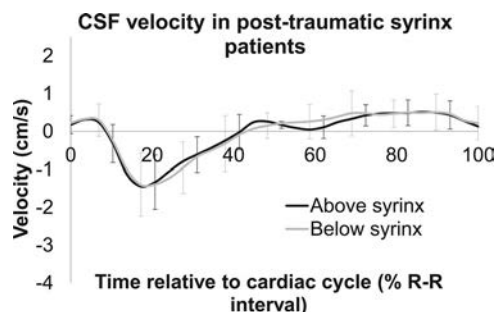


**FIG 2.** Mean CSF velocity-time profiles in participants with syrinx for above and below the syrinx. SDs are represented by error bars.

**Table 2: Summary of features of CSF velocity-time profile above and below the syrinx<sup>a</sup>**

	Above Syring	Below Syring	<i>P</i> Value
Timing of peak cranial velocity	8.8 (2.5)	9.0 (1.8)	.9
Timing of peak caudal velocity	2.3 (1.1)	2.3 (0.7)	1.0
Duration of caudal flow	3.5 (0.5)	4.3 (2.5)	.5
Onset time of caudal flow	1.0 (0.2)	1.1 (0.5)	.6
Time of return to cranial flow	4.6 (0.6)	5.5 (2.2)	.3
Peak cranial velocity (cm/s)	0.6 (0.3)	0.7 (0.40)	.7
Peak caudal velocity (cm/s)	1.6 (0.9)	1.7 (0.9)	.7

<sup>a</sup> Data are mean (SD). All temporal features are expressed as % R-R interval.

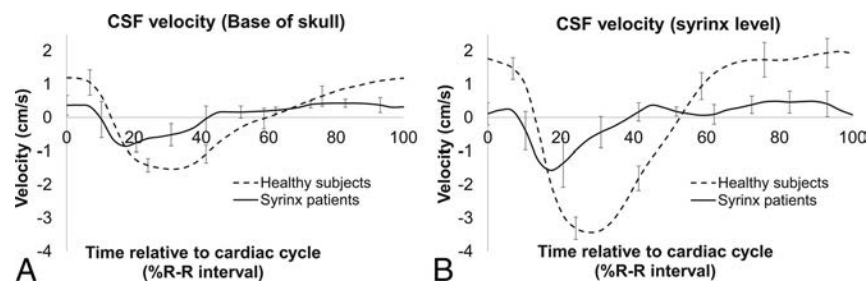


**FIG 3.** Average CSF velocity-time profile in participants with syrinx (black line) and controls (dotted line) at the skull base (A) and near the syrinx (B) (see Table 1 for locations of measurements in participants with syrinx) and at the C5 spinal level in controls. Error bars represent SDs.

## RESULTS

Syrinxes were observed in the T1-weighted MR images in all participants with syringomyelia. Syring size varied among participants. Table 1 summarizes the location of the syrinx and spinal levels where flow measurements were obtained. CSF flow velocity at the base of the skull was not measured for participant SP5 because of an existing irregular heartbeat, which made cardiac gating difficult. The scan was terminated due to prolonged scan time and patient discomfort. In addition, CSF velocity was measured 2 spinal levels (C4) above the syrinx for participant SP2 because the immediate spinal level (C5) above the syrinx could not be visualized because the spinal cord was obscured by spinal injury.

### CSF Velocity in Participants with Syrinx

Figure 2 shows the average CSF flow velocity above and below the syrinxes. Despite differences in syrinx size, location, and spinal subarachnoid space geometry in the participants with syringomyelia, there was very little difference in CSF flow velocity above and below the syrinx, and this is demonstrated by the small SDs in Fig 2. In addition, there were no significant differences in any features of the CSF velocity-time profiles above and below the syrinx (paired *t* tests, all *P* > .1, see Table 2 for details). In general, CSF flow was initially cranially directed (positive velocity); then, it was reversed to caudal flow at ~10% of the cardiac cycle and then reversed again to cranial flow at ~40% of the cardiac cycle. There was little variation in this timing along the spinal canal in the participants with syrinx (Table 2). The peak caudal and cranial velocities above and below the syrinx were similar despite the differences in syrinx location along the spine. In addition, in the participants with syrinx, the CSF flow velocity at the base of the skull (Fig 3A, black line) was also similar to the CSF flow velocity above and below the syrinx.

### CSF Velocity in Patients with Syringomyelia and Healthy Participants

Figure 3A shows the comparison between CSF flow velocity at the base of the skull in the controls and the participants with post-traumatic syringomyelia. Although the onset time of caudal flow appeared to be ~3% earlier in the participants with syringomyelia than in the controls, this was not significantly different (*P* = .15). However, the average peak cranial and caudal velocities in the participants with syringomyelia were 46% and 65% lower than those in controls, respectively, and these were significantly different between groups (peak cranial velocity, *P* = .01; peak caudal velocity, *P* = .03).

The average CSF flow-velocity profiles obtained at the syrinx level (spinal levels between C4 and T12) in the participants with syringomyelia and at spinal level C5 in the controls are shown in Fig 3B. All the features of the CSF velocity-time profile at this level were significantly different between patients and controls (see Table 3 for details) except for the timing of peak cranial velocity (8.8 ± 2.5 seconds for participants with syringomyelia, 8.3 ± 4.5 seconds in con-

**Table 3: Summary of features of CSF velocity time-profile in participants with syrinx and controls at the base of the skull and syrinx spinal level<sup>a</sup>**

	Base of Skull			Syrinx Spinal Level		
	Patients with Syrinx	Controls	P Value	Patients with Syrinx	Controls	P Value
Timing of peak cranial velocity	8.8 (2.3)	4.2 (5.2)	.21	8.8 (2.5)	8.3 (4.5)	.4
Timing of peak caudal velocity	2.3 (0.9)	3.7 (1.2)	.07	2.3 (1.1)	3.6 (0.7)	.03
Duration of caudal flow	3.5 (0.9)	5.4 (0.5)	.05	3.5 (0.5)	4.9 (0.6)	.003
Onset time of caudal flow	1.3 (0.5)	1.6 (0.4)	.15	1.0 (0.2)	1.7 (0.4)	.002
Time of return to cranial flow	4.8 (1.3)	7 (0.9)	.04	4.6 (0.6)	6.6 (0.9)	.002
Peak cranial velocity (cm/s)	0.6 (0.2)	1.3 (0.3)	.01	0.6 (0.3)	2.0 (0.5)	.00004
Peak caudal velocity (cm/s)	1.1 (0.2)	1.7 (0.2)	.03	1.6 (0.9)	3.2 (0.7)	.007

<sup>a</sup>Data are mean (SD). All temporal features are expressed as % R-R interval. P values are from unpaired t tests between participants with syrinx and controls.

trols, unpaired *t* test, *P* = .4). The average peak cranial and caudal velocities in the controls were 3.3 and 2 times higher, respectively, than those in the participants with syringomyelia. The CSF flow profile relative to the cardiac cycle was shifted earlier in the participants with syrinx relative to the controls (Fig 3B).

## DISCUSSION

There were 2 key observations in this novel study of CSF flow profiles in patients with posttraumatic syringomyelia. First, all the features of the CSF velocity-time profile were significantly different between the participants with syringomyelia and matched controls, with most flow features occurring earlier in the cardiac cycle in participants with syringomyelia than in healthy controls. In addition, while there were obvious differences in CSF flow velocity at different spinal levels (base of the skull and C5) in healthy controls, CSF flow along the spine was more uniform in the participants with syringomyelia.

Results from this study support the hypothesis that syrinxes are associated with altered CSF flow. This study shows that the timing of the peak caudal velocity in the participants with syringomyelia was earlier by 3%–5% of the cardiac cycle than in matched controls. This difference in timing of the CSF flow implies that there will also be an earlier arrival of peak spinal CSF pressure relative to cardiac systole in the participants with syringomyelia.<sup>10</sup> A modest change in the time of arrival of peak CSF pressure relative to the arrival of peak arterial pressure in systole may enhance CSF flow into the spinal cord through the perivascular spaces,<sup>11,12</sup> though this possibility remains to be confirmed experimentally. Syringomyelia is associated with CSF flow obstructions. CSF flow obstructions in Chiari malformation,<sup>10,13</sup> spinal stenosis, and arachnoiditis<sup>14</sup> are associated with increased velocity at the level of obstruction and a large pressure drop across the obstruction on the basis of existing computational modeling studies on CSF flow in the spinal subarachnoid space. According to existing hypotheses, syrinxes occur due to the development of pressure differences along the spinal subarachnoid space. This pressure difference could either drive CSF into the spinal cord<sup>15</sup> or distend the spinal cord radially due to Venturi effects.<sup>16</sup>

Most interesting, this study shows that both the peak caudal and cranial CSF velocities above and below the syrinx were similar; therefore, any CSF pressure drop across the syrinx in the spinal subarachnoid space would be small. In fact, the CSF pressure drop along the spinal subarachnoid space would be higher in the healthy controls because of a significant change in CSF flow velocity. This can be observed in the average peak caudal velocity,

where the velocity at C5 was almost 2 times higher compared with that in the base of the skull. It is therefore tempting to believe that the CSF pressure drop across a syrinx has little to do with the pathogenesis of syringomyelia, at least in posttraumatic participants. Longitudinal monitoring of patients after spinal cord injury would be required to confirm this belief by capturing any differences in CSF flow before the formation of a syrinx and during syrinx enlargement. However, this was not possible in this cross-sectional study design. Furthermore, this study was unable to investigate specific changes in the temporal features of CSF flow as a syrinx enlarges.

Nevertheless, although there were minimal differences in CSF velocity (and therefore pressure) above and below the syrinx, the absolute CSF pressure in the participants with syringomyelia may be higher than in controls because the disease is known to be related to decreased craniospinal compliance.<sup>17</sup> The decrease in craniospinal compliance may increase the effects of arterial pulsations, which may increase perivascular flow into the spinal cord parenchyma and syrinx.

Most interesting, alterations in the CSF flow profile in patients with posttraumatic syringomyelia differed from those in studies that compared patients with Chiari type I malformation with matched controls.<sup>9</sup> In patients with posttraumatic syringomyelia, peak caudal velocity occurred earlier in the cardiac cycle than in matched controls. Conversely, there was no significant difference in the timing of peak caudal velocity between patients with Chiari malformation and matched controls. Nevertheless, several temporal features of the CSF velocity profiles being different between patients with Chiari malformation with and without a syrinx suggests that the temporal effects of CSF flow velocity are still likely to play a role in syrinx development. In patients with Chiari malformation without a syrinx, the onset of caudal flow, return to cranial flow, and peak caudal velocity all occurred significantly earlier in the cardiac cycle compared with patients with a syrinx. It is unclear whether treatment can effectively reverse the temporal changes in CSF flow dynamics in syringomyelia, but there are at least 2 studies that showed that treatment of CSF flow disorders could delay the onset time of caudal flow and peak caudal velocity. A study that investigated CSF flow velocity in patients with Chiari malformation (after a decompression operation) showed that the duration of caudal CSF flow appeared to be shorter than that in flow measured postoperatively.<sup>18</sup> Temporal changes in CSF flow may also be associated with other CSF disorders, such as hydrocephalus. A computational modeling study of hydrocephalus found that the peak caudal velocity occurred later in the cardiac

cycle after a simulated endoscopic third ventriculostomy at the third ventricle.<sup>19</sup>

There were several limitations to this study. First, the primary motivation of this research was to understand CSF flow velocity above and below the syrinx in posttraumatic patients. However, there was a discrepancy in the comparison of spinal levels between participants with syringomyelia and healthy controls in some cases. Although the average CSF flow velocity obtained adjacent to the syrinx varied between C4 and T12 in our participants, it was compared with CSF flow velocity at a standard spinal location (C5) in the matched controls. Nevertheless, given that there was minimal difference in CSF flow velocities along the spine in the patients with syrinx, we expected the effect of these differences in measurement locations to be small. Comparing the magnitude of CSF velocity measurements in the participants with syringomyelia with that in the healthy controls at a different spinal location (eg, T1) may yield different results because CSF velocity is highest at the C5 level in healthy humans and can be reduced by as much as 20%–30% at the thoracic spinal region.<sup>20</sup> However, when CSF velocity in the participants with syringomyelia was compared with a simulated CSF velocity-time profile that has peak velocity reduced by 20%, the results were still significantly different for both the cranial and caudal velocities.

Second, it was not anticipated before this study that the CSF velocity of participants with posttraumatic syringomyelia would be in the range of 1–3 cm/s, and because this was only identified as a consistent observation midway in the study, the encoding velocity was left unchanged to ensure consistencies in the protocol used. While this feature may affect the measurement accuracy of the velocity magnitude, it is unlikely to change the conclusions of this study.

Another limitation was that data were not collected from spinal patients without a syrinx for comparison. Because this was a cross-sectional study and neither prior nor subsequent measurements of syrinx dimensions were available from the participants' clinical records, we are unable to comment on whether syrinxes in the participants were stable. Understanding longitudinal changes in CSF flow measurements and syrinx size in the participants with syringomyelia may help provide insights into the mechanisms of syrinx development, but this was not designed as part of this study. It would also be ideal to compare the CSF velocity-time profile with spinal arterial blood flow to assess the theory that change in the relative timing of arterial blood and CSF pulses is important for syrinx development and progression.<sup>2</sup> However, neither arterial blood flow nor additional spinal level scans were measured in this study because patient discomfort precluded additional scan acquisitions. Finally, the sample size of this study, though small, was appropriate, and while a larger sample size will provide a more robust conclusion to the study, it is unlikely to affect the key findings.

## CONCLUSIONS

This study provides new information on CSF flow profiles in patients with a syrinx with spinal cord injuries. In the participants with syringomyelia, there was very little difference in peak caudal and cranial velocities above and below the syrinx. This suggests that there was an absence of a large pressure drop across the syrinx. However, peak CSF caudal and cranial velocities in the par-

ticipants with syringomyelia were significantly lower compared with those in the healthy controls. Furthermore, temporal features of the CSF flow profile were significantly different between the 2 groups; peak flow and change in flow direction were earlier in the cardiac cycle in participants with syringomyelia. Additional work to study the specific changes in the temporal features of CSF flow when a syrinx enlarges and posttreatment is important to further elucidate the mechanisms of syringomyelia development. This work could assist in predicting treatment response.

## ACKNOWLEDGMENTS

The authors thank Mr Segar Suppiah from Neuroscience Research Australia for his help with MR imaging.

Disclosures: Shaokoon Cheng—RELATED: Grant: Column of Hope. Marcus Stoodley—RELATED: Grant: National Health and Medical Research Council, Column of Hope. Comments: standard competitive research grants\*. Lynne Bilston—RELATED: Grant: National Health and Medical Research Council of Australia\*. UNRELATED: Grants/Grants Pending: National Health and Medical Research Council, Australian Research Council, Column of Hope, University of New South Wales, Rebecca Cooper Foundation\*. \*Money paid to the institution.

## REFERENCES

1. Brodbelt AR, Stoodley MA. **Post-traumatic syringomyelia: a review.** *J Clin Neurosci* 2003;10:401–08 CrossRef Medline
2. Bilston LE, Fletcher DF, Brodbelt AR, et al. **Arterial pulsation-driven cerebrospinal fluid flow in the perivascular space: a computational model.** *Comput Methods Biomech Biomed Engin* 2003;6:235–41 CrossRef Medline
3. Hemley SJ, Tu J, Stoodley MA, et al. **Role of the blood-spinal cord barrier in posttraumatic syringomyelia.** *J Neurosurg Spine* 2009;11:696–704 CrossRef Medline
4. Naruse H, Tanaka K, Kim A, et al. **A new model of spinal cord edema.** *Acta Neurochir Suppl* 1997;70:293–95 Medline
5. Enzmann DR, Pelc NJ. **Normal flow patterns of intracranial and spinal cerebrospinal fluid defined with phase-contrast cine MR imaging.** *Radiology* 1991;178:467–74 CrossRef Medline
6. Mauer UM, Gottschalk A, Mueller C, et al. **Standard and cardiac-gated phase-contrast magnetic resonance imaging in the clinical course of patients with Chiari malformation type I.** *Neurosurg Focus* 2011;31:E5 CrossRef Medline
7. Maynard FM, Bracken MB, Creasey G, et al. **International Standards for Neurological and Functional Classification of Spinal Cord Injury: American Spinal Injury Association.** *Spinal Cord* 1997;35:266–74 CrossRef Medline
8. Heiberg E, Sjögren J, Ugander M, et al. **Design and validation of Segment: freely available software for cardiovascular image analysis.** *BMC Med Imaging* 2010;10:1 CrossRef Medline
9. Clarke EC, Stoodley MA, Bilston LE. **Changes in temporal flow characteristics of CSF in Chiari malformation type I with and without syringomyelia: implications for theory of syrinx development.** *J Neurosurg* 2013;118:1135–40 CrossRef Medline
10. Clarke EC, Fletcher DF, Stoodley MA, et al. **Computational fluid dynamics modelling of cerebrospinal fluid pressure in Chiari malformation and syringomyelia.** *J Biomech* 2013;46:1801–09 CrossRef Medline
11. Bilston LE, Stoodley MA, Fletcher DF. **The influence of the relative timing of arterial and subarachnoid space pulse waves on spinal perivascular cerebrospinal fluid flow as a possible factor in syrinx development.** *J Neurosurg* 2010;112:808–13 CrossRef Medline
12. Stoodley MA, Brown SA, Brown CJ, et al. **Arterial pulsation-dependent perivascular cerebrospinal fluid flow into the central canal in the sheep spinal cord.** *J Neurosurg* 1997;86:686–93 CrossRef Medline
13. Martin BA, Kalata W, Shaffer N, et al. **Hydrodynamic and longitudinal impedance analysis of cerebrospinal fluid dynamics at the**

- craniovertebral junction in type I Chiari malformation.** *PLoS One* 2013;8:e75335 CrossRef Medline
14. Cheng S, Stoodley MA, Wong J, et al. **The presence of arachnoiditis affects the characteristics of CSF flow in the spinal subarachnoid space: a modelling study.** *J Biomech* 2012;45:1186–91 CrossRef Medline
  15. Williams B. **On the pathogenesis of syringomyelia: a review.** *JR Soc Med* 1980;73:798–806 Medline
  16. Greitz D. **Unraveling the riddle of syringomyelia.** *Neuros Rev* 2006; 29:251–63; discussion 264 CrossRef Medline
  17. Rusbridge C, Greitz D, Iskandar BJ. **Syringomyelia: current concepts in pathogenesis, diagnosis, and treatment.** *J Vet Intern Med* 2006;20: 469–79 CrossRef Medline
  18. Sivaramakrishnan A, Alperin N, Surapaneni S, et al. **Evaluating the effect of decompression surgery on cerebrospinal fluid flow and intracranial compliance in patients with Chiari malformation with magnetic resonance imaging flow studies.** *Neurosurgery* 2004;55: 1344–50; discussion 1350–51 CrossRef Medline
  19. Farnoush A, Tan K, Juge L, et al. **Effect of endoscopic third ventriculostomy on cerebrospinal fluid pressure in the cerebral ventricles.** *J Clin Neurosci.* 2016;23:63–67 CrossRef Medline
  20. Heidari Pahlavian S, Bunck AC, Loth F, et al. **Characterization of the discrepancies between four-dimensional phase-contrast magnetic resonance imaging and in-silico simulations of cerebrospinal fluid dynamics.** *J Biomech Eng* 2015;137:051002 CrossRef Medline

# Syringomyelia Fluid Dynamics and Cord Motion Revealed by Serendipitous Null Point Artifacts during Cine MRI

C.M. Honey, K.W. Martin, and M.K.S. Heran



## ABSTRACT

**SUMMARY:** Dynamic MR imaging was used to evaluate a cervical syrinx in an adolescent boy with an associated hindbrain herniation. Null artifacts were present on one of the sequences that allowed simultaneous high-resolution visualization of syrinx fluid motion and the anatomy of the syrinx walls. A brief review of the theories of syrinx formation and propagation is provided with a comment on why the Williams “slosh” theory of syrinx progression is supported by our unique imaging.

“Syringomyelia” was originally coined by Ollivier<sup>1</sup> in 1827 and has come to be defined as a tubular cavitation of the spinal cord extending over many segments.<sup>2</sup> A variety of conditions may cause syringomyelia, including hindbrain herniations, trauma, arachnoiditis, and tumors.<sup>3</sup> Many different theories have been advanced to explain their cause and growth.<sup>4,5</sup> The more modern theories all revolve around abnormal fluid dynamics within the spinal canal. MR imaging sequences, which can visualize and measure CSF flow, have been used to elucidate the pathophysiology underpinning syringomyelia.<sup>6</sup> Unfortunately, these sequences often trade anatomic detail for quantification of CSF movement. During the investigation of a case of syringomyelia associated with a Chiari I malformation, the patient was imaged with dynamic cine balanced steady-state free precession sequences.<sup>7</sup> Unexpected null artifacts were present that placed a band of low signal through the middle of the syrinx. The dephased water protons could then be visualized as they moved during the cardiac cycle. We describe this hydrodynamic motion of the syrinx fluid and the associated movements of the surrounding spinal cord walls and briefly review the various theories of syrinx formation and growth.

## MATERIALS AND METHODS

A 17-year-old adolescent boy with an asymptomatic C5–6 syrinx detected during screening for a known Chiari I malformation was studied with dynamic MR imaging.<sup>7</sup> Sequences included a cardiac-gated cine balanced steady-state free precession study on a 1.5T scanner (Intera; Philips Healthcare, Best, the Netherlands). Images were viewed in a video loop to correlate any motion with the cardiac cycle.

## RESULTS

Examples of the sagittal cine MR imaging with and without the null artifacts<sup>8</sup> are presented in On-line Videos 1 and 2, respectively. During systole, the cerebellar tonsils descended. At the same time, the dilated spinal cord walls surrounding the superior portion of the syrinx collapsed. Within the syrinx, a jet of fluid then moved rostral to caudal, hitting and dilating the inferior walls of the syrinx. During diastole, the syrinx fluid then “sloshed” rostrally, re-expanding the superior walls and allowing the inferior walls to recoil.

Representative diagrams highlighting the spinal cord wall motion and syrinx fluid pulsation at rest (Fig 1A), during systole (Fig 1B), and during diastole (Fig 1C) are presented.

## DISCUSSION

The mechanisms causing and enlarging syringes may be different, but most authors have considered them together. Early theories favored a congenital or neoplastic origin.<sup>3</sup> Gardner and Angel<sup>4</sup> popularized the “hydrodynamic theory.” In patients with a hindbrain abnormality obstructing CSF egress from the fourth ventricle, they postulated that fluid was pushed down into the central canal of the cord, dilating the canal to produce a syrinx. Williams<sup>5</sup> argued that these mechanisms should cause hydrocephalus not hydromyelia. He measured pressure gradients of >100 mm Hg

Received March 14, 2017; accepted after revision April 15.

From the Division of Neurosurgery (C.M.H.), University of Manitoba Health Sciences Centre, Winnipeg, Manitoba, Canada; Department of Radiology (K.W.M.), University of California, San Francisco, Benioff Children’s Hospital, Oakland, California; and Department of Radiology (M.K.S.H.), University of British Columbia, Vancouver, British Columbia, Canada.

Please address correspondence to C. Michael Honey, MD, GB 129-820 Sherbrook St, Health Sciences Centre, Winnipeg, MB Canada R3A 1R9; e-mail: c.michael.honey@gmail.com

Indicates open access to non-subscribers at [www.ajnr.org](http://www.ajnr.org)

Indicates article with supplemental on-line video.

<http://dx.doi.org/10.3174/ajnr.A5328>

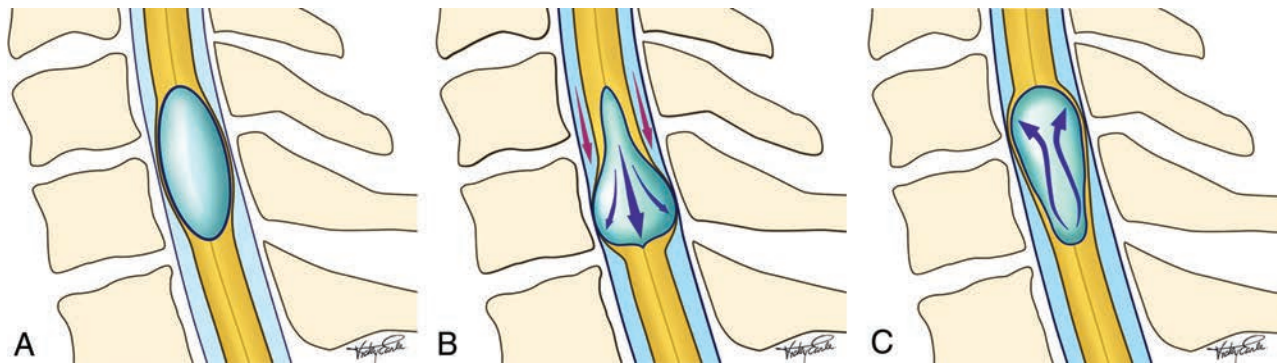


**FIG 1.** Diagram of the syrinx wall and fluid movement during the cardiac cycle. A, The syrinx “at rest” during late diastole with its classic ovoid shape. B, During systole, the superior portion of the syrinx is compressed, forcing a fluid jet caudally, which distends the inferior portion of the syrinx. C, During early diastole, the ballooned inferior portion of the syrinx recoils and forces the fluid rostrally to re-expand the superior portion of the syrinx. Images courtesy of Ms Vicky Earle (vearlemedicalart.com).

across the foramen magnum during Valsalva maneuvers in patients with hindbrain hernias and postulated that this craniospinal pressure dissociation, a force he called “suck,” caused fluid to be pulled into the syrinx from the ventricle. The subsequent enlargement of the syrinx was thought to be due to fluid movement within the syrinx during Valsalva maneuvers, what he called “slosh.”

Subsequent authors have highlighted the lack of communication between the syrinx and fourth ventricle and postulated that the fluid entered the syrinx from the spinal subarachnoid space.<sup>6,9,10</sup> With the advent of dynamic MR imaging and intraoperative sonography, Oldfield et al<sup>6</sup> proposed that the downward movement of the tonsils seen during systole caused a “pistonlike” effect, resulting in a CSF pressure wave that contracted the cord and forced fluid into it. Researchers argued, however, that if fluid pressure caused the cord to contract, it would be unlikely that any fluid could enter the cord. Grietz<sup>11</sup> and Koyanagi and Houkin<sup>12</sup> suggested that the syrinx fluid was extracellular in nature rather than CSF. Grietz proposed the “intramedullary pulse pressure theory,” in which CSF moving abnormally rapidly past the cord caused a low pressure within the cord, promoting extracellular fluid (not CSF) to build up and eventually form a syrinx.<sup>11</sup>

We now know that various etiologies can produce syringes. The pathophysiology causing a fluid-filled cavity to form within the spinal cord is undoubtedly different following the absorption of a traumatic hematoma, the secretion of proteinaceous fluid from a neoplasm, or the altered CSF dynamics accompanying a hindbrain herniation. The pathophysiology underpinning the enlargement of syringes, however, may have a common theme. Across the years, imaging studies have helped elucidate the pathophysiology underpinning syrinx enlargement.

Initially, fluoroscopic images of dye within syringes were documented to pulsate with each heartbeat, and the rostral movement induced by cough was described as “impressive.”<sup>25</sup> With the advent of MR imaging and quantification of spinal CSF pulsations,<sup>11</sup> the noninvasive analysis of CSF hydrodynamics became possible.<sup>13</sup> MR imaging studies have measured the pulsatile motion of the cerebellar tonsils<sup>14</sup> and lamina terminalis<sup>15</sup> and have documented sinusoidal CSF flow linked to the cardiac cycle within syringes, along the spinal subarachnoid space, and across the foramen magnum.<sup>16,17</sup> Most studies have used

phase contrast techniques, which have allowed quantification of CSF velocities but with reduced anatomic resolution.

Our imaging was able to simultaneously demonstrate high anatomic resolution and fluid movement within the syrinx and spinal subarachnoid space. On-line Video 1 shows that during systole and concurrent with the downward displacement of the tonsils, the superior portion of the outer syrinx wall was initially impacted by the CSF systolic pulse pressure. This force distorted the shape of the syrinx, collapsing its upper portion and forcing the fluid within to jet inferiorly, impacting and ballooning the lower portion of the syrinx. During diastole, as the pressure gradient reversed, the distended lower portion of the syrinx recoiled and pushed fluid rostrally to expand the upper portion of the syrinx. The unexpected null artifacts extending through the syrinx and adjacent subarachnoid space (On-line Video 1) produced contrast in the syrinx fluid, enabling visualization of its movement. With each heartbeat, the syrinx walls were distorted unevenly, causing a jet of syrinx fluid to impact the inferior pole of the cavity. Slow caudal growth of the syrinx may follow 42 million such impacts during a year. Greater CSF pressure gradients follow Valsalva maneuvers, and asymmetric contraction of the syrinx may be responsible for the sudden rostral expansion described in the literature.<sup>18</sup> Our study did not visualize the cord during a Valsalva maneuver. The current study provides direct visual confirmation of the CSF movement previously calculated by phase contrast MR imaging studies. Although the technique may not have had the necessary sensitivity to be definitive, there was no obvious transparenchymal movement of CSF visualized during our study, in keeping with the theories postulating that syrinx fluid accumulates from within the cord rather than from CSF being forced into it.

## CONCLUSIONS

This novel imaging study of a cervical syrinx allowed simultaneous high-resolution visualization of syrinx fluid motion and the anatomy of the syrinx walls. The study supports the hypothesis that syrinx enlargement is due to the slosh of fluid with each heartbeat (and the Valsalva maneuver). The external asymmetric contraction of the rostral portion of the cord around the syrinx during systole caused a jet of fluid within the syrinx to extend caudally impacting and dilating the caudal portion of the syrinx.

With diastole, the fluid moved more slowly to its original position as the dilated caudal portion of the syrinx returned to its original shape.

## REFERENCES

1. Ollivier CP. *Traité des Maladies de la Moelle Epinière: Contenant L'histoire Anatomique, Physiologique et Pathologique de Ce Centre Nerveux chez l'Homme*. 2nd ed. Paris: Méquignon-Marvis père et fils; 1827:178–83
2. Harding BN, Copp AJ. **Malformations**. In: Grenfield JG, Graham DI, Lantos P, eds. *Greenfield's Neuropathology*. 7th ed. London: Arnold; 2002:443
3. Lotbinière AC. **Historical considerations**. In: Anson JA, Benzel EC, Awad IA, eds; AANS Publications Committee. *Syringomyelia and the Chiari Malformations*. Park Ridge: American Association of Neurological Surgeons; 1997:1–26
4. Gardner WJ, Angel J. **The mechanism of syringomyelia and its surgical correction**. *Clin Neurosurg* 1958;6:131–40 Medline
5. Williams B. **On the pathogenesis of syringomyelia: a review**. *JR Soc Med* 1980;73:798–806 Medline
6. Oldfield EH, Muraszko K, Shawker TH, et al. **Pathophysiology of syringomyelia associated with Chiari I malformation of the cerebellar tonsils: implications for diagnosis and treatment**. *J Neurosurg* 1994;80:3–15 CrossRef Medline
7. Wang DD, Martin KW, Auguste KI, et al. **Fast dynamic imaging technique to identify obstructive lesions in the CSF space: report of 2 cases**. *J Neurosurg Pediatr* 2015;15:519–23 CrossRef Medline
8. Storey P, Li W, Chen Q, et al. **Flow artifacts in steady-state free precession cine imaging**. *Magn Reson Med* 2004;51:115–22 CrossRef Medline
9. Alboulker J. **Syringomyelia and intra-rachidian fluids, I: syringomyelia, 2: conceptions** [in French]. *Neurochirurgie* 1979;25(suppl 1): 9–22 Medline
10. Milhorat TH, Miller JI, Johnson WD, et al. **Anatomical basis of syringomyelia occurring with hindbrain lesions**. *Neurosurgery* 1993; 32:748–54; discussion 754 CrossRef Medline
11. Greitz D. **Unraveling the riddle of syringomyelia**. *Neurosurg Rev* 2006;29:251–63; discussion 264 CrossRef Medline
12. Koyanagi I, Houkin K. **Pathogenesis of syringomyelia associated with Chiari type I malformations: review of evidences and proposal of a new hypothesis**. *Neurosurg Rev* 2010;33:271–84; discussion 284–85 CrossRef Medline
13. Enzmann DR, Pelc NJ. **Normal flow patterns of intracranial and spinal cerebrospinal fluid defined with phase-contrast cine MR imaging**. *Radiology* 1991;178:467–74 CrossRef Medline
14. Sharma A, Parsons MS, Pilgram TK. **Balanced steady-state free-precession MR imaging for measuring pulsatile motion of cerebellar tonsils during the cardiac cycle: a reliability study**. *Neuroradiol* 2012;54:133–38 CrossRef Medline
15. Reubelt D, Small LC, Hoffmann MH, et al. **MR imaging and quantification of the movement of the lamina terminalis depending on the CSF dynamics**. *AJNR Am J Neuroradiol* 2009;30:199–202 Medline
16. Rubin JB, Enzmann DR. **CSF flow effects during MRI of the central nervous system**. *Magn Reson Annu* 1988;147–87 Medline
17. Tanghe HL. **Magnetic resonance imaging (MRI) in syringomyelia**. *Acta Neurochir* 1995;134:93–99 CrossRef Medline
18. Bertrand G. **Chapter 26: dynamic factors in the evolution of syringomyelia and syringobulbia**. *Clin Neurosurg* 1973;20:322–33 Medline

# Celebrating 35 Years of the AJNR

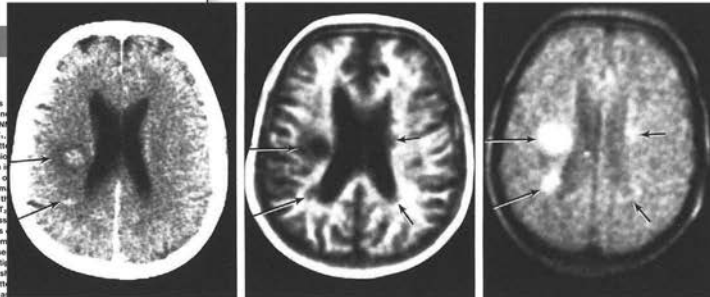
September 1982 edition

## Clinical NMR Imaging of the Brain: 140 Cases

G. M. Bydder<sup>1</sup>  
R. E. Steiner<sup>2</sup>  
I. R. Young<sup>2</sup>  
A. S. Hall<sup>2</sup>  
D. J. Thomas<sup>3</sup>  
J. Marshall<sup>4</sup>  
C. A. Pallas<sup>5</sup>  
N. J. Legg<sup>6</sup>

Cranial nuclear magnetic resonance (NMR) scans of 140 patients with a broad spectrum of pathology were compared with x-ray computed tomography (CT) scans. The NMR sequences reflecting proton density, blood flow, T<sub>1</sub> sagittal, and coronal images. White matter, gray matter, and cerebrospinal fluid were clearly distinguished in the normal brain with inversion-recovery sequences. Normal progressive myelination was demonstrated in children. Acute hemorrhages displayed short T<sub>1</sub> values, but on T<sub>2</sub> images they displayed long T<sub>2</sub> values, and on long T<sub>2</sub> values. Cysts had very long T<sub>2</sub> values (about 1000 ms). Echo (SE) sequences showed increased values of T<sub>1</sub> and T<sub>2</sub> for lesions against the relatively featureless brain. With inversion-recovery scans, different stages of the hemispheres. NMR was more useful than CT in demonstrating white matter lesions in demyelinating diseases. NMR scans. Many more lesions were observed in multiple sclerosis. Benign tumors were well seen and usually had a characteristic appearance. Mass effects from tumors were generally better seen with CT, including more subtle mass effects such as compression of the caudate nucleus in Huntington chorea. Abnormalities were seen in diseases of the basal ganglia, including marked atrophy of the head of the caudate nucleus in Huntington chorea.

Advantages of NMR imaging include the high level of gray-white matter contrast, lack of bone artifact, variety of possible sequences, transverse, sagittal, and coronal imaging, sensitivity to pathologic change, and lack of known hazard. Disadvantages include lack of bone detail, limited spatial resolution, lack of contrast agents, and cost. Promising directions for future clinical research include developmental neurology, tissue characterization with T<sub>1</sub> and T<sub>2</sub>, assessment of blood flow, and the development of contrast agents. Much more detailed evaluation will be required, but NMR seems to be a potentially important addition to existing techniques of neurologic diagnosis.



This article appears in the August 1982 issue of AJNR and the September/October 1982 issue of AJNR.

Received March 18, 1982; accepted April 16, 1982.

<sup>1</sup>Department of Diagnostic Radiology, Royal Postgraduate Medical School, Hammersmith Hospital, Du Cane Road, London W12 0HS, England. Address reprint requests to G. M. Bydder.

<sup>2</sup>Fickler International, Wexley, London, England.

<sup>3</sup>Institute for Neurology and National Hospital for Nervous Diseases, Queen Square, London, England.

<sup>4</sup>Department of Medicine (Neurology), Royal Postgraduate Medical School, Hammersmith Hospital, London, England.

AJNR 3:459-490, September/October 1982  
0195-4108/82/0305-0459 \$00.00  
© American Roentgen Ray Society

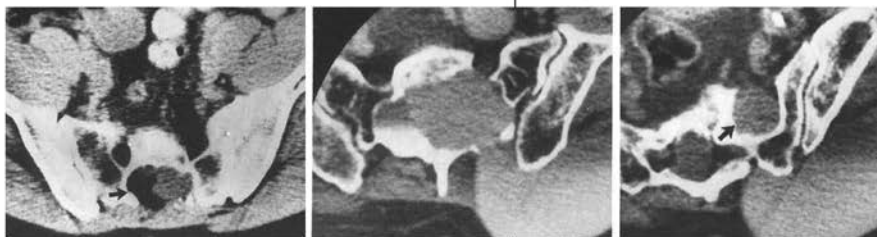
Although NMR imaging was initially proposed in the United States [1, 2], much of the early development was carried out by small groups of physicists and engineers in Britain based at the Department of Bio-medical Physics in Aberdeen [3], the Department of Physics in Nottingham [4], and the Central Research Laboratories of Thorn-EMI Ltd. The highlights published results of NMR imaging of the brain largely reflect the activities of these groups, although major contributions are expected from other centers in the near future. Head images were produced by the Thorn-EMI group in 1978 [5], and a series of brain scans was published by the Nottingham group during 1980 [6-10]. The Aberdeen group produced normal head images in 1980 [11] and have described abnormal cases during 1981 [12]. Nevertheless the total volume of published cerebral cases remains small. Fewer than 40 cases have been described with the largest series a group of 10 patients with multiple sclerosis [13].

In previous studies we have emphasized the high level of gray-matter contrast

## Computed Tomography of the Sacrum: 2. Pathology

Margaret Anne Whelan<sup>1,2</sup>  
Sadok K. Hilal<sup>1</sup>  
Richard Palmer Gold<sup>1</sup>  
Marlin G. Luken<sup>3</sup>  
W. Jost Michelson<sup>4</sup>

Fifteen cases of primary sacral pathology were analyzed. High-resolution computed tomography was found to be the most accurate means of studying these cases. Certain anatomic changes involving the central canal and sacral foramina were found to be helpful in determining the type of pathology. Although conventional plain films, radionuclide bone scans, and myelography were useful in certain cases, computed tomography was found to be the procedure of choice in the workup of sacral problems.



scans of 15 patients with sacral abnormalities were performed in the supine position with no angulation of the table or the patient. The patients were examined using the Pizcor model 450 scanner with a 10 sec, and a slice thickness of 2-10 mm. Of the 15 patients (three adults, six children and six had children).

Diagnoses included as meningocele (case 1), lipoma (cases 2-3), meningocele (case 4), low conus, tethered cord (case 5). All but one of the six children in this series had a congenital lesion either because of a neural tube defect (hemimelia) or associated anomalies such as spina bifida. Three had histories strongly suggestive of spina bifida (cases 2 and 3), while one patient (case 1) was first examined. All the patients with congenital lesions had varying degrees of spinal dysraphism on plain films. In two cases, the defect was minimal and not appreciated on the initial films, while in one case of adult meningocele the sacral deformity was believed to represent neoplasm. Bone scanning was not performed in any of the patients with congenital lesions. Myelography was performed in six patients, two with metrizamide and four with Pantopaque. A low conus with tethered cord was demonstrated in five patients; an associated lipoma was present in four and a dermoid in one. However, the most informative study of the sacrum in all these patients was the high-resolution CT scan.

All the congenital lesions demonstrated dorsal dysraphism with widening of the central sacral canal and sparing of the sacral foramina. The four lipomas clearly displayed fat density (Fig. 1) while the dermoid showed calcium, fat, and soft-tissue density. In the patient with meningocele (case 1), CT demonstrated the widening of the central canal as well as extrusion of the meningocele into the buttock via a dorsal defect in the sacrum (Fig. 2A). In addition, CT was able to

Received October 14, 1980; accepted after revision April 20, 1982.

Presented at the annual meeting of the American Society of Neuroradiology, Los Angeles, March 1980.

<sup>1</sup>Department of Radiology, Columbia-Presbyterian Medical Center, New York, NY 10032.

<sup>2</sup>Present address: Department of Radiology, New York University Medical Center, 560 First Ave., New York, NY 10016. Address reprint requests to M. A. Whelan.

<sup>3</sup>Department of Neurosurgery, Columbia-Presbyterian Medical Center, New York, NY 10032.

AJNR 3:555-559, September/October 1982  
0195-4108/82/0305-0555 \$00.00  
© American Roentgen Ray Society

## LAST<sub>2</sub> CH<sub>2</sub>ANCE: A Summary of Selection Criteria for Thrombectomy in Acute Ischemic Stroke

In 2015 and 2016, six randomized controlled trials (MR CLEAN, ESCAPE, SWIFT PRIME, REVASCAT, EXTEND-IA, and THRACE), which focused on the endovascular treatment of patients with acute ischemic stroke caused by large vessel occlusion, were published in *The New England Journal of Medicine*<sup>1</sup> and *Lancet Neurology*.<sup>2</sup> All of these trials favor thrombectomy for patients with acute ischemic stroke with large vessel occlusion, which can significantly improve patients' 90-day outcomes. The impact of these trials is huge. Cerebrovascular physicians all over the world have started putting more efforts on thrombectomy. However, there are many indications and contraindications for thrombectomy, which are a challenge for the physician to remember and may cause potential errors and delays in the process of selecting candidates.

To handle this problem, we carefully reviewed the literature and guidelines<sup>3,4</sup> and summarized the indications and contraindications as "LAST<sub>2</sub> CH<sub>2</sub>ANCE," which represents different aspects of patient selection. The details of "LAST<sub>2</sub> CH<sub>2</sub>ANCE" are shown in the Table.

We have used this to do many training sessions in China. During the posttraining survey, most physicians were impressed by this summary. They can remember complex patient selection criteria in a few minutes even though they knew very little before the training. Therefore, we feel it is better to let the entire community know this system to make rapid and accurate patient selection for

thrombectomy. Because thrombectomy is the last chance for patients with acute ischemic stroke with large vessel occlusion to recover, we hope this patient selection summary, "LAST<sub>2</sub> CH<sub>2</sub>ANCE," will be helpful.

### REFERENCES

1. Goyal M, Menon BK, van Zwam WH, et al. **Endovascular thrombectomy after large-vessel ischaemic stroke: a meta-analysis of individual patient data from five randomised trials.** *Lancet* 2016;387:1723–31 CrossRef Medline
2. Bracard S, Ducrocq X, Mas JL, et al. **Mechanical thrombectomy after intravenous alteplase versus alteplase alone after stroke (THRACE): a randomised controlled trial.** *Lancet Neurol* 2016;15:1138–47 CrossRef Medline
3. Franssen PS, Beumer D, Berkhemer OA, et al. **MR CLEAN, a multi-center randomized clinical trial of endovascular treatment for acute ischemic stroke in the Netherlands: study protocol for a randomized controlled trial.** *Trials* 2014;15:343 CrossRef Medline
4. Powers WJ, Derdeyn CP, Biller J, et al. **2015 American Heart Association/American Stroke Association focused update of the 2013 guidelines for the early management of patients with acute ischemic stroke regarding endovascular treatment: a guideline for healthcare professionals from the American Heart Association/American Stroke Association.** *Stroke* 2015;46:3020–35 CrossRef Medline

● P. Yang

● Y. Zhang

● J. Liu

Department of Neurosurgery  
Changhai Hospital  
Second Military Medical University  
Shanghai, China

<http://dx.doi.org/10.3174/ajnr.A5249>

### Details of LAST<sub>2</sub> CH<sub>2</sub>ANCE

Symbol	Meaning	Details
L	Large vessel occlusion	Internal carotid artery or proximal MCA <sup>a</sup>
A	Age	≥18 yrs <sup>a</sup>
S	Symptom	NIHSS score ≥6 <sup>a</sup>
T	Time	Onset to groin puncture time <6 h <sup>a</sup>
T <sub>2</sub>	Thrombocytopenia	PLT ≥40*10 <sup>9</sup> /L <sup>b</sup>
C	Crippled/disabled	mRS <2 <sup>a</sup>
H	Hypoglycemia	CBG ≥2.7 mmol/L <sup>b</sup>
H <sub>2</sub>	Hypertension	BP ≤185/110 mmHg <sup>b</sup>
A	Anticoagulation	INR ≤3.0 <sup>b</sup>
N	Nonsalvageable brain tissue	ASPECTS ≥6 <sup>a</sup>
C	Collateral	ACG >1 <sup>c</sup>
E	Expectancy of life	>90 d <sup>b</sup>

**Note:**—ACG indicates American Society of Interventional and Therapeutic Neuroradiology collateral grading; BP, blood pressure; CBG, capillary blood glucose; INR, international normalization ratio; PLT, platelet count.

<sup>a</sup> Criterion from the American Heart Association/American Stroke Association guidelines.

<sup>b</sup> Criterion from the protocol of MR CLEAN trial.

<sup>c</sup> Criterion we use in our daily practice but without consensus in the literature.

## Is Hippocampal Volumetry Really All That Matters?

I read with interest the recent article in AJNR, “Predictive Utility of Marketed Volumetric Software Tools in Subjects at Risk for Alzheimer Disease: Do Regions Outside the Hippocampus Matter?”<sup>1</sup>

It is an interesting study, yet I will elaborate below why I do not fully agree with the conclusions of this article: “Therefore, future prognostic studies in mild cognitive impairment, combining such tools with demographic and other biomarker measures, are justified in using hippocampal volume as the only volumetric biomarker.”<sup>1</sup>

The authors demonstrated that 2 different MR volumetry software packages provide equivalent results with respect to hippocampal volumetry. As a consequence, the conclusion is justified that the postprocessing software does not systematically bias the MR morphometry results, at least for the 2 implemented software packages.

The second finding is that hippocampal atrophy alone performed as well as the additionally performed analysis of other anatomic regions. However, it must be noted that the regions used in the tested software packages are anatomically defined regions that only partially overlap with the established Alzheimer disease (AD) signature regions (ie, those regions that are consistently found to be abnormal in AD).<sup>2,3</sup> Because of partial volume effects, these large anatomic regions are not necessarily the most sensitive regions for this specific purpose. The current study assessed 3D T1 voxel-based morphometry (VBM)–derived gray matter concentration, whereas the more demanding analyses of 3D T1–derived cortical thickness and related volume estimates are generally more sensitive with less interindividual variability.<sup>4</sup> A direct comparison between the presented VBM-type hippocampal volumetry and cortical thickness–derived volumetry (eg, in AD signature regions) was not performed. Consequently, I challenge the conclusion that hippocampal volume can be suggested as the only volumetric biomarker because the authors did not demonstrate that the presented hippocampal volumetry outperforms, for instance, AD signature regions.

When looking into the data in more detail, the area under the curve (AUC) for hippocampal volumetry is 0.69 or 0.68, depend-

ing on the software. In the abstract, this is not noted, yet it is stated in the manuscript that the AUC was 0.76 and 0.68 for the Alzheimer’s Disease Assessment Scale–13 (ADAS-13) and the Mini-Mental State Examination (MMS), respectively. The MMS is a very simple and fast clinical test that costs almost nothing and can be done everywhere. The MMS performed as well as the much more time-consuming and expensive hippocampal volumetry. Moreover, the MMS worked in all cases, whereas MR hippocampal volumetry was impossible in 30% of cases. Based on the provided results, it can be concluded that MR volumetry provided no added value with respect to the simple and established MMS. The ADAS-13 clearly outperformed hippocampal volumetry. So, playing the devil’s advocate, one might conclude that hippocampal MR volumetry is useless because it provided no added value.

Moreover, the dataset is derived from the Alzheimer’s Disease Neuroimaging Initiative dataset, a strongly preselected dataset with “super-patients” and “super-controls” excluding all microvascular lesions. Such microvascular lesions contribute to cognitive decline and are very frequent in this age group in typical clinical populations.<sup>5</sup> MR parameters are strictly standardized in this dataset, yet in clinical application, even small modifications of MR parameters significantly bias estimated volumetry results.<sup>6</sup> Therefore, I might speculate that the presented results for MR morphometry in this current article are over-optimistic with respect to typical real-world clinical applications. I would like to repeat that already in this specific and preselected sample, the simple MMS performed as well as MR volumetry, and the ADAS-13 even outperformed MR volumetry.

Personally, I do believe that MR volumetry can provide added value. Yet, I argue that simple hippocampal volumetry is not the best MR biomarker, notably for the detection of individual cases. On average, there is a normal interindividual variation in hippocampal volume of approximately 20% in controls, but also in patients with mild cognitive impairment (MCI) and AD,<sup>7</sup> whereas the disease-related change (eg, for patients with MCI versus controls) is in the range of 7%. This means that direct hippocampal volumetry may identify a substantial volume difference of 7% at the group level, yet because of the larger interindividual variability of approximately 20% per group, this measure is of limited use for the diagnosis of individual cases. Moreover, the current results of hippocampal atrophy are not compared with

patterns of atrophy, such as the AD signature regions mentioned above, DTI,<sup>8,9</sup> arterial spin labeling,<sup>10-12</sup> and, ideally, a combination of multiple MR parameters and advanced data analysis.<sup>13</sup>

Finally, MR imaging in dementia is used for more than discriminating MCI/AD versus controls, but should also include a differential diagnosis between various types of dementia. This differential diagnosis can be challenging, particularly in the early stages of the disease. As indicated by the authors, future treatment trials of MCI should therefore also discriminate Alzheimer type-MCI/AD pathology from other types of dementia to include only the desired treatment group. For example, behavioral variant frontotemporal dementia (bvFTD) is characterized by predominant frontotemporal atrophy, yet, in most cases, has associated mesiotemporal atrophy. Consequently, hippocampal atrophy alone cannot discriminate AD versus bvFTD, but the volumetry assessment of atrophy pattern has added value. This means that hippocampal volumetry alone might lead to the false inclusion of patients with bvFTD in MCI/AD trials. In Lewy body dementia, hippocampal volumetry will be noncontributive. However, because of the pathologic overlap with Parkinson disease, susceptibility-weighted imaging of nigrosome 1 has added value,<sup>14,15</sup> and quantitative volumetric assessment tools for nigrosome 1 based on quantitative susceptibility mapping are under development. Likewise, vascular pathology often coexists with, for example, AD pathology and cannot be detected by using hippocampal volumetry alone, and volumetric tools exist to assess vascular burden.

In summary, I agree with the conclusion that the 2 tested software tools provide equivalent results for hippocampal volumetry. Hippocampal volumetry alone was as good as the analysis of a predefined anatomic region, with the limitation that anatomically defined regions are not necessarily the most sensitive approach for this specific purpose. I disagree with the statement that hippocampal volumetry alone can be suggested as the only volumetric biomarker for future prognostic studies. This is not supported by the presented results and is an oversimplification of the available evidence.

## REFERENCES

1. Tanpitukpongse TP, Mazurowski MA, Ikkena J, et al; Alzheimer's Disease Neuroimaging Initiative. **Predictive utility of marketed volumetric software tools in subjects at risk for Alzheimer disease: do regions outside the hippocampus matter?** *AJNR Am J Neuroradiol* 2017;38:546–52 CrossRef Medline
2. Dickerson BC, Bakkour A, Salat DH, et al. **The cortical signature of Alzheimer's disease: regionally specific cortical thinning relates to symptom severity in very mild to mild AD dementia and is detectable in asymptomatic amyloid-positive individuals.** *Cereb Cortex* 2009;19:497–510 CrossRef Medline
3. Dickerson BC, Stoub TR, Shah RC, et al. **Alzheimer-signature MRI biomarker predicts AD dementia in cognitively normal adults.** *Neurology* 2011;76:1395–402 CrossRef Medline
4. Hutton C, Draganski B, Ashburner J, et al. **A comparison between voxel-based cortical thickness and voxel-based morphometry in normal aging.** *Neuroimage* 2009;48:371–80 CrossRef Medline
5. Haller S, Barkhof F. **Interaction of vascular damage and Alzheimer dementia: focal damage and disconnection.** *Radiology* 2017;282:311–13 CrossRef Medline
6. Haller S, Falkovskiy P, Meuli R, et al. **Basic MR sequence parameters systematically bias automated brain volume estimation.** *Neuroradiology* 2016;58:1153–60 CrossRef Medline
7. Frankó E, Joly O, Alzheimer's Disease Neuroimaging Initiative. **Evaluating Alzheimer's disease progression using rate of regional hippocampal atrophy.** *PLoS One* 2013;8:e71354 CrossRef Medline
8. Haller S, Nguyen D, Rodriguez C, et al. **Individual prediction of cognitive decline in mild cognitive impairment using support vector machine-based analysis of diffusion tensor imaging data.** *J Alzheimers Dis* 2010;22:315–27 CrossRef Medline
9. O'Dwyer L, Lamberton F, Bokde AL, et al. **Using support vector machines with multiple indices of diffusion for automated classification of mild cognitive impairment.** *PLoS One* 2012;7:e32441 CrossRef Medline
10. Xekardaki A, Rodriguez C, Montandon ML, et al. **Arterial spin labeling may contribute to the prediction of cognitive deterioration in healthy elderly individuals.** *Radiology* 2015;274:490–99 CrossRef Medline
11. Binnewijzend MA, Kuijter JP, Benedictus MR, et al. **Cerebral blood flow measured with 3D pseudocontinuous arterial spin-labeling MR imaging in Alzheimer disease and mild cognitive impairment: a marker for disease severity.** *Radiology* 2013;267:221–30 CrossRef Medline
12. Collij LE, Heeman F, Kuijter JP, et al. **Application of machine learning to arterial spin labeling in mild cognitive impairment and Alzheimer disease.** *Radiology* 2016;281:865–75 CrossRef Medline
13. Haller S, Lovblad KO, Giannakopoulos P, et al. **Multivariate pattern recognition for diagnosis and prognosis in clinical neuroimaging: state of the art, current challenges and future trends.** *Brain Topogr* 2014;27:329–37 CrossRef Medline
14. Haller S, Fällmar D, Larsson EM. **Susceptibility weighted imaging in dementia with Lewy bodies: will it resolve the blind spot of MRI?** *Neuroradiology* 2016;58:217–18 CrossRef Medline
15. Kamagata K, Nakatsuka T, Sakakibara R, et al. **Diagnostic imaging of dementia with Lewy bodies by susceptibility-weighted imaging of nigrosomes versus striatal dopamine transporter single-photon emission computed tomography: a retrospective observational study.** *Neuroradiology* 2017;59:89–98 CrossRef Medline

© S. Haller

Affidea Centre de Diagnostic Radiologique de Carouge CDRC  
Geneva, Switzerland  
Faculty of Medicine of the University of Geneva  
Geneva, Switzerland  
Department of Surgical Sciences, Radiology  
Uppsala University  
Uppsala, Sweden  
Department of Neuroradiology  
University Hospital Freiburg  
Freiburg, Germany

**REPLY:**

**W**e thank Dr Haller for his recent letter regarding our publication, “Predictive Utility of Marketed Volumetric Software Tools in Subjects at Risk for Alzheimer Disease: Do Regions Outside the Hippocampus Matter?”

We restricted our study to NeuroQuant (CorTechs Labs, San Diego, California) and Neuroreader (Brainreader, Horsens, Denmark) because they have received FDA 510(k) marketing clearance and physicians are likely to use them in everyday practice. Also, these packages use a probabilistic atlas-based segmentation on non-uniformity-corrected 3D T1-weighted images to derive absolute volumes of a variety of cortical and subcortical structures (and are not voxel-based morphometry–derived gray matter concentrations, as stated by Dr Haller).

We fully agree with Dr Haller that areas outside the medial temporal lobe play a role in the evolution of Alzheimer disease (AD); indeed, we and others have previously documented the value of using multiple markers, including other brain regions.<sup>1,2</sup> Nevertheless, the earliest synaptic lesions in AD are thought to be in the medial temporal lobe, and MR imaging hippocampal volumes are one of the markers used in newer diagnostic criteria for mild cognitive impairment (MCI) due to AD.<sup>3</sup>

<http://dx.doi.org/10.3174/ajnr.A5259>

Clearly, MCI and dementia are heterogeneous in their pathology, presentation, and outcomes; using multiple anatomic and molecular biomarkers will no doubt help us better personalize diagnosis and therapy.<sup>4</sup>

**REFERENCES**

1. Shaffer JL, Petrella JR, Sheldon FC, et al; Alzheimer’s Disease Neuroimaging Initiative. **Predicting cognitive decline in subjects at risk for Alzheimer disease by using combined cerebrospinal fluid, MR imaging, and PET biomarkers.** *Radiology* 2013;266:583–91 CrossRef Medline
2. Hostage CA, Choudhury KR, Murali Doraiswamy P, et al; Alzheimer’s Disease Neuroimaging Initiative. **Mapping the effect of the apolipoprotein E genotype on 4-year atrophy rates in an Alzheimer disease-related brain network.** *Radiology* 2014;271:211–19 CrossRef Medline
3. Albert MS, DeKosky ST, Dickson D, et al. **The diagnosis of mild cognitive impairment due to Alzheimer’s disease: recommendations from the National Institute on Aging–Alzheimer’s Association workgroups on diagnostic guidelines for Alzheimer’s disease.** *Alzheimers Dement* 2011;7:270–79 CrossRef Medline
4. Petrella JR. **Neuroimaging and the search for a cure for Alzheimer disease.** *Radiology* 2013;269:671–91 CrossRef Medline

● **T.P. Tanpitukpongse**

UNC Rex Healthcare  
Raleigh, North Carolina

● **J.R. Petrella**

Duke University Health System  
Durham, North Carolina

## FDG-PET/CT or MRI for the Diagnosis of Primary Progressive Aphasia?

We have read with interest the article by Sajjadi et al<sup>1</sup> concerning the use of MR imaging for the diagnosis of primary progressive aphasia (PPA). The authors studied the sensitivity and specificity of the visual analysis of MR imaging for the diagnosis of each PPA variant. They found that accuracy values were appropriate for the semantic variant, but somewhat disappointing for logopenic and nonfluent aphasia. Although specificity values were above 90% for the 3 variants, sensitivity for nonfluent and logopenic PPA was 21% and 49%, respectively. This issue is relevant because a biomarker showing focal neurodegeneration (eg, MR imaging) is included in the current diagnostic criteria and clinical diagnosis of PPA variants may be difficult.<sup>2</sup>

We published a similar study 2 years ago, but with FDG-PET/CT.<sup>3</sup> In our study, FDG-PET images from a cohort of 33 patients with PPA and 11 controls were visually reviewed by 5 nuclear medicine physicians to evaluate the diagnostic accuracy of the technique and the interrater agreement. Another 5 raters also reviewed the maps using Statistical Parametric Mapping (SPM), comparing each patient individually with a healthy control group (statistical analysis). Interrater agreement was moderate for visual analysis (Fleiss  $\kappa = 0.568$ ) and substantial for statistical analysis ( $\kappa = 0.756-0.881$ ). Sensitivity and specificity for the diagnosis of PPA (to discriminate it from healthy controls) was 87.8% and 89.9%, respectively, in the visual analysis. Interrater agreement was high in semantic and logopenic variants (at least 4 of 5 raters agreed in 100% and 84% of cases, respectively), and it was lower in nonfluent aphasia (at least 4 of 5 raters agreed in only 20% of cases). Furthermore, using images statistically preprocessed by SPM improved the agreement among raters, especially in the nonfluent variant.

We reanalyzed the data of our previous study<sup>2</sup> with the same method as that used by Sajjadi et al.<sup>1</sup> We estimated the sensitivity and specificity for the diagnosis of each type of PPA. Mean sensitivity and specificity of expert raters using FDG-PET was, respectively, 65% and 98.5% for the nonfluent variant, 62.5% and 96.2% for the semantic variant, and 89.4% and 86% for the logopenic type. With statistical analysis, the mean sensitivity and specificity

were 70% and 94.1% for nonfluent, 75% and 93.5% for semantic, and 82.1% and 88% for the logopenic variant.

Thus, our study revealed higher diagnostic accuracy, especially regarding sensitivity, for the diagnosis of PPA and its variants with FDG-PET than that reported by Sajjadi et al<sup>1</sup> with MR imaging. This might support a better diagnostic performance of FDG-PET/CT compared with MR imaging in the specific setting of diagnosing and classifying PPA. However, studies directly comparing FDG-PET/CT and MR imaging accuracy are necessary to clarify the superiority of one technique over the other<sup>4</sup> or to evaluate a potential benefit of the combination of both techniques at an individual level. Furthermore, the assessment of statistical maps may reduce some of the limitations encountered when performing direct visual analysis of images.

Disclosures: Jorge Matias-Guiu—UNRELATED: Board Membership: Spanish Neurological Society, Comments: Editor-in-Chief of *Neurologia*, official journal of the Spanish Neurological Society; Employment: Hospital Clinico San Carlos, Universidad Complutense de Madrid, Comments: Professor of Neurology, Director of Neuroscience Institutes, Head of Neurology Department.

### REFERENCES

1. Sajjadi SA, Sheikh-Bahaei N, Cross J, et al. **Can MRI visual assessment differentiate the variants of primary progressive aphasia?** *AJNR Am J Neuroradiol* 2017 Mar 24. [Epub ahead of print] CrossRef Medline
2. Gorno-Tempini ML, Hillis AE, Weintraub S, et al. **Classification of primary progressive aphasia and its variants.** *Neurology* 2011;76:1006–14 CrossRef Medline
3. Matias-Guiu JA, Cabrera-Martín MN, Pérez-Castejón MJ, et al. **Visual and statistical analysis of <sup>18</sup>F-FDG PET in primary progressive aphasia.** *Eur J Nucl Med Mol Imaging* 2015;42:916–27 CrossRef Medline
4. Panegyres PK, McCarthy M, Campbell A, et al. **Correlative studies of structural and functional imaging in primary progressive aphasia.** *Am J Alzheimers Dis Other Demen* 2008;23:184–91 CrossRef Medline

● J.A. Matias-Guiu

Department of Neurology

● M.N. Cabrera-Martín

Department of Nuclear Medicine

● J. Matias-Guiu

Department of Neurology

● J.L. Carreras

Department of Nuclear Medicine

Hospital Clinico San Carlos

San Carlos Institute for Health Research, University Complutense

Madrid, Spain

## REPLY:

We thank Dr Matias-Guiu et al for their interest in our study on the role of MR imaging in the syndromic classification of primary progressive aphasia (PPA).<sup>1</sup> Their proposal that FDG-PET might be a more sensitive method than structural MR imaging is highly plausible. We also agree with Matias-Guiu et al that direct comparison would be necessary to definitively resolve the issue. For instance, both structural MR imaging and FDG-PET measure neurodegeneration. The greater the degree of neurodegeneration, therefore, the more likely it is to be detectable with these types of imaging. In other words, the sensitivity of any technique that operates through detecting degeneration is also a function of disease severity. To this end, it is possibly relevant that their PPA group as a whole was more advanced than those with PPA in our series—mean Mini-Mental State Examination and Addenbrookes cognitive examination scores of  $18.5 \pm 8.1$  and  $46.1 \pm 22.0$ ,<sup>2</sup> respectively, compared with scores of  $22.1 \pm 3.9$  and  $56.4 \pm 14.1$ .<sup>1</sup> Whether this confounder offers a credible explanation for the apparent increased sensitivity of FDG-PET of Matias-Guiu et al is perhaps debatable, but nonetheless important to address with a direct comparison.

A further methodologic feature that we would strongly advocate in designing a future study is the inclusion of a good number of negative (healthy age-matched) and positive (non-PPA degenerative dementia) controls. If raters know a priori that the scans they are evaluating come from a few predefined groups, the rating

essentially becomes a forced-choice paradigm; this, in turn, may artificially inflate the accuracy compared with a real-world clinical environment in which the differential diagnosis is more open-ended.

Finally, as noted by Matias-Guiu et al, a new study could also assess the potential benefit of the combination of FDG-PET and MR imaging. To this end, we would add the possibility that the decision of whether to combine them is likely to vary according to the precise clinical question. For instance, our study showed that MR imaging returns near-perfect accuracy in detecting the lesions of semantic-variant PPA, making FDG-PET redundant in this scenario. In contrast, the terrible sensitivity yet good specificity for nonfluent and logopenic PPA with MR imaging suggest that a hierarchic algorithm in which one proceeds to FDG-PET if the MR imaging is nonspecific might be sensible.

## REFERENCES

1. Sajjadi SA, Sheikh-Bahaei N, Cross J, et al. **Can MRI visual assessment differentiate the variants of primary-progressive aphasia?** *AJNR Am J Neuroradiol* 2017 Mar 24. [Epub ahead of print] CrossRef Medline
2. Matias-Guiu JA, Cabrera-Martín MN, Pérez-Castejón MJ, et al. **Visual and statistical analysis of <sup>18</sup>F-FDG PET in primary progressive aphasia.** *Eur J Nucl Med Mol Imaging* 2015;42:916–27 CrossRef Medline

● S.A. Sajjadi

Department of Neurology  
University of California, Irvine  
Irvine, California

● P.J. Nestor

German Center for Neurodegenerative diseases  
Magdeburg, Germany

<http://dx.doi.org/10.3174/ajnr.A5261>

**NEW**

# Indication for Trevo<sup>®</sup> Retrievers

A New Standard of Care in Stroke



**FIRST**

mechanical thrombectomy device  
indicated to reduce disability in stroke.\*

**FIRST**

new treatment indication for  
stroke in 20 years.

## Trevo XP

PROVUE RETRIEVER

Success accelerated.

\*The Trevo Retriever is indicated for use to restore blood flow in the neurovasculature by removing thrombus for the treatment of acute ischemic stroke to reduce disability in patients with a persistent, proximal anterior circulation, large vessel occlusion, and smaller core infarcts who have first received intravenous tissue plasminogen activator (IV t-PA). Endovascular therapy with the device should start within 6 hours of symptom onset.



Not for sale within the territory of the United States

## UNIQUE FLEXIBILITY

### ACCLINO<sup>®</sup> flex plus Stent

Highly flexible closed-cell stent with enhanced visibility allowing sequential stent and coil placement using the same microcatheter for the treatment of intracranial aneurysms.

FLEXIBLE. VISIBLE. SMOOTH.

[www.acandis.com](http://www.acandis.com)



**acandis<sup>®</sup>**

ENGINEERING STROKE SOLUTIONS